THE UNIVERSITY
of EDINBURGH

Cenozoic volcanism in Northeast Brazil and its links to the Cameroon Line

André Rezende Guimarães

THE UNIVERSITY *of* EDINBURGH

Thesis submitted for the degree of
Doctor of Philosophy

University of Edinburgh
School of Geosciences

2018

Volume 1 of 2

Cenozoic volcanism in Northeast Brazil and its links to the Cameroon Line

André R. Guimarães

Abstract

Cenozoic volcanism in Northeast Brazil occurs in three distinct regions: the Macau-Queimadas volcanic lineament (MQVL) and the Mecejana volcanic field, both in the Borborema Province, and the Fernando de Noronha archipelago. They are the only significant occurrences of Cenozoic magmatism along the South American passive margin and their location matches the position of the Cameroon Line in Africa, to which they were adjacent before the opening of the South Atlantic. The Cameroon Line is one of the few and the largest occurrence of Cenozoic volcanism along the African Atlantic passive margin. Volcanic activity in the two conjugate margins postdate continental separation by 10s of millions of years. Here, the Brazilian occurrences are compared with one another and with the Cameroon Line using sixteen new $^{40}Ar/^{39}Ar$ ages obtained for Borborema, which for the first time include Mecejana, major and trace element data and $^{87}Sr/^{86}Sr$ and $^{140}Nd/^{139}Nd$ isotopic ratios. Activity in Mecejana dates to the late Eocene to early Oligocene (35.03 ± 0.28 to 30.80 ± 0.22 Ma). Volcanism in the MQVL is synchronous with Mecejana but also continues intermittently to the Miocene (12.39 ± 0.34 Ma), with a peak in the late Oligocene to the early Miocene marked by activity in the local basins. Comparisons with other published ages show that volcanism in the MQVL also continues into the late Miocene and is synchronous with activity in Fernando de Noronha. There are no age progression patterns in the region, and a deep mantle plume is not a suitable model to explain local magmatism. Geochemical results show a compositional continuum in Northeast Brazil, with variability controlled by depth and degrees of partial melting of a stratified sublithospheric source that includes both spinel and garnet lherzolite and extends across both

continental and oceanic lithospheres. Northeast Brazil volcanic occurrences result from the same magmatic processes and should be treated as a single volcanic province. They are also synchronous and geochemically virtually identical to the Cameroon Line, indicating a continental lithospheric control in their genesis. We propose a model that relies on edge-driven convection and the rheological characteristics of the lithospheric thermal boundary layer (TBL) to explain magmatism in both conjugate margins, where edge-driven convection triggered by the local continental lithospheric morphology affects the continental TBL and cause it to flow laterally towards the oceanic sector. The intermediate rheology of the TBL explains the mainly asthenospheric characteristics of the magmatic source in both conjugate margins, but with the presence of subtle geochemical enrichment that must be caused by relatively recent enrichment events. The model finds strong support in the distribution of volcanism along the Atlantic passive margins, including seamounts and other volcanic provinces that also straddle continental and oceanic lithospheres such as the Canaries and the adjacent Moroccan volcanism, and the New England seamount chain.

Declaration

This thesis is my own original work, except where acknowledgment is made in the text. It does not exceed the word limit. The work has not been submitted as part of any other degree or professional qualification at any other institution.

André Rezende Guimarães

September 2018

Collaborative work statement

Analytical geochemical results for all the Northeast Brazil samples were shared with Marthe Klöcking, from the Earth Sciences Department at the University of Cambridge. We have worked together collecting samples in Borborema and subsequently cutting, crushing and powdering them at the University of Cambridge. ICP-MS analyses for both the Borborema and the Fernando de Noronha samples were done by Marthe Klöcking at Cambridge. All the XRF work was done at the University of Edinburgh, as well as all the preparation of the Fernando de Noronha samples. Fieldwork in Fernando de Noronha was also done solely by the author. $^{40}Ar/^{39}Ar$ dating and isotopic analytical measurements were conducted at the Scottish Universities Environmental Research Centre (SUERC) by Dr. Dan Barfod, Mrs. Anne Kelly and Mr. Vincent Gallagher, with me working as an assistant and conducting all the sample preparation procedures.

Acknowledgments

This work would not have been possible with the help and support from a great many people. First and foremost, I must thank my supervisors Godfrey Fitton and Linda Kirstein. Godfrey not only suggested this project, but also secured a University of Edinburgh Scholarship, funding for the Ar analyses through the NERC Isotope Geoscience Facilities Steering Committee, and support from the School of GeoSciences and SUERC, East Kilbride, for most of the other analyses required in the course of this work. He also provided all the samples from the Cameroon Line. The remining funds for my studentship were granted by the Edinburgh Global Research Scholarship, for which I am grateful. Thank you to Richard Hinton, for acting as my advisor. I must also thank Nicholas Odling for the X-ray fluorescence analyses, Mike Hall for the thin sections, Dan Barfod for $^{40}Ar/^{39}Ar$ ages, and Anne Kelly and Vincent Gallagher for the isotope analyses. Thank you to Gillian McCay and John Craven for all the help in the labs, and to John Stevenson for all the computing support. I am also grateful to all those who helped me at the Scottish Universities Environmental Research Centre during my trips there: Jim Imlach, Ross Dymock, Ben Cohen, Rona McGill and Ryan Ickert. Thank you to the staff at the Postgrad office at the School of GeoSciences at the University of Edinburgh. A special thank you to Marthe Klöcking, my collaborator in this project, who provided all the inductively coupled plasma mass spectrometry data, and with whom I zig-zagged through the desert in Northeast Brazil looking for rocks. Also thank you to Patrick Ball and Bruna Carvalho, who were also with us during field work in Borborema. I thank Alcides Sial from the Federal University of Pernambuco for his advice on all fieldwork. I am grateful to Wellington, who accompanied me as guide in Fernando de Noronha, and all the staff from the ICMBio Institute and the Fernando de Noronha Marine National Park who helped me with the necessary paperwork and permits to do fieldwork there. Thank you to my PhD colleagues Amelia Bain and Guohui Chen for all the help, the

discussion and chats in the office. Thank you to my family, Toni and Leo, for all the patience and support during this time. I hope you can forgive me for these messy four years. I must also apologise if I have forgotten anyone. I am grateful to all those who have contributed in any way so that this work could be completed.

Table of Contents

VOLUME 1 OF 2

LIST OF FIGURES

LIST OF TABLES

Chapter 1: Introduction and Geological Context

Introduction

Intraplate volcanic activity occurs worldwide and affects both continental and oceanic lithospheres. It is marked by significant physical and geochemical variability between volcanic centres and, contrasting with plate boundary process of spreading ridges and subduction zones, has so far resisted any explanation attempts under a unified model. Current hypotheses may be divided into those based on plate processes and those that rely on deep mantle plumes. The former is a widely variable group of models that focus on how the relationship between the lithosphere and the asthenosphere affects the geodynamics of the asthenospheric upper mantle, whilst the latter relies on deep mantle processes as the trigger for intraplate magmatism in the form of ascending deep mantle plumes. Although the large variability of different plate models seems more adequate to accommodate such a heterogeneous group of rocks, such variability also risks leading to overly specific interpretations that only work for individual cases and therefore cannot be satisfactorily tested. Plume models, on the other hand, suffer the opposite problem of establishing too many specific predictions that often do not find adequate support in observations across the wide range of intraplate occurrences.

Predictions of plume models have evolved since it was first proposed in 1971 by W. J. Morgan (Morgan, 1971; Foulger, 2010). Today, they include an initial stage of domal uplift followed by flood basalt eruptions, a time-progressive volcanic chain, evidence for an elevated geotherm and often a conduit down to the core-mantle boundary beneath the most recent spot of activity (Foulger, 2010). Whilst some intraplate volcanism bear typical signatures of deep mantle plumes, such as Iceland and Hawaii, most centres still challenge the model. The Atlantic Ocean and its continental passive margins contain several intraplate volcanic centres that are difficult to explain

using deep mantle plumes, and this study will focus on two such centres: the Cameroon Volcanic Line and the Cenozoic volcanism of Northeast Brazil (Figure 1-1).

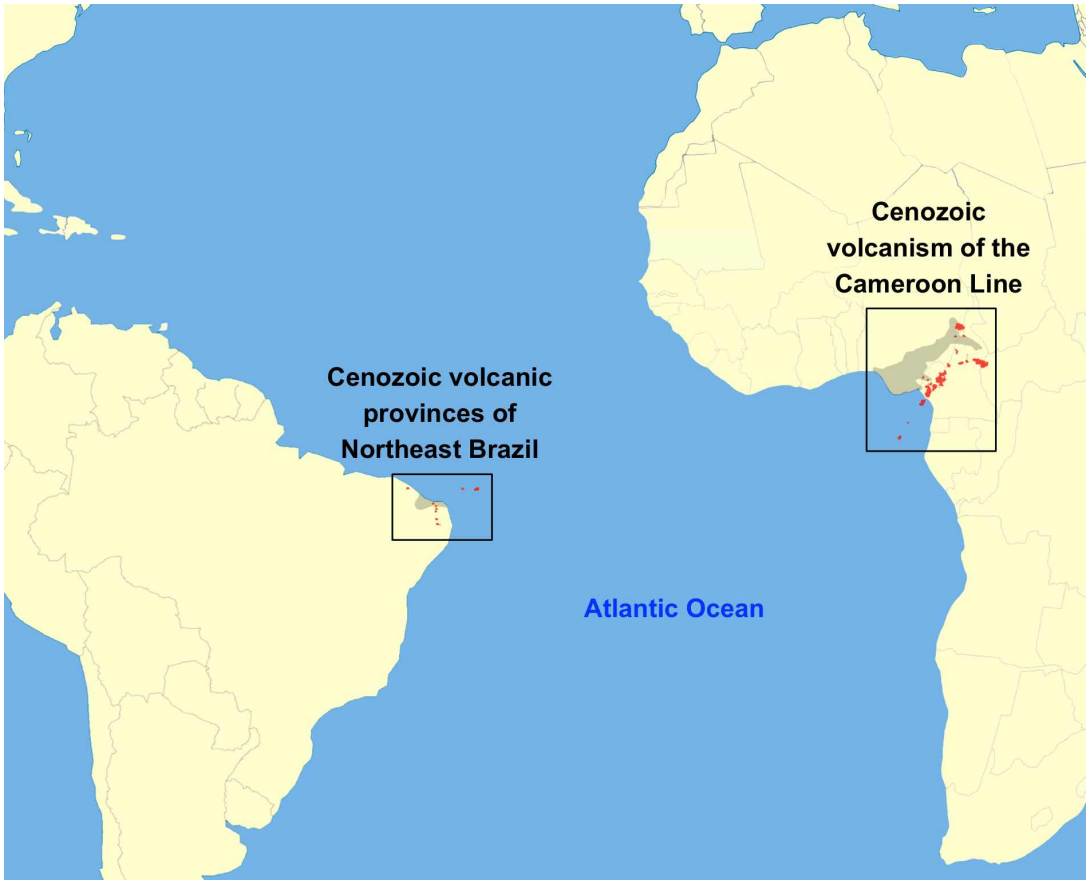

Figure 1-1: Position of the Cenozoic volcanic provinces of Northeast Brazil and the Cameroon Line in relation to the South American and African continents. Adapted from www.wikipedia.com. Red areas show volcanic occurrences. The grey areas represent the onshore branch of the Potiguar Basin, in Northeast Brazil, and the Benue Trough, north of the Cameroon Line.

These two magmatic areas extend across both continental and oceanic lithospheres and would be adjacent in the pre-rift continental configuration (Figure 1-2). On the continental sector, both are located over Proterozoic fold belts abutting cratonic terranes and share similar geological field relations. Current chronological data also suggests that their volcanism started almost synchronously and have spanned similar time periods, even though volcanic activity only started ~40-50 m.y. after continental separation happened in the area at ~100 Ma (Nürnberg and Müller, 1991; Mizusaki *et*

al., 2002). Continental breakup between Africa and South America started sometime between 150 and 130 Ma and developed from south to north, with the point connecting Borborema and the Cameroon Line being the last segment of the two continents to separate (Nürnberg and Müller, 1991; Turner *et al.*, 1994). There are no other volumetrically significant continental occurrences of Cenozoic volcanism along the whole South American and African conjugate margins, and the new geochemical data that will be discussed here demonstrates that lavas in both volcanic regions are not only synchronous, but also show remarkable similarity in composition despite being on opposite sides of the Atlantic Ocean.

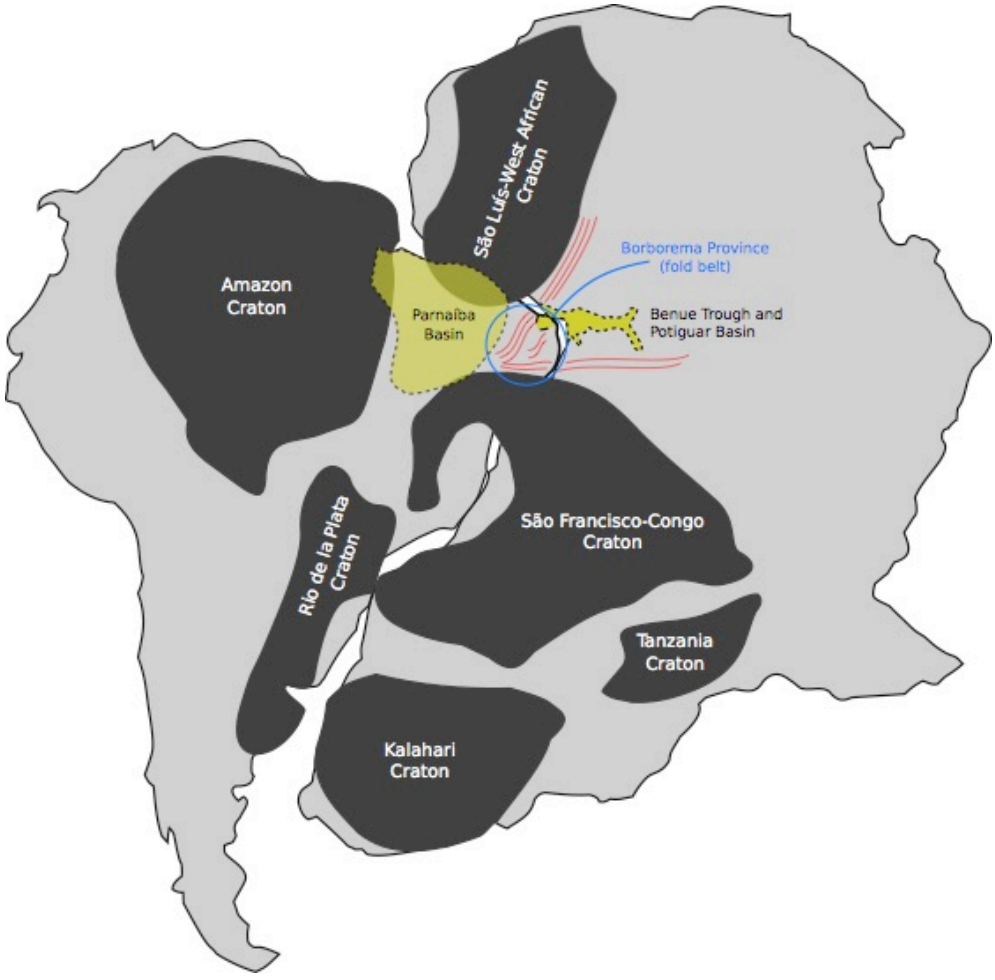

Figure 1-2: Positions of South American and African cratons, highlighting the Parnaíba Basin, the Benue Trough, the onshore branch of the Potiguar Basin and the Borborema Province. Adapted from Heilbron *et al.* (2008).

Cenozoic volcanism in Northeast Brazil has been traditionally subdivided and studied as three distinct volcanic areas: the ocean island of Fernando de Noronha, the Macau-Queimadas Volcanic Lineament (MQVL) and the Mecejana volcanic field (Figure 1-3). The last two are continental occurrences emplaced in the Borborema Province, a Proterozoic fold belt between the São Francisco-Congo and the São Luís-West African cratons (Figure 1-2). For this study, we have collected samples from all three areas, which are given in Figure 1-4, with those selected for $^{40}Ar/^{39}Ar$ dating in Chapter 2 being highlighted. Locality coordinates and sample contexts are given on Table 1-1. Continental Cenozoic magmatic activity elsewhere in Brazil is significantly restricted and relatively insignificant when compared to the country's northeast province (Mizusaki *et al.*, 2002). Nonetheless, direct comparisons between volcanic occurrences in Northeast Brazil have focused exclusively on the MQVL and Fernando de Noronha and have never included the Mecejana volcanic field. These comparisons have often attempted to test the hypothesis that the MQVL and Fernando de Noronha are the products of the same deep mantle plume, which up until recently has been a common explanation for the similarities amongst these volcanic areas (Sial, 1976a; Morgan, 1983; O'Connor and Duncan, 1990; Fodor *et al.*, 1998; Mizusaki *et al.*, 2002; Sleep, 2003). These comparisons include previous geochemical studies by Fodor *et al.* (1998, 2002) and Rivalenti *et al.* (2000, 2007), most of which focus on mantle xenoliths and how they highlight potential differences between the processes that have affected the continental and oceanic lithospheres, and how these processes support or undermine the presence of a deep mantle plume.

However, the plume hypothesis started to be challenged by recent chronological studies in the area, which show no age progression patterns (Knesel *et al.*, 2011; Perlingeiro *et al.*, 2013; Souza *et al.*, 2013) and indicate that there must be another explanation for the geochemical similarities between Borborema and Fernando de Noronha and their apparently dominantly sublithospheric origin. Similar conclusions have been reached by

analysing the patterns of the South American plate motion and how they relate to known or potential hotspots in the Atlantic (Ernesto, 2005). Furthermore, the lack of evidence for any disturbance at the transition zone below the region, which could indicate an ascending plume conduit from the core-mantle boundary to the upper mantle, also undermines a plume model for the area (Pinheiro and Julià, 2014).

Another issue is the complete exclusion of the Mecejana volcanic field in these analyses, despite its geochemical similarities with Fernando de Noronha having been noted by Guimarães *et al.* (1982) and Rao & Sial (1972), and similar K/Ar ages to the MQVL reported by Mizusaki et al. (2002). Its absence in any analysis significantly restricts what may be said about the magmatic processes operating underneath Northeast Brazil.

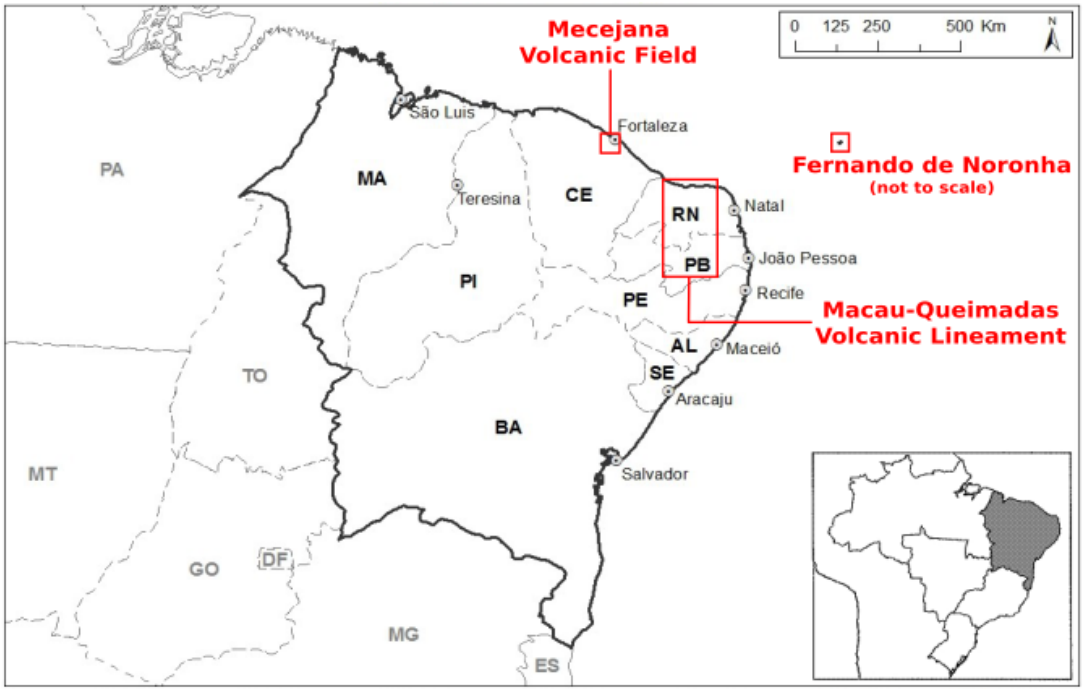

Figure 1-3: Occurrences of Cenozoic volcanic rocks in Northeast Brazil (adapted from www.mapasparacolorir.via12.com, which is based on the cartographic dataset from the Brazilian Institute of Geography and Statistics, IBGE).

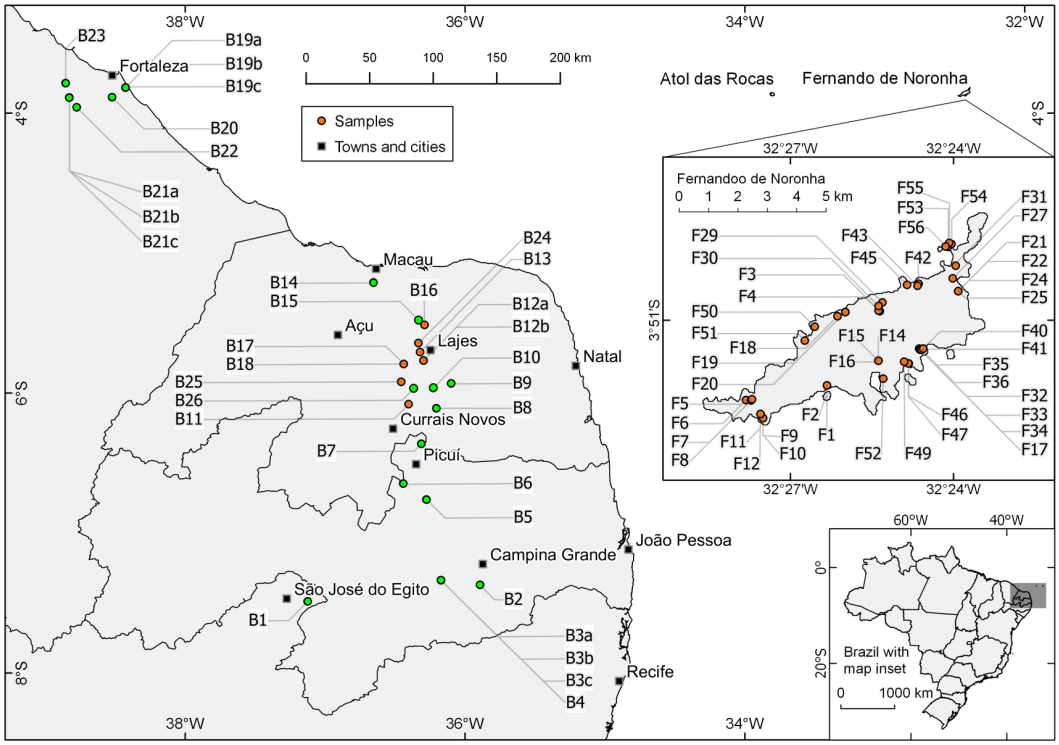

Figure 1-4: Sample localities. Samples marked in *green* were selected for $^{40}Ar/^{39}Ar$ dating (Chapter 2).

Table 1-1: Locality and sample information. Rock type according to petrographic observations (Chapter 3). Map code refers to Figure 1-4. Samples selected for $^{40}Ar/^{39}Ar$ dating (Chapter 2) highlighted in *grey*. *Pdt.* = peridotitic; Ol. = olivine; Krs. = kaersutite.

Sample	Map code	Locality (Borborema) Formation (FN)	Context	Rock type	Overall texture	Groundmass texture	Pdt. xenolith	UTM		
Borborema										
15BP1-1	B1	São Pedro	Plug	Basanite	porphyritic hypocrystalline	glassy (mostly) to cryptocrystalline	Yes	24 M	706900	9171830
15BP3-2	B2	Queimadas Lava Flow	Flow	Alkali basalt	porphyritic holocrystalline	fine-grained intergranular	Uncert.	25 M	810652	9184292
15BP4-6	B6	Picuí	Flow (?)	Basanite	porphyritic holocrystalline	fine-grained to micro-crystalline with *ne* oykocrysts	Uncert.	24 M	782830	9264610
15BP4-7	B7	Serra Saco do Inferninho	Neck	Olivine basalt	aphyric holocrystalline	microcrystalline	Uncert.	24 M	797362	9296008
15BP5-8	B8	Socavão	Plug	Basanite	porphyritic hypocrystalline	crypto- to microcrystalline heterogeneous	Yes	24 M	809376	9323977
15BP5-9	B9	Carnaubinha Quarry	Plug	Basanite	porphyritic holocrystalline	microcrystalline	Yes	24 M	821209	9343608
15BP5-10	B10	Serrote Preto	Plug	Ol. alkali basalt	aphyric holocrystalline	microcrystalline	Yes	24 M	807014	9340068
15BP5-11	B11	Pedreira Vale Vulcanico	Plug	Ol. alkali basalt	aphyric holocrystalline	microcrystalline to fine-grained	Yes	24 M	787392	9327351
15BP6-12a	B12	Cabugizinho	Neck	Ol. alkali basalt	porphyritic hypocrystalline	crypto- to microcrystalline heterogeneous	Yes	24 M	799425	9361786
15BP6-13	B13	Cabugi	Neck	Ol. alkali basalt	porphyritic holocrystalline	fine-grained	No	24 M	796669	9368499
15BP7-15	B15	Serra Preta (Pedro Avelino)	Plug	Ol. nephelinite	porphyritic holocrystalline	crypto- to microcrystalline heterogeneous	Yes	24 M	795593	9393723

Table 1-1 (cont.)

Sample	Map code	Locality (Borborema) Formation (FN)	Context	Rock type	Overall texture	Groundmass texture	Pdt. xenolith	UTM		
Borborema (cont.)										
15BP7-16	B16	Serra Aguda	Neck	Ol. alkali basalt	porphyritic holocrystalline	microcrystalline	Yes	24 M	800303	9389957
15BP8-17	B17	Pico Cabelo de Negro (North)	Plug (Dyke?)	Titanaugite-phyric basanite	porphyritic hypocrystalline	microcrystalline	Uncert.	24 M	783662	9359122
15BP8-18	B18	Pico Cabelo de Negro (South)	Plug (Dyke?)	Ol. alkali basalt	porphyritic hypocrystalline	microcrystalline	Yes	24 M	783662	9359122
15BP10-24	B24	Carcarazinho	Plug	Ol. alkali basalt	porphyritic hypocrystalline	cryptocrystalline	Uncert.	24 M	795384	9375622
15BP12-25	B25	Serra Preta (Residência)	Plug (Dyke?)	Ol. nephelinite	porphyritic holocrystalline	microcrystalline	Uncert.	24 M	781659	9345034
15BP12-26	B26	Serra Preta (Cerro Corá)	Plug	Ol. alkali basalt	porphyritic holocrystalline	microcrystalline to fine-grained	Yes	24 M	791541	9339752
Borborema Basins										
15BP3-3a	B3a	Juá Quarry	Hyalo-clastite	Hyalo-basalt	porphyritic hypocrystalline	Interstitial glass (> 95%)	Yes	24 M	812220	9187991
15BP3-3b	B3b	Juá Quarry	Pillow	Subalkali basalt	hypocrystalline	glassy (> 60%) to microcrystalline	No	24 M	812220	9187991
15BP3-4	B4	Juá Quarry	Flow	Ol. basalt	porphyritic holocrystalline	fine-grained to microcrystalline interstitial	Uncert.	24 M	812220	9187991
15BP3-5	B5	Cubati	Flow	Ol. basalt	porphyritic holocrystalline	fine-grained to microcrystalline interstitial	No	24 M	801112	9251874
15BP7-14	B14	Macau Lava Flow	Flow	Ol. subalkali basalt	aphyric hypocrystalline	glassy to fine-grained	No	24 M	760006	9423646

Table 1-1 (cont.)

Sample	Map code	Locality (Borborema) Formation (FN)	Context	Rock type	Overall texture	Groundmass texture	Pdt. xenolith	UTM		
Mecejana volcanic field										
15BP9-19a	B19a	Caruru Quarry	Plug	Phonolite	porphyritic holocrystalline	microcrystalline	No	24 M	563649	9578075
15BP9-19c	B19c	Caruru Quarry	Plug	Aegirine phonolite	porphyritic holocrystalline	microcrystalline lightly trachytic	Uncert.	24 M	563649	9578075
15BP10-20	B20	Ancuri	Plug	Aegirine-phyric phonolite	porphyritic holocrystalline	crypto- to microcrystalline heterogeneous	No	24 M	553001	9570444
15BP10-21a	B21a	Pao de Acucar	Neck	Aegirine-phyric phonolite	porphyritic holocrystalline	microcrystalline to fine-grained, trachytic	Uncert.	24 M	519046	9570156
15BP10-21b	B21b	Pao de Acucar	Neck	Aegirine phonolite	porphyritic holocrystalline	microcrystalline, felty	No	24 M	519046	9570156
15BP10-22	B22	Japarara	Plug	Phonolite	aphyric holocrystalline	fine-grained lightly trachytic	No	24 M	524924	9562443
15BP10-23	B23	Salgadinho	Plug	Aegirine phonolite	porphyritic holocrystalline	fine-grained lightly trachytic	No	24 M	516133	9581566
Fernando de Noronha										
FN01-01	F1	Remédios	Dome	Trachyte	porphyritic holocrystalline	microcrystalline trachytic	No	25 M	562310	9572224
FN01-02	F2	Remédios	Dome	Trachyte	porphyritic (almost aphyric) holocrystalline	microcrystalline trachytic	No	25 M	562310	9572224
FN02-03	F3	Remédios	Dome	Phonolite	porphyritic holocrystalline	crypto- to microcrystalline lightly trachytic	No	25 M	564109	9574736

Table 1-1 (cont.)

Sample	Map code	Locality (Borborema) Formation (FN)	Context	Rock type	Overall texture	Groundmass texture	Pdt. xenolith	UTM		
FN03-04	F4	Remédios	Dome	Phonolite	porphyritic holocrystalline	crypto- to microcrystalline trachytic	No	25 M	564065	9574757
Fernando de Noronha (cont.)										
FN04-05	F5	Quixaba	Flow	Ol. alkali basalt	porphyritic holocrystalline	microcrystalline	No	25 M	559553	9571730
FN04-06	F6	Quixaba	Flow	Ol. alkali basalt	porphyritic hypocrystalline	crypto- to microcrystalline heterogeneous	No	25 M	559553	9571730
FN05-07	F7	Quixaba	Flow	Ol. alkali basalt	porphyritic hypocrystalline	cryptocrystalline heterogeneous	No	25 M	559726	9571717
FN06-08	F8	Quixaba	Flow	Basanite	porphyritic hypocrystalline	crypto- to microcrystalline heterogeneous	No	25 M	559758	9571757
FN07-09	F9	Quixaba	Flow	Basanite	porphyritic hypocrystalline	microcrystalline	No	25 M	560133	9571119
FN07-10	F10	Quixaba	Flow	Basanite	porphyritic hypocrystalline	microcrystalline	No	25 M	560133	9571119
FN10-14	F14	Remédios	Dome	Phonolite	porphyritic holocrystalline	microcrystalline	No	25 M	564060	9573060
FN10-15	F15	Remédios	Dome	Phonolite	porphyritic holocrystalline	microcrystalline	No	25 M	564060	9573060
FN10-16	F16	Remédios	Dome	Phonolite	porphyritic holocrystalline	microcrystalline	No	25 M	564060	9573060
FN11-17	F17	Remédios	Dome	Phonolite	aphyric holocrystalline	crypto- to microcrystalline	No	25 M	565446	9573469
FN14-18	F18	Quixaba	Flow	Ol.-phyric nephelinite	porphyritic holocrystalline	microcrystalline	Uncert.	25 M	562669	9574566

Table 1-1 (cont.)

Sample	Map code	Locality (Borborema) Formation (FN)	Context	Rock type	Overall texture	Groundmass texture	Pdt. xenolith	UTM		
FN15-19	F19	Quixaba	Flow	Tephrite	porphyritic hypocrystalline	microcrystalline	No	25 M	562936	9574709
Fernando de Noronha (cont.)										
FN15-20	F20	Quixaba	Flow	Ol.-phyric nephelinite	porphyritic hypocrystalline	microcrystalline	No	25 M	562936	9574709
FN13-21	F21	Remédios	Dyke	Trachyte	porphyritic (almost aphyric) holocrystalline	Microcrystalline to fine-grained trachytic	No	25 M	566778	9575415
FN13-25	F25	Remédios	Dyke	Krs. trachyandesite	porphyritic holocrystalline	microcrystalline trachytic	No	25 M	566778	9575415
FN16-27	F27	Quixaba	Flow	Tephrite	porphyritic hypocrystalline	crypto- to microcrystalline heterogeneous	Uncert.	25 M	566591	9575849
FN17-29	F29	Remédios	Dome	Phonolite	porphyritic hypocrystalline	crypto- to microcrystalline heterogeneous lightly trachytic	No	25 M	564197	9575034
FN18-30	F30	Remédios	Dome	Phonolite	porphyritic holocrystalline	microcrystalline trachytic	No	25 M	564065	9574915
FN19-31	F31	Quixaba	Flow	Titanaugite-phyric tephrite	porphyritic hypocrystalline	microcrystalline	No	25 M	566691	9576277
FN12-32	F32	Remédios	Sill	Krs.-phyric tephriphonolite	porphyritic holocrystalline	microcrystalline felty	No	25 M	565480	9573434
FN12-33	F33	Remédios	Sill	Krs.-phyric tephriphonolite	porphyritic holocrystalline	crypto- to microcrystalline lightly trachytic	No	25 M	565480	9573434
FN12-36	F36	Remédios	Sill	Basaltic trachyandesite	porphyritic holocrystalline	crypto- to microcrystalline	No	25 M	565528	9573429

Table 1-1 (cont.)

Sample	Map code	Locality (Borborema) Formation (FN)	Context	Rock type	Overall texture	Groundmass texture	Pdt. xenolith	UTM		
FN20-40	F40	Remédios	Sill	Basaltic trachyandesite	porphyritic holocrystalline	microcrystalline	No	25 M	565585	9573470
Fernando de Noronha (cont.)										
FN21-42	F42	Remédios	Dome	Phonolitic nephelinite	aphyric holocrystalline	crypto- to microcrystalline	No	25 M	565430	9575668
FN22-43	F43	Remédios	Dyke	Phonolite	aphyric holocrystalline	microcrystalline trachytic	No	25 M	565393	9575598
FN24-45	F45	Remédios	Dome	Phonolite	porphyritic (almost aphyric) holocrystalline	microcrystallinelightly trachytic	No	25 M	565037	9575630
FN25-46	F46	Remédios	Flow	Trachybasalt	aphyric holocrystalline	microcrystalline	Uncert.	25 M	565094	9572965
FN25-47	F47	Remédios	Dyke	Basaltic trachyandesite	porphyritic holocrystalline	microcrystalline to fine-grained	No	25 M	565080	9572966
FN26-49	F49	Remédios	Dome	Trachyte	porphyritic holocrystalline	microcrystalline lightly heterogeneous	No	25 M	564935	9573026
FN27-50	F50	Quixaba	Flow	Ol. alkali basalt	porphyritic holocrystalline	microcrystalline	Yes	25 M	561893	9574215
FN28-51	F51	Quixaba	Flow	Ol. alkali basalt	porphyritic holocrystalline	microcrystalline	Yes	25 M	561556	9573743
FN29-52	F52	Remédios	Dome	Phonolite	aphyric holocrystalline	crypto- (mostly) to microcrystalline lightly trachytic	No	25 M	564224	9572453
FN30-53	F53	São José	Flow	Olivine alkali basalt	porphyritic holocrystalline	microcrystalline	Yes	25 M	-	-

Table 1-1 (cont.)

Sample	Map code	Locality (Borborema) Formation (FN)	Context	Rock type	Overall texture	Groundmass texture	Pdt. xenolith	UTM		
FN30-54	F54	São José	Flow	Olivine alkali basalt	porphyritic holocrystalline	microcrystalline	Yes	25 M	-	-
Fernando de Noronha (cont.)										
FN30-55	F55	São José	Flow	Olivine alkali basalt	porphyritic holocrystalline	microcrystalline	Yes	25 M	-	-
FN30-56	F56	São José	Flow	Olivine alkali basalt	porphyritic hypocrystalline	crypto- to microcrystalline	Yes	25 M	-	-
Fernando de Noronha basaltic dykes										
FN13-22	F22	Remédios	Dyke	Alkali basalt	porphyritic holocrystalline	microcrystalline	No	25 M	566778	9575415
FN12-34	F34	Remédios	Dyke	Tephrite	porphyritic holocrystalline	crypto- to microcrystalline heterogeneous	No	25 M	565480	9573434
FN12-35	F35	Remédios	Dyke	Tephrite	porphyritic holocrystalline	crypto- to microcrystalline	No	25 M	565528	9573429
FN20-41	F41	Remédios	Dyke	Titanaugite-phyric basanite/tephrit.	porphyritic hypocrystalline	glassy to cryptocrystalline	Uncert.	25 M	565585	9573470

Despite receiving more attention than Northeast Brazil, the Cameroon Line also remains controversial, with no consensus about the origins of its volcanic activity (Njome and de Wit, 2014). It is, however, generally agreed that a deep mantle plume is not an adequate model for the region, in spite of magmatism being clearly sublithospheric (Fitton, 1980, 1987, 2007; Fitton and Dunlop, 1985; Foulger, 2010; Njome and de Wit, 2014). Problems with this model often parallel what is seen in Northeast Brazil, and include lack of age progression along the volcanic chain (Fitton, 1980, 1987, 2007; Fitton and Dunlop, 1985; Njome and de Wit, 2014), its forked shape that follows the outline of the Benue Trough to the north (Fitton, 1980; Reusch *et al.*, 2010), the lack of disturbances in the mantle transition zone under the province according to seismic data, which undermines the hypothesis of a mantle plume ascending from the core-mantle boundary to the upper mantle (Reusch *et al.*, 2011), and the fact that volcanism has been continuous and geographically fixed, independently of plate movement, for tens of millions of years (Fitton, 1980).

Lack of consensus around the origins of Cenozoic magmatism in both conjugate margins also extends to other models. Decompression melting due to extension is unlikely on the African side, as the region lacks evidence for extension (Fitton, 2007; Reusch *et al.*, 2010; Njome and de Wit, 2014), although this process may have had a localised effect in the basins of Borborema (Souza *et al.*, 2013). Decompression through other means such as lithospheric basal or surface erosion is also unlikely, given that it would imply astenospheric melting and would not explain synchronous and identical volcanism on both conjugate margins. Although it has been argued that there is some contribution of lithospheric material to the lavas of both the Cameroon Line and Northeast Brazil, which would be expected in the case of lithospheric basal erosion, it is still very limited (Fitton and Dunlop, 1985; Fitton, 1987; Fodor *et al.*, 1998; Njome and de Wit, 2014).

An alternative explanation for the Cameroon Line would be a large degree of rift asymmetry along the Benue Through, with the base of its

control fault/shear zone located a long way to the south. However, this would be at odds with the positive gravity anomalies directly under the basin itself (Fairhead and Okereke, 1987, 1991, Poudjom Djomani *et al.*, 1995, 1997; Adams *et al.*, 2015), which imply local thermal re-equilibration and subsidence. Moreover, thermal re-equilibration would likely be faster than the more than 60 m.y. of volcanic activity along the Cameroon Line, and a model based on the Benue rift is also not applicable to Northeast Brazil, failing to explain the volcanic similarities between the two conjugate margins.

Lithospheric instabilities that generate areas of downwelling and upwelling at the base of the lithosphere, which lead respectively to compression and extension, have been proposed as an alternative interpretation for the Cameroon Line (Milelli *et al.*, 2012; Adams *et al.*, 2015). The model implies that all intraplate volcanism in Africa may result from the same process, but this fails to accommodate the heterogeneity of the continent's volcanic provinces more generally and, more specifically, is undermined by the lack of evidence for extension in the Cameroon Line.

More adequate candidates would be models based on small scale edge-driven convection, which have been proposed for the Cameroon Line based on seismic imaging and geophysical evidence (King and Ritsema, 2000; Reusch *et al.*, 2010, 2011). Such models are based on lithospheric morphology and may be applied to the volcanic provinces on both sides of the Atlantic, since the lithospheric block on either side are continuations of one another. An edge-driven convection hypothesis gains strength if applied specifically to thickness gradients underlying the continental block, as opposed to the gradient between continental and oceanic lithospheres, as this helps explaining why Cenozoic volcanism along these conjugate margins does not occur along the whole passive margin.

Despite their matching characteristics and the lack of an adequate model, to date there are no in-depth discussions about possible connections between Cenozoic igneous processes in Northeast Brazil and the Cameroon Line. Potential comparisons seem to have been precluded by the fact that

the two continents were already separated for 10s of millions of years when magmatism started either side of the Atlantic. However, comparing the two provinces is likely to be key to understanding them, and this will be the focus of this study. The degree of similarities between both volcanic regions in terms of geochemistry, chronology and geological settings show that they must be somehow related petrogenetically. These relationships, in turn, expose patterns in intraplate volcanism that are as yet unexplored, and which may add to our understanding of how the Earth's mantle operates.

The implications of a genetic relationship between the two provinces are many. First, simultaneous volcanic activity on equivalent areas of two conjugate margins already separated for 10s of millions of years, with magmatism then remaining coupled with plate movement up until the present, would indicate some form of lithospheric control, since the two areas must share the same lithospheric structures. Second, similarities between primitive rocks from both the continental and oceanic sectors of the two margins, and between the two margins themselves would indicate that the source must be sub-lithospheric but also somehow coupled with each plate, since volcanism follows plate movement but does not vary between continental and oceanic lithospheres. Third, their virtual synchronicity would indicate that the magmatic processes responsible for their genesis must have a well-defined timeframe of operation that is somehow associated with continental breakup, implying also a tectonic control to the process. These points relate directly to many of the issues concerning our current understanding of intraplate volcanism, and the conjugate margins of Northeast Brazil and the Cameroon Line offer a unique opportunity whereby direct correlations may be established between intraplate magmatic processes from different provinces or even plates. They allow comparisons and testing of hypotheses across two different plates, including the specific effects that differences between oceanic and continental lithospheres (e.g. thickness and composition) may have in these processes, and highlight

potential consistencies in the diverse and heterogeneous array of intraplate volcanic occurrences that are not related to mantle plumes.

Therefore, the main objective of this work is to examine Cenozoic volcanic occurrences in northeast Brazil as a whole, with new $^{40}Ar/^{39}Ar$ dates and geochemical data obtained through XRF and ICPMS analyses, and to compare them with the Cameroon Line, for which equivalent XRF data, obtained in the same laboratory and using the same methods as the XRF data presented here, is also available (Fitton and Dunlop, 1985; Fitton, 1987). These new $^{40}Ar/^{39}Ar$ ages and geochemical data further support the argument against a mantle plume as the driving mechanism for magmatism in Northeast Brazil. The new $^{40}Ar/^{39}Ar$ dates demonstrate that the lack of age progression patterns in the region is not only a trend between the MQVL and Fernando de Noronha as pointed out by Knesel et al. (2011), but extends to the entire MQVL as a distinct lineament, and into the Mecejana volcanic field. The new geochemical data show that lavas in the three Cenozoic volcanic regions of Northeast Brazil, which have been previously studied independently, are in fact geochemically related, and therefore must be treated as a single unit resulting from the same process. The geochemical datasets are also virtually identical to those of the Cameroon Line. Having shown that, we introduce a new model for the magmatic process operating on both conjugate margins, which accommodates both their similarities and differences, and argue that intraplate volcanism along the Equatorial and South Atlantic passive margins must obey lithospheric controls that are associated with the continental lithosphere and somehow triggered by plate separation, even when these processes tap sources that are compositionally mainly asthenospheric.

The model we propose brings together edge-driven convection (King and Anderson, 1998; King and Ritsema, 2000; King, 2007), erosion of the continental sublithospheric thermal boundary layer (TBL) and flow of hot ductile material (including from the TBL) at the base of the lithosphere (Sleep, 1996, 2003; Ebinger and Sleep, 1998), and provides an adequate

explanation encompassing all the observed similarities and differences between the two conjugate margins analysed here. These are all familiar geodynamic concepts, but are not normally applied together, even though they are not mutually exclusive. Although the concept of lateral flow of hot enriched material has usually been applied in conjunction with plume models, there is no reason why it wouldn't be applicable to other types of thermal anomalies. For instance, continental lithospheric morphology may lead to the development of an edge-driven convection cell and a localised thermal anomaly, which may in turn erode the continental TBL by affecting its thermal structure and cause it to flow along the base of the lithosphere. The TBL convects very slowly and in practical terms may remain coupled with the rigid lithosphere during plate movement (Anderson, 1995). However, due to its intermediate rheology between the lithosphere and asthenosphere, it is not a permanent layer, and may become more ductile under the effects of a localised thermal anomaly. These characteristics also imply that the TBL may be subject to localised processes of enrichment and metasomatism and retain their record for some time, developing a distinct albeit similar geochemical signature to the asthenospheric upper mantle. Therefore, the compositional and rheological characteristics of the TBL, combined with edge-driven convection models, may account for the geochemical and chronological similarities across both continents, as well as their enriched signatures (both in terms of isotopic ratios and trace element concentrations). The combination of these models not only provides an interpretation for both Northeast Brazil and the Cameron Line, but it also associates them with the broader context of intraplate volcanism in the Equatorial and South Atlantic, where similar patterns seem to be in operation and manifesting themselves through seamount chains.

The methods used is this study for obtaining the new chronological and geochemical data are given in Appendix A. Chapter 2 will present the new $^{40}Ar/^{39}Ar$ dates for the volcanic centres in Borborema, together with comparisons with other published dates for the area and a discussion of how

the local chronology relates to the Cameroon Line. It will be clear how Cenozoic volcanism on the South American passive margin is virtually synchronous with its African counterpart, and how both lack any age progression pattern that may indicate the presence of a deep mantle plume. Once chronological correlations have been established, Chapter 3 will discuss the geochemical similarities of the three different volcanic areas of Northeast Brazil, including new isotopic data, and demonstrate that they should be treated as a single province sharing a common origin. Chapter 4 will then address the geochemical correlations between the South American and African conjugate margins in terms of major and trace element patterns. Their similarities are remarkable and demonstrate that they must be related petrogenetically. Finally, Chapter 5 will present our proposed model for how these patterns may be explained, in light of a broader discussion of edge-driven convection cells and how they may affect an enriched sub-continental TBL.

First, however, it is important to provide an overview of the geological context and current state of research for both provinces, including our current understanding of how the Equatorial and South Atlantic opened and the correlations between terranes in the South American and African passive margins.

Geological context

Fernando de Noronha

Fernando de Noronha is a volcanic archipelago located about 365 km northeast of Natal, in the State of Rio Grande do Norte, Brazil. It has a total area of 18.4 km^2, comprising an eponymous main island with 16.9 km^2 and 20 other islets, and is the easternmost and only offshore exposure of a submerged seamount chain that continues to the west towards the city of Fortaleza, in the State of Ceará (Figure 1-5). The Macejana volcanic field has sometimes been interpreted as the onshore manifestation of the same

processes that created the offshore chain (Sial, 1976b; Ernesto, 2005; Almeida, 2006). The seamount at Fernando de Noronha has a base 4000 m below sea level and extends for 60 km in its longest axis (Cordani, 1970; Mitchell-Thomé, 1970).

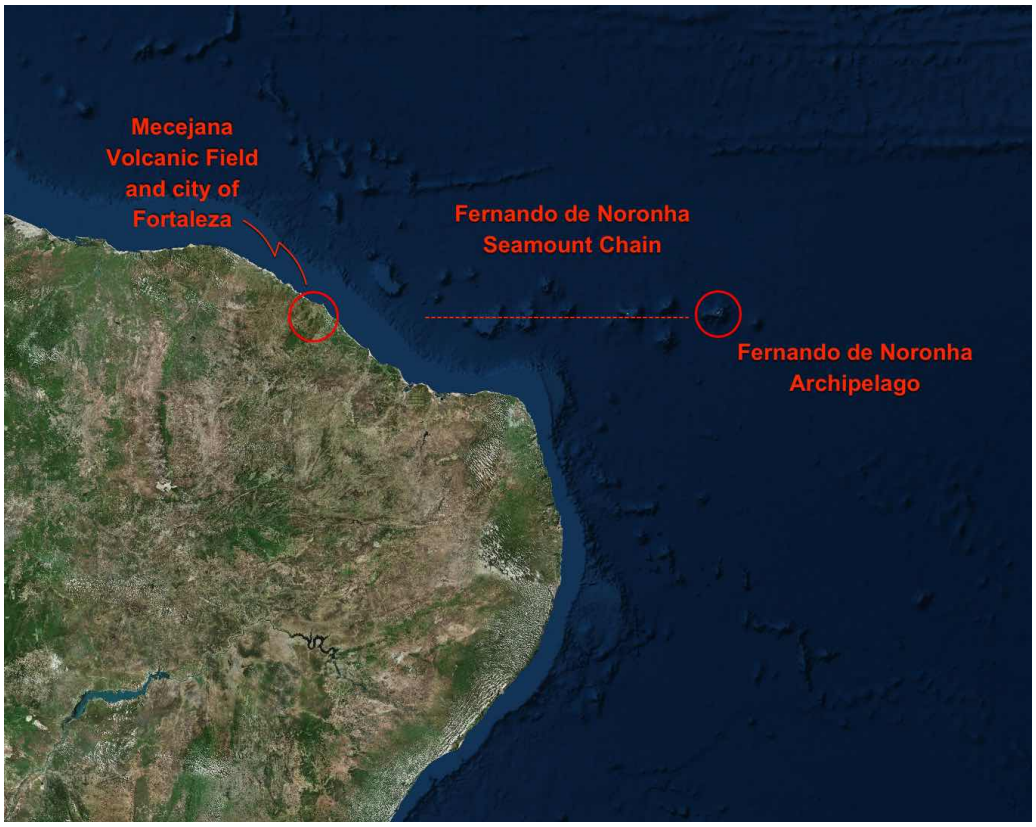

Figure 1-5: Fernando de Noronha seamount chain and its association with the Mecejana Volcanic Field.

It is perhaps the most studied of the three volcanic provinces in Northeast Brazil, and important works include Almeida (2006, 1955), Gerlach et al. (1987), Lopes (2002), Lopes et al. (2014), Mitchell-Thomé (1970), Perlingeiro et al. (2013), Ulbrich (1993), Ulbrich et al. (1994), Ulbrich and Lopes (2000) and Weaver (1990). Most of these, however, focus on detailed petrological, petrographical and geochemical descriptions of the local rocks, and only a few try objectively to insert the archipelago into a broader context of intraplate occurrences.

The archipelago is dominated by extrusive and hypabyssal rocks divided into three Formations: Remédios, Quixaba and São José. Small

occurrences of Quaternary calcarenites are also present as a distinct rock group (Almeida, 1955; Mitchell-Thomé, 1970; Lopes, 2002). Volcanic activity in the exposed areas lasted for over 10 m.y., from the Miocene (Serravallian) to the Pleistocene, with the most current ages published by Perlingeiro et al. (2013) using the $^{40}Ar/^{39}Ar$ technique. These will be the dates used in this work.

The Remédios Formation (9.4-12.5 Ma) is heterogeneous, ranging from basanite and alkali basalt to phonolite. It comprises a series of alkaline aphanitic and porphyritic domes, necks and dykes cutting through pyroclastic deposits. The latter contain clasts of the exposed lithologies and plutonic examples otherwise not exposed in the archipelago (Cordani, 1970; Ulbrich, 1993; Ulbrich *et al.*, 1994; Ulbrich and Lopes, 2000; Perlingeiro *et al.*, 2013).

The Quixaba Formation (1.3-6.2 Ma) is more homogeneous, comprising lava flows of nephelinite (often classified as ankaratrite), basanite (often classified as ankaramite) and alkali basalt whose eruption peaked at ~3 Ma (Cordani, 1970; Perlingeiro *et al.*, 2013). The flows pile up for 10s of meters (reaching close to 200 m in the northwest of the main island), and have interbedded cogenetic volcanic breccias (Cordani, 1970; Ulbrich, 1993; Lopes, 2002). There is no evidence of palaeosols or erosional surfaces between these flows, and identification of independent units can be ambiguous (Leonhardt et al., 2003). Nonetheless, palaeomagnetic studies have confirmed the existence of at least six distinct units, which must have had relatively short time intervals between them (ibid.). They were emplaced unconformably over an irregular relief formed over the Remédios Formation after a hiatus in volcanic activity of a few million years (Weaver, 1990; Ulbrich, 1993; Lopes, 2002; Almeida, 2006).

The São José Formation (9.0-9.2 Ma) comprises thick alkali basalt lava flows with well-developed basal columnar jointing and is particularly rich in peridotite xenoliths up to ~30 cm in diameter. The Formation is restricted to the three islets of São José, Cuscuz and de Fora, to the northeast of the main island. Some researchers argue that the São José Formation is

dominated by basanite rather than alkali basalt, and that it is petrologically more similar to the Quixaba than to the Remédios Formation, in spite of being chronologically closer to the latter (Ulbrich, 1993). The São José samples analysed here are limited to alkali basalt in terms of composition, but overlap with the least alkaline Quixaba specimens in a total alkalis-silica (TAS) diagram, and are also petrographically very similar to some of this Formation's flows (see Chapter 3).

Fernando de Noronha's volcanics are exclusively alkaline, and the Remédios Formation is the only one with intermediate and evolved rocks. Intermediate samples have limited exposure and are concentrated on the east and southeast of the main island, where erosion is more intense and rocks most altered. These conditions have caused an apparent loss of Na from those rocks that is reflected in their relatively lower content of total alkalis in the TAS diagram, and which also correlates directly with loss on ignition (LOI) values (see Chapter 3 and Figure 1-9 below). Geochemical data and current dates suggest a continuous sequence of magma differentiation and relatively uninterrupted volcanic activity in the Remédios Formation that, together with the coeval São José Formation, are less undersaturated than the younger Quixaba events.

The Remédios Formation dataset also includes a dyke swarm (Figure 1-6) cutting through basaltic trachyandesites and pyroclastic deposits in the Atalaia and Caieiras beaches, respectively on the southeast and east of the main island, the area most affected by erosion and alteration due to the prevailing currents. It is not clear if these dykes are indeed part of the Remédios Formation or if they are associated with the overlying Quixaba lava flows or the nearby São José Formation. They form a small heterogeneous group that has been previously interpreted as a distinct subgroup dominated by lamprophyre (Ulbrich, 1993; Ulbrich *et al.*, 1994; Lopes, 2002), and as such suffer from the same levels of inconsistency and variability that usually accompany this loose term.

Figure 1-6: Part of the Atalaia beach dyke swarm in Fernando de Noronha.

The Borborema Province

The Borborema Province, on the northeast coast of Brazil, comprises Proterozoic fold belts bounded by the São Francisco craton to the south, the Parnaíba Basin to the west and the São Luís craton to the northwest (Figure 1-2). It may be divided between north and south of the Pernambuco shear zone, with Cenozoic magmatism only occurring in the northern area (Mizusaki et al., 2002; Figure 1-7). Rifting and crustal stretching directly associated with volcanic centres are limited to the southernmost localities around the Patos Shear Zone, within the Boa Vista and Cubati Basins (Souza et al., 2013, 2005), whilst the northernmost occurrences are within the Cretaceous Potiguar Basin.

Cenozoic volcanism in the area is dominated by alkaline and transitional rocks that cut mainly through Precambrian basement, although some occurrences also intrude the Cretaceous sediments of the Potiguar Basin. They contrast markedly with the Mesozoic tholeiites and plutonic occurrences found in the area (Sial, 1976a), and occur in two geographically and lithologically distinct groups: the Macau-Queimadas Volcanic Lineament (MQVL), comprising solely basic and ultrabasic assemblages; and the

Mecejana volcanic field, formed entirely by phonolites (Figures 1-3 and 1-7). Published dates for Mecejana are limited to the K/Ar method and range from 26 to 34 Ma (Cordani, 1970; Mizusaki *et al.*, 2002), whereas current $^{40}Ar/^{39}Ar$ dates for the MQVL range from 7.1 ± 0.3 to 51.8 ± 0.9 Ma (Silveira, 2006; Knesel *et al.*, 2011; Souza *et al.*, 2013). The younger dates for the MQVL significantly overlap with Fernando de Noronha, and the two areas together show no age progression pattern indicative of a plume track.

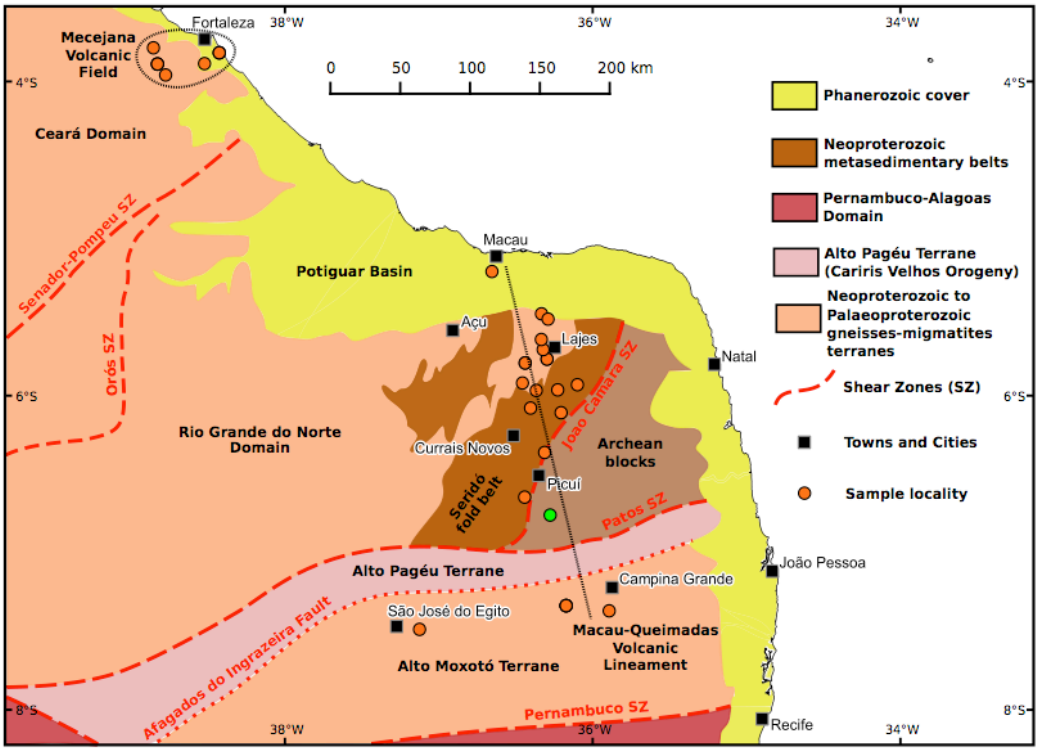

Figure 1-7: Simplified representation of the main geological units in Borborema. Adapted from van Schmus et al. (2008) and the DNPM Geological Map of Rio Grande do Norte (1998). The Cubati volcanic centre (marked in *green* on the Figure) is the only Cenozoic volcanic occurrence between the João Câmara and the Patos Shear Zones, in an area marked by the presence of Archean blocks, and there has been no reported Cenozoic volcanism south of the Pernambuco shear zone.

Assessment of the MQVL was carried out during the 1970s (Cordani, 1970; Sial, 1975a, 1975b, 1976b, 1976a; Sial *et al.*, 1981), and resumed again only in the late 1990s with the work by Fodor et al. (1998), with the exception of occasional limited studies of the local xenoliths (Comin-Chiaramonti *et al.*, 1986; Princivalle *et al.*, 1989, 1994). Since then, works

have been diverse, including discussions of the local lavas, their ubiquitous peridotite xenoliths, geochronology and tectonic context (Fodor *et al.*, 1998, 2002, Rivalenti *et al.*, 2000, 2007; Mizusaki *et al.*, 2002; Ernesto, 2005; Souza *et al.*, 2005, 2013; Silveira, 2006; Knesel *et al.*, 2011). Broad similarities with the Cameroon Line have been hinted at by Sial (1976b) and Fodor et al. (1998).

Outcrops along the MQVL are dominated by plugs, necks and flows, roughly in this order of proportion. They occur roughly on a linear strip trending NNW-SSE, ~50 km wide and ~300 km long, from the town of Macau in the north to the Boa Vista Basin and Queimadas lava flows in the south (Figures 1-4 and 1-7). Their linear arrangement, age and compositional affinities distinguishes them as a distinct group. The lineament straddles over the States of Rio Grande do Norte and Paraíba. The São Pedro plug (sample 15BP1-1), located to the east of São José do Egito in the State of Pernambuco and ~100 km WSW of the Boa Vista Basin, although technically outside the MQVL, will be considered together with it. Apart from São Pedro, plugs and necks concentrate in the middle of the lineament, whilst flows dominate in the north and south (Sial, 1976b, 1976a). Rocks range from transitional basalt to nephelinite, but subalkaline basaltic andesite also occurs around Macau in the Potiguar Basin, and in the Boa Vista Basin in the south. Lava flows associated with basin environments have fine-grained groundmass textures and are more silica saturated, contrasting with the microcrystalline, cryptocrystalline and hypocrystalline fabrics and more undersaturated compositions of plugs and necks. These characteristics reflect the dominance of thicker, more viscous and slower cooling lava bodies in the basins, contrasting with the less viscous and more rapidly cooling hypabyssal intrusions in other areas. The basins also contain pillow lavas (Figure 1-8) and subaqueous sediment deposits (fossiliferous carbonates and chert) that transition laterally and vertically to subaerial lava flows. A few occurrences of plutonic rocks with ages ~50 Ma have also been

reported (Silveira, 2006), and add to the chronological and lithological similarities with the Cameroon Line.

Figure 1-8: Lava pillows in the Boa Vista Basin. The card on the photo shows a cm-scale.

The Mecejana volcanic field has often been interpreted as the continuation of the Fernando de Noronha seamount chain that lies over a fracture zone abutting the continental lithosphere (Almeida, 2006; Ernesto, 2005; Sial, 1976a; Figure 1-5). However, as yet, the area has not been studied in any detail, and publications are limited to a couple of conference communications that point out the overall similarities with phonolites from Fernando de Noronha (Rao and Sial, 1972; Guimarães et al., 1982). The area is named after a suburb of the city of Fortaleza, State of Ceará, but volcanic occurrences dot an area just under 50 km radius around the city. Outcrops are dominated by plugs and pipes, some of which are quarried for building material. They lie ~250 km northwest from the northernmost volcanic occurrence of the MQVL near the town of Macau, and no Cenozoic igneous

rocks have been reported in the space between the two areas. The Mecejana phonolites are relatively diverse, but overall are highly evolved, with high alkali content, rich in nepheline phenocrysts, and some carry K-feldspar megacrysts or wall-rock xenoliths. They also contain occasional kaersutite amphiboles, and overall are very similar to the phonolites in Fernando de Noronha.

The Cameroon Line

The continental volcanic segment of the Cameroon Line is located in the Precambrian fold-belt just north of the Congo craton, and is roughly aligned with the suture zone between the two terranes. It covers mainly Cameroon but its northern occurrences cross into southeast Nigeria. The chain continues into the oceanic sector, more or less perpendicular to the passive margin, and forms the islands of Bioko, Príncipe, São Tomé and Annobón. Compared to Northeast Brazil, the Cameroon Line is a significantly more extensive, voluminous and vigorous volcanic chain reaching nearly 1700 km in length and 200 km in width in its broadest segments. It also reproduces the exact shape and shows remarkable alignment with the Benue Trough just north of it (Fitton, 1980, 1987).

The volcanic chain is dominated by alkaline compositions, but rocks from the continental sector also evolve to rhyolitic compositions due to the effects of the continental lithosphere on melt evolution during magma ascent (Fitton, 1987). Furthermore, similarly to Northeast Brazil, only the oceanic sector produced a continuous development from primitive to evolved rocks through intermediate compositions, whilst the continental sector, although still more compositionally widespread than the MQVL, also shows a relative lack of intermediate samples (Figure 1-9). Although the African oceanic sector does not show Na loss to the same extent as Fernando de Noronha, the few samples there with low total alkalis also have high LOI values (Figure 1-9). Plutonic occurrences are more common than in Northeast Brazil, but

similarly to their South American counterparts have also produced the oldest dates in the chain (Njome and de Wit, 2014).

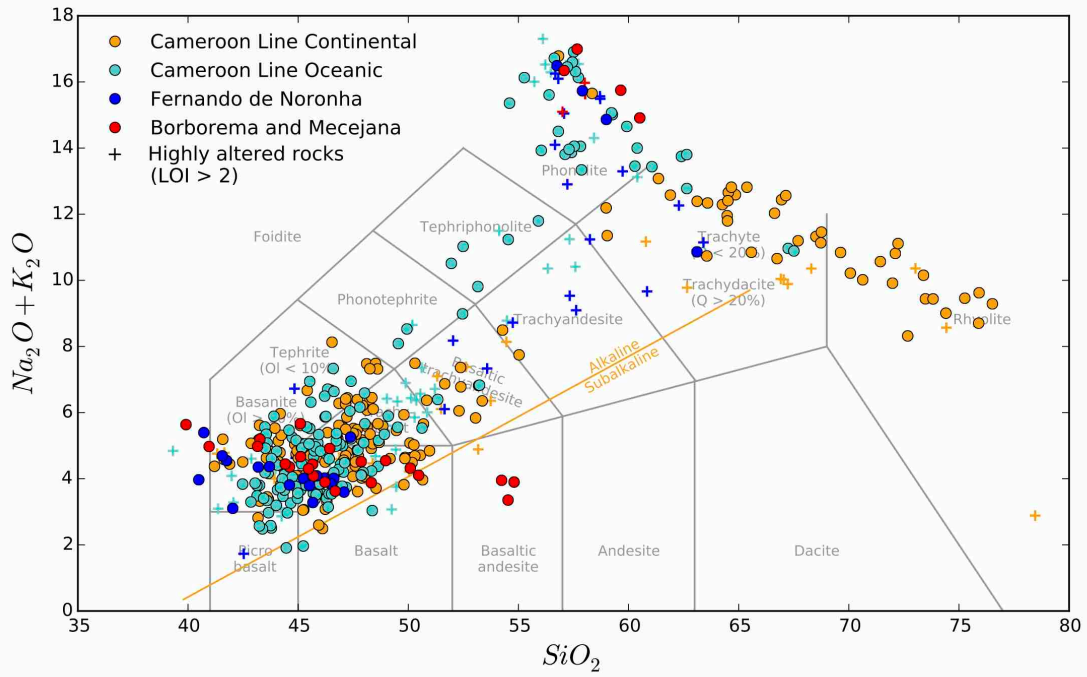

Figure 1-9: Total Alkalis and Silica diagram after Le Maitre (2002) using the data given in Appendix C and discussed in detail in Chapter 3. Data plotted on a volatile free basis and ΣFeO. It is clear how samples with higher LOI values are much more common in the oceanic sectors. They also correlate with relatively low total alkalis, which result in transitional compositions that still run parallel to alkaline compositions with LOI ≤ 2 wt.%. These effects are particularly strong in Northeast Brazil, and are likely a result of Na loss due to alteration. The line dividing alkaline and subalkaline compositions is taken from MacDonald and Katsura (1964).

The most recent review of the published literature and current understanding of the Cameroon Line was presented by Njome and de Wit (2014). Although some studies still try to associate the chain or parts of it directly with a deep mantle plume (Ebinger and Sleep, 1998; Kuepouo *et al.*, 2006), this hypothesis is generally seen as inadequate for the area (Fitton, 1980, 2007; Fitton and Dunlop, 1985; Foulger, 2010; Njome and de Wit, 2014). However, some interpretations argue for the involvement of a deep mantle plume in the enrichment event of the upper mantle that gives the Cameroon Line its enriched geochemical signatures (Halliday *et al.*, 1990; Aka *et al.*, 2004), although this does not explain the Cenozoic magmatism

itself. Other mechanisms for triggering magmatism, such as decompression melting due to lithospheric stretching, also fail to provide an adequate explanation (see above), and the reasons for these failures may also be extrapolated to Northeast Brazil.

Geological correlations and continental breakup

Parallels between the geological settings of Northeast Brazil and the Cameroon Line are a natural consequence of the two areas being extensions of one another that only separated with continental breakup. Therefore, lithospheric morphology and composition should be very similar, if not virtually identical, on both conjugate margins.

The opening of the South Atlantic started sometime between 150 and 130 Ma at the southernmost regions of the newly forming South American and African continents (Nürnberg and Müller, 1991; Turner *et al.*, 1994). Separation then developed gradually northwards, with each stage of extension being accommodated and temporarily buffered by shear zones and basins developing at progressively lower latitudes. This process continued up to the Pernambuco-Adamawa fault, which represents the last one of these buffers (Nürnberg and Müller, 1991; Matos, 1992). During this time, the onshore branch of the Potiguar Basin was also extending, forming a significant basin, whilst movement along the Benue Trough was dominated by lateral shearing (Nürnberg and Müller, 1991; Matos, 1992). Extension in the Benue Trough would not start until sometime between the late Berremian and the mid-Aptian (~118-124 Ma), which would also mark the development of the offshore branch of the Potiguar Basin and the separation of the northern coast of Brazil from Africa (Matos, 1992). At ~118 Ma the Equatorial Atlantic would also begin to open, but formation of the oceanic basin would not start until ~100 Ma, when the area between these two accommodation zones represented by the Benue Trough and the Pernambuco-Adamawa fault, the last segment of continental lithosphere connecting the two continents, finally separates (Nürnberg and Müller, 1991; Mizusaki *et al.*,

2002). The initial sinistral strike-slip movement along the Benue Trough as the South American plate rotated clockwise during most of the continental separation shifted to dextral trans-tensional during the final breakup (Nürnberg and Müller, 1991). The MQVL today runs perpendicular to this final movement direction that is also roughly the same as the present-day South American plate motion (i.e. ESE), and parallel to the last stretch of the two conjugate margins to separate (Figure 1-7). The Cameroon Line, on the other hand, is roughly parallel to the Benue Trough, and more or less perpendicular to both the MQVL and the adjacent passive margin.

Tectonic accommodation continued in the Benue Trough until ~84 Ma, marked to some extent by transpressional processes that seem absent in the Potiguar Basin, which suggests distinct tectonic accommodation processes in each of the newly formed continents (Nürnberg and Müller, 1991). Magmatic activity associated with continental breakup in Northeast Brazil seems to have continued up until around the same period (Mizusaki *et al.*, 2002), even though earlier studies argue that the South American plate started to behave rigidly from the moment of separation (Nürnberg and Müller, 1991). There are no observable magnetic anomalies along the Equatorial Atlantic for the period between 118.7 Ma and 84 Ma, limiting the evidence available for building a chronological sequence of events during the final stages of continental breakup (Nürnberg and Müller, 1991; Mizusaki *et al.*, 2002).

The Potiguar and Benue Basins are therefore continuations of each other, and they share many structural and tectonic similarities (Castro *et al.*, 2012). Geophysical studies in the Benue Trough consistently show high positive gravity anomalies on its SW section, but lower measurements on its NE segments, especially the eastern arm (Fairhead and Okereke, 1987, 1991, Poudjom Djomani *et al.*, 1995, 1997; Adams *et al.*, 2015). These lower values for gravity anomalies coincide with areas where volcanism crosses the Benue Trough whilst still not overlapping with it significantly (Figure 1-10). High positive gravity anomalies also exist at the centre of the Potiguar

Basin (Castro *et al.*, 2012), where Cenozoic volcanism is relatively more subdued than in the terranes further south. High positive anomalies on both sides of the Atlantic indicate the presence of denser material resulting from the thermal re-equilibration after lithospheric thinning, which in turn may lead to subsidence.

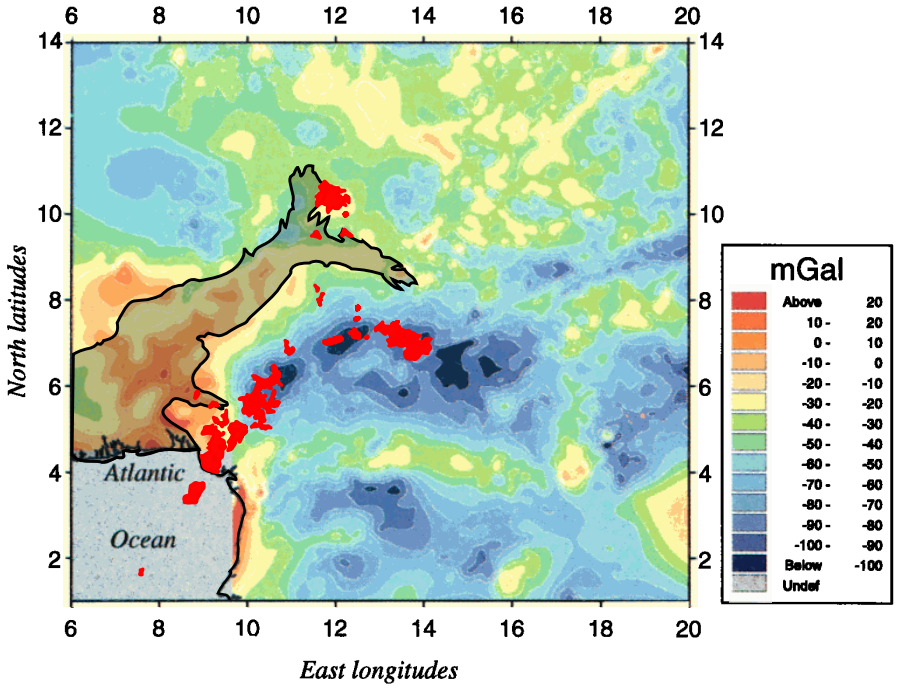

Figure 1-10: Map of the Benue Trough and the Cameroon Volcanic Line superimposed on a map of local gravity anomalies. Taken respectively from Fitton (1987) and Poudjom Djomani et al. (1995). Gravity anomalies appear slightly offset from the basin contour, likely as a result of the horizontal uncertainties associated with seismic measurements (Priestley *et al.*, 2008; Priestley and McKenzie, 2013). It is clear how the Biu plateau, the northernmost volcanic occurrence, is located across the Benue Trough but still does not intersect with it significantly.

The tectonic fabrics of northern Borborema and the Benin-Nigeria Provinces, on the northern side of the Potiguar-Benue Basins, are virtually the same, but the fit along Borborema's eastern shore and the NW Cameroon terrane in Africa, both on the southern side of the Potiguar-Benue Basins, is more problematic in its details. The continental sectors on both sides of the Atlantic contain blocks of accreted terranes in complex arrangements, and, in that respect, are broadly similar. They are also

surrounded by cratonic terranes where Cenozoic volcanic activity is absent. An overview of the Proterozoic formation of these regions and their correlations with each other is given by Arthaud et al. (2008), Castro et al. (2012), Santos et al. (2008) and van Schmus et al. (2008). The areas are the product of long and complex Proterozoic continental cycles and terrane accretion affecting both Archean and Palaeoproterozoic blocks, which created a heterogeneous shield of fold belts covering both South America and Africa, and which has been mostly stable since the Upper Neoproterozoic and the Cambrian (Figures 1-2 and 1-7).

Most of the MQVL mainly cuts through the Seridó Belt and Palaeoproterozoic gneiss-migmatite terranes (Arthaud *et al.*, 2008), but also through the Cretaceous sediments of the Potiguar Basin to the north, the Ceará Group to the west and the Alto Moxotó terrane to the south (Figure 1-7). No Cenozoic volcanism is found south of the Pernambuco shear zone or to the west of the Transbrasiliano Lineament, which are respectively where the São Francisco and São Luís Cratons begin (Santos *et al.*, 2008; van Schmus *et al.*, 2008).

The Seridó Group is a Neoproterozoic autochthonous fold belt dominated by metasedimentary suites that is truncated to the east by the João Câmara shear zone (Arthaud *et al.*, 2008). There is no significant Cenozoic volcanism beyond the João Câmara shear zone (JCSZ) and north of the Patos shear zone (PtSZ; Figure 1-7). In Nigeria, the Seridó Group seems to correspond to the Igarra Sequence on the SW of the country and adjacent to the northern edge of the Benue Trough (Arthaud *et al.*, 2008). The Alto Pajéu and Alto Moxotó terranes south of the PtSZ in Borborema comprise what is called the Transverse terrane, and seem to correspond to the Eastern Nigeria shield in Africa (van Schmus *et al.*, 2008). Although Alto Moxotó is very similar to other gneiss and migmatite terranes in Borborema, Alto Pajéu is dominated by the effects of the Cariris Velho orogeny and the PtSZ represents a major terrane boundary between the Transverse terrane and the Rio Grande do Norte domain (van Schmus *et al.*, 2008). The Ceará

Group is a highly deformed and migmatized Neoproterozoic allochthonous fold belt comprising metasedimentary suites that seems to continue into Nigeria (Arthaud *et al.*, 2008). It ends at the Transbrasiliano Lineament to the west, a major crustal-block boundary that, according to seismic evidence, separates the Ceará Group from the São Luís craton underlying the Parnaíba Basin. The Lineament also continues into Africa as the suture underlying the Dahomeyide Belt, marking the boundaries of the West African Craton roots (Santos *et al.*, 2008).

There is no overall agreement for the precise fit between the equatorial passive margins of South America and Africa. This is particularly clear in the different ideas around the precise fit between the Tcholliré-Banyo and Adamawa lineaments in Africa, and the Pernambuco and Macururé shear zones in Northeast Brazil (Arthaud *et al.*, 2008; van Schmus *et al.*, 2008; Castro *et al.*, 2012). The palimpsest of so many shear zones and accreted terranes on both sides pose a significant challenge to an unequivocal fit (Nürnberg and Müller, 1991; Arthaud *et al.*, 2008; Santos *et al.*, 2008; van Schmus *et al.*, 2008; Castro *et al.*, 2012). Nonetheless, it is clear that the origin of Cenozoic volcanism on the two conjugate margins is independent of local geological terranes, since the terranes affected are not the same across the two continents. African Cenozoic volcanism is limited to the NW Cameroon terrane, which seems to match the Brazilian Pernambuco-Alagoas terrane (van Schmus *et al.*, 2008), which lies south of the Pernambuco shear zone and where Cenozoic volcanism is absent. Conversely, there is no significant Cenozoic volcanism north of the Benue Trough on the African side, but the continuation of these terranes into Brazil include the Ceará Group, the Seridó Belt and the Transverse terrane, which are affected by Cenozoic volcanism. Once it has been demonstrated that Cenozoic volcanism in Northeast Brazil and the Cameroon Line are both synchronous and geochemically virtually identical (next Chapters), the mismatch between the geological terranes affected by Cenozoic volcanic

activity on both sides of the Atlantic reinforces the argument that the main magmatic process must be sublithospheric.

Chapter 2: $^{40}Ar/^{39}Ar$ geochronology

Introduction

Linear age progression in volcanic activity is one of the main criteria used to identify deep mantle plume tracks. Therefore, lack of age progression is a central argument against this model as an explanation for Cenozoic volcanism in Northeast Brazil and the Cameroon Line (Fitton, 1980, 1987, 2007; Fitton and Dunlop, 1985; Silveira, 2006; Knesel *et al.*, 2011; Perlingeiro *et al.*, 2013; Souza *et al.*, 2013; Njome and de Wit, 2014). For instance, recent $^{40}Ar/^{39}Ar$ dates show that volcanism in the central segment of the Macau-Queimadas Volcanic Lineament (MQVL) is synchronous with volcanic activity in Fernando de Noronha (Knesel *et al.*, 2011; Perlingeiro *et al.*, 2013), and previous studies based on K/Ar fail to show clear age progression patterns in Northeast Brazil as a whole (Cordani, 1970; Sial *et al.*, 1981; Mizusaki *et al.*, 2002). In the Cameroon Line, available dates not only show no age progression patterns, but also demonstrate synchronous activity along almost the entire chain in the last 10 m.y. (Fitton and Dunlop, 1985; Njome and de Wit, 2014). However, most available chronological data for both regions comes from K/Ar analyses (Cordani, 1970; Mizusaki *et al.*, 2002; Njome and de Wit, 2014). In Borborema, the duration of Cenozoic volcanism was still poorly constrained by more reliable $^{40}Ar/^{39}Ar$ dates prior to the present study, despite some published ages (Silveira, 2006; Knesel *et al.*, 2011; Souza *et al.*, 2013), noticeably with no $^{40}Ar/^{39}Ar$ ages available for the Mecejana volcanic field or the northernmost occurrences of the MQVL.

In this chapter, new $^{40}Ar/^{39}Ar$ ages for Borborema are presented. For the first time, the Mecejana volcanic field and one northern occurrence of the MQVL (i.e. near the town of Macau) are included. The results further highlight the lack of age progression of Cenozoic volcanism in Northeast Brazil, and also show that Cenozoic volcanism in Northeast Brazil and the

Cameroon Line are both synchronous and share a similar chronological development.

$^{40}Ar/^{39}Ar$ method

Dating through the $^{40}Ar/^{39}Ar$ method uses the same principles applied in K/Ar dating, but instead of measuring K and Ar isotopes separately to track the radioactive decay of ^{40}K to radiogenic ^{40}Ar, the sample is irradiated in a nuclear reactor to transform part of the ^{39}K isotopes in the sample, which are stable, into ^{39}Ar isotopes, allowing for a single measurement of Ar isotopic ratios instead (relevant equations are shown and discussed below). Measuring a single aliquot and relying on isotopic ratios rather than absolute values respectively decreases potential errors due to sample and method inhomogeneities, improves accuracy and allows smaller samples to be analysed. During irradiation, ^{39}K is transmuted to ^{39}Ar, and since $^{40}K/^{39}K$ is constant in nature, $^{40}Ar/^{39}Ar$ is proportional to age. By relying on isotopic ratios from a single element, the technique also allows for an incremental heating approach when degassing the sample for the measurements, which allows for a detailed assessment of the distribution of Ar isotopic ratios within the sample, considering that different phases will degas at different temperatures, and higher temperatures will reach deeper into the crystals being measured. Assessing the distribution of Ar isotopic ratios within the sample also allows the identification of potential loss of radiogenic ^{40}Ar, such as through surface alteration, or excess ^{40}Ar from contamination by foreign material that may also degas at distinct temperatures (see below).

The half-life $t_{1/2}$ of a radioactive element is given by:

$$t_{\frac{1}{2}} = \frac{\ln 2}{\lambda} \tag{1}$$

and the simplest definition of the relationship between radioactive decay and age is given by:

$$N = N_0 \exp(-\lambda t)$$

(2)

where λ is the decay constant, N is the present quantity of a given radiogenic element in a sample, N_0 is the initial amount of the same element and t is the age (McDougall and Harrison, 1999). For ^{40}K, $\lambda = \lambda_\varepsilon + \lambda_{\beta^-}$, which results in $\lambda = 5.5305\ (\pm 0.0134) \times 10^{-10}\ a^{-1}$ (according to values from Renne *et al.*, 2011) and half-life = $1.253\ (\pm 0.002) \times 10^9$ a. However, ^{40}K has a dual decay to both ^{40}Ar and ^{40}Ca, and the value of λ also includes the decay to the latter. Therefore, only the proportion of ^{40}K decaying to ^{40}Ar must be considered when using the $^{40}Ar/^{39}Ar$ method for dating, which is 10.32% of the total ^{40}K (McDougall and Harrison, 1999).

The method also relies on the measurement of $^{39}Ar_K$ produced from ^{39}K during neutron irradiation, which will depend on the duration of irradiation, the neutron flux and the neutron capture cross section (i.e. the likelihood the irradiating neutron will trigger the desired reaction through which ^{39}K converts to ^{39}Ar). Accounting for both these issues is achieved by defining a dimensionless J parameter as:

$$J = \frac{^{39}K}{^{40}K} \frac{\lambda}{\lambda_e + \lambda'_e} \Delta \int \emptyset(E)\sigma(E)dE$$

(3)

where $\lambda_e + \lambda'_e$ are the decay constants for the proportion of ^{40}K that produces radiogenic ^{40}Ar during decay (dominated by electron capture as opposed to the electron emissions that characterise the formation of radiogenic ^{40}Ca), Δ is the duration of irradiation, $\phi(E)$ is the neutron flux at energy E and $\sigma(E)$ is the neutron capture cross section at energy E for the $^{39}K(n,p)^{39}Ar$ reaction. The details of all the relevant equations and their derivations are given in McDougall and Harrison (1999), with the final equation for the age t used in the $^{40}Ar/^{39}Ar$ method given as:

$$t = \frac{1}{\lambda} \ln\left(1 + J \frac{^{40}Ar*}{^{39}Ar_K}\right)$$

(4)

where ^{40}Ar* refers to radiogenic ^{40}Ar produced from ^{40}K decay. Given the difficulties in measuring precisely the relevant integrated fast-neutron dose that a sample receives during irradiation and which is required for determining *J*, a mineral of accurately know K/Ar age is also irradiated together with the sample of unknown age. Measurements from this standard sample then allow *J* to be calculated through the equation:

$$J = \frac{(\exp \lambda t) - 1}{^{40}Ar * / \, ^{39}Ar_K} \tag{5}$$

where *t* is the known age of the standard sample. The derivation of this last equation is also given in McDougall and Harrison (1999), but may be summarised simply as applying Equation 4 to a sample of know age in order to determine *J*.

Presentation of results

Results of ^{40}Ar/^{39}Ar analyses are presented in the form of three distinct diagrams: age spectrum, inverse isochron and age probability. The age spectrum diagram shows the relationship between ^{40}Ar/^{39}Ar for each incremental heating step and the amount of released ^{39}Ar. The inverse isochron diagram shows the relationship between ^{39}Ar/^{40}Ar and ^{36}Ar/^{40}Ar, which reflect the mixture of radiogenic and trapped Ar in the sample and is used to assess the composition of the trapped component. The latter is normally atmospheric in origin, but may also contain excess ^{40}Ar that can affect the age calculations and therefore has to be taken into account during the analyses. In addition, the slope in the inverse isochron diagram also reflects the age of the sample, which may be compared with results from the age spectrum diagram. The age probability spectrum shows the distribution of individual age results. Therefore, final results include both a plateau age from the age spectrum diagram and an inverse isochron age, both of which will be explained below. A value for the total integrated age in the age spectrum diagram is also given, which indicates the age for the total

degassing of the sample and not just the plateau steps. The latter age should be equivalent to an age obtained through the K/Ar method. Differences between the integrated age and the plateau age show potential biases in the total data. For example, the presence of xenoliths with older ages would lead to an older integrate age than the plateau age, whilst significant alteration could generate the opposite trend. Effects of Ar recoil (see below) also affect the integrated age.

Age spectrum diagram:

The age spectrum diagram illustrates the age, and by inference the $^{40}Ar^*/^{39}Ar_K$ ratio, for each heating step towards progressively higher temperatures, already corrected for atmospheric contamination and the production of interfering Ar isotopes generated during irradiation (see below). The measurement of persisting $^{40}Ar/^{39}Ar$ ratios that do not vary beyond potential error margins over several heating steps should indicate the dominant ratios in the sample and thereby reflect the closure temperature age. Secondary processes such as alteration or recoil are more likely to be irregular and not form recurrent $^{40}Ar^*/^{39}Ar$ ratios during incremental heating. A good result therefore is the characteristic 'plateaued' diagram of $^{40}Ar/^{39}Ar$ dating. Nonetheless, there are no fixed formulas for defining such plateau, and different studies may adopt slightly different criteria when deciding, for example, the amount of variability acceptable between heating steps, the number of heating steps with invariant $^{40}Ar/^{39}Ar$ ratios, the proportion of ^{39}Ar release that each step or the plateau as a whole must represent, etc. (McDougall and Harrison, 1999; Koppers *et al.*, 2000). Plateau criteria are interpretation guidelines, and some flexibility is warranted when applying them. For example, a common criterion is that plateaus should represent at least 50% of the total released ^{39}Ar, but some studies have demonstrated how meaningful ages may be obtained at lower thresholds (Koppers *et al.*, 2000, 2003), especially in the case of fine-grained basaltic rocks. Our own criteria will be given below but, accordingly, failing such criteria does not lead

necessarily to an immediate rejection of the sample, but instead a more thorough inspection of it.

The age spectrum diagram also tracks the proportion of radiogenic ^{40}Ar and K/Ca ratios being released during each heating step. This information helps distinguishing the types of phases that are producing the results of each step (i.e. K-rich vs Ca-rich) and if the total ^{40}Ar being released doesn't simply reflect non-radiogenic atmospheric content. This information may also be useful in detecting the effects of alteration. Although efforts are made to purify the samples to a high degree, potential alteration material may still lie along crystal surfaces, fractures or, in the case of groundmass, altered glass domains. This material is dominated by phyllosilicates and, if present, will readily breakdown during early heating steps, producing younger ages than the rest of the rock that should also coincide with high K/Ca and low proportion of radiogenic ^{40}Ar.

Inverse isochron

The inverse isochron illustrates the relationship between $^{40}Ar/^{39}Ar$, which is used to calculate age, and $^{40}Ar/^{36}Ar$, which is used to track the isotopic Ar composition of the trapped component in the sample and may also be used to identify excess ^{40}Ar (i.e. a trapped $^{40}Ar/^{36}Ar$ component that is above atmospheric values). This relationship is illustrated through their inverse ratios so it doesn't extend to infinity and uses ^{40}Ar, the more precisely measured of the three relevant isotopes, as the denominator on both axes (McDougall and Harrison, 1999). It also allows the *y*-intercept (i.e. *y*-axis being $^{36}Ar/^{40}Ar$) to indicate the value of the trapped component (i.e. when $^{39}Ar/^{40}Ar = 0$), whilst the *x*-intercept indicates the age based on the isochron best-fitting line. The data presented in the isochron is already corrected for irradiation-induced interferences that are listed in Appendix B. Therefore, calculations assume that all ^{36}Ar is atmospheric, and, ideally, the trapped component should represent atmospheric values, for which $^{40}Ar/^{36}Ar$ ratios are well known, to show that Ar degassing and full equilibration with the

atmosphere has been reached during eruption. In this case, all ^{40}Ar beyond atmospheric values should have been produced through the radioactive decay of ^{40}K since the closure temperature has been reached. The measurement of ^{36}Ar abundances in a sample also allows for a precise correction (i.e. subtraction) of the trapped component (i.e. the ^{40}Ar associated with it) during age calculations, given our knowledge of atmospheric $^{40}Ar/^{36}Ar$ ratios. An intercept indicating $^{40}Ar/^{36}Ar$ ratios above atmospheric values indicates the presence of excess ^{40}Ar, which may come from mantle xenoliths or melt inclusions. It can potentially distort the final results towards older ages, and therefore has to be considered. Sometimes, $^{40}Ar/^{36}Ar$ values in volcanic rocks are somewhat below those of the current atmosphere. The reasons for this are not fully understood, but it has been suggested that equilibration of the lava's Ar content with atmospheric values prior (e.g. through interaction with percolating surface fluids) or during eruption also involves some mass fractionation that leads to somewhat low $^{40}Ar/^{36}Ar$ (McDougall and Harrison, 1999). On rare occasions, kinetic effects such as outgassing can also yield values below atmospheric ones, but differences are generally small. However, in most cases, intercept values reflecting $^{40}Ar/^{36}Ar$ ratios below atmospheric values are caused by artifacts in the data.

Age probability spectrum

Age probability spectrum diagrams show the same data as those presented in the age spectrum diagrams, and as such are already corrected for atmospheric contamination and irradiation-induced interferences, but they do not consider the sequential order of heating steps. The distribution of individual age results helps calculating the probability that the final result represents the most likely age for the sample, and may be used to assess the significance of the age obtained in the age spectrum diagram. It also allows the identification of distinct age peaks that may indicate distinct age populations and thereby specific geological phenomena. The latter may result from analytical artefacts, but can also potentially indicate the presence

of xenoliths or other grains with distinct ages from the host rock. These diagrams show two distribution spectra superimposed, one for all the data (dotted line), and another representing a coherent population (solid line).

Uses and problems of distinct Ar isotopes formed during irradiation

During irradiation, Ar isotopes are produced through interaction with Ca and K atoms, namely ^{36}Ar, ^{37}Ar, ^{39}Ar and ^{40}Ar. Interaction with Cl also produces ^{38}Ar and ^{36}Ar, although interference cause by the latter daughter isotope is often insignificant. However, Cl interference may become an issue in Cl-rich samples or when there is a long delay (~1 year) between irradiation and analyses, due to the relatively slow decay of ^{36}Cl to ^{36}Ar (McDougall and Harrison, 1999). All the other Ar isotopes always have to be accounted for during calculations. For instance, $^{39}Ar_{Ca}$ cannot be confused with $^{39}Ar_K$, and $^{36}Ar_{Ca}$ and $^{37}Ar_{Ca}$ are used for specific corrections during analysis that affect the final determination of $^{40}Ar_K/^{39}Ar_K$ ratios. $^{37}Ar_{Ca}$ is used to measure the amount of $^{39}Ar_{Ca}$ being produced, since they are produced at constant ratios, in order for $^{39}Ar_{Ca}$ to be subtracted from $^{39}Ar_K$. Because $^{40}Ar/^{36}Ar$ is a constant ratio in the atmosphere ($^{40}Ar/^{36}Ar = 298.6$; Lee et al., 2006), ^{36}Ar is used to calculate the amount of atmospheric ^{40}Ar present in the sample, so it can be distinguished from radiogenic ^{40}Ar. Therefore, $^{36}Ar_{Ca}$ also needs to be accounted for to avoid overcorrections of atmospheric ^{40}Ar during measurements. The relevance of tracking the amounts of all Ar isotopes produced specifically by the transmutation of Ca during irradiation are made clear in the formulas used for calculating radiogenic ^{40}Ar (Jourdan and Renne, 2013):

$$^{40}Ar* = {}^{40}Ar_m - {}^{39}Ar_K\left(\frac{^{40}Ar}{^{39}Ar}\right)_K - \left(\frac{^{40}Ar}{^{36}Ar}\right)_{atm}\left[{}^{36}Ar_m - {}^{37}Ar_{Ca}\left(\frac{^{36}Ar}{^{37}Ar}\right)_{Ca}\right] \quad (6)$$

where $^{40}Ar^*$ is radiogenic ^{40}Ar, *m* denotes measured, $(^{40}Ar/^{39}Ar)_K$ is the production ratio of K and $(^{40}Ar/^{39}Ar)_{atm}$ is the atmospheric composition of Ar.

The calculation of $^{39}Ar_K$, also according to Jourdan and Renne (2013), is given by:

$$^{39}Ar_K = {}^{39}Ar_m - {}^{37}Ar_{Ca}\left(\frac{^{39}Ar}{^{37}Ar}\right)_{Ca} \quad (7)$$

where $^{39}Ar_K$ is the ^{39}Ar produced from ^{39}K, $^{39}Ar_m$ is the total ^{39}Ar measured, and $^{37}Ar_{Ca}$ is the total ^{37}Ar measured and corrected according to its radioactive decay since irradiation (i.e. ^{37}Ar has a half-life of 35.1 days; ibid.).

^{39}Ar and ^{37}Ar recoil

The equations above show how errors in the measurements of interfering Ar isotopes can lead to errors in determining $^{40}Ar/^{39}Ar$. More specifically, they expose the method's susceptibility to the problems of Ar loss or redistribution through recoil during irradiation (Onstott *et al.*, 1995; McDougall and Harrison, 1999; Jourdan *et al.*, 2007; Jourdan and Renne, 2013). In other words, the atoms hit by the neutron bombardment move (recoil) as a result of the neutron flux energy and the energy of the subsequent reaction. This issue is particularly relevant when analysing fine-grained groundmass where recoil distances may approach crystal sizes (Koppers *et al.*, 2000; Jourdan *et al.*, 2007), and therefore relevant to our results.

The formation of ^{37}Ar and ^{39}Ar through neutron bombardment during irradiation is accompanied by omnidirectional recoil of the product isotopes. The same happens to ^{36}Ar, but the effects are much more subdued (Jourdan *et al.*, 2007). In addition to the recoil itself, differences in recoil distance between different Ar isotopes may distort their ratios even further. Loss or redistribution of Ar isotopes creates a depleted layer around the edge of the crystal. The thickness of this layer is dependent on recoil distances, which in turn vary between different isotopes and according to mineral phases. For silicates, it has been calculated as ~0.07-0.09 μm for ^{39}Ar (Jourdan et al.,

2007; Jourdan and Renne, 2013; McDougall and Harrison, 1999), and 3.3 ± 0.4 μm for ^{37}Ar in Ca-rich silicates (Jourdan and Renne, 2013). The latter is substantially larger and shows that the effects of ^{37}Ar loss may be more significant for dating basaltic groundmass than ^{39}Ar loss. The reasons for such disparity in the behaviour of the two isotopes is not yet understood (Jourdan and Renne, 2013). These effects will increase for finer textures. They start to become an issue for crystals ≤ 50 μm (Jourdan and Renne, 2013), but do not greatly affect larger sizes. Such scales, however, certainly affect cryptocrystalline textures, and may also have an effect on microcrystalline granularity.

A common effect of recoil redistribution is the association of older ages with high K/Ca ratios during early heating steps (lower temperatures), and a drop in the apparent age and K/Ca ratios at later heating steps (higher temperatures), because ^{39}Ar may get redistributed during irradiation from low temperature to high temperature phases (McDougall and Harrison, 1999; Koppers *et al.*, 2000). The result is an increase in $^{40}Ar/^{39}Ar$ ratios and apparent older ages during the early heating steps, and a decrease in $^{40}Ar/^{39}Ar$ ratios and apparent younger ages in later heating steps, creating a spurious age spectrum. Conversely, recoil loss of ^{39}Ar directly affects $^{40}Ar/^{39}Ar$ measurements, leading to overall older ages in the affected phases. The loss of ^{37}Ar will lead to an over-correction of the trapped ^{40}Ar component due to an under-correction of $^{39}Ar_{Ca}$, leading to apparently younger ages (Equations 1 and 2), especially amongst Ca-rich phases. Such effects may produce progressively younger ages at later heating steps, as Ca-rich phases tend to degas at higher temperatures. The similar effects of ^{39}Ar redistribution and ^{37}Ar loss (i.e. progressively younger ages at higher heating steps) are difficult to disentangle from one another and a clear, widely tested mechanism for that is not yet available.

Although attempts have been made to design correction mechanisms for this problem (Jourdan *et al.*, 2007; Jourdan and Renne, 2013), the complexity of polymineralic, crypto- to microcrystalline, Ca-rich basaltic

groundmass is a major obstacle. For example, it is difficult to calculate how much recoiled material is redistributed or lost, and many of the correction calculations rely on knowing the dimensions and volume of groundmass crystals, which are difficult to generalise. Therefore, problems of recoil persist, and need to be accounted for when dealing with $^{40}Ar/^{39}Ar$ analyses of basaltic groundmass. Although these effects must be kept in mind when interpreting the groundmass results from the MQVL and Mecejana volcanic field, reliable groundmass ages for basalts and other compositions were still obtained.

Analyses

Sample selection

Twelve basaltic samples from the MQVL and seven phonolites from the Mecejana volcanic field were selected for dating. An attempt was made to select localities previously not dated by $^{40}Ar/^{39}Ar$, although there is still some overlap with previous chronological work in the MQVL that allows for comparisons with previously published ages (Silveira, 2006; Knesel *et al.*, 2011; Souza *et al.*, 2013). Textural and locality details for all samples are given in Table 1-1 in Chapter 1, where those selected for $^{40}Ar/^{39}Ar$ dating have been highlighted. A map showing their distribution is also given in Chapter 1 (Figure 1-4).

The MQVL basaltic samples analysed came from the São Pedro volcanic neck (15BP1-1), Queimadas lava field (15BP3-2), Juá quarry in the Boa Vista basin (15BP3-3b), Cubati basin (15BP3-5), the outskirts of Nova Palmeira village near Picuí (15BP4-6), Saco do Inferninho peak (15BP4-7), Socavão plug (15BP5-8), Carnaubinha plug (15BP5-9), Serrote Preto plug (15BP5-10), the onshore section of the Potiguar basin at the oceanic-continental boundary (15BP7-14), the nephelinite plug from the Serra Preta near Pedro Avelino (15BP7-15) and the plug from the Serra Preta near Cerro Corá (15BP12-26). These were selected in an attempt to both extend the

spatial distribution covered by currently available $^{40}Ar/^{39}Ar$ dates along the MQVL and to include new localities along segments of the lineament that were already dated by this technique. Some overlap with previous studies was allowed where comparisons were desirable. Nevertheless, sample selection was also constrained by sample quality and geochemical representativeness, which were assessed through thin-section examinations and geochemical analyses (Chapter 3). The Mecejana phonolite samples analysed were from the Caruru quarry (15BP9-19a and 15BP9-19c), Ancurí quarry (15BP10-20), Pão de Açucar neck (15PB10-21a and 15BP10-21b), Japarara plug (15BP10-22) and Salgadinho neck (15BP10-23). They represent all sampled localities in Mecejana and offer a substantial set of $^{40}Ar/^{39}Ar$ dates for an area that previously lacked them.

The group of MQVL samples located in the space between and including the continental edges of the Potiguar basin to the north, and the area around the João Câmara shear zone (JCSZ) to the south will be referred to as the central segment of the MQVL (Figure 2-1). The group includes all MQVL samples north of the town of Picuí except for sample 15BP7-14. The latter lies in the oceanic-continental boundary (OCB) virtually on the shore and is the sole representative of what will be referred to as the northern segment of the MQVL. All samples south of the JCSZ and of Picuí will be referred to as the the southern segment of the MQVL.

Material selection

Both groundmass and sanidine phenocrysts were used in the analyses. All MQVL ages were obtained from groundmass measurements. In Mecejana, all localities were dated through sanidine phenocrysts, but most of them were also accompanied by groundmass measurements, sometimes from the same hand specimen. Therefore, all sampled Mecejana localities are represented by at least one age measurement, sometimes two. When two samples come from the same hand specimen, the letter suffix to the sample code is between brackets. Conversely, the letter suffix is without

brackets if the samples represent two distinct hand specimens but come from the same locality.

There are distinct issues related to $^{40}Ar/^{39}Ar$ dating of groundmass grains or monomineralic phenocryst separates. Single mineral aliquots will behave similarly throughout the step heating stages, but polymineralic grains are likely to degas at different steps due to the different thermal stability ranges of each mineral. This may trigger specific effects such as ^{39}Ar redistribution (see above) or ^{37}Ar loss amongst Ca-rich phases. There is also a marked difference in crystal sizes between groundmass or phenocryst aliquots. Although different minerals and crystal sizes will all have the same age in a rapidly cooling volcanic rock, they will react differently to the effects of recoil loss and redistribution (see above), as well as atomic diffusion that may also cause some Ar loss (McDougall and Harrison, 1999).

Glass content in the groundmass is also a significant variable in the quality of the $^{40}Ar/^{39}Ar$ age data. Any phase in a glass matrix will be so small that the effects of Ar loss and redistribution due to recoil will be significant. For example, crystals < 5 μm may be subject to > 98% ^{37}Ar loss during irradiation (Jourdan *et al.*, 2007). Groundmass containing high proportions of glass domains and/or devitrified material may also be more susceptible to alteration, such as the breakdown to palagonite (Gill, 2010).

Although K-feldspar phenocrysts provide the ideal material for $^{40}Ar/^{39}Ar$ dating, basaltic samples in our assemblage could only be represented by groundmass grains. Despite efforts to avoid altered samples and favour coarser groundmass textures, hypo- and cryptocrystalline textures could not be fully avoided in our assemblage, despite these samples potentially hiding altered domains and their very small crystal sizes. Nonetheless, we have obtained robust results.

Sample preparation and analyses criteria

Groundmass grains were obtained by crushing the samples to a size of 250-500 μm, leaching them in nitric acid (25% dilute HNO_3), using

repeated runs of magnetic separation in order to separate phenocrysts (i.e. mainly olivine and clinopyroxene in the case of basaltic samples, and mainly aegirine and amphibole in the case of phonolite samples), and finally handpicking grains free of phenocrysts for groundmass measurements, or sanidine phenocrysts for the sanidine measurements. Detailed methods of sample preparation are given in Appendix A. The selected size range should make the effects of recoil negligible amongst the sanidine phenocrysts, according to published recoil distances in silicate structures (Onstott *et al.*, 1995; McDougall and Harrison, 1999; Jourdan *et al.*, 2007; Jourdan and Renne, 2013).

All samples were irradiated in the Oregon State University reactor. Fish Canyon sanidine (28.294 ± 0.036 Ma at 1σ; Renne et al. 2011)[1] was used to monitor ^{39}Ar production and establish neutron flux (*J*) values. All gas measurements were made via step-heating using a CO_2 laser with a 3.5 mm beam diameter and data collected on a GVi Instruments ARGUS V multi-collector mass spectrometer. Each step of the step heating process of an individual sample is identified with a letter. More detailed analytical methods are given in Appendix A.

Inverse-variance-weighted plateau ages were chosen as the best estimates of the emplacement ages. Plateau age criteria include a minimum of three contiguous steps overlapping in age within 2σ uncertainty and together representing a minimum of 50% of released ^{39}Ar, with each step representing ≥ 0.1% of total ^{39}Ar. Plateau steps should also have an indistinguishable inverse isochron age within 2σ uncertainty and a trapped component composition derived from the inverse isochron indistinguishable from current atmospheric values (298.6 ± 0.31; Lee et al., 2006) at 2σ uncertainty. Consistency between the plateau and isochron ages when there is no excess ^{40}Ar reinforces the validity of both ages. More detailed criteria are given in Appendix A.

[1] In reference to Renne et al. (2010) and Schwarz et al. (2011).

Results

Results are illustrated in Figures 2-1 and 2-2, the latter giving the age spectrum, inverse isochron and age probability spectrum for each sample, and summarised in Tables 2-1 and 2-2. A full table of all results, including *J* values, is given in Appendix B. The complete raw dataset for the $^{40}Ar/^{39}$ Ar ages, obtained during measurements, is given in Appendix F, which is presented in the Volume 2of 2 of this thesis. Some samples provided a reliable age with a single run of measurements, but in some cases two or three runs were conducted. All ages are given as millions of years (Ma). Unfortunately, samples 15BP1-1, 15BP4-6, 15BP4-7 and 15BP12-26 did not produce resolvable ages. As a result, volcanic occurrences in the southern segment of the MQVL that are not related to the local extensional basins are still not dated by the $^{40}Ar/^{39}Ar$ method.

All sanidine phenocrysts and some groundmass samples for both basalt and phonolite produced very robust age results. Other groundmass samples showed variable effects of alteration and recoil loss or redistribution that in some cases led to no resolvable age (see aforementioned samples). However, recoil effects do not necessarily compromise a sample and meaningful ages can be obtained (Koppers *et al.*, 2000), and some of our samples demonstrate that. Despite the effects of alteration and/or recoil loss or redistribution amongst some groundmass samples, some of them still fall within our plateau criteria and show remarkably consistent ages with the remaining assemblage and other published ages (Silveira, 2006; Knesel *et al.*, 2011; Souza *et al.*, 2013).

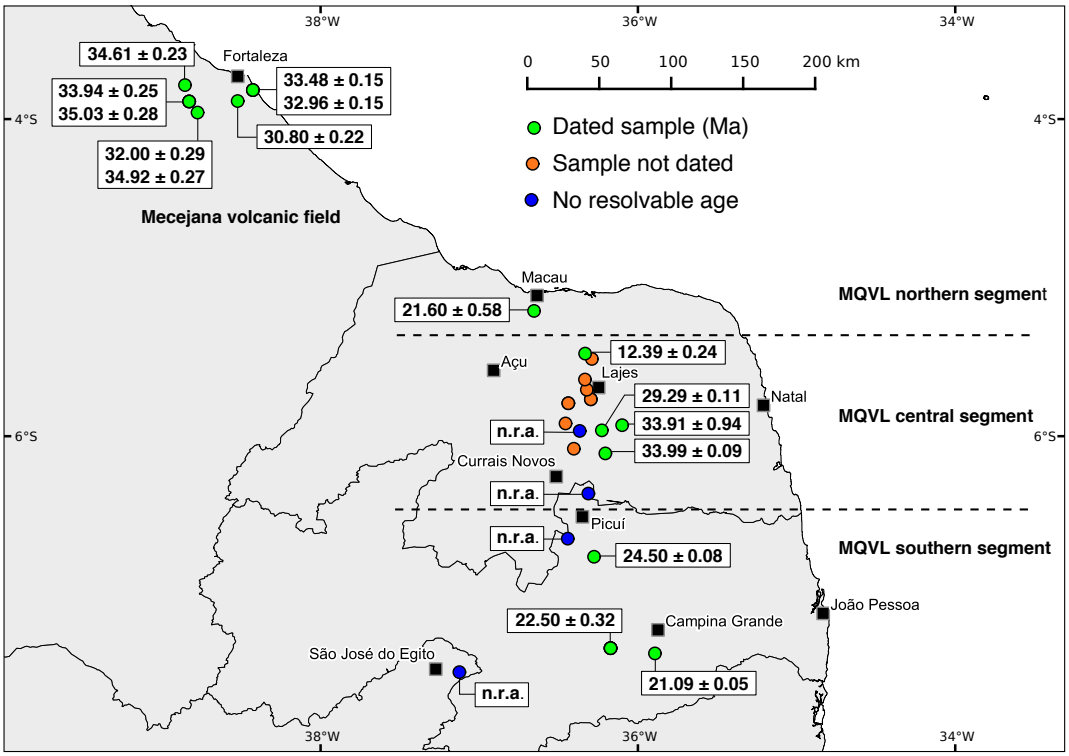

Figure 2-1: Map of sample distribution highlighting the dated samples and their age results in Ma. The map also shows the division of the MQVL into its northern, central and southern segments. *n.r.a = no resolvable age*.

Table 2-1: $^{40}Ar/^{39}Ar$ age results for basaltic rocks from the MQVL. Plateau ages are considered the best results for the region, and the accepted ages are given in bold. Ages in bold (i.e. accepted ages) are the only ones shown in the following figures. *Mat.* = material; *g.m.* = *groundmass; n.p. = no plateau; MSWD = mean square weighted deviation; n = number of heating steps in age plateau; $n_{tot.}$ = total number of heating steps; (i) = intercept; *comments on main text.*

Sample	Run ID	Mat.	Plateau Age (Ma) ±2σ	MSWD	n	$n_{tot.}$	Steps	$\%^{39}Ar$ release	Integrated age (Ma) ± 2σ	Trapped $^{40}Ar/^{36}Ar$	Isochron age (Ma) ± 2σ	MSWD	$^{40}Ar/^{36}Ar(i)$ ± 2σ	Status
15BP1-1	92902-1	g.m.	n.p.						30.8 ± 2.6	298.6		164.1		no resolvable age
15BP1-1	92902-2	g.m.	n.p.						30.9 ± 1.7	298.6				
15BP1-1	92902-1 92902-2	g.m.	n.p.						30.8 ± 1.3	298.6				
15BP3-2	92900-1	g.m.	**21.09 ± 0.05**	1.8	9	12	g-o	82,0	21.1 ± 0.2	298.6	20.87 ± 0.22	1.0	432.9 ± 139.9	accepted age
15BP3-3b	92897-1	g.m.	n.p.						30.4 ± 5.6	298.6				*see text for comments on accepted age
15BP3-3b	92897-1	g.m.	**22.50 ± 0.32**	1,0	9	14	g-o	56.3	25.0 ± 3.8	**562.5**	22.50 ± 2.65	1.2	562.5 ± 169.4	
15BP3-3b	92897-2	g.m.	n.p.						29.6 ± 4.8	298.6				
15BP3-5	92912-1	g.m.	**24.50 ± 0.08**	1.1	6	14	e-j	75.4	24.4 ± 0.5	298.6	24.55 ± 0.11	1.0	282.1 ± 27.6	accepted age
15BP4-6	92910-1	g.m.	n.p.						75.0 ± 14	298.6		165		no resolvable age
15BP4-6	92910-2	g.m.	n.p.						72.8 ± 9.1	298.6		79		
15BP4-7	92907-1	g.m.	n.p.						32.1 ± 2.3	298.6		1221		no resolvable age
15BP4-7	92907-2	g.m.	n.p.						31.4 ± 1.5	298.6		263		
15BP5-8	92905-1	g.m.	34.01 ± 0.47	4.1	6	14	b-g	70.7	33.4 ± 2.0	298.6	34.00 ± 0.10	5.0	300.2 ± 3.7	*see text for comments on accepted age
15BP5-8	92905-2	g.m.	**33.99 ± 0.09**	1.2	12	21	b-m	68.5	32.9 ± 1.9	298.6	33.97 ± 0.08	1.0	301.2 ± 3.2	
15BP5-8	92905-all plat. steps	g.m.	34.00 ± 0,17	2.1	17	18	b-m	99.8	34.0 ± 0.2	298.6	33.98 ± 0.07	1.9	300.8 ± 2.4	
15BP5-9	92922-2	g.m.	**33.91 ± 0.94**	1.3	8	22	m-t	58.1	35.2 ± 4.1	298.6	33.51 ± 1.67	1.5	315.1 ± 59.8	accepted age

Table 2-1 (cont.)

Sample	Run ID	Mat.	Plateau Age (Ma) ±2σ	MSWD	n	$n_{tot.}$	Steps	%^{39}Ar release	Integrated age (Ma) ± 2σ	Trapped ^{40}Ar/^{36}Ar	Isochron age (Ma) ± 2σ	MSWD	^{40}Ar/^{36}Ar(i) ± 2σ	Status
15BP5-10	93274-1	g.m.	**29.29 ± 0.11**	0.9	9	22	i-q	51.4	28.9 ± 0.5	298.6	29.15 ± 0.19	0.6	325.4 ± 31.3	accepted age
15BP7-14	92920-2	g.m.	**21.60 ± 0.58**	2.4	7	22	a-g	42.5	21.0 ± 0.8	298.6	21.45 ± 0.24	2.2	302.6 ± 4.4	accepted age despite somewhat high MSWD
15BP7-15	93281-1	g.m.	**12.39 ± 0.24**	1.2	18	22	e-v	88.5	12.36 ± 0.84	298.6	12.50 ± 0.29	12	297.2 ± 2.1	accepted age
15BP12-26	93282-1	g.m.	n.p.						25.63 ± 0.87	298.6				no resolvable age

Table 2-2: ^{40}Ar/^{39}Ar age result for phonolites from the Mecejana Volcanic Field. Plateau ages are considered the best results for the region, and the accepted ages are given in bold. Sample code letter suffixes between brackets indicate two samples from the same hand specimen. Letter suffixes without brackets indicate samples from the same locality but not the same hand specimen. Ages for sample 15BP10-20(a) have all been rejected. *Mat.* = material; *g.m. = groundmass; n.p. = no plateau; MSWD = mean square weighted deviation; n = number of heating steps in age plateau; $n_{tot.}$ = total number of heating steps; (i) = intercept; *comments on main text*.

Sample	Run ID	Mat.	Plateau Age (Ma) ±2σ	MSWD	n	n_{tot}	Steps	%^{39}Ar release	Integrated age (Ma) ± 2σ	Trapped ^{40}Ar/^{36}Ar	Isochron age (Ma) ± 2σ	MSWD	^{40}Ar/^{36}Ar(i) ± 2σ	Status
15BP9-19a	92917-1	Snd.	**33.48 ± 0.15**	1.2	16	18	d-s	97.7	33.4 ± 0.3	298.6	33.57 ± 0.14	1.0	263.8 ± 36.5	accepted age
15BP9-19c	92916-1	g.m.	32.88 ± 0.15	1,0	7	18	f-l	54.4	32.9 ± 0.4	298.6	33.21 ± 0.20	1.1	249.5 ± 26.4	*see text for comments on accepted age
15BP9-19c	92916-2	g.m.	**32.96 ± 0.15**	1.3	13	22	h-t	72.1	32.9 ± 0.4	298.6	32.97 ± 0.16	1.4	297.4 ± 16.4	
15BP9-19c	92916-all plat. steps	g.m.	32.92 ± 0.16	1.7	20	20	f-t	100	32.9 ± 0.1	298.6				

Table 2-2 (cont.)

Sample	Run ID	Mat.	Plateau Age (Ma) ±2σ	MSWD	n	n_{tot}	Steps	%^{39}Ar release	Integrated age (Ma) ± 2σ	Trapped ^{40}Ar/^{36}Ar	Isochron age (Ma) ± 2σ	MSWD	^{40}Ar/^{36}Ar(i) ± 2σ	Status
15BP10-20(a)	92915-1	g.m.	24.65 ± 0.15	2,0	6	14	j-o	40.6	25.2 ± 1.4	298.6	25.89 ± 1.27	2.0	215.6 ± 87.7	ages rejected
15BP10-20(a)	92915-2	g.m.	24.50 ± 0.15	1.9	5	22	r-v	26.1	25.2 ± 1.3	298.6	27.29 ± 1.25	0.8	109.4 ± 80.3	
15BP10-20(a)	92915-all plat. steps	g.m.	24.57 ± 0.21	3.3	11	11	j-v	100	24.6 ± 0.2	298.6				
15BP10-20(b)	92944-1	Snd.	**30.80 ± 0.22**	1.6	10	19	g-p	67.1	34.0 ± 0.5	298.6	31.22 ± 0.33	1.0	261.6 ± 26	accepted age
15BP10-21a	92943-1	Snd.	**33.94 ± 0.25**	1.4	8	18	f-m	71,0	34.0 ± 0.5	298.6	33.98 ± 0.27	1.7	292.4 ± 23.9	accepted age
15BP10-21b	92942-1	Snd.	**35.03 ± 0.28**	1.4	16	18	d-s	96.2	35.0 ± 0.2	298.6	35.03 ± 0.24	1.5	294.8 ± 58.6	accepted age
15BP10-22(a)	92939-1	g.m.	**32.00 ± 0.29**	1.8	7	14	i-o	53.7	32.3 ± 0.7	298.6	32.13 ± 0.65	1.9	291.7 ± 31.2	accepted age
15BP10-22(a)	92939-2	g.m.	31.81 ± 0.29	1.6	6	21	q-v	52,0	32.3 ± 0.7	298.6	31.01 ± 1.20	1.3	341.2 ± 61.8	
15BP10-22(a)	92939-all plat. steps	g.m.	31.92 ± 0.33	2.8	13	13	i-v	100	31.9 ± 0.3	298.6				
15BP10-22(b)	92937-1	Snd.	35.43 ± 0.27	2,0	8	18	g-n	48.1	36.3 ± 1.6	298.6	34.92 ± 0.41	0.5	411.4 ± 80.1	*see text for comments on accepted age
15BP10-22(b)	92937-1	Snd.	**34.92 ± 0.27**	0.4	8	18	g-n	48.1	35.7 ± 1.3	**411.4**				
15BP10-23	92936-2	Snd.	**34.61 ± 0.23**	1.5	12	15	ca-n	91.9	34.6 ± 0.2	298.6	34.62 ± 0.17	1.6	293.8 ± 17.6	accepted age

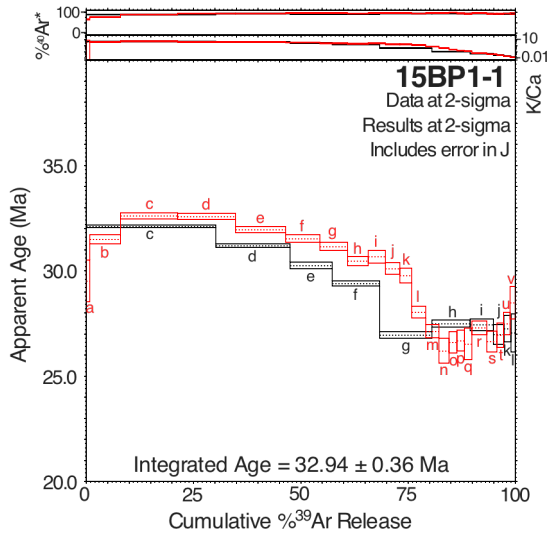
15BP1-1
Data at 2-sigma
Results at 2-sigma
Includes error in J
Integrated Age = 32.94 ± 0.36 Ma
Apparent Age (Ma)
Cumulative %39Ar Release
%40Ar*
K/Ca

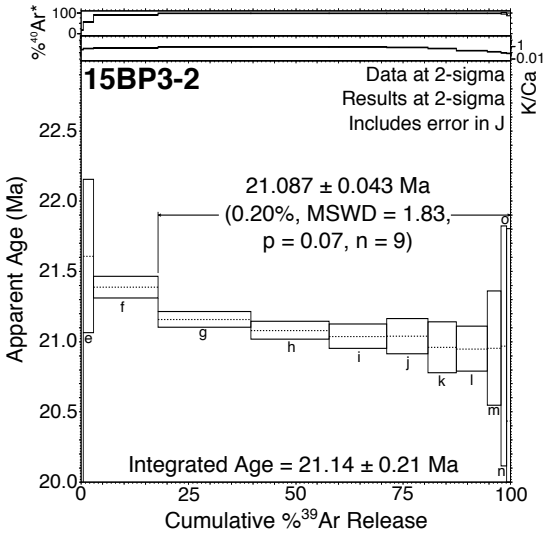
15BP3-2
Data at 2-sigma
Results at 2-sigma
Includes error in J
21.087 ± 0.043 Ma
(0.20%, MSWD = 1.83,
p = 0.07, n = 9)
Integrated Age = 21.14 ± 0.21 Ma
Apparent Age (Ma)
Cumulative %39Ar Release
%40Ar*
K/Ca

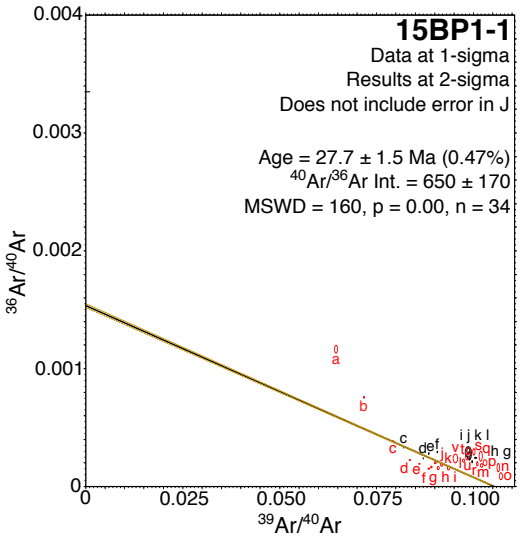
15BP1-1
Data at 1-sigma
Results at 2-sigma
Does not include error in J
Age = 27.7 ± 1.5 Ma (0.47%)
40Ar/36Ar Int. = 650 ± 170
MSWD = 160, p = 0.00, n = 34
36Ar/40Ar
39Ar/40Ar

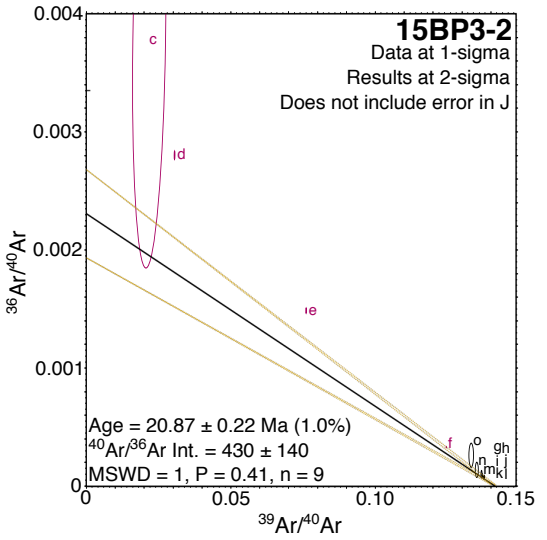
15BP3-2
Data at 1-sigma
Results at 2-sigma
Does not include error in J
Age = 20.87 ± 0.22 Ma (1.0%)
40Ar/36Ar Int. = 430 ± 140
MSWD = 1, P = 0.41, n = 9
36Ar/40Ar
39Ar/40Ar

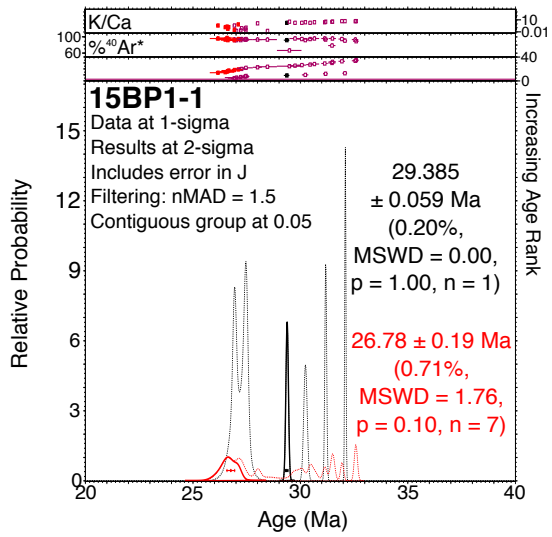
15BP1-1
Data at 1-sigma
Results at 2-sigma
Includes error in J
Filtering: nMAD = 1.5
Contiguous group at 0.05
29.385
± 0.059 Ma
(0.20%,
MSWD = 0.00,
p = 1.00, n = 1)
26.78 ± 0.19 Ma
(0.71%,
MSWD = 1.76,
p = 0.10, n = 7)
Relative Probability
Age (Ma)
Increasing Age Rank
K/Ca
%40Ar*

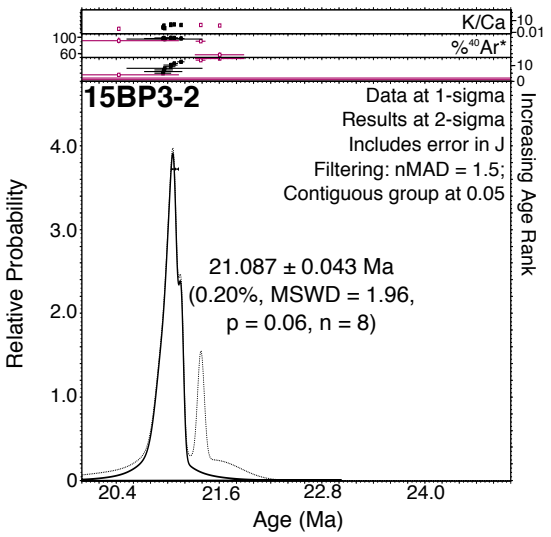
15BP3-2
Data at 1-sigma
Results at 2-sigma
Includes error in J
Filtering: nMAD = 1.5;
Contiguous group at 0.05
21.087 ± 0.043 Ma
(0.20%, MSWD = 1.96,
p = 0.06, n = 8)
Relative Probability
Age (Ma)
Increasing Age Rank
K/Ca
%40Ar*

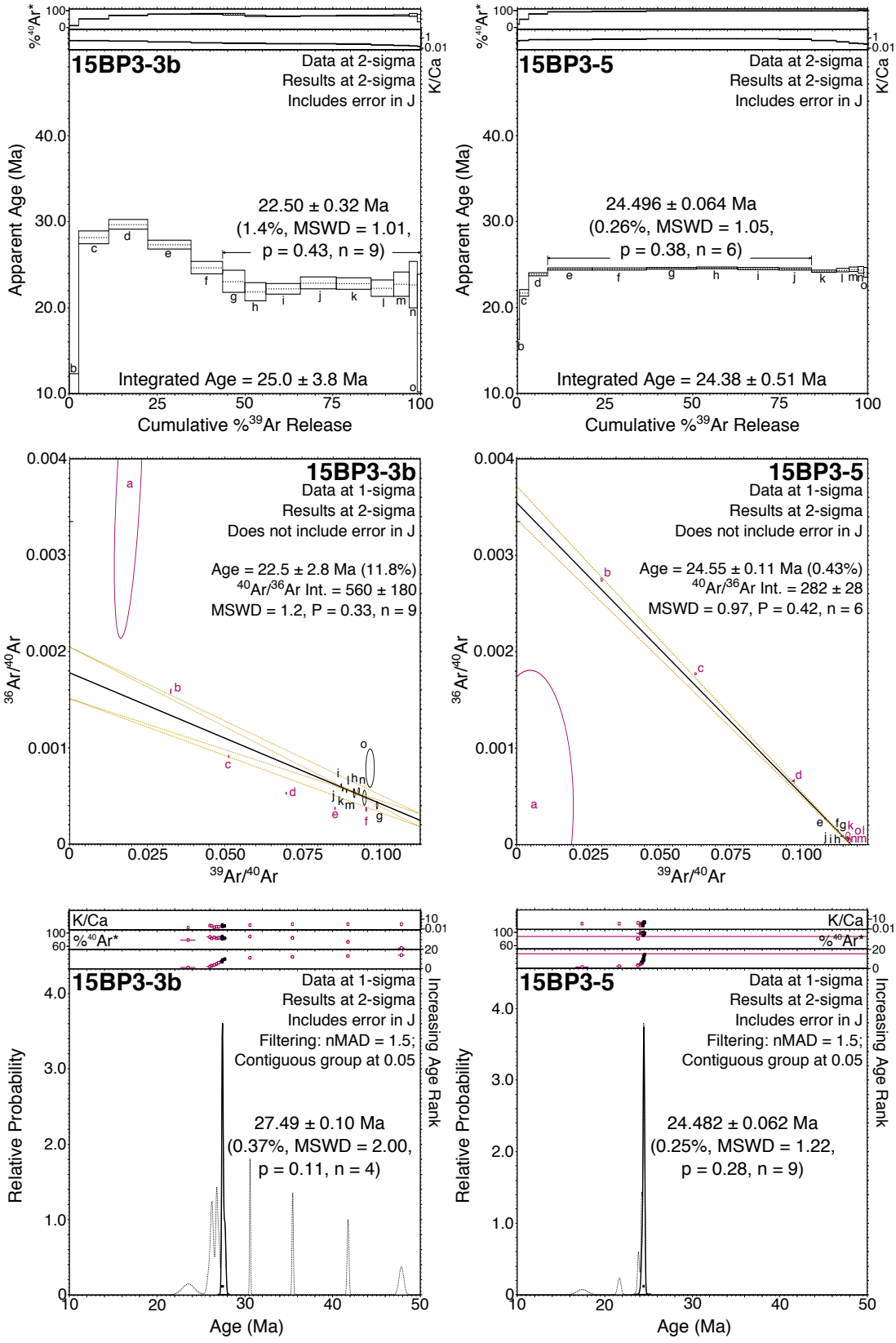
15BP3-3b
Data at 2-sigma
Results at 2-sigma
Includes error in J
22.50 ± 0.32 Ma
(1.4%, MSWD = 1.01,
p = 0.43, n = 9)
Integrated Age = 25.0 ± 3.8 Ma
Apparent Age (Ma)
Cumulative %39Ar Release
%40Ar*
K/Ca
15BP3-5
Data at 2-sigma
Results at 2-sigma
Includes error in J
24.496 ± 0.064 Ma
(0.26%, MSWD = 1.05,
p = 0.38, n = 6)
Integrated Age = 24.38 ± 0.51 Ma
Apparent Age (Ma)
Cumulative %39Ar Release
%40Ar*
K/Ca
15BP3-3b
Data at 1-sigma
Results at 2-sigma
Does not include error in J
Age = 22.5 ± 2.8 Ma (11.8%)
40Ar/36Ar Int. = 560 ± 180
MSWD = 1.2, P = 0.33, n = 9
36Ar/40Ar
39Ar/40Ar
15BP3-5
Data at 1-sigma
Results at 2-sigma
Does not include error in J
Age = 24.55 ± 0.11 Ma (0.43%)
40Ar/36Ar Int. = 282 ± 28
MSWD = 0.97, P = 0.42, n = 6
36Ar/40Ar
39Ar/40Ar
15BP3-3b
Data at 1-sigma
Results at 2-sigma
Includes error in J
Filtering: nMAD = 1.5;
Contiguous group at 0.05
27.49 ± 0.10 Ma
(0.37%, MSWD = 2.00,
p = 0.11, n = 4)
Relative Probability
Age (Ma)
K/Ca
%40Ar*
Increasing Age Rank
15BP3-5
Data at 1-sigma
Results at 2-sigma
Includes error in J
Filtering: nMAD = 1.5;
Contiguous group at 0.05
24.482 ± 0.062 Ma
(0.25%, MSWD = 1.22,
p = 0.28, n = 9)
Relative Probability
Age (Ma)
K/Ca
%40Ar*
Increasing Age Rank

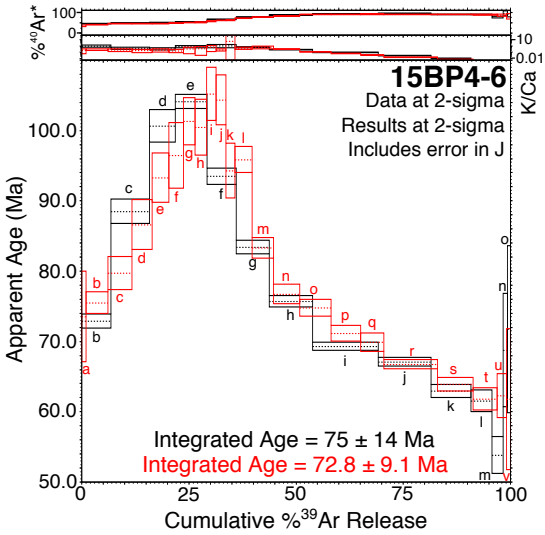
15BP4-6
Data at 2-sigma
Results at 2-sigma
Includes error in J
Integrated Age = 75 ± 14 Ma
Integrated Age = 72.8 ± 9.1 Ma
Apparent Age (Ma)
Cumulative %39Ar Release
%40Ar*
K/Ca

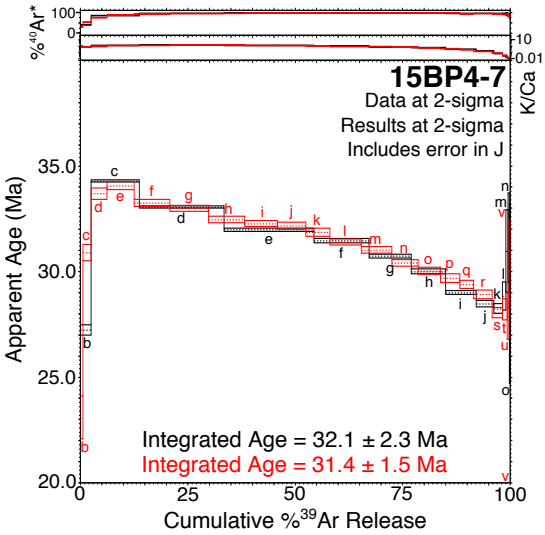
15BP4-7
Data at 2-sigma
Results at 2-sigma
Includes error in J
Integrated Age = 32.1 ± 2.3 Ma
Integrated Age = 31.4 ± 1.5 Ma
Apparent Age (Ma)
Cumulative %39Ar Release
%40Ar*
K/Ca

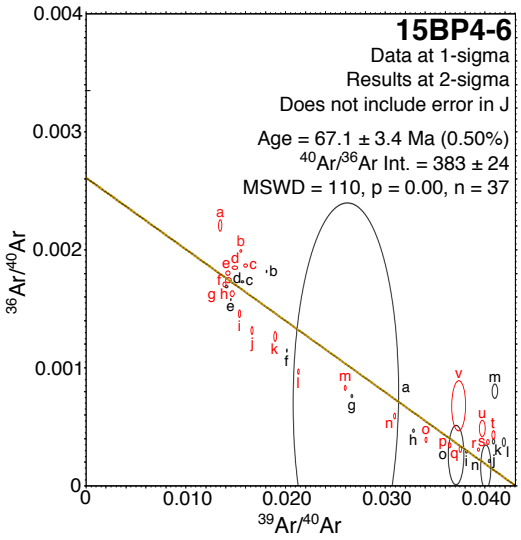
15BP4-6
Data at 1-sigma
Results at 2-sigma
Does not include error in J
Age = 67.1 ± 3.4 Ma (0.50%)
40Ar/36Ar Int. = 383 ± 24
MSWD = 110, p = 0.00, n = 37
36Ar/40Ar
39Ar/40Ar

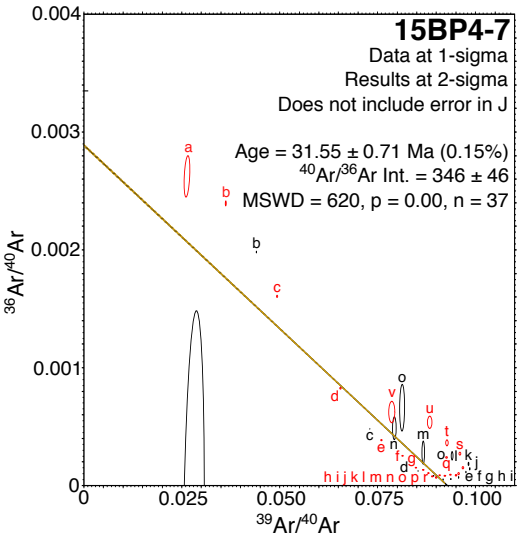
15BP4-7
Data at 1-sigma
Results at 2-sigma
Does not include error in J
Age = 31.55 ± 0.71 Ma (0.15%)
40Ar/36Ar Int. = 346 ± 46
MSWD = 620, p = 0.00, n = 37
36Ar/40Ar
39Ar/40Ar

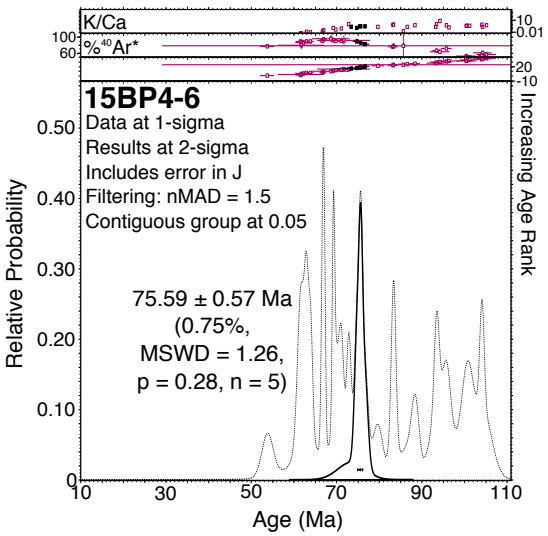
K/Ca
%40Ar*
15BP4-6
Data at 1-sigma
Results at 2-sigma
Includes error in J
Filtering: nMAD = 1.5
Contiguous group at 0.05
75.59 ± 0.57 Ma
(0.75%,
MSWD = 1.26,
p = 0.28, n = 5)
Relative Probability
Age (Ma)
Increasing Age Rank

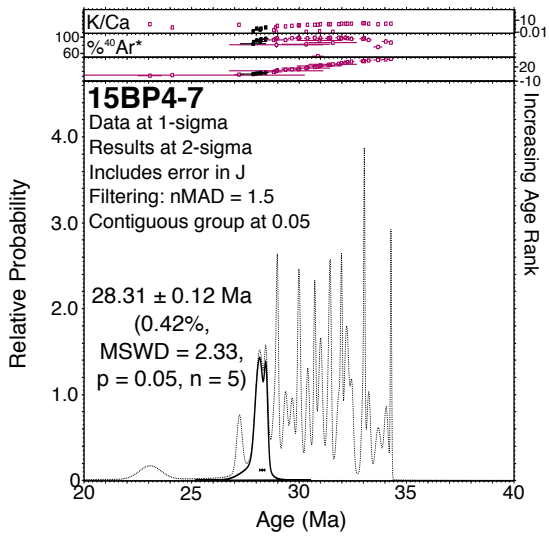
K/Ca
%40Ar*
15BP4-7
Data at 1-sigma
Results at 2-sigma
Includes error in J
Filtering: nMAD = 1.5
Contiguous group at 0.05
28.31 ± 0.12 Ma
(0.42%,
MSWD = 2.33,
p = 0.05, n = 5)
Relative Probability
Age (Ma)
Increasing Age Rank

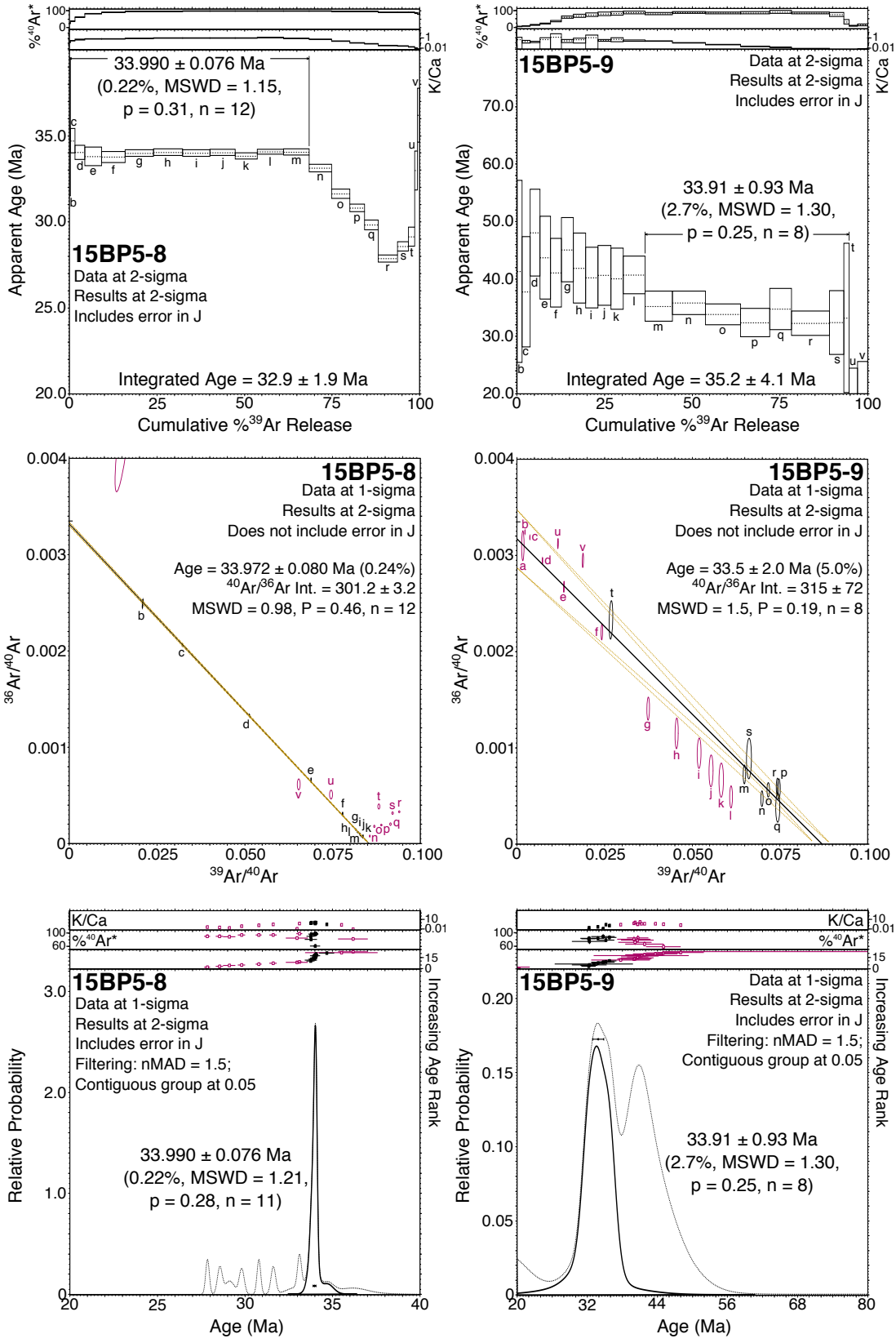
15BP5-8
Data at 2-sigma
Results at 2-sigma
Includes error in J
33.990 ± 0.076 Ma
(0.22%, MSWD = 1.15,
p = 0.31, n = 12)
Integrated Age = 32.9 ± 1.9 Ma
Apparent Age (Ma)
Cumulative %39Ar Release
%40Ar*
K/Ca
15BP5-9
Data at 2-sigma
Results at 2-sigma
Includes error in J
33.91 ± 0.93 Ma
(2.7%, MSWD = 1.30,
p = 0.25, n = 8)
Integrated Age = 35.2 ± 4.1 Ma
15BP5-8
Data at 1-sigma
Results at 2-sigma
Does not include error in J
Age = 33.972 ± 0.080 Ma (0.24%)
40Ar/36Ar Int. = 301.2 ± 3.2
MSWD = 0.98, P = 0.46, n = 12
36Ar/40Ar
39Ar/40Ar
15BP5-9
Data at 1-sigma
Results at 2-sigma
Does not include error in J
Age = 33.5 ± 2.0 Ma (5.0%)
40Ar/36Ar Int. = 315 ± 72
MSWD = 1.5, P = 0.19, n = 8
15BP5-8
Data at 1-sigma
Results at 2-sigma
Includes error in J
Filtering: nMAD = 1.5;
Contiguous group at 0.05
33.990 ± 0.076 Ma
(0.22%, MSWD = 1.21,
p = 0.28, n = 11)
Relative Probability
Age (Ma)
Increasing Age Rank
15BP5-9
Data at 1-sigma
Results at 2-sigma
Includes error in J
Filtering: nMAD = 1.5;
Contiguous group at 0.05
33.91 ± 0.93 Ma
(2.7%, MSWD = 1.30,
p = 0.25, n = 8)

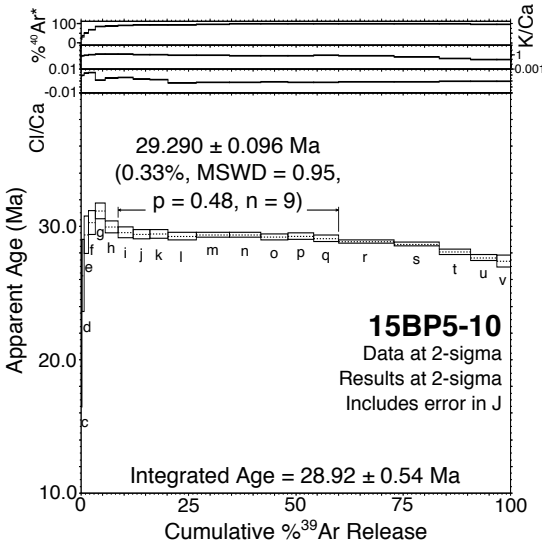
%40Ar*
K/Ca
Cl/Ca
29.290 ± 0.096 Ma
(0.33%, MSWD = 0.95,
p = 0.48, n = 9)
15BP5-10
Data at 2-sigma
Results at 2-sigma
Includes error in J
Integrated Age = 28.92 ± 0.54 Ma
Apparent Age (Ma)
Cumulative %39Ar Release

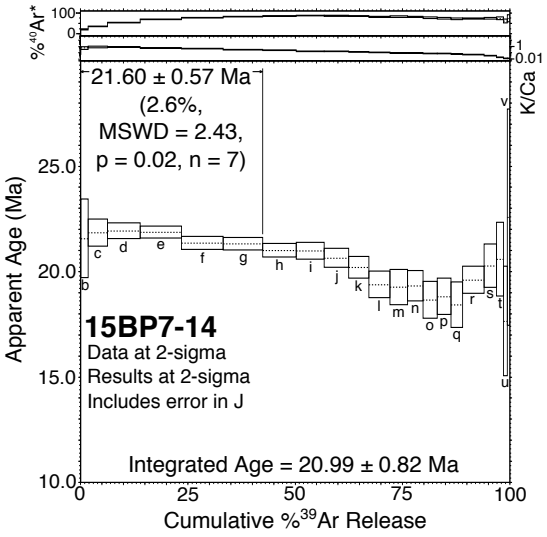
%40Ar*
K/Ca
21.60 ± 0.57 Ma
(2.6%,
MSWD = 2.43,
p = 0.02, n = 7)
15BP7-14
Data at 2-sigma
Results at 2-sigma
Includes error in J
Integrated Age = 20.99 ± 0.82 Ma
Apparent Age (Ma)
Cumulative %39Ar Release

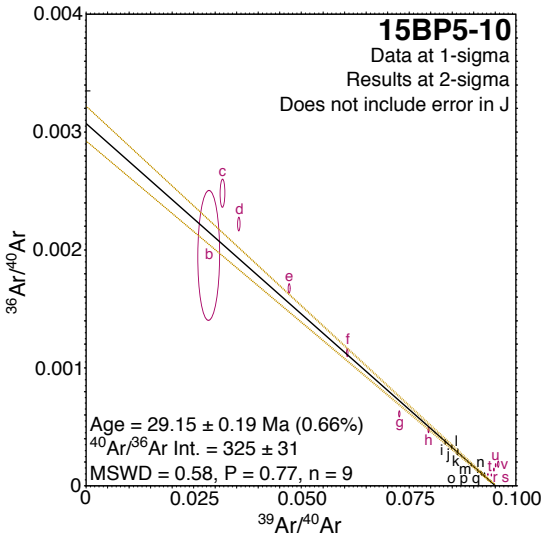
15BP5-10
Data at 1-sigma
Results at 2-sigma
Does not include error in J
Age = 29.15 ± 0.19 Ma (0.66%)
40Ar/36Ar Int. = 325 ± 31
MSWD = 0.58, P = 0.77, n = 9
36Ar/40Ar
39Ar/40Ar

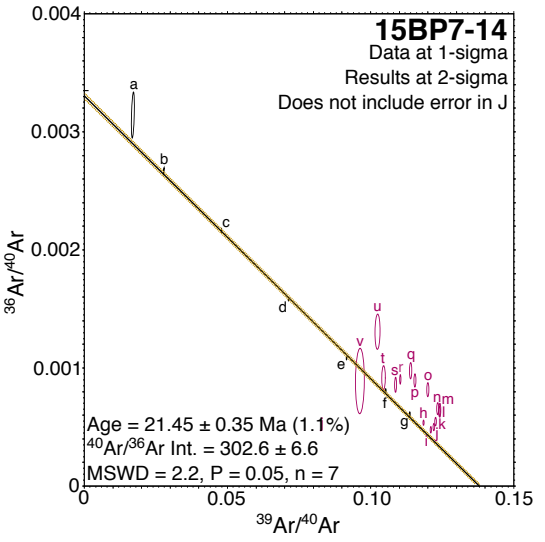
15BP7-14
Data at 1-sigma
Results at 2-sigma
Does not include error in J
Age = 21.45 ± 0.35 Ma (1.1%)
40Ar/36Ar Int. = 302.6 ± 6.6
MSWD = 2.2, P = 0.05, n = 7
36Ar/40Ar
39Ar/40Ar

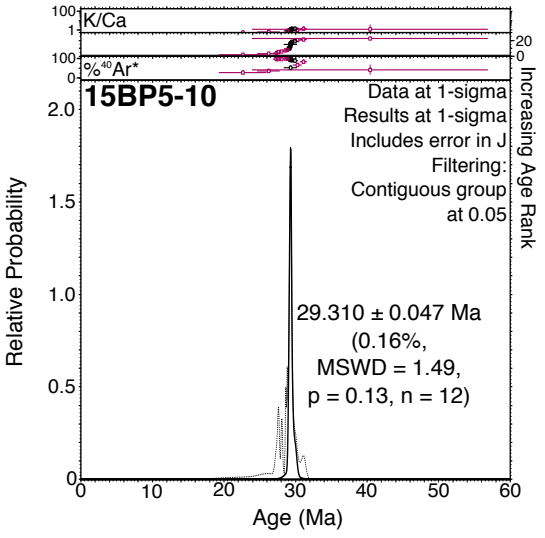
K/Ca
%40Ar*
15BP5-10
Data at 1-sigma
Results at 1-sigma
Includes error in J
Filtering:
Contiguous group
at 0.05
29.310 ± 0.047 Ma
(0.16%,
MSWD = 1.49,
p = 0.13, n = 12)
Relative Probability
Increasing Age Rank
Age (Ma)

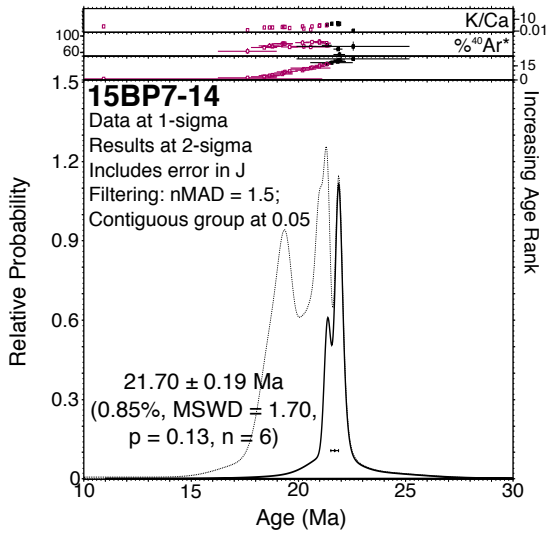
K/Ca
%40Ar*
15BP7-14
Data at 1-sigma
Results at 2-sigma
Includes error in J
Filtering: nMAD = 1.5;
Contiguous group at 0.05
21.70 ± 0.19 Ma
(0.85%, MSWD = 1.70,
p = 0.13, n = 6)
Relative Probability
Increasing Age Rank
Age (Ma)

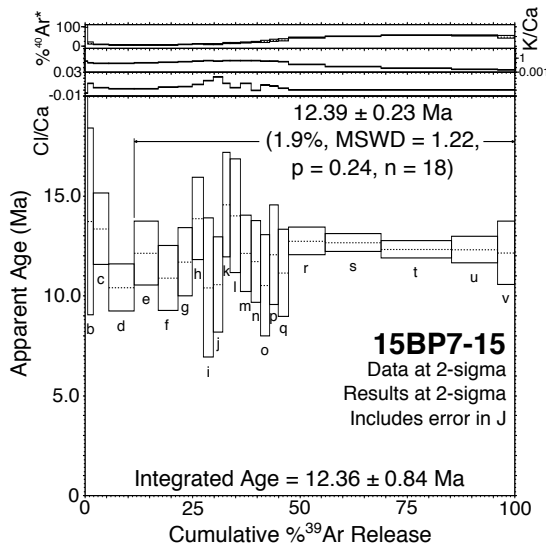
%40Ar*
K/Ca
Cl/Ca
Apparent Age (Ma)
12.39 ± 0.23 Ma
(1.9%, MSWD = 1.22,
p = 0.24, n = 18)
15BP7-15
Data at 2-sigma
Results at 2-sigma
Includes error in J
Integrated Age = 12.36 ± 0.84 Ma
Cumulative %39Ar Release

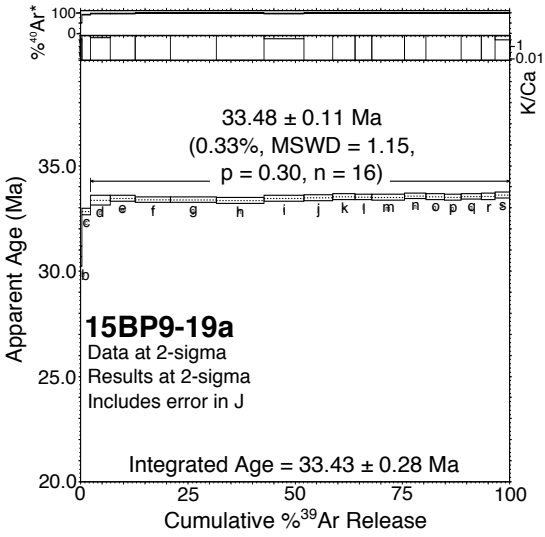
%40Ar*
K/Ca
Apparent Age (Ma)
33.48 ± 0.11 Ma
(0.33%, MSWD = 1.15,
p = 0.30, n = 16)
15BP9-19a
Data at 2-sigma
Results at 2-sigma
Includes error in J
Integrated Age = 33.43 ± 0.28 Ma
Cumulative %39Ar Release

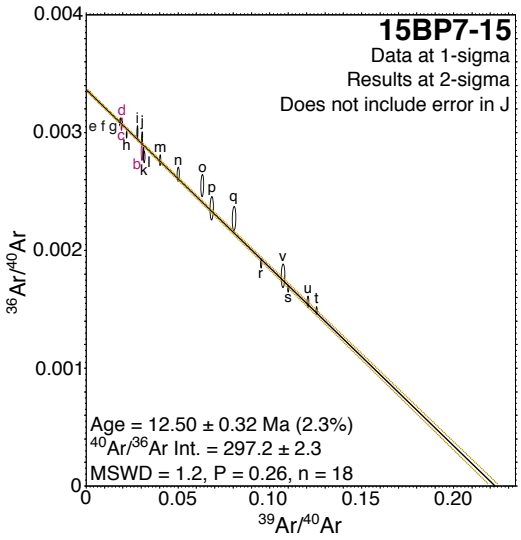
15BP7-15
Data at 1-sigma
Results at 2-sigma
Does not include error in J
Age = 12.50 ± 0.32 Ma (2.3%)
40Ar/36Ar Int. = 297.2 ± 2.3
MSWD = 1.2, P = 0.26, n = 18
36Ar/40Ar
39Ar/40Ar

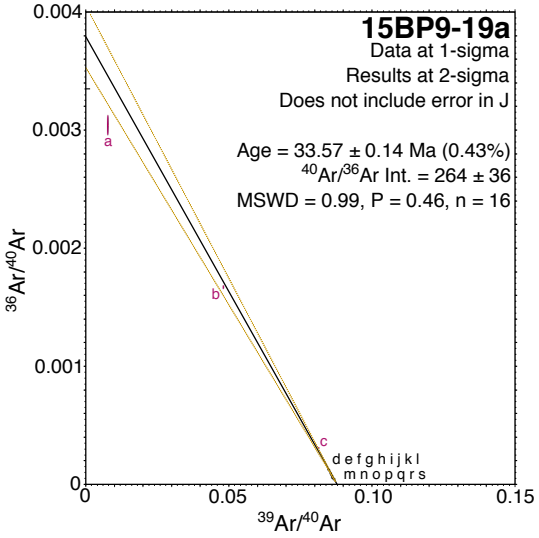
15BP9-19a
Data at 1-sigma
Results at 2-sigma
Does not include error in J
Age = 33.57 ± 0.14 Ma (0.43%)
40Ar/36Ar Int. = 264 ± 36
MSWD = 0.99, P = 0.46, n = 16
36Ar/40Ar
39Ar/40Ar

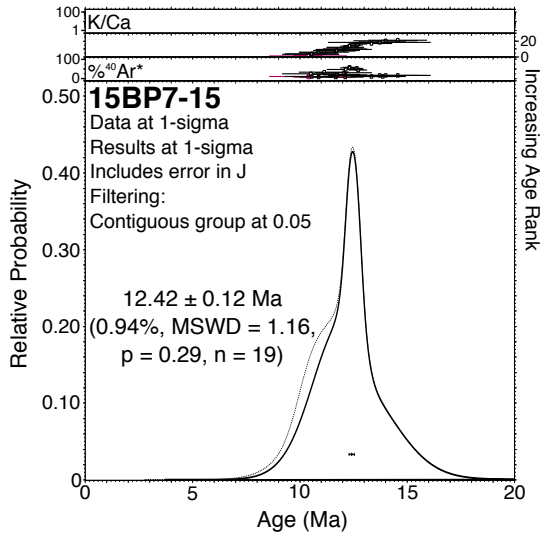
K/Ca
%40Ar*
15BP7-15
Data at 1-sigma
Results at 1-sigma
Includes error in J
Filtering:
Contiguous group at 0.05
12.42 ± 0.12 Ma
(0.94%, MSWD = 1.16,
p = 0.29, n = 19)
Relative Probability
Increasing Age Rank
Age (Ma)

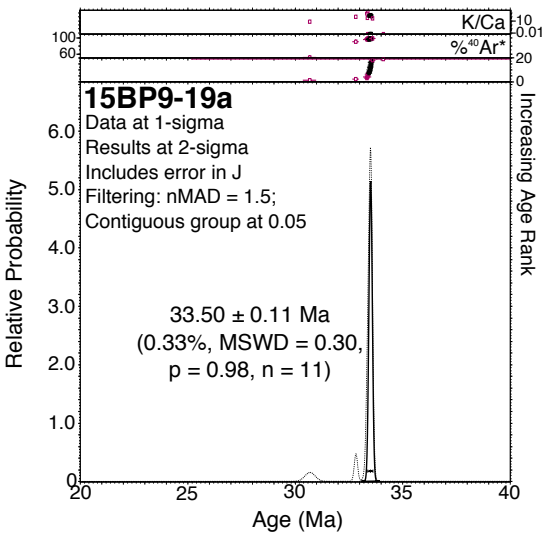
K/Ca
%40Ar*
15BP9-19a
Data at 1-sigma
Results at 2-sigma
Includes error in J
Filtering: nMAD = 1.5;
Contiguous group at 0.05
33.50 ± 0.11 Ma
(0.33%, MSWD = 0.30,
p = 0.98, n = 11)
Relative Probability
Increasing Age Rank
Age (Ma)

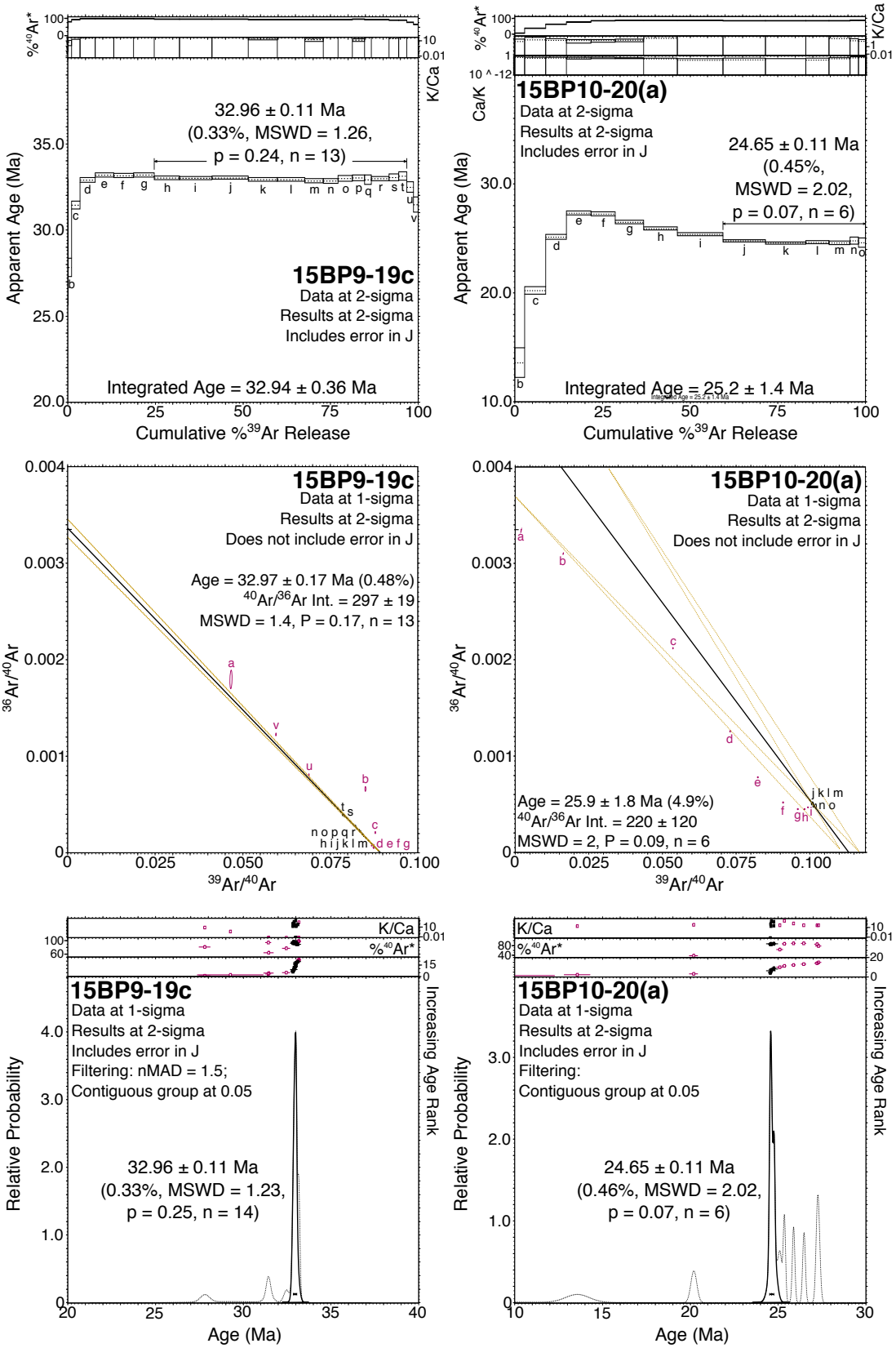
15BP9-19c
Data at 2-sigma
Results at 2-sigma
Includes error in J
32.96 ± 0.11 Ma
(0.33%, MSWD = 1.26,
p = 0.24, n = 13)
Integrated Age = 32.94 ± 0.36 Ma
Apparent Age (Ma)
Cumulative %39Ar Release
%40Ar*
K/Ca
15BP10-20(a)
Data at 2-sigma
Results at 2-sigma
Includes error in J
24.65 ± 0.11 Ma
(0.45%,
MSWD = 2.02,
p = 0.07, n = 6)
Integrated Age = 25.2 ± 1.4 Ma
Ca/K
15BP9-19c
Data at 1-sigma
Results at 2-sigma
Does not include error in J
Age = 32.97 ± 0.17 Ma (0.48%)
40Ar/36Ar Int. = 297 ± 19
MSWD = 1.4, P = 0.17, n = 13
36Ar/40Ar
39Ar/40Ar
15BP10-20(a)
Data at 1-sigma
Results at 2-sigma
Does not include error in J
Age = 25.9 ± 1.8 Ma (4.9%)
40Ar/36Ar Int. = 220 ± 120
MSWD = 2, P = 0.09, n = 6
15BP9-19c
Data at 1-sigma
Results at 2-sigma
Includes error in J
Filtering: nMAD = 1.5;
Contiguous group at 0.05
32.96 ± 0.11 Ma
(0.33%, MSWD = 1.23,
p = 0.25, n = 14)
Relative Probability
Increasing Age Rank
Age (Ma)
15BP10-20(a)
Data at 1-sigma
Results at 2-sigma
Includes error in J
Filtering:
Contiguous group at 0.05
24.65 ± 0.11 Ma
(0.46%, MSWD = 2.02,
p = 0.07, n = 6)

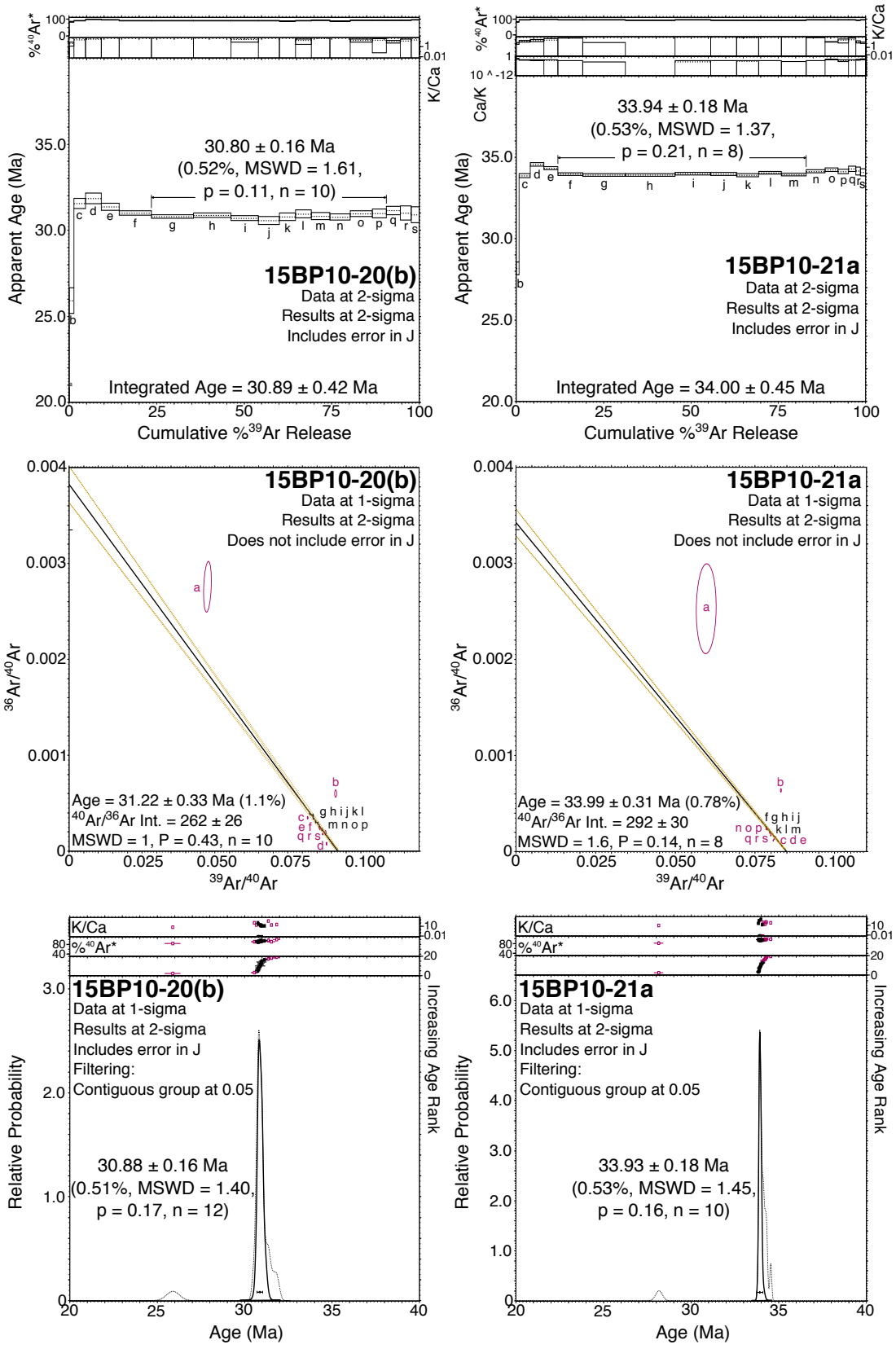
%40Ar*
K/Ca
Apparent Age (Ma)
30.80 ± 0.16 Ma
(0.52%, MSWD = 1.61,
p = 0.11, n = 10)
15BP10-20(b)
Data at 2-sigma
Results at 2-sigma
Includes error in J
Integrated Age = 30.89 ± 0.42 Ma
Cumulative %39Ar Release
Ca/K
33.94 ± 0.18 Ma
(0.53%, MSWD = 1.37,
p = 0.21, n = 8)
15BP10-21a
Data at 2-sigma
Results at 2-sigma
Includes error in J
Integrated Age = 34.00 ± 0.45 Ma
Cumulative %39Ar Release
15BP10-20(b)
Data at 1-sigma
Results at 2-sigma
Does not include error in J
36Ar/40Ar
39Ar/40Ar
Age = 31.22 ± 0.33 Ma (1.1%)
40Ar/36Ar Int. = 262 ± 26
MSWD = 1, P = 0.43, n = 10
15BP10-21a
Data at 1-sigma
Results at 2-sigma
Does not include error in J
Age = 33.99 ± 0.31 Ma (0.78%)
40Ar/36Ar Int. = 292 ± 30
MSWD = 1.6, P = 0.14, n = 8
15BP10-20(b)
Data at 1-sigma
Results at 2-sigma
Includes error in J
Filtering:
Contiguous group at 0.05
30.88 ± 0.16 Ma
(0.51%, MSWD = 1.40,
p = 0.17, n = 12)
Relative Probability
Increasing Age Rank
Age (Ma)
15BP10-21a
Data at 1-sigma
Results at 2-sigma
Includes error in J
Filtering:
Contiguous group at 0.05
33.93 ± 0.18 Ma
(0.53%, MSWD = 1.45,
p = 0.16, n = 10)

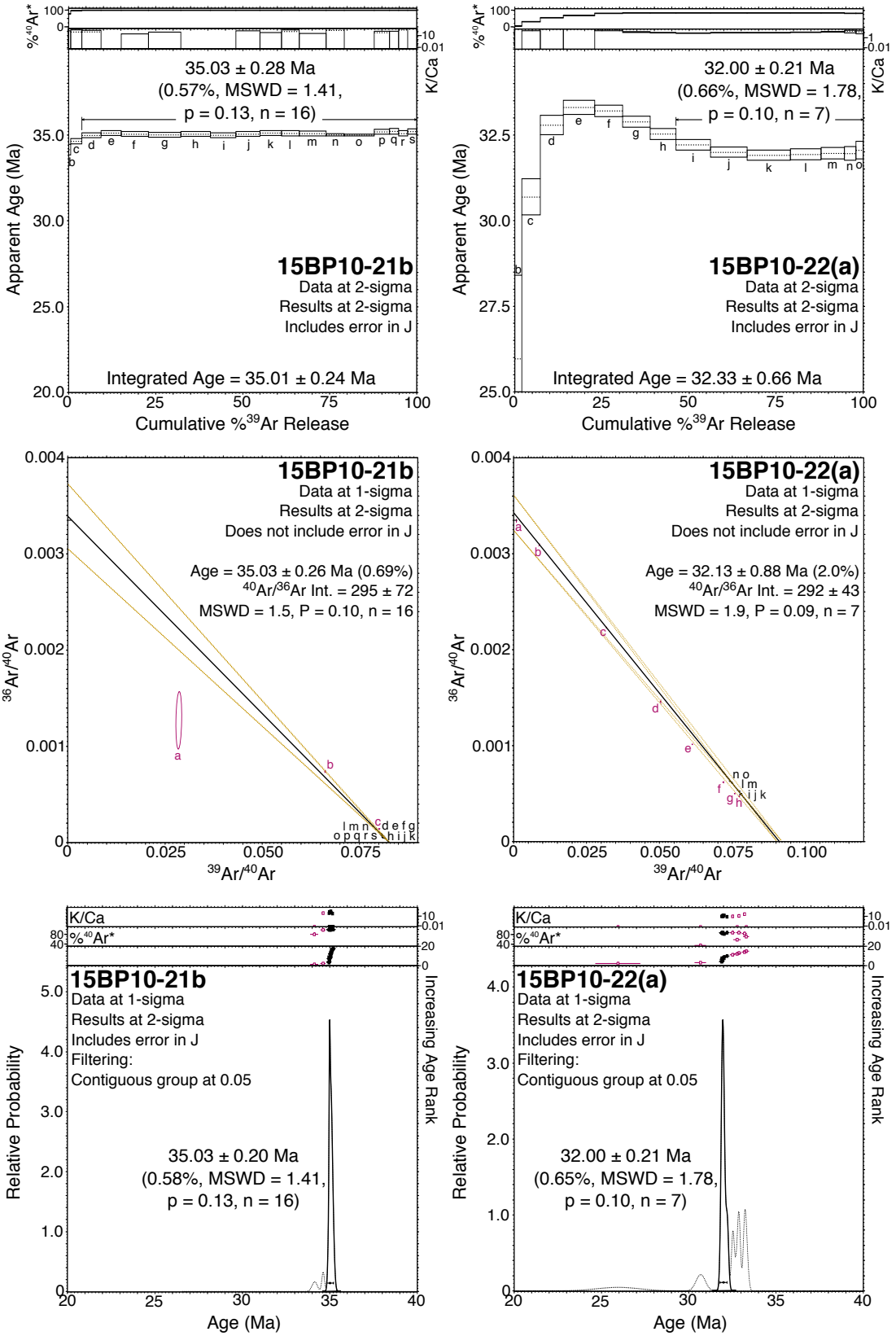
%40Ar*
K/Ca
35.03 ± 0.28 Ma
(0.57%, MSWD = 1.41,
p = 0.13, n = 16)
Apparent Age (Ma)
15BP10-21b
Data at 2-sigma
Results at 2-sigma
Includes error in J
Integrated Age = 35.01 ± 0.24 Ma
Cumulative %39Ar Release
32.00 ± 0.21 Ma
(0.66%, MSWD = 1.78,
p = 0.10, n = 7)
15BP10-22(a)
Data at 2-sigma
Results at 2-sigma
Includes error in J
Integrated Age = 32.33 ± 0.66 Ma
Cumulative %39Ar Release
15BP10-21b
Data at 1-sigma
Results at 2-sigma
Does not include error in J
Age = 35.03 ± 0.26 Ma (0.69%)
40Ar/36Ar Int. = 295 ± 72
MSWD = 1.5, P = 0.10, n = 16
36Ar/40Ar
39Ar/40Ar
15BP10-22(a)
Data at 1-sigma
Results at 2-sigma
Does not include error in J
Age = 32.13 ± 0.88 Ma (2.0%)
40Ar/36Ar Int. = 292 ± 43
MSWD = 1.9, P = 0.09, n = 7
K/Ca
%40Ar*
15BP10-21b
Data at 1-sigma
Results at 2-sigma
Includes error in J
Filtering:
Contiguous group at 0.05
35.03 ± 0.20 Ma
(0.58%, MSWD = 1.41,
p = 0.13, n = 16)
Relative Probability
Increasing Age Rank
Age (Ma)
15BP10-22(a)
Data at 1-sigma
Results at 2-sigma
Includes error in J
Filtering:
Contiguous group at 0.05
32.00 ± 0.21 Ma
(0.65%, MSWD = 1.78,
p = 0.10, n = 7)

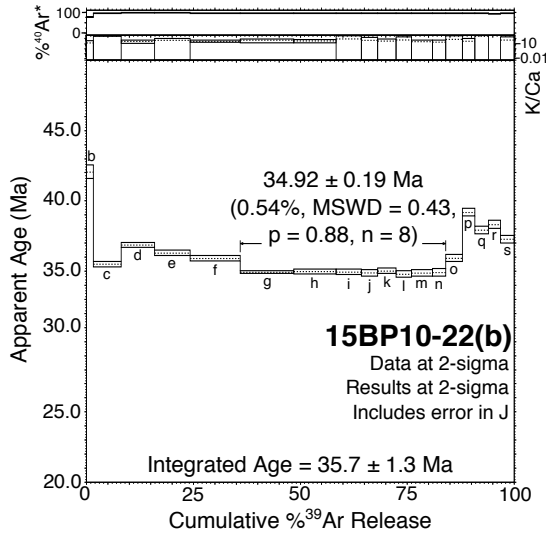
%40Ar*
100
0
10
0.01
K/Ca
34.92 ± 0.19 Ma
(0.54%, MSWD = 0.43,
p = 0.88, n = 8)
15BP10-22(b)
Data at 2-sigma
Results at 2-sigma
Includes error in J
Integrated Age = 35.7 ± 1.3 Ma
Apparent Age (Ma)
Cumulative %39Ar Release

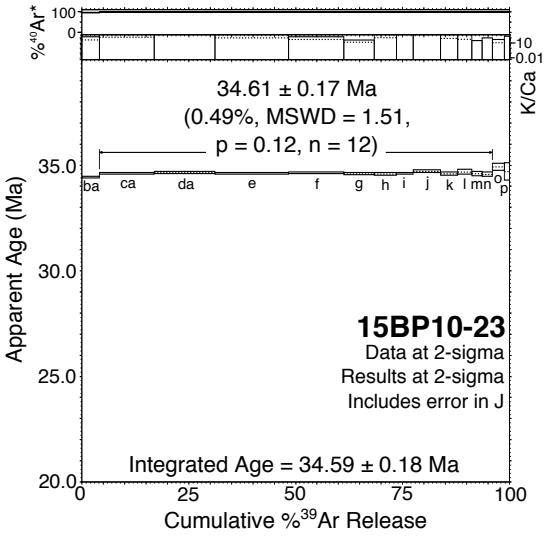
%40Ar*
100
0
10
0.01
K/Ca
34.61 ± 0.17 Ma
(0.49%, MSWD = 1.51,
p = 0.12, n = 12)
15BP10-23
Data at 2-sigma
Results at 2-sigma
Includes error in J
Integrated Age = 34.59 ± 0.18 Ma
Apparent Age (Ma)
Cumulative %39Ar Release

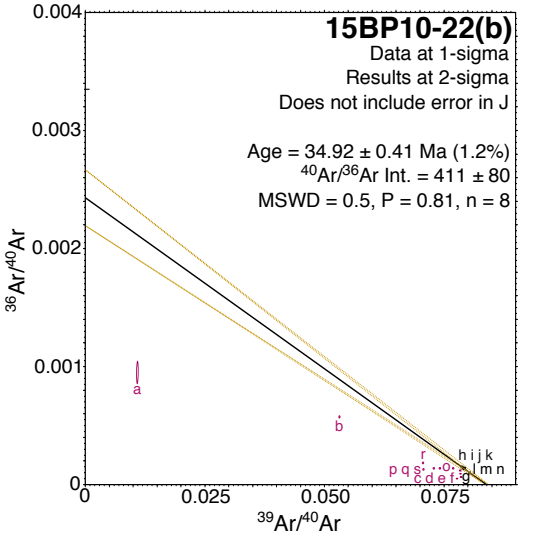
15BP10-22(b)
Data at 1-sigma
Results at 2-sigma
Does not include error in J
Age = 34.92 ± 0.41 Ma (1.2%)
40Ar/36Ar Int. = 411 ± 80
MSWD = 0.5, P = 0.81, n = 8
36Ar/40Ar
39Ar/40Ar

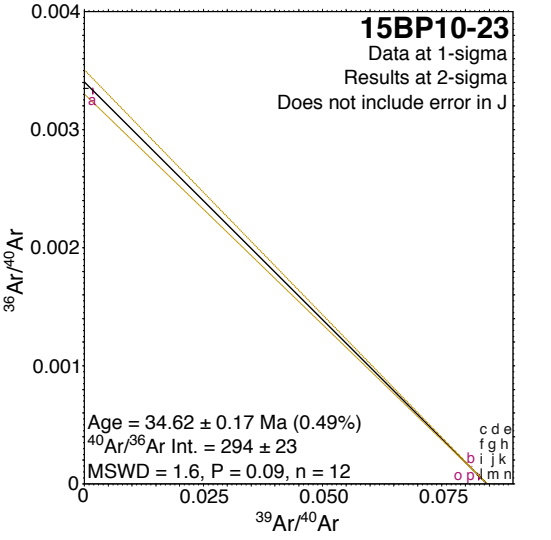
15BP10-23
Data at 1-sigma
Results at 2-sigma
Does not include error in J
Age = 34.62 ± 0.17 Ma (0.49%)
40Ar/36Ar Int. = 294 ± 23
MSWD = 1.6, P = 0.09, n = 12
36Ar/40Ar
39Ar/40Ar

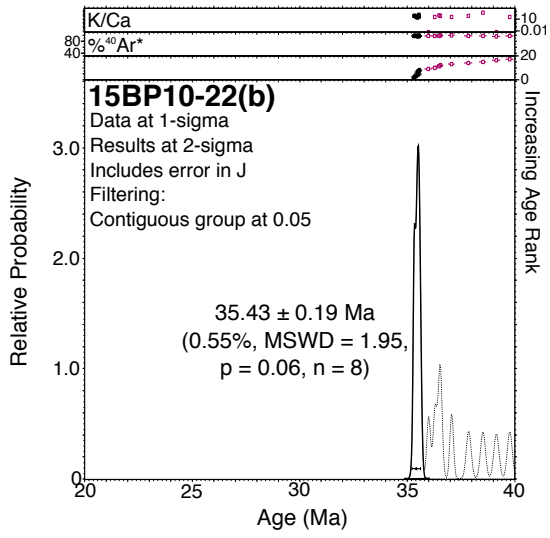
K/Ca
%40Ar*
10
0.01
20
0
15BP10-22(b)
Data at 1-sigma
Results at 2-sigma
Includes error in J
Filtering:
Contiguous group at 0.05
35.43 ± 0.19 Ma
(0.55%, MSWD = 1.95,
p = 0.06, n = 8)
Relative Probability
Increasing Age Rank
Age (Ma)

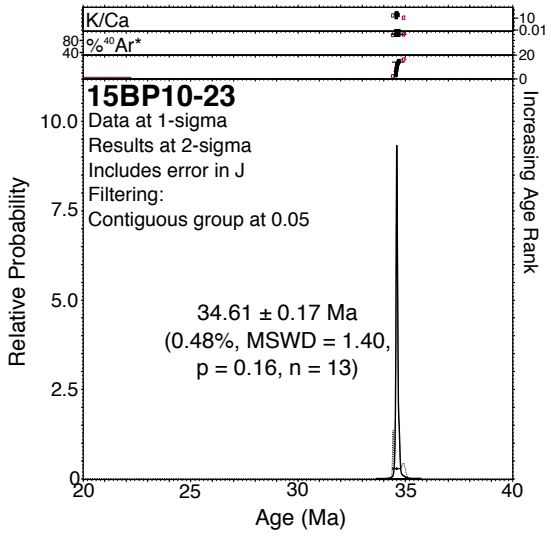
K/Ca
%40Ar*
10
0.01
20
0
15BP10-23
Data at 1-sigma
Results at 2-sigma
Includes error in J
Filtering:
Contiguous group at 0.05
34.61 ± 0.17 Ma
(0.48%, MSWD = 1.40,
p = 0.16, n = 13)
Relative Probability
Increasing Age Rank
Age (Ma)

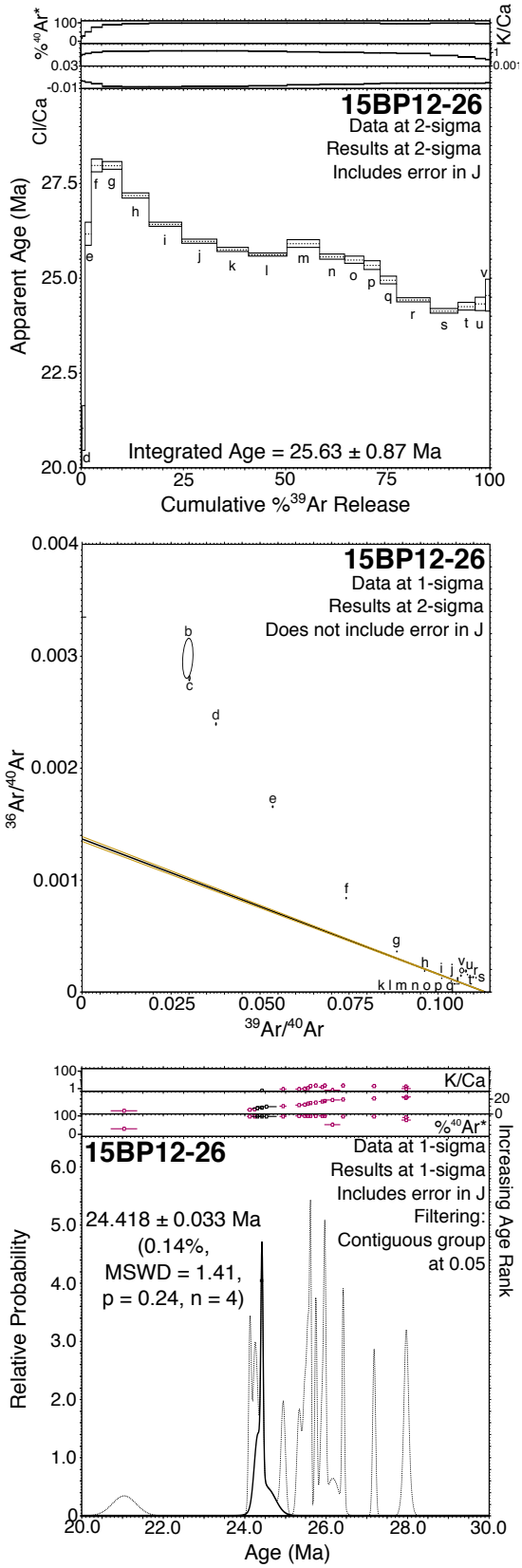

Figure 2-2: $^{40}Ar/^{39}Ar$ age spectra (*upper*), inverse isochron (*middle*) and age probability spectra (*lower*) diagrams of all dated samples, including those that did not produce resolvable ages, given in columns. Samples 15BP1-1, 15BP4-6, 15BP4-7 and 15BP12-26 did not produce resolvable ages. Results for samples 15BP10-20(a) were rejected (see main text).

Overall issues concerning the results

Recoil loss, recoil redistribution and alteration effects

A combination of different recoil effects is clear in the oscillating age spectra of some groundmass measurements, and is particularly strong in the basaltic samples 15BP1-1, 15BP4-6, 15BP4-7 and 15BP12-26, for which resolvable ages were not obtained. Similar effects also affect the phonolite groundmass sample 15BP10-20(a), which has also been rejected, although based also on other grounds (see below). The characteristic age spectra in these cases show steep climbing apparent ages during the very early heating steps associated with high K/Ca ratios (i.e. alteration combined with recoil loss or redistribution of ^{39}Ar), followed by a gradual drop in apparent age spectra and K/Ca, with no resolvable age plateau (recoil loss of ^{37}Ar and/or redistribution of ^{39}Ar). Overall, the oscillating age spectra patterns that may indicate ^{37}Ar recoil loss and ^{39}Ar recoil loss and redistribution are clearly more significant amongst groundmass samples, reflecting their fine-grained textures, and affect both basaltic and phonolitic compositions and does not seem to be affected by the higher Ca content of basalt. Nonetheless, reliable plateau ages could still be obtained from many groundmass measurements, following the plateau definition criteria described above.

Samples failing the plateau criteria

Some plateaus fell short of representing 50% of released ^{39}Ar (i.e. 15BP7-14, 15BP10-20(a) and 15BP10-22(b), with ^{39}Ar yields of 43%, 41% and 48%, respectively). Lack of adherence to a plateau definition does not mean a sample should be immediately rejected, but rather examined more closely (McDougall and Harrison, 1999). Furthermore, it has been argued in other studies that a 30% threshold of total ^{39}Ar yield in basaltic rocks, instead of the traditional 50%, can still produce robust ages through careful sample

preparation, Ar measurements and data analyses (Koppers *et al.*, 2000, 2003).

Sample 15BP10-20(a), in addition to failing plateau criteria, also shows the largest difference between plateau and isochron ages of all samples (respectively 24.65 ± 0.15 and 25.89 ± 1.26), with a relatively significantly high standard deviation for the latter, and substantial discrepancy with the sanidine phenocryst age from the same hand specimen (i.e. sample 15BP10-20(b), with its plateau age of 30.80 ± 0.22) and all the other ages from Mecejana. The sample also shows a very high standard deviation for the trapped component value, despite still being within atmospheric values. The combination of all these issues casts doubt in the reliability of the age obtained from sample 15BP10-20(a), and therefore its results were rejected.

Conversely, despite failing plateau criteria, the ages for samples 15BP7-14 and 15BP10-22(b) are still reliable. This is supported by their data as a whole, including inverse isochrons and age probability spectra, and by comparisons with other dates produced in this study or published elsewhere (Mizusaki *et al.*, 2002; Souza *et al.*, 2013). This is despite the presence of some excess ^{40}Ar in sample 15BP10-22(b), which had to be accounted for during the step heating measurements and calculations. The lack of a plateau beyond the 50% threshold of released ^{39}Ar for this sample could be due to the trapped component itself, something reinforced by the overall higher ages amongst heating steps outside the plateau and the higher integrated age. A more detailed discussion of all the three samples that failed the plateau criteria is given below.

Consistency of plateau ages with the inverse isochron ages and y-intercepts

Most samples produced inverse isochron ages and age probability spectra that match the plateau ages within 2σ. Most samples also produced inverse isochron *y*-intercepts that match current $^{40}Ar/^{36}Ar$ atmospheric

values, although samples 15BP3-2 and 15BP5-9 showed relatively high standard deviations, and samples 15BP10-22(b) and 15BP3-3b have produced high intercept values for some of the measurements that indicate some excess ^{40}Ar. In the latter case, trapped component ratios were calculated from the inverse isochron and used for the correction of non-radiogenic ^{40}Ar instead of current atmospheric values (Equation 6), as a way to filter out the effects of excess ^{40}Ar and calculate a reliable age. Excess ^{40}Ar can be a significant problem in xenolith-rich samples, which are ubiquitous in the continental sector of Northeast Brazil and make this problem particularly relevant for $^{40}Ar/^{39}Ar$ chronology in the region.

Specific issues of individual samples

Sample 15BP5-8 was subject to two groundmass measurement runs that produced plateau ages of 34.01 ± 0.47 and 33.99 ± 0.09. However, the plateau for the first run was forced from steps *b* to *g* in the age spectrum (up to 70% of ^{39}Ar degassing), since step *d* fell somewhat outside the 2σ uncertainty of steps *f* and *g*, which led to a high mean square weighted deviation (MSWD) value of 4.1. This was done because the difference to the 2σ uncertainty was small and establishing a plateau allowed for a combination of the results of the two runs and comparison between the two. Nonetheless, the second run, which shows higher precision with a clear age plateau and MSWD of 1.2, still produced more robust results and was chosen as the better age.

Sample 15BP7-14 is one example that didn't meet the 50% threshold of ^{39}Ar yields. It is a basaltic andesite from the coastal area near Macau, Rio Grande do Norte, and is likely from an underwater extrusive event, based on its ubiquitous, rounded and evenly distributed vesicles and hyalopilitic texture. The locality is at the onshore branch of the Potiguar basin, but at the transition to its offshore section. One groundmass measurement produced a plateau age of 21.6 ± 0.58 based on 43% ^{39}Ar degassing and a somewhat

high MSWD of 2.4. However, the matching inverse isochron age (21.45 ± 0.24) and age probability spectra (21.7 ± 0.19), and absence of excess ^{40}Ar ($^{40}Ar/^{36}Ar$ intercept of 302.6 ± 4.4) give further credibility to the plateau results. The plateau was also obtained in the lower temperature heating steps, marked by gradually increasing proportions of radiogenic ^{40}Ar and high K/Ca ratios. Higher temperature steps, which did not produce a plateau, coincide with the peak in radiogenic ^{40}Ar degassing, a gradual drop in K/Ca ratios and lower apparent age spectra. Although these patterns seem to highlight the possible effects of ^{37}Ar recoil loss in the measurements, these appear to be small and the sample's age data is considered robust.

Sample 15BP3-3b is a basaltic andesite collected from the core of a lava pillow in the Juá Quarry in the Boa Vista basin (Figure 1-8 in Chapter 1). Two groundmass measurements produced no plateau or isochron ages, high integrated ages (29.6 ± 4.8 and 30.4 ± 5.6), scattered age probability spectra (26.77 ± 0.15 with MSWD = 1.7, and 27.49 ± 0.1 with MSWD = 2,0) and evidence for significant excess ^{40}Ar in the second analysis ($^{40}Ar/^{36}Ar$ intercept of 562.5 ± 169.4). Therefore, an estimated value for the excess ^{40}Ar calculated from the inverse isochron results was used as the trapped component value in the calculations of a third measurement (Equation 6), producing a plateau age of 22.50 ± 0.32 for just over 55% of released ^{39}Ar. This matches the $^{40}Ar/^{39}Ar$ ages obtained with somewhat different methods by Souza et al. (2013) for a chilled margin from the same suite of pillow lavas (i.e. a plateau age of 22.3 ± 0.1 and an inverse isochron age of 22.0 ± 0.2), which strengthens the validity of the method used here to compensate for excess ^{40}Ar and the age thus obtained. The inverse isochron and age probability spectra for the calibrated measurement are also coherent with the plateau age (respectively 22.50 ± 2.65 and 22.51 ± 0.32). Although the standard deviation for the inverse isochron age is high, this comes from adjusting the isochron to exclude the excess ^{40}Ar. The MSWD for the age probability spectra for this third measurement dropped to 0.8, which is significantly lower than before. Therefore, despite the original excess ^{40}Ar,

we believe that the calibrated age is acceptable. The sample is a good example of a reliable age obtained from a hypocrystalline groundmass (see Table 1-1 in Chapter 1 for groundmass textures). The overall trends in the age spectrum, with a convex-up pattern during early heating steps after a sharp increase in the apparent age, which is then followed by a gradual decrease in apparent ages, also indicate some effects of alteration and recoil loss and/or redistribution. However, the high temperature, late heating steps stabilised in an acceptable plateau after calibration of its trapped component, and the resulting age is robust.

In the case of sample 15BP10-22(b), which comprises sanidine phenocrysts from a phonolite plug at the Serrote Japarara, the age plateau (35.43 ± 0.27) accounted for 48% of total ^{39}Ar degassing, falling short of the 50% threshold, and the inverse isochron $^{40}Ar/^{36}Ar$ intercept (411.4 ± 80.1) indicates some excess ^{40}Ar. Therefore, a second measurement was made and calibrated using the same method as for 15BP3-3b to account for the non-atmospheric trapped component. This produced a plateau age of 34.92 ± 0.27 with a matching inverse isochron age (34.92 ± 0.41) but a somewhat higher age in the age probability spectrum (35.43 ± 0.19). These ages are ~2.5 m.y. older than those obtained from the groundmass in the same hand specimen (i.e. sample 15BP10-22(a)). This difference could reflect excess ^{40}Ar in the sanidine phenocrysts, for example in the form of melt inclusions, or a less pure sanidine aliquot, as this is one of two samples (the other being 15BP10-20) where the paucity of good phenocrysts led to the measurement of both groundmass and phenocrysts. However, such difference is more likely to reflect some effects of ^{37}Ar loss or ^{39}Ar redistribution due to recoil in the younger, groundmass sample. For instance, two measurement runs were conducted for the groundmass sample 15BP10-22(a), and one plateau result (32.00 ± 0.29) was chosen based on its better agreement with both the inverse isochron age (32.13 ± 0.62) and age probability spectrum (32.00 ± 0.21), and a $^{40}Ar/^{36}Ar$ intercept (291.7 ± 31.2) closer to current atmospheric values. However, both measurement runs seem somewhat affected by

alteration and recoil loss or redistribution, with an age spectrum showing a convex-up pattern during early heating steps after a sharp increase in the apparent age, followed by a gradual decrease in age patterns. Considering that the apparent age spectra plateaus for this sample were obtained in the high temperature heating steps, they could be underestimations if recoil loss or redistributions are indeed significant. Therefore, the Japarara locality shows issues with both its groundmass and sanidine measurements, although both are still well within the overall age range for Mecejana. Since both aliquots come from the same hand specimen, the best age estimate for the outcrop would be the sanidine phenocryst result, since the effects of excess ^{40}Ar are easier to account for during calculations than those of recoil loss and/or redistribution.

Samples 15BP10-20(a) and 15BP10-20(b) are from the same phonolite plug hand specimen, collected from what is now an abandoned quarry (Ancurí). They represent respectively the sample's groundmass, for which two measurement runs were conducted (24.56 ± 0.15 chosen as the better plateau age result), and its sanidine phenocrysts, which produced a good plateau age from one measurement (30.80 ± 0.22). The age gap of almost 6 m.y. between the groundmass and phenocrysts taken from the same hand specimen cannot be readily explained. The groundmass plateau age represents 41% of released ^{39}Ar and is below our criteria threshold. It also produced a relatively high MSWD of 1.4 and an $^{40}Ar/^{36}Ar$ intercept of 208 ± 124.1 that, although in accordance with current atmospheric values, also has a high standard deviation. Its inverse isochron age (25.83 ± 1.81) also produced a high standard deviation. Furthermore, the initial sharp increase from very low values to relatively high apparent ages in the low temperature steps, followed by a gradual decrease at high temperature steps indicate some effects of alteration, and recoil loss or redistribution. This can potentially have caused underestimations that may be the reason for the age gap between the groundmass and phenocryst results. This sample is the only one amongst the Mecejana phonolites with a cryptocrystalline texture

(see Table 1-1 in Chapter 1 for groundmass textures), which could be the cause for a more substantial effect of recoil loss. Conversely, the plateau age for the sanidine phenocryst is robust, with a matching inverse isochron age (31.22 ± 0.33) and age probability spectra (30.88 ± 0.16) based on 67.1% of ^{39}Ar release. However, the $^{40}Ar/^{36}Ar$ intercept (261.6 ± 26) is somewhat lower than current atmospheric values (298.6). The reasons for somewhat low $^{40}Ar/^{36}Ar$ in occasional volcanic rocks is not fully understood, but has been associated with some mass fractionation of Ar isotopes during the lava's equilibration with atmospheric content just prior to or during eruption (McDougall and Harrison, 1999). Therefore, given the issues with the groundmass measurements and its significant disparity with a robust phenocryst age, the groundmass result has been rejected, leaving the sanidine result as representative of the outcrop.

Inconclusive ages

Out of 19 selected hand specimens, samples 15BP1-1, 15BP4-6 and 15BP4-7 failed to produce age plateaus concordant with our criteria, and their data as a whole did not offer resolvable ages. Sample 15BP1-1 was subject to three measurement runs, whilst samples 15BP4-6 and 15BP4-7 were subject to two runs each (Table 2-1).

Sample 15BP1-1 is a basanite from the São Pedro volcanic neck. The apparent age spectra and age probability diagrams, although not resolvable, suggest an age between 25 and 33 Ma. The $^{40}Ar/^{36}Ar$ intercept (651.6 ± 13.6) is well above current atmospheric values and indicates significant excess ^{40}Ar. Although very fresh, the sample comes from a locality rich in mantle xenoliths that could be the source of excess ^{40}Ar. The percentage of radiogenic, as opposed to atmospheric ^{40}Ar remained high and close to 100% throughout all the heating steps, including early ones, suggesting that the results have suffered little effects from alteration. Although sample preparation should have removed most peridotitic material, thin-sections show that their presence is ubiquitous even on a microscopic scale (Chapter

3), and contamination would be difficult to avoid. The sample also has a hypocrystalline texture (see Table 1-1 in Chapter 1 for groundmass textures) that has likely been affected by Ar recoil loss and redistribution, especially ^{37}Ar loss. The correlation between changes in the apparent age spectra and the K/Ca ratios support this. For instance, the shift in K/Ca ratios from ≥ 1 to ≤ 1 correlates with decreasing ages.

Sample 15BP4-6 is a basanite collected from a small ill-defined exposure. The apparent age spectra are inconclusive and produced significant variability between 50 and 110 Ma, which potentially puts the sample outside the range of available $^{40}Ar/^{39}Ar$ dates for the MQVL (Knesel et al., 2011; Silveira, 2006; Souza et al., 2013; and this study) or the Cenozoic. Variability is especially accentuated in early heating steps, which also produced the oldest ages and correlate with high K/Ca ratios and low radiogenic ^{40}Ar. This pattern represents significant effects of both alteration and recoil loss or redistribution. Age probability spectra are scattered and also inconclusive. Inverse isochrons produced ages of 66.71 ± 0.42 and 67.54 ± 0.49, with $^{40}Ar/^{36}Ar$ intercepts at 394 ± 3 and 366.7 ± 3.5 respectively, suggesting excess ^{40}Ar and the corollary age overestimation. There is no discernible structure for the outcrop, and one cannot tell if it is a dyke similar to the Early Cretaceous volcanic events such as the Rio Ceará Mirim dyke swarm, dated to ~120-140 Ma (Mizusaki *et al*., 2002), or if it is a plug or lava flow, more similar to the Cenozoic structures. Despite the inconclusive age and dubious outcrop characteristics, it will be clear in Chapter 3 that the sample's geochemistry is still well within the range of the local Cenozoic lavas and indicates that it must be associated with the same magmatic event that led to the formation of the MQVL.

Sample 15BP4-7 is a transitional basalt collected from the large volcanic neck at the Serra do Saco do Inferninho. Apparent age spectra vary between 22 and 35 Ma and maintain high values for radiogenic ^{40}Ar (except for the very early heating steps) and K/Ca ratios (except for the very last steps) throughout the heating process. Although inconclusive, an attempt to

process the results produced age probability spectra (28.41 ± 0.13 and 28.07 ± 0.23) and inverse isochron ages (31.63 ± 0.05 and 31.43 ± 0.06) that suggest an age range within the Early Oligocene, which is in agreement with some of the oldest available ages for the MQVL (Silveira, 2006; and this study). It also agrees with the integrated ages of 32.1 ± 2.3 and 31.4 ± 1.5. However, $^{40}Ar/^{36}Ar$ intercepts (352.7 ± 2.3 and 319.8 ± 3.2) indicate excess ^{40}Ar, likely because of the ubiquitous peridotitic xenoliths in the sample, which could cause age overestimations.

Sample 15BP12-26 is an olivine alkali basalt from a plug NNW of Cerro Corá. Its age spectrum is the most irregular in the whole assemblage, varying mainly between 24 and 29 Ma after a sharp increase from significantly lower values during early heating steps. Integrated age and the age probability spectrum suggest ages of 25.63 ± 0.87 and 24.42 ± 0.1, respectively. Although the age spectrum values gradually decrease, they also have a slight peak towards relatively higher values in the middle heating steps, which is a unique feature when compared to the rest of the assemblage, and cannot be readily explained. No isochron could be plotted, and it is not clear why this sample failed to produce a resolvable age.

Discussion

Mecejana

$^{40}Ar/^{39}Ar$ ages for Mecejana indicate recurrent volcanic activity in the area between 31.71 and 35.31 Ma (Table 2-2; Figures 2-1, 2-2 and 2-3), and the results are similar to previous published ages obtained through other methods. Previous K/Ar ages vary between 29.9 ± 0.9 and 32 ± 1 (Cordani, 1970; Almeida *et al.*, 1988), whereas a Rb-Sr age of 36 ± 2 has also been mentioned (Almeida *et al.*, 1988; Mizusaki *et al.*, 2002). There are also K/Ar ages of 32-44 Ma for basaltic rocks from drill cores ~40-80 km off the coast of Ceará, which lie along or just north of the State's eponymous platform (ibid.). Basaltic seamounts ~40 km NNE of Fortaleza, north of and somewhat

outside the Fernando de Noronha fracture zone, produced the youngest of these ages, at 32 ± 1 Ma (Almeida *et al.*, 1988). These offshore ages and the Mecejana age of 32 ± 1 were obtained through K/Ar in the 1970s and 1980s and published in reports of the oil company Petrobras that are not readily available to the general public. We therefore cannot check the data directly and must rely on secondary references. Considering the problems with dating submarine basalts (see above), these ages should be treated with caution. Furthermore, relatively recent $^{40}Ar/^{39}Ar$ dates for Cenozoic volcanism in Northeast Brazil have sometimes produced younger ages than previous K/Ar results from the same samples, raising concerns that K/Ar may lead to overestimations due to the difficulty in measuring excess ^{40}Ar (Knesel *et al.*, 2011). These issues would also apply to these drill-core ages from Northeast Brazil, which therefore could also be overestimations. However, despite being significantly older, their range still overlaps and is consistent with our ages for Mecejana. For instance, samples 15BP10-21(b) (35.03 ± 0.28) and 15BP10-23 (34.61 ± 0.23), respectively from the Pão de Açucar and Serrote Salgadinho phonolite necks, produced two of the most robust ages in our dataset, and establish very reliably that the Mecejana volcanic field was active at the end of the Eocene.

One of the main issues concerning the measurements from the Mecejana phonolites is the disparity between groundmass and phenocryst ages from the same hand specimen from the localities of Japarara and the Ancurí quarry. Differences vary from ~0.5 to ~6.5 m.y. and phenocrysts are invariably older. Although sanidine phenocrysts will be a completely open system to Ar at magmatic temperatures, they can potentially hold melt inclusions that carry with them excess ^{40}Ar and lead to older apparent ages for phenocrysts in relation to groundmass. Although such inclusions were not identified petrographically, they could still be present. This could explain the difference of ~2.5 m.y. between the groundmass sample 15BP10-22(a) (32.00 ± 0.29) and the phenocryst sample 15BP10-22(b) (34.92 ± 0.27) from Japarara, where excess ^{40}Ar has been identified in the phenocryst

measurements. Although the calculations performed to produce the age spectrum diagram have been calibrated to account for it, the potential for an overestimation cannot be completely ruled out, given the significant difference with the groundmass sample. On the other hand, results for the groundmass sample also suggest some Ar recoil loss and/or redistribution, and could itself be an underestimation. If we rely on the sanidine measurement, the age range for the Mecejana volcanic field given above would be contracted to 32.81 to 35.31 Ma, which is ~1 m.y. shorter at its youngest threshold. Considering that the effects of excess ^{40}Ar are measured quantitatively and therefore are easier to deal with numerically during the calculations, and the effects of Ar recoil and redistribution are observed more qualitatively than quantitatively in the results, we believe that the phenocryst age is a better representation of the age of the Japarara locality. In the case of the groundmass sample 15BP10-20(a) (24.65 ± 0.15) and phenocryst sample 15BP10-20(b) (30.80 ± 0.22), both from the same hand specimen from the Ancurí quarry, there are too many issues with the groundmass age and we concluded it should be discarded altogether in favour of the phenocryst age for the locality.

The groundmass sample 15BP9-19c and the phenocryst sample 15BP9-19a both come from the same locality (Caruru quarry) but from two distinct hand specimens. They produced consistent ages that are close to each other, reinforcing the strength of our results for the locality. Sample 15BP9-19a was taken from the bottom of the central section of the quarry, 10s of meters deep, and had its sanidine phenocrysts dated, whilst sample 15BP9-19c is stratigraphically higher, coming from the margin of the quarry at surface level, and had its groundmass dated. Sample 15BP9-19a had one measurement run that produced a good plateau age of 33.48 ± 0.15 Ma, whilst sample 15BP9-19c produced an age of 32.96 ± 0.15 Ma based on two measurement runs, from which the one with an inverse isochron intercept value of 297.4 ± 16.4 was chosen, as it matches current atmospheric values (the intercept value for the other measurement being 249.5 ± 26.4).

Together, these ages indicate a relatively continuous period of activity at the Caruru volcanic centre.

The Pão de Açucar locality also had two distinct samples dated. The locality consists of a phonolite neck containing texturally and chemically distinct rocks, of which two had their sanidine phenocrysts dated. Unfortunately, field relations between the different rock types could not be obtained due to the heavily wooded terrane. Sample 15BP10-21a is an aegirine-phyric phonolite with strong trachytic texture, and sample 15BP10-21b is a hyalopilitic amphibole phonolite with a more subdued trachytic texture. The samples produced good plateau ages of 33.94 ± 0.25 Ma and 35.03 ± 0.28 Ma respectively, suggesting that volcanic activity recurred in the same volcanic centre over a relatively long period of time.

MQVL

Despite the lack of age progression along the MQVL, our $^{40}Ar/^{39}Ar$ results highlight some patterns within and between individual volcanic centres in the lineament. For instance, 15BP3-5 is a transitional basalt lava flow sample collected northwest of Sossêgo, State of Paraíba, in the Cubati basin and on the northwest corner of the Cubati lava field, for which exposure covers 10s of square km, despite keeping close to ground level (Figure 2-1). One groundmass measurement produced a very good plateau age of 24.50 ± 0.08 Ma, comprising over 75% of released ^{39}Ar and maintaining low standard deviation, with matching ages (within 2σ) from the inverse isochron and age probability spectra. Souza et al. (2013), using somewhat different methods, also calculated an $^{40}Ar/^{39}Ar$ age of 24.9 ± 0.1 Ma for a sample collected on the southern area of the same lava field, several kilometres away. The almost overlapping ages at both ends of the exposure suggests that the Cubati lava flow, despite its size, was the result of relatively continuous activity in the same centre.

Other chronological patterns within the MQVL include the relationship between sample 15BP5-8 (33.99 ± 0.09 Ma), a basanite sample from the

Socavão plug, and sample 15BP5-9 (33.91 ± 0.94 Ma), a basanite plug sample from the Carnaubinha quarry (Figure 2-1). They are located respectively to the southeast and northeast of the town of Cerro Corá, just under 25 km from each other, and at the central segment of the MQVL. Their virtually identical ages have good resolvability, and together with their geographical proximity suggest that they could be related to a single period/event of volcanic activity. These two volcanic centres also produced the oldest basalt ages in this study and are synchronous with activity in the Mecejana volcanic field ~350 km to the northwest (Figure 2-1). Sample 15BP5-10 (29.29 ± 0.11 Ma), ~14 km to the west, also produced consistent ages with these two centres and clearly sets the earliest recorded activity on the central segment of the MQVL at beginning of the Oligocene, perhaps stretching back to the late Eocene (Figure 2-3). Conversely, according to previously published work, other basaltic centres around Cerro Corá (i.e. Cabugizinho, Cabelo de Negro and Serra Preta near Residência, represented here respectively by samples 15BP6-12a, 15BP8-17 & 15BP8-18 and 15BP12-25) and geographically close to samples 15BP5-8 and 15BP5-9 (i.e. 20-40 km) also produced the youngest ages in the MQVL (8.9 ± 0.5 Ma to 7.1 ± 0.3 Ma), which are in turn synchronous with activity in Fernando de Noronha over 450 km to northeast (Knesel et al., 2011; Perlingeiro et al., 2013; Silveira, 2006; Figure 2-3).

Sample 15BP7-15 (12.39 ± 0.24 Ma), the most northern sample of the MQVL that is not associated with any basins, but sill located in the central segment of the MQVL, produced the youngest age in our assemblage. The result is also consistent with the age of 14.7 ± 0.9 Ma obtained by Silveira (2006). These patterns indicate intermittent volcanic activity in the central segment of the MQVL recurring for ~25 m.y., as well as synchronicity with other volcanic centres 100s of kilometres away at what could be considered the extremities of any supposed plume track in the region (i.e. the Mecejana volcanic field and Fernando de Noronha).

Basaltic volcanic occurrences in the basins on the northern and southern extremities of the MQVL are also not only synchronous with each other (i.e. samples 15BP3-2 and 15BP7-14) but also with occurrences at the centre of the lineament (Silveira, 2006; Figure 2-3). For example, despite a distance of > 120 km, volcanism in the Cubati basin (24.5 ± 0.08 Ma) produced ages close to those published for the Cabugi peak (25.5 ± 0.6 Ma; Silveira, 2006), the largest volcanic edifice in the continental sector of Northeast Brazil and located in the central segment of the MQVL (see Chapter 1 and Figure 1-4, where the Cabugi locality is represented by sample 15BP6-13 and point B13 on the map). Our results for the MQVL basins also show remarkable agreement with other published ages for basaltic occurrences in the Cubati and Boa Vista basins that range from ~27.3 Ma to ~22.0 Ma (Souza *et al.*, 2013). This further reinforces the synchronicity of volcanic activity in the southern basins with the central segment of the MQVL (e.g. samples 15BP5-10 and ages from Silveira, 2006) and the Potiguar basin to the north (sample 15BP7-14), and shows that basaltic volcanism in the basins lies chronologically between activity in Mecejana and Fernando de Noronha. Souza et al. (2013) also obtained an age of ~12.5 Ma for a trachyte dyke cutting through the Boa Vista basalts and all other lithologies in the basin. This date brings volcanism in the southern basins closer to the occurrences in Fernando de Noronha and the younger activity in the central segment of the MQVL (i.e. sample 15BP7-15 with an age of 12.39 ± 0.24 Ma), and also suggests a shift in petrogenetic and/or tectonic processes in the basin. Volcanic outcrops change from extensive primitive to intermediate subalkaline lava flows to small evolved transitional dykes.

Notwithstanding the relatively young date of the Boa Vista trachyte dyke (Souza *et al.*, 2013), volcanism in the northern and southern basins of the continental sector are relatively contracted chronologically when compared to the central segment of the MQVL. The basin outcrops are also dominated by extensive lava flows of relatively more silica saturated and

evolved basaltic rocks, contrasting with the dominance of hypabyssal outcrops that are more silica undersaturated in the other areas (see Chapter 1 and Table 1-1; the detailed geochemistry of the region will be discussed in Chapter 3). A similarly contracted time range is seen in Mecejana, which is mostly concentrated at the Eocene-Oligocene boundary, and permanently ceases around the time activity starts in the basins during the late Oligocene.

Northeast Brazil as a whole

Despite the limited chronological range of Mecejana and the MQVL basins, volcanism in Northeast Brazil as a whole is more or less continuous from ~35 Ma to ~21 Ma, recurring between different centres at relatively short intervals (Silveira, 2006; Souza et al., 2013; and this study). This span of activity is followed by a period ~6-8 m.y. of apparent volcanic quiescence, before resuming again more or less synchronously with Fernando de Noronha (~12-14 Ma; Perlingeiro et al., 2013; Souza et al., 2013). It is also preceded by sparse volcanic activity dating back to 51.8 ± 0.9, which also include plutonic outcrops (Silveira, 2006). These patterns are clear in Figure 2-3. Synchronous volcanism in the northern and southern basins of the MQVL, the two extremities of the lineament and where its most silica saturated and evolved rocks are located, represent the last stages of this more or less continuous span of activity that extends from the late Eocene and throughout the Oligocene, and is the strongest evidence against age progression along the MQVL. Synchronous volcanism in the central segment of the MQVL with both the Mecejana volcanic field (Eocene-Oligocene) and Fernando de Noronha (Miocene) are the strongest evidence against age progression between the different Cenozoic volcanic areas of Northeast Brazil. The apparent period of volcanic quiescence (between ~20 Ma and ~14 Ma) that follows after activity in the basins has ceased, therefore, separates a period of intense and widespread volcanism, marked by a significant representation of alkali basalt and some transitional basalt and basaltic andesite, from one of geographical contraction and significant

increase in the proportion of nephelinite, with basanite being a common rock type in the two periods.

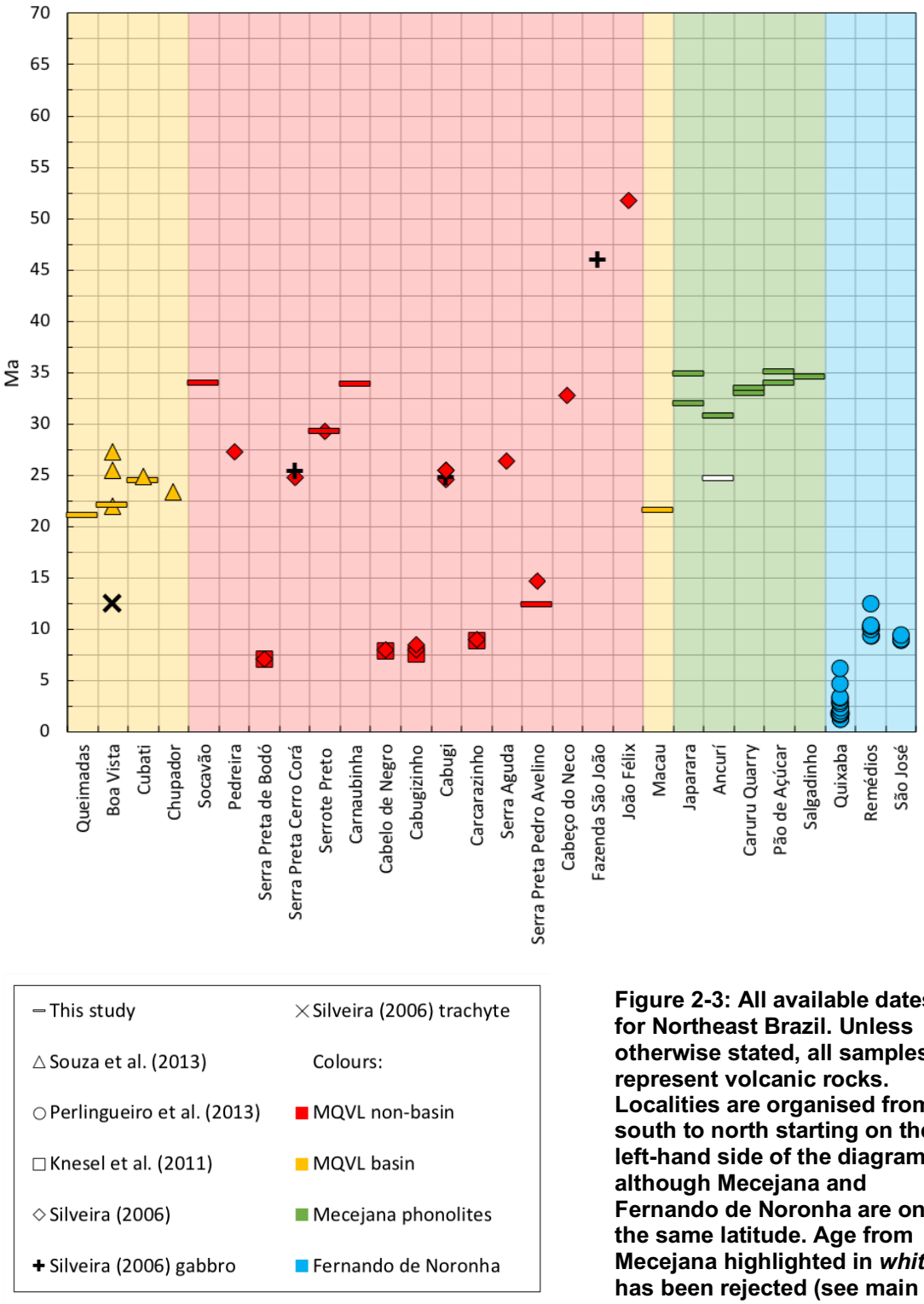

Figure 2-3: All available dates for Northeast Brazil. Unless otherwise stated, all samples represent volcanic rocks. Localities are organised from south to north starting on the left-hand side of the diagram, although Mecejana and Fernando de Noronha are on the same latitude. Age from Mecejana highlighted in *white* has been rejected (see main text).

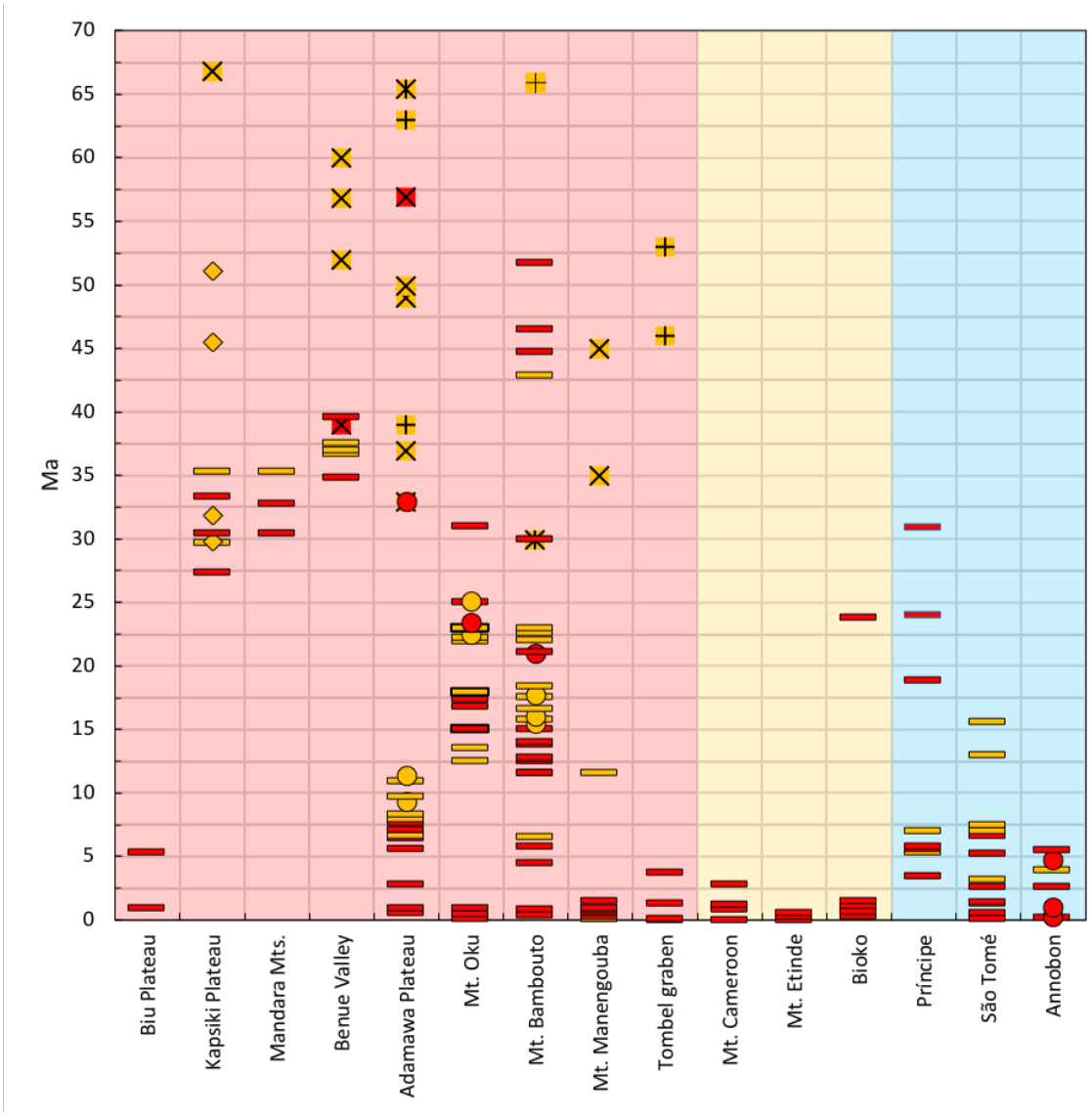

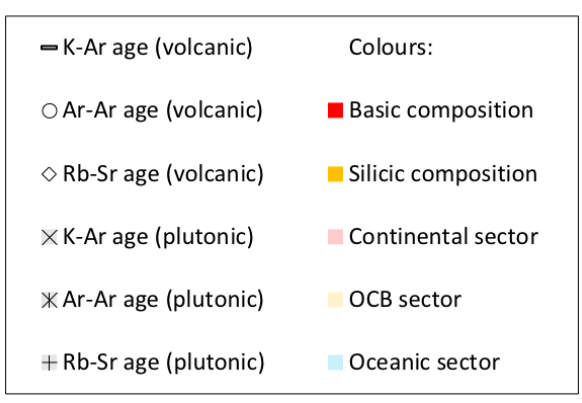

Figure 2-4: Ages for the Cameroon Line compiled in Njome and de Wit (2014). Localities are organised from north to south (i.e. Biu plateau to the Adamawa plateau) then from east to west (i.e. from the Adamawa plateau to the oceanic islands), starting on the *left-hand side* of the diagram. The order from east to west is reversed for better comparison with ages for Northeast Brazil illustrated in Figure 2-3. *OCB = oceanic-continental boundary*.

The lack of age progression along the MQVL or between the different volcanic areas of Northeast Brazil seriously undermines a model based on a deep mantle plume to explain magmatism in the region. One possibility that would favour the plume model and that is still left untested is the potential age progression along the seamount chain connecting the Fernando de Noronha archipelago and the Mecejana volcanic field. However, if this chain were to be caused by a deep mantle plume, it would have to be synchronous with a continuous and independent magmatic process active in the MQVL abutting to the south. It is unlikely that two independent magmatic processes would remain active for so long and so close to each other without significant mutual interference. Furthermore, in Chapter 3 we will demonstrate that all these centres are geochemically virtually identical, indicating that they are the result of the same process of magmatism.

The stratigraphy of the Boa Vista basin shows a vertical and lateral transition from subaqueous environments represented by pillow lavas (sample 15BP3-3b; Figure 1-8 in Chapter 1) to subaerial eruptions represented by extensive lava flows within the basin (sample 15BP3-4) and, during later stages, around the basin (sample 15BP3-2). This development has been discussed in detail by Souza et al. (2013) and is confirmed by the ages obtained here. Phonolite and trachyte are also absent during the period of basin extension and the build-up of some of the largest volcanic edifices in the area, but appear both before and after it, even though they are only volumetrically significant in the geographically peripheral areas of Mecejana and Fernando de Noronha. It is difficult to establish what, if any, are the relationships between basin extension and what seems to be the period of most intense magmatism in the continental sector, or between activity in the basins and the decrease in the proportions of evolved alkaline lavas in favour of subalkaline intermediate ones. It is likely that basin extension locally boosts the surface expression of sublithospheric magmatism that is affecting the MQVL as a whole, assuming that lithospheric stretching facilitates magma ascent and provides a positive feedback for the increase in melt

fractions and silica saturation through decompression melting. Facilitating magma ascent should also work against sluggish magma movement through the lithosphere and stagnant magma chambers, and thereby hinders magma evolution to phonolitic or trachytic compositions. Therefore, chronological patterns for Cenozoic volcanism in Northeast Brazil show that magmatic activity may be divided in two distinct stages that also reflect changes in lithology, with a period of quiescence in between them, with the first stage also showing a chronological development of its lithologies and volcanic processes.

Comparisons with Cameroon Line

Cenozoic magmatism along the Cameroon Line (Figure 2-5) is marked by continental activity from ~66 Ma to the present, but with a dominance of plutonic occurrences in the period before ~35 Ma, and volcanic occurrences in the period after ~35 Ma (Fitton, 1987; Njome and de Wit, 2014). Activity on the oceanic sector coincides with the continental volcanic period, starting at ~33 Ma (ibid.). Activity in the oceanic-continental boundary (OCB), which includes Mt. Cameroon, Mt. Etinde and the island of Bioko, comprises almost exclusively activity since ~4 Ma (ibid.). Whilst the continental sector of the OCB is completely contained within this age interval, there is a single date that is older (~24 Ma) for the island of Bioko.

In light of all available dates for Northeast Brazil, it becomes clear that Cenozoic magmatism in the region is synchronous with the Cameroon Line, on the other side of the Atlantic. All the available chronological data for the latter has been synthesised in the review paper by Njome and de Wit (2014), which may be compared to Northeast Brazil (Figures 2-3 and 2-4). Both provinces correspond to matching regions along the South American and African conjugate margins, but despite their Cenozoic volcanic activity being synchronous, the oldest available dates for either region (i.e. ~52 Ma for Northeast Brazil and ~66 Ma for the Cameroon Line) significantly postdate continental separation, which was completed by ~100 Ma (Chapter 1). By

comparing the oldest ages from both conjugate margins with available ages for magnetic anomalies on the Atlantic ocean floor (Njome and de Wit, 2014; Pérez-Diaz and Eagles, 2014; Pérez-Díaz and Eagles, 2017), it is clear that volcanism in the two provinces reflects magmatic processes acting on two independent plates (Figure 2-6). Plate reconstruction shows that volcanism only started once the two continents were well apart from each other and a significant stretch of the Atlantic Ocean basin had formed, with ~2000 km separating the two conjugate margins (see also Nürnberg and Müller, 1991).

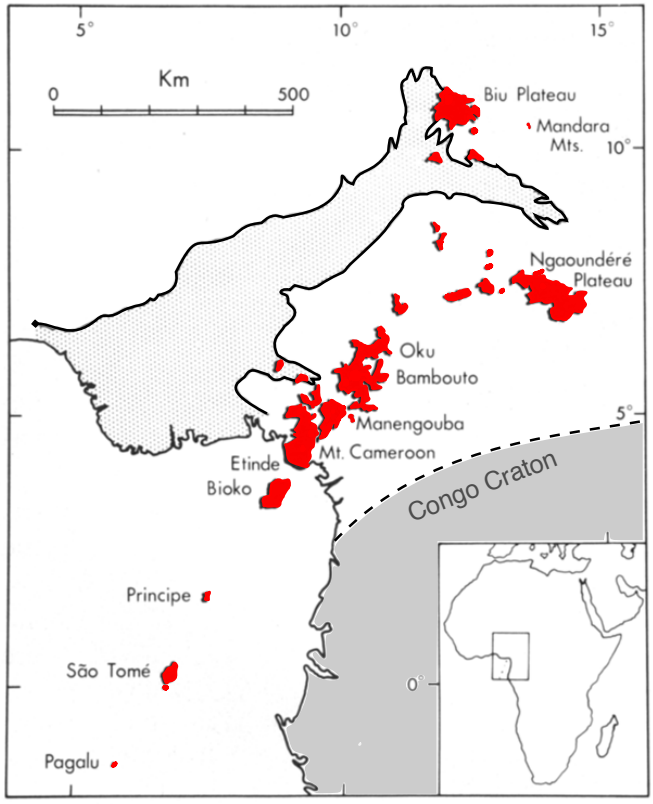

Figure 2-5: Distribution of volcanism along the Cameroon Line with the approximate position of the Congo craton. Adapted from Fitton and Dunlop (1985).

The Cameroon Line also shows patterns of chronological development that are somewhat similar to those in Northeast Brazil. Volcanism ceased in centres northeast of Mt. Oku and north of the Adamawa plateau (i.e. Mandara mountains and the Benue Valley, including the Kapsiki Plateau; Figures 2-4 and 2-5) in the middle Oligocene (~27 Ma). Cessation of activity in the north-eastern segment of the Cameroon Line would only be broken by relatively recent activity in the Biu plateau (~5 Ma to the present), but this is

markedly contracted chronologically and geographically when compared with activity up to the middle Oligocene at the Mandara mountains, the Benue Valley and the Kapsiki plateau. The Adamawa plateau, representing the eastern arm of the Cameroon Line, also goes through a period of inactivity lasting ~20 m.y., from ~32 to ~13 Ma, which also starts roughly together with cessation of activity in the north-eastern segment of the chain (Figure 2-4). However, notwithstanding this quiescence period, magmatic activity in the Adamawa plateau persists throughout the entire chronological range of the Cameroon Line, similarly to the central segment of the lineament (i.e. from Mt. Oku to the southwest to the Mt. Manengouba and the Tombel graben; Figures 2-4 and 2-5).

The quiescence period in the northern and eastern arms of the Cameroon Line marks a geographical shift, when the bulk of activity shifts to the central (continental) segment of the lineament, and commences in the oceanic sector in the early Oligocene (Njome and de Wit, 2014). In Northeast Brazil, this period also coincides with the onset of activity in Mecejana. Therefore, Cenozoic volcanism in both Northeast Brazil and the Cameroon Line saw significant geographical restructuring in the late Eocene to the early Oligocene, and volcanism in both oceanic sectors postdates activity in the continent, despite the lack of age progression between the continental or oceanic centres.

Moreover, plutonic occurrences lie amongst the oldest reported ages in both conjugate margins (Silveira, 2006; Njome and de Wit, 2014). In Northeast Brazil, the microgabbro of the São João locality produced the region's second oldest available $^{40}Ar/^{39}Ar$ date (46 ± 4), and in the Cameroon Line, the oldest $^{40}Ar/^{39}Ar$ age (65.0 ± 0.8) is for the Hossere Nigo plutonic occurrence associated with the Adamawa plateau (Kamdem *et al.*, 2002), with the oldest overall age for the Cameroon Line being a Rb-Sr age of 66 ± 3 for Golda Zuelva at the Kapsiki plateau (Jacquemin *et al.*, 1982).

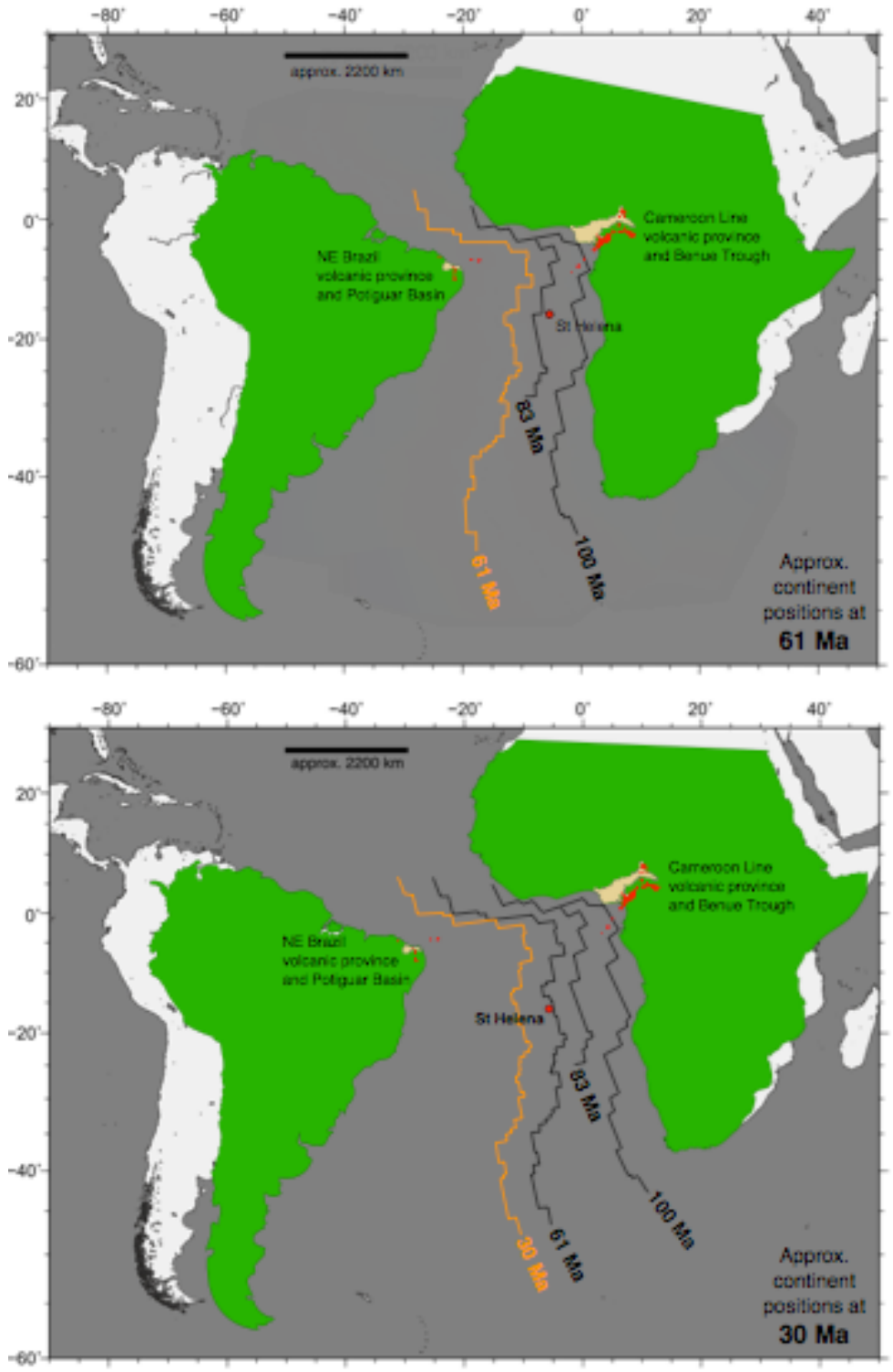

Figure 2-6: Approximate positions of South America and Africa at 61 Ma (*above*) and 30 Ma (*below*), in *green*, compared with their current position, the ages of the ocean basin magnetic anomalies and the coeval position of the mid-ocean spreading ridge (in *black* and *orange*). Adapted from Njome and de Wit (2014), Pérez-Diaz and Eagles (2014) and Pérez-Díaz and Eagles (2017). The reconstructions indicate over 2000 km of oceanic lithosphere between South America and Africa at the time volcanism started at the Cameroon Line. The current position of the St Helena island is shown for comparison.

It is also noteworthy that volcanism in the oceanic sectors of both conjugate margins concentrate in the past 7 m.y. Although this could reflect sampling bias, since early stages of oceanic activity are inaccessible and some localities have at least 4 km of volcanic edifice (e.g. Fernando de Noronha), swells in the oceanic lithosphere along the Cameroon Line are the result of uplift within the past 30 m.y., in accordance with ages for the oceanic sector (Meyers et al., 1998, according to Njome and de Wit, 2014).

Although volcanism in Northeast Brazil is more restricted geographically and volumetrically, and lacks any recent activity as seen in the Cameroon Line, it could simply reflect less vigorous magmatism in the region and does not necessarily point to significantly different magmatic processes. Instead, the remarkably similar chronological patterns argue in favour of similar magmatic process with roughly parallel timeframes operating in the two conjugate margins and likely triggered by continental separation.

Overall, there is a slight offset between the published dates for Northeast Brazil and those for the Cameroon Line, with the former being younger. Summarising all the available dates shows that the Cameroon Line has had magmatic activity since ~66 Ma on the continental sector and ~31 Ma on the oceanic sector (Njome and de Wit, 2014), whereas in Brazil these dates are respectively ~52 Ma and ~12 Ma (Silveira, 2006; Perlingeiro *et al.*, 2013). However, if we consider the ages from the Petrobras drill cores (Almeida *et al.*, 1988), activity in the Brazilian oceanic sector is pushed back to ~ 44 Ma. Nonetheless, drill-core ages are likely to be older, being stratigraphically deeper, and drill-cores in the oceanic sector of the Cameroon Line would also likely push the local ages further back. Furthermore, most of the African dates for extrusive rocks were obtained through K/Ar, and $^{40}Ar/^{39}Ar$ measurements for volcanic samples remain limited to ages < 33 Ma in the continental sector and < 5 Ma in the oceanic sector. As mentioned above, K/Ar ages in Northeast Brazil have shown a tendency towards overestimations due to the difficulty in tracking the

presence of excess ^{40}Ar (Knesel *et al.*, 2011), which would also apply to the drill-core ages from Northeast Brazil. The same issue has been reported in the Cameroon Line in a study by Kamdem et al. (2002) that compares K/Ar and $^{40}Ar/^{39}Ar$ ages for the same sample directly with each other and show a difference of ~7 m.y. If this is the case, ages form both oceanic sectors could potentially be brought closer together by further $^{40}Ar/^{39}Ar$ dates along the Cameroon Line ocean islands, and the drill-core ages from Northeast Brazil could also be brought closer to activity in Mecejana. The overall lack of $^{40}Ar/^{39}Ar$ ages for the Cameroon Line is one of the main problems with the local chronology (Njome and de Wit, 2014). Nonetheless, these issues are not so significant when assessing the overall geological timescale of the magmatic processes affecting both conjugate margins, and it is clear that Cenozoic volcanism in Northeast Brazil and the Cameroon Line are synchronous and share remarkable chronological parallels. These patterns become even more significant in light of the two areas being geochemically virtually identical, which will be the topic of the next chapter.

Chapter 3: Petrography and Geochemistry of Cenozoic Volcanism in Northeast Brazil

Introduction

This chapter concerns the geochemistry of rocks from the Borborema Province and Fernando de Noronha in Northeast Brazil. It will be demonstrated that lavas from Northeast Brazil must be geochemically related to one another, regardless of their continental or oceanic contexts, and that variability is controlled mainly by differences in depth and degrees of partial melting. Some variability trends are especially clear in the extensional basins of the Macau-Queimadas Volcanic Lineament (MQVL), where shallow melting and large melt fractions are more accentuated. Xenocryst and xenolith contamination and occasional alteration have also affected rocks in the assemblage. The former is especially common amongst primitive samples in the continental sector, whilst the latter is particularly strong amongst intermediate samples in the oceanic sector. Although the effects of these processes are limited in scope, discussing them emphasises the similarity between the continental and oceanic sectors, as it highlights the circumstantial nature of some of the more obvious differences within the assemblage. Similarities between the two sectors also extend to evolved rocks, which are represented in the continental sector solely by the Mecejana phonolites. The degree of variability between continental and oceanic evolved samples is greater than for primitive compositions. However, this should be expected, and despite localised differences that represent their distinct evolutionary contexts, continental and oceanic phonolites are remarkably similar.

We will start with a brief note on the methods and definitions used in this discussion. Then we will present a summary of our petrographic observations, and the major and trace element geochemistry for all rocks in

the assemblage. This will be followed by a discussion of the main trends in the dataset. Finally, we will present and discuss the isotopic data.

Methods and Definitions

The geochemical data discussed in this chapter include major and trace element concentrations obtained through x-ray fluorescence (XRF), trace element concentrations obtained through inductively coupled plasma mass spectrometry (ICP-MS), and $^{87}Sr/^{86}Sr$ and $^{143}Nd/^{144}Nd$ isotopic ratios obtained in a thermal ionisation mass spectrometer after samples had been prepared through cation exchange column chemistry. Methods are described in detail in Appendix A. For the purpose of plotting the major element data, the analyses have been normalised on a volatile-free basis, and all iron is recalculated as Σ FeO. The original data are given in the data tables in Appendix C. In the XRF trace element dataset, K, P and Ti concentrations that are given in parts per million (ppm) were calculated from their major element oxide weight percentages (i.e. K_2O, P_2O_5 and TiO_2). The ICP-MS trace element dataset covers more elements than the XRF analyses, and will be the dataset most used for comparisons between the continental and oceanic sectors of Northeast Brazil (i.e. Borborema and Fernando de Noronha). However, there is also a wide range of XRF data available for oceanic islands across the world that were obtained in the same laboratory and using the same techniques as our own XRF data. Therefore, when making comparisons with this global dataset, the XRF trace element data will be used instead of the ICP-MS.

Details about sample locations and context are given in Chapter 1. All hand specimens from the MQVL selected for petrographic and geochemical analyses appear fresh. Basaltic samples are overall unremarkable fine-grained dark grey rocks, but stand out for their ubiquitous peridotitic mm- and cm-scale xenoliths and xenocrysts. In Fernando de Noronha, a similar ubiquitous presence of peridotitic material is only seen in the São José

Formation, where xenoliths are also significantly larger (up to ~30 cm). These xenoliths were avoided as much as possible during sample preparation for geochemical analyses. Details of how these xenoliths affect our analyses will be discussed below.

Amongst basaltic samples, primitive compositions will be defined as those with MgO ≥ 8 wt.% and SiO_2 ≤ 50 wt.%. Petrographic observations and major element data for the whole assemblage show that MgO values of 5-7 wt.% are dominated by basaltic trachyandesite and basaltic andesite in both sectors, indicating significant degrees of fractional crystallisation. The trachybasalt sample FN25-46 (MgO = 5.63 wt.%) is the only exception to this trend, but for the sake of consistency it will not be considered within our definition of primitive samples. The Remédios basaltic dykes in Fernando de Noronha (i.e. FN13-22; FN12-34; FN12-35 and FN20-41), the only basaltic samples in that Formation, although in the range of 7-8 wt.% MgO, form a geochemically and petrographically distinct subgroup in the assemblage that is not volumetrically representative and therefore will be excluded or treated separately for most of the discussion. Basaltic rocks comprise all those defined as primitive plus all basaltic andesite, all basaltic trachyandesite and the trachybasalt FN25-46. Intermediate samples comprise those between and excluding the classification fields of basalt, trachybasalt and tephrite-basanite on the one hand, and rhyolite, trachyte and phonolite on the other, according to the total-alkalis and silica classification scheme given in Le Maitre et al. (2002). Evolved samples refer to rhyolite, trachyte and phonolite. Geochemical and petrographic classifications were based mainly on Le Maitre et al. (2002) and Mackenzie et al. (1982).

Petrography

Petrographic observations are given in detail in Appendix E and summarised in Table 3-1. They are consistent with the geochemical analyses that will be presented below. The primitive assemblage is dominated by alkali

basalt, basanite, nephelinite and transitional basalt roughly in this order of proportion. Representative samples from the MQVL are given in Figure 3-1. Samples petrographically classified as subalkali basalt also include those geochemically classified as basaltic andesite (see geochemical data below), since their glassy textures and sparsity of phenocrysts hinders the assessment of plagioclase compositions and therefore the distinction between the two rock types. Except for sample FN25-46, there are no trachybasalt or picro-basalt in the assemblage. The Remédios dykes in Fernando de Noronha are petrographically distinct, dominated by titanaugite tephrite but with virtually all their original olivine replaced by calcite and/or smectite pseudomorphs. Virtually all Remédios dyke samples are also vesiculated, which is unusual in the archipelago, but could be the result of their distinct emplacement setting and inability to easily degas. Apart from the dykes, tephrite is proportionally rare in the assemblage, and represented only by samples FN16-27; FN19-31 and FN15-19.

Overall, rocks in Fernando de Noronha are more varied than in Borborema, even when only primitive samples and phonolites are considered. Nonetheless, the Remédios dykes and the alkali basalt from the São José Formation represent two internally homogeneous subgroups in the archipelago. The transitional and subalkaline basaltic samples from the continental basins are also relatively homogeneous both texturally and mineralogically.

Table 3-1: Summary of petrographic observations. *g.m.* = groundmass; *pdt* = peridotite; uncert. = uncertain; *ab* = albite; *agr* = aegirine; *amph* = amphibole; *antc* = anorthoclase; *aug* = augite; *bt* = biotite; *cpx* = clinopyroxene; *dp* = diopside; *fds* = feldspar; *K-fds* = K-feldspar; *krs* = kaersutite; *ne* = nepheline; *ol* = olivine; *opq* = opaques; *opx* = orthopyroxene; *plg* = plagioclase; *sgm* = sodalite-group mineral; *snd* = sanidine; *sph* = sphene; *spl* = spinel; *Ti-aug* = titanaugite.

Sample	Rock	Phenocrysts (modal%)	*g.m.* minerals	Acces. minerals	Xenocrysts and xenoliths	Other features
MQVL						
15BP1-1	Basanite	*ol* (10-15%); *aug** (50-60%)	*aug; opq*	*Ti-aug*	*pdt* (rare); *ol* (5-7%); *opx* (rare)	-
15BP3-2	Alkali basalt	*Ti-aug* (20-25%); *ol* (1-2%)	*plg; Ti-aug; ol; opq*	-	*ol* (uncert.)	-
15BP4-6	Basanite	*ol* (10-15%)	*aug; ne; ol; opq*; *plg* (rare)	*Ti-aug*	*pdt* (uncert.)	-
15BP4-7	Ol. basalt	aphyric	*ol; aug; plg; opq*	-	*ol* (uncert.)	ocelli
15BP5-8	Basanite	*ol* (10-15%)	*aug*; *ol; plg* (rare); *opq*	*Ti-aug*	*ol* (5-7%); *opx; spl* sandstone xenolith (1 grain)	ocelli
15BP5-9	Basanite	*ol* (7-10%); *Ti-aug* (1%)	*aug; ol; plg* (rare); *opq*	-	*ol* (5-7%); *spl* (1 crystal)	ocelli
15BP5-10	Ol. alkali basalt	aphyric	*plg; aug; ol; opq*	-	*ol* (2-3%); *Ti-aug* (rare)	ocelli amygdales (rare)
15BP5-11	Ol. alkali basalt	aphyric	*plg; Ti-aug; ol; opq*	-	*ol* (< 3%)	ocelli (≤ 2 cm) amygdales (< 1%)
15BP6-12a	Ol. alkali basalt	*ol* (10-15%)	*plg; aug; ol; opq*	*Ti-aug*	*pdt* (≤ 2 cm); *ol* (5-7%); *opx; spl; dp*	ocelli
15BP6-13	Ol. alkali basalt	*ol* (10-15%)	*Ti-aug; ol; plg; opq*	-	-	-
15BP7-15	Ol. nephelinite	*ol* (7-10%); *aug** (1-2%)	*aug; ne; opq*	-	*pdt* (5-7%)	ocelli
15BP7-16	Ol. alkali basalt	*ol* (15-20%); *Ti-aug* (1%)	*ol; Ti-aug; plg; opq*	-	*ol* (10-15%); *opx* (rare)	ocelli
15BP8-17	Titanaugite-phyric basanite	*ol* (10-15%); *Ti-aug* (15-20%); *plg* (rare)	*Ti-aug; ol; plg; opq*	-	*ol* (uncert.)	ocelli
15BP8-18	Ol. alkali basalt	*ol* (10-15%); *Ti-aug* (15-20%)	*Ti-aug; ol; plg* (rare); *opq*	-	*pdt; ol* (< 2%)	ocelli
15BP11-24	Ol. alkali basalt	*ol* (10-15%)	*ol; aug; plg; opq*	-	*plg* (2-3%); *pdt* (uncert.)	ocelli (2-3%)
15BP12-25	Ol. nephelinite	*ol* (5-7%); *Ti-aug* (3-5%)	*ol; aug; ne; opq*	-	*pdt* (uncert.)	-
15BP12-26	Ol. alkali basalt	*ol* (10-15%); *Ti-aug* (3-5%)	*ol; Ti-aug; plg; opq*	-	*ol; opx; spl; total* = 3-5%	ocelli (1-2%)

Sample	Rock	Phenocrysts (modal%)	*g.m.* minerals	Acces. minerals	Xenocrysts and xenoliths	Other features
MQVL basins						
15BP3-3a	Hyalo-basalt	*ol; aug; plg;* total < 5%	*plg; aug;* total < 5%	-	*pdt; ol; opx; dp*	vesicles + amygdales (10-15%) pseudomorphs after *ol*
15BP3-3b	Subalkali basalt	*plg** (rare); *ol** (2-3%)	*plg; ol*	-	-	vesicles + amygdales (rare) pseudomorphs after *ol*
15BP3-4	Ol. basalt	*ol; aug; plg;* total = 7-10%	*plg; aug; opq*	-	*pdt* (uncert.)	-
15BP3-5	Ol. basalt	*ol* (5-7%); *aug* (3-5%)	*plg; aug; ol; opq*	-	-	-
15BP7-14	Ol. subalkali basalt	aphyric	*ol; plg*	-	-	vesicles (5-7%, ≤ 0.5 cm)
Mecejana volcanic field						
15BP9-19a	Phonolite	*snd* (20-25%); *krs* (< 2%); *Ti-aug* (< 2%)	*snd; agr; opq*	*sph; ne*	-	-
15BP9-19c	Aegirine phonolite	*snd* (15-20%); *ne* (3-5%); *krs* (< 2%); *sgm* (1-2%)	*snd; agr; ne*	*sph; opq*	-	-
15BP10-20	Aegirine-phyric phonolite	*agr* (3-5%); *ne* (3-5%); *snd* (rare)	*snd; ne*	-	-	-
15BP10-21a	Aegirine-phyric phonolite	*agr* (7-10%); ne (5-7%); snd (2-3%)	*snd; ne*	*krs*	-	-
15BP10-21b	Aegirine phonolite	*snd* + *ne* (10-15%); *agr** (3-5%); *krs* (1-2%); *aug* (rare)	*snd; agr; ne*	*sph; opq*	-	-
15BP10-22	Phonolite	aphyric	*snd*; *agr; ne*	*krs; sph*	-	-
15BP10-23	Aegirine phonolite	*snd* (7-10%); *ne* (≤ 1%); agr* (1-2%)	*snd; agr; ne*	*sph; opq*	-	-
Fernando de Noronha						
FN01-01	Trachyte	*snd* (3-5%); *sgm* (3-5%)	*snd; opq*	*ne; agr; sph*	-	-
FN01-02	Trachyte	*snd* (2-3%)	*snd; agr; opq*	*sph; sgm; amph*	-	pseudomorphs after *sgm*

Sample	Rock	Phenocrysts (modal%)	*g.m.* minerals	Acces. minerals	Xenocrysts and xenoliths	Other features
Fernando de Noronha (cont.)						
FN02-03	Phonolite	*snd* (2-3%); *ne* (3-7%); *sgm* (2-3%); *krs* (1-2%)	*snd; agr; opq*	*sph*	-	-
FN03-04	Phonolite	*snd* (1-2%); *ne* (3-7%); *agr** (1-2%); *sgm* (1-2%)	*snd; agr*	*krs; sph*	-	-
FN04-05	Ol. alkali basalt	*ol* (7-10%); *Ti-aug** (2-3%)	*aug; plg; opq*	-	-	-
FN04-06	Ol. alkali basalt	*ol* (3-5%); *Ti-aug** (5-7%)	*aug; opq*	*plg*	-	vesicles (5-7%, ≤ 0.6 cm)
FN05-07	Ol. alkali basalt	*ol* (10-15%); *Ti-aug** (7-10%)	*aug; opq*	*plg*	-	-
FN06-08	Basanite	*ol* (10-15%); *aug* (7-10%)	*aug; opq*	-	-	vesicles + amygdales (25-30%)
FN07-09	Basanite	*ol* (10-15%); *Ti-aug* (≤ 1%)	*Ti-aug; ne; opq*	*bt*	-	-
FN07-10	Basanite	*ol* (10-15%); *Ti-aug* (≤ 1%)	*Ti-aug; ol; ne; opq*	*plg; bt*	-	-
FN10-14	Phonolite	*snd* (3-5%); *sgm* (3-5%); *krs* (3-5%); ne (2-3%); agr (1-2%); *sph* (1%)	*snd; agr; opq*	-	-	-
FN10-15 & FN10-16	Phonolite	*snd* (3-5%); *ne* (2-3%); *agr* (1-2%); *krs* (3-5%)	*snd; agr; opq*	*sph; bt*	-	pseudomorphs after *sgm* (1-2%) tear-shaped ocellus (0.5 cm)
FN10-17	Phonolite	aphyric	*snd; agr; opq*	*krs; sgm*	-	-
FN14-18	Ol.-phyric nephelinite	*ol* (7-10%)	*aug; ne; opq*	*Ti-aug*	*ol* (very rare, uncert.)	-
FN15-19	Tephrite	*ol* (5-7%)	*aug; ne; opq*	*plg; Ti-aug*	-	vesicles + amygdales + devitrified glass (15-20%)
FN15-20	Ol.-phyric nephelinite	*ol* (5-7%)	*aug; ne; opq*	*Ti-aug*	-	vesicles + devitrified glass (3-5%)
FN13-21	Trachyte	*snd*; *agr; amph*; total = 1-2%	*snd; opq*	*sph*	-	-
FN13-25	Kaersutite trachyandesite	*krs* (2-3%); *opq** (1-2%)	*snd; opq*	*aug*	*krs* (1 crystal, 0.8 cm)	-
FN16-27	Tephrite	*ol* (7-10%)	*aug; opq; ne* (rare)	*plg; bt*	*ol* (2-3%, uncert.)	-
FN17-29	Phonolite	*sgm* (2-3%); *agr** (2-3%); *snd* (1-2%)	*snd; agr*	*krs; ne; sph; opq*	-	-
FN18-30	Phonolite	*snd* (1-2%); *agr** (1-2%)	*snd; agr*	*ne; krs; opq; sph*	-	pseudomorphs after *sgm* + *ne* (1-2%)

Sample	Rock	Phenocrysts (modal%)	*g.m.* minerals	Acces. minerals	Xenocrysts and xenoliths	Other features
Fernando de Noronha (cont.)						
FN19-31	Titanaugite-phyric tephrite	*Ti-aug* (10-15%); *ol* (5-7%)	*aug; ne; opq*	-	-	-
FN12-32	Kaersutite-phyric tephriphonolite	*krs* (7-10%); *sgm* (5-7%); *snd* (3-5%); *agr* (2-3%); *ne** (1-2%)	*agr + aug; opq; ne* (rare)	*sph*	*krs + fds* (uncert.)	-
FN12-33	Kaersutite-phyric tephriphonolite	*snd* (10-15%); *krs* (5-7%); *ne* (3-5%); *sph* (1%)	*snd; cpx; opq*	-	-	-
FN12-36	Basaltic trachyandesite	*Ti-aug* (3-5%); *krs* (3-5%)	*plg; aug; opq*	*sph; bt*	*K-fds* (uncert.)	pseudomorphs after *sgm*
FN20-40	Basaltic trachyandesite	*Ti-aug* (5-7%); *krs* (1-2%); *sgm* (1-2%)	*plg* (oikocrysts); *aug; opq*	*sph; bt*	-	pseudomorphs after *Ti-aug* (2-3%)
FN21-42	Phonolitic nephelinite	aphyric	*ne*	*snd*	-	-
FN22-43	Phonolite	aphyric	*snd; agr; ne* (2-3%)	-	-	-
FN23-45	Phonolite	*ne; snd; agr** (rare); total = 1-2%	*snd; agr; ne*	*sph; opq*	-	-
FN25-46	Trachybasalt	aphyric	*plg; aug; opq;* unident. min.	-	*cpx* + *K-fds* + *krs* + *opq* (< 1%)	-
FN25-47	Basaltic trachyandesite	*krs* (5-7%); *Ti-aug* + *aug* (2-3%)	*plg; aug; opq*	*sgm; sph*	-	vesicles + amygdales (3-5%)
FN26-49	Trachyte	*snd* (5-10%); *sgm* (2-3%); *agr* (1-2%)	*snd; agr*	*krs; sph*	*ort* + *snd* (1-2%, uncert.)	-
FN27-50	Ol. alkali basalt	*ol* (20-25%); *Ti-aug** (1-2%)	*plg; aug; opq*	-	*ol*	-
FN28-51	Ol. alkali basalt	*ol* (15-25%); *Ti-aug** (2-3%)	*plg; Ti-aug; opq*	-	*ol*	-
FN29-52	Phonolite	aphyric	*snd; ne*	-	-	-
Fernando de Noronha São José						
FN30-53	Ol. alkali basalt	*ol* (7-10%); *Ti-aug* (3-5%); *plg* (rare)	*plg; aug; ol; opq*	-	*pdt; ol* (1-2%)	amygdales ocelli (rare)
FN30-54	Ol. alkali basalt	*ol* (1-2%); *Ti-aug* (10-15%); *plg* (rare)	*plg; aug; ol; opq*	-	*opx; ol* (< 1%)	ocelli (rare)

Sample	Rock	Phenocrysts (modal%)	*g.m.* minerals	Acces. minerals	Xenocrysts and xenoliths	Other features
Fernando de Noronha São José (cont.)						
FN30-55	Ol. alkali basalt	*ol* (7-10%); *Ti-aug* (5-7%); *plg* (rare)	*plg; aug; ol; opq*	-	*ol* (~1%)	-
FN30-56	Ol. alkali basalt	*ol* (10-15%); *Ti-aug* (2-3%); *plg* (rare)	*plg; aug; ol; opq*	-	*pdt; ol* (< 1%); *spl;* basalt xenolith (1 grain)	-
Fernando de Noronha dykes						
FN13-22	Alkali basalt	*Ti-aug (10-15%); ol* (2-3%); *opq** (1-2%)	*Ti-aug; plg; ne; opq*	-	-	-
FN12-34	Tephrite	*Ti-aug* (3-5%)	*aug; opq*	-	-	vesicles + amygdales (2-3%, ≤ 0.5 cm) pseudomorphs after *ol* + *aug* (3-5%)
FN12-35	Tephrite	*Ti-aug* (7-10%)	*aug; opq*	*plg*	-	amygdales + cavities (1%) pseudomorphs after *ol* (7-10%)
FN20-41	Titanaugite-phyric basanite/tephrite	*Ti-aug* (10-15%)	*aug; opq*	-	*ort* (rare)	amygdales (1-2%) pseudomorphs after *ol* (7-15%)
Fernando de Noronha kaersutite nodules						
FN12-39	Kaersutite nodule	-	*krs* (40-50%); *cpx* (30-40%); apatite (7-10%); *sph* (5-7%); *opq*	-	-	-
FN25-48	Kaersutite nodule	-	*krs; plg; ort; cpx; opq*	*sph;* apatite	-	Serrated boundaries between *krs*

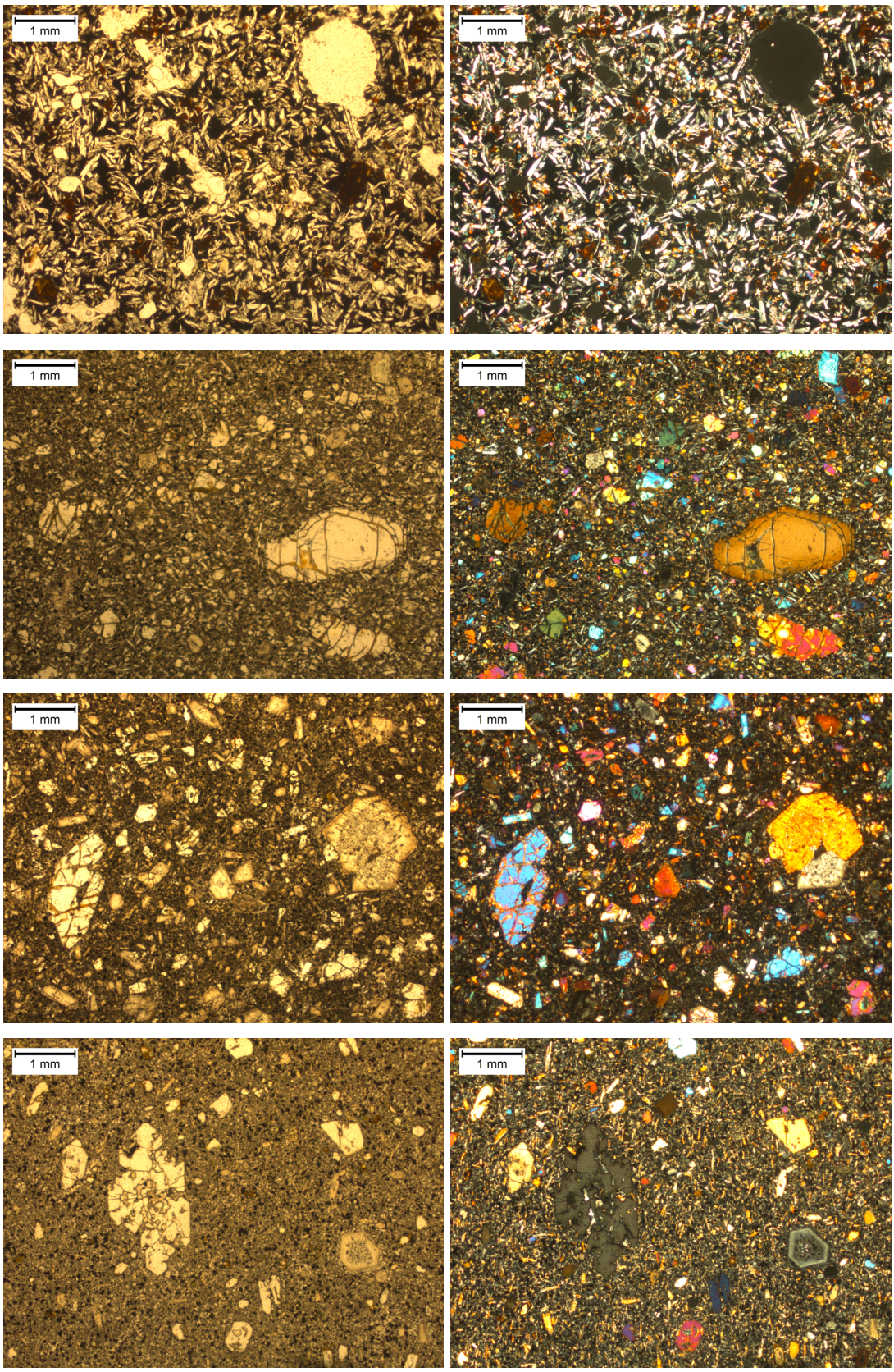

Figure 3-1: Representative samples from the MQVL in plane-polarised light (*left*) and crossed polars (*right*). From top to bottom: basaltic andesite (basin sample 15BP7-14), alkali basalt (15BP12-26), basanite (15BP8-17) and nephelinite (15BP12-25).

Titanaugite is the dominant clinopyroxene phenocryst phase in the alkaline assemblage. It is somewhat proportionally more common in Fernando de Noronha than in the MQVL amongst alkali basalt, basanite and nephelinite (Figure 3-2). Although most of the groundmass clinopyroxene is marked as augite in Table 3-1, it is difficult to distinguish between different clinopyroxene varieties in crypto- to microcrystalline groundmass, and it is likely that titanaugite is also substantially present as a groundmass phase. Nepheline is also somewhat proportionally more common in Fernando de Noronha than in the MQVL amongst alkali basalt, basanite and nephelinite, whilst the opposite occurs for plagioclase amongst alkali basalt and basanite. Both nepheline and plagioclase occur predominantly as groundmass phases. The proportions of alkali basalt, basanite and nephelinite between the two sectors are very similar (Figure 3-3), and therefore differences in modal titanaugite, nepheline and plagioclase indicate differences in degrees of silica saturation. Considering that the mineralogical modal shift from alkali basalt to basanite and nephelinite is marked by a gradual decrease in plagioclase and gradual increase in nepheline, modal proportions in the assemblage indicate higher degrees of undersaturation in Fernando de Noronha. This is also supported by the higher proportions of titanaugite there. Furthermore, this is reflected in the exclusive occurrence of tephrite, trachybasalt and trachyandesite in Fernando de Noronha, and basalt and subalkali basalt in the MQVL (Figure 3-3), indicating two distinct incipient evolutionary trends because of differences in degrees of silica saturation. However, considering that phonolite is the only example of evolved composition in the continental sector, and basalt and subalkali basalt are restricted to the continental extensional basins, evolution towards silica oversaturated compositions in the MQVL must be at least in part controlled by local tectonic settings.

Virtually all amphibole has been petrographically identified as kaersutite (Figure 3-4), which is in accordance with published mineral geochemical analyses for the area (Lopes, 1997, 2002; Lopes *et al.*, 2014). The mineral is most common amongst trachyandesite, tephriphonolite and

phonolite in both the continental and oceanic sectors, occurring in ~2/3 of these rocks. Conversely, trachyte is dominated by hornblende. Although the number of samples showing kaersutite is similar in both sectors, proportions of the mineral within individual samples are within or just above accessory levels (up to 2 modal%) in the continental sector, whilst amongst oceanic samples they are often > 2 and may reach 10 modal% (Figure 3-5).

Kaersutite also occurs in xenolith nodules < 10 cm in intermediate rocks from Fernando de Noronha (e.g. samples FN12-39 and FN25-48). In hand specimen they appear monomineralic, but in thin section it is possible to identify clinopyroxene, feldspars, sphene, apatite and opaques (Table 3-1). Given their context and the petrography of the rest of the assemblage, these are likely to come from cumulate layers developed during significant kaersutite fractional crystallisation, a proposition also supported by the geochemical data (see below).

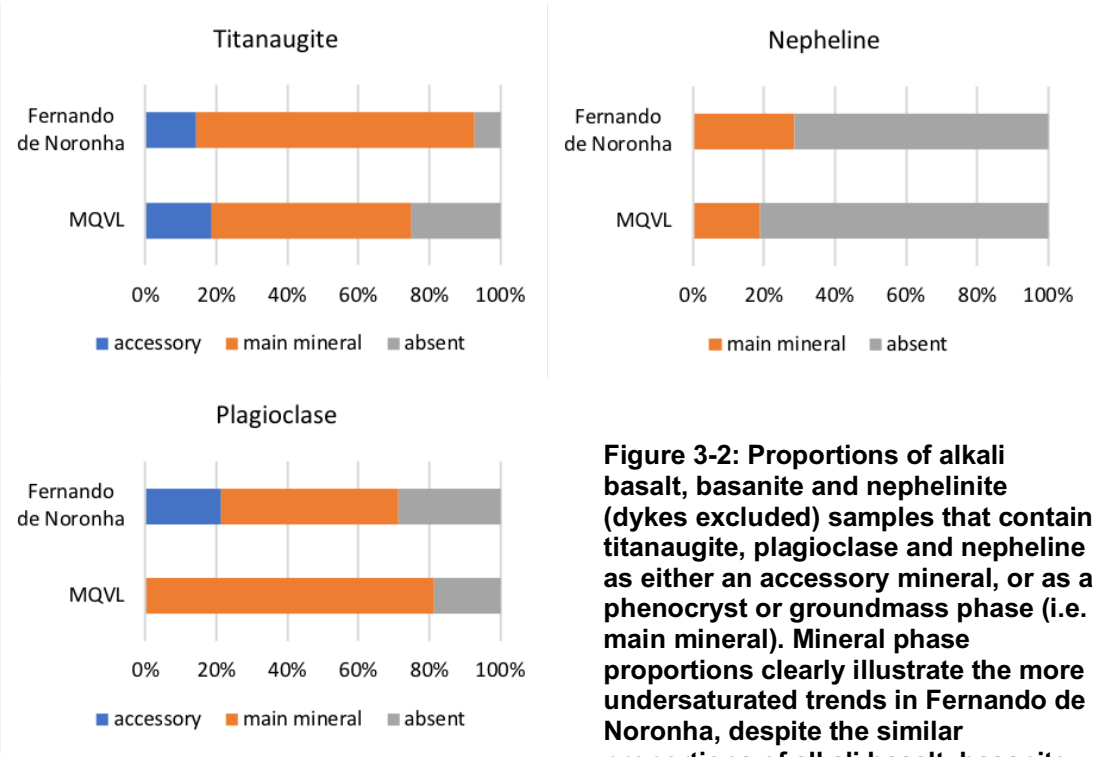

Figure 3-2: Proportions of alkali basalt, basanite and nephelinite (dykes excluded) samples that contain titanaugite, plagioclase and nepheline as either an accessory mineral, or as a phenocryst or groundmass phase (i.e. main mineral). Mineral phase proportions clearly illustrate the more undersaturated trends in Fernando de Noronha, despite the similar proportions of alkali basalt, basanite and nephelinite as rock types.

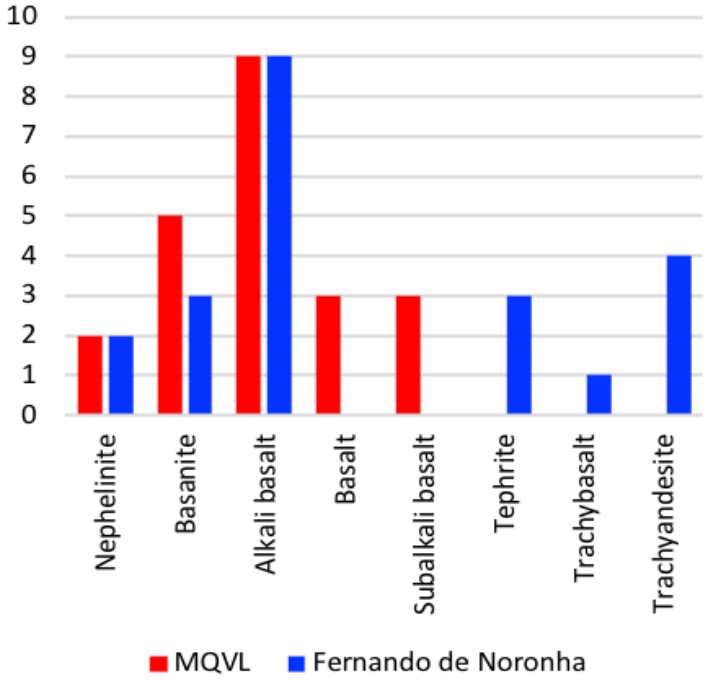

Figure 3-3: Count of basaltic rock types according to petrographic classification (Fernando de Noronha dykes excluded).

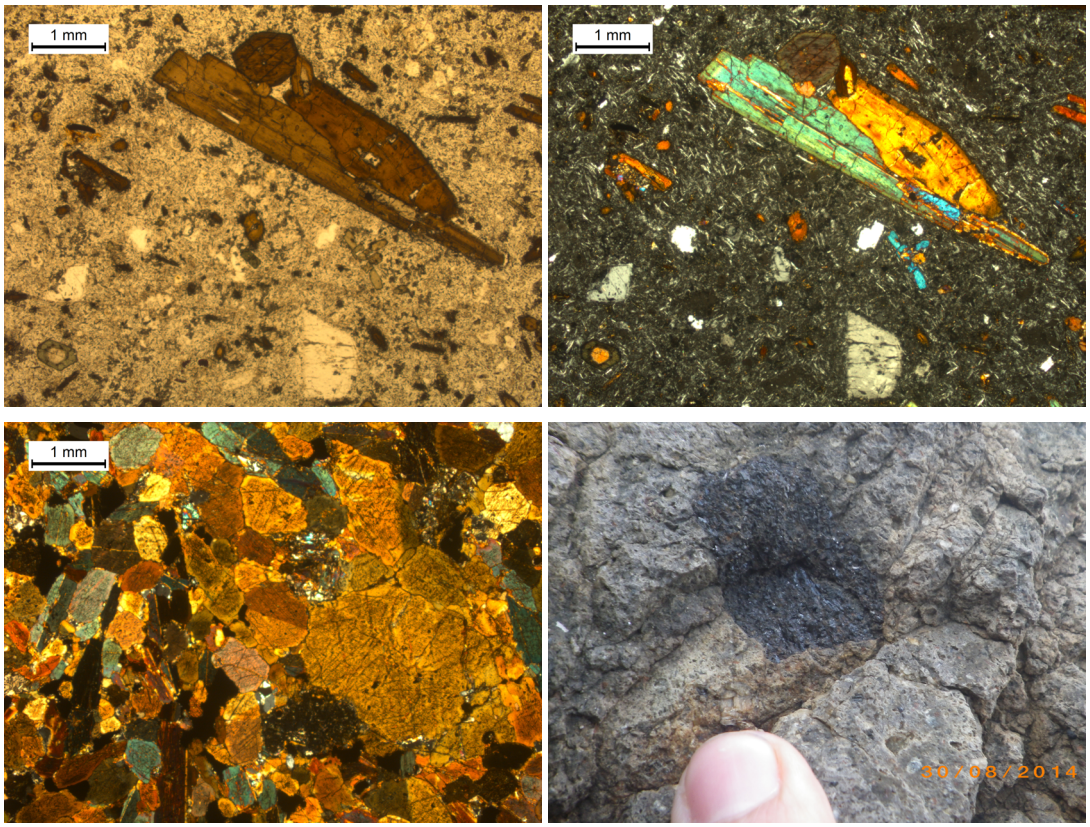

Figure 3-4: *Top two*: kaersutite phenocryst in sample FN12-32 (*left*: plane-polarised light; *right*: crossed polars). *Lower two*: kaersutite cumulate nodules from the Atalaia beach (*left*: in thin section under crossed polars; *right*: in the outcrop).

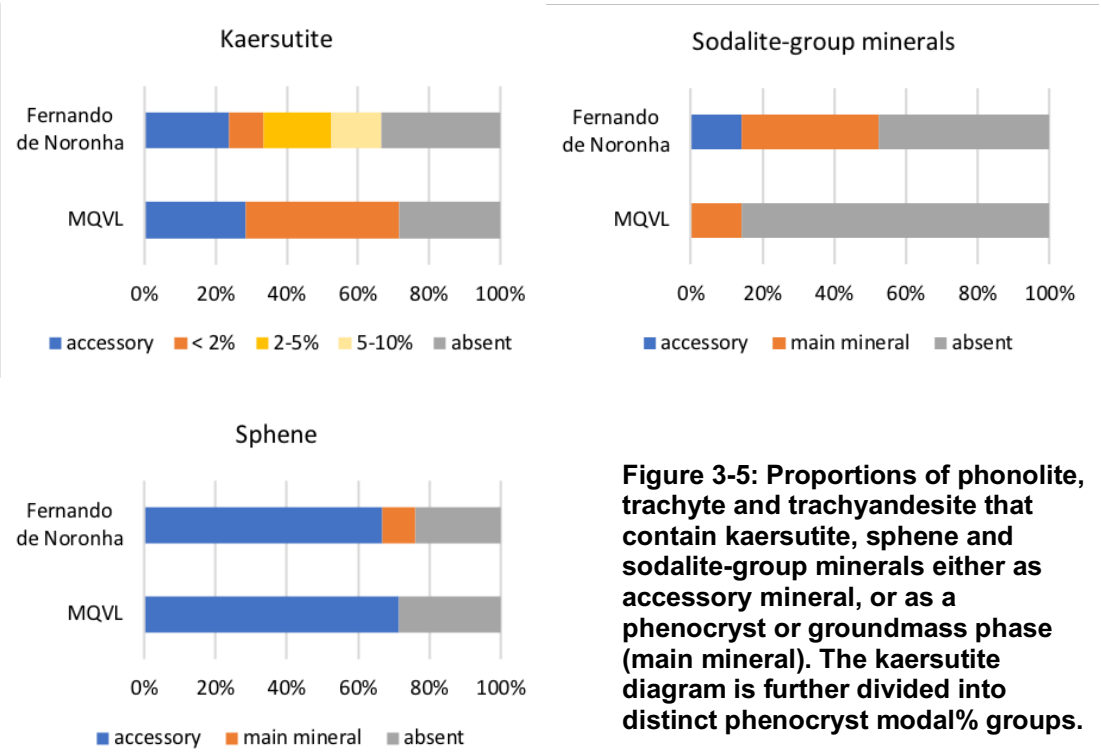

Figure 3-5: Proportions of phonolite, trachyte and trachyandesite that contain kaersutite, sphene and sodalite-group minerals either as accessory mineral, or as a phenocryst or groundmass phase (main mineral). The kaersutite diagram is further divided into distinct phenocryst modal% groups.

Sphene occurs in ~3/4 of all intermediate and evolved rocks, with somewhat higher proportions in the oceanic sector (Figure 3-5). It is absent from basaltic samples. Although the number of samples with sphene is similar in both sectors, in Mecejana it invariably occurs as an accessory phase, whereas in Fernando de Noronha it is relatively more ubiquitous in the samples where it occurs. Although it is difficult to quantity sphene's modal differences between the two sectors because individual sample proportions are mostly accessory (≤ 1 modal%), it is clear in the thin sections that in Mecejana proportions are << 1 modal%, whereas in Fernando de Noronha they are ~1, sometimes reaching 1-2 modal% (i.e. beyond accessory proportions).

Sodalite-group minerals appear exclusively in intermediate and evolved rocks. In Mecejana they occur only in one phonolite sample, where they appear as phenocrysts at 1-2 modal%. They are significantly more common in Fernando de Noronha (Figure 3-5), appearing in trachyandesite, tephriphonolite, trachyte and phonolite as phenocrysts in proportions up to 7

modal%, and sometimes substituted by calcite or zeolite pseudomorphs. Petrographically, it has not been possible to identify them either as sodalite, haüyne or nosean, but published mineral geochemical analyses for the area report the presence of all three phases (Lopes, 1997, 2002; Lopes *et al.*, 2014).

Olivine is present in all basaltic rocks from both sectors, except for the trachybasalt FN25-46. It is the mineral most affected by alteration, which ranges from slight alteration to iddingsite or smectite along fractures and boundaries, to complete calcite or smectite substitution forming pseudomorphs. The latter process is especially common in the Fernando de Noronha basaltic dykes.

Peridotitic xenoliths and xenocrysts from disaggregated xenoliths are present in virtually all basaltic rocks of the continental sector and in all those from the São José Formation in Fernando de Noronha. It is not possible to quantitatively determine the degree of peridotitic contamination because of the difficulty in distinguishing olivine xenocrysts from phenocrysts, especially in cases where there is stronger olivine alteration. Textural features such as size discrepancies, polygonal (non-euhedral) shapes, joined crystals in granular texture, etched boundaries, resorption textures and undulose extinction may be indicative of xenocrysts (Figure 3-6), but no certainty can be attained without crystal chemical data. This has been carried out by Fodor et al. (1998), who have reported the presence of olivine, clinopyroxene and plagioclase xenocrysts in lavas from the central segment of the MQVL, based on direct compositional analyses and textural evidence for disequilibrium (e.g. sieve or 'spongy' textures). Based solely on petrographic textural interpretations, potential plagioclase and clinopyroxene xenocrysts are rare in the samples described here, but potential olivine xenocrysts are ubiquitous. However, due to the uncertainty in this method of identification, these samples have been marked as containing *uncertain xenocrysts* (Table 3-1).

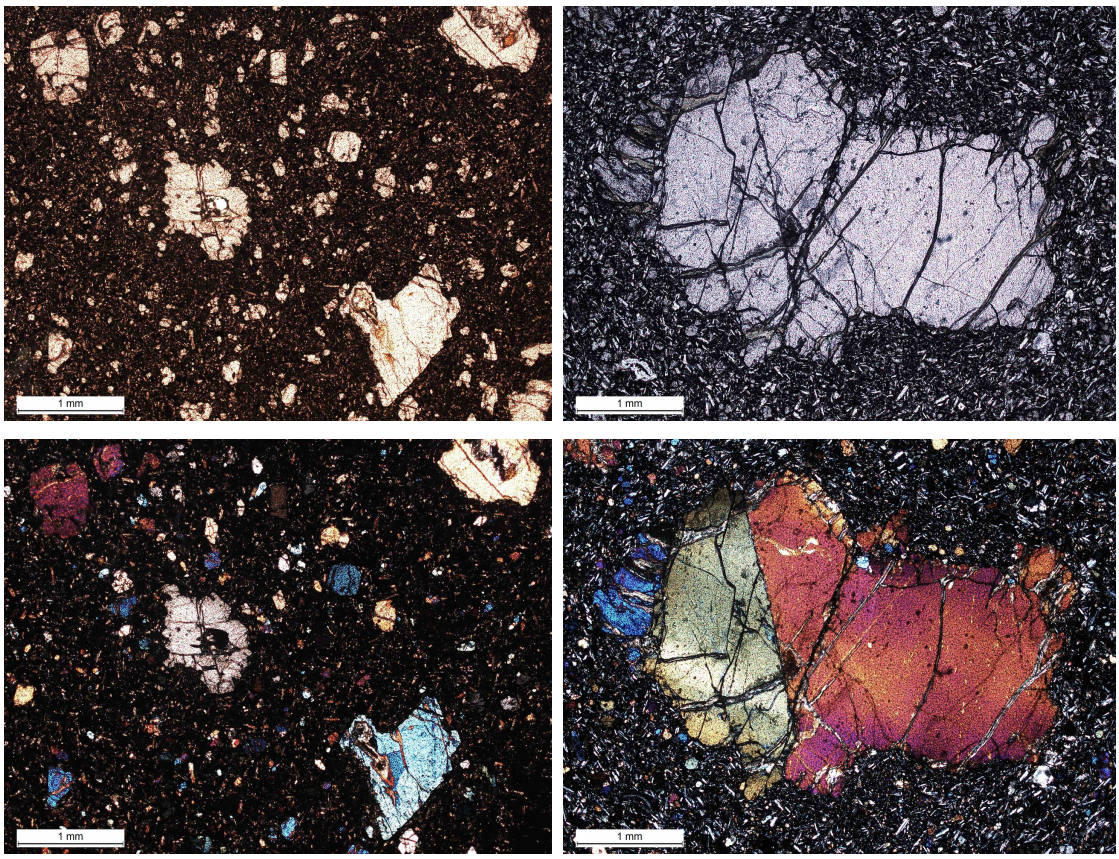

Figure 3-6: Two distinct thin section fields showing possible olivine xenocrysts in sample 15BP5-9. The irregular polygonal shapes, joined crystals in apparent granular texture and etched boundaries suggest these are not phenocrysts. *Left-hand side:* plane-polarised light. *Right-hand side:* crossed polars.

There is also a ubiquitous presence of ocellar features in the MQVL (Figure 3-7). They are relatively heterogenous, and some clearly indicate reactions with peridotitic xenoliths. They are dominated by augite crystals, but may also contain glass, olivine and, occasionally, an orthopyroxene grain in its core, indicating reactions with peridotite xenoliths, especially between orthopyroxene and the undersaturated melt. Furthermore, ocelli are only present in samples containing peridotitic xenocrysts, and are absent from the continental phonolites and samples from the MQVL basins (Table 3-1).

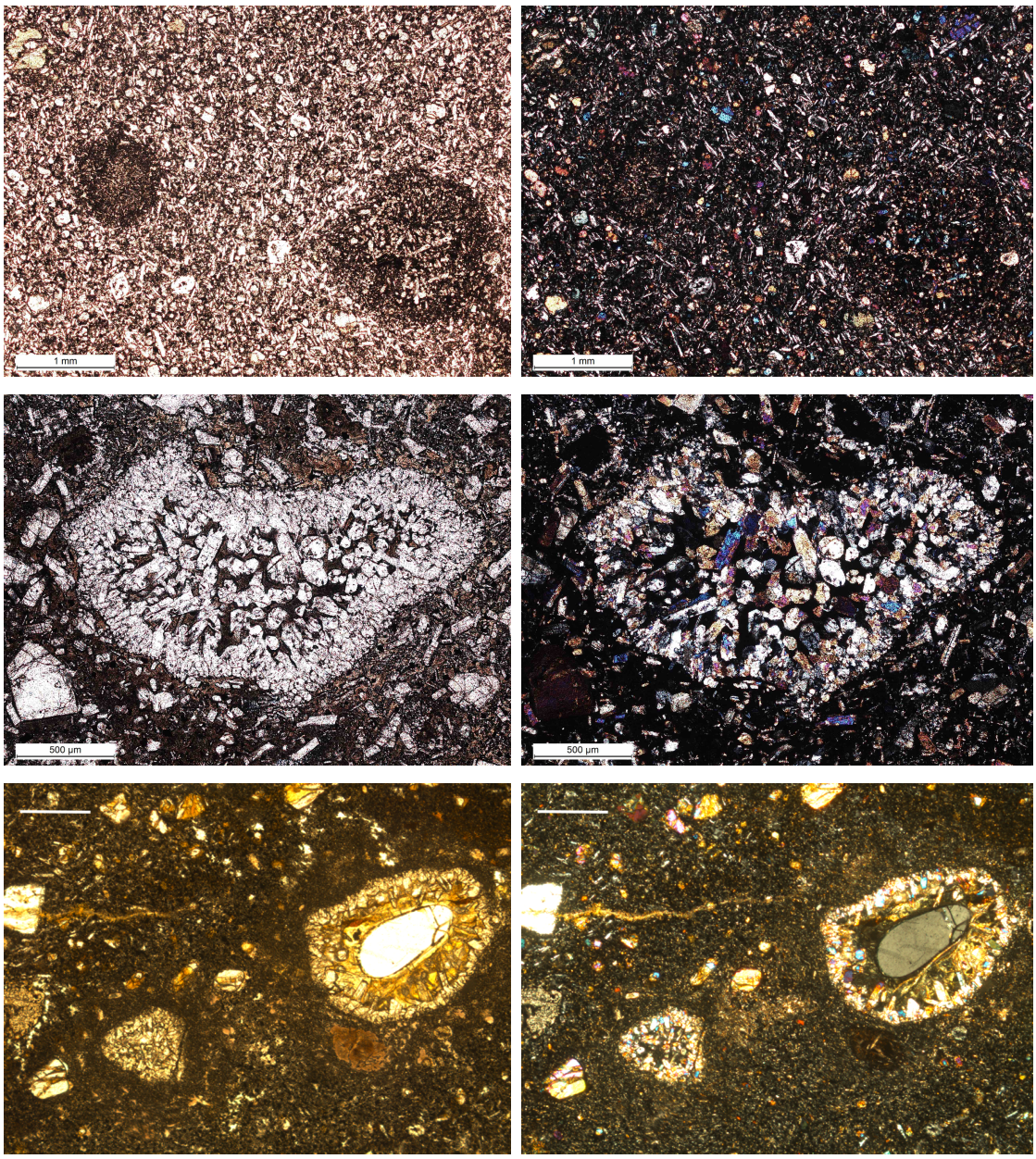

Figure 3-7: Ocellar features in lavas from the MQVL *(left:* plane-polarised light; *right:* crossed polars). *Top pair*: the most ubiquitous type of occeli, containing only clinopyroxene and glass. *Middle pair*: an ocellar feature also continaing olivine. *Lower pair*: an ocellr feature containing a potential quartz (or orthopyroxene) grain.

Although xenoliths and xenocrysts are dominated by mantle material, there is one occurrence of an obvious crustal xenolith (a quartz-rich sandstone) in sample 15BP5-8. Furthermore, some of the glassy ocelli amongst the MQVL samples may also indicate resorption of more fusible crustal material such as quartz. It has not been possible to adequately distinguish quartz from orthopyroxene in all cases where these features

occur, due to the small size and sparsity of colourless and low-birefringent grains in the cores of ocelli. However, quartz xenocrysts bearing clinopyroxene coronas that indicate incomplete resorption have been reported by Fodor et al. (1998) for the MQVL, and by Kuepouo et al. (2006) for the Cameroon Line. Therefore, in addition to the orthopyroxene identified in our observations, there is potentially some quartz as well. One such dubious examples is illustrated in Figure 3-7. Despite the potential presence of crustal material in the MQVL lavas, their proportions must nonetheless be significantly limited.

Major elements

Major element analyses are presented in Appendix C and illustrated in variation diagrams in Figures 3-8 and 3-9. Primitive compositions from the two sectors are virtually indistinguishable in SiO_2 variation diagrams, but with clear disparities in MgO concentrations that are generally more scattered and particularly higher in the continental sector (Figure 3-8). This disparity is clear in variation diagrams that use MgO as reference (Figure 3-9), which show an apparent degree of variability between the two sectors that is not seen in relation to SiO_2, and which can be explained in terms of MgO enrichment in the continent. It results in continental trends sometimes appearing offset from the oceanic sector, contrasting with the overlapping and contiguous trends in the SiO2 variation diagrams. Despite MgO enrichment, MgO variation diagrams still highlight higher contents of Al_2O_3, K_2O, Na_2O and SiO_2, and lower FeO, CaO, TiO_2 and P_2O_5 amongst primitive samples in the continental sector, which indicate incipient fractional crystallisation of mafic phases amongst some continental samples. Evolved compositions are also virtually indistinguishable in SiO_2 variation diagrams, but intermediate samples from the continental and oceanic sectors are somewhat offset from one another.

In the Total Alkalis and Silica (TAS) diagram (Figure 3-10), primitive samples from the continental and oceanic sectors of Northeast Brazil form a

compositional continuum with overlapping values and a negative slope from the field of nephelinite to alkali basalt, with continental samples dominating the more silica-saturated end of the spectrum and oceanic ones being more undersaturated. The assemblage is also almost exclusively alkaline, with only three samples well within the subalkaline field, plotting as basaltic andesite (i.e. 15BP3.3a; 15BP3.3b and 15BP7.14). There are also two samples overlapping the alkaline-subalkaline dividing line in the basalt field, and which may be classified as transitional basalt (i.e. 15BP3.4 and 15BP3.5). All subalkaline and transitional samples come from the MQVL basins and therefore are associated with specific tectonic environments. The distinct composition of some the Fernando de Noronha basaltic dykes is also clear in the diagram.

The TAS diagram also highlights the dominance of high loss on ignition (LOI) values amongst intermediate and evolved rocks in Fernando de Noronha. For instance, all intermediate samples, virtually all trachyte and more than half of the phonolite have LOI > 2 wt.%. Except for the phonolite, these samples were collected along the southern and eastern shore of archipelago's main island, where the effects of erosion by the sea and outcrop weathering are particularly strong (Chapter 1). Intermediate samples have also produced more transitional, as opposed to clearly alkaline compositions, and exclusively *potassic* or *ultrapotassic* characters (respectively $K_2O > Na_2O$ and $K_2O/Na_2O > 2$), as defined by Gill (2010), in contrast with the rest of the assemblage that is exclusively *sodic* or *mildly potassic* (respectively $K_2O + 2 < Na_2O$ and $K_2O + 2 > Na_2O$) and dominated by LOI < 2wt.% (Figure 3-11).

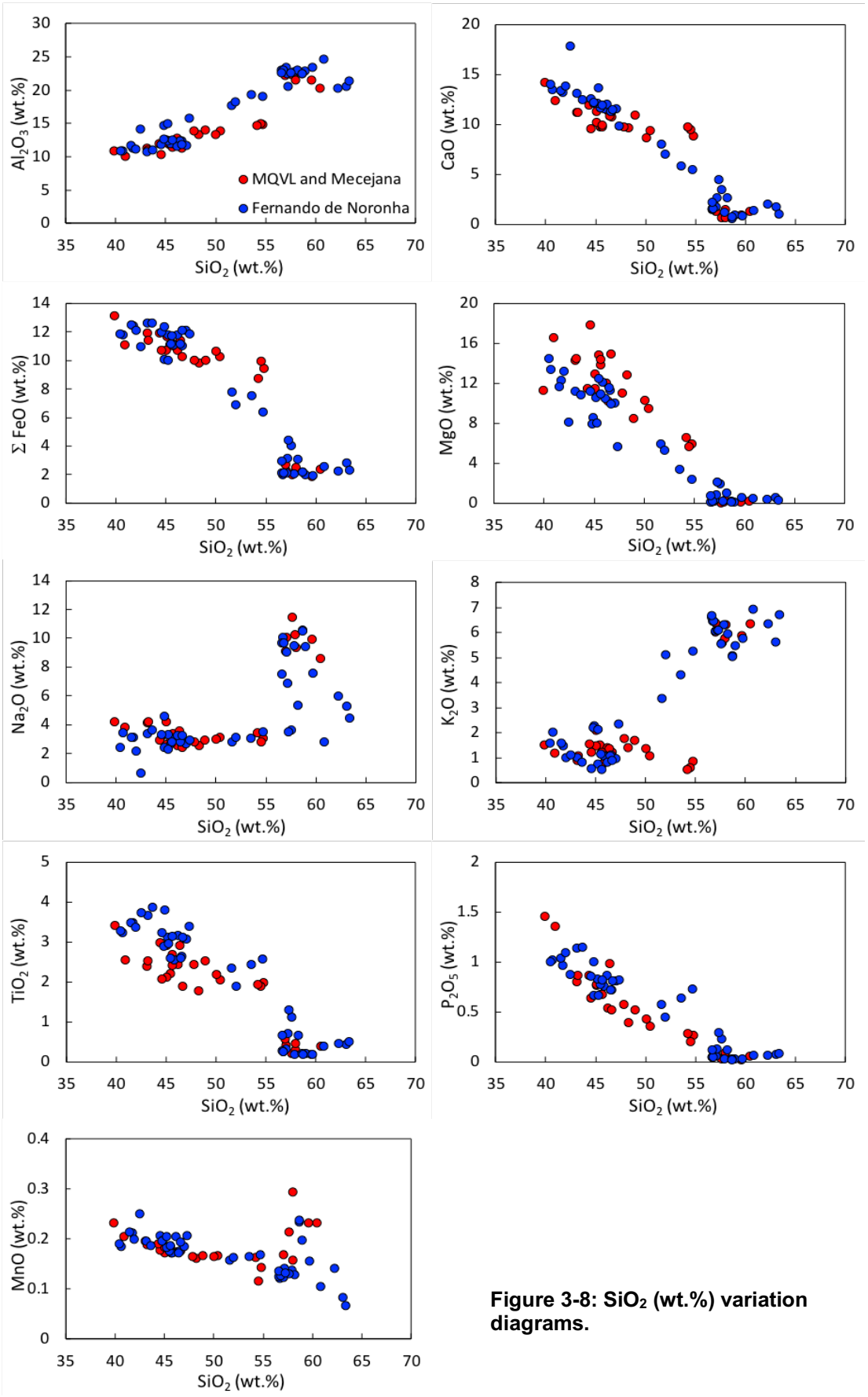

Figure 3-8: SiO_2 (wt.%) variation diagrams.

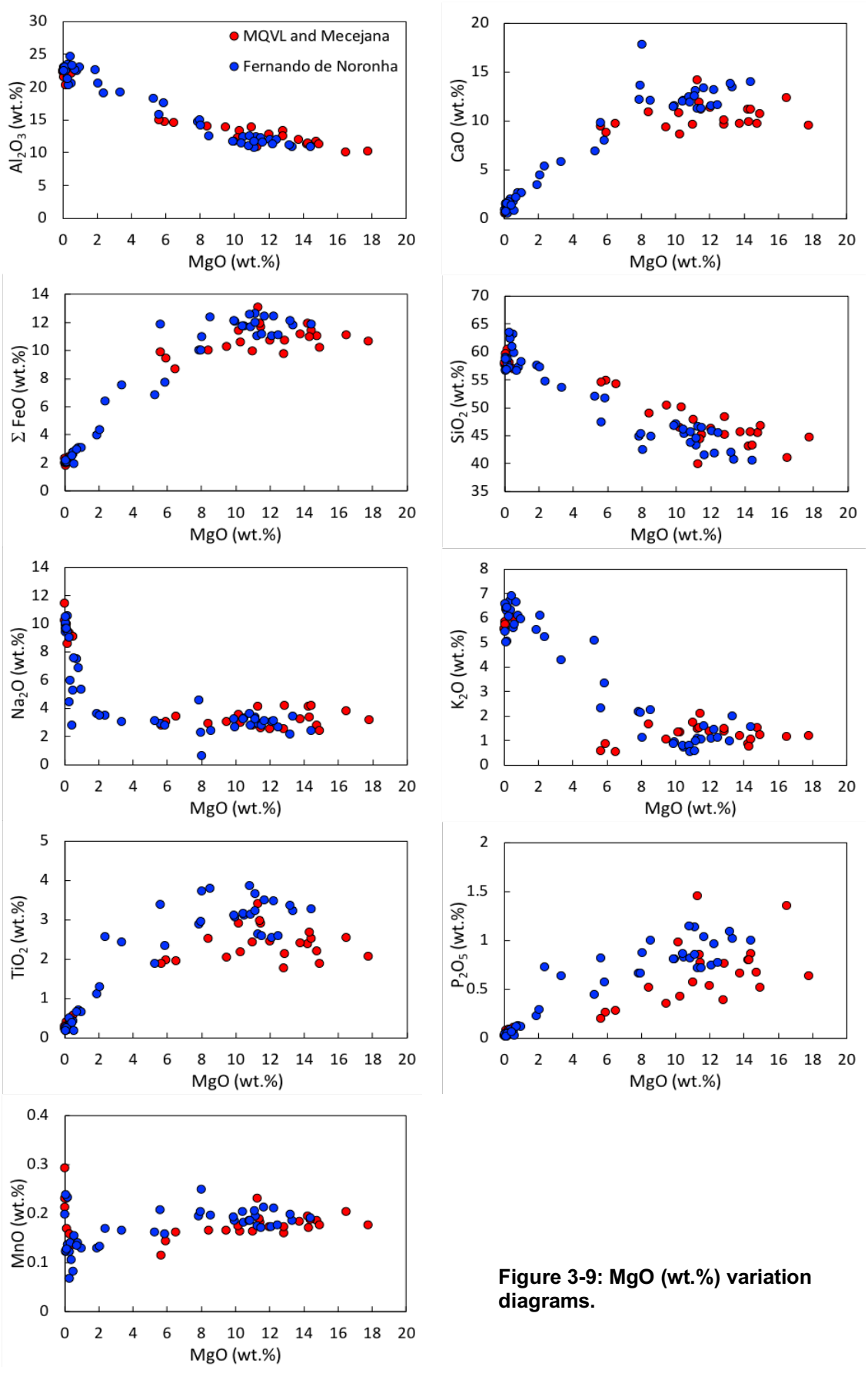

Figure 3-9: MgO (wt.%) variation diagrams.

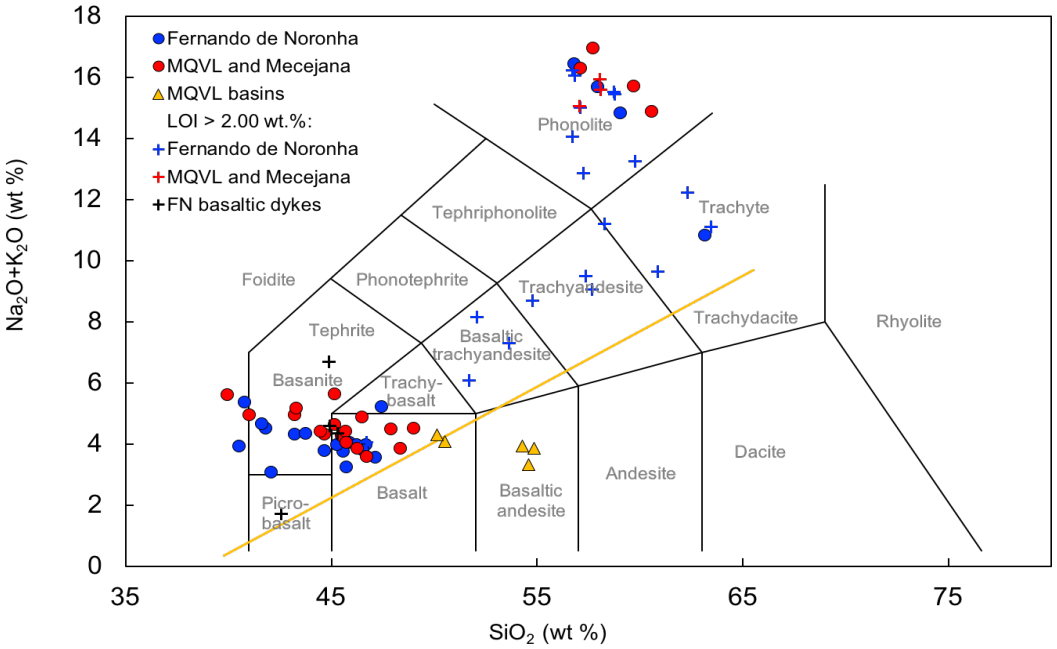

Figure 3-10: Total Alkalis and Silica (TAS) diagram, according to Le Maitre (2002) and plotted on a volatile free basis and ΣFeO. Samples with loss on ignition (LOI) > 2wt.% (marked as crosses) are more common in the oceanic sector and clearly dominate amongst intermediate and trachytic rocks, forming an array that plots within the transitional classification fields. The yellow line, from MacDonald and Katsura (1964), separates Hawaiian tholeiitic and alkaline basalts.

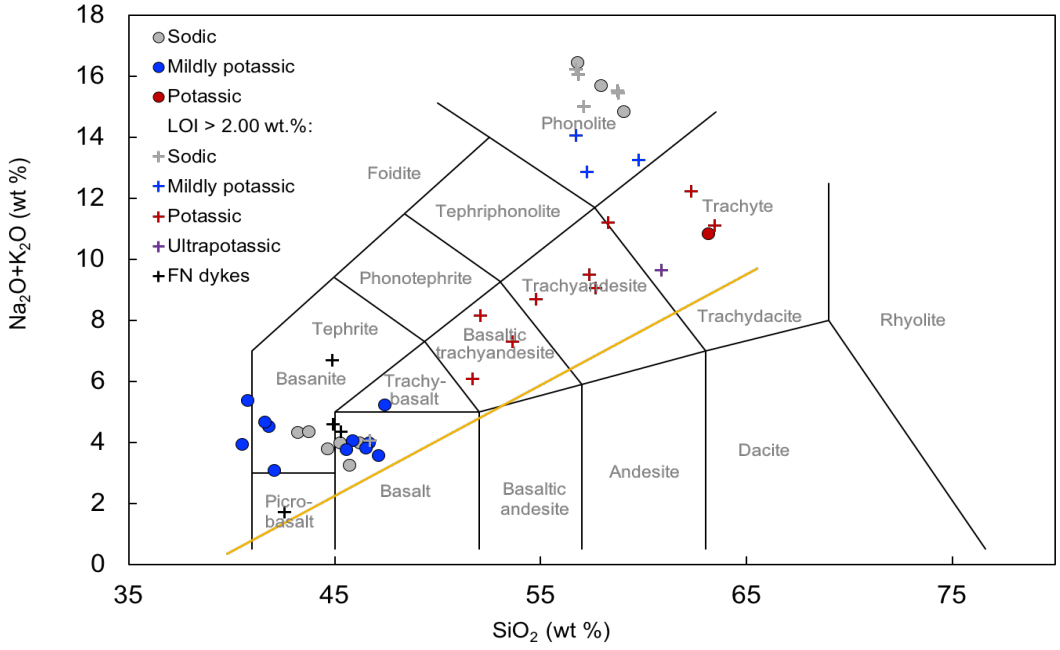

Figure 3-11: TAS diagram according to Le Maitre (2002) and plotted on a volatile free basis and ΣFeO, for Fernando de Noronha samples subdivided by potassic character, highlighting how *potassic* and *ultrapotassic* compositions correlate with LOI > 2wt.% and a more transitional rather than alkaline trend. The yellow line, from MacDonald and Katsura (1964), separates Hawaiian tholeiitic and alkaline basalts.

A similar pattern of compositional continuum between basaltic samples from the two sectors also emerges by comparing normative compositions (Figure 3-12). These are almost exclusively undersaturated and with overlapping patterns where each sector represents one end of a compositional spectrum within the nepheline-olivine-diopside field in the classification tetrahedron from Thompson (1984). Continental samples show more normative olivine and a few samples plot within the saturated field. Some continental samples have also evolved to oversaturated compositions, which are exclusively basaltic andesites. All saturated and oversaturated samples come from the MQVL basins and represent all samples from these localities, with all oversaturated samples coming specifically from the Boa Vista and Potiguar basins. Oversaturated samples are also from dominantly subaqueous eruption environments, and contain the only such examples in the assemblage, in outcrops that shift vertically and laterally to subaerial environments (Chapter 1), according to stratigraphy and the $^{40}Ar/^{39}Ar$ dates (Chapter 2).

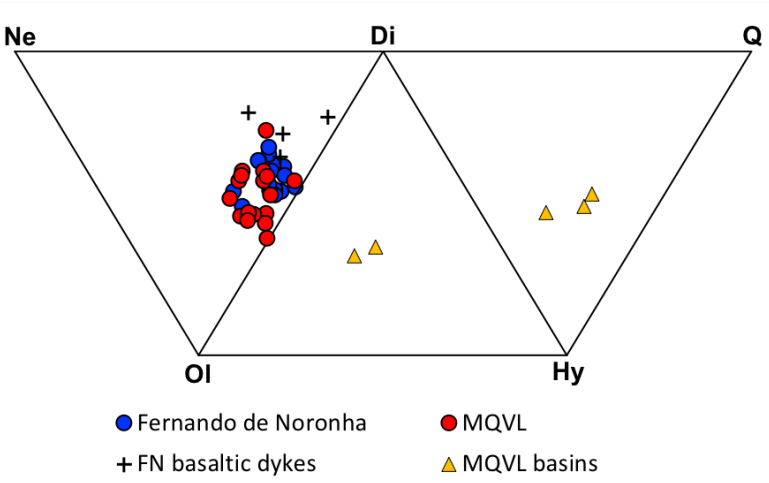

Figure 3-12: CIPW norm distribution in the tetrahedron classification scheme of Thompson (1984). All oversaturated compositions are basaltic andesites from the Boa Vista and Potiguar basin.

Trace elements

Trace element patterns for the continental and oceanic sectors of Northeast Brazil are also remarkably similar for both primitive and evolved rocks. Results from both XRF and ICP-MS analyses are given in Appendix C.

Primitive samples (MgO ≥ 8 wt.%) from the two sectors have virtually identical patterns for most incompatible trace elements, both in terms of absolute concentrations and element ratios (Figure 3-13). This is emphasised by taking the average of concentration values for primitive samples in both sectors, which also further highlights the distinctiveness of the dyke swarm in Fernando de Noronha (Figure 3-14). Geometric averages or the inclusion of all continental basaltic samples in the average calculation produce virtually the same results. Normalising the same data to ocean island basalt (OIB) using data from Sun and McDonough (1989) also highlights the data's robust affinities with OIB characteristics, which are stronger in the continental sector than in the oceanic one (Figure 3-15).

Although primitive rocks from Fernando de Noronha are somewhat more enriched than those from Borborema, they still retain the same absolute values for Lu and Yb and gradually diverging values for Y, Tb and Gd, whilst ratios for most other elements remain virtually unchanged. This applies to both XRF and ICPMS analyses, showing that these patterns are independent of the methods. The only exceptions to this trend are the highly mobile elements Rb and K, as well as Th, all of which, especially Rb, show higher concentrations in the continental sector. The patterns for Lu, Yb, Tb and Gd indicate differences in the behaviour of heavy rare-earth elements (HREE) between the two sectors. Y usually behaves similarly to HREE, and therefore shows similar patterns.

There are also clear similarities between the REE patterns for both primitive samples and phonolites in the two sectors, despite greater homogeneity in the Fernando de Noronha primitive group (Figure 3-16). Differences within the oceanic sector dataset (Figure 3-17) are subtle and limited to the Remédios basaltic dykes, of which three out of the four samples show a subtle depletion in medium-range rare-earth elements (MREE), and the overall greater enrichment of samples FN16-27 and FN19-31. Depletion of MREE continues and becomes more pronounced amongst intermediate and evolved oceanic samples, but does not affect the basaltic

andesite from the continental basins. These patterns indicate distinct processes of fractional crystallisation amongst intermediate samples from Fernando de Noronha and the MQVL basins, but not between Fernando de Noronha and the Mecejana phonolites, similarly to what was observed petrographically and in major element variation diagrams.

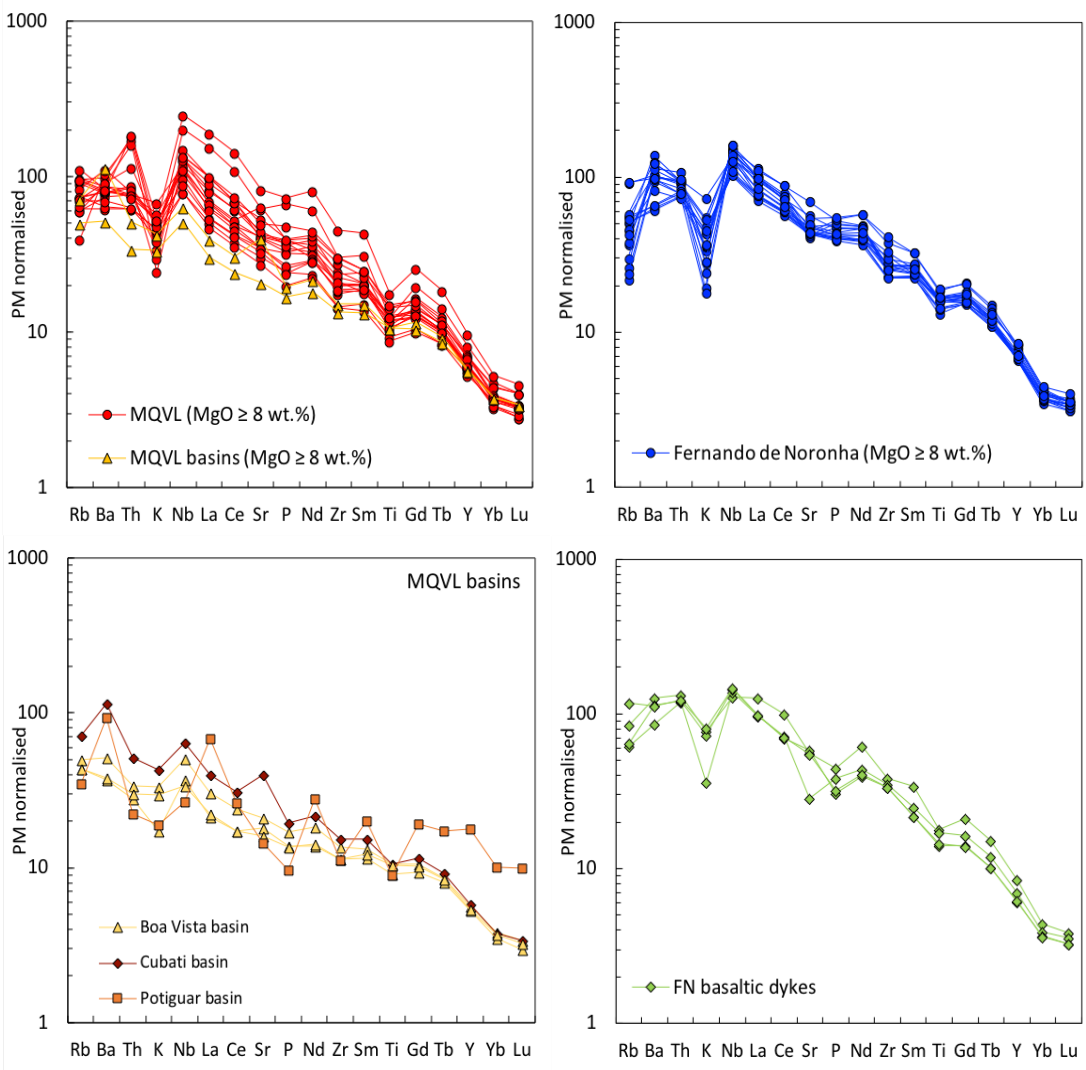

Figure 3-13: Multi-element diagrams for basaltic and primitive samples normalised to Primitive Mantle according to McDonough and Sun (1995). Fernando de Noronha basaltic dykes show distinct variability.

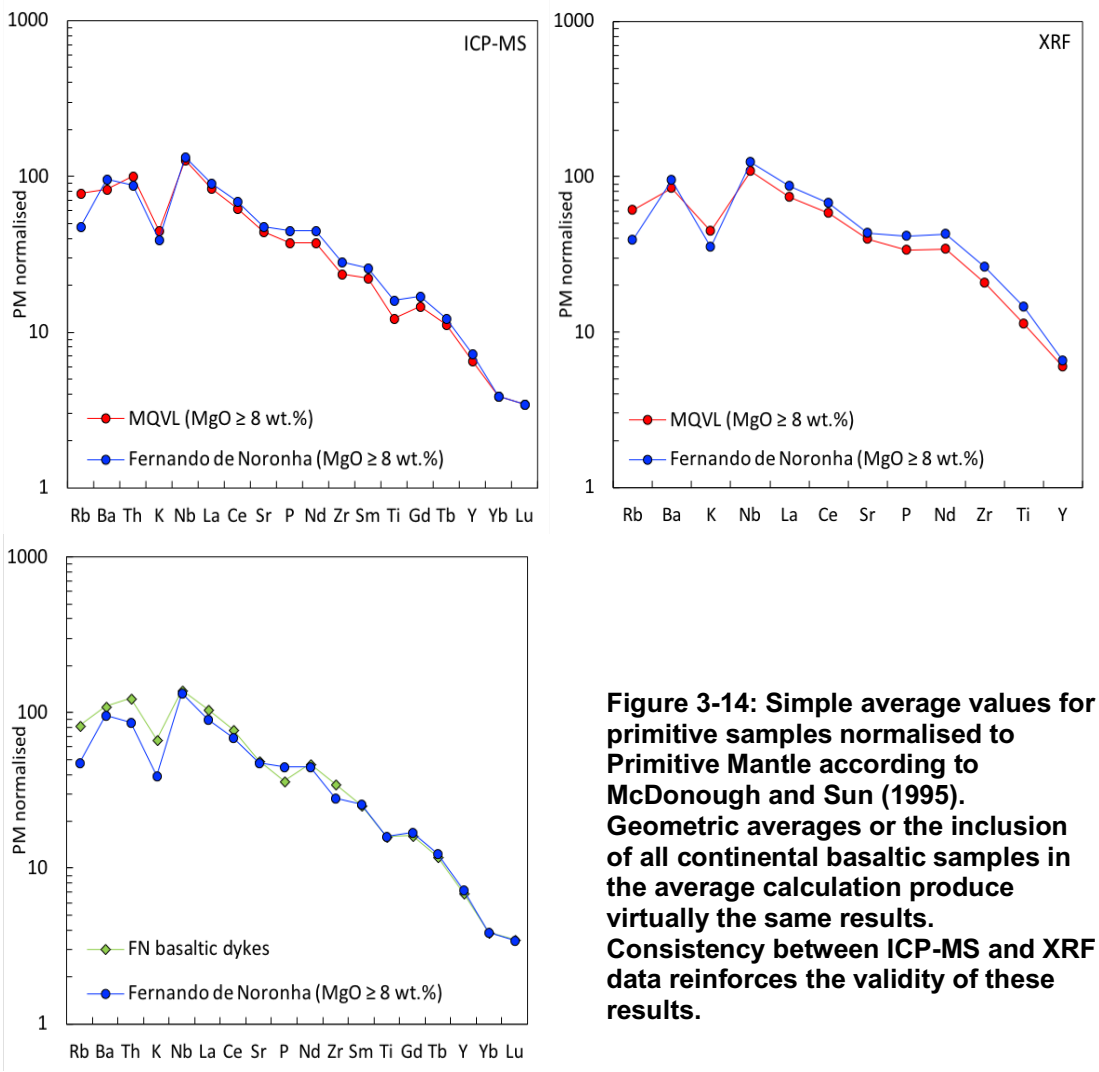

Figure 3-14: Simple average values for primitive samples normalised to Primitive Mantle according to McDonough and Sun (1995). Geometric averages or the inclusion of all continental basaltic samples in the average calculation produce virtually the same results. Consistency between ICP-MS and XRF data reinforces the validity of these results.

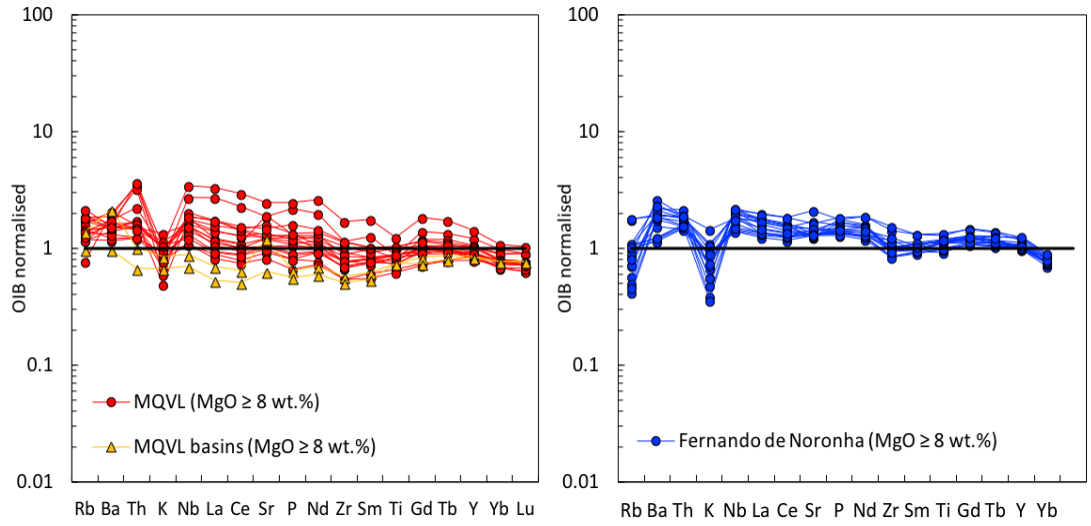

Figure 3-15: Multi-element diagrams normalised to ocean island basalt (OIB) according to Sun and McDonough (1989). Continental samples show overall stronger OIB signatures than oceanic ones.

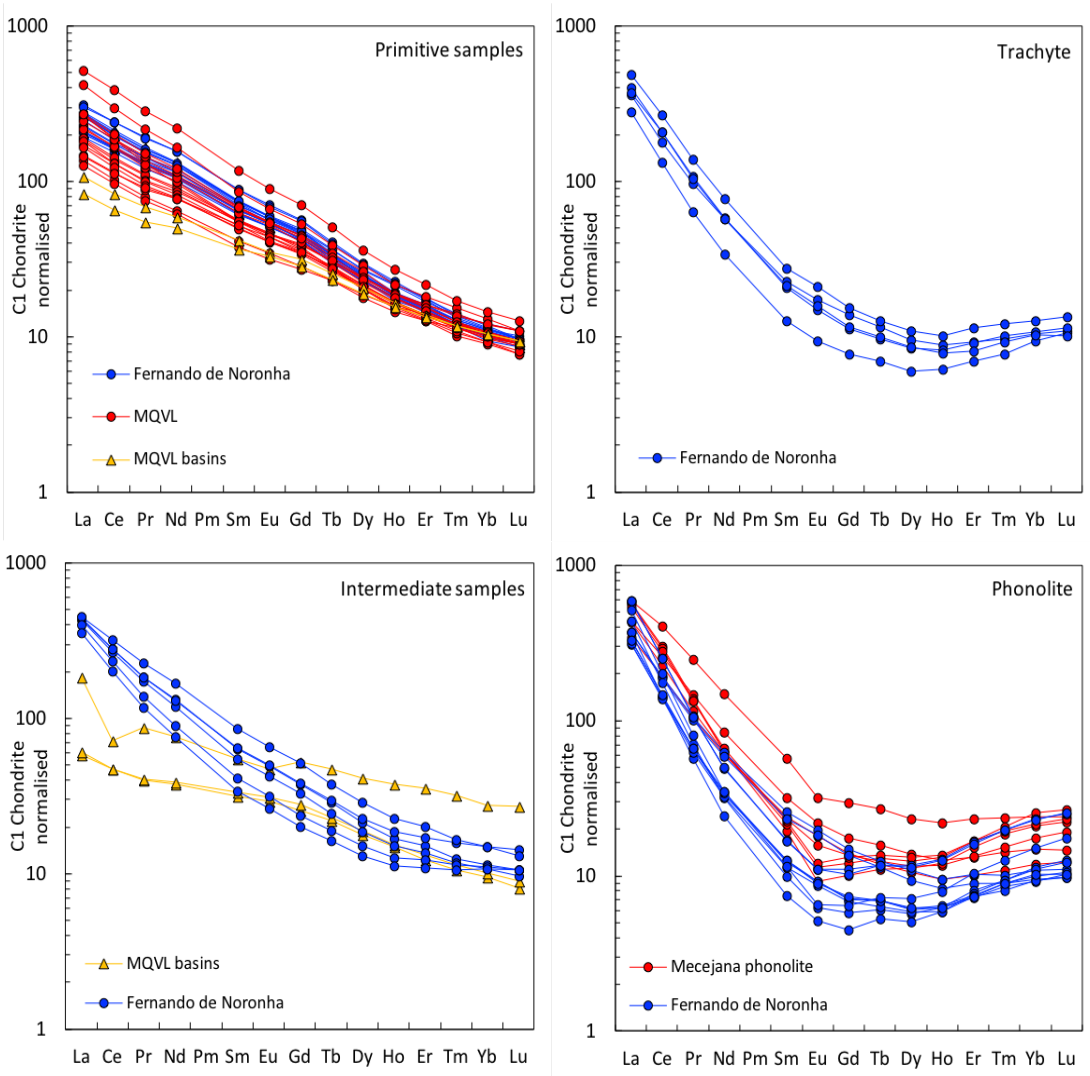

Figure 3-16: REE diagrams according to rock types, normalised to C1 Chondrite according to McDonough and Sun (1995). Similarities between primitive samples from the two sectors are clear. Intermediate samples in Fernando de Noronha clearly show the onset of MREE depletion, which becomes stronger in more evolved samples. Fernando de Noronha dykes are excluded.

Ratios between light rare-earth elements (LREE) and MREE amongst primitive continental samples are lowest within the basins, indicating higher melt fractions (Figure 3-18). Low LREE/MREE also coincides with somewhat lower MREE/HREE and higher HREE absolute concentrations, indicating a larger contribution of spinel- rather than garnet lherzolite in the source, and an inverse correlation between melt fractions and depths of melting that is accentuated in the MQVL basins. The two continental nephelinite samples (i.e. 15BP7-15 and 15BP12-25) show the strongest REE evidence for

fractional crystallisation in the MQVL, with high absolute concentrations for both LREE and HREE (Figure 3-18). Apart from these differences amongst basin samples and nephelinites, the REE patterns for continental primitive compositions are relatively homogeneous.

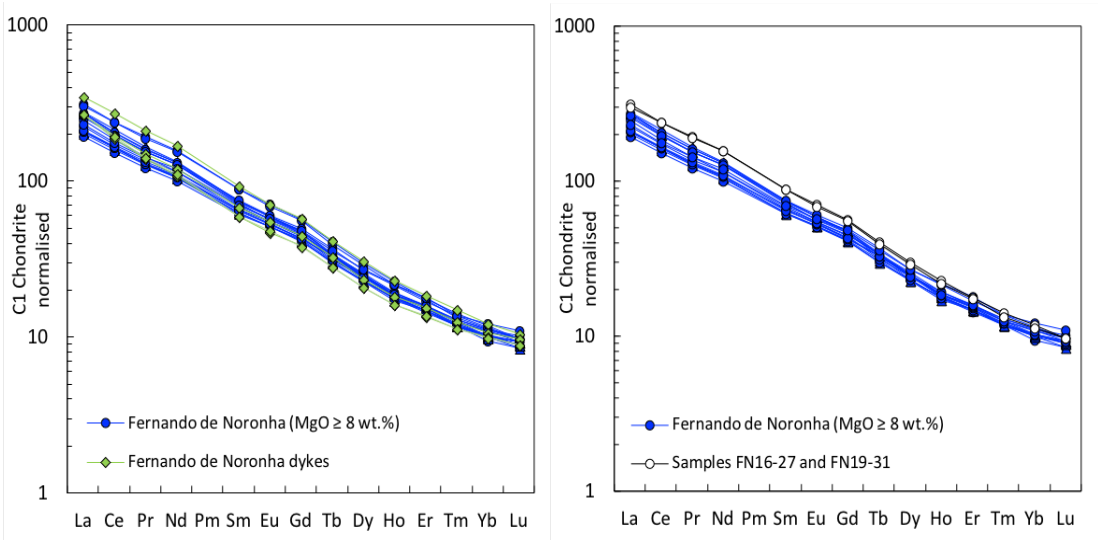

Figure 3-17: REE patterns normalised to C1 Chondrite according to McDonough and Sun (1995). (*Left*) REE patterns for Fernando de Noronha showing the differences between primitive samples and the Remédios basaltic dykes where three out of four samples show incipient depletion of MREE. (*Right*) REE patterns for Fernando de Noronha primitive compositions highlighting the differences of the two most enriched samples in the group, FN16-27 and FN19-31.

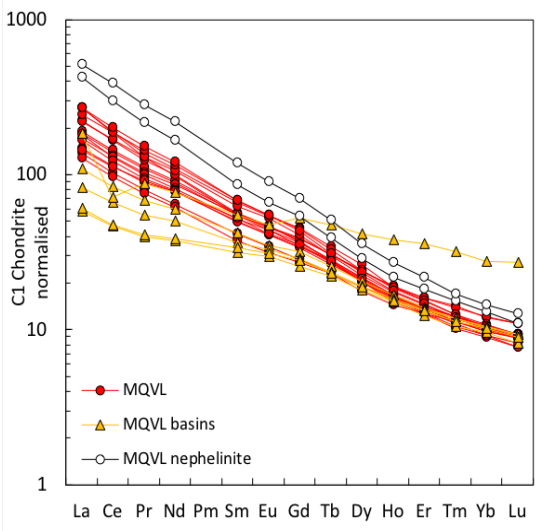

Figure 3-18: REE patterns highlighting the MQVL basin samples and the two MQVL nephelinite samples, 15BP7-15 and 15BP12-25. Normalised to C1 Chondrite according to McDonough and Sun (1995).

Trace-element variation diagrams for basaltic samples using Zr (ppm) as index further highlight the trends illustrated in multi-element diagrams (Figures 3-19 and 3-20). Zr is incompatible in most mafic phases and was considered a better index than MgO wt.%, given the latter's enrichment in continental samples that was observed in the major element patterns. Most incompatible trace elements show stable behaviour against Zr, but the highly mobile elements Rb, Ba and K show scattered patterns, and a few samples are enriched in Th. There are also some differences between the two sectors in the patterns of Ni and Cr, which are elements compatible in mafic phases. For instance, whilst Fernando de Noronha shows roughly constant concentrations for Ni and Cr, the continental sector produced scattered results towards higher values.

Phonolite multi-element diagrams are also virtually identical for both sectors, despite small differences that include lower concentrations of MREE, Y and Nb in Fernando de Noronha, and somewhat lower Sr content in the continental sector (Figure 3-21). These differences are highlighted by comparing the average of concentrations in each sector, where it is clear that only the differences in Nb and Sr alter the patterns of the plot (Figure 3-21). Variability in MREE and Y were already highlighted in the REE patterns presented above but the patterns in Nb may be further stressed by Zr and SiO_2 variation diagrams that include intermediate and evolved samples (Figure 3-22). The diagrams show two distinct evolution trends for samples with $SiO_2 > 52$ wt.%. Zr and SiO_2 variation diagrams for Ta, which is an element that behaves similarly to Nb in andesitic compositions, also show similar patterns in both sectors. Given the similar behaviour of these two elements amongst primitive compositions in both sectors (Figure 3-19), their patterns amongst intermediate and evolved samples are likely the result of fractional crystallisation rather than source differences.

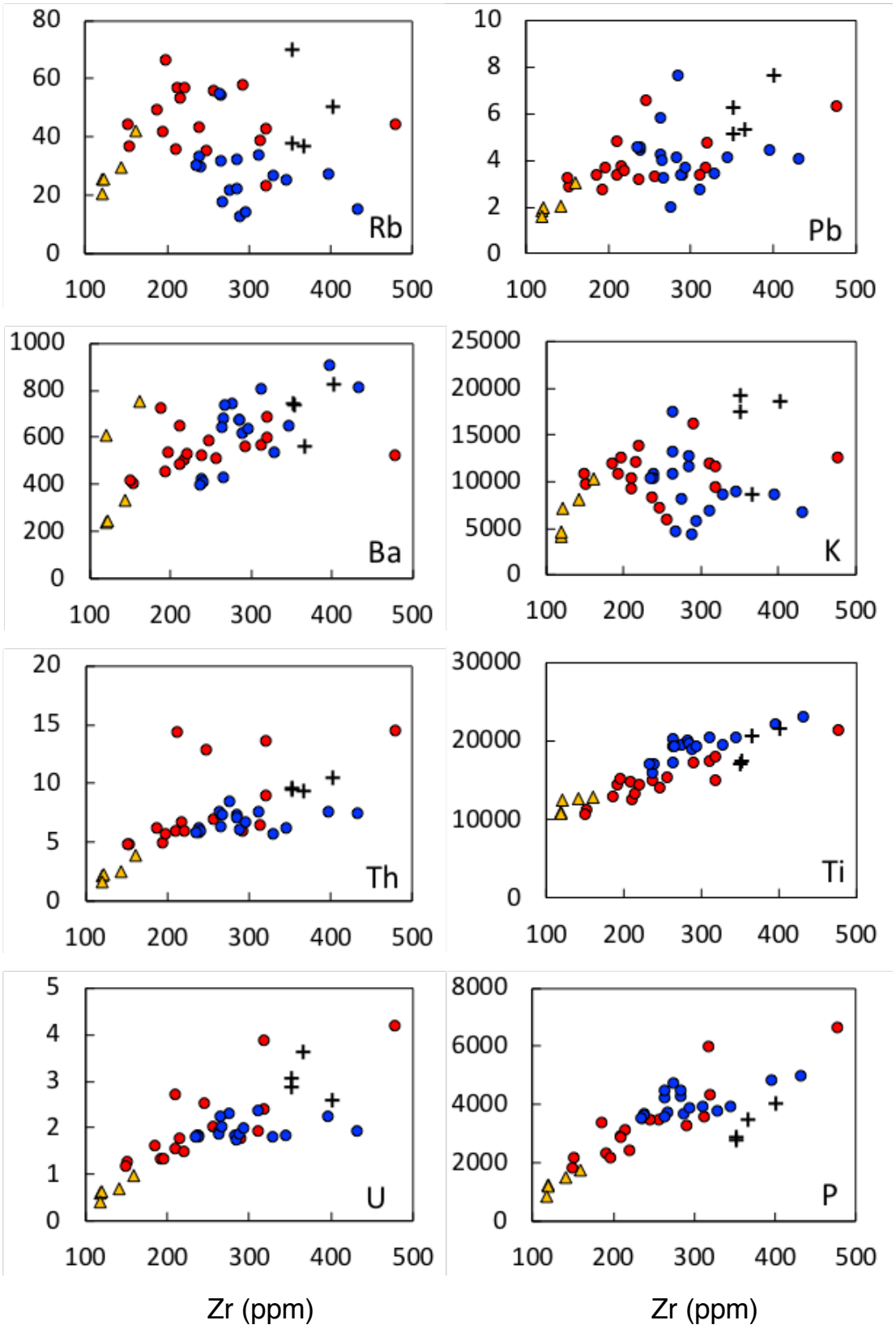

Figure 3-19: Continues on the next page.

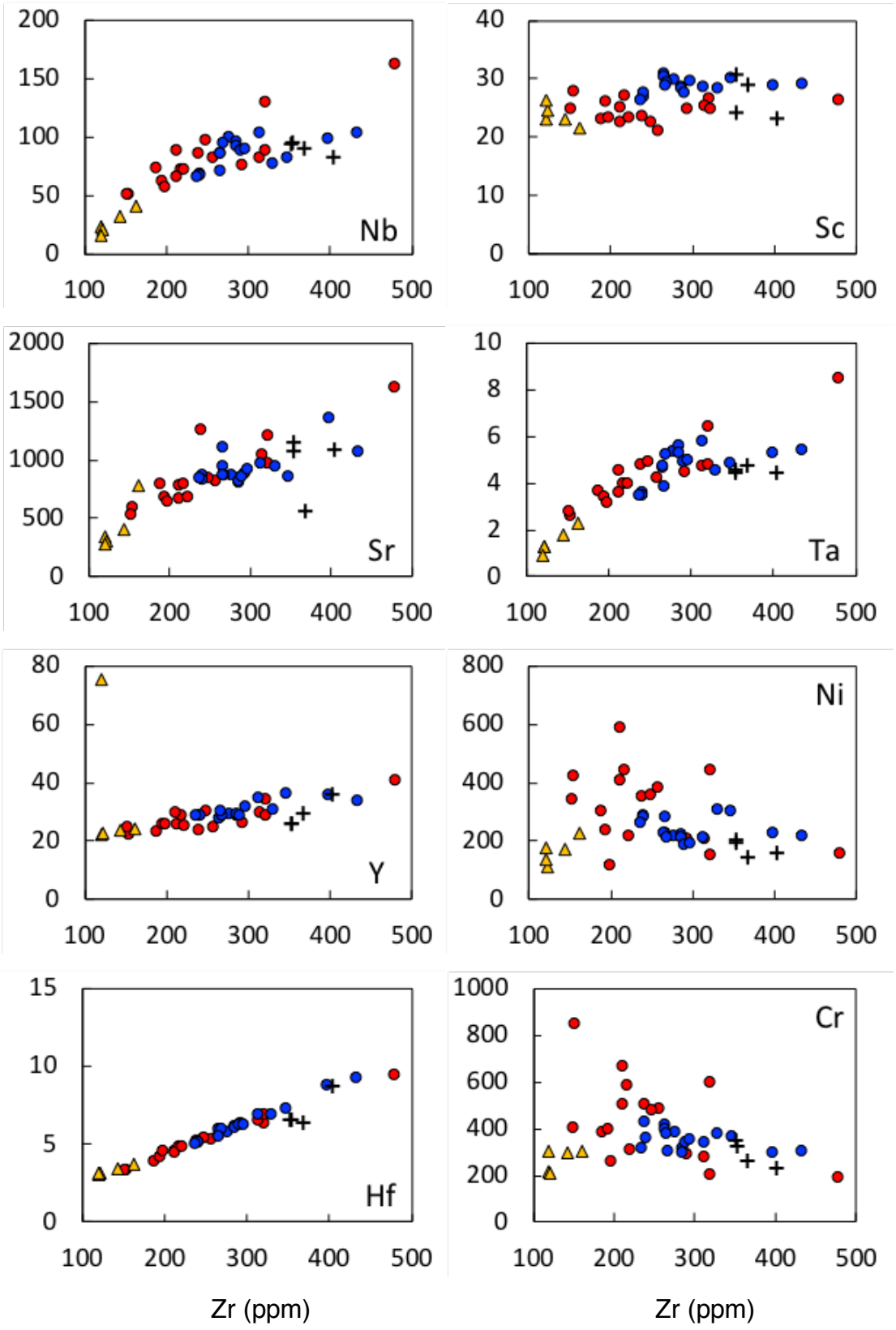

Figure 3-19: Trace elements Zr variation diagrams for basaltic samples. All values in ppm. Legend as in Figure 3-20.

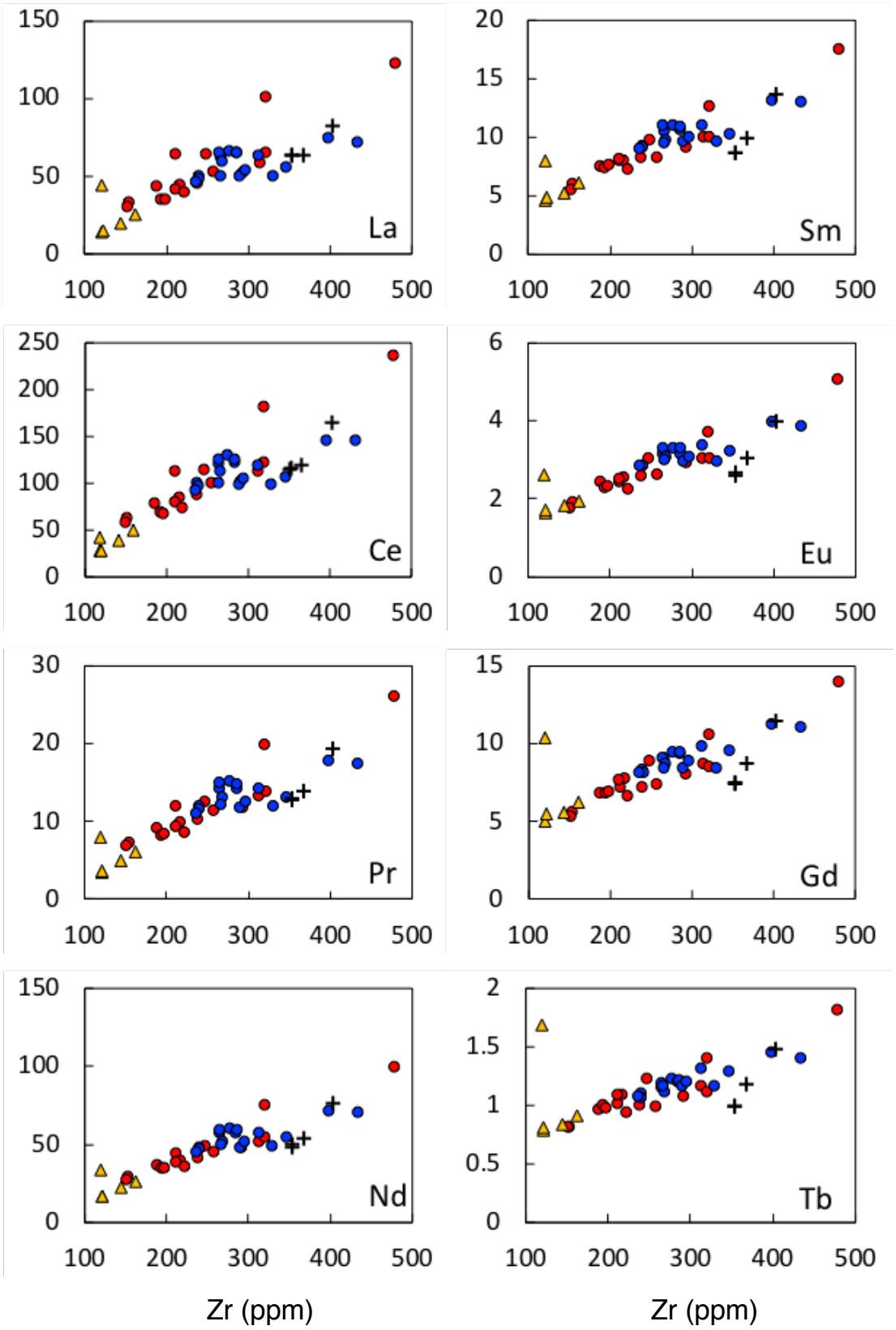

Figure 3-20: Continues on the next page.

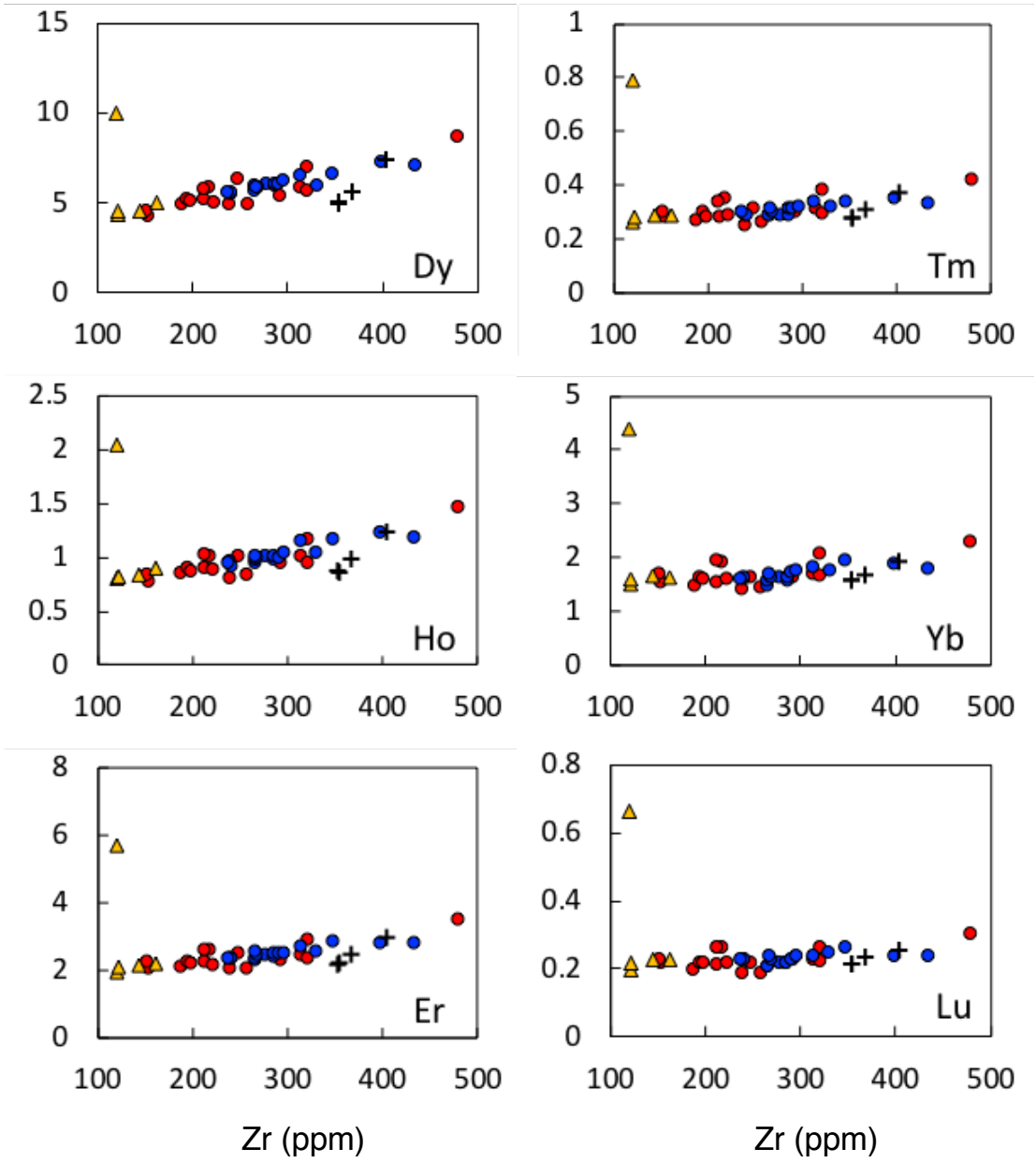

Figure 3-20: Rare-Earth elements (REE) Zr variation diagrams for basaltic samples. All values in parts per million (ppm).

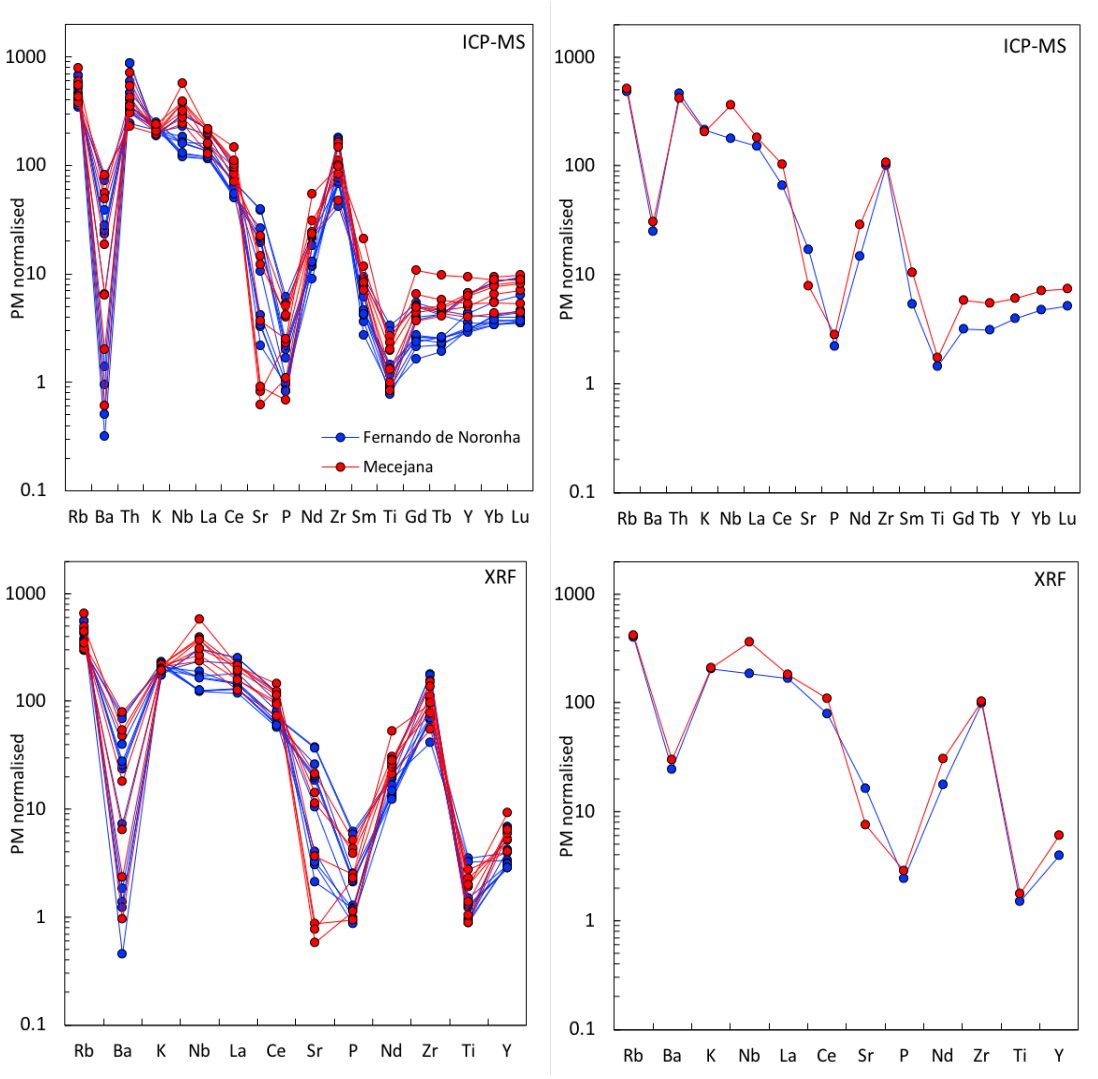

Figure 3-21: Phonolite multi-element diagrams. The *top* two diagrams are based on the ICP-MS data and the *lower* two on the XRF data. Both are included for comparison and to show that the overserved trends are not a product of the methods used. Both diagrams on the *right* show the average of values for the two sectors and highlight the main differences between them, namely the behaviour of MREE, Y and Nb, and different degrees of Sr depletion.

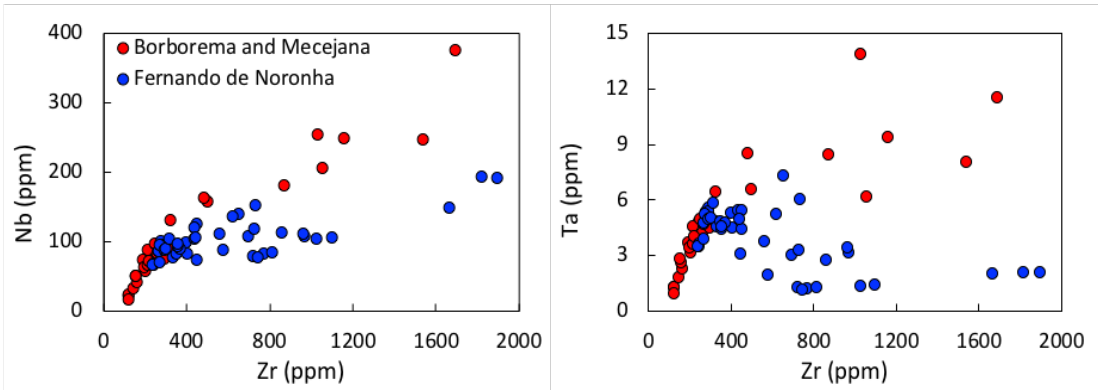

Figure 3-22: Continues on the next page.

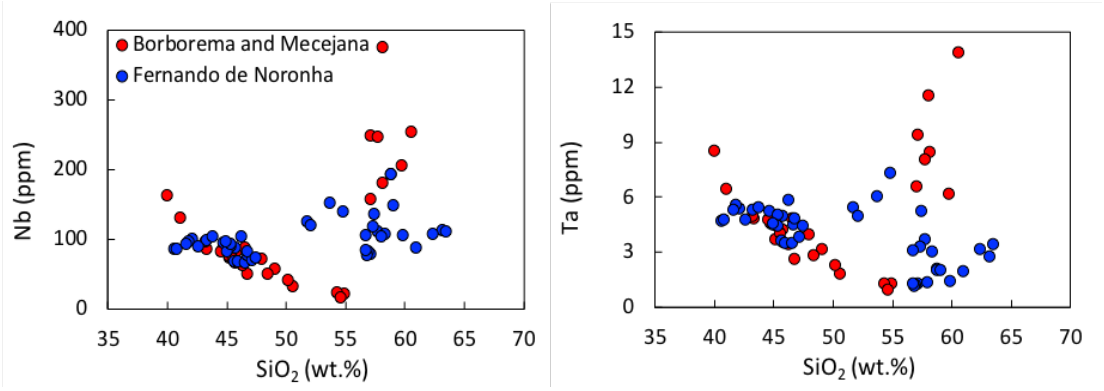

Figure 3-22: Zr and SiO_2 variation diagrams for Nb and Ta, highlighting the distinct evolutionary trends for intermediate and evolved rocks from the continental and oceanic sectors.

Discussion

Alteration

Despite the fresh appearance of hand specimens and most thin sections, some degree of alteration has affected some samples in the assemblage, especially in Fernando de Noronha. It is important to address these issues before proceeding, as they affect both major and trace elements and may influence our analysis. The two main effects of alteration have been a loss of Na_2O content of intermediate and some evolved rocks in Fernando de Noronha, and variable effects on the very mobile trace elements Rb, K and Ba.

Na_2O loss directly affect the alkali content of some samples and therefore the TAS diagram and any classification based on it. Although the transitional compositions of intermediate and trachytic samples in Fernando de Noronha seen in the TAS diagram form a continuous transitional trend, their exclusively *potassic* and *ultrapotassic* characters and virtually exclusive LOI values > 2 wt.% are clearly distinct from the rest of the assemblage (Figure 3-11). Furthermore, all rocks that plot as transitional come from sections of the Remédios Formation comprising the most weathered exposures in the archipelago (Chapter 1) and which have produced the most altered oceanic samples according to LOI values (Appendix C; Table C-1). A

transitional trend is also in sharp contrast with samples from the Cameroon Line oceanic sector. Although the latter dataset will be discussed in detail in Chapter 4, we bring forward this particular comparison to emphasise some of the effects of alteration in Northeast Brazil. In the Cameroon Line oceanic sector, despite the overall lack of *potassic* or *ultrapotassic* samples, all intermediate transitional compositions also have LOI > 2 wt.%, whilst most alkaline ones do not. In addition, most alkaline samples are sodic, whilst most transitional ones are mildly potassic (Figure 4-10 in Chapter 4). The correlation between high LOI and low total alkalis on both sides of the Atlantic and the distinct potassic indices of these samples suggest that the apparent transitional character of intermediate samples in Fernando de Noronha is the result of depletion in total alkalis. In Fernando de Noronha, this depletion has affected Na_2O more strongly than K_2O, giving rocks exclusively *potassic* or *ultrapotassic* characters, in contrast with the rest of the whole assemblage that is exclusively *sodic* or *mildly potassic*. Stronger Na_2O depletion in relation to K_2O has been reported as a common phenomenon in weathering associated with seawater, due to the breakdown of plagioclase and its alteration to orthoclase during early stages (Pearce, 1976). Therefore, any analysis of intermediate and trachytic rocks from Fernando de Noronha must be treated with caution.

The scattered trends of Rb and K in multi-element and variation diagrams (Figures 3-13, 3-14 and 3-19) indicate alteration leading to depletion, especially in Fernando de Noronha. They show scattered distributions in Zr variation diagrams that are similar for the two elements, which suggests similar controls behind their scattering. Rb is highly incompatible in mafic phases and its concentrations should decrease with increasing melt fractions. However, comparing Ce/Y, which may be used as a measure of degrees of partial melting, with Ce/Rb from our XRF data shows increasing Ce/Rb at constant Ce/Y in the oceanic sector, indicating decreasing values for Rb (Figure 3-23). Furthermore, despite the overall higher content of incompatible trace elements and more undersaturated

lithology and geochemistry in Fernando de Noronha, its Ce/Rb ratios are higher than those for the MQVL, and well above OIB published values (Sun and McDonough, 1989) and other primitive (MgO ≥ 8 wt.%) OIB XRF dataset collected at the same laboratory at the University of Edinburgh (Fitton, 2007). Extending this comparison to Ce/Ba and Ce/Nb, Ba and Nb also being incompatible elements, show that the patterns in Northeast Brazil are indeed due to Rb depletion. Ce/Nb and Ce/Ba ratios show that trends in the region are in accordance with other OIB data, except for its high Ce/Rb ratios. These diagrams also show that trends in Northeast Brazil lean towards low Ce/Nb, Ce/Ba and, in the case of continental samples, Ce/Rb. These ratios indicate lavas that are relatively enriched in more incompatible trace elements in relation to available OIB datasets, including values from Sun and McDonough (1989), thus further highlighting how relatively low Rb concentrations diverge from the overall trends in Northeast Brazil and must indicate secondary processes that to a small extent also affect OIB around the world. Although phlogopite fractionation could be an alternative explanation for Rb depletion in Fernando de Noronha, it may be excluded on the basis of scant evidence for fractional crystallisation, the lack of correlation between Ce/Y and Rb depletion and the opposite behaviour of Ba in the archipelago (see below). Consequently, their behaviour is likely the result of more advanced weathering in the oceanic environment. Figure 3-19 shows how K behaves very similarly to Rb. Although Th is not very mobile, it still produced a few outliers with relatively higher Th content that are more clearly visible in Figures 3-13 and 3-14, although the reasons for this are not clear. These elements should therefore be avoided in comparisons between the two sectors. Nonetheless, K depletion also leads to the conclusion that low total alkalis amongst oceanic samples, despite reflecting a proportionally greater depletion of Na, is also due to some loss of K.

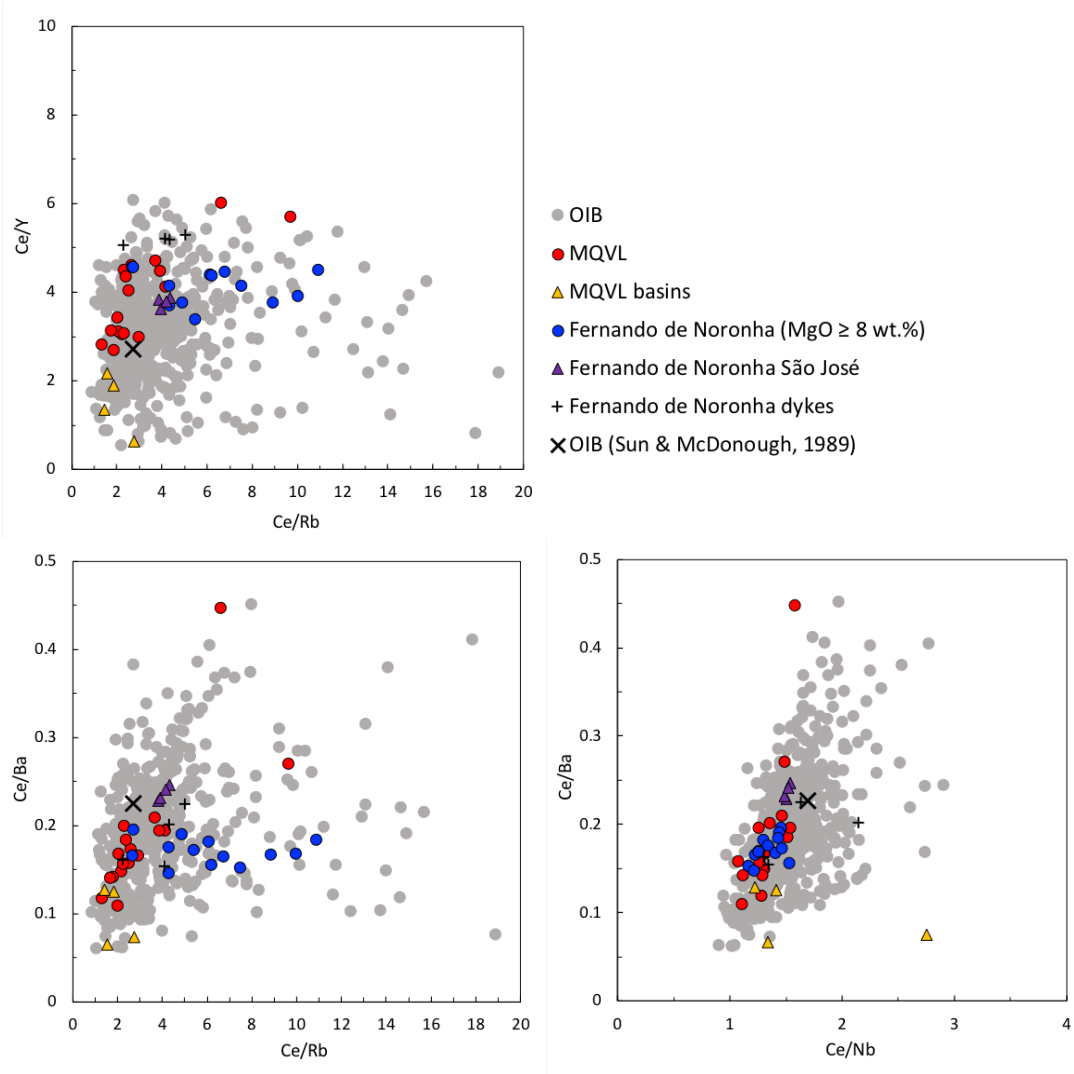

Figure 3-23 (previous page): Relationship between Ce/Rb with other incompatible elements. Ce/Y represents degrees of partial melting and shows that scattered and increasing Ce/Rb ratios in Fernando de Noronha are independent of it. Ce/Be and Ce/Nb illustrate how other incompatible elements behave closer to general OIB trends, emphasising the unusual behaviour of Rb. Primitive (MgO ≥ 8 wt.%) OIB data are from Fitton (2007) and Sun and McDonough (1989).

Contamination by peridotitic xenoliths and xenocrysts

Hand specimens and petrographic observations highlight the ubiquity of peridotite xenoliths and their disaggregated products such as olivine, which dominated amongst xenocrysts, and reaction textures consuming orthopyroxene in the assemblage. Table 3-1 gives a summary of these observations. Any discussion of the assemblage from Northeast Brazil must first address the issue of contamination by mantle material, since their

presence has had an effect on the MgO content and other geochemical signatures associated with early fractional crystallisation amongst primitive samples.

Ni and Cr, two very compatible elements in mantle phases and highly sensitive to mantle xenolith contamination, show a positive correlation with the presence of peridotitic nodules, especially in the continental sector (Figure 3-24). Conversely, their clustered values in Fernando de Noronha, except for the xenolith-rich São José Formation and two other samples containing xenoliths, indicates the small extent to which both fractional crystallisation and peridotitic contamination has affected the oceanic sector. This is based on the distinct behaviour of very compatible trace elements during partial melting or fractional crystallisation, and Ni and Cr are particularly useful in mafic and ultramafic rocks, as the former is highly compatible in olivine, and the latter in spinel and clinopyroxene. Their strong affinities to mantle phases means that their concentrations in the melt are mostly unaffected at small degrees of partial melting, but become quickly depleted in the early stages of fractional crystallisation, making them useful for distinguishing between these processes (Minster and Allègre, 1978). Accordingly, some of the relatively more evolved continental samples show Ni and Cr depletion that indicates some fractional crystallisation (Figure 3-25). This includes the MQVL basaltic andesites from the basins and the nephelinite sample that happens to be free of xenoltiths and xenocrysts (i.e. 15BP12-25). The latter has also produced REE patterns that indicate some fractional crystallisation (see above; Figure 3-18). Samples affected by fractional crystallisation also correlate with the absence of xenoliths, potentially reflecting greater residence times and/or slower ascent, and the consequent resorption or settling of any contaminant nodules together with phenocrysts. The continental trends of xenolith contamination and fractional crystallisation observed in the Ni and Cr diagram, indicated respectively by high and low concentrations of these elements, intersect precisely at the median Ni and Cr values for Fernando de Noronha (219 ppm and 339 ppm,

respectively) and thus suggest that both sectors had initially similar Ni and Cr concentrations before being affected by these two opposing process, and are likely to have come from a similar source.

Since these fragments are compositionally indistinguishable from early fractionation phases in terms of major elements, they also explain MgO enrichment (Figures 3-8 and 3-9) and the significant proportions of normative olivine amongst continental rocks. Xenolith contamination also explains the Ni and Cr patterns in the Zr variation diagrams (Figure 3-19). Their patterns show scattered and enriched concentrations in the continent that reflect contamination by mantle material, and contrast with the invariant values in oceanic sector. Zr variation diagrams may be combined with petrographic observations and compared with SiO_2 and MgO variation diagrams to demonstrate the correlation between the presence of peridotitic xenoliths and scattered Ni and Cr patterns (Figure 3-26). SiO_2 variation diagrams not only shows the same trends observed in relation to Zr, but also highlights the invariant Ni and Cr values across different silica content, and thereby demonstrate the dominance of different degrees of partial melting rather than fractional crystallisation as the dominant process behind variability in the assemblage. Conversely, MgO variation diagrams show positive linear trends in the continental sector that reflect the correlation of MgO, Ni and Cr contents with peridotitic nodules. The xenolith-rich rocks from the Fernando de Noronha São José Formation, however, show a subtle enrichment in Ni but not in Cr (Figure 3-26). The reason for this difference is not clear, but there are reported differences between continental and oceanic xenoliths in Northeast Brazil (Rivalenti *et al.*, 2000, 2007; Fodor *et al.*, 2002), and given that Ni and Cr are not compatible in the same mantle phases, some difference in their behaviour could represent differences in the mantle material that they carry.

Apart from the effects on MgO and on elements that are compatible in mantle phases, contamination by mantle xenoliths does not seem to have affected the assemblage further. However, it hinders the possibility of

identifying primary magmas or adequately assessing the effects of early fractional crystallisation (see below). Overall, contamination is dominated by mantle material, and only one obvious crustal xenolith was identified (i.e. in sample 15BP5-8; see above). Although there is the possibility that some of the ocelli identified in these rocks during petrographic observations represent resorbed quartz, the potential presence of crustal material in the MQVL would be minor, and there is no indication that any crustal contamination significantly affected the assemblage.

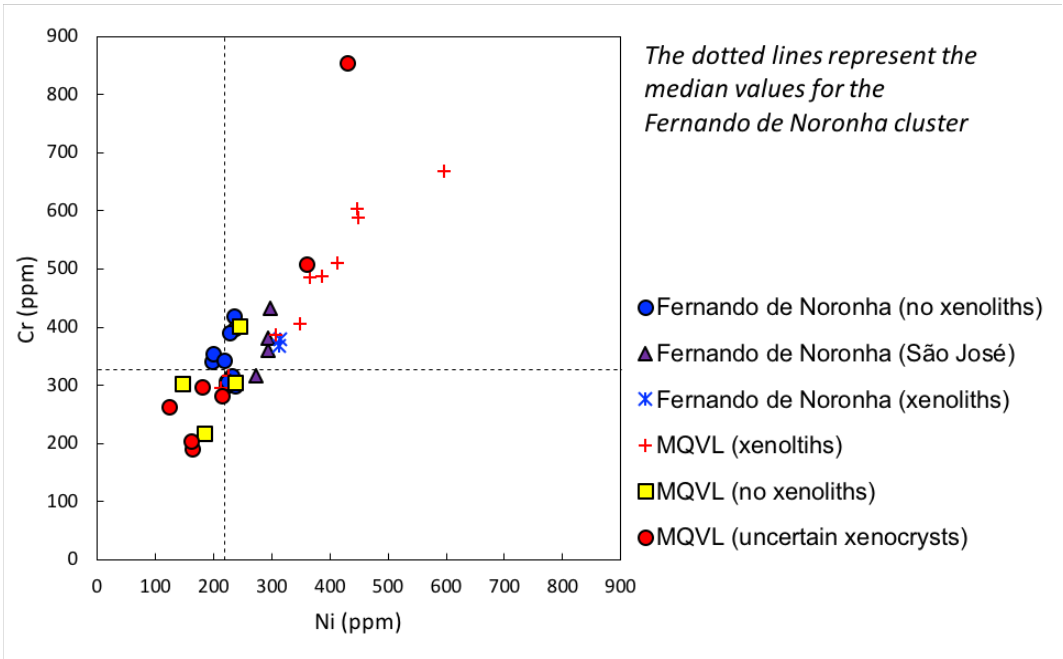

Figure 3-24: Ni and Cr patterns show a restricted range of concentrations in Fernando de Noronha and correlate with the presence of peridotitic xenoliths and other evidence for fractional crystallisation in the MQVL (see also Figure 3-25). The uncertainty in relation to the presence of xenocrysts in some samples is due to the difficulty in distinguishing them from phenocrysts, as discussed above. All Fernando de Noronha São José samples contain xenoliths. The crossed lines mark the median Ni and Cr values for Fernando de Noronha (219 ppm and 339 ppm, respectively), and coincide roughly with where the MQVL linear trends of fractional crystallisation and xenolith contamination come together, indicating that their original Ni and Cr values before these processes could be similar to values in Fernando de Noronha.

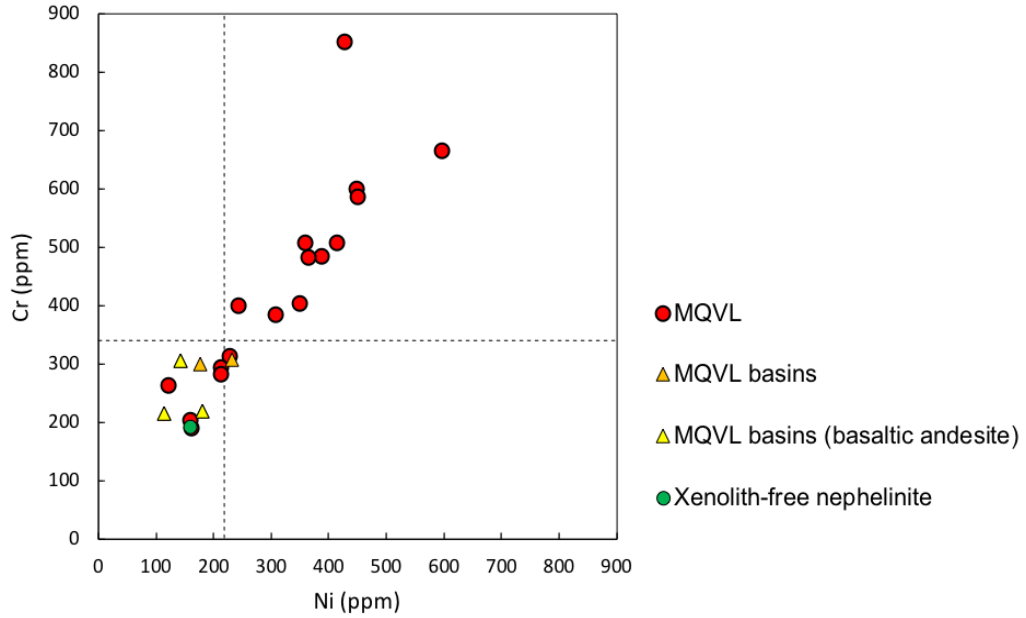

Figure 3-25: Ni and Cr patterns in relation to sample context and rock type in the MQVL. Lower Ni and Cr contents are clear amongst samples that show other types of evidence for fractional crystallisation, and dominate amongst the MQVL basins.

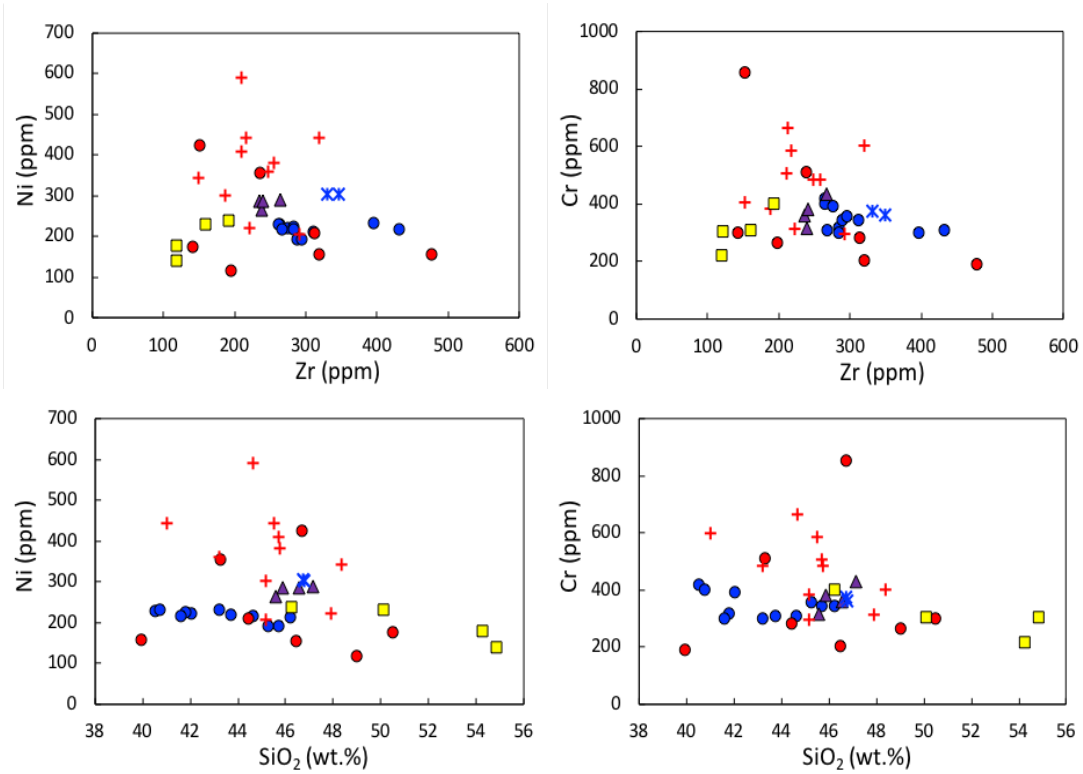

Figure 3-26: Continues on the next page.

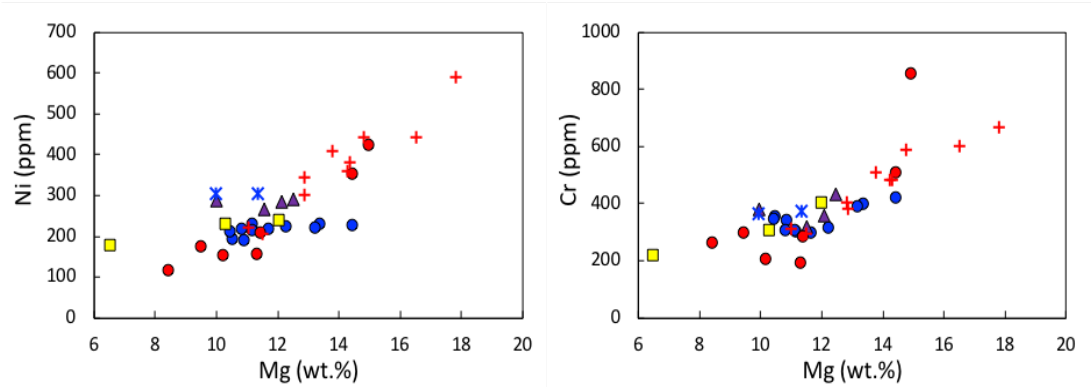

Figure 3-26: Zr (ppm), SiO_2 (wt.%) and MgO (wt.%) variation diagrams for Ni and Cr in primitive rocks from the MQVL and Fernando de Noronha. Legend as in Figure 3-24. Scattered and higher Ni and Cr values clearly correlate with the presence of xenoliths, and form a linear positive correlation with MgO. Conversely, the mainly invariant Ni and Cr trends in Fernando de Noronha reflect the dominance of partial melting processes rather than fractional crystallisation as responsible for variability in the assemblage.

Early fractional crystallisation

Although primitive samples in the assemblage (MgO ≥ 8 wt.%) have been affected by some degree of fractional crystallisation, the effects are not significant. However, it shows that these rocks do not represent primary magmas. In the continental sector MgO variation diagrams, the higher content of Al_2O_3, K_2O, Na_2O and SiO_2, which are more incompatible in mafic systems, and lower contents FeO, CaO and TiO_2, which are compatible in early crystallising mafic phases, combined with higher silica saturation in relation to Fernando de Noronha, reflect some incipient fractional crystallisation. P_2O_5 also shows lower content and a downward trend that could be attributed to the early crystallisation of apatite.

The Ni and Cr patterns discussed above also show clear evidence for some fractional crystallisation amongst some samples, which match similar evidence for major- and incompatible trace elements, despite the difficulty in disentangling early fractional crystallisation from peridotitic contamination in the geochemical data. Since these two processes affect the data similarly but in opposite directions (e.g. their effects on the Ni and Cr patterns in Figure 3-24), it is difficult to assess the extent to which each processes has affected the composition of Cenozoic lavas in Northeast Brazil, and to identify

samples potentially close to primary compositions. The consistency of evidence for fractional crystallisation across different elements with different behaviours reinforces their validity. Nonetheless such evidence is also consistently sparse and localised, emphasising the limited role that this process has had in geochemical variability amongst primitive rocks in Northeast Brazil.

The effects of early fractional crystallisation on major elements amongst primitive samples and the problems of peridotitic xenolith and xenocryst (i.e. disaggregated xenoliths) contamination may be further illustrated by combining CaO trends with petrographic observations and plotting them against olivine and augite compositions in a MgO variation diagram (Figure 3-27). The diagram shows the correlation between xenolith contamination and deviation from a qualitatively ankaramitic (olivine + clinopyroxene) fractionation line. Higher and scattered MgO values correlate directly with the presence of xenoliths, whereas xenolith-free samples form a curvilinear array intersecting a compositional line connecting augite and olivine that suggests fractional crystallisation of these two minerals. These trends also highlight the dominance of olivine in the contaminants, over other peridotitic phases such as clinopyroxenes. Small degrees of olivine and clinopyroxene fractionation amongst Cenozoic lavas from the MQVL has also been noted by Fodor et al. (1998), based on olivine compositions ~Fo_{80-86} and pyroxene zoning, despite their high MgO contents that must result from xenolith and xenocryst inclusions. The distinct characteristics of the Fernando de Noronha dykes are also highlighted in the diagram.

Figure 3-27: (*next page*) Ankaramitic (olivine + clinopyroxene) fractional crystallisation in basaltic rocks illustrated by CaO in relation to MgO. Augite and olivine compositions from webmineral.com. There is a clear correlation between xenolith content and higher MgO that leads to deviation from the qualitative ankaramitic line of descent that is represented by the dashed line (i.e. fractional crystallisation of olivine + clinopyroxene with gradually increasing modal content of clinopyroxene). The Fernando de Noronha basaltic dykes (7-8 MgO wt.%) form a clearly distinct group.

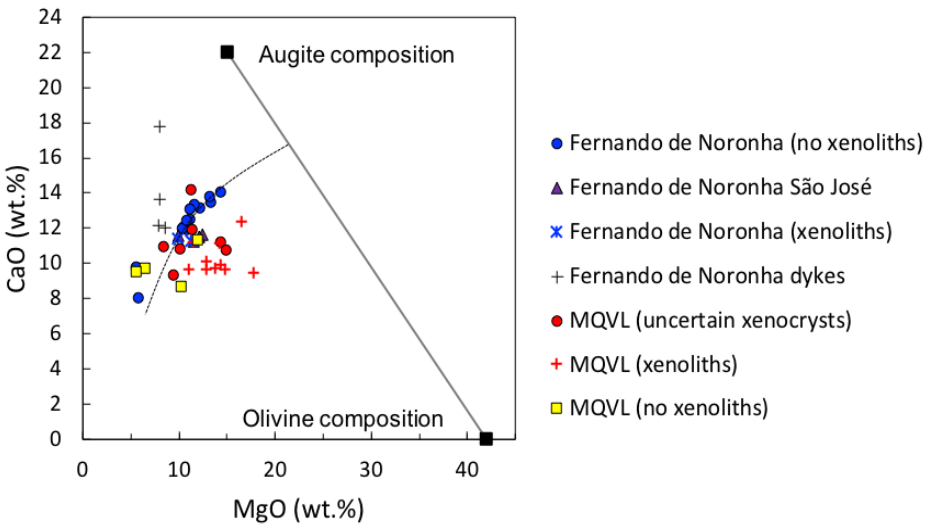

Figure 3-27: Caption on the previous page.

Phonolites and other evolved rocks

Despite the small effects of fractional crystallisation amongst primitive rocks in Northeast Brazil, evolved rocks are still part of both the continental and oceanic assemblages. Continental phonolites come exclusively from the Mecejana Volcanic Field, and there are no significant amounts of evolved rocks in the MQVL where examples are limited to occasional small-scale veins and dykes (Souza *et al.*, 2005, 2013; Silveira, 2006). Conversely, phonolite is the only rock type in the Mecejana volcanic field, over 250 km NW of the northern tip of the MQVL. Fernando de Noronha has ubiquitous phonolite and trachyte in addition to some occurrences of intermediate rocks. The latter are the least abundant rock types in Northeast Brazil, being restricted to the shoreline of the archipelago's main island and marked by high levels of erosion. Although it is not possible to directly compare Mecejana with the MQVL, both areas are associated with Fernando de Noronha in terms of chronology and geochemistry, in addition to being synchronous with one another, which highlights their interconnection despite the lack of directly comparable lithologies.

Although the Mecejana Volcanic Field is located on the continent, it sits on the coast and is aligned with the Fernando de Noronha seamount

chain and fracture zone. Similarities between phonolites from the two areas are significant and have been noted before, but studies are limited (Rao and Sial, 1972; Guimarães *et al.*, 1982). Despite their trace element patterns showing somewhat greater variability than those of basaltic samples, multi-element diagrams are still virtually identical (Figure 3-21). Small differences include lower concentrations of MREE, Y and Nb in Fernando de Noronha and somewhat lower Sr content in Mecejana. Petrographic differences between the two sectors include the significantly greater presence of sodalite-group minerals in Fernando de Noronha, whilst petrographic similarities include the ubiquitous presence of kaersutite and sphene, although that is stronger in Fernando de Noronha. The strong similarities between phonolites from the two areas, together with their tectonic context (proximity to the same fracture zone), could indicate that oceanic processes extend to the edges of the continental lithosphere or vice-versa.

The depletion of MREE amongst intermediate and evolved rocks and the ubiquitous presence of amphibole phenocrysts shows that melt evolution in both areas is marked by amphibole fractional crystallisation, according to Winter (2010) and Rollinson (1993) and amphibole partition coefficients listed therein (Figures 3-5 and 3-16). Depletion of MREE in Fernando de Noronha is clear from intermediate composition onwards, coinciding with the appearance of kaersutite cumulate nodules in the assemblage, and also slightly affects the basaltic dykes in the archipelago. MREE depletion continues and becomes more pronounced in more evolved oceanic samples, but does not affect the continental intermediate compositions represented by the basaltic andesite of the Boa Vista and Potiguar basins. Amphibole fractionation may be also illustrated by Y depletion, which was used by Fitton (1987) to demonstrate amphibole fractional crystallisation amongst intermediate and evolved rocks in the Cameroon Line oceanic sector. In Northeast Brazil, Y depletion is clear amongst evolved rocks from both Mecejana and Fernando de Noronha (Figure 3-28), although it is less pronounced in the continental sector. Nonetheless, there is a clear affinity

between the Mecejana phonolites with the oceanic evolved samples (comparisons with the Cameroon Line will be explored further in Chapter 4).

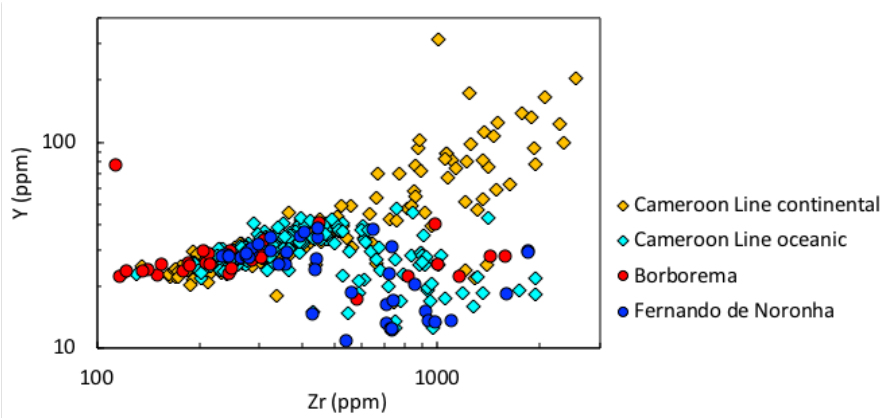

Figure 3-28: Relationship between Zr and Y, indicating the fractional crystallisation of amphibole through Y depletion amongst evolved rocks in both Northeast Brazil and the Cameroon Line. It is clear the affinity of the Mecejana phonolites with rocks from the oceanic sector in both Northeast Brazil and the Cameroon Line, even though Y depletion trends in Mecejana are less pronounced.

The greater depletion of Y and MREE in Fernando de Noronha in relation to Mecejana may be explained in terms more accentuated fractional crystallisation of amphibole, dominated by kaersutite, but also sphene fractionation. Y is also highly compatible in sphene (Winter, 2010), and the ubiquitous kaersutite cumulate nodules in intermediate rocks in Fernando de Noronha, which are absent from the continental sector, also contain sphene, clinopyroxene and plagioclase (Table 3-1). Petrographic observations also reinforce the greater proportions of these minerals in the oceanic phonolites, where in some cases the presence of sphene phenocrysts reaches modal content beyond accessory levels (> 1%).

The greater presence of kaersutite and sphene in the oceanic sector suggests distinct processes controlling the activity of Ti. Although early TiO_2 depletion in Borborema is clear in SiO_2 variation diagrams, and highlights the only difference other than MgO content between the major element patterns of the two sectors (Figure 3-8), we will see in the next Chapter that the Cameroon Line continental sector has similar TiO_2 content to Fernando de Noronha and the African oceanic sector, and yet did not fractionate any

amphibole or sphene (Figure 3-28). Therefore, although TiO_2 content decreases in Fernando de Noronha to values below Mecejana amongst evolved compositions, reflecting the greater fractionation of kaersutite and sphene, the early TiO_2 depletion seen in Borborema cannot be the control behind these differences. In the case of amphibole, greater access to water could be the reason behind its stronger fractionation in both oceanic sectors. This would also explain why evolved samples in Mecejana, which may be affected by the adjacent oceanic fracture zone, carry amphibole phenocrysts but the Cameroon Line continental sector does not (Fitton, 1987).

The greater participation of kaersutite and sphene in fractional crystallisation processes in Fernando de Noronha is also reflected in Nb and Ta patterns. Nb and Ta are High Field Strength Elements that tend to substitute for Ti in Ti-rich phases (Winter, 2010), but Ta is even more compatible in sphene, which has a partition coefficient D_{Ta} between 10.8 and 19.6 that is at least three times greater than D_{Nb} values, which lie between 3.5 and 7.6 (Green and Pearson, 1987; Weaver, 1990). Variation diagrams for Nb and Ta emphasise the stronger depletion of Ta in the oceanic sector amongst intermediate and evolved composition, and the distinct evolutionary trends between the two sectors in relation to these two elements, which may be explained in terms of stronger kaersutite and sphene fractionation in the oceanic sector, but with an even greater participation of sphene (Figure 3-22). This may be illustrated more clearly by Nb/Ta patterns (Figure 3-29) where the significant Ta depletion amongst evolved rocks in the oceanic sector is not matched in the continent, and leads to significantly higher Nb/Ta ratios in Fernando de Noronha, despite the proportionally higher Nb content in continental samples. Conversely, basaltic samples (i.e. Nb ≤ ~100 ppm) show a clear linear array with no significant differences between Ta and Nb, emphasising the presence of some fractional crystallisation in these trends. High Nb/Ta ratios in the archipelago have also been noted by Weaver (1990) and also attributed to sphene fractionation.

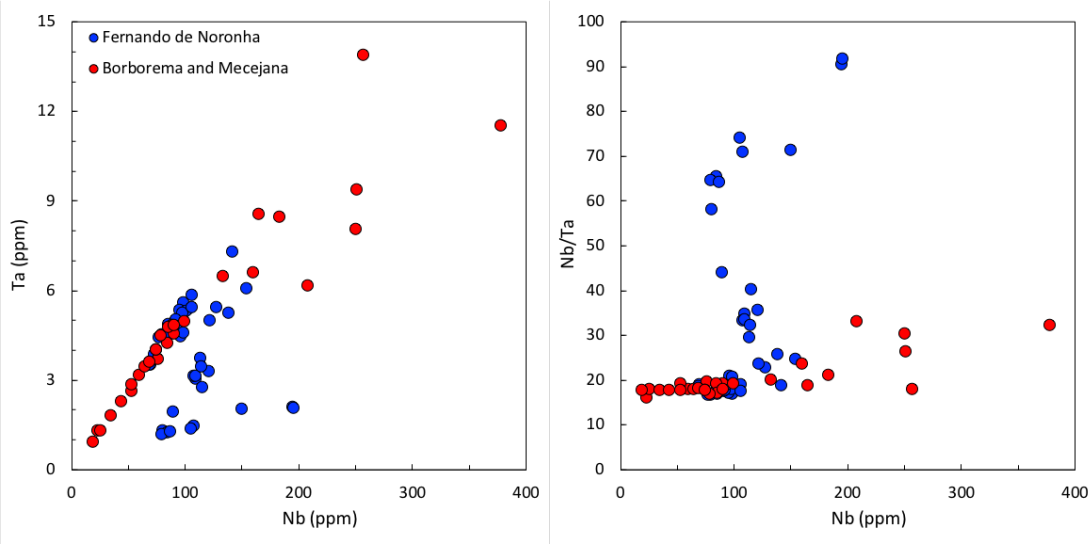

Figure 3-29: Behaviour of Ta in relation to Nb. Their identical behaviour amongst basaltic samples (i.e. Nb ≤ ~100 ppm) is clear, but amongst intermediate and evolved samples in the oceanic sector there is clear and significant depletion of Ta, as well as some Nb.

Higher proportions of kaersutite, sphene and sodalite-group minerals in Fernando de Noronha mark the main mineralogical difference between intermediate and evolved rocks from the continental and oceanic sectors. We have discussed the presence of the first two minerals, but the reasons for greater proportions of sodalite-group minerals in Fernando de Noronha are not clear. They may reflect higher degrees of undersaturation in the oceanic sector, since these minerals are often associated with nephelinites and melilitites (Deer *et al.*, 1992). The reasons for the lower Sr content in the continental phonolites are also not clear. It could result from more significant fractionation of feldspar during melt evolution in the continental sector, which would further distinguish the liquid line of decent in Mecejana from that in Fernando de Noronha in addition to the differences in sphene fractional crystallisation.

Variability due to depth and degrees of partial melting

Despite the presence of some incipient fractional crystallisation amongst primitive samples in both sectors, the negative slope in their TAS diagram distribution (Figure 3-10) indicates that it cannot be the main control

affecting variability amongst these rocks, and that different degrees of partial melting must be the dominant process involved. This is further reinforced by the virtually identical values of Yb and Lu in both sectors, but gradually diverging concentrations for the lighter REE (Figure 3-16). The latter trend shows that LREE are behaving somewhat differently from HREE, supporting the interpretation that degrees of partial melting and not fractional crystallisation is the main control of the assemblage's variability.

Incompatible trace elements in an igneous system behave differently during fractional crystallisation and partial melting, and may be used to show the dominance of one process over the other. During fractional crystallisation, the behaviour of moderately incompatible elements (for which the partition coefficient $D \sim 0.1$) and highly incompatible elements ($D \leq 0.01$) will be virtually indistinguishable. During partial melting, however, enrichment of highly incompatible elements in the melt will be more accentuated towards smaller melt fractions when compared with moderately incompatible ones (Minster and Allègre, 1978; Rollinson, 1993), causing their ratios to change with degrees of partial melting. Their behaviour will also vary slightly between batch melting and fractional melting, although for melt fractions below ~0.02, the distinction becomes less pronounced, and the behaviour of incompatible trace elements during fractional melting will approach that of batch melting. At such small melt fractions, it is also reasonable to assume that the modal composition of the parent rock and the melt, and therefore the bulk partition coefficients for both (i.e. D and P respectively), will remain constant (Allègre and Minster, 1978; Minster and Allègre, 1978). When P is constant and very small, the batch melting equation:

$$\frac{C_l}{C_0} = \frac{1}{D + F(1 - P)} \tag{8}$$

which may be rearranged as:

$$\frac{1}{C_l} = \frac{D + F(1-P)}{C_0} \tag{9}$$

becomes a linear function of the melt fraction *F*, where C_l is the concentration in the liquid and C_0 is the initial concentration in the parent rock (Minster and Allègre, 1978). In this particular case, the pattern of two trace elements plotted against each other as $1/C_l$ must therefore be a straight line that does not intersect the origin (Minster and Allègre, 1978), since both concentrations may be directly related to each other as linear functions of the same *F*.

A positive linear correlation should also be expected for the ratio between a highly incompatible and a moderately incompatible element against the concentration of the same highly incompatible element (Minster and Allègre, 1978). In this case, subsequent fractional crystallisation creates linear patterns with flat slopes branching out of the main positive linear trend, reflecting the similar behaviour of the two elements during this process, as opposed to their different behaviour during partial melting (Figure 3-30). For the same reasons, plotting a moderately incompatible element against a highly incompatible should generate an exponential curve during partial melting and a straight line during fractional crystallisation.

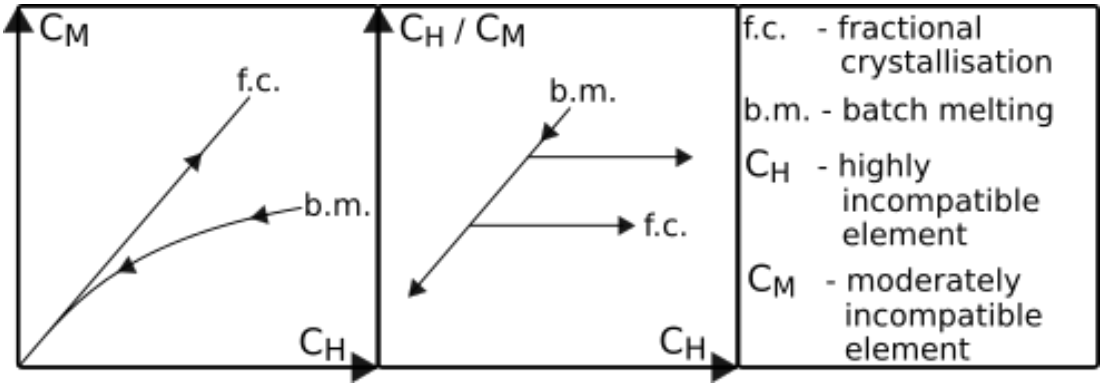

Figure 3-30: Qualitative trends for the behaviour of incompatible trace elements during fractional crystallisation and batch melting (partial melting). Adapted from Minster & Allègre (1978).

Applied to Cenozoic basaltic lavas from Northeast Brazil, these principles point to partial melting as the dominant process behind their

variability, as illustrated by La and Gd (Figure 3-31), with the exception only of the continental basins. In the latter (i.e. samples 15BP3-3a; 15BP3-3b; 15BP3-4; 15BP3-5; 15BP7-14), there are some limited effects of fractional crystallisation and evidence for changes in partition coefficients during melt generation, with samples deviating from a straight line. Similar results are also obtained by pairing any of Nb, La, Ce, Zr and Nd as highly incompatible elements, with Sm, Sr, Gd or Tb as relatively moderately incompatible.

According to these principles, the strongest effects of fractional crystallisation in Fernando de Noronha are found in the Quixaba lava flows unconformably overlying the Remédios Formation directly (i.e. FN16-27 and FN19-31) and marking the break of a hiatus in volcanic activity, but such effects are still clearly minor. Evidence for relatively more significant fractional crystallisation in these two samples is also clear in their REE patterns, where they stand out with distinctively more enriched concentrations across all REE (Figure 3-17). Petrographically, these samples are also marked by relatively less olivine and were classified as tephrite instead of basanite. Not only basanite is significantly more common in the archipelago, but these two samples also represent the only tephrite in the assemblage except for the Fernando de Noronha dykes, and thereby reflect somewhat more advanced fractional crystallisation. Sample 15BP12-25 also shows subtle evidence for fractional crystallisation that is also matched by its REE patterns. Sample 15BP5-8 also stands out in the diagrams. It is the only sample clearly contaminated by crustal xenoliths, which could explain its unusually high LREE/MREE ratios. Samples from MQVL extensional basins show the strongest effects of fractional crystallisation. Although it is difficult to disentangle this process from the effects of changing partition coefficients during partial melting, this interpretation matches other evidence such as the behaviour of Ni and Cr (Figures 3-24 and 3-25), the TAS diagram (Figure 3-10) and normative compositions (Figure 3-12). Nonetheless, the diagrams show that partial melting in the MQVL basins differs from the same process in the rest of the assemblage.

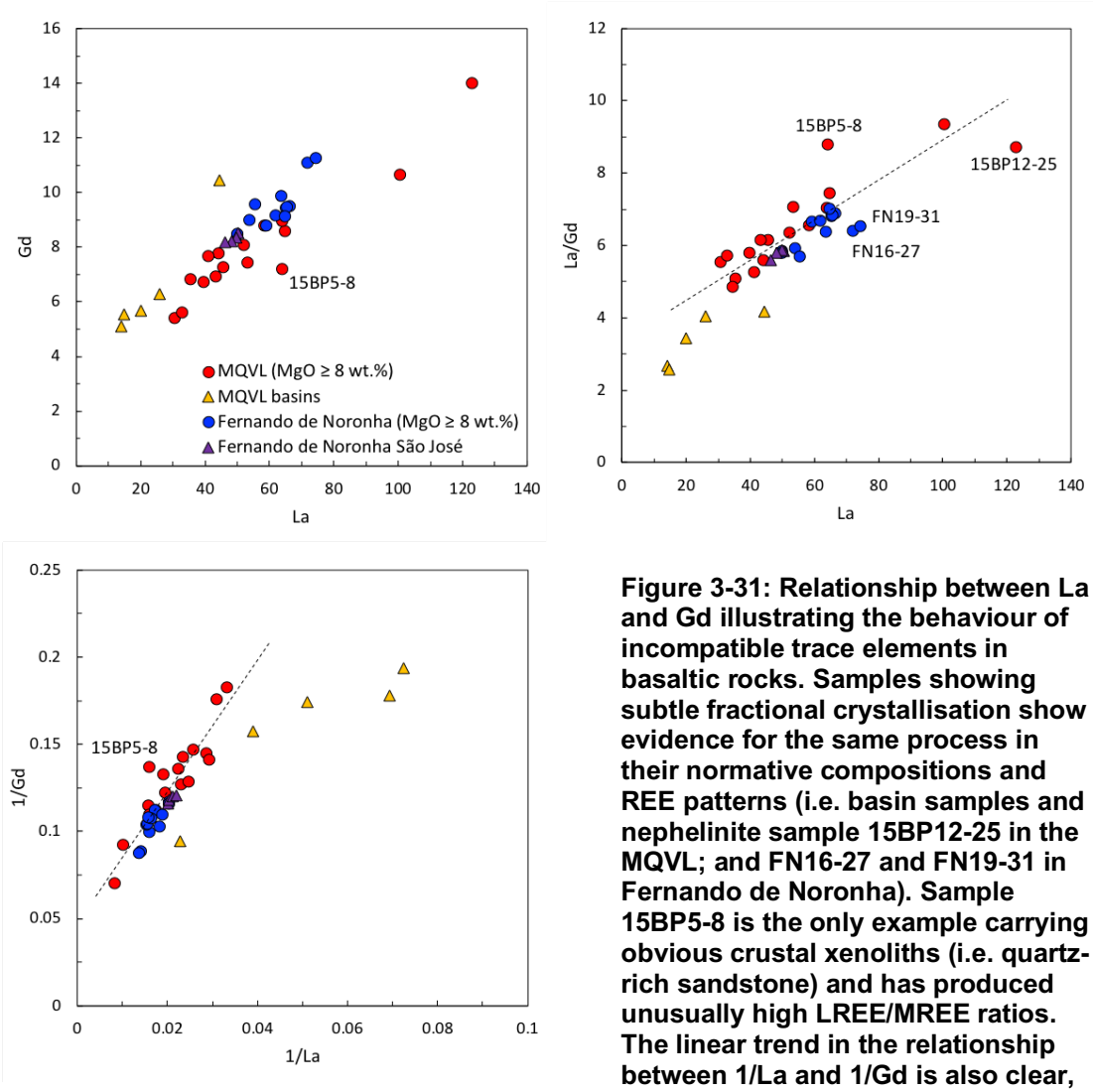

Figure 3-31: Relationship between La and Gd illustrating the behaviour of incompatible trace elements in basaltic rocks. Samples showing subtle fractional crystallisation show evidence for the same process in their normative compositions and REE patterns (i.e. basin samples and nephelinite sample 15BP12-25 in the MQVL; and FN16-27 and FN19-31 in Fernando de Noronha). Sample 15BP5-8 is the only example carrying obvious crustal xenoliths (i.e. quartz-rich sandstone) and has produced unusually high LREE/MREE ratios. The linear trend in the relationship between 1/La and 1/Gd is also clear, except also for samples from the continental basins, which indicates changing *P* during partial melting.

Plotting Y or REE heavier than Tb as moderately incompatible elements against La produces irregular trends and a gradual increase in scattering towards higher atomic numbers, especially in the MQVL, indicating changing partition coefficients for these elements (Figure 3-32). Different contributions of garnet- and spinel lherzolite to the original melts could specifically affect the partition coefficients and behaviour of HREE without much effect on other elements, and therefore these trends must indicate changing contributions of these two types of lherzolite, which in turn point to variations in the depths of melting.

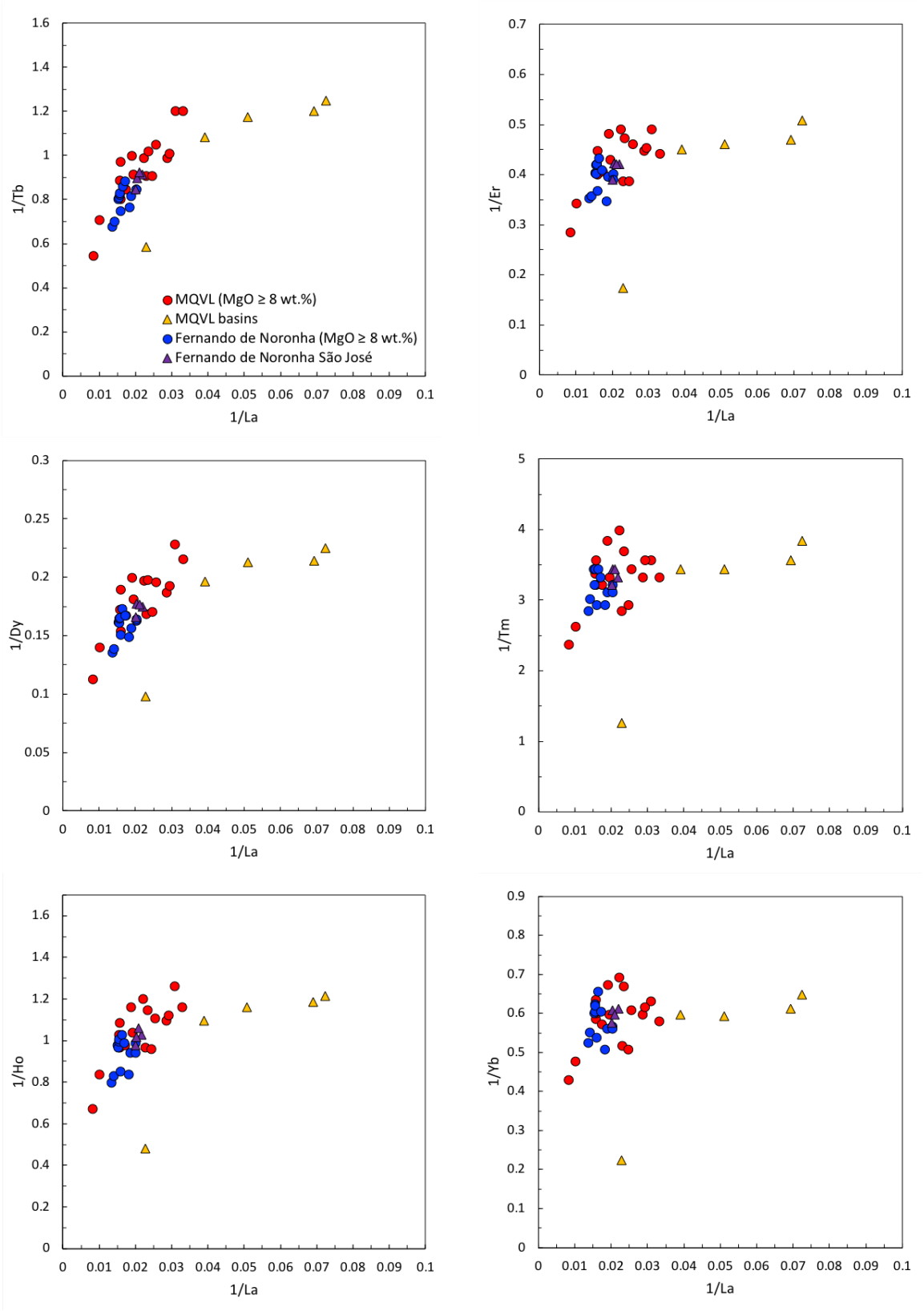

Figure 3-32: Continues on the next page.

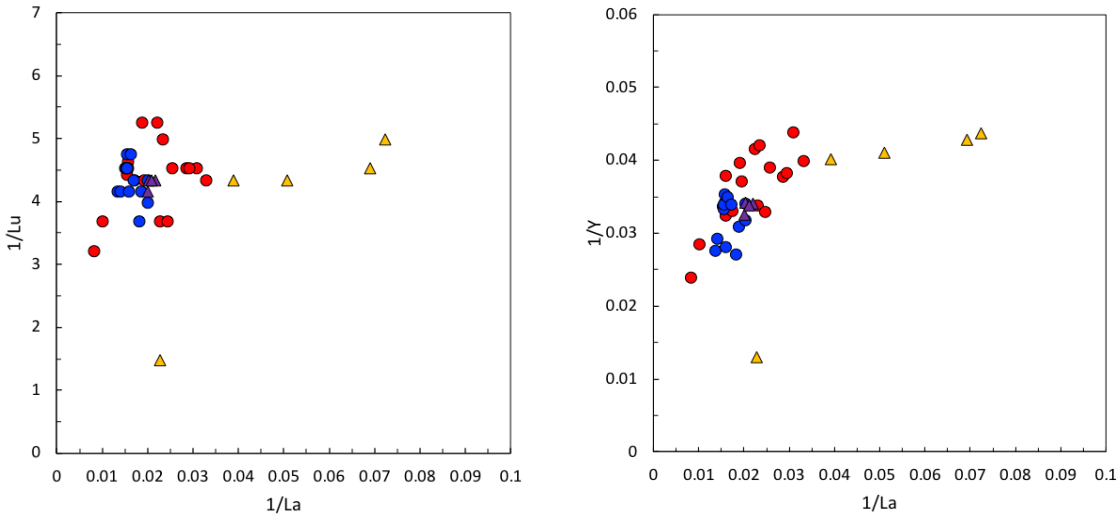

Figure 3-32: (*continues on previous page*) Sequence of HREE and Y compared to La. Partial melting at constant *D* and *P* should have produced linear trends, similar to those for Gd (Figure 3-31). Instead, trends progressively deviate from that behaviour. These elements are more compatible in garnet, and their changing partition coefficients indicate varying contributions of garnet- and spinel lherzolite, which in turn represents different depths of melting.

Despite xenolith and xenocrysts contamination, continental lavas also show a correlation between increasing MgO and increasing incompatible trace element absolute concentrations towards higher element incompatibility (i.e. to the left of Sm and excluding Rb and K; Figure 3-33). This is indicative of differences in degrees of partial melting, as opposed to fractional crystallisation that would show the opposite trend. These differences are absent from the Fernando de Noronha samples, where trace element concentrations in basaltic rocks are independent of MgO. However, the archipelago retains higher trace element concentrations that reflect the higher degrees of undersaturation and lower degrees of melting there. Both these trends in the oceanic and continental sectors are also in part reflected in the more homogeneous REE patterns for primitive samples in Fernando de Noronha that show little difference in relative concentrations between LREE and HREE, and in the greater differences in relative concentrations seen from Lu to La in the MQVL (Figures 3-13 and 3-16).

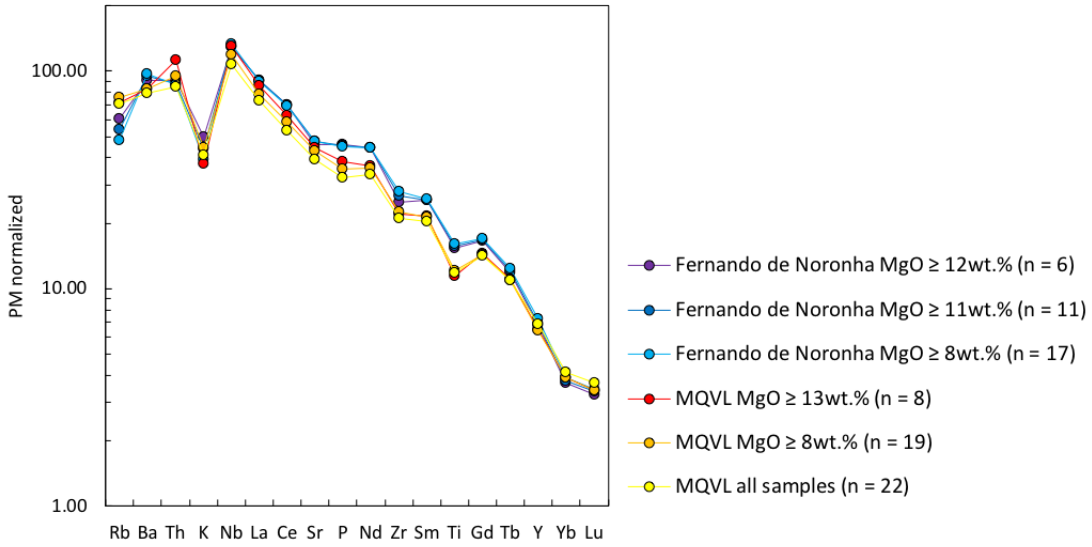

Figure 3-33: Averaged multi-element patterns according to MgO content. Number of samples in each group is given by *n*. Variability in Fernando de Noronha is negligible, whilst in the MQVL it is limited to the relatively more incompatible elements to the left of Sm. The restriction of MgO content to gradually higher values in the MQVL increases the average concentration of incompatible trace elements to the left of Sm.

Degrees of partial melting and contributions of garnet- and spinel lherzolite:

The gradually diverging concentrations of Lu, Yb, Tb and Gd, which are all HREE, and Y, which behaves very similarly to HREE, in multi-element diagrams, as well as the evidence for changing partition coefficients amongst HREE, indicate some role of garnet in the source. Variability in garnet- and spinel lherzolite contributions also work as a measure of depth of melting. Moreover, we have demonstrated how degrees of partial melting, and not fractional crystallisation, must be the dominant petrogenetic process behind variability in the assemblage. Therefore, we may test the relationship between variability in melt fractions and contributions of garnet- or spinel lherzolite as a measure of depth by modelling the behaviour of Sm/Yb ratios against Ce/Sm, both normalised to chondrite (McDonough and Sun, 1995), as described by Fitton et al. (in press). The former ratio indicates the role of garnet in the melting process, whilst the latter is more sensitive to degrees of partial melting. Ce is chosen instead of La because of the greater availability of *D* values for Ce, and Sm is a suitable choice of MREE because Gd or

heavier REE are compatible in garnet and Eu is sensitive to the presence of plagioclase. Fitton et al. (in press) estimated the composition of the mantle from the composition of primitive Ontong Java Plateau basalt and an estimated melt fraction of 0.3 (Fitton and Godard, 2004). They estimated *D* and *P* by averaging published values, and used published modal compositions for garnet lherzolite, spinel lherzolite and harzburgite, and melt modes from Baker and Stolper (1994) and Walter (1998). Values are given in Table 3-2. Comparing our data to the modelled behaviour of Ce/Sm and Sm/Yb (Figures 3-34 and 3-35) illustrates the relationship between melt fractions and the relative proportions of garnet- and spinel lherzolite involved in the original melts forming our assemblage. The effect of fractional crystallisation should be negligible, since during such process the behaviour of elements with $D \leq 0.1$ is virtually indistinguishable and ratios should remain constant (see above). Furthermore, as discussed above, our data do not show evidence for significant fractional crystallisation.

Table 3-2: Values used in the (Ce/Sm)n and (Sm/Yb)n model.

Concentrations	**Ce**	**Sm**	**Yb**
Mantle source†	1.2362	0.3459	0.4322
Chondrite††	0.613	0.148	0.161

***D* and *P* values (lherzolite)**	**Ce**	**Sm**	**Yb**
D (spl lhz)	0.0109	0.0363	0.0878
P (spl lhz)	0.0560	0.1824	0.3043
D (gt lhz)	0.0094	0.0579	0.6169
P (gt lhz)	0.0651	0.2797	1.7172

D values (minerals)	**Ce**	**Sm**	**Yb**
olivine	0.0003	0.0009	0.02
orthopyroxene	0.01	0.02	0.12
clinopyroxene	0.07	0.24	0.37
spinel	0.01	0.01	0.01
garnet	0.02	0.29	4.8*

Modal composition	**Mantle spl-lhz**	**gt-lhz**	**Melt spl**	**gt**
olivine	0.578	0.598	-0.22	0.08
orthopyroxene	0.27	0.211	0.38	-0.19
clinopyroxene	0.119	0.076	0.71	0.81
spinel	0.033	0	0.13	0
garnet	0	0.115	0	0.3

† mantle source concentrations calculated from the Ontong Java Plateau using a harzburgite source and 0.3 melt fraction; †† chondrite concentrations from (McDonough and Sun, 1995); * 4.8 is increased from 3.7, which was the original average from the cited publications (see main text for discussion); *spl* = spinel; *gt* = garnet; *lhz* = lherzolite.

Figure 3-34 shows that this simple model fails to account for the high Sm/Yb in rocks from Fernando de Noronha and one of the MQVL nephelinites. However, raising the *D* value for Yb in garnet from the average value of 3.7 to 4.8, which is still well within the range of published values, changes the model in a way that fits the data (Figure 3-35). Despite the uncertainties in this model, the relative relationship between chondrite normalised Ce/Sm and Sm/Yb is robust, and reflects relative differences in degrees of partial melting and involvement of garnet- and spinel lherzolite.

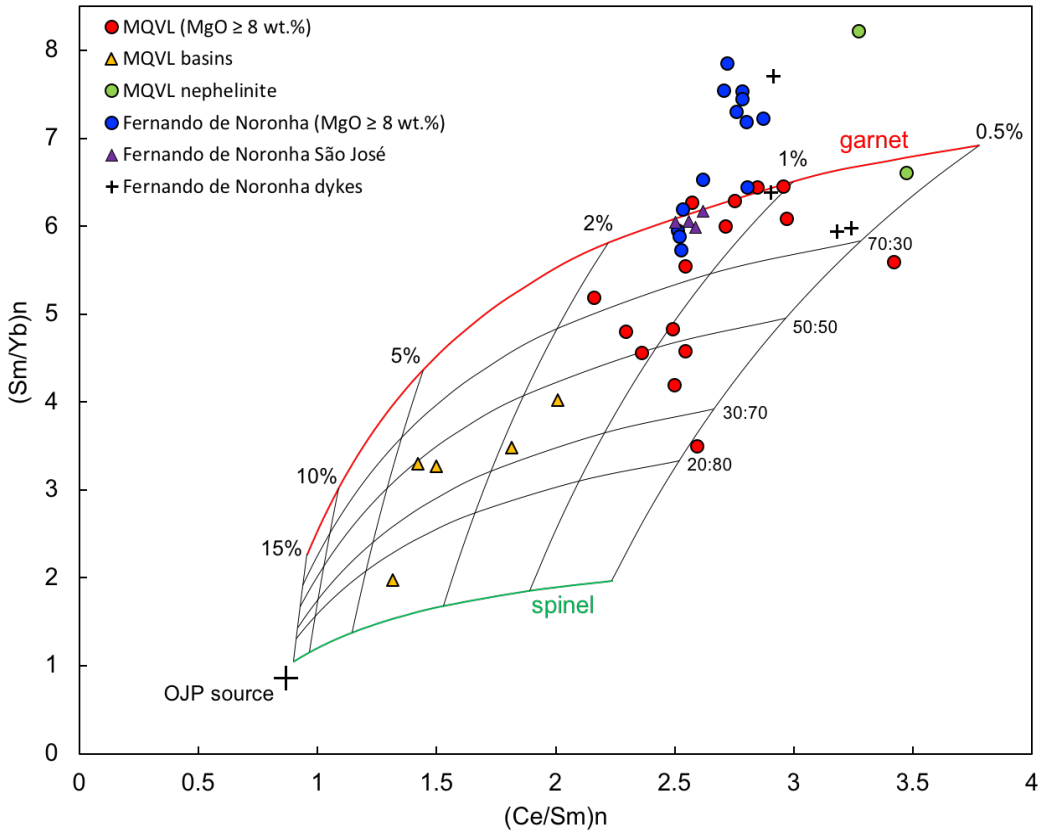

Figure 3-34: Relationship between (Ce/Sm)n and (Sm/Yb)n normalised to chondrite (McDonough and Sun, 1995) in relation to the upper mantle, using the average of published *D* values and calculating the mantle source composition from the Ontong Java Plateau lavas using 0.3 melt fraction (Fitton et al., in press; Fitton and Godard, 2004). The diagram does not model the data from Fernando de Noronha adequately.

The results in Figure 3-35 show that basaltic samples from Fernando de Noronha have a dominantly garnet lherzolite source and generally lower melt fractions compared with the continental sector. The latter shows a

greater range in both ratios, with larger involvement of spinel lherzolite, and both higher and lower melt fractions. The model suggests that melt fractions in the continental sector range from < 0.005 to ~0.05, although only basin samples and the lava flow 15BP3-2 adjacent to the Boa Vista basin produced values > 0.01. In the oceanic sector, melt fractions concentrate at ~0.01, although oceanic dykes have values as low as ~0.005. Garnet lherzolite contributions in the oceanic sector range from 100% to 50%, and in the continent from 70% to < 20%, although one continental nephelinite sample shows garnet lherzolite contributions close to 100%. It is worth noting that, despite the size of its dataset, Fernando de Noronha is a single locality whose rock variability is mostly the product of melt evolution, and therefore greater homogeneity amongst primitive rocks there is unsurprising.

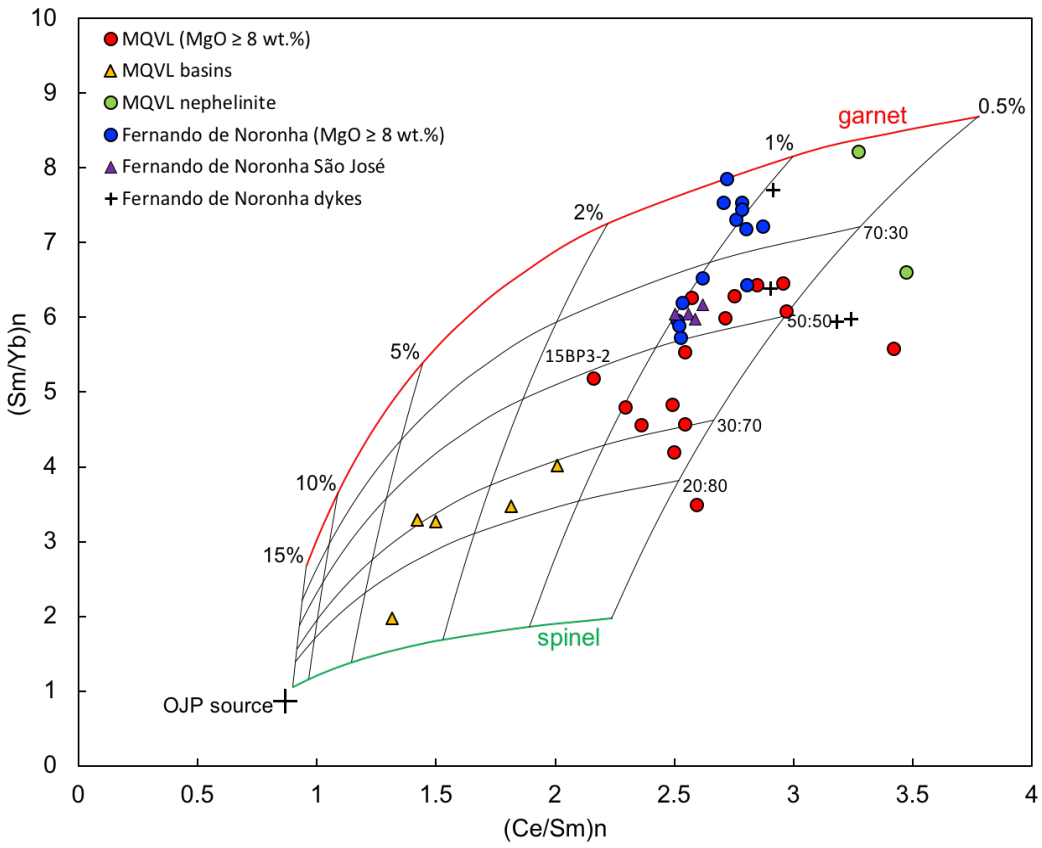

Figure 3-35: Relationship between (Ce/Sm)n and (Sm/Yb)n normalised to chondrite (McDonough and Sun, 1995) in relation to the upper mantle, using the same parameters as Figure 3-34, except for the partition coefficient *D* for Yb in garnet, for which a value of 4.8 was used instead of 3.7. This is still well within the range of published values, and the resulting diagram accommodates all of the data adequately.

Modelled REE behaviour suggests that melting beneath the continent was generally shallower than beneath the oceanic sector, even outside the continental basins, which points to significant levels of lithospheric thinning in the MQVL. These results are in agreement with the geophysical model by Priestley and McKenzie (2013), which indicates that the lithosphere under Borborema is at least as thin as the adjacent oceanic lithosphere (Figure 3-36). Their lithospheric thickness map also shows how both Borborema and the continental sector of the Cameroon Line, which were joined together before continental separation, represent the thinnest lithospheric segments along the equatorial and south Atlantic's passive margins, as well as being provinces surrounded by cratons with large thickness gradients.

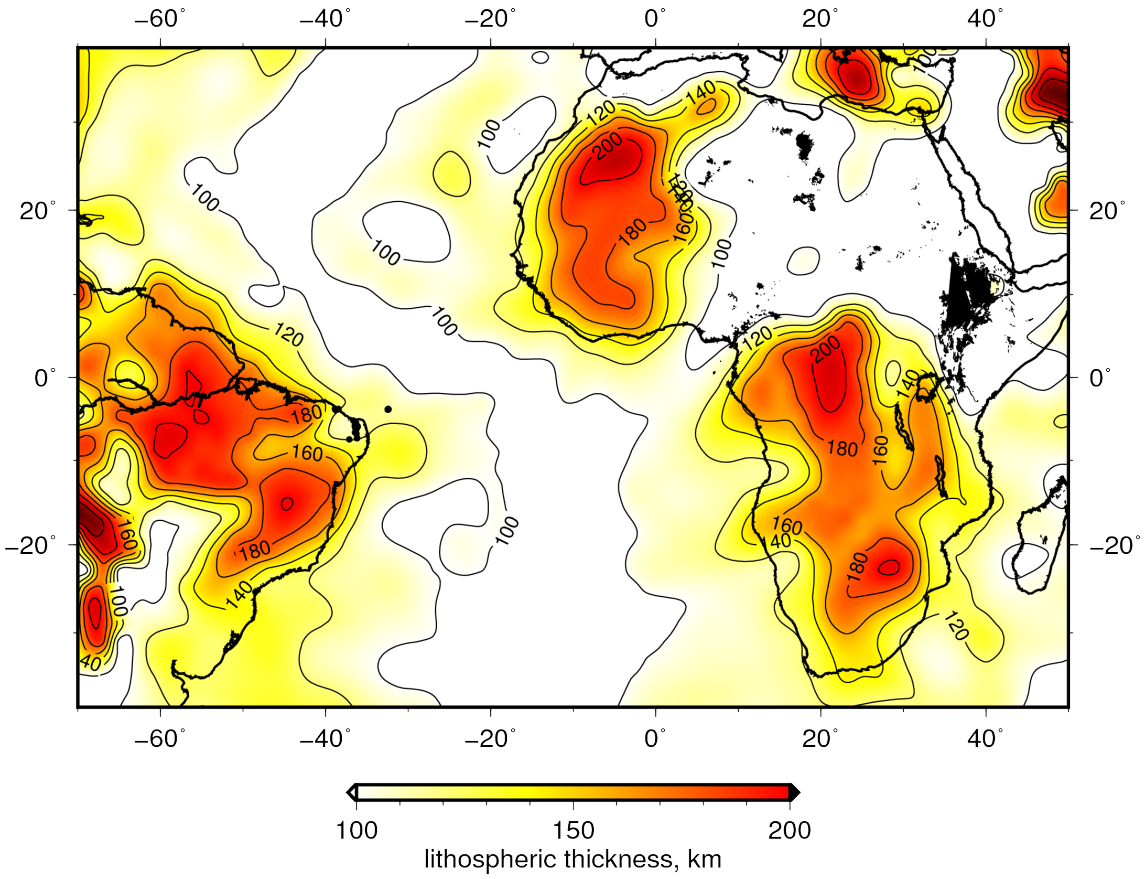

Figure 3-36: Lithospheric thickness map for the equatorial and south Atlantic according to Priestley and McKenzie (2013). Locations of Northeast Brazil samples marked as black dots.

The results also illustrate the localised effects of extensional settings, such as larger melt fractions, in accordance with other geochemical evidence and petrography observations. All saturated and oversaturated samples come from the continental basins, have strong spinel lherzolite contributions (≥ ~70%) and represent higher melt fractions than the rest of the assemblage, demonstrating a direct correlation between silica saturation and tectonic environment, namely well-developed extensional settings. However, not all spinel lherzolite contributions are limited to the basins, indicating that lithospheric thinning in the region is not limited to these settings.

Vertically heterogeneous source

Higher proportions of spinel lherzolite also seem to control the degree of assimilation of vertically stratified continental lithospheric material. In the continental sector, contributions of spinel lherzolite (and therefore depths of melting) and degrees of partial melting correlate with relative concentrations of Ba and Nb. This was first noted by Fodor et al. (1998) who, following a strategy similar to Fitton et al. (1991), have argued that increasing relative Ba concentrations correlate with decreasing LREE content and decreasing LREE/HREE ratios in the MQVL, and represent increasing contributions of continental lithospheric material accompanying higher degrees of partial melting. Based on Ba/Nb, La/Nb and La/Y ratios, they argue that the continental lithosphere must have been affected by long periods of enrichment by asthenospheric melts representing low melt fractions and carrying low La/Nb (~0.64, compared to ~0.96 in a primitive mantle source), and that subsequent larger melt fractions in the asthenosphere directly underlying the lithosphere would be more likely to assimilate this overlying material, leading to low La/Y and low La/Nb (Fodor et al., 1998). The same material should also be enriched in Ba, leading to increasingly higher Ba/Nb with decreasing La/Y, despite the simultaneous increase in Nb content. Nonetheless, they estimate that lithospheric contributions are still < 10% by modelling Ba behaviour.

In our dataset, using the same trace element ratios, or Ce/Sm against Ce/Nb instead of La/Y against La/Nb in order to remain consistent with the model discussed above and to better distinguish melt fractions from depth of melting, produces similar results (Figure 3-37). However, contrasting with Fodor et al. (1998), whose analyses only include samples from the central segment of the MQVL, our dataset shows that samples from the continental basins deviate from the linear positive correlation between La/Y (or Ce/Sm) and La/Nb (or Ce/Nb) that is dominant in the rest of the assemblage. These samples have the lowest La/Y and Ce/Sm values but show a sudden increase in La/Nb and Ce/Nb. A similar shift also exists for Ce/Ba in relation to Ce/Sm, but it is significantly more subdued. Comparing Ce/Nb and Ce/Ba to Sm/Yb, the latter ratio representing spinel lherzolite contributions to the source and hence indicating depth, shows a similar sudden increase in Ce/Nb at low Sm/Yb, but a linear relationship between Ce/Ba and Sm/Yb (Figure 3-37). The sudden increase in Ce/Nb at low Sm/Yb, however, is not limited to the continental basins, and also includes samples 15BP4-7 and 15BP5-10, which are located in the central segment of the MQVL and represent large contributions of spinel lherzolite at relatively lower melt fractions.

These trends indicate that Nb content sees a relatively significant and sudden decrease at shallower depths that deviates from its linear behaviour when deeper. Conversely, Ce/Ba only shows a non-linear relationship to Ce/Sm (i.e. to degrees of partial melting). Superimposing the group of samples that shows the sudden increase in Ce/Nb (Figure 3-37) on our Ce/Sm-Sm/Yb model produces a clear depth threshold at 70% spinel lherzolite contributions for this trend (Figure 3-38). Moreover, comparing Nb and Ce concentrations directly shows that the same group has clearly defined Ce/Nb ratios that are distinct from the rest of the assemblage (Figure 3-39). For instance, samples with ≥ 70% spinel lherzolite develop along Ce/Nb = 1.14, whereas samples with < 70% follow Ce/Nb = 1.66. Depth of melting, therefore, correlates with changes in relative Nb content at the

source, independently of degrees of partial melting. This indicates vertical compositional stratification at the base of the continental lithosphere of an element that is generally used as proxy for contrasting subduction-related magmatism (which tend to produce relatively low-Nb melts) with intraplate igneous processes.

Conversely, the relationship between Ba and Ce shows scattered trends in the continental sector that generally lean towards higher Ba content, but also show a sharp decrease in concentrations for all nephelinite (Figure 3-39). The general increase in Ba concentrations and its scattered behaviour in the continent at relatively higher melt fractions, and its decrease amongst the nephelinite are also clear on multi-element and variation diagrams (Figures 3-13 and 3-19). These patterns contrast with the linear trends seen for Ce in the same diagrams, which shows that changes in Ce/Ba ratios must reflect changing Ba concentrations, as opposed to Ce. Furthermore, scattered and irregular patterns suggest that changes in Ba reflect contamination rather than characterising the melt's source. Nonetheless, it still supports the model put forward by Fodor et al. (1998) that attributes increasing Ba content with the assimilation of continental lithospheric material, although the assimilation of Ba seems to be due to a secondary processes rather than or in addition to reflecting source characteristics. Using La and Zr variation diagrams to compare our data with that of Fodor et al. (1998) shows that both datasets produce scattered trends for Ba and linear ones for Nb, as well as relatively lower Nb at low Zr and La (Figure 3-40), reinforcing these interpretations.

In addition to their distinct Nb content and Ba contamination, continental samples also produced relatively low Ti in relation to the oceanic sector (Figures 3-8 and 3-9), and a few samples, especially from the Cubati and Boa Vista basins, show relative subtle to strong positive Sr anomalies (Figure 3-41). When combined, these trends indicate some subtle effects of arc signatures affecting the dominantly OIB patterns (Sun and McDonough, 1989), especially in the continental basins. Therefore, shallower sources with

relatively lower Nb content indicate the influence of older continental lithosphere marked by the relict effects of past subduction zones. Conversely, deeper sources marked by relatively higher Nb may represent younger enrichment events associated with asthenospheric alkaline or carbonatite low melt fractions. Similar patterns of vertical lithospheric stratification in Northeast Brazil have been observed in relation to xenolith heterogeneity (Rivalenti *et al.*, 2000, 2007; Fodor *et al.*, 2002), and are in agreement with the conclusions of Fodor et al. (1998), despite the lack of samples from the continental basins in their analysis. Conversely, Ba patterns in the continent are more haphazard and are more likely due to contamination and degrees of melt than source characteristics.

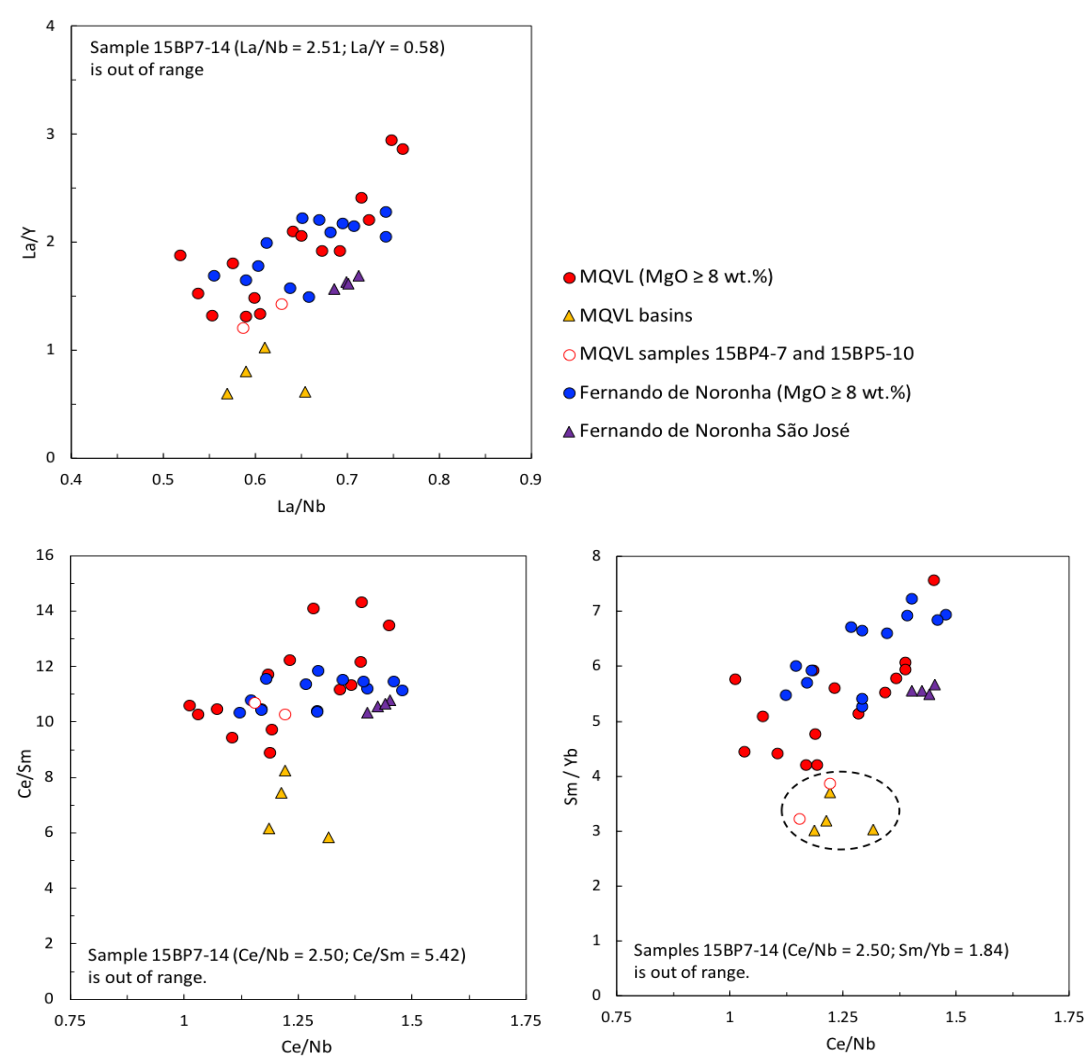

Figure 3-37: Continues on the next page.

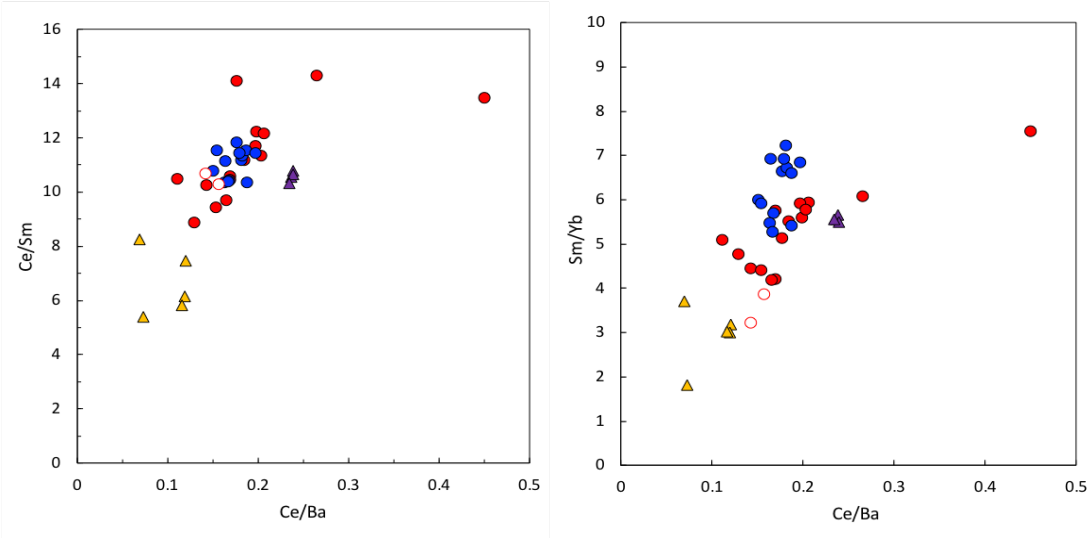

Figure 3-37: Relationship between degrees of partial melting, as represented by La/Y and Ce/Sm, and the relative contents of Ba and Nb. There is a clear correlation between degrees of partial melting (decreasing Ce/Sm) and enrichment in Ba and Nb amongst continental samples, except for samples with large spinel lherzolite contribution (i.e. low Sm/Yb), which show a sudden increase in Ce/Nb and include

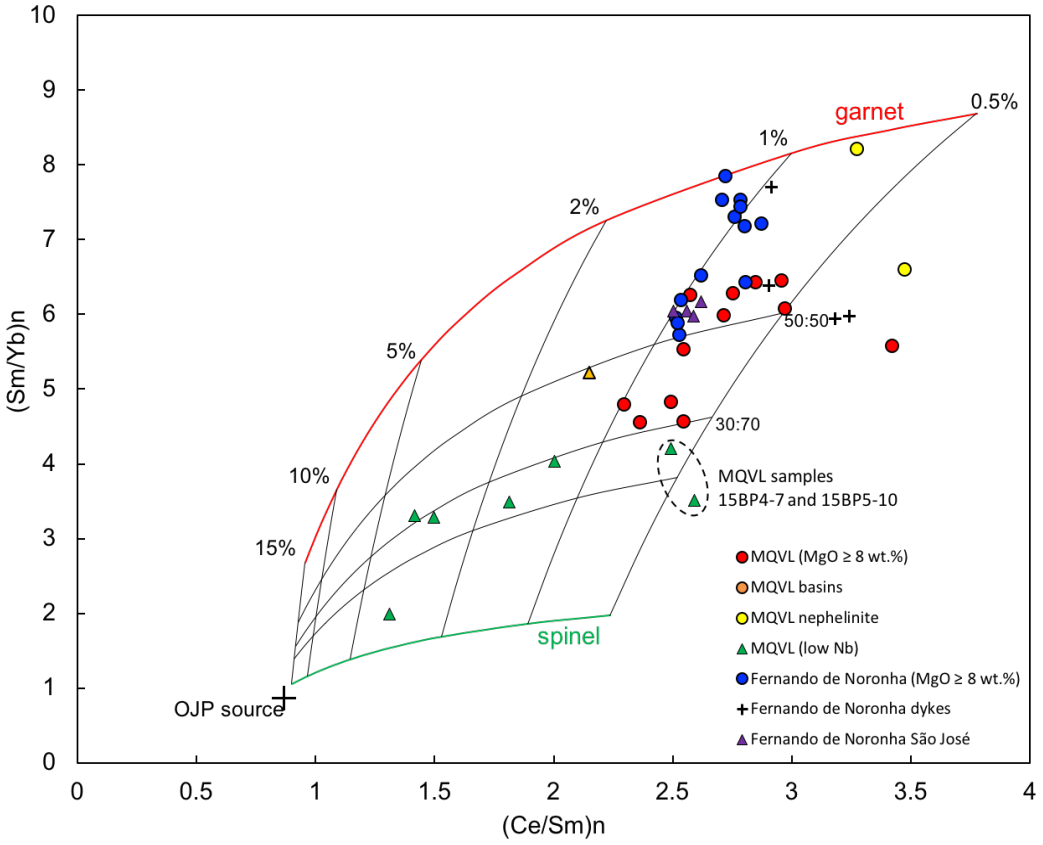

Figure 3-38: Samples with low Nb highlighted on the (Ce/Sm)n against (Sm/Yb)n model (see above), indicating a threshold of ~70% spinel lherzolite contributions for the shift in Nb behaviour. Samples 15BP4-7 and 15BP5-10 are highlighted and represent high spinel lherzolite contributions and low Nb at relatively lower melt fractions.

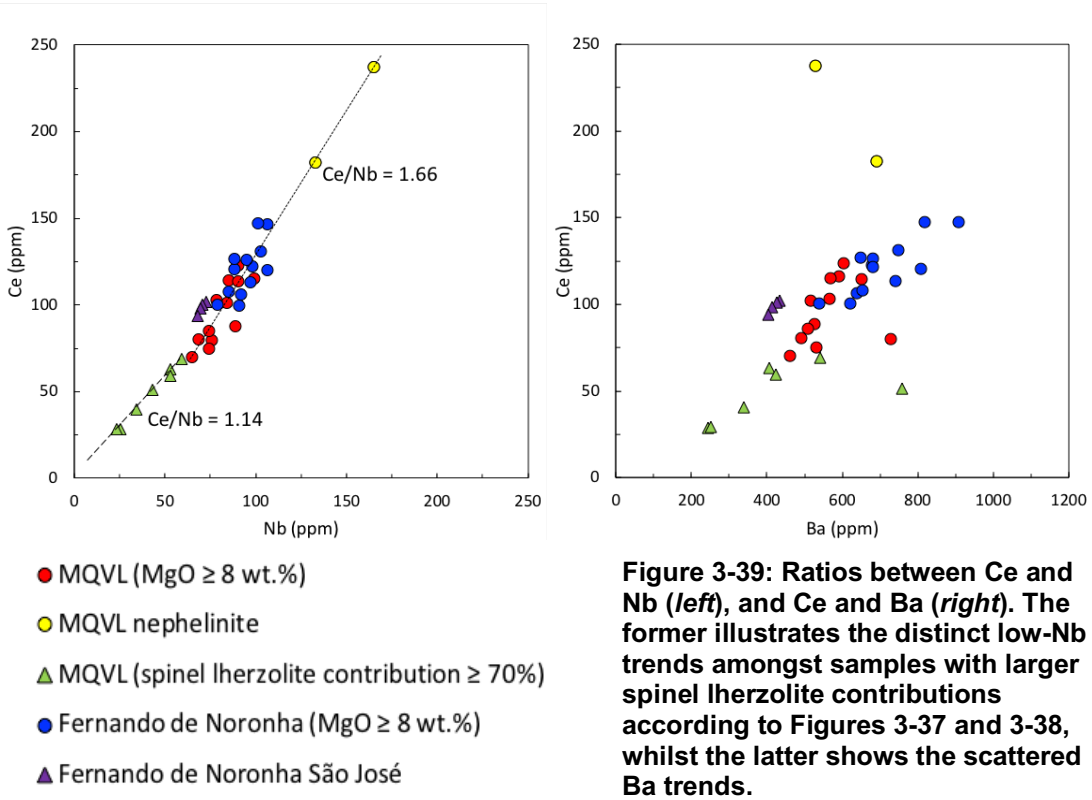

Figure 3-39: Ratios between Ce and Nb (*left*), and Ce and Ba (*right*). The former illustrates the distinct low-Nb trends amongst samples with larger spinel lherzolite contributions according to Figures 3-37 and 3-38, whilst the latter shows the scattered Ba trends.

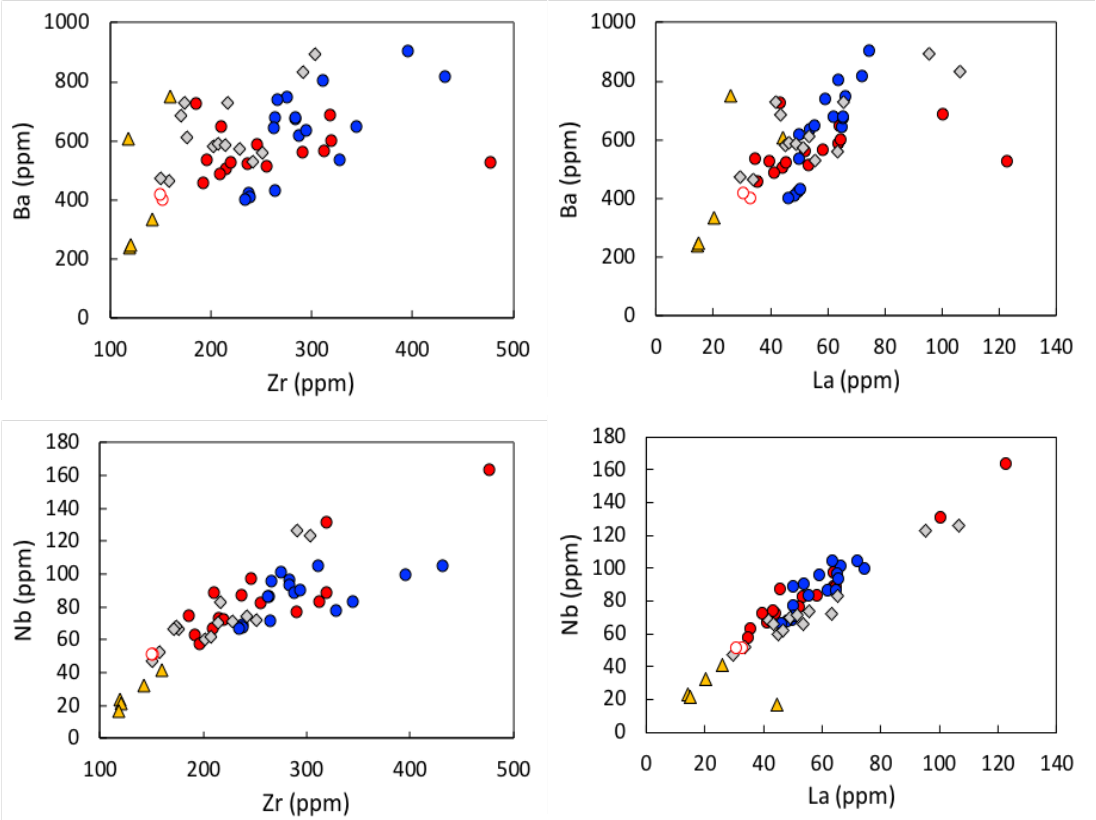

Figure 3-40: Legend and caption on the next page.

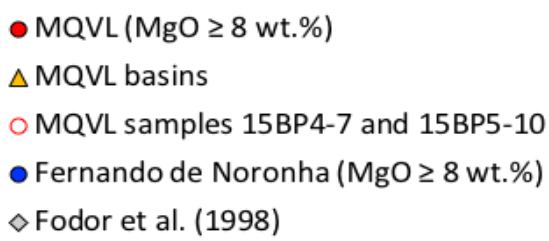

Figure 3-40: Variation diagrams contrasting the scattered behaviour of Ba with the more coherent behaviour of Nb using La and Zr as reference and including the dataset from Fodor et al. (1998). Samples 15BP4-7 and 15BP5-10 from the MQVL are also highlighted.

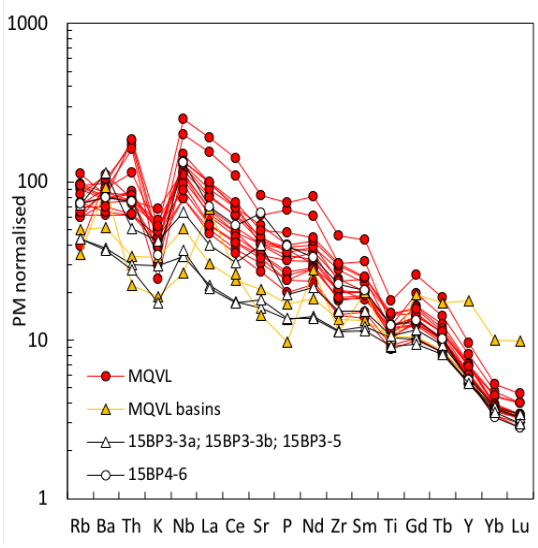

Figure 3-41: Multi element diagram for the MQVL showing the relative Sr anomalies amongst some samples (highlighted in *white*). Most samples from the basins have a subtle or strong Sr anomaly, whereas it is present in one sample in the rest of the lineament (i.e. 15BP 4-6).

Therefore, Nb and Ba patterns do not indicate significant qualitative differences between the oceanic and continental sectors in terms of melting processes, but instead reflect shallower and more vigorous magmatism with access to continental lithospheric material in the continental block. Despite the localised effects of such material in the contents of Ba and Nb in the MQVL, both continental and oceanic datasets from Northeast Brazil still fall within OIB concentration ranges as defined by the XRF OIB dataset from Fitton (2007). This is clear in a diagram comparing La/Nb with La/Ba (Figure 3-42), similarly to what was done in Fitton et al. (1991) who worked with the same OIB dataset, and reinforces that the effects of continental lithospheric material are limited. However, the same dataset also illustrates how larger degrees of partial melting amongst OIB from around the world also correlate with decreasing Nb content (Figure 3-43).

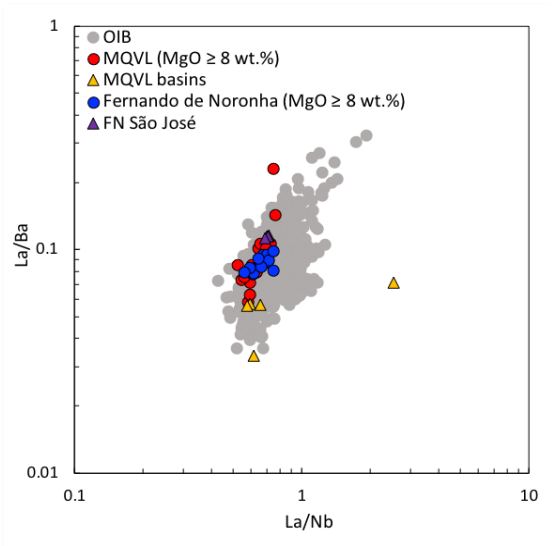

Figure 3-42: Relationship between Ba, Nb and La, as used in Fitton et al. (1991), showing how Ba and Nb contents in Northeast Brazil, despite showing evidence for some contributions from continental lithospheric material, still carries clear OIB characteristics.

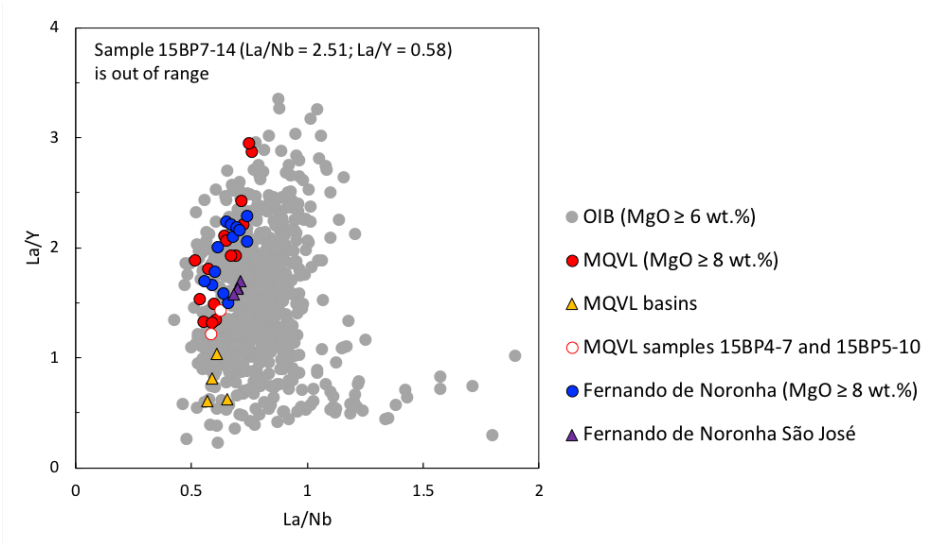

Figure 3-43: Relationship between degrees of partial melting as illustrated by La/Y ratios and Nb content. It is clear how Nb decreases at low La/Y.

Chronological patterns

Despite the lack of geographical age progression patterns, combining the ages presented in Chapter 2 with the geochemical data shows that there is compositional variability over time in Northeast Brazil. Considering all $^{40}Ar/^{39}Ar$ ages and major element geochemical data available for basaltic rocks from the region (Souza *et al.*, 2005, 2013; Silveira, 2006; Knesel *et al.*, 2011; Perlingeiro *et al.*, 2013) together with our own geochemical and

chronological results, and using the silica saturation index (SI) given in Fitton et al. (1991) and derived from the CIPW norm scheme, where:

$$SI = 100\left(Si - \frac{Al + Fe2 + Mg + 3Ca + 11Na + 11K + Mn - Fe3 - Ti - 4P}{2}\right) \quad (10)$$

and *Si*, *Al*, *Mg* etc. are molecular proportions of SiO_2, Al_2O_3, MgO etc., it is clear how continental lavas become increasingly silica saturated from the late Eocene to the early Miocene, reaching a peak at around 20-25 Ma, but then shift back to undersaturated compositions (Figure 3-44). Although geochemical data are not available for the samples dated in Souza et al. (2013), geochemical analyses for samples from the same localities in the Boa Vista basin, representing its *lower* and *upper* basalts, are reported in Souza et al. (2005). For the *lower* basalts, there is one sample analysed geochemically and two samples dated from which the freshest one was chosen as representative of the group's age. For the *upper basalts*, there is only one sample dated but eleven geochemical analyses from which the highest and lowest silica indices were chosen and given the same age to represent the set within a range of values.

The peak of silica saturation also represents the period of extensional activity in the continental basins (both north and south; see Chapter 2), the formation of by far the largest volcanic edifice in the MQVL (i.e. the Cabugi peak at ~25 Ma; Silveira, 2006) and the largest proportions of spinel lherzolite contributions to the lavas (i.e. all the dated basin samples and lavas from the Serrote Preto locality, the latter represented here by sample 15BP5-10; Figure 3-38 and dates in Chapter 2). In the continental basins and their surroundings, changes in silica saturation are also accompanied by a vertical and lateral shift from subaqueous to subaerial environments, according to stratigraphy, outcrop characteristics and $^{40}Ar/^{39}Ar$ ages (see Chapters 1 and 2). Compositional changes over time are also reflected in the spatial rearrangement of the MQVL. Whilst magmatism extended over the entire length of the lineament during the peak of silica saturation, subsequent

volcanism concentrated on its central segment. Furthermore, tomographic models (Klöcking, 2017) indicate upwelling in the area since magmatism started, and outcrop spatial patterns not only support this but also suggest that upwelling may have been centred in the central segment of the MQVL. Exposures in this segment are dominated by hypabyssal conduits (e.g. volcanic necks) and have no surviving lava flows or other surficial structures associated with them, indicating strong erosion. Meanwhile, the vertical and lateral transition from vesiculated pillow lavas to subaerial lava flows in the basins, which represent both the northern and southern extremities of the lineament, indicate basin drainage that could result from uplift, but contrary to the central segment of the MQVL, these flows still survive today and there are no hypabyssal exposures.

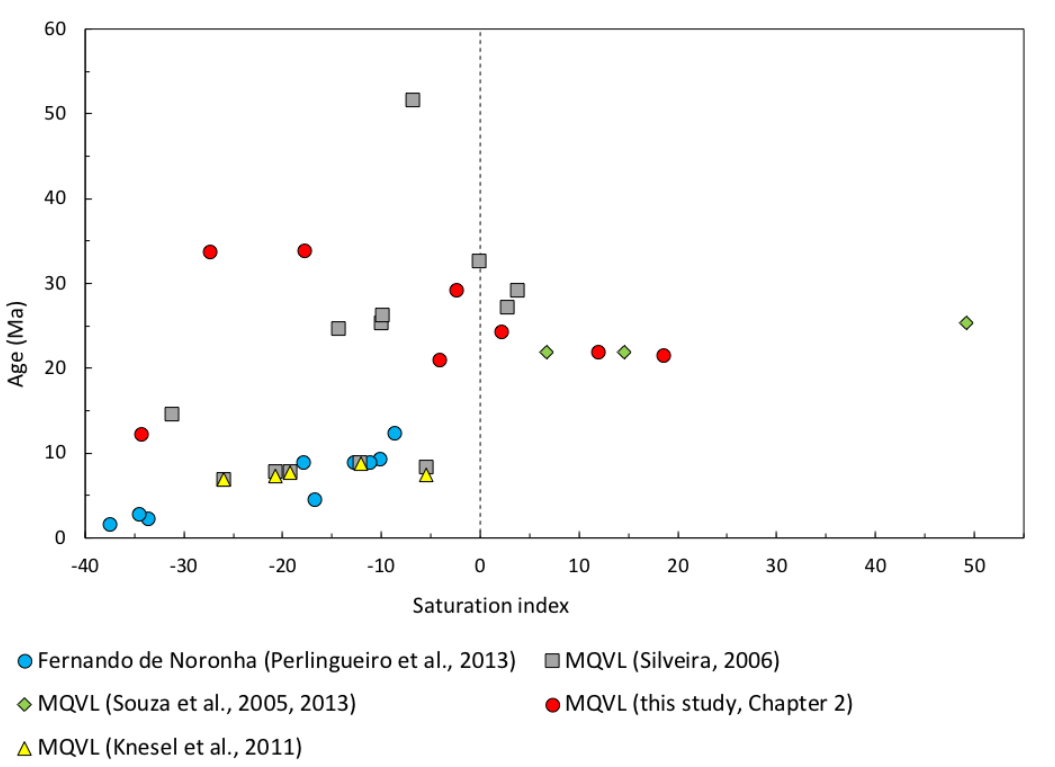

Figure 3-44: Comparison between available $^{40}Ar/^{39}Ar$ ages and major element geochemistry for basaltic rocks from the MQVL and Fernando de Noronha (Souza *et al.*, 2005, 2013; Silveira, 2006; Knesel *et al.*, 2011; Perlingeiro *et al.*, 2013) with the silica saturation index defined by Fitton et al. (1991). See text for a description of the selection process for the data from Souza et al. (2005) and Souza et al. (2013).

These patterns indicate a period of vigorous, widespread and relatively shallow magmatic activity producing relatively high melt fractions between periods of deeper and more subdued magmatism, with the younger periods of activity in the continent also being significantly restricted geographically. The youngest occurrences in the continental sector are also synchronous with Fernando de Noronha, which is also dominated by more undersaturated compositions. Therefore, magmatism in Northeast Brazil seems to have developed gradually towards a well-defined peak of activity, and then subsided.

Summary

The discussion above shows that primitive rocks from both the oceanic and continental sectors have virtually identical geochemistry, with linear and continuous geochemical variability amongst samples from the two areas that may be explained in terms of degrees of partial melting. Melt fraction variability also affects the amount of assimilation and contamination by continental lithospheric material, which creates variability in Ba content in the assemblage. Higher melt fractions are mostly restricted to shallower depth and specific tectonic environments (i.e. continental extensional basins), according to geochemical modelling that indicates access to spinel lherzolite at the source. However, the opposite does not apply, and melting in the spinel lherzolite zone is not restricted to high melt fractions. Shallow melting also allows access to a distinct layer at the base of the lithosphere marked by relatively lower Nb content. Nonetheless, the overall variability caused by changes in depth and degrees of partial melting is localised, and limited to differences in HREE (i.e. reflecting garnet- and spinel lherzolite contributions to the source), Ba and Nb. Fractional crystallisation and contamination by peridotitc xenoliths and xenocrysts are also present but also limited, affecting the content of MgO and compatible elements such as Ni and Cr. Fractional crystallisation also has some incipient effects on major elements and, in very few samples, trace elements as well. Alteration affects

Na and the highly mobile elements Rb and K, but its effects are also limited, and easily discernible.

Geochemical variability in the assemblage does not require distinct sources or petrogenetic processes to be explained and such interpretations unnecessarily complicate the history of the area. Furthermore, establishing that internal variability between the two sectors may be explained in terms of changes in depth and degrees of partial melting, as opposed to fractional crystallisation, highlights their cogenetic relationship and strengthens the validity of bringing together primitive Cenozoic rocks from all the three volcanic areas in Northeast Brazil and the conclusions obtained therefrom. It is also important to point out their small differences and the reasons behind them when, in the next Chapter, we compare these samples with the Cameroon Line, where the significantly larger dataset shows greater degrees of fractional crystallisation, but contains no occurrences of extensional settings to the same extent (both quantitatively and qualitatively) found in Northeast Brazil.

Isotopes

$^{87}Sr/^{86}Sr$ and $^{143}Nd/^{144}Nd$ data

For this study, twelve samples from the MQVL, three from the Mecejana Volcanic Field and three from Fernando de Noronha were analysed for their $^{87}Sr/^{86}Sr$ and $^{143}Nd/^{144}Nd$ ratios. Samples were prepared using cation exchange column chemistry and analysed in a VG sector 54-30 Thermal Ionisation Mass Spectrometer, with methods described in detail in Appendix A. Results are presented in Table 3-3, including Rb-Sr isochron ages and the age-corrected isotopic ratios. In the absence of absolute ages from this study, ages from Perlingueiro *et al.* (2013), Souza *et al.* (2013) and Knesel *et al.* (2011) were used. Where multiple ages were available for a single locality, the average age was used. Where no ages were available, 20.5 Ma was used, which is the average between the oldest (33.99 Ma; this

study) and youngest (7.1 Ma; Knesel *et al.*, 2011) $^{40}Ar/^{39}Ar$ ages available for the MQVL. $^{87}Rb/^{86}Sr$ and $^{147}Sm/^{144}Nd$ were calculated from our ICP-MS dataset, respectively as $2.89\left(\frac{Rb}{Sr}\right)$ and $0.6048\left(\frac{Sm}{Nd}\right)$, and decay constants λ being 1.42×10^{-11} for ^{87}Rb and 6.54×10^{-12} for ^{147}Sm (White, 2015).

Using the mantle isotopic reservoirs commonly invoked in the published literature, our age-corrected $^{87}Sr/^{86}Sr$ and $^{143}Nd/^{144}Nd$ results show a linear array roughly between the depleted mantle (DM) and high-μ (HIMU) reservoirs, and bulk silicate Earth (BSE), with some compositions extending towards enriched mantle reservoirs I and II (EM-I and EM-II) in correlation with degrees of partial melting and geographical location (Figure 3-45). These reservoirs are defined here according to Winter (2010) and Rollinson (1993). One phonolite also extends into the HIMU field. However, it is difficult to define precisely the contributions of HIMU, given the uncertainties in defining this reservoir. For instance, HIMU is a source better defined in terms of Pb isotopes, and for which there is more than one defined isotopic field in the $^{87}Sr/^{86}Sr$-$^{143}Nd/^{144}Nd$ diagram. Therefore, we will focus on DM and EM isotopic signatures, and avoid relying on HIMU.

Basaltic samples that represent high melt fractions (i.e. samples from the continental basins and their vicinities) cluster around BSE or are more enriched in $^{87}Sr/^{86}Sr$ and/or depleted in $^{143}Nd/^{144}Nd$. For instance, sample 15BP7-14 from the Potiguar basin, a basaltic andesite and the only basaltic sample from the oceanic-continental boundary (OCB), produced significantly lower $^{143}Nd/^{144}Nd$ and a strong EM-I signature, deviating from the main linear array. The other outlier is a single Mecejana phonolite sample within the HIMU field. Two samples from the central segment of the MQVL lie in-between the main sample cluster and those representing high melt fractions. Continental nephelinites and basaltic samples collected south of the João Câmara shear zone (JCSZ) but which are not associated with any basin produced the strongest DM signatures in the continental sector, and plot together with samples from Fernando de Noronha.

Table 3-3: Isotopic data, including Rb-Sr isochron ages and age-correction data. $^{87}Rb/^{86}Sr$ and $^{147}Sm/^{144}Nd$ defined respectively as 2.89(Rb/Sr) and 0.6048(Sm/Nd) (both using ICP-MS data; Appendix C). Ages from Perlingueiro et al. (2013) and Souza et al. (2013) are averaged from several $^{40}Ar/^{39}Ar$ ages for equivalent localities in those publications. * = age average from the oldest and youngest $^{40}Ar/^{39}Ar$ ages available.

Sample	SUERC lab n.	$^{87}Sr/^{86}Sr$	$^{87}Sr/^{86}Sr$ %SdErr	$^{143}Nd/^{144}Nd$	$^{143}Nd/^{144}Nd$ %SdErr	Age (Ma)	Age source	$^{87}Rb/^{86}Sr$	$^{147}Sm/^{144}Nd$	$^{87}Sr/^{86}Sr$ (age-corrected)	$^{143}Nd/^{144}Nd$ (age-corrected)
15BP1-1	H787	0.7040848	0.0013	0.5127413	0.0008	*20.5	Averaged	0.154	0.123	**0.7040329**	**0.5127248**
15BP3-2	H788	0.7058103	0.0012	0,5125934	0.0006	21.09	This study	0.256	0.132	**0.7057211**	**0.5125752**
15BP3.3b	H804	0.7056075	0.0012	0.5126406	0.0008	22.5	This study	0.184	0.163	**0.7055403**	**0.5126165**
15BP3-4	H789	0.7051176	0.0013	0.5125829	0.0006	26.4	Souza et al. (2013)	0.176	0.143	**0.7050389**	**0.5125582**
15BP4-6	H790	0.7040844	0.0013	0.5127818	0.0007	*20.5	Averaged	0.091	0.121	**0.7040554**	**0.5127656**
15BP4-7	H791	0.7036375	0.0012	0.512814	0.0006	*20.5	Averaged	0.151	0.126	**0.7035860**	**0.5127971**
15BP5-9	H792	0.7046157	0.0013	0.5127539	0.0006	33.91	This study	0.102	0.120	**0.7045572**	**0.5127274**
15BP7-14	H793	0.7048553	0.0013	0.5119682	0.0005	21.6	This study	0.179	0.141	**0.7047902**	**0.5119483**
15BP7-15	H794	0.703847	0.002	0.5127577	0.0008	12.39	This study	0.048	0.101	**0.7038372**	**0.5127495**
15BP8.17	H795	0.703903	0.0011	0.5127577	0.0008	7.9	Knesel et al. (2011)	0.092	0.116	**0.7038911**	**0.5127517**
15BP9.19a	H796	0.7048312	0.0012	0.5126937	0.0007	33.48	This study	1.376	0.078	**0.7040632**	**0.5126766**
15BP10-21a	H797	0.7051305	0.0013	0.5126722	0.0007	24.63	This study	2.348	0,075	**0.7041844**	**0.5126602**
15BP10-23	H798	0.708161	0.0012	0.5126711	0.0007	34.61	This study	8.441	0.075	**0.7031830**	**0.5126541**
15BP11-24	H799	0.7045327	0.0015	0.5126544	0.0006	8.9	Knesel et al. (2011)	0.109	0.110	**0.7045166**	**0.5126480**
15BP12-25	H800	0.7038161	0.0011	0.512751	0.0008	7.1	Knesel et al. (2011)	0.069	0.106	**0.7038081**	**0.5127461**
FN04-05	H801	0.7037764	0.0013	0.5128269	0.0006	3.7	Perlingueiro et al. (2013)	0.040	0.118	**0.7037741**	**0.5128241**
FN17-29	H802	0.7040032	0.0013	0.5128137	0.0007	11	Perlingueiro et al. (2013)	1.590	0.068	**0.7037110**	**0.5128088**
FN30-54	H803	0.7039364	0.0013	0.5128253	0.0016	9.1	Perlingueiro et al. (2013)	0.093	0.120	**0.7039230**	**0.5128182**

Rb-Sr isochron ages

Area	Isochron ages (Ma)	Area	Isochron ages (Ma)
MQVL basaltic	35.20	Mecejana phonolite	35.20
MQVL basaltic (high melt fractions)	596.06	Fernando de Noronha	7.04
MQVL basaltic (high melt fractions) after age correction	477.25	Fernando de Noronha (Gerlach et al., 1987)	7.04

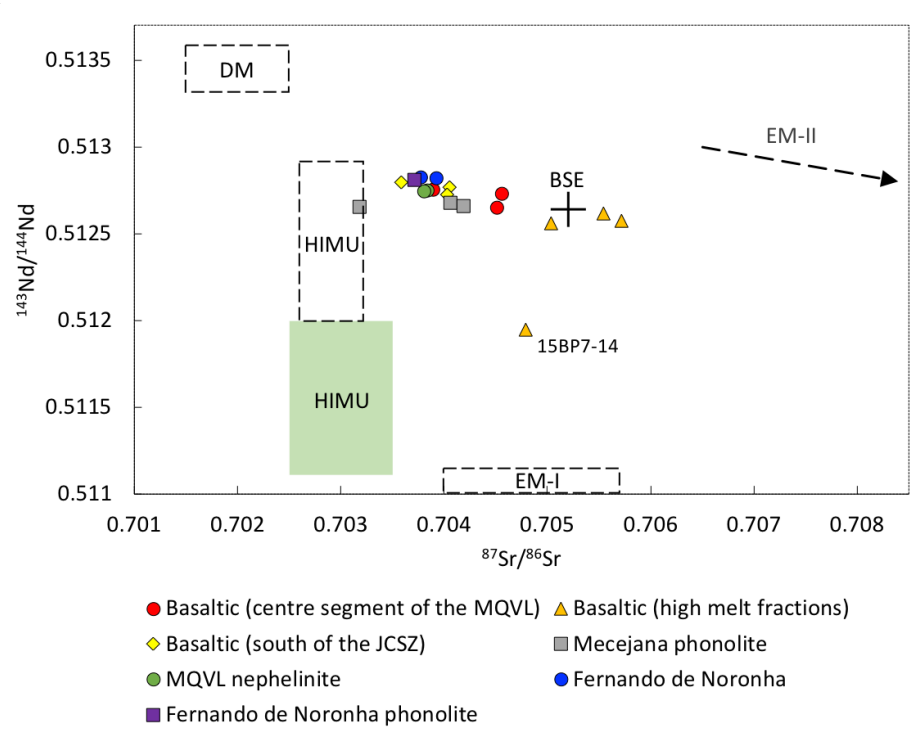

Figure 3-45: Age-corrected isotope data in relation to possible mantle reservoirs. All basaltic samples are from the MQVL. Reservoir domains (*dashed lines*) from Rollinson (1993), and *green* HIMU field from Winter (2010). Samples from Fernando de Noronha include two alkali basalts and one phonolite. Sample 15BP7-14 has been highlighted in the diagram. *JCSZ* = João Câmara Shear Zone (see main text).

Rb-Sr isochron ages

Rb-Sr isochron ages *t* can be obtained from the slope of data arrays on a plot of $^{87}Sr/^{86}Sr$ against $^{87}Rb/^{86}Sr$ (Figure 3-46), through:

$$t = \frac{\ln(slope + 1)}{\lambda_{Rb}} \quad (11)$$

where λ_{Rb} is the ^{87}Rb decay constant (1.42×10^{-11}). The Mecejana phonolites and MQVL samples which are not associated with basins produced the same slope and isochron ages of ~35 Ma independently of one another (Figure 3-46). Despite the very low R^2 value for the MQVL regression line, the Mecejana phonolites produced $R^2 = 0.998$, and results agree with the older ages obtained by $^{40}Ar/^{39}Ar$ in this study (Chapter 2). On the other hand, samples representing high melt fractions, which in this case are associated with the MQVL basins, produced an isochron age ~596 Ma (late

Neoproterozoic). This age matches the late- to post-Pan-African/Brasiliano orogeny, a period of orogenic collapse marked by intensive plutonism that became one of the main characteristics of the Borborema Province as a geological terrane (Cordani and Sato, 1999; Cordani *et al.*, 2000; Arthaud *et al.*, 2008; van Schmus *et al.*, 2008). As would be expected, age-corrected samples produced sub-horizontal isochrons, except for samples from the MQVL basins (i.e. representing high melt fractions), which produced an isochron age ~477 Ma (Early Palaeozoic), which still falls within the aforementioned period of intense plutonism in the Borborema Province.

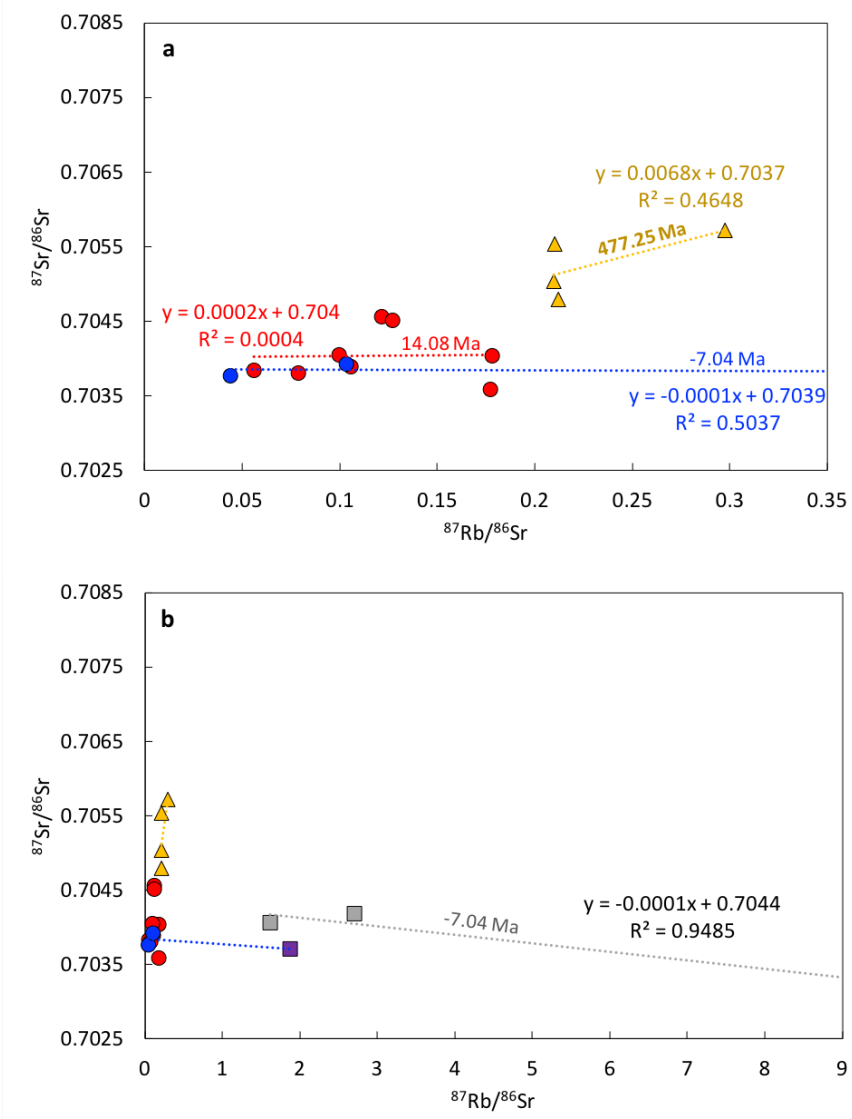

Figure 3-46: Continues on the next page.

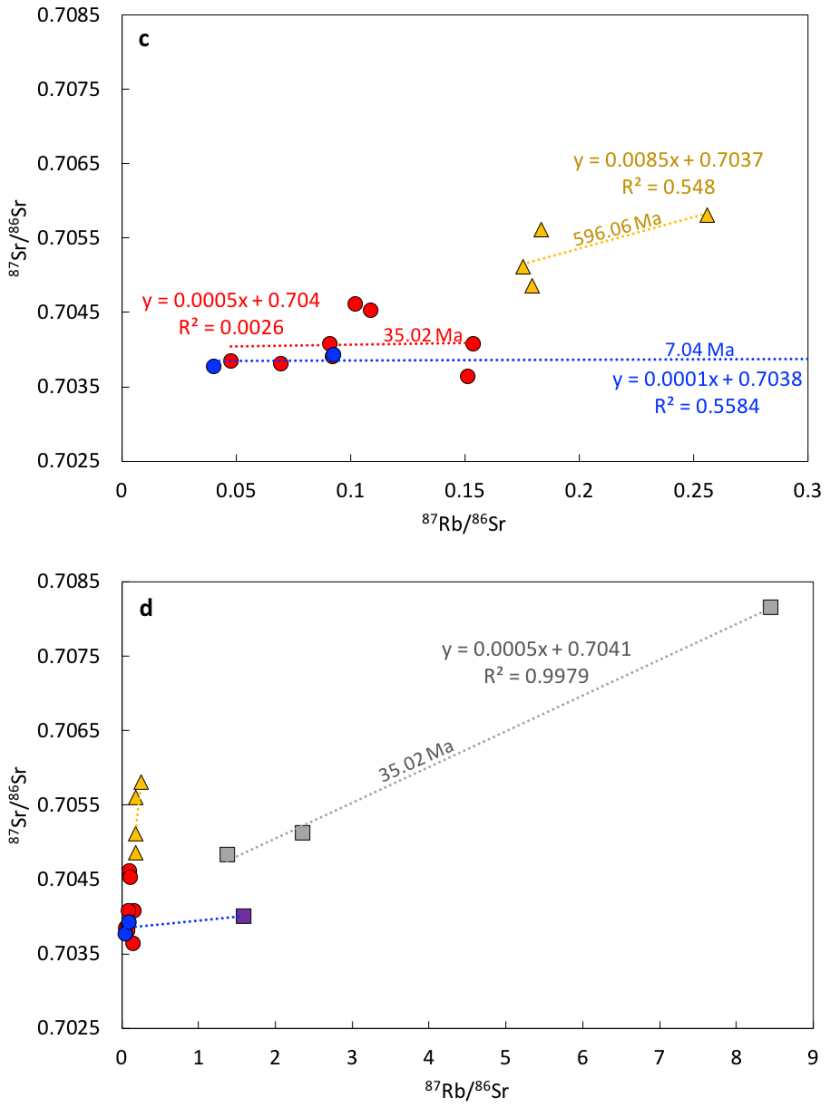

Figure 3-46: Regression lines defining Rb-Sr isochrons, with respective line equations and R^2 for the different sample groups in Northeast Brazil. Symbols as in Figure 3-45. *a* and *b*: age-corrected diagrams showing sub-horizontal slopes. *c* and *d*: diagrams before age-correction, showing ages in agreement with those obtained through $^{40}Ar/^{39}Ar$ dating. The Fernando de Noronha phonolite used in defining the archipelago's regression line in *b* and *d* is outside the range of the diagrams, but may be seen in *a* and *c*.

Discussion

Isotope analyses constitute a significant proportion of previous work done in Northeast Brazil since the late 1980s, although most of it focuses on mantle xenoliths, and there is some consensus about isotopic trends in the region, including comparisons between the continental and oceanic lithospheres (Gerlach *et al.*, 1987; Fodor *et al.*, 1998, 2002, Rivalenti *et al.*,

2000, 2007). In Fernando de Noronha, Gerlach et al. (1987) show a correlation between higher melt fractions and EM-I, which is more dominant amongst the more silica saturated or evolved samples of the Remédios Formation and interpreted as representing a finite source of delaminated subcontinental lithospheric material. Conversely, the authors identify a correlation between lower melt fractions and HIMU and DM, which is stronger in the younger Quixaba Formation and interpreted as representing asthenospheric material. The MQVL isotopic data discussed in Fodor *et al.* (1998) also show similar trends to that of Gerlach *et al.* (1987), displaying a correlation between isotopically enriched material and Ba content, which they use as a proxy for contributions of continental material to the lavas (see above).

Rivalenti *et al.* (2000) studied the geochemistry, isotopic characteristics and geothermobarometry of clinopyroxenes from mantle xenoliths from the Pico do Cabugi, in the MQVL, and from the Fernando de Noronha São José Formation, and compared their radiogenic isotopic data with published data for local lavas (Gerlach *et al.*, 1987; Fodor *et al.*, 1998). Their results show that the isotopic patterns for oceanic xenoliths consistently match those of the lavas and are more homogeneous in terms of temperature and pressure than the continental ones. Conversely, results for continental xenoliths do not match those for the local lavas, and variability is significantly higher. For instance, protogranular continental xenoliths produced equilibration temperatures ~825ºC, which have been interpreted as reflecting an old salic igneous process that affected the continental lithosphere, whilst porphyroclastic continental xenoliths equilibrated ~1248ºC and produced significantly stronger EM-I isotopic signatures. Calculated equilibration pressures in the Pico do Cabugi xenoliths vary from 1.9 to 2.7 GPa. On the other hand, in the oceanic sector, both protogranular and porphyroclastic xenoliths seem to have equilibrated at ~1035 ºC and between 1-1.9 and 2.3 GPa. Rivalenti et al. (2000) did not obtain isotopic data for continental protogranular xenoliths, but their results show that isotopic

signatures in the oceanic lithosphere are dominated by an array between DM and BSE, with occasional contributions of EM-I, whilst continental samples are significantly influenced by EM-I signatures. The same pattern repeats itself amongst the lavas, albeit more subdued. They also identified distinct patterns of metasomatic enrichment in the lithospheric mantle underneath Pico do Cabugi and underneath Fernando de Noronha. In the former, metasomatic events both predate and are coeval with Cenozoic magmatism, whilst in the latter metasomatism is exclusively coeval. Greater variability in terms of isotopic characteristics, metasomatism, temperature and pressure in the continent indicates a compositionally and texturally stratified lithosphere affected by previous magmatic events.

Therefore, the results presented here for $^{87}Sr/^{86}Sr$ and $^{143}Nd/^{144}Nd$ isotopic ratios are in good agreement with previous interpretations. They indicate mainly sources with stronger DM-HIMU affinities, which are likely asthenospheric, with some gradual contributions of enriched material that bring compositions closer to BSE and EM sources in direct correlation with melt fractions, silica saturation and depths of melting, indicating potential degrees of interaction with lithospheric material, especially in the continent. Overall, EM signatures are stronger in the continental sector. For instance, our MQVL sample at the oceanic-continental boundary (15BP-7-14) produced a distinctively strong EM-I signature, which is also strong amongst continental mantle xenoliths but virtually absent amongst oceanic ones. One continental phonolite also produced a strong HIMU signatures not observed for any other sample.

Fodor et al. (1998) discusses why the trace element patterns for lavas from the MQVL do not indicate significant crustal contributions to their compositions. Following their argument, sample 15BP7-14 is the only basaltic sample in our dataset with trace elements patterns that could suggest some crustal contamination (e.g. high La/Nb), but, conversely, its isotopic signatures argue against it, reinforcing that local crustal contamination is not significant. In the case of Fernando de Noronha, our

limited dataset lies well within the main cluster of samples, at the end of the array that shows the relatively stronger DM affinities (perhaps also with HIMU contributions), and do not contradict results published elsewhere.

Isotopic signatures correlate not only with melt fractions, but also with contributions of spinel lherzolite at the source, the latter reflecting depth of melting. This may be illustrated by the relationship of $^{87}Sr/^{86}Sr$ with chondrite-normalised (McDonough and Sun, 1995) Ce/Sm and Sm/Yb ratios (Figure 3-47). The array of basaltic rocks clearly shows an increase in $^{87}Sr/^{86}Sr$ with decreasing Ce/Sm and Sm/Yb, and samples from the continental basin and their surroundings, which includes the lava flow 15BP3-2 that is adjacent to the Boa Vista basin but post-dates basin inversion (Chapter 2 and ages from Souza et al., 2013), form a distinct group amongst basaltic rocks at high $^{87}Sr/^{86}Sr$ and low (Ce/Sm)n and (Sm/Yb)n. Conversely, the nephelinite concentrate on low $^{87}Sr/^{86}Sr$ and high (Ce/Sm)n and (Sm/Yb)n. Continental and oceanic phonolites also have low $^{87}Sr/^{86}Sr$ (age-corrected) ratios, noting however that Fernando de Noronha samples will lean towards higher (Ce/Sm)n and lower (Sm/Yb)n due to the depletion of MREE amongst them. Overall, however, the correlation of high $^{87}Sr/^{86}Sr$ with degrees of partial melting represented by (Ce/Sm)n appears stronger than the correlation with contributions of spinel lherzolite represented by (Sm/Yb)n.

Isotopic data from Fodor et al. (1998) produces the same results, despite only three overlapping localities with our dataset, although their sample from Serrote Preto (indicated in Figure 3-47) plots together with our group associated with the continental basins. This latter locality is represented in our dataset by sample 15BP5-10, which comes from the central segment of the MQVL and produced high (Ce/Sm)n and low (Sm/Yb)n. Therefore, the sample supports a correlation between high $^{87}Sr/^{86}Sr$ and large contributions of spinel lherzolite to the melt and not necessarily with geographical patterns or extensional settings. It also shows that high $^{87}Sr/^{86}Sr$ does not correlates exclusively with degrees of partial melting, despite its apparently stronger correlation with (Ce/Sm)n, indicating

that both shallower and higher degrees of partial melting increase access to enriched $^{87}Sr/^{86}Sr$ signatures.

In addition to the patterns across the continental and oceanic sectors, and correlations with depth and degrees of partial melting, our results also point to potential geographical patterns in isotopic signatures. Samples south of the João Câmara shear zone that are not associated with extensional basins produced some of the strongest DM affinities in the continental sector, matching the continental nephelinites and samples from Fernando de Noronha (Figure 3-45). Conversely, samples from the central segment of the MQVL include more enriched signatures, and samples associated with the basins are clearly enriched. Furthermore, whilst the Potiguar basin in the oceanic-continental boundary produced a uniquely strong EM-I signature, the Boa Vista basin and its associated lava flows lean towards BSE and EM-II. Therefore, there seems to be a decrease of EM signatures towards the south, away from the oceanic-continental boundary, except for the case of extensional settings. In this case, basins in the continental hinterland are marked by BSE and EM-II characteristics, and those in oceanic-continental boundary by EM-I. As we have discussed above, the central segment of the MQVL also seems to mark the epicentre of volcanic activity and uplift in the continental sector, and an increase in DM signatures towards the south coincides with more subdued and likely deeper magmatism.

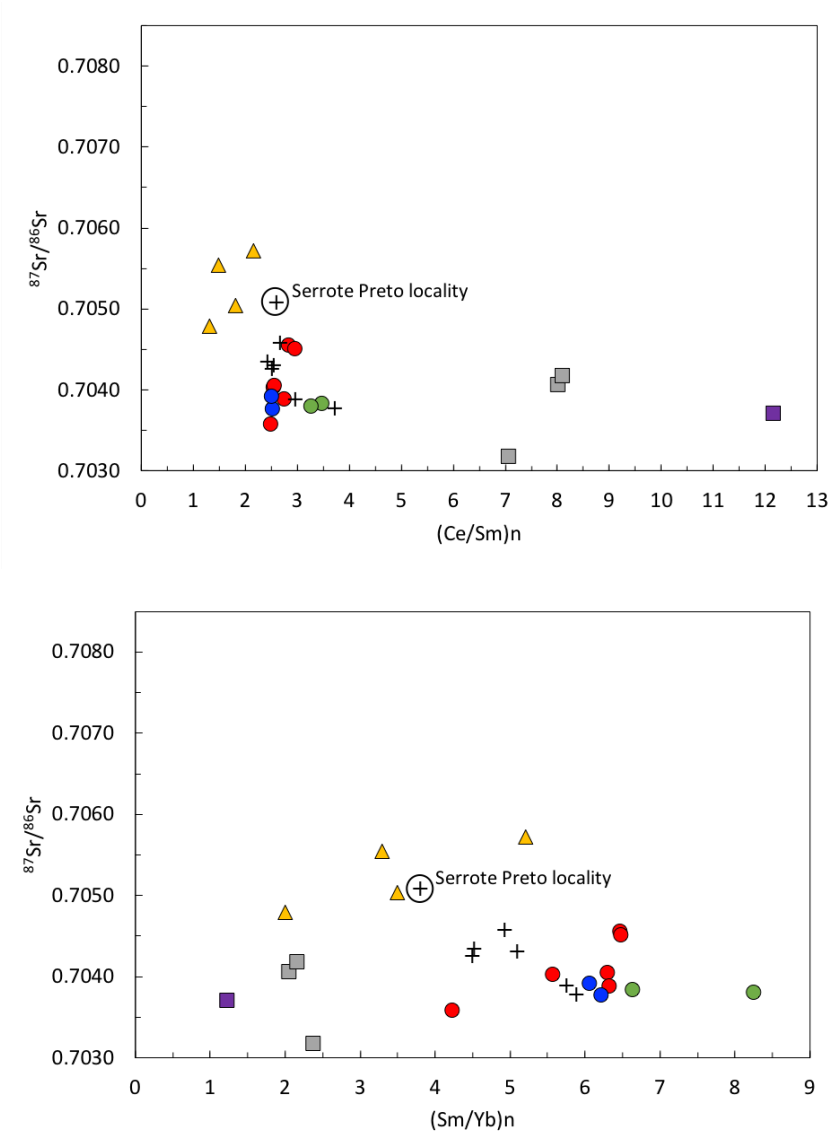

Figure 3-47: Relationship between $^{87}Sr/^{86}Sr$ and chondrite-normalised Ce/Sm and Sm/Yb ratios. Chondrite data according to McDonough and Sun (1995). Data from Fodor et al. (1998), with the Serrote Preto locality highlighted (see main text), are included for comparison, and show the same overall trends as our dataset. (Ce/Sm)n and (Sm/Yb)n respectively represent degrees of partial melting and contributions of garnet- and spinel-lherzolite to the primary melt. The negative correlation amongst basaltic rocks and greater $^{87}Sr/^{86}Sr$ in continental phonolites when compared with oceanic ones are clear, despite the REE ratios in the latter having been affected by stronger depletion of MREE (see above).

Rb-Sr isochron ages

Although based on few data points, the synchronicity between the MQVL and the Mecejana phonolites according to Rb-Sr isochron ages and their agreement with the $^{40}Ar/^{39}Ar$ results (Chapter 2) reinforces the reliability of our results. It is also interesting that samples associated with the continental basins form an independent isochron that roughly matches the last major tectonic event to affect the area prior to continental separation, in agreement with the geochemical patterns discussed above that suggest assimilation of continental lithospheric material in the basins and amongst samples with high contributions of spinel lherzolite to their source or representing high melt fractions.

In Fernando de Noronha, the three data points are each from one of the archipelago's three Formations and, although limited in number, the resulting isochron of ~7 Ma also coincides with the average age for the archipelago according to published $^{40}Ar/^{39}Ar$ dates (Perlingeiro *et al.*, 2013). Moreover, the larger Fernando de Noronha dataset published by Gerlach et al. (1987) also produces identical model ages (Figure 3-48). Rb depletion in Fernando de Noronha (see above) has led to relatively low $^{87}Rb/^{86}Sr$ amongst trachyte, intermediate rocks and some basaltic ones (which form a group of apparently high $^{87}Sr/^{86}Sr$ in Figure 3-49), but they have nonetheless kept the same slope in relation to $^{87}Sr/^{86}Sr$ and therefore the same isochron age. Rb-Sr isochron ages, therefore, correlate with geological contexts and show remarkable consistency with $^{40}Ar/^{39}Ar$ dates and data from different studies.

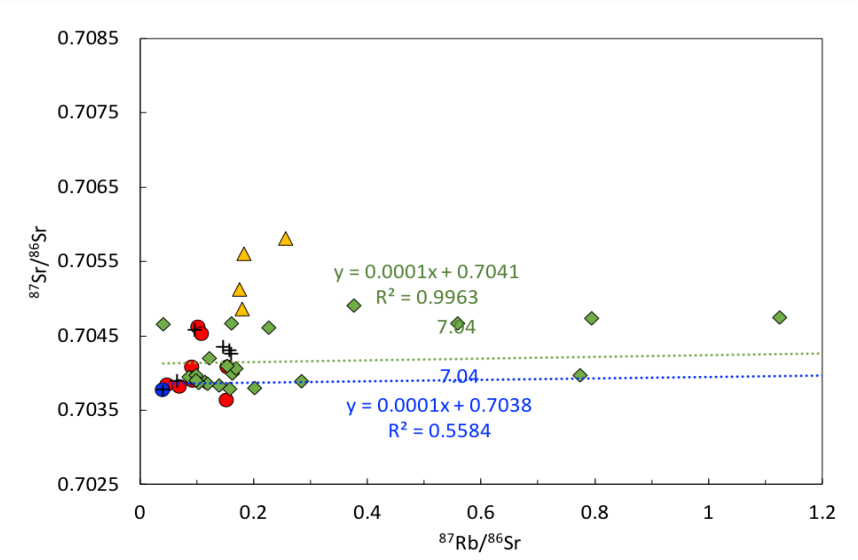

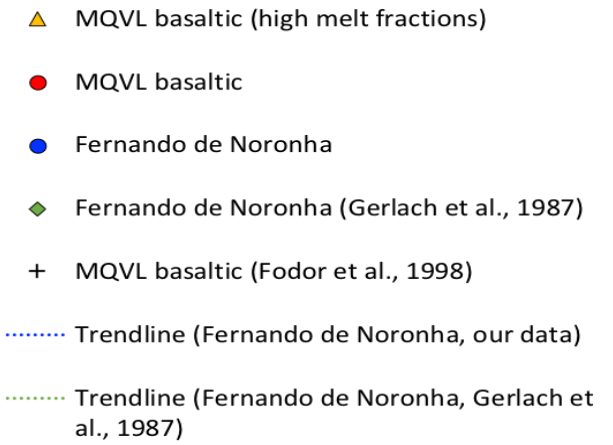

Figure 3-48: Regression line for the Fernando de Noronha dataset from Gerlach et al. (1987) in *green*, and that for our own data in *blue,* with virtually the same slope, despite the limited number of data points in our analysis. The diagram also shows the distinct pattern of samples associated with the MQVL basins. Some data points used to define the regression lines lie outside the range of the diagram.

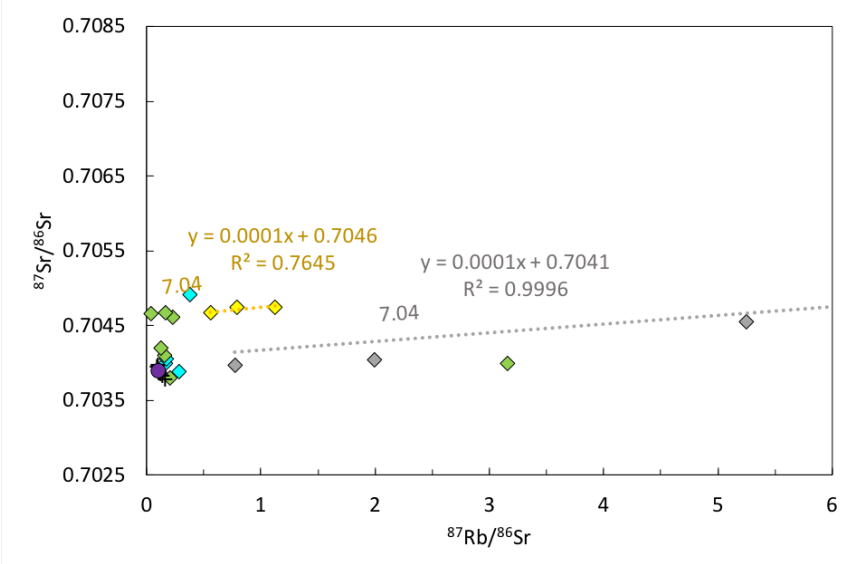

Figure 3-49: Legend and caption on the next page.

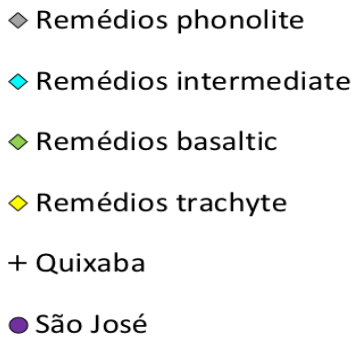

Figure 3-49: Data from Gerlach et al. (1987) subdivided by rock type and Formation. Remédios intermediate samples, trachyte and transitional basalt are the most subject to alteration and show unusually low $^{87}Rb/^{86}Sr$ ratios that result in an apparent parallel trend at high $^{87}Sr/^{86}Sr$, for which the regression line is shown in *yellow*. However, it is clear how they keep the same slope as the rest of the assemblage. Some data points used to define the regression lines lie outside the range of the diagram.

Conclusions

All three Cenozoic volcanic provinces in Northeast Brazil, namely the MQVL, the Mecejana volcanic field and Fernando de Noronha are virtually identical geochemically and form a compositional continuum with one another that may be explained in terms of degrees of partial melting as the dominant underlying process behind the variability of their basaltic rocks, and fractionation of Ti-bearing phases in the case of phonolites. Other differences amongst basaltic rocks may be accounted for in terms of depth of melting. Both depth and degrees of partial melting also correlate with small amounts of assimilation of continental lithospheric mantle material, reflected in some localised variability in Ba, Nb and isotopic trends. There are some effects of contamination by peridotitic xenoliths (e.g. MgO, Ni and Cr contents) and low-temperature alteration. The latter process is limited, and affects mainly highly mobile elements such as Rb and K. Contamination by peridotitic xenoliths affects mainly contents of MgO, Ni and Cr, but can be easily demonstrated and disentangled from the main petrogenetic processes. Differences between the continental and oceanic phonolites manifest mainly through the fractional crystallisation of kaersutite and sphene, which is stronger in the oceanic sector. The reasons for these differences in fractional crystallisation processes between the two sectors are not clear.

Isotopic evidence is in good agreement with major and trace element geochemistry, supporting the idea that melts are mainly asthenospheric but

may incorporate vertical heterogeneities according to depth and degrees of partial melting. Such vertically heterogeneous source seems to include continental lithospheric material, indicating some assimilation of the base of the continental lithosphere. Although our Rb-Sr isochron ages are based on few data points, and therefore must be treated with caution, they still show remarkable agreement with the local geological context, $^{40}Ar/^{39}Ar$ ages (both from this study and other published sources) and other published isotope data.

Despite the similarities between Cenozoic volcanism in the MQVL, the Mecejana volcanic field and Fernando de Noronha, including their proximity in time and space, other published interpretations of the region have failed to bring these volcanic areas together under a unified model. Whilst Fernando de Noronha has generally been discussed in isolation (Ulbrich, 1993; Ulbrich *et al.*, 1994; Ulbrich and Lopes, 2000; Lopes, 2002), attempts have been made to identify the signatures of a supposed hotspot underlying the archipelago, often associated with a deep mantle plume, in adjacent continental lavas (Fodor *et al.*, 1998, 2002, Rivalenti *et al.*, 2000, 2007). We have shown that a better explanation is to treat the two sectors as the product of the same magmatic process. Although published data for mantle xenoliths indicate similarities between lithospheric metasomatic events at the base the oceanic and continental sectors, which are likely associated with magmatism producing small degrees of melting (Rivalenti *et al.*, 2007), studies of the lavas themselves have up until now not produced conclusive connections between them. However, we believe that our analysis establishes these connections, in agreement with the matching metasomatism at the base of both continental and oceanic lithospheres and coeval with magmatism, which were reported by Rivalenti et al. (2007). The difficulties in establishing these connections between the continental and oceanic lavas have been partially due to the continental lithospheric component and higher degrees of silica saturation in some of the MQVL lavas, which gives the impression of distinct processes and sources in the

continental sector. However, we have shown that these effects are limited to specific tectonic settings and variability in depths and degrees of melting, and there is in fact a compositional continuum and chronological synchronicity within and between the three Cenozoic volcanic areas of Northeast Brazil.

Some authors also still argue for the presence of a local plume to explain the enrichment characteristics of some xenolith samples and their elevated equilibrium temperatures (Rivalenti *et al.*, 2000; Fodor *et al.*, 2002). However, there is no reason why previous episodes of continental lithospheric enrichment must be associated with a mantle plume, instead of simply reflecting the developmental history of the Borborema continental block. For example, the vertical variability indicated by Nb patterns that may indicate the effects of past subduction zones, the increase in enriched isotopic signatures at higher melt fractions and Rb-Sr isochron ages that match previous major tectonic events all support this proposition. Furthermore, the elevated geotherm indicated by these calculations is limited (~1250^{o}C at ~20-22 kbar according to Fodor *et al.*, 2002; or a potential temperature of 1315-1320^{o}C according to Klöcking *et al.*, 2017) and far from the order of magnitude expected from a deep mantle plume. Instead, it may be explained through lithospheric thinning or other kinds of thermal anomalies. For instance, edge-driven convection has been suggested recently as a more feasible model for Cenozoic volcanism in Borborema (Knesel *et al.*, 2011; Pinheiro and Julià, 2014). Alternatively, Souza *et al.* (2013) argue that tectonic controls are a more plausible explanation, at least for the MQVL southern basins, which would imply that volcanism there is different from the rest of the lineament. However, based on our analyses, this is unlikely, and Souza *et al.* (2013) also recognise that edge-driven convection and extensional regimes in the area are not mutually exclusive and may be combined as an explanation for magmatism. We believe such combination is more plausible, and in accordance with our data.

Overall, our arguments and interpretations find remarkable support in previous studies, including some limited and localised continental lithospheric

assimilation (i.e. in extensional settings), a vertically stratified heterogeneous continental lithosphere, more vigorous and shallower magmatism in the continental sector, and a continuous development from DM to EM isotopic signatures that correlates with melt fractions and access to continental lithospheric material. Our more encompassing approach brings together the three largest Cenozoic volcanic provinces in Northeast Brazil, bridging the gaps of previous studies and demonstrating the need for a unified model that treats the region as a single group. We believe that subcontinental edge-driven convection provides a suitable candidate to explain the evidence discussed above, as well as accommodating the similarities between Northeast Brazil and the Cameroon Line, which will be the topic of the next chapter. The model itself will be addressed in the final chapter.

Chapter 4: Comparisons between Cenozoic volcanism from Northeast Brazil and the Cameroon Line

Introduction

It has been demonstrated in previous chapters how Cenozoic volcanism in Northeast Brazil, encompassing the archipelago of Fernando de Noronha, the Macau-Queimadas Volcanic Lineament (MQVL) and the Mecejana volcanic field, the last two located in the continent in the Borborema Province, must all be related and part of the same sublithospheric process. It has also been demonstrated how this process is synchronous with volcanic activity along the Cameroon Line, on the other side of the Atlantic (Chapter 2). These two Cenozoic volcanic provinces lie on equivalent segments of the South American and African conjugate margins, and were therefore adjacent to one another before continental separation, which happened ~50 Ma before the onset of magmatism.

Now, we will compare the Brazilian and African provinces geochemically, using major and trace element data from both areas that were produced in the same laboratory and with the same techniques. It will become clear how lavas in both continents are not only synchronous, but also geochemically identical. The two provinces therefore provide unique constraints on the origin of intraplate alkaline volcanism. They indicate that some form of localised lithospheric control, triggered by continental separation, must be in operation to allow synchronous and identical volcanism to occur on equivalent areas of two conjugate margins. Concomitantly, any model proposed for one region, must also work for the other. The comparison below will highlight recurring characteristics as well as some limited local variability, allowing for the establishment of what must be the relevant variables for building a common model. This is a unique case in the wide realm of intraplate volcanism. For the first time, the possibility of

testing specific hypotheses concerning plume-independent intraplate magmatism against a 'control' group becomes available, and further studies addressing these two areas together might bring some consistency to a type of volcanism that has otherwise resisted attempts at defining general models to explain it.

Methods and Definitions

The geochemical data for Northeast Brazil analysed in this chapter include the major and trace element concentrations obtained through x-ray fluorescence (XRF), and $^{87}Sr/^{86}Sr$ and $^{143}Nd/^{144}Nd$ isotopic ratios that were presented in Chapter 3. Methods are described in detail in Appendix A. For the purpose of plotting geochemical data, all major element analyses have been normalised on a volatile-free basis, and all iron is reported as Σ FeO. Loss on ignition (LOI) was measured in the Brazilian samples but not in those from the Cameroon Line. LOI in the latter is estimated from the analytical totals for the purpose of identifying the more altered samples in variation diagrams. For the Northeast Brazil assemblage, details about sample locations, context and petrography were also given Chapters 1 and 3.

Major and trace element concentrations for the Cameroon Line were obtained through XRF at the same laboratory at the University of Edinburgh and using the same techniques. There is also a wide range of XRF data available for oceanic islands across the world that were obtained likewise and will sometimes be used for comparison. These values are published in Fitton (2007) and Fitton et al. (1991). Radiogenic isotopic data for the Cameroon Line were collected from published sources (Halliday *et al.*, 1988, 1990; Lee *et al.*, 1994; Ballentine *et al.*, 1997; Marzoli *et al.*, 1999; Ngounouno *et al.*, 2000; Aka *et al.*, 2004; Rankenburg *et al.*, 2005; Njome and de Wit, 2014). The dataset from Mount Etinde is very distinct from the rest of the African assemblage in terms of major and trace elements, especially for intermediate and evolved samples, and since it comprises a

single locality it will not be included in the discussion. However, its isotopic characteristics are comparable with the rest of the assemblage and will be included in the discussion. Our reasoning is that Etinde's distinct major and trace element characteristics, which are more pronounced in intermediate and evolved samples, suggest differences in petrogenetic processes, but its sources still tap the same isotopic reservoir.

Amongst basaltic samples, primitive compositions will be defined as those with MgO ≥ 6 wt.%. Our choice of an 8 wt.% MgO threshold in the previous chapter to discuss the assemblage from Northeast Brazil was justified on the basis that the range of 6-8 wt.% MgO includes solely the Remédios Formation dyke swarm and one basaltic andesite from the Boa Vista basin (i.e. 15BP3-3b, with 6.5 wt.% MgO). However, the same does not apply to the Cameroon Line, which includes several samples of alkali basalt, trachybasalt and basanite samples in this range. Therefore, we believe it is productive to lower the cut-off to 6 wt.%. The one aforementioned basaltic andesite from the Boa Vista basin (15BP3-3b), however, is clearly an exception to this trend and will be excluded from our definition of primitive samples. Samples from the MQVL have had their MgO content affected by xenolith contamination (Chapter 3), and the MgO compositional gap between 6 and 8 wt.% could be a result of that, further justifying a lower MgO threshold when comparing the assemblage with the Cameroon Line. The Remédios basaltic dykes in Fernando de Noronha are the only basaltic samples in that Formation and, despite being partially within the 6-8 wt.% MgO range, form a geochemically and petrographically distinct subgroup in the assemblage that is not volumetrically representative. Therefore, they will be highlighted as a distinct group in the discussion and might be excluded from some comparisons where they clearly represent outliers.

Intermediate samples comprise those between and excluding the classification fields of basalt, trachybasalt and tephrite-basanite on the one hand, and rhyolite, trachyte and phonolite on the other, according to the total-alkalis and silica classification scheme. Evolved samples refer to rhyolite,

trachyte and phonolite. Geochemical classifications are based on Le Maitre et al. (2004).

Major elements

Major element values for Northeast Brazil and the Cameroon Line are given in Appendix C. Data from Northeast Brazil was discussed in detail in Chapter 3. Although the Cameroon Line dataset is significantly larger than the one for Northeast Brazil, major element trends amongst basaltic rocks in both provinces overlap each other on SiO_2 and MgO variation diagrams (Figures 4-1 and 4-2). Differences between the two areas are limited to intermediate samples in the oceanic sectors and intermediate and evolved samples in the continental sectors. These patterns are also clear on a total alkalis and silica diagram (TAS diagram; Figure 4-3). In the oceanic sector of Northeast Brazil, intermediate samples are dominated by transitional compositions whilst evolved ones have a relatively high proportion of trachyte in relation to phonolite, whereas in the Cameroon Line oceanic sector, intermediate samples are clearly alkaline and evolved ones are dominated by phonolite with proportionally few trachyte samples. There are proportionally very few intermediate samples in the Cameroon Line continental sector, but they are clearly transitional as opposed to alkaline. In the continental sector of Northeast Brazil, intermediate compositions are virtually absent, except for the basaltic andesites from the MQVL basins, which stand out from the main trends in all other areas. Primitive samples from the Brazilian continental sector also produced higher MgO and lower TiO_2 than all other areas. Evolved continental samples in Northeast Brazil comprise exclusively phonolite, whereas in the Cameroon Line they show an evolution line from trachyte to rhyolite. The clear linear trend with a negative slope amongst primitive samples in Northeast Brazil on the TAS diagram is also absent in the Cameroon Line, which shows instead a greater spread of data points towards higher SiO_2 and higher total alkalis. This suggests greater influence

of fractional crystallisation in the local variability of African occurrences when compared to the dominance of degrees of partial melting on the South American side. Primitive samples from Northeast Brazil are also marked by a larger proportion of silica-poor specimens and concomitantly a proportionally high number of nephelinite samples.

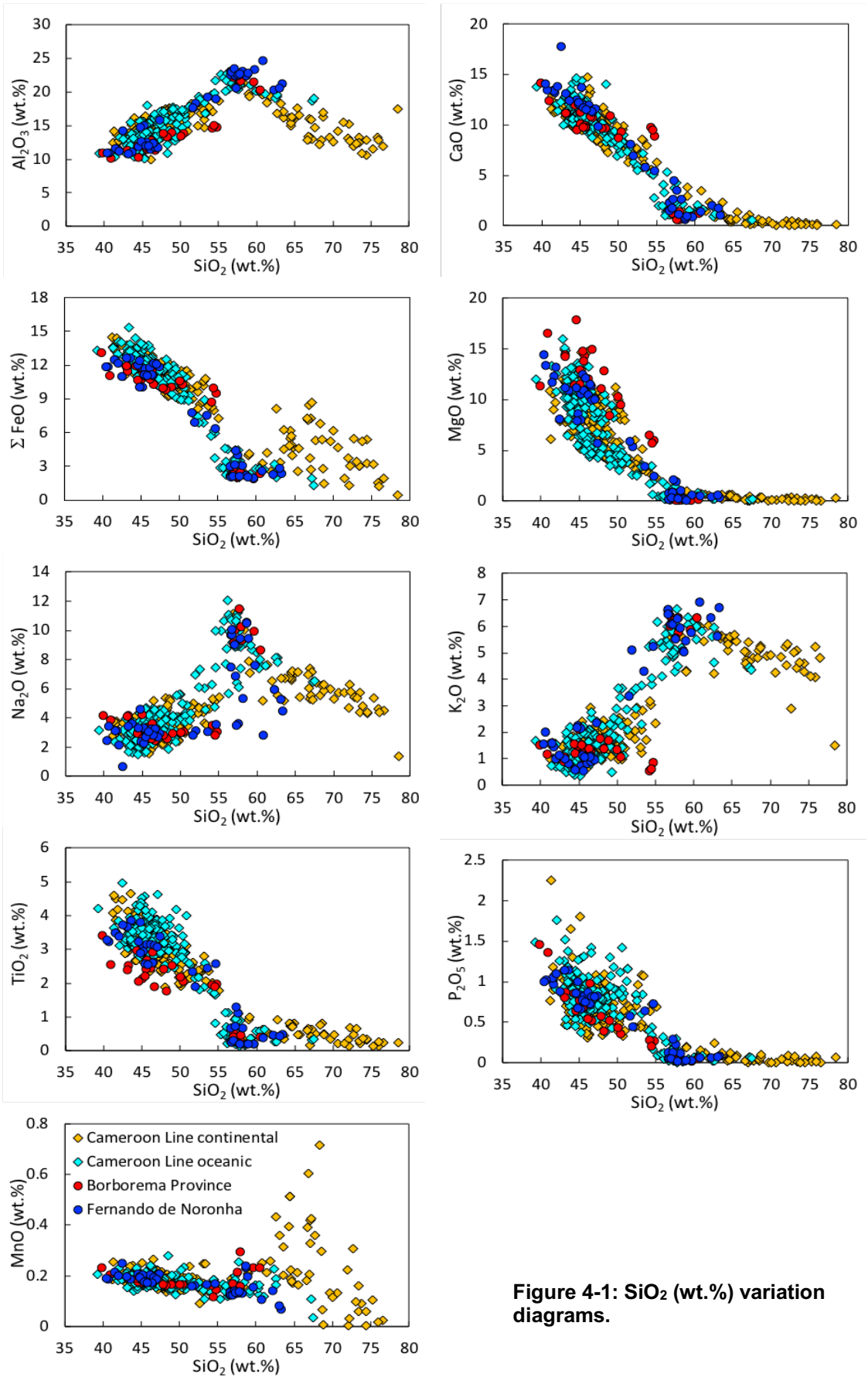

Figure 4-1: SiO_2 (wt.%) variation diagrams.

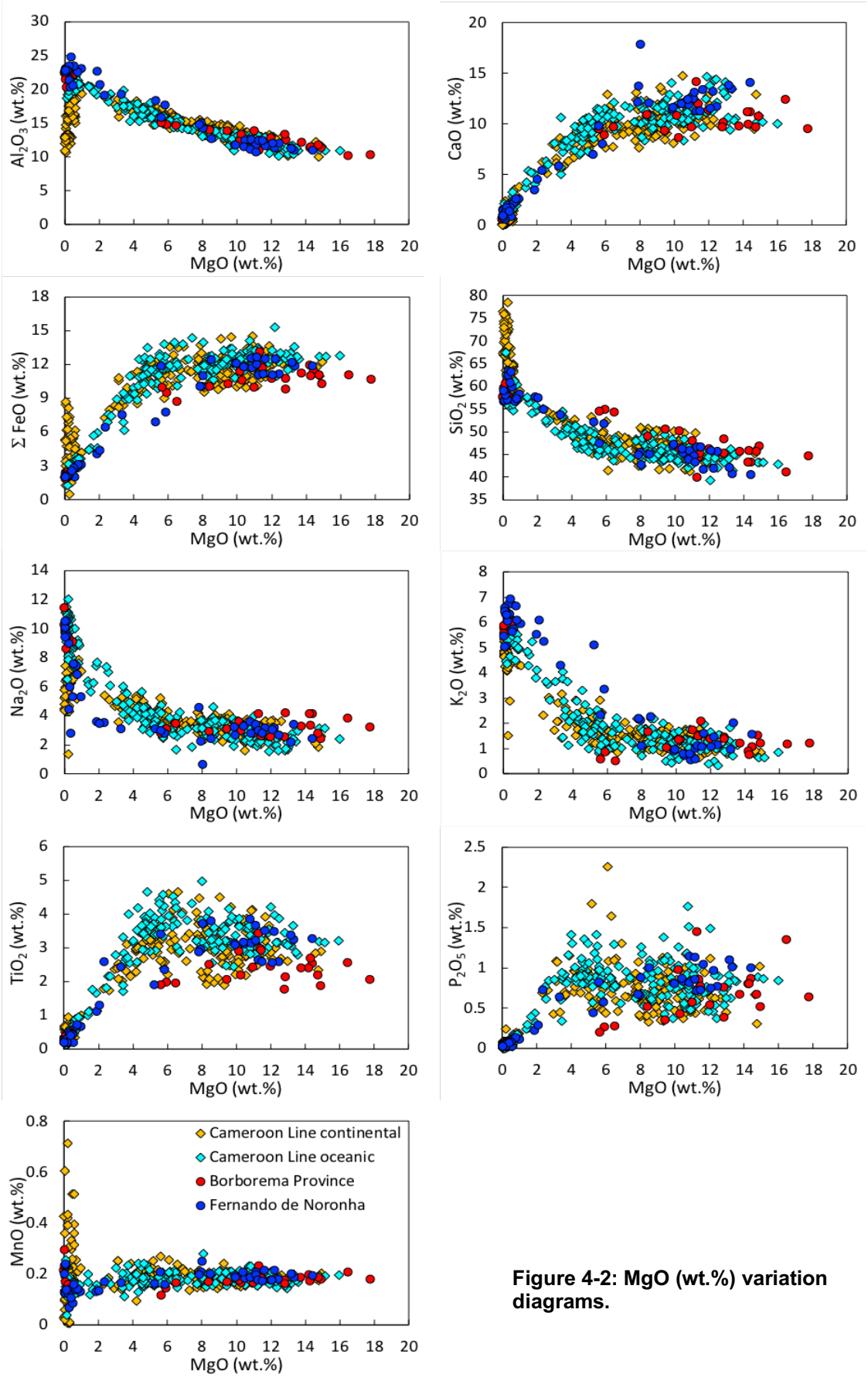

Figure 4-2: MgO (wt.%) variation diagrams.

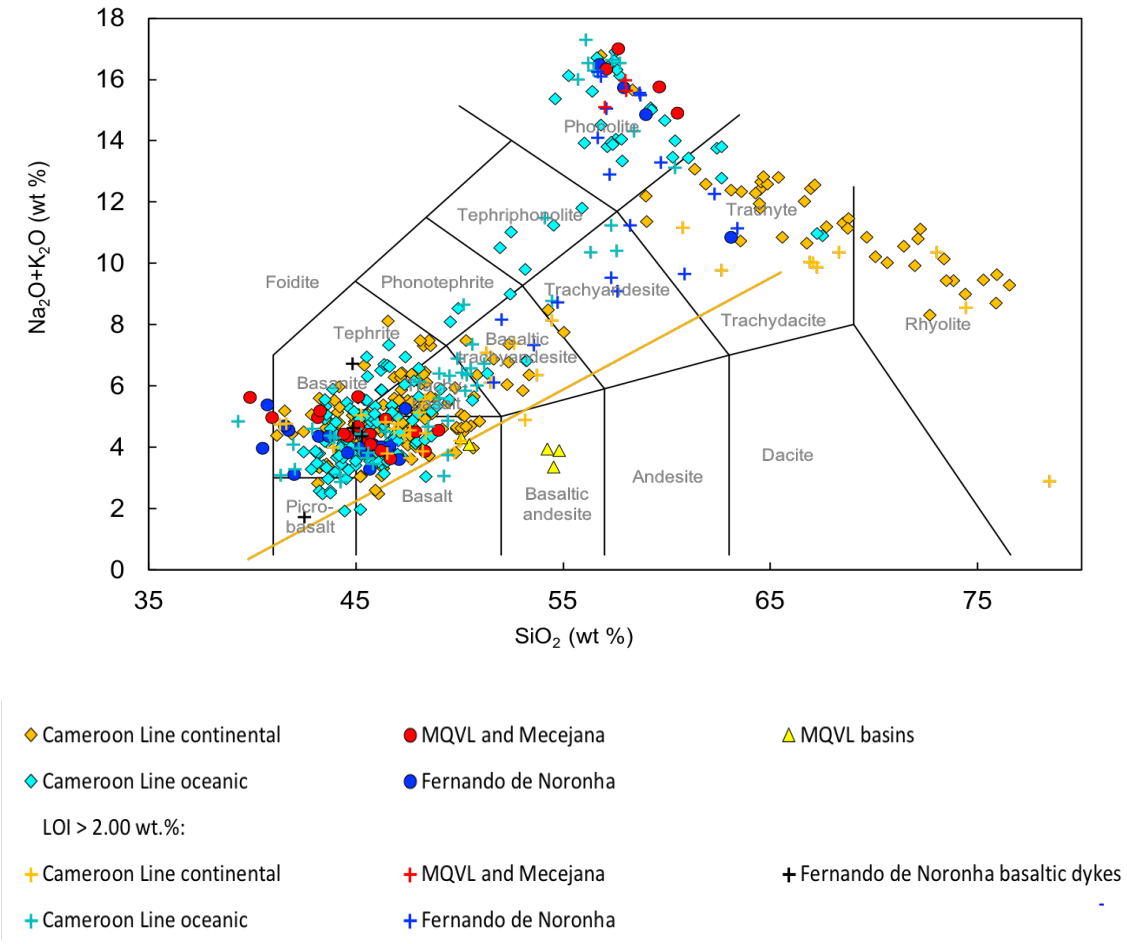

Figure 4-3: Total alkalis vs. silica (TAS) diagram for all areas, produced as in Figure 1-9 and plotted on a volatile free basis and ΣFeO. Cameroon Line data from Fitton (2007) and Fitton et al. (1991).

Trace elements

Comparisons between trace element patterns in Zr variation diagrams amongst primitive samples (MgO ≥ 6 wt.%) from Northeast Brazil and the Cameroon Line indicate matching concentrations and trends for most elements in both continents (Figure 4-4). Values are given in Appendix C. The scattered Rb and K values, with some depletion in the oceanic sector, discussed in Chapter 3 in relation to Northeast Brazil, are also present in the Cameroon Line, albeit proportionally less so. The same occurs for Ba enrichment amongst some continental samples. The Cr and Ni enrichment present in Northeast Brazil, especially in the continental sector and interpreted as a result of xenocryst contamination (Chapter 3), does not

occur in the Cameroon Line to the same extent. Although Cr enrichment is present in the Cameroon Line, the concomitant Ni enrichment remains dominant in the Brazilian continental sector, affecting only a proportionally small number of samples from the African oceanic sector and a few continental ones. The main differences between the two conjugate margins noticeable in these diagrams are the higher values for Sc, Cu and Sr amongst some African samples, especially in the oceanic sector in the case of Sc and Cu, and in the continent in the case of Sr.

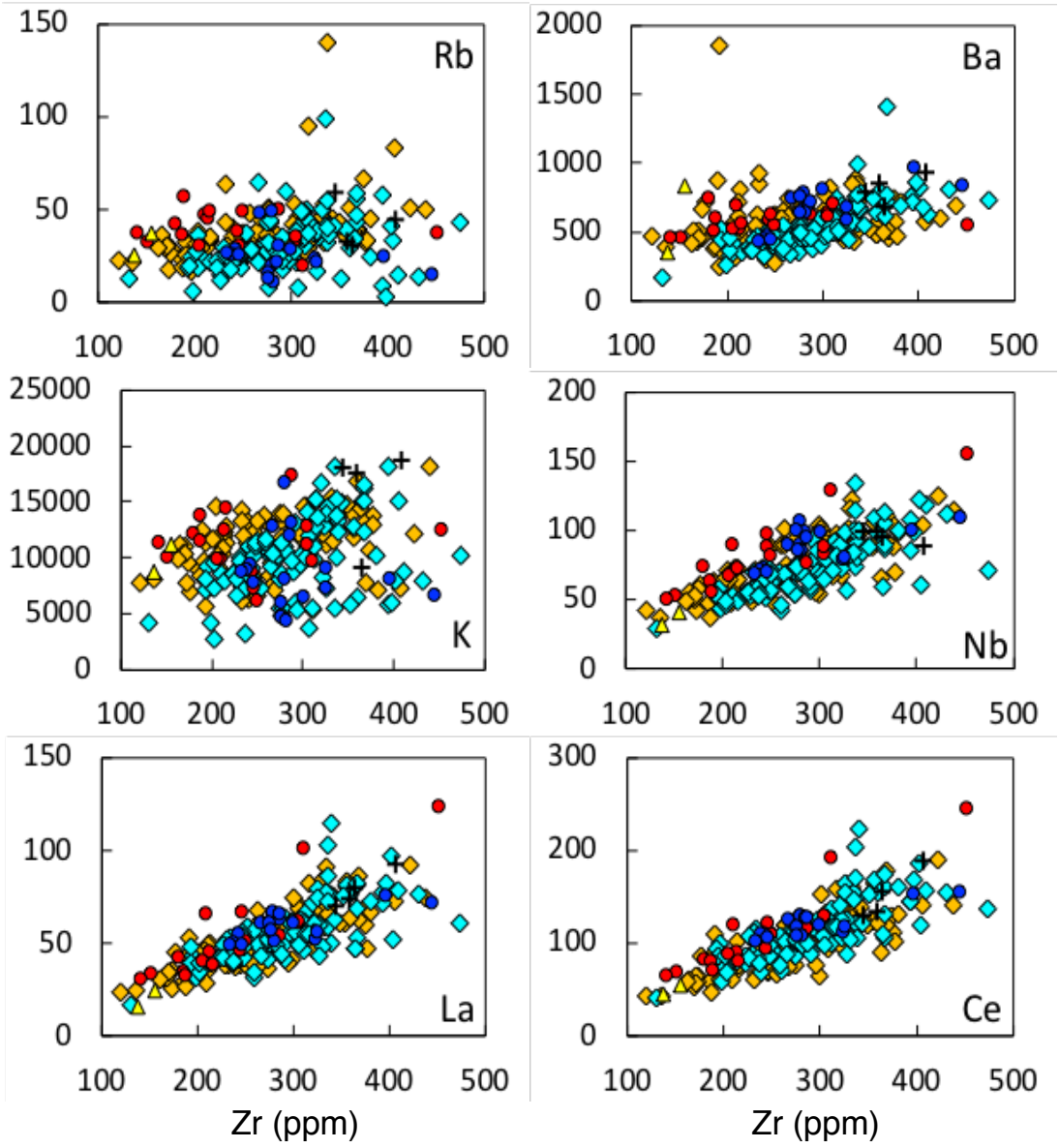

Figure 4-4: Continues on the next page.

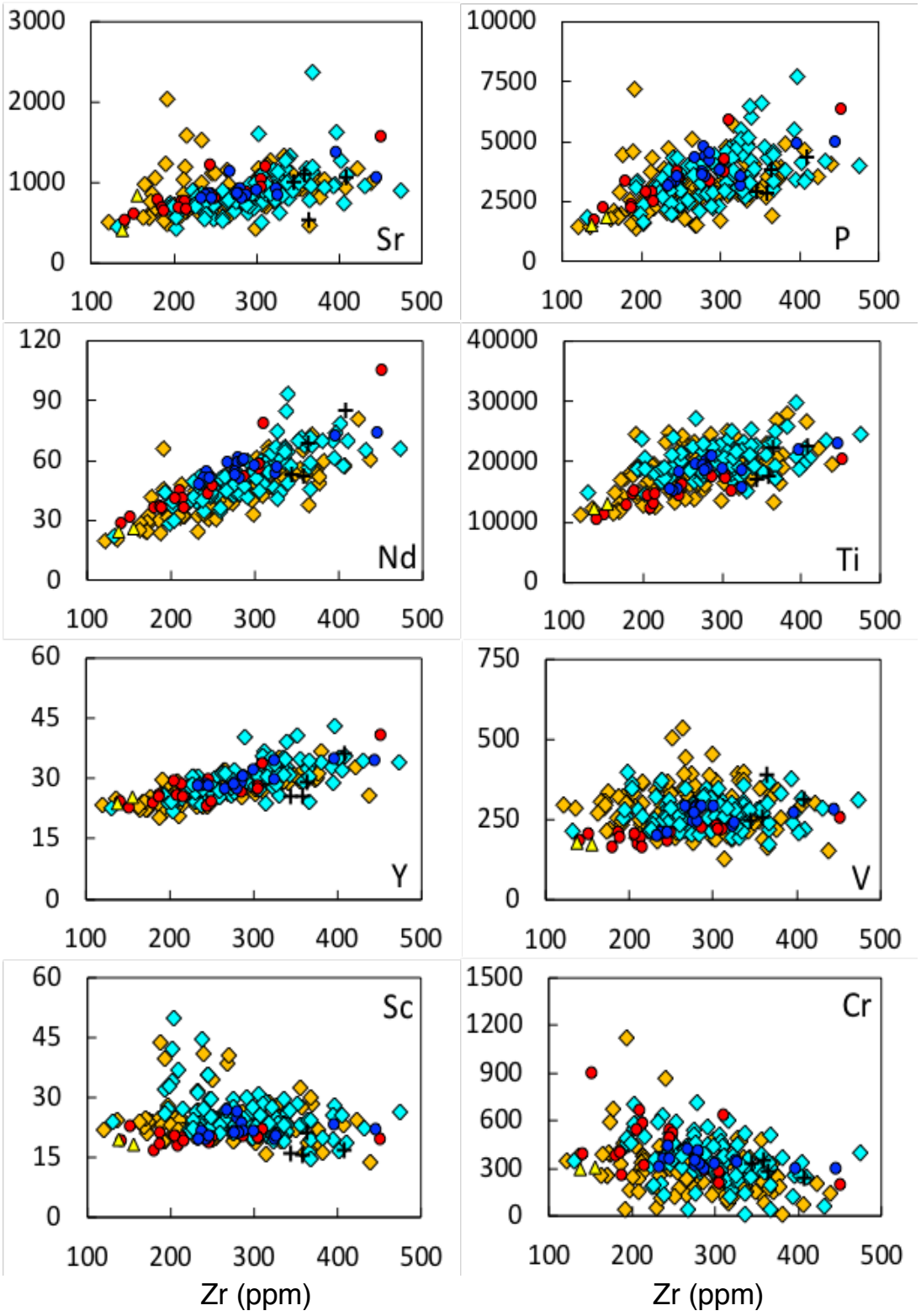

Figure 4-4: Continues on the next page.

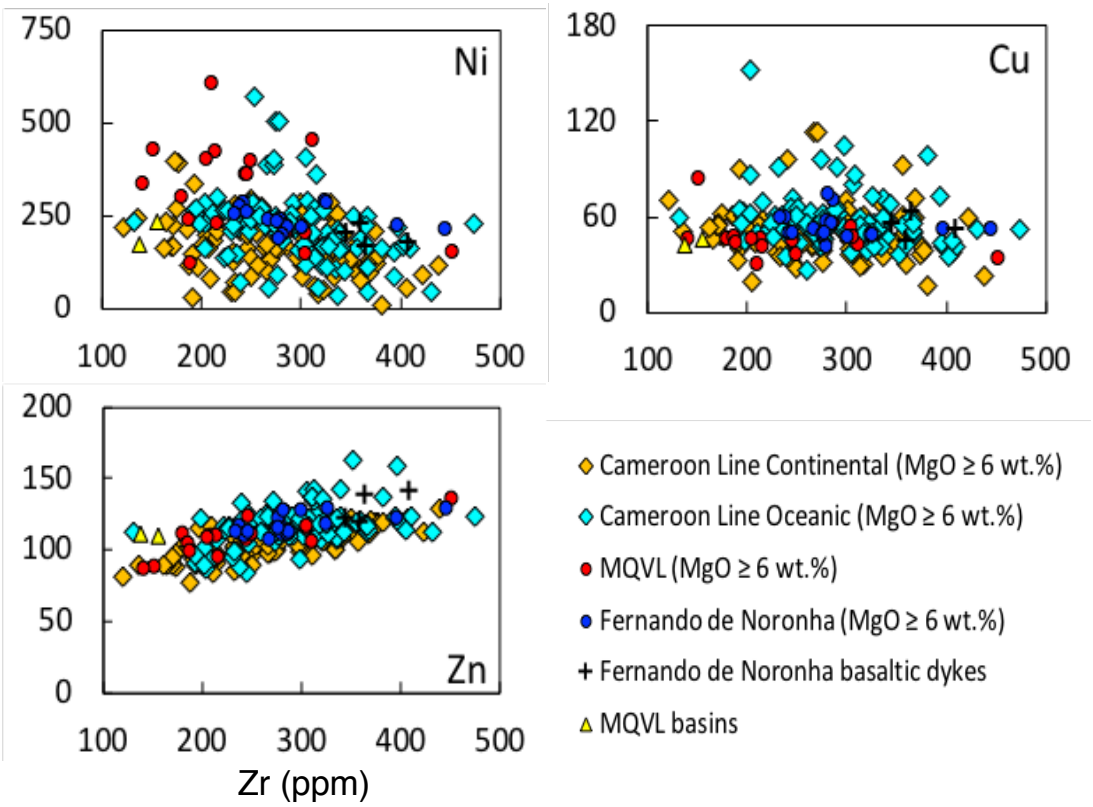

Figure 4-4: Zr variation diagrams for primitive samples (MgO ≥ 6 wt.%).

Multi-element diagrams normalised to primitive mantle (McDonough and Sun, 1995) for both the continental and oceanic sectors in Northeast Brazil and the Cameroon Line provide an even clearer illustration of the striking similarity between basaltic rocks from the two conjugate margins (Figure 4-5). The illustrated ranges of element concentrations for the Cameroon Line given in diagrams **c** and **d** of Figure 4-5 for comparison with Northeast Brazil were produced after the removal of four samples from each sector that have extreme outlying values that distort the final diagram. These samples are marked individually in diagrams **a** and **b** of Figure 4-5, but, despite their outlying values, four of these samples (two from each sector) are still remarkably similar to the nephelinite and basin samples from the MQVL (Figure 4-6), which are also end-member examples from the continental assemblage from Northeast Brazil. Concomitantly, Brazilian basin samples and nephelinite fall somewhat outside the Cameroon Line range. Samples from Fernando de Noronha also lie somewhat outside the African

continental range, especially in relation to the highly mobiles elements Rb, Ba and K, but not the oceanic one, showing the same low Rb and K values as the latter. Samples from the MQVL also show somewhat lower values for Zr, Ti and Y than the Cameroon Line oceanic sector, but lie within the African continental range. Both oceanic sectors show somewhat higher incompatible trace element concentrations than their continental counterparts. The somewhat higher Sr values in the Cameroon Line continental sector may be seen in the diagrams in the form of common positive Sr anomalies amongst its samples, which do not appear in the MQVL. The higher Sr content in the Cameroon Line continental sector must reflect the stronger effects of continental lithospheric material amongst those rocks (Fitton and Dunlop, 1985; Fitton, 1987).

The two datasets become virtually identical when their average values are compared with each other (Figure 4-7). This diagram emphasises how incompatible trace element patterns from the two conjugate margins are similar in both their absolute values and relative proportions, the latter reflected in the overall patterns and shape of the multi-element diagrams. Averaged values also highlight a similar Rb and K depletion in both oceanic sectors, and the lower Zr and Ti values in the Brazilian continental sector in relation to all other areas. As in the diagrams showing all values in Figure 4-5, continental samples are more similar to each other than they are to their oceanic counterparts, and vice-versa. Nonetheless, the Cameroon Line oceanic sector shows the lowest Nb content of all areas. Average values for individual oceanic islands along the Cameroon Line also show how Fernando de Noronha resembles more closely the islands of Annobón and São Tomé, which are those farthest away from the continental margin (Figure 4-8).

Figure 4-5: (next page) Multi-element diagrams for the Cameroon Line and Northeast Brazil. Individual samples highlighted in diagrams *a* and *b* have been removed from the range of values shown for the Cameroon Line in diagrams *c* and *d*. Normalised to the primitive mantle values of McDonough and Sun (1995).

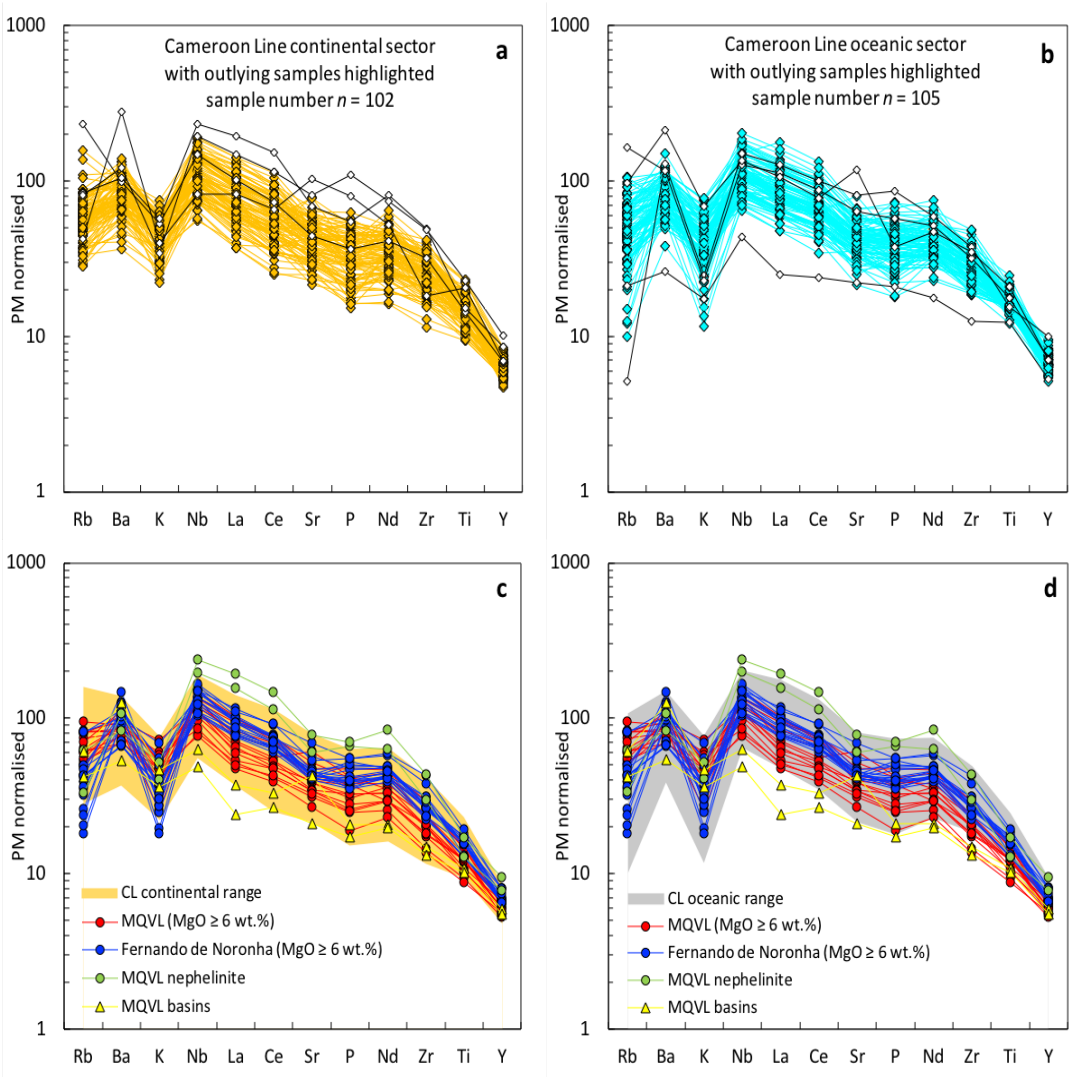

Figure 4-5: Caption on previous page.

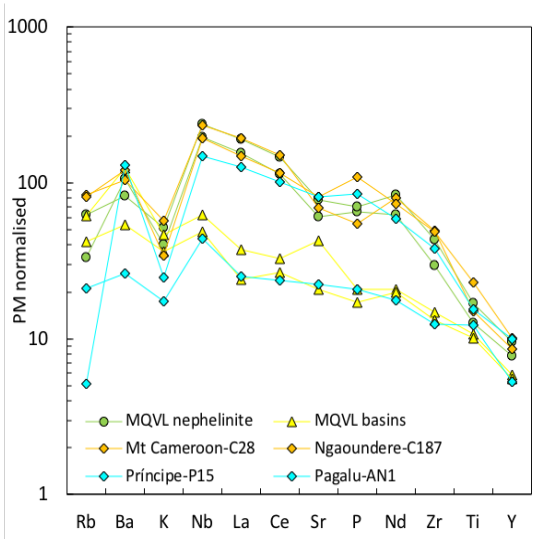

Figure 4-6: Four outliers (two from each sector) illustrated in diagrams *a* and *b* of Figure 4-5 compared with end-member samples from the MQVL (i.e. two nephelinite and two basin samples). Normalised to primitive mantle values according to McDonough and Sun (1995).

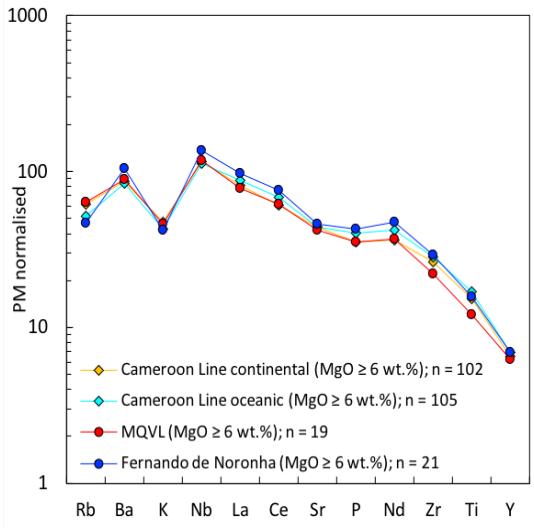

Figure 4-7: Average concentrations of incompatible trace elements for primitive samples (MgO ≥ 6 wt.%) from Northeast Brazil and the Cameroon Line (*n = number of averaged samples*). Normalised to primitive mantle values according to McDonough and Sun (1995).

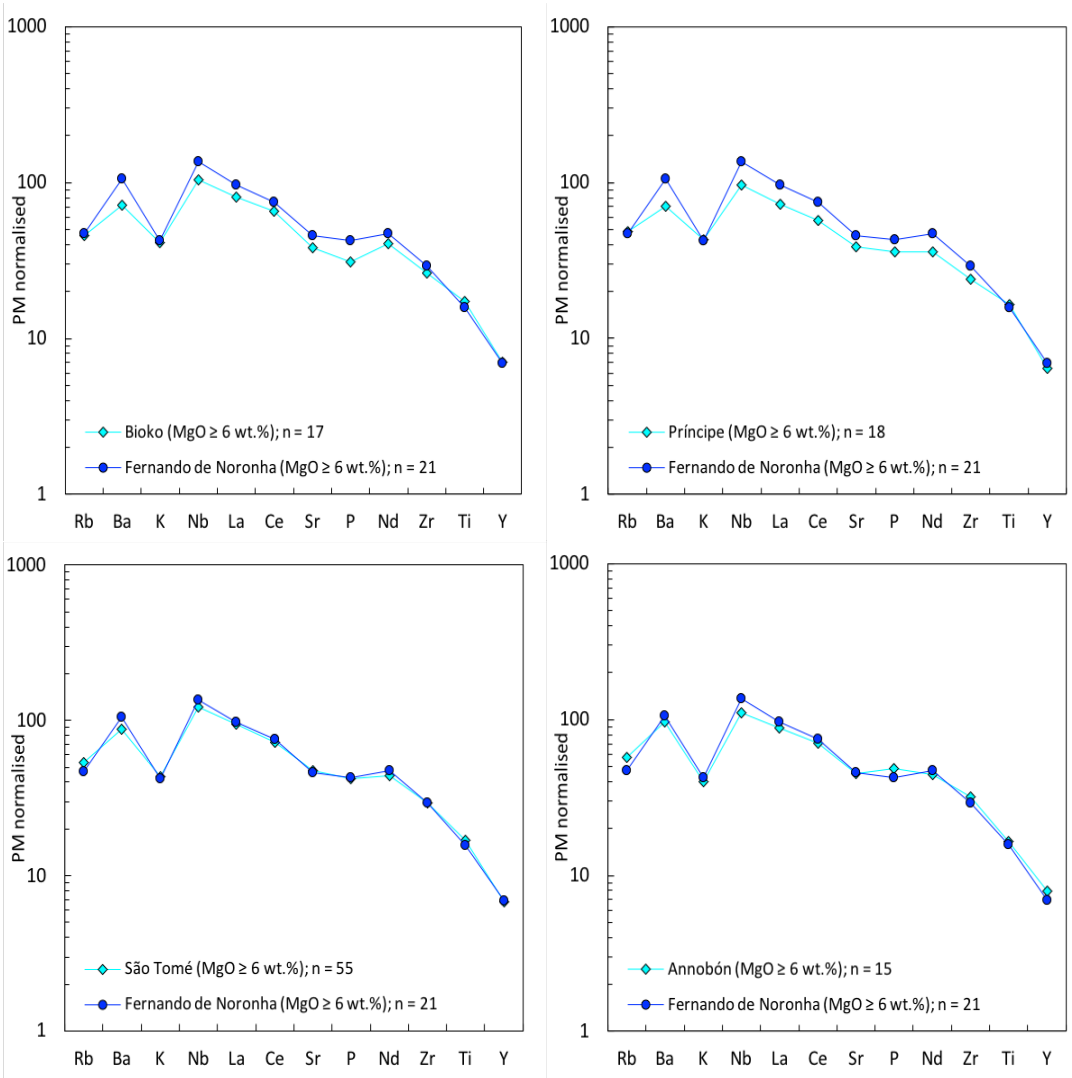

Figure 4-8: Average values for trace elements from Fernando de Noronha primitive samples (MgO ≥ 6 wt.%) compared with those from individual islands of the Cameroon Line oceanic sector (*n = number of averaged samples*). Normalised to primitive mantle values according to McDonough and Sun (1995).

The overall trace element patterns for phonolite, despite small differences, is also virtually identical for all regions (Figure 4-9). Similarities may be highlighted by illustrating the average values of all areas as shown in diagram **b** of Figure 4-9. Overall, all areas fall within the range of the Cameroon Line oceanic sector, although a few Mecejana samples have somewhat higher values. Although the range of the Cameroon Line oceanic sector illustrated in Figure 4-9 has its phosphorous values distorted by a single outlier, removing this sample still leaves all the other areas within the range of the African oceanic samples. Although variability is still somewhat higher for phonolitic than for basaltic samples, this is to be expected for evolved rocks. Overall, there are higher incompatible trace element absolute concentration in Mecejana, although the area also shows a distinctly strong depletion in Sr that distinguishes it from all other assemblages from both sides of the Atlantic. Both sectors of Northeast Brazil are also significantly more depleted in Ba. The noticeable Nb disparity between the two sectors of Northeast Brazil, where Mecejana produced higher values and Fernando de Noronha lower ones, is absent in the Cameroon Line, where average values lie in between those from Brazil. In fact, concentrations for Nb and most other elements in the Cameroon Line oceanic sector spread across the whole range of both sectors of Northeast Brazil, and are significantly more variable than any other area. African oceanic islands also show particularly high values for Ba and Sr, although these are compensated by low values and the final average agrees with the other areas. In the Cameroon Line, average oceanic values are equal or higher than continental ones, except for Nb, for which the average continental value is somewhat higher and match that of the continental sector of Northeast Brazil. Relatively lower Nb concentrations are a distinct characteristic of both oceanic sectors in relation to their continental counterparts amongst both primitive and evolved compositions, and is particularly strong in the African oceanic sector.

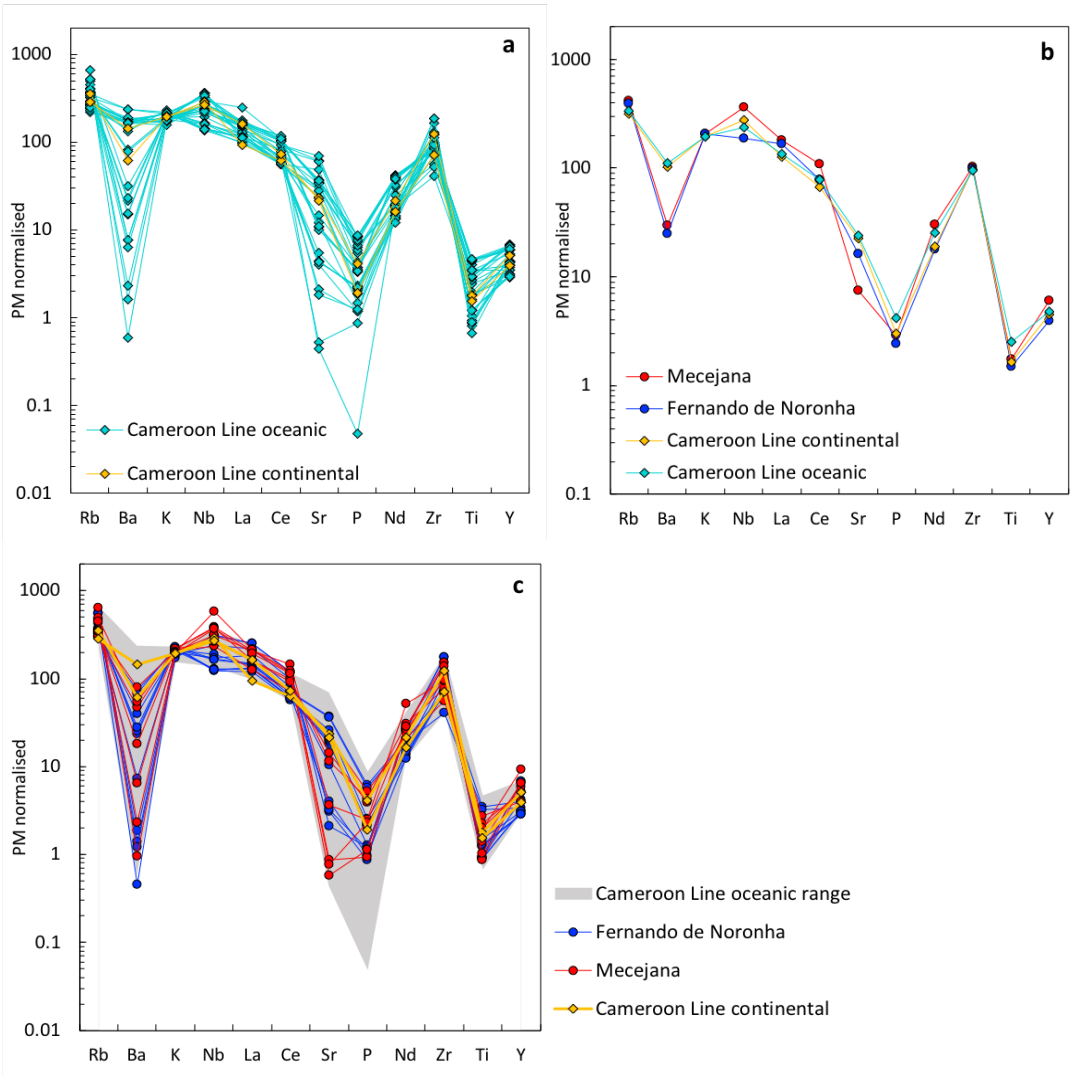

Figure 4-9: Multi-element diagrams for phonolites classified according to the TAS diagram (Figure 4-3). *a*: individual analyses for the Cameroon Line using data from Fitton (2007) and Fitton et al. (1991); *b*: averaged values for all areas; *c*: individual analyses from Northeast Brazil and the Cameroon Line continental sector compared with the range of values from the Cameroon Line oceanic sector.

Discussion

Alteration

In the TAS diagram (Figure 4-3), intermediate compositions from the two oceanic sectors show differences in their total alkali contents. This is caused by Na loss in Fernando de Noronha, which was discussed in Chapter 3. Such loss is associated with outcrops subject to strong weathering and alteration along the archipelago's shoreline and coincides with loss on

ignition (LOI) values > 2 wt.%. It has caused samples from Fernando de Noronha to show a transitional trend of melt evolution, as opposed to the clearly alkaline patterns in the African oceanic sector. However, the same process also affects the Cameroon Line oceanic samples, albeit to a smaller extent. The latter also shows the same correlation amongst intermediate samples between LOI > 2 wt.% and transitional characters, and LOI ≤ 2 wt.% and alkaline compositions. Although transitional compositions do not occur in the Cameroon Line oceanic sector to the same extent as in Northeast Brazil, this correlation between total alkalis and LOI affects virtually all intermediate samples, and therefore has an effect on their apparent transitional or alkaline characters.

The association between low total-alkalis and Na loss becomes clear in its correlation with increasing relative proportions of K_2O to Na_2O, which leads to apparently *mildly potassic* samples ($N_2O - K_2O < 2$) dominating transitional compositions, and *sodic* samples ($N_2O - K_2O > 2$) dominating alkaline ones (Figure 4-10). Furthermore, all apparently *mildly potassic* and *potassic* samples have LOI > 2 wt.%. The trends are the same as the ones observed for Fernando de Noronha (Chapter 3), albeit more subdued. For instance, there are only two apparently *potassic* ($K_2O > N_2O$) and no *ultrapotassic* ($K_2O > 2 \times N_2O$) samples in the whole Cameroon Line oceanic sector. These patterns on the African side further reinforce the argument presented in Chapter 3 for Na loss in Fernando de Noronha, where all intermediate transitional samples appear to be *potassic* or even *ultrapotassic*, and contrast sharply with the *mildly potassic* and *sodic* compositions of all other samples from the archipelago and other areas in both conjugate margins.

These trends also appear to affect the rhyolite and trachyte samples from the Cameroon Line continental sector, which are dominantly *mildly potassic* but due to Na loss several samples fall into the *potassic* field. All but two *potassic* evolved continental samples have LOI > 2 wt.%. These rocks have been significantly affected by continental lithospheric material (Fitton

and Dunlop, 1985; Fitton, 1987) and relatively higher K content should be expected, explaining why the trends of Na loss cause a transition from *mildly potassic* to *potassic*, as opposed to the changes from *sodic* to *mildly potassic* seen in the rest of the assemblage.

Therefore, apparently transitional compositions, as opposed to alkaline, amongst intermediate rocks in the oceanic sectors of both conjugate margins do not reflect intrinsic compositional or evolutionary difference between the areas. Instead, they seem to have been caused by alteration in oceanic environments, which in its early stages has a particularly strong effect on the breakdown of Na-plagioclase (Pearce, 1976). This is further supported by the Cameroon Line data published in Njome and de Wit (2014), which shows no hawaiite in the oceanic sector (a rock type that by definition should be *sodic* or *mildly potassic*; Gill, 2010), but potassic trachybasalt instead. Conversely, the continental sector in their dataset is dominated by hawaiite with limited occurrences of potassic trachybasalt, highlighting Na loss amongst oceanic samples. The clearly stronger effects of Na loss in Northeast Brazil reflect the small exposure of seamounts above sea level on the Brazilian side, which is limited to the small island of Fernando de Noronha (< 20 km^2), and its proportionally greater exposure to weathering caused by the oceanic environment, and contrast with the significantly larger African oceanic islands.

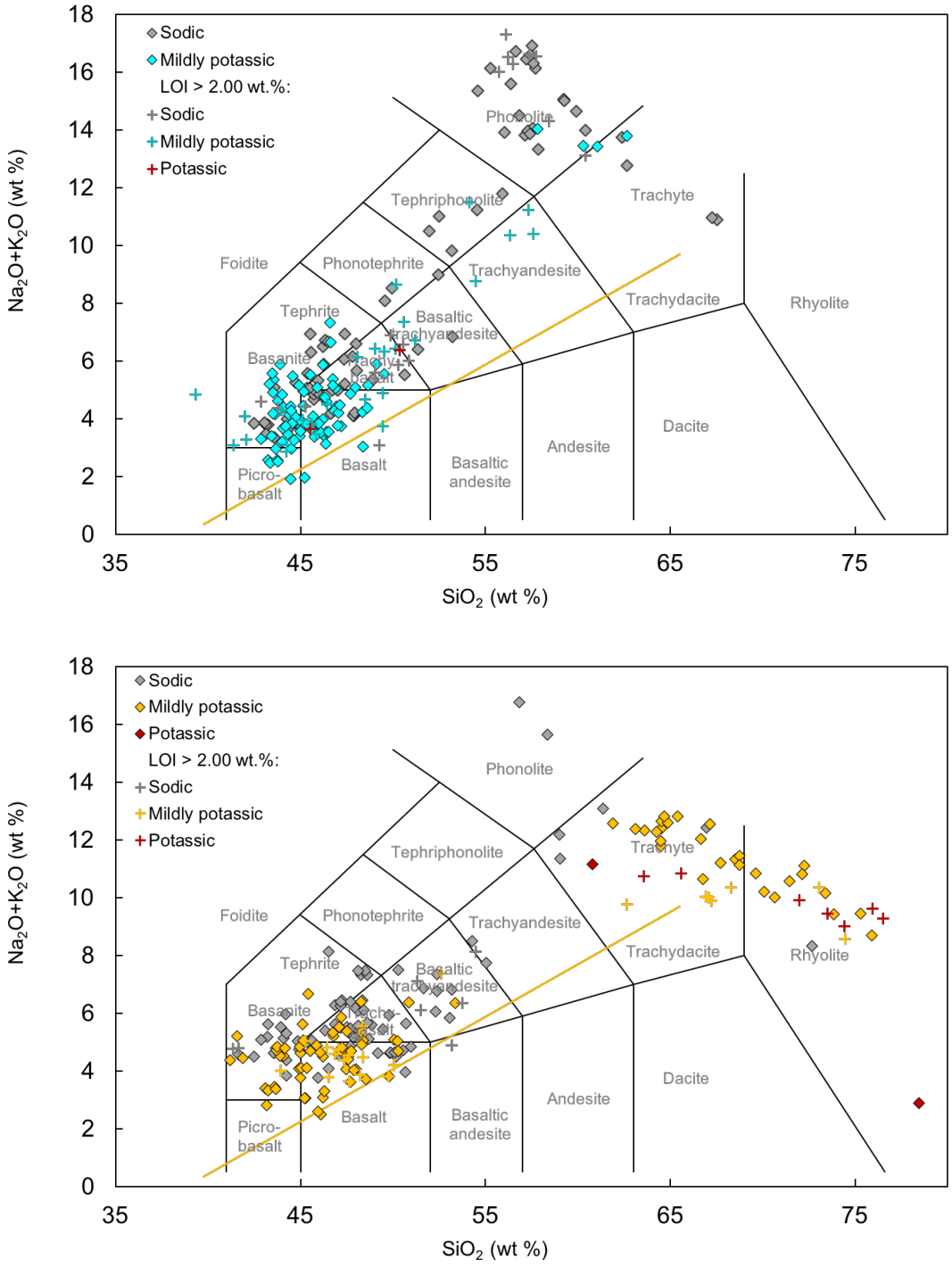

Figure 4-10: Apparently potassic character of the Cameroon Line oceanic (*upper diagram*) and continental (*lower diagram*) sectors plotted on a TAS diagram (volatile free and using ΣFeO). Cameroon Line data from Fitton (2007) and Fitton et al. (1991). It Is clear that intermediate oceanic samples with mildly *potassic* or *potassic* affinities have lower total alkalis and thereby an almost exclusively transitional character, which in turn correlate with LOI > 2 wt.% (see Figure 4-3). The same process affects the rhyolite and trachyte from the continental sector, where all but two *potassic* samples have LOI > 2 wt.%, in an assemblage otherwise dominated by *mildly potassic* compositions.

Rocks from the Cameroon Line oceanic sector also have low Rb and K contents, similarly to those from Fernando de Noronha, although the effects are proportionally less substantial (Figures 4-4, 4-5 and 4-7). In Chapter 3 we have attributed these trends to higher degrees of alteration in the oceanic environment, which seems to affect oceanic island basalts (OIB) around the world to a small extent. We can show that the same processes are affecting the Cameroon Line oceanic sector by also comparing Rb with Nb (Figure 4-11). The latter is an element that produces linear trends against other incompatible elements such as Zr, La and Ce, despite its somewhat lower values in the Cameroon Line oceanic sector (see above), and against which Rb should also show a similar correlation. However, Rb shows irregular patterns that reflect depletion in the oceanic sector, and somewhat scattered trends amongst continental samples in particular. Published average OIB values from Sun and McDonough (1989) are included in the diagrams (i.e. represented by a *black cross*) to emphasise these trends. By comparing Nb/Rb, two highly incompatible elements, against Nb/Ce, Ce being relatively less incompatible, demonstrates that the Rb trends against Nb result from Rb depletion rather Nb enrichment. Nb/Rb ratios should ideally remain more or less constant during changes in Nb/Ce or show some form of correlation if Nb is the element varying in relation to the others. Although the diagram shows a dominant trend of invariant Nb/Rb ratios in relation to changing Nb/Ce, especially in the continental sectors, it also shows some scattered high Nb/Rb values, particularly amongst oceanic samples, which do not correlate with Nb/Ce and are significantly higher than OIB values from Sun and McDonough (1989). The same trends may be observed in Northeast Brazil for the ICPMS data (Figure 4-12), showing that this is not an issue with the analytical methods. Comparing these trends with Ce/Y also shows how these processes are independent of depth and degrees of partial melting. K behaves similarly to Rb and is also affected by similar processes. Therefore, the trends of low total alkalis discussed above must also reflect some K loss, albeit proportionally less than Na. Kuepouo et

al. (2006) has also reported similar alteration effects amongst transitional basalts of the Bana complex in the Cameroon Line continental sector, which has also affected specifically Na, K and Rb, and has been attributed to the breakdown of interstitial glass and alkali-bearing phases.

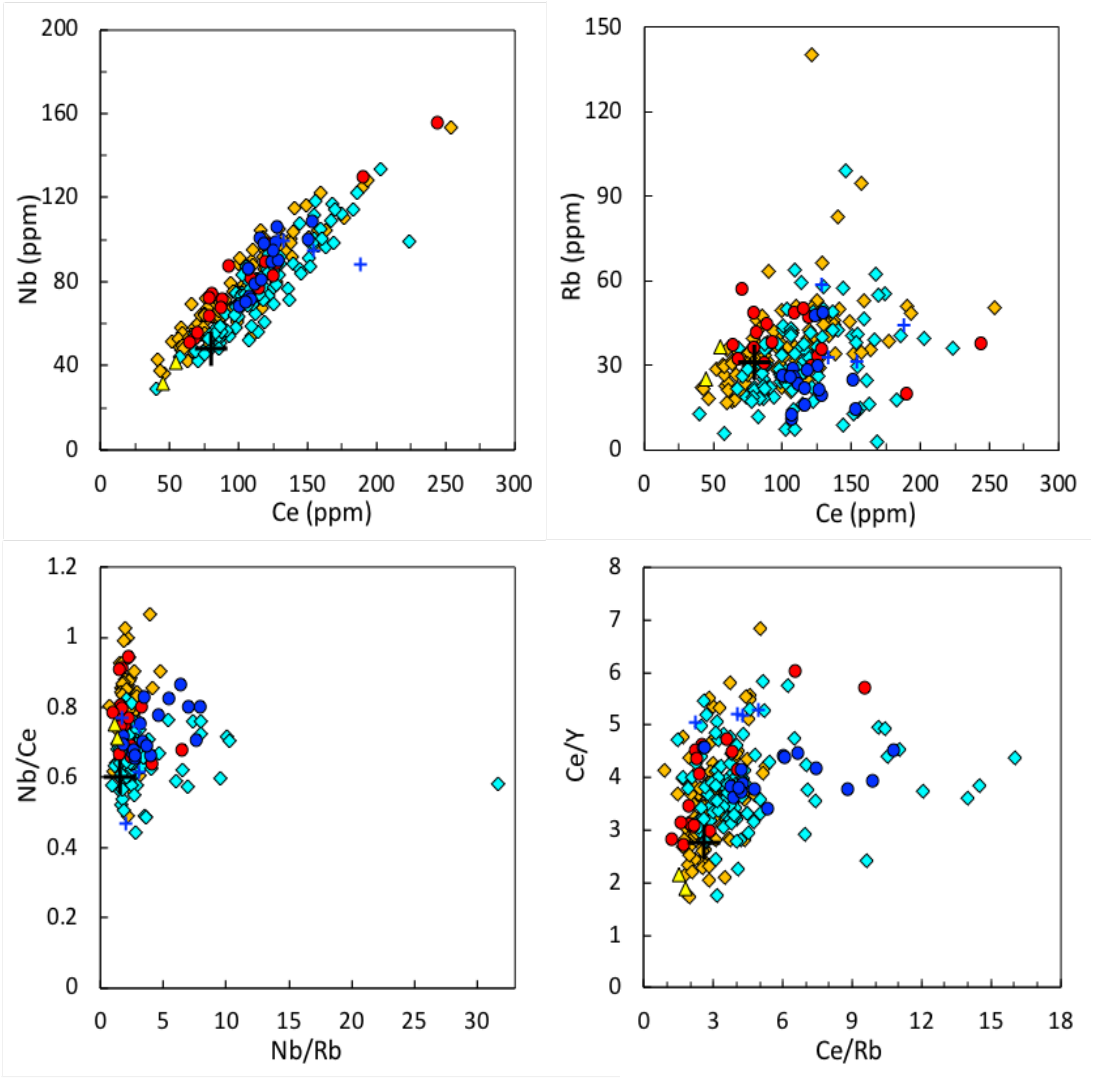

Figure 4-11: Relationship between Rb and Nb, showing Rb depletion in both oceanic sectors and scattered trends amongst some samples, particularly in the continents. The scattered increase in Nb/Rb ratios uncorrelated with the linear trend for Nb/Ce suggests that Rb depletion is the process behind it, rather than Nb enrichment. OIB values are from Sun and McDonough (1989).

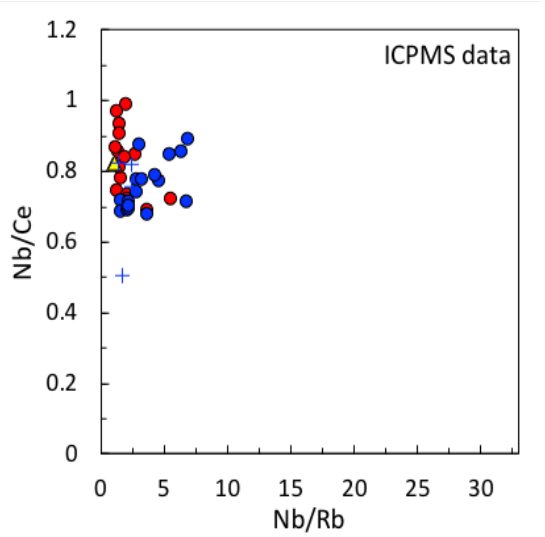

Figure 4-12: Relationship between Rb, Nb and Ce for the Northeast Brazil ICPMS data, showing the same Rb depletion in the oceanic sector as the XRF data above (Figure 4-11) and showing that these patterns are independent of the analytical methods.

Variability in melt evolution from major elements and the TAS diagram

The clear negative slope amongst primitive samples from Northeast Brazil in the TAS diagram contrasts with the greater spread, especially towards higher SiO_2 and total alkalis, in the Cameroon Line dataset, although sample distribution from the two conjugate margins still overlap. This suggests a greater influence of fractional crystallisation processes on the African side and does not indicate intrinsic differences between the two datasets. However, the TAS diagram shows a clearly distinct evolutionary trend amongst continental lavas from the Cameroon Line, which evolve to rhyolitic compositions. Conversely, evolved compositions in Borborema are restricted to the Mecejana volcanic field and are exclusively phonolitic. They also plot together with phonolites from both Fernando de Noronha and the Cameroon Line oceanic sector (Figure 4-3). The development of rhyolite in the Cameroon Line continental sector is therefore unique in the dataset, whereas the similarities between primitive rocks from both conjugate margins, independently of coming from a continental or oceanic context, also extends to phonolite wherever they occur. The distinct patterns of evolved samples in the Cameroon Line continental sector have been linked to the effects of the continental lithosphere in the processes of melt evolution (Fitton and Dunlop, 1985; Fitton, 1987). Continental phonolites in Northeast

Brazil are geographically limited to the oceanic-continental lithospheric boundary and are potentially associated with the adjacent fracture zone in the oceanic lithosphere (also named Fernando de Noronha; see Chapter 1). Therefore, they may be linked to oceanic processes, which may explain the lack of similar patterns between evolved rocks from the Brazilian and African continental sectors, and further reinforces the argument that the cause for the latter's distinct patterns is indeed the effects of the continental lithosphere in processes of melt evolution (Fitton and Dunlop, 1985; Fitton, 1987).

Despite the lack of rhyolite in the continental sector of Northeast Brazil, Borborema produced the only basaltic samples clearly within the subalkaline field (i.e. basaltic andesite). These occurrences are limited to local extensional basins that have caused significant localised increases in melt fractions and produced transitional compositions that have become oversaturated during early stages of fractional crystallisation (Chapter 3). The same tectonic contexts are not so significant in the Cameroon Line, and despite the presence of transitional compositions and more intense volcanic activity in the region, basaltic subalkaline occurrences are completely absent from our African dataset and only limited occurrences have been reported elsewhere (e.g. the rocks from the Bana complex reported by Kuepouo et al., 2006). Although the African plate seems to have been affected by significant extension during changes in the tectonic stress regime at ~80 Ma (Nürnberg and Müller, 1991; Njome and de Wit, 2014), the degree of lithospheric extension and basin formation on the South American side during the Cretaceous is clearly greater, and not matched in west Africa (Nürnberg and Müller, 1991; Matos, 1992). This helps to explain why subalkaline volcanic suites were produced in the Borborema basins, even though the intensity of magmatism in Northeast Brazil was more subdued than in Africa.

We can demonstrate the differences in silica saturation between the areas more clearly by using the method in Fitton et al. (1991) for calculating

a silica saturation index (SI) for basaltic samples from their major elements, which is derived from the CIPW norm calculation scheme, where:

$$SI = 100\left(Si - \frac{Al + Fe2 + Mg + 3Ca + 11Na + 11K + Mn - Fe3 - Ti - 4P}{2}\right) \quad (11)$$

and *Si*, *Al*, *MgO* etc. are molecular proportions of the respective oxides. This method shows how both oceanic sectors are somewhat more undersaturated than their respective continental counterparts (Figure 4-13), a pattern that is also reflected in the higher concentration of incompatible trace elements in both oceanic sectors (Figures 4-5 and 4-7), and demonstrates a similar type of variability between oceanic and continental sectors on both conjugate margins. All three samples with SI ≥ 10 are from the MQVL basins. Although they are not within our definition of primitive samples, the represent a significant group of basaltic lavas in the MQVL and therefore are included. Samples from the Cameroon Line are all primitive (MgO ≥ 6 wt.%).

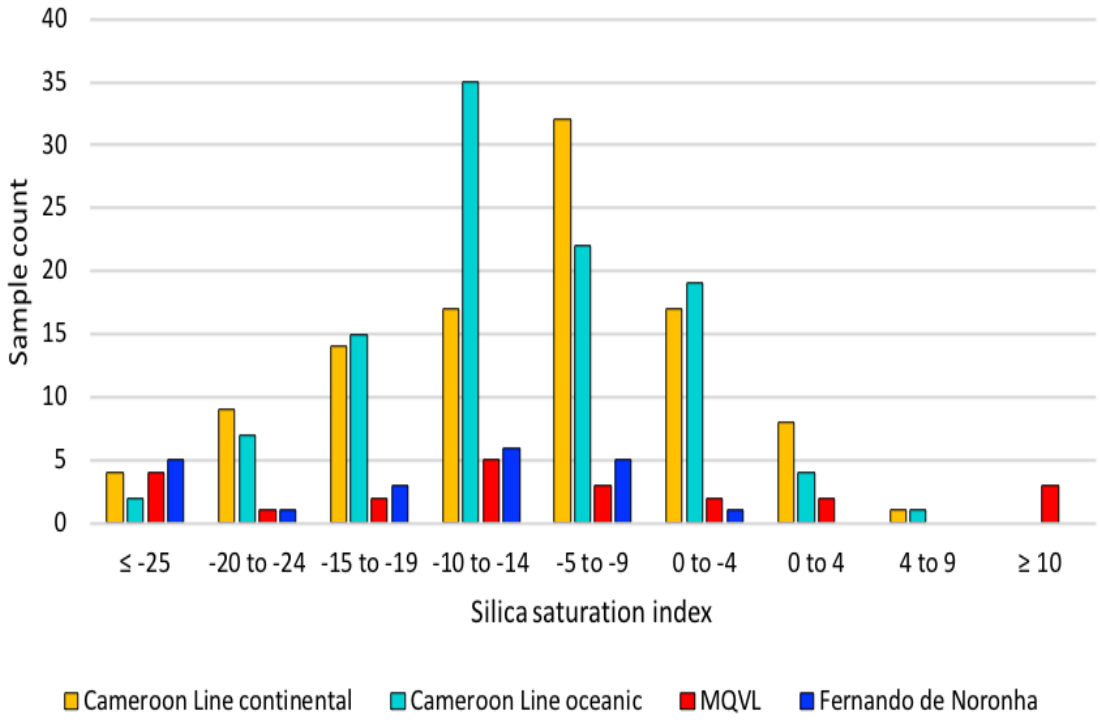

Figure 4-13: Sample count according to the silica saturation index (SI) of Fitton et al. (1991). All MQVL samples with SI ≥ 10 are from the MQVL basins.

Trace elements patterns

Basaltic rocks from Northeast Brazil and the Cameroon Line demonstrate very similar trends. However, the larger dataset and more vigorous volcanism on the African side shows greater variability than its South American counterpart, including stronger effects of fractional crystallisation and contamination by continental lithospheric material that are also clear in the major element patterns discussed above.

Ni and Cr patterns amongst primitive samples (MgO ≥ 6 wt.%) in both the Cameroon Line and Northeast Brazil are virtually identical, and trends from both conjugate margins overlap each other. However, they also show the stronger effects of fractional crystallisation on the African side, where the two elements correlate linearly towards lower values; the higher degrees of melting in the Cameroon Line, indicated by higher Cr/Ni ratios; and the proportionally stronger effects of xenolith contamination in the MQVL, where higher Ni and Cr concentrations correlate linearly (Figure 4-14). The range of values from all areas converge on the cluster of samples from Fernando de Noronha, which is not affected by fractional crystallisation to the same extent, indicating similar initial concentrations of Ni and Cr and therefore likely similar sources and petrogenetic processes in their formation, despite the aforementioned effects. This may be highlighted by illustrating in Figure 4-14 the Fernando de Noronha Ni and Cr median values (respectively 219 and 339 ppm). Higher Cr concentrations in relation to Ni in the Cameroon Line reflect the higher *D* values for Cr in clinopyroxene (Rollinson, 1993), which may cause some relative enrichment in relation to Ni at somewhat higher melt fractions during early stages of melting. Higher Cr in relation to Ni is also clear in MgO wt.% variation diagrams (Figure 4-15). The effects of xenolith and xenocryst contamination in the MQVL, discussed in Chapter 3, also seem to affect a few samples in the Cameroon Line, especially in the oceanic sector, leading to the higher contents of both Ni and Cr and a positive correlation between these elements and MgO > ~12 wt.% (Figure 4-15).

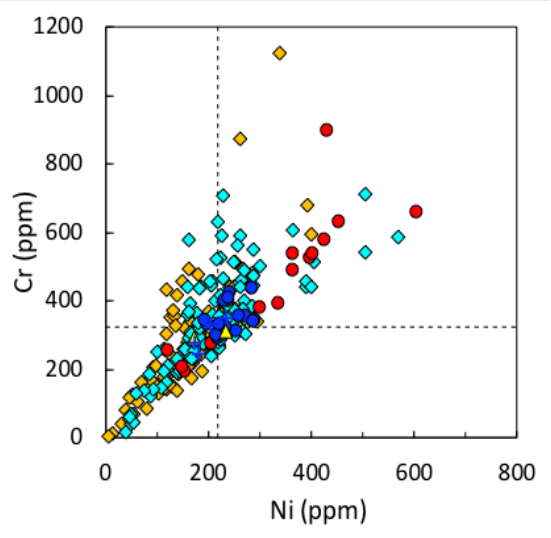

Figure 4-14: Relationship between Ni and Cr in Northeast Brazil and the Cameroon Line. The clustered pattern of Fernando de Noronha indicates limited fractional crystallisation (Chapter 3) and its median values of Ni = 219 and Cr = 339 coincide with where samples from all the other areas converge. Higher values for Cr result from its higher *D* value in clinopyroxene and the consequent subtle enrichment of the at somewhat higher melt fractions. Legend as in Figure 4-11.

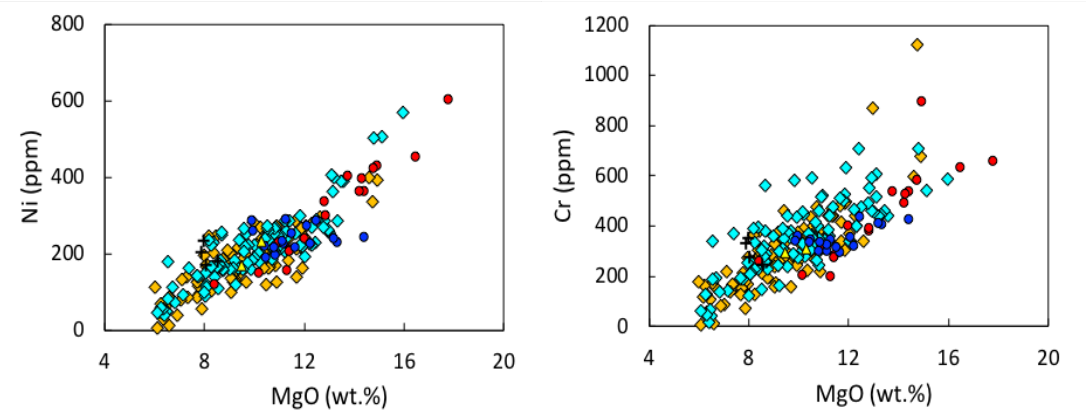

Figure 4-15: Behaviour of Ni and Cr (ppm) against MgO (wt.%). In Northeast Brazil, magmas with MgO values above ~12 wt.% were affected by significant contamination of peridotitic xenoliths and xenocrysts, which affects their contents of MgO, Ni and Cr (Chapter 3). It is likely that the same applies to some samples in the Cameroon Line that show trends matching those from the MQVL. For all the other samples, there is a greater spread towards higher Cr content in the Cameroon Line that cannot be seen in Northeast Brazil and is not matched in the behaviour of Ni, reflecting differences in the partition coefficient *D* of Cr in clinopyroxene. Legend as in Figure 4-11.

Although the trace element concentrations in the continental and oceanic sectors virtually overlap each other in both conjugate margins, both oceanic sectors still show somewhat higher values than their continental counterparts for most incompatible elements (Figures 4-5 and 4-7). This reflects the somewhat more undersaturated characters of oceanic lavas in relation to continental ones (Figure 4-13), and is clearer in Northeast Brazil, where the size and geographical distribution of the data are more restricted. Nonetheless, these patterns show how the oceanic sectors on each side of

the Atlantic are more similar to each other than they are to their respective adjacent continental terranes, and the same applies to the two continental sectors. Therefore, not only are the trace element patterns in the two conjugate margins virtually identical, but the small concentration differences between continental and oceanic sectors repeat themselves on both sides of the Atlantic.

Trace-element similarities between the two conjugate margins become even more significant in face of the differences with ocean islands from other parts of the world, for which some data obtained in the same laboratory and using the same methods are also available (Fitton *et al.*, 1991; Fitton, 2007). Figure 4-16 shows the average value of trace elements from different ocean islands across the world compared to Northeast Brazil and the Cameroon Line. Only localities with 9 or more samples were included in the diagrams, based on the number of samples available for the Canary Islands, the dataset that most approach Northeast Brazil and the Cameroon Line, but localities with fewer samples also show the same patterns. Geographically, the Canaries are one of the closest localities to ours, and the closest one with an observable seamount chain connecting it to the continent (see Chapter 5). Cape Verde, which also neighbour the African west passive margin, is also somewhat more similar to Northeast Brazil and the Cameroon Line than other oceanic islands, although it is not connected to the continent by a seamount chain.

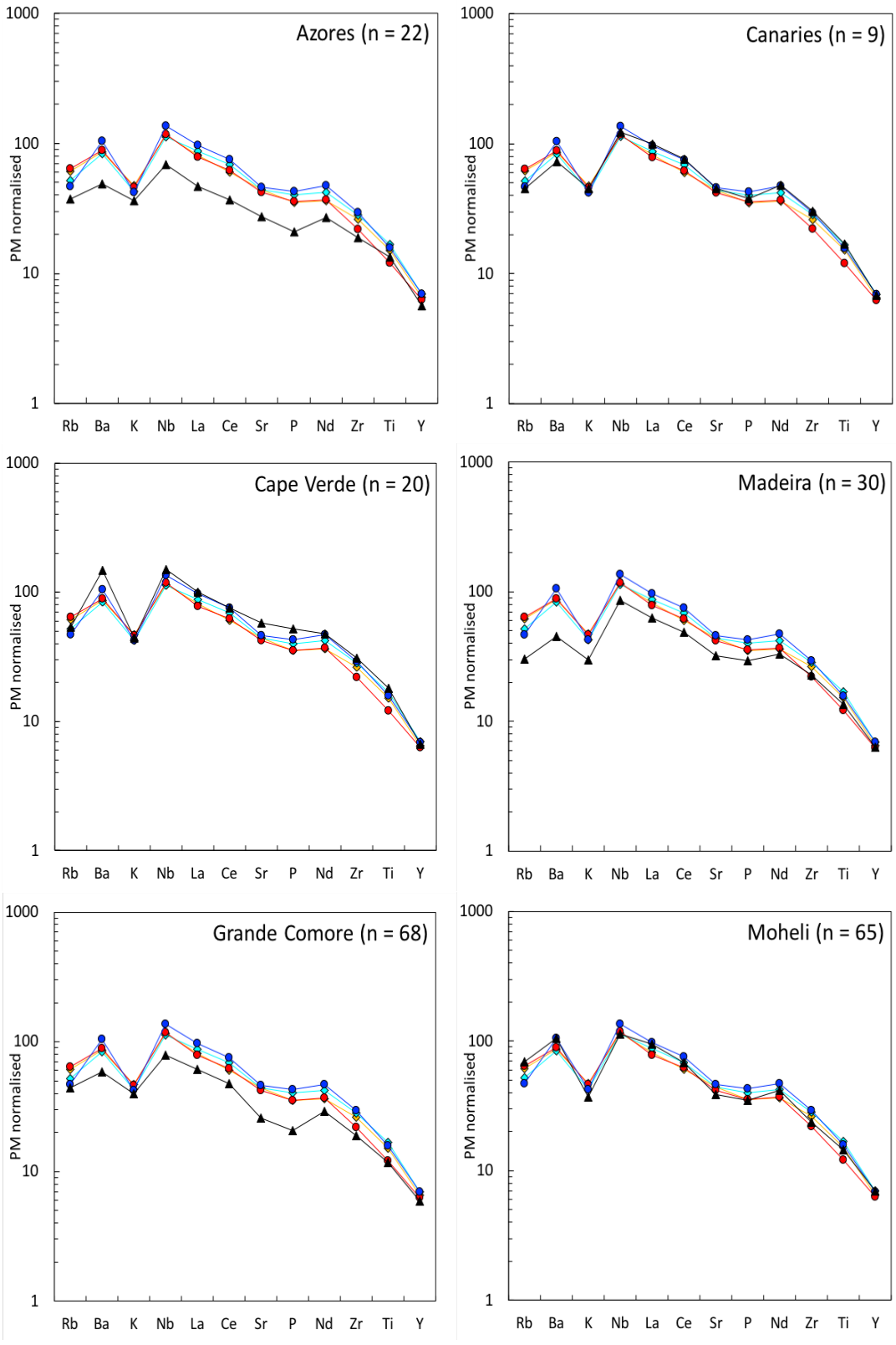

Figure 4-16: Continues on the next page.

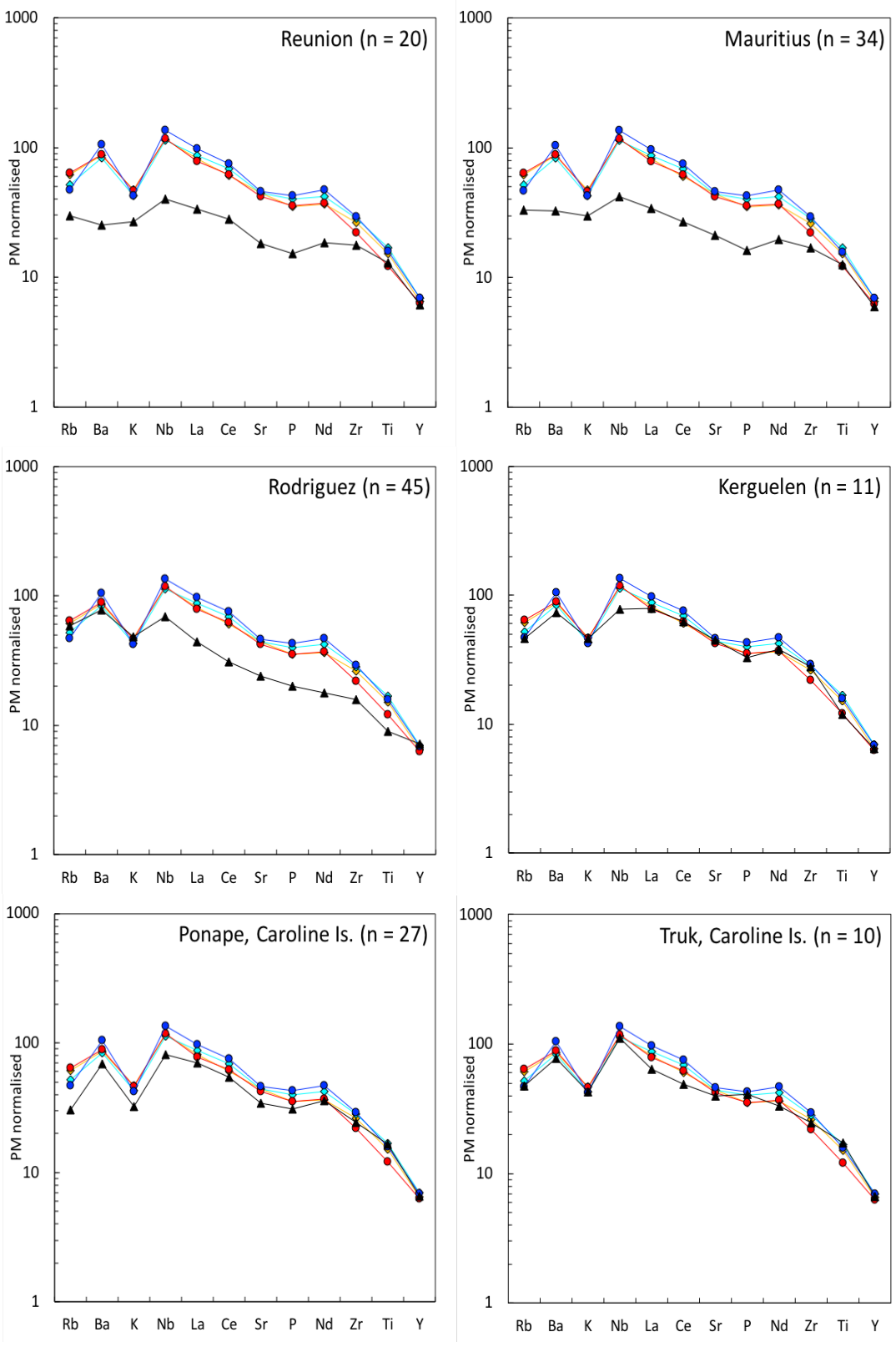

Figure 4-16: Continues on the next page.

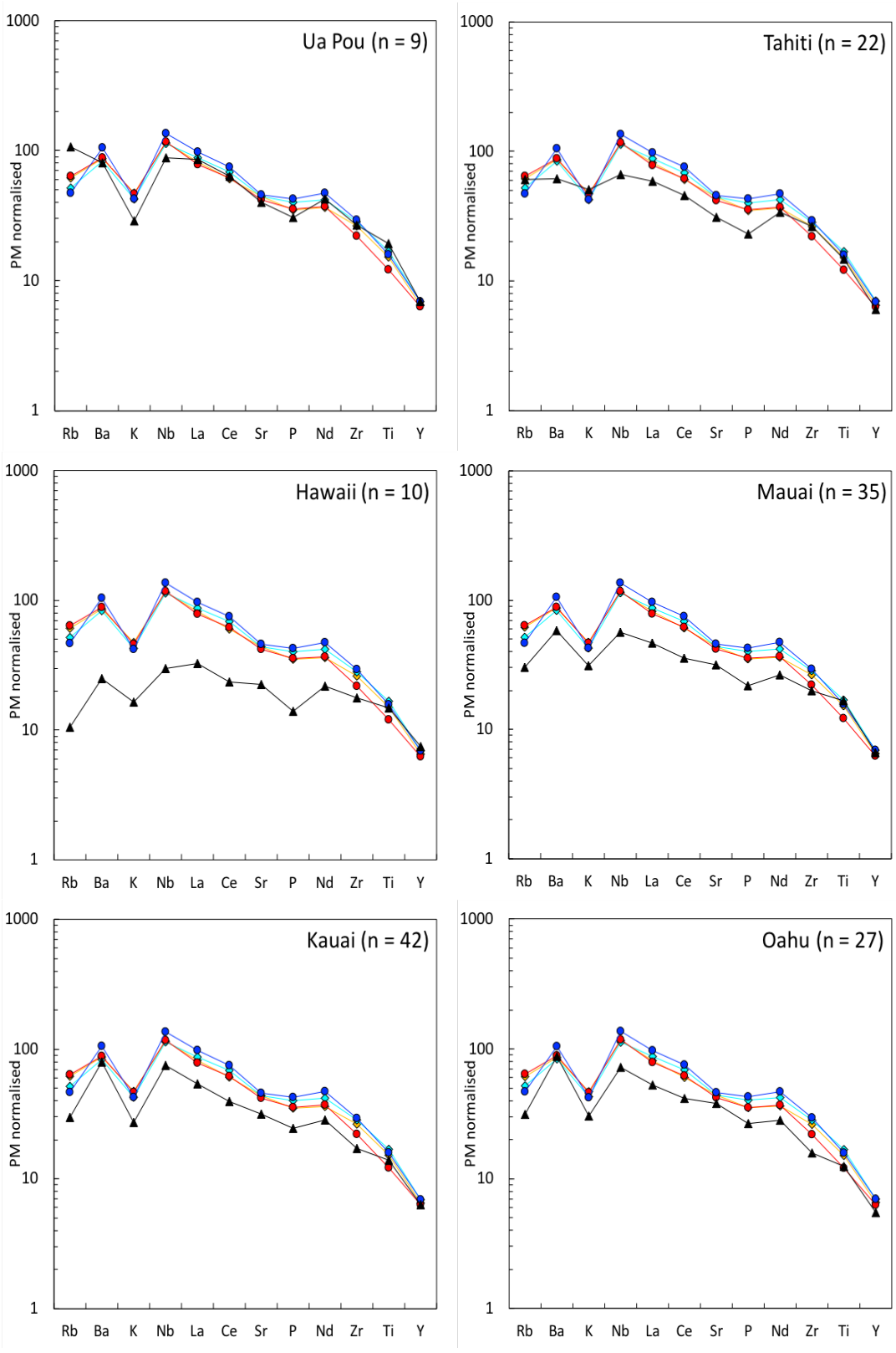

Figure 4-16: Continues on the next page.

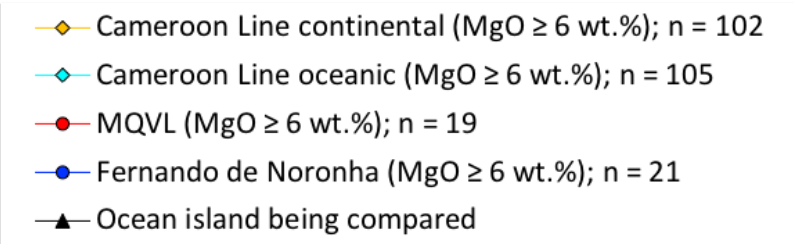

Figure 4-16: Average values of trace element concentrations measured through XRF at the University of Edinburgh for different oceanic islands across the world (Fitton *et al.*, 1991; Fitton, 2007) compared with the Cameroon Line and Northeast Brazil. Only localities with number of samples *n* ≥ 9 were included, but the pattern is the same if localities with fewer samples are also considered. Legend on previous page.

There are also incompatible trace element similarities with intraplate volcanic occurrences in continental Africa. Ratios between highly incompatible elements should be relatively constant at a given magmatic region and evolve along locally distinctive trends (Rollinson, 1993; Winter, 2010). Kampunzu and Mohr (1991) used Zr/Y and Zr/Nb ratios to show how the signatures of different extensional settings in Africa vary, including data from the Western Rift and Kenya Rift valleys, Ethiopian flood basalts, the Afar Rift, and the Red Sea and Gulf of Tajura. In our dataset, trends between these ratios match those from the Western Rift and Kenya Rift valleys, whilst being significantly different from the other African extensional settings (Figure 4-17). This extensional setting is the closest one geographically to the Cameroon Line, and also borders the Congo craton. These similarities are also clear in a multi-element diagram normalised to the Kenya Rift valley (Figure 4-18) as published in Gill (2010). Published isotopic data also indicate greater similarities between the Cameroon Line and Kenya than with other intraplate occurrences in Africa, the Atlantic or other areas of the globe (Halliday et al., 1988; Figure 2 therein). Similarities with both the Western Rift/Kenya Rift and the Canaries suggests that volcanic occurrences that extend across oceanic and continental lithospheres along the African Atlantic passive margin may somehow be associated with the African continental block, and this association has also been maintained on the South American conjugate margin.

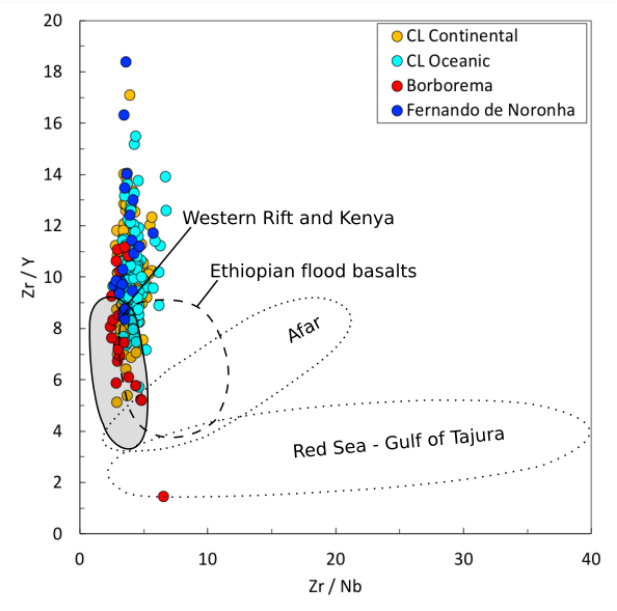

Figure 4-17: Trends of Zr/Y against Zr/Nb in Northeast Brazil and the Cameroon Line compared with those from Kampunzu and Mohr (1991), as published in Winter (2010). The similarities between the two areas and the Western Rift and Kenya Rift valleys in Africa are clear, in contrast to the other extensional localities farther away in Africa.

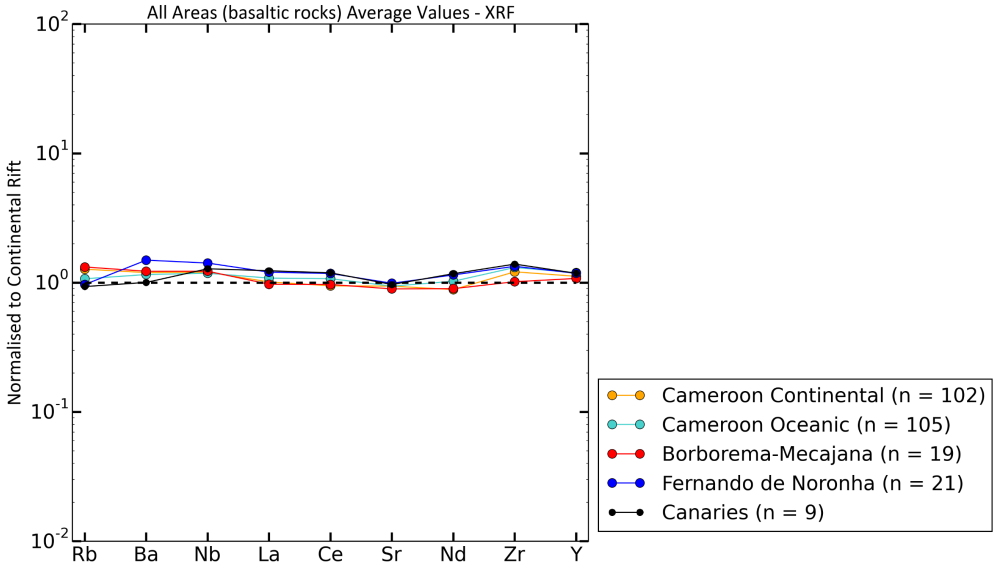

Figure 4-18: Multi-element diagram normalised to basalts from the Kenya Rift valley using data from Gill (2010). The Canaries are also included for comparison.

Highly incompatible trace elements have also been used by Njome and de Wit (2014), who compared ratios between Rb, K, Ba, Th, Nb, La and Zr in basaltic rocks from the Cameroon Line with common mantle and lithospheric reservoirs, namely depleted mantle (DM), primitive mantle (PM), enriched mantle I (EM-I), enriched mantle II (EM-II), high-μ (HIMU) and continental crust (CC). They concluded that subalkaline basaltic compositions (e.g. those reported in Kuepouo et al., 2006; further references

discussed in Njome and de Wit, 2014) matched ratios of enriched mantle (EM) sources and fell outside the range of HIMU, which they interpreted as indicating shallower and higher degrees of partial melting in the continent carrying signatures of lithospheric material, and contrasting with the deeper and smaller melt fractions of alkaline basaltic rocks that fall well within the HIMU range. They also identified EM-II as an almost exclusively continental signature. Similar conclusions were obtained in Chapter 3 from the trace element and isotopic patterns in Northeast Brazil, where higher melt fractions, especially the subalkaline samples from the MQVL basins, have increasingly higher contributions of spinel lherzolite (i.e. shallower sources) and lithospheric material, both in terms of trace elements (i.e. Ba, Nb and REE) and isotopic signatures. Concomitantly, they contrast with the stronger DM signatures and garnet lherzolite contributions amongst alkaline compositions.

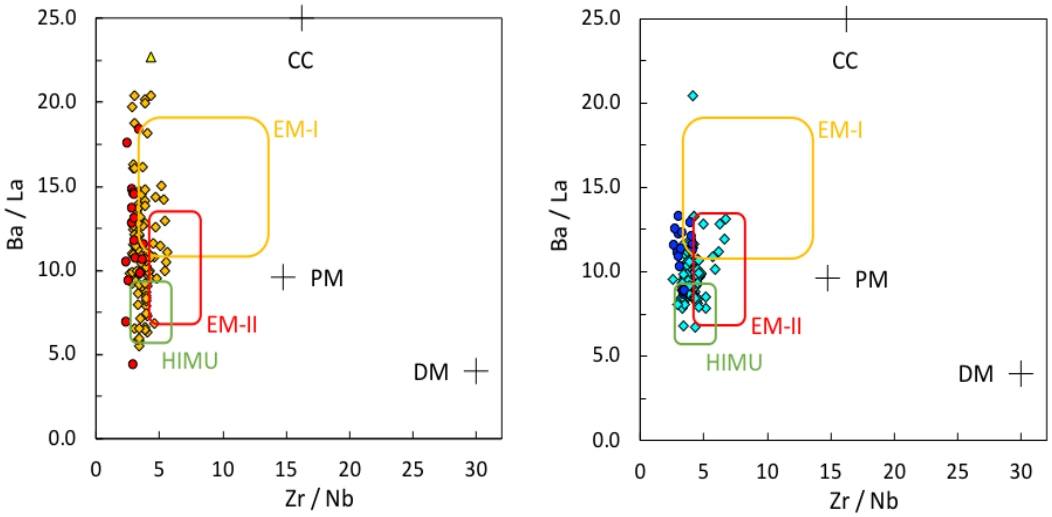

Figure 4-19: Incompatible trace element ratios compared with common mantle reservoirs according to Njome and de Wit (2014). Legend as in Figure 4-11. The Fernando de Noronha basaltic dykes and MQVL basaltic andesites are excluded. *CC = continental crust; DM = depleted mantle; PM = primitive mantle; HIMU = high-μ; EM = enriched mantle*.

Of the elements used in Njome and de Wit (2014), Rb and K have been affected by alteration in our dataset, especially in the oceanic sector of

Northeast Brazil (see above and Chapter 3), which hinders their comparative value. Also, we do not have Th data available for the Cameroon Line. Nonetheless, comparisons between Zr/Nb, Ba/La, La/Nb and La/Ba (Figure 4-19) show overlapping values between Northeast Brazil and the Cameroon Line, highlighting the affinities between the two conjugate margins. Their relationship to mantle reservoir fields also indicate the larger heterogeneity of the two continental sectors, which agrees with the trace element and isotopic data for Northeast Brazil discussed in Chapter 3. It also shows how somewhat higher Zr/Nb ratios on the African side pushes its samples slightly more into the EM fields. Despite these small differences, the data clearly fall within the field of OIB from Fitton (2007), acquired at the same laboratory at the University of Edinburgh, and agrees with the average OIB values published by Sun and McDonough (1989), represented in the diagram by a grey cross (Figure 4-20). The same dataset and the same relationship between La/Nb and La/Ba was also used in Fitton et al. (1991) to distinguish between OIB signatures and those from subduction-modified lithospheric mantle. The overall matching ratios of highly incompatible elements in both conjugate margins indicate a similar source for these lavas, as well as clear OIB characteristics.

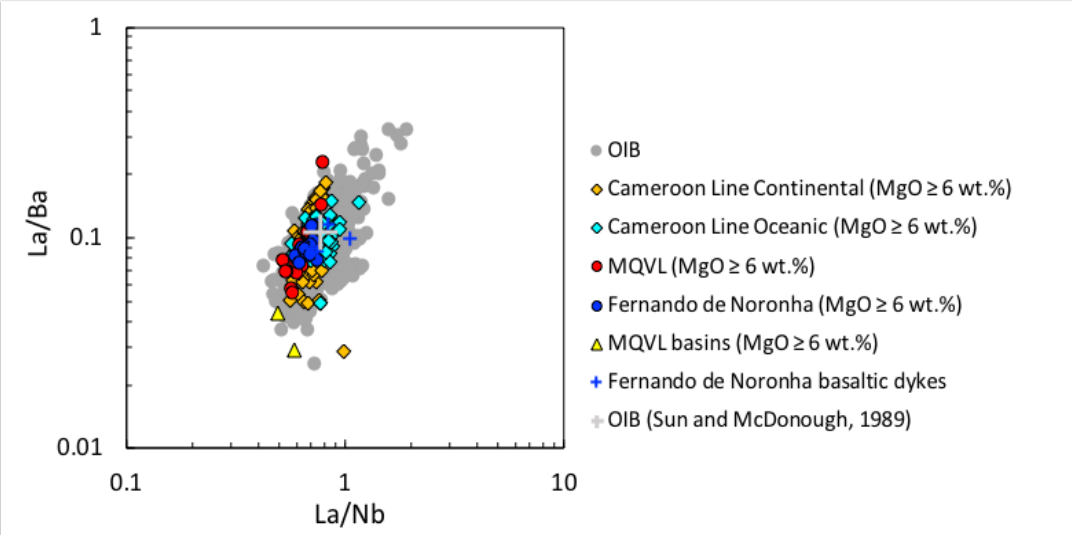

Figure 4-20: Incompatible trace element ratios compared with other OIB data from Fitton (2007), Fitton et al. (1991) and Sun and McDonough (1989). The latter is marked on the diagram by the *grey cross*.

We have discussed in Chapter 3 how magmatism in Northeast Brazil has affected a vertically stratified source, with shallower melts showing a distinct shift in the proportions of Nb content towards lower values. Despite all similarities between Northeast Brazil and the Cameroon Line, this trend only affects the Brazilian samples, especially those from the MQVL basins. Although we do not have the full range of REE data for the Cameroon Line, this may be illustrated by comparing Ce/Y to Ce/Nb, in a similar way to what was done for Northeast Brazil in Chapter 3, and using a MgO threshold of 5 wt.% to increase the selection from the Cameroon Line to a similar range of that of the MQVL basin samples (Figure 4-21). The diagram shows a proportionally significant divergence from the main trend towards high Ce/Nb amongst the MQVL basin samples, but the same trend is absent in the Cameroon Line. These patterns show that the specific context of extensional basins in the MQVL has allowed for assimilation of continental lithospheric material from shallower depths (Chapter 3) to a degree not seen in other areas from both conjugate margins, highlighting the circumstantial nature of differences seen in the MQVL basins. Although some African samples show somewhat higher Ce/Nb ratios, especially in the oceanic sector, they are proportionally much less significant and somewhat scattered, showing no correlation with Ce/Y or a significant shift in the main trend. Since Ce/Y ratios respond to both changes in melt fractions and in the contributions of either garnet- or spinel-lherzolite to the source (i.e. a reflection of depth of melting), it is difficult to assess if the Cameroon Line samples that show relatively higher Ce/Nb correlate with depth in the same way as in Northeast Brazil. A more detailed assessment of the Cameroon Line REE data would be warranted for more definite conclusions to be taken.

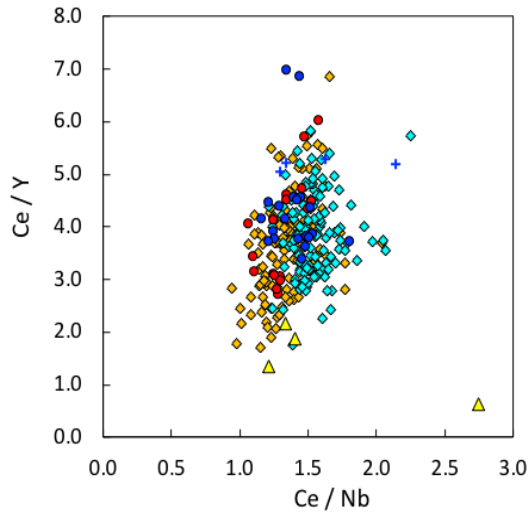

Figure 4-21: Illustration of the shift towards higher Ce/Nb at low Ce/Y amongst the MQVL basin samples, indicating a decrease in Nb content. The same process either absent or negligible amongst samples from the Cameroon Line. Legend as in Figure 4-20.

Phonolites and other evolved rocks

Data for evolved rocks in Northeast Brazil have been discussed in Chapter 3. In the Cameroon Line, evolved rocks are dominated by phonolite in the oceanic sector and trachyte and rhyolite in the continental sector, which suggests some role of continental lithospheric contamination in controlling melt evolution and silica saturation in the continent (Fitton, 1987; Njome and de Wit, 2014).

For the oceanic sector of the Cameroon Line, Fitton (1987) uses the relationship between Zr and Y to demonstrate how the evolution of intermediate rocks is marked by the fractional crystallisation of amphibole. The same pattern occurs in Northeast Brazil (Figure 4-22; Chapter 3). Amphibole-bearing xenoliths dominated by kaersutite and similar to those from Fernando de Noronha have also been reported from São Tomé in the Cameroon Line oceanic sector (Fitton, 1987; Fitton, pers. comm.), which reinforces the affinities between the two conjugate margins and indicates that their similarities extend beyond basaltic compositions. Despite the presence of kaersutite phenocrysts in continental phonolites from Northeast Brazil and the clear evidence for significant amphibole fractionation during their development (e.g. Y depletion), the aforementioned xenoliths are absent

there and have not been reported in the continental sector of the Cameroon Line either, which suggests more pervasive amphibole fractionation in both oceanic sectors than in their continental counterparts. This difference between oceanic and continental sectors has already been discussed in relation to the Northeast Brazil assemblage (Chapter 3) and repeats itself in Africa. Considering the dependence of amphibole fractionation to water vapour pressure in the source, greater access to water in the oceanic sector during melt evolution at shallower depths could be the main control behind this difference (Fitton, 1987).

On the Brazilian side, kaersutite-bearing xenoliths are also rich in sphene, leading to the strong Ta depletion observed in some intermediate and evolved lavas in Fernando de Noronha, and the absence of such a trend in the Mecejana phonolites (Chapter 3). Y is also compatible in sphene. Therefore, stronger Y depletion in both oceanic sectors when compared to the more subdued trends in Mecejana might be due not only to greater degrees of amphibole fractionation in the oceanic islands, but also the added fractionation of sphene in the oceanic sectors on both sides of the Atlantic.

Differences between evolved samples from the two oceanic sectors and Mecejana are also clear in Nb variation diagrams, which show that continental and oceanic trends contrast with one another on both conjugate margins (Figure 4-23). Although we do not have Ta data available for the Cameroon Line, Nb patterns indicate that different fractionation paths between continental and oceanic sectors also repeats itself on both sides of the Atlantic, and are likely related to Ti-rich phases.

In Fernando de Noronha, kaersutite-bearing xenoliths are ubiquitous in intermediate rocks from basaltic trachyandesites onwards, and coronas around kaersutite phenocrysts, observed in phonolite thin-sections, together with reported crystal compositional zoning (Guimarães *et al.*, 1982) indicate that they formed relatively early in the melts' evolutionary sequence (Chapter 3). If the same is true for the Cameroon Line, it shows that similarities between the phonolites in both conjugate margins are not a coincidence but

must reflect similar evolutionary processes that start with virtually identical basaltic assemblages. These processes seem to vary only slightly in the Mecejana volcanic field, and reinforce that despite its location in the continental sector, it is likely to have been affected by the adjacent oceanic fracture zone and oceanic processes.

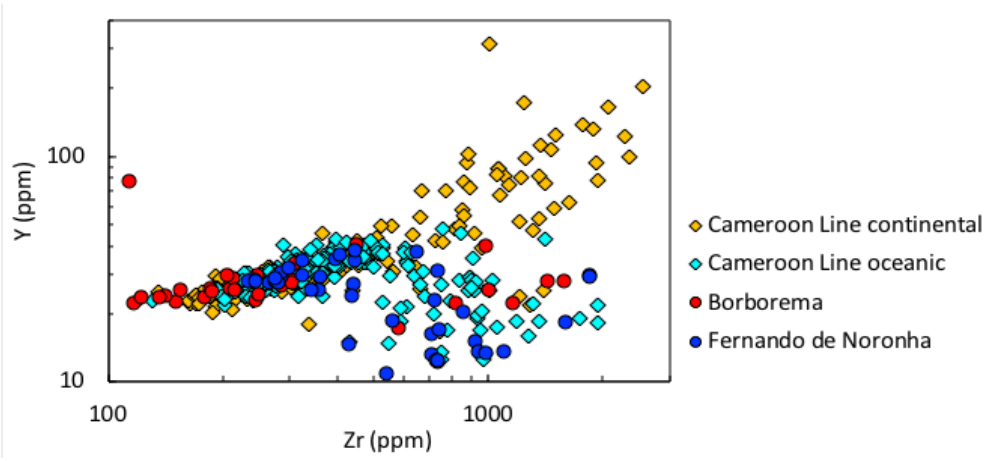

Figure 4-22: Relationship between Zr and Y, indicating the fractional crystallisation of amphibole amongst evolved rocks of all areas, except those from the Cameroon Line continental sector. It is clear that the Borborema phonolites (i.e. from the Mecejana volcanic field) have greater affinity with rocks from the oceanic sectors of both passive margins than with their African continental counterpart. It is also clear how the process of Y depletion is more subdued in Borborema than in Fernando de Noronha.

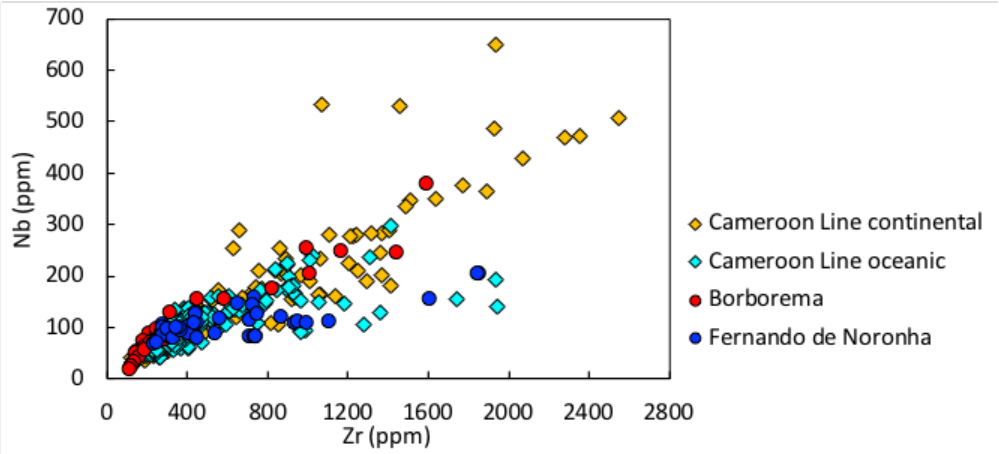

Figure 4-23: Zr variation diagram for Nb. It is clear how the evolution line for both oceanic sectors is marked by relative Nb depletion.

Multi-element and SiO_2 variation diagrams (Figures 4-1, 4-5 and 4-7) comparing both conjugate margins highlight how the low Ti content in the

Northeast Brazil continental sector is exclusive to that area and does not occur on its African counterpart. This difference cannot be the reason behind why kaersutite and sphene fractionation were stronger in the oceanic sector of Northeast Brazil, because the Cameroon Line continental sector does not show such low Ti concentrations, but its Y and Nb patterns indicate no amphibole or sphene fractionation. Instead, differences between both continental and oceanic sectors must play a stronger role.

Despite these small differences, the overall trace element patterns for phonolites is virtually identical for all regions (Figure 4-9). As in the case of basalt, the two sectors of Northeast Brazil also show greater variability between them than their African counterparts, the latter showing greater consistency both in terms of trace element concentrations and ratios. This may be due to differences in the sizes of assemblages. Cameroon Line continental phonolites are represented by only two samples, whilst the Cameroon Line's oceanic assemblage is considerably larger than that of Fernando de Noronha. The most significant difference between the two conjugate margins as two distinct groups (independently of their oceanic and continental characteristics) is the significantly greater Ba depletion and somewhat lower Sr values on the Brazilian side. These elements may be associated with contamination by continental lithospheric material, including sub-continental lithospheric mantle material and crust (Chapter 3; Fitton et al., 1991; Fodor et al., 1998; Sun and McDonough, 1989) and suggest that there could be some influence of continental mantle material (since there is no evidence for crustal contributions to these lavas; Fitton, 1987; Fodor et al., 1998) on the Cameroon Line oceanic sector. The model we propose for synchronous and virtually identical magmatism on the two conjugate margins that will be discussed in Chapter 5 argues for some level of continental influence on the adjacent oceanic sector, and helps to explain these patterns.

Isotopes

According to published radiogenic isotopic data for the Cameroon Line (Halliday *et al.*, 1988, 1990; Lee *et al.*, 1994; Ballentine *et al.*, 1997; Marzoli *et al.*, 1999; Ngounouno *et al.*, 2000; Aka *et al.*, 2004; Rankenburg *et al.*, 2005; Njome and de Wit, 2014), Sr, Nd and Pb isotopic signatures for both the continental and oceanic sectors are dominated by high-μ (HIMU; μ = $^{238}U/^{204}Pb$ ratios) and depleted mantle (DM) sources, but with strong contributions of enriched mantle I (EM-I; i.e. low $^{87}Sr/^{86}Sr$ and low $^{143}Nd/^{144}Nd$) in the oceanic-continental boundary (OCB, which includes Mt. Cameroon, Mt. Etinde and the island of Bioko), and some divergence towards enriched mantle II (EM-II; i.e. high $^{87}Sr/^{86}Sr$ and low $^{143}Nd/^{144}Nd$) that leads to compositions approaching bulk silicate Earth (BSE). The $^{87}Sr/^{86}Sr$ and $^{143}Nd/^{144}Nd$ data are illustrated in Figure 4-24 and compared to Northeast Brazil. More specifically, Figure 4-24 shows that lavas from the continental sector are the most affected by EM-II and the ones that most approach BSE, whilst the oceanic-continental boundary produced the strongest EM-I and HIMU signatures, with relatively little EM-II contributions in relation to other continental localities. HIMU and, to some extent, EM-I signatures decrease away from the OCB, and also away from the Congo craton boundary in the continental sector (i.e. from south to north in the continental hinterland), giving way to patterns lying between DM as one endmember and BSE and/or EM-II as the other. For instance, the Biu plateau shows the weakest HIMU and EM-I contributions (i.e. high $^{143}Nd/^{144}Nd$), whilst the isotopic signatures of the Adamawa/Ngaoundéré plateau clearly lie in the lower end of the continental $^{143}Nd/^{144}Nd$ ratios and approaches the OCB, with the Mandara mountains lying in-between (Figures 4-24 and 4-25). Furthermore, the highest $^{87}Sr/^{86}Sr$ and lowest $^{143}Nd/^{144}Nd$ values (i.e. strong EM-II signature) in the CL continental field (Figure 2-24) are dominated by samples from Bambouto and Oku, well away from the OCB (Figure 4-25). Ballentine et al. (1997) has also demonstrated how the distal oceanic island

of Annobón has the weakest HIMU signatures in the Cameroon Line oceanic sector. Moreover, DM signatures become more significant away from the oceanic-continental boundary along both the continental and the oceanic volcanic lineament according to Pb-isotope ratios (Halliday *et al.*, 1988, 1990). Similar symmetrical patterns pivoting around the oceanic-continental boundary exist also for He isotopes, which become more MORB-like away from it along both the oceanic and continental sectors (Aka *et al.*, 2004).

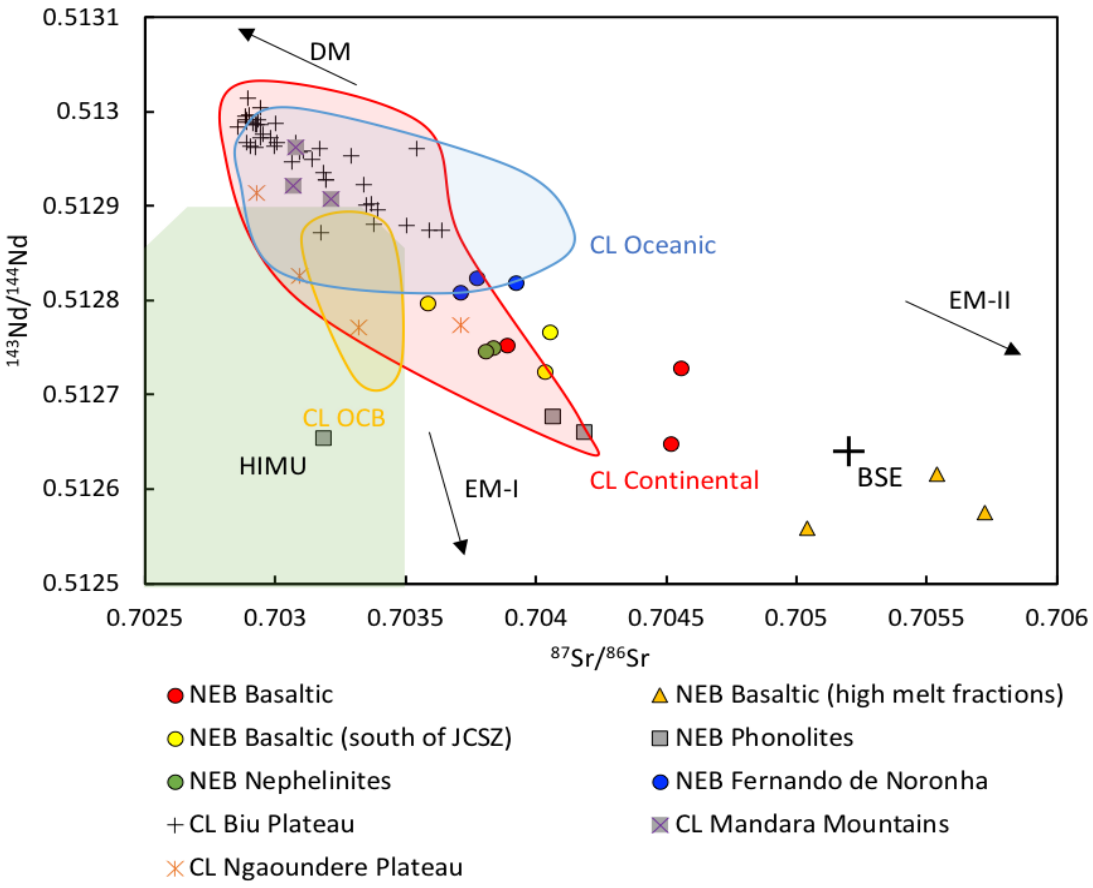

Figure 4-24: Fields of isotopic signatures of the Cameroon Line from other published studies (Halliday *et al.*, 1988, 1990; Lee *et al.*, 1994; Ballentine *et al.*, 1997; Marzoli *et al.*, 1999; Ngounouno *et al.*, 2000; Aka *et al.*, 2004; Rankenburg *et al.*, 2005) subdivided between continental, oceanic and oceanic-continental boundary (OCB), compared to Northeast Brazil (age-corrected values from this study). Samples from the Cameroon Line hinterland are also shown individually (i.e. those around the Adamawa-Ngaoundéré plateau, those from the Mandara Mountains-Kapsiki plateau, and those from the Biu plateau-Jos locality), and show the distinct trends between the south-eastern arm of the Cameroon Line, which lies adjacent to the Congo craton boundary and is isotopically closer to the OCB, and its northern arm, represented by the Biu plateau and showing the weakest EM signatures (see also Figure 4-25). Reservoir domains from Rollinson (1993) and Winter (2010). *CL = Cameroon Line; NEB = Northeast Brazil; JCSZ = João Câmara Shear Zone.*

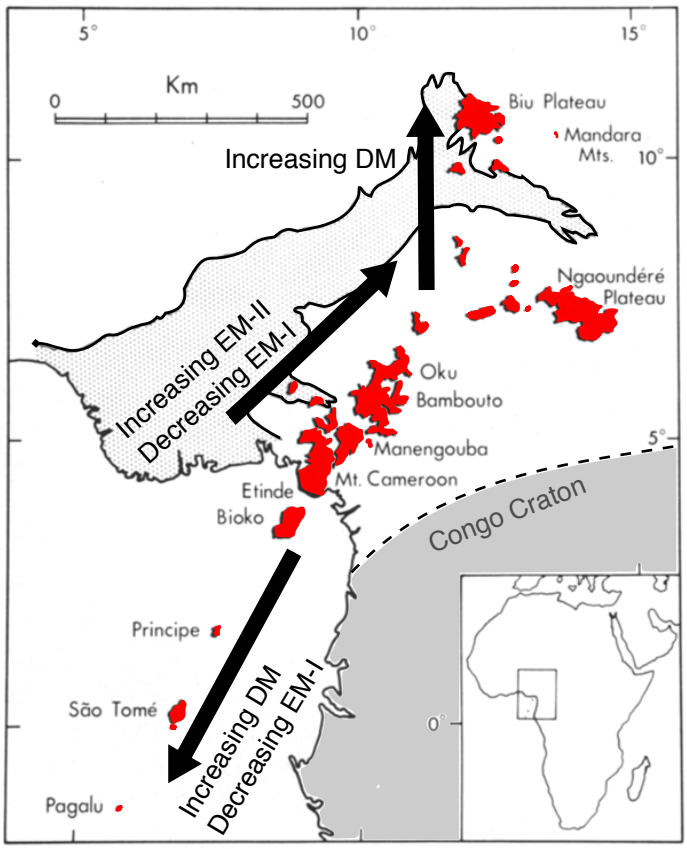

Figure 4-25: Isotopic trends along the Cameroon line. Adapted from Fitton and Dunlop (1985). EM-I signatures focus on the oceanic-continental boundary (OCB), which includes the island of Bioko, Mt. Etinde and Mt. Cameroon (see OCB in Figure 4-24). EM-II signatures become stronger along the continental sector away from the OCB, peaking in Bambouto and Oku. DM signatures become stronger in the continent away from the main axis of the lineament (i.e. the segment between Mt. Cameroon and the Ngaoundéré plateau) towards the Biu Plateau, and into the oceanic sector away from the OCB.

These patterns indicate horizontal variability that seems to correlate with changes in lithospheric thickness and type of lithosphere (i.e. oceanic or continental). The gradual increase in DM signatures away from areas of thin continental lithosphere (i.e. the OCB), and away from cratonic boundaries (i.e. the Adamawa/Ngaoundéré plateau), suggests that melts generated below oceanic lithosphere and, in the case of continental occurrences, away from both the OCB and craton boundary are less likely to tap HIMU or EM material. Simultaneously, shallower and higher melt fractions increase the chances of EM contributions, significantly more so in the continents (Njome and de Wit, 2014), and EM-I concentrates in the OCB. Very similar patterns are also found in Northeast Brazil, where the strongest EM-I and HIMU signatures come respectively from the Macau locality (sample 15BP7-14) and Mecejana (sample 15BP10-23), both at the OCB, and oceanic samples and deep and/or small fractions of continental melts produced the strongest

DM isotopic affinities. Moreover, the high melt fractions in the MQVL extensional basins show isotopic signatures matching BSE and are influenced by EM-II (Figure 4-24; see also Chapter 3).

Horizontal variability suggests a correlation between EM-II and shallower depths in both conjugate margins, although these signatures are proportionally more significant in Northeast Brazil where extensional basins play a larger role and EM-II signatures also correlate with degrees of partial melting. In the Cameroon Line, similar signatures to those from the MQVL basins also affect localised occurrences of transitional suites with tholeiitic affinities in the Bana complex (Kuepouo *et al.*, 2006; Njome and de Wit, 2014). Conversely, the dominance of EM-I and HIMU in the OCB, also found in both conjugate margins, is significantly stronger in the Cameroon Line, but in Northeast Brazil the OCB is represented only by one basaltic sample and the Mecejana phonolites. These trends suggest that the sub-continental lithospheric base is vertically stratified, with EM-II representing a lower, deeper layer, and EM-I and HIMU representing a shallower layer that is associated with lithospheric segments most affect by continental separation (i.e. the OCB).

Nonetheless, it is also important to emphasise that despite EM contributions to isotopic signatures on both margins, the great majority of samples still have lower $^{87}Sr/^{86}Sr$ and higher $^{143}Nd/^{144}Nd$ than BSE, and therefore have relatively depleted mantle compositions. It implies that melting processes are predominantly affecting the asthenosphere but close to the base of the lithosphere or, more specifically, the base of the thermal boundary layer (TBL), with EM-II sources only tapped during proportionally and significantly shallower and/or more pervasive melting, and EM-I tapped mostly in areas directly affected by continental breakup.

Conclusions

Cenozoic volcanism in Northeast Brazil and the Cameroon Line are remarkably similar to each other geochemically, irrespective of their oceanic

or continental setting. Although similarities are stronger amongst primitive compositions, they also extend to evolved samples in both oceanic sectors and the Mecejana volcanic field, the latter located on the oceanic-continental lithospheric boundary of Northeast Brazil. Differences between all these areas are localised, circumstantial and may be accounted for in terms of access to continental material, presence of mantle xenoliths/xenocrysts or subtle alteration (i.e. in the case of Na and highly mobile elements), not requiring distinct sources or processes to be explained. In the case of phonolite, access to percolating seawater may also play a role as it may affect the crystallisation of amphibole.

It was shown in Chapter 3 that magmas from Borborema and Fernando de Noronha must have shared the same sources and processes for the past 35 m.y. The geochemical patterns presented in the previous chapter and discussions in other studies (e.g. Fodor et al., 2002, 1998, Rivalenti et al., 2007, 2000) also show that, in Northeast Brazil, the primitive lavas that are most different from Fernando de Noronha are also those most likely contaminated by continental lithospheric material, namely those from the continental basins. Effects of the continental lithosphere are also behind the differences between intermediate and evolved rocks from the continental and oceanic sectors in the Cameroon Line, where continental intermediate and evolved rocks are dominated by silica saturated and oversaturated compositions due to the influence of continental material (Fitton and Dunlop, 1985; Fitton, 1987). However, the African basaltic samples do not show the same degree of silica saturation and Nb depletion seen for the shallower melts from Northeast Brazil, namely those from the MQVL basins, and do not seem to have had access to the same relatively shallow lithospheric layers during melt generation.

Despite the vigorous magmatism seen in the Brazilian basins, the Cameroon Line, overall, is a much more significant Cenozoic volcanic province than Northeast Brazil, being substantially more voluminous, chronologically continuous and horizontally widespread. More favourable

tectonic conditions (as opposed to compositional, since both continents produced identical lavas) may be the reason for the more intense magmatism along the Cameroon Line, which in turn may have led to the diminished differences between oceanic and continental lavas there. The horizontal variability seen in isotopic signatures and its correlation with lithospheric thickness suggests that more subtle vertical stratification, in accordance with lithospheric thickness, also affects the lavas outside the extensional basin settings, and further highlight the lithospheric and tectonic controls in the two provinces.

The effects of alteration in volcanic rocks from Northeast Brazil (Chapter 3) also find parallels on the African side. The correlation between Na loss, LOI values and potassic character, as well as the same patterns of Rb and K depletion are found in both conjugate margins. Patterns of rock evolution also seem to repeat themselves on both sides of the Atlantic, where the composition of phonolitic melts is strongly influenced by the fractionation of kaersutite and sphene. Isotopic patterns indicate a correlation between access to continental material and access to enriched isotopic signatures, in patterns that vary horizontally according to lithospheric thickness and composition (i.e. continental or oceanic). Similar patterns were discussed for Northeast Brazil in Chapter 3.

Although up until now there have been no definite attempts to directly compare the two conjugate margins, similarities between them have been hinted at in previous studies. For example, Sial (1976b) compared the crystallisation sequence of rocks from the MQVL with Osborn's 1962 scheme for calc-alkaline melts, and pointed out that their general AFM trends indicate some resemblance with Cenozoic lavas from West Africa. Fodor et al. (1998) also drew comparisons between the trace element and isotopic patterns in Northeast Brazil and other continental intraplate provinces such as Tanzania, Pannonian Basin (Hungary), Slovakia, Hannuoba (China) and Cameroon, and their data reinforces the similarities between the Brazilian and African passive margins in comparison with the other regions (Fodor et al. 1998;

Figure 9b therein). Despite their differences with other parts of the world, we have also shown how they still keep some resemblance to oceanic islands along the African Atlantic passive margin, and the Western Rift and Kenya Rift valleys in the African rift system, another intraplate occurrence that may be tapping material from the base of the African lithosphere in the vicinity of the Congo craton.

In the next chapter, we will propose a model to explain synchronous and identical volcanism on both conjugate margins. The model needs to accommodate not only these remarkable similarities, but also the subtle differences between and within the two provinces. For that, the relatively greater differences between oceanic and continental lavas in Northeast Brazil, even though they are still part of the same geochemical, isotopic and chronological continuum, provide a useful starting point and helps to constrain the model.

Chapter 5: A geodynamic model for Northeast Brazil and the Cameroon Line

Introduction

In this chapter we will discuss how the geochemical and chronological patterns established so far may fit into a specific interpretation model relevant for both conjugate margins. First, we will present a general summary of the observations and conclusions about Cenozoic volcanism in Northeast Brazil and the Cameroon Line discussed in this work. Any proposed model has to accommodate these observations. Then we will establish what is the lithospheric structure underneath Northeast Brazil, based on our results and results published elsewhere. This lithospheric structure is the main shared element between the two conjugate margins, and must be considered in order to explain identical volcanism postdating continental separation on both sides. After that, we will propose a model that can accommodate all the observations, including a shared lithospheric structure by both provinces. The model we propose is based on the concepts of edge-driven convection and the characteristics of the lithospheric thermal boundary layer (TBL), which will initially be discussed individually in order to establish clearer definitions of the elements we use in our interpretation. They may then be combined with our data, discussions and conclusions in order to present a conceptual model that, we believe, is applicable to Cenozoic volcanism in both Northeast Brazil and the Cameroon Line. We will further support this model by comparing its predictions with general patterns of volcanism in other localities along the Atlantic Ocean and its passive margins.

Summary of Cenozoic volcanism in Northeast Brazil and the Cameroon Line

The identical nature of volcanism in both conjugate margins is most clear in their trace element patterns and synchronicity. Limited isotopic data

also support the trace element interpretations, despite being relatively restricted in the case of Northeast Brazil, and collected from many different published sources in the case of the Cameroon Line. Effects of alteration and contamination by mantle peridotite xenoliths and xenocrysts in Northeast Brazil are limited and have not affected the main geochemical trend in the region. On the contrary, they account for some of the limited geochemical variability identified in the region and thereby reinforce the circumstantial nature of differences between the different Brazilian volcanic areas (i.e. the Macau-Queimadas volcanic lineament, Fernando de Noronha and the Mecejana volcanic field) and Cenozoic volcanism in Northeast Brazil and the Cameroon Line.

Other internal patterns of geochemical variability in Northeast Brazil are related to differences in depth and degrees of partial melting, changes in silica saturation over time and access to material from the base of the lithosphere, all of which help constrain the controls on magmatism. Such variability is nonetheless generally limited, and primitive lavas still retain strong mantle-like signatures, albeit somewhat enriched, in terms of major elements, trace elements and isotopes. Although some of these patterns of internal variability repeat themselves on both side of the Atlantic, they are more obvious in Northeast Brazil, where the dataset is less diluted due to being more restricted numerically and geographically, and fractional crystallisation being more limited.

More specifically, in Northeast Brazil, basaltic rocks show correlations between depth and degrees of partial melting, which in turn correlate with access to Ba-rich and Nb-poor sources and enriched mantle (EM) isotopic reservoirs. Variability in depth and degrees of partial melting is greater in the continental sector, where melt sources are also potentially shallower. Changes in silica saturation with age of volcanism correlate with intensity of volcanic activity and spatial spread along the lineament. There is also spatial variability in isotopic EM signatures. The effects of localised tectonic controls on petrogenetic processes is also clearly demonstrated by the increase in

melt fractions and decrease in melting depth in the Borborema basins. The basin samples are particularly useful in highlighting the validity of the aforementioned correlations, given that their distinct geological context accentuates some of the geochemical trends but remain clearly related geochemically to the rest of the assemblage. All these results are in good agreement with previous studies, but also go further inasmuch as they bring together the Macau-Queimadas volcanic lineament (MQVL), Fernando de Noronha and the Mecejana volcanic field for the first time, and address Cenozoic lavas from the region in more detail than has been done before.

It is more difficult to identify this level of detail in geochemical variability in the Cameroon Line. The significantly larger dataset seems to dilute many of the patterns. There is also a general lack of relatively extreme cases like those from the Borborema basins that may highlight specific trends. Furthermore, our dataset for the Cameroon Line, despite being quantitatively larger, is qualitatively more restricted, not including ICP-MS data, petrography or new chronological or isotope analyses. Nonetheless, the comparison of XRF analyses conducted at the same laboratory clearly shows how the two provinces are geochemically identical, and comparisons with previously published chronological and isotopic data demonstrate how they are also synchronous and isotopically very similar. When combined with their geographical positioning, it is clear that they must be related, and therefore much of our discussion of Northeast Brazil may be extrapolated to the Cameroon Line.

The lithospheric structure under Northeast Brazil

Temperature, depth and thickness

The relationship between Ce/Sm and Sm/Yb, and the patterns of heavy rare-earth elements (HREE) discussed in previous chapters show that the melting column in Northeast Brazil must extend from the garnet- into the spinel lherzolite zone, creating an assemblage marked by both peridotite

types. However, there is greater participation of spinel lherzolite in the continental sector, where it reaches > 50% (Chapter 3), whilst garnet lherzolite dominates in Fernando de Noronha, where spinel lherzolite contributions are always < 50%. Spinel lherzolite contributions increase significantly within the continental extensional basins (≥ ~70%), but also affect a few localities in the central segment of the MQVL. Overall, these patterns agree with but also expand on previous interpretations of the MQVL lavas that indicate mainly a spinel zone origin, although inferred depths vary according to different analyses. Sial (1976b) suggests a single source at least 64 km deep (~20 kbar), which in turn agrees with later studies that place the origin of local xenoliths in a zone between ~30 and ~65-90 km deep based on estimates from clinopyroxene equilibration temperatures, Ca-in-olivine geobarometers, estimates of local crustal thickness (~30 km) and the fact that only spinel zone peridotite mantle xenoliths have been found in the region (Rivalenti *et al.*, 2000; Fodor *et al.*, 2002). Despite favouring a dominantly spinel lherzolite source for the local lavas, interpretations do not exclude sources within the garnet zone. Klöcking (2017) modelled the melting behaviour of basaltic lavas from Borborema and concluded that they originated at ~70 km depth through adiabatic melting producing < 2% melt fractions, with a thinner lithosphere in the area acting as a significant control. Her analysis does not include the basaltic andesites (Chapter 3). Her results match the lower end of depths calculated from porphyroclastic xenolith equilibration pressures (i.e. through Ca-in-olivine geobarometer) by Rivalenti et al. (2000), who reported pressures 1.9-2.7 GPa (~65-90 km) for the Cabugi peak xenoliths. They also match the lower depth threshold of ~65 km suggest by Fodor et al. (2002) and Sial (1976b), and calculated lithospheric thickness based on shear wave velocities from tomographic models, which suggest lithospheric thicknesses of 70-120 km in the region (Klöcking, 2017; Priestley and McKenzie, 2013; see lithospheric thickness map in Chapter 3, Figure 3-36). For Fernando de Noronha, Rivalenti et al. (2000) calculated

similar but much more homogeneous pressures for porphyroclastic xenoliths (i.e. 2.3 GPa, indicating ~75-80 km).

Temperature profiles based on shear wave velocity calculations from tomographic models indicate mantle potential temperatures of 1280-1330˚C in the region (Priestley and McKenzie, 2013; Klöcking, 2017). Similar results were obtained by Fodor et al. (2002) who, based on pyroxene equilibration temperatures and the lack of garnet lherzolite nodules amongst the MQVL xenoliths, estimated a high heat flow (~70-80 mW/m^2) and geotherm (~12˚C/km) through the spinel lherzolite zone in the area. However, they attributed this to the effects of an alleged Fernando de Noronha plume in the area, given that these are supposedly high values for a continental block. Rivalenti et al. (2000) calculated an average temperature of 1248 ± 19ºC for the 1.9-2-7 GPa pressure range for their porphyroclastic xenoliths from the Cabugi peak, and 1035 ± 80 ºC for the 2.3 GPa for those from Fernando de Noronha. Their results for the Cabugi peak indicate somewhat lower temperatures than the aforementioned estimates, but still indicate higher temperatures in the continental sector, and lithospheric thickness similar to fully developed oceanic blocks (i.e. 100-125 km for oceanic lithosphere older than ~60 Ma).

Overall, there is good agreement between the different interpretations of the local lithospheric structure in Northeast Brazil. Although these models suggest that there is no substantially anomalous hot mantle material in the region, potential temperatures are somewhat elevated and the continental lithosphere significantly thin, potentially even more so than the adjacent oceanic sector. Higher contributions of spinel lherzolite in the continental sector are stronger in the basin environments but are not limited to them, showing that shallower melting and therefore thinner continental lithosphere occurs across the whole MQVL, and is not exclusive to extensional settings. Locations of volcanic centres along the MQVL also do not correlate with surficial tectonic lineaments, such as faults or shear zones (i.e. the only exception being the overall lack of volcanism south of the João Câmara and

north of the Patos shear zones), and these features therefore cannot explain shallower melting outside the basins. Conversely, noticeably higher degrees of partial melting (> ~1% and up to ~3-4%) are unique to the basins. Therefore, because magmatism in the region is independent of extensional structures, there must be an independent sub-lithospheric process generating melt, but which in turn becomes amplified in extensional settings, increasing the degrees of partial melting and silica saturation in these settings. Smaller melt fractions and deeper conditions in Fernando de Noronha point to less vigorous magmatism and less (if any) lithospheric thinning in the oceanic sector. A thinner continental lithosphere must indicate processes postdating continental breakup, because the same processes of thermal equilibration acting under the oceans would also have affected the continental sector since continental separation, and continental lithospheric thickness should be equal to or greater than the adjacent oceanic lithosphere. If we associate this thinner continental lithosphere with magmatism in some way, either as part of the cause or result of it, and considering the geochemical continuity between the continental and oceanic sectors, we may infer that the main focus of magmatism must be located under Borborema (i.e. the continental sector), despite the process continuing under the oceanic lithosphere. This is also supported by the greater range of degrees of partial melting in the continental sector, even when the higher degrees of partial melting of extensional settings are excluded.

A locally elevated geotherm and thin lithosphere has been interpreted as potentially the result of thermal erosion of the base of the continental lithosphere by a supposed Fernando de Noronha plume (Fodor *et al.*, 2002; Rivalenti *et al.*, 2007). A plume model, however, does not fit the chronological data presented in Chapter 2 and in other studies (Knesel *et al.*, 2011), and is not required to explain either the area's geochemical patterns presented in Chapter 3 or the somewhat elevated geotherm. Neither is it required to explain melting, which can be modelled with only a slightly higher local potential temperature for the adiabat (Klöcking, 2017). Furthermore,

given the results presented here and in other studies, the elevated geotherm in the region is not substantial enough to justify a plume and may be more adequately explained by a more subdued type of thermal anomaly and lithospheric thinning.

A plume model is not required to explain the geochemical patterns along the Cameroon Line either, and also contradicts the local chronological development (Fitton and Dunlop, 1985; Fitton, 1987; Njome and de Wit, 2014). In addition, the same aforementioned lithospheric thickness models based on shear wave velocities from tomographic models (Priestley and McKenzie, 2013) also indicate a similarly thin continental lithosphere under the Cameroon Line (Chapter 3, Figure 3-36).

Despite the absence of a plume, explaining continental lithospheric thinning in the region by the presence of another type of thermal anomaly implies a change in the local thermal structure of the mantle that brings the geotherm closer to the solidus both in terms of pressure and temperature. Lithospheric thinning alone, although in principle capable of generating a locally elevated geotherm, cannot explain magmatism in the two regions. For instance, lithospheric thinning inherited from continental breakup fails to explain the delay for the onset of magmatic activity, as the plates would have been subject to thermal re-equilibration since continental separation. The same applies to thinning due to other tectonic processes predating continental separation. Furthermore, these two scenarios also fail to account for magmatism in the oceanic sector, where the lithosphere was not subject to these processes. Lithospheric thinning due to Cenozoic extension in the area is also unlikely. Despite Borborema being one of the most seismically active areas in Brazil, there is no evidence for significant Cenozoic extension in Fernando de Noronha or the MQVL, except for the Oligocene events in the Boa Vista and Cubati basins (Souza *et al.*, 2005, 2013), which have had only localised effects in magmatism. This hypothesis also fails to explain synchronous and identical volcanism in the African conjugate margin, where, in addition, evidence for extension is also lacking (Fitton, 2007; Reusch *et al.*,

2010; Njome and de Wit, 2014). Lithospheric basal erosion by gravitational instability and material breaking off from its base could potentially generate synchronous melting by asthenospheric upwelling on both conjugate margins, considering that lithospheric instabilities could occur on similar timescales after continental separation. However, this model fails to explain their identical geochemistry, as it implies a source decoupled from the lithosphere.

Vertical and horizontal compositional heterogeneities

Vertical variability in the source of lavas in Northeast Brazil is not limited to changes between garnet- and spinel lherzolites. The evidence presented in previous chapters also demonstrate some degree of vertical stratification related to incompatible trace elements. The gradual increase in Ba content with increasing contributions of spinel lherzolite at the source and, to a lesser extent, with increasing degrees of partial melting, together with the sharp shift in Nb content at high proportions of spinel lherzolite contributions, both within and outside the continental basins (Chapter 3), also indicate a mantle source vertically stratified compositionally. The patterns suggest that shallower melts (i.e. within the spinel zone) had access to sublithospheric domains that were imprinted by previous subduction events (low Nb relative to similarly incompatible elements) at some point in their history, and sources generally more enriched in highly incompatible trace elements (increasing Ba content). Conversely, deeper melts show patterns closer to asthenospheric mantle signatures and depleted mantle. Rivalenti et al. (2007, 2000), through the analyses of lithospheric mantle xenoliths, conclude that deeper specimens from both the continental and oceanic sectors show metasomatism that is coeval with the emplacement of the Northeast Brazil Cenozoic lavas, but, in the continental sector, shallower specimens carry evidence from older metasomatic events.

Vertical variability in the lithosphere may also be inferred from the correlation of enriched mantle (EM) isotopic signatures with tectonic context

and lithospheric thickness in both conjugate margins: i.e. the extensional basins in Northeast Brazil, proximity to the Congo craton in the Cameroon Line, and distance from the oceanic-continental boundary (OCB) in both provinces. Both regions, although these patterns are seen more clearly in the Cameroon Line (Chapter 4, Figure 4-25), show decreasing EM-I signatures away from the OCB farther into both the oceanic and continental sectors, increasing depleted mantle (DM) signatures farther into the oceanic sectors, and an increase followed by a decrease in EM-II influences towards the continental hinterland. Hence, vertical variability also translates into horizontal patterns as it correlates with lithospheric thickness.

In Northeast Brazil, decreasing EM-II continental signatures start south of the João Câmara Shear Zone (excluding basin samples), whilst in the Cameroon Line it happens north of the Adamawa plateau, in the Mandara mountains and the Kapsiki and Biu plateaus (Chapter 4; Figure 4-25). These centres also produced the strongest isotopic DM signatures in both continental sectors. They are also the volcanic occurrences located farther into the continental hinterland (e.g. sample 15BP1-1 in the MQVL and the Biu plateau in the Cameroon Line), and away from what appear to be the main magmatic centres of both provinces, and away from their respective OCBs.

Although only one sample from the OCB in Northeast Brazil has been analysed (15BP7-14), it produced a distinctively strong EM-I type signature, as well as representing the shallowest and highest degree of melting in the whole assemblage (i.e. > ~90% spinel lherzolite contributions to the source and ~4% melt fraction according to modelled Ce/Sm and Sm/Yb relationships; Chapter 3). In the Cameroon Line, the OCB comprises Bioko, which is an island that abuts the continental shelf and is the closest oceanic occurrence to the continental block, and the continental volcanic centres along the coast (i.e. Mt. Cameroon and Etinde), and it is remarkable that they also produced strong EM-I signatures (Halliday *et al.*, 1990; Njome and de Wit, 2014), similarly to the patterns seen in the OCB of Northeast Brazil.

Conversely, DM signatures become increasingly dominant away from the OCB along the African oceanic chain, and are also the dominant signatures amongst the Fernando de Noronha basaltic samples. The greater similarities between Fernando de Noronha (~350 km off the Brazilian coast) and the Cameroon Line oceanic islands that are farthest from the continental block (i.e. Annobón and São Tomé, ~480 km and ~710 km off the African coast, respectively; see Chapter 3), including their stronger DM isotopic signatures, indicate how the more vigorous magmatism in the African side may have extended its OCB influences farther, causing seamounts closer to the continent (i.e. Bioko) to retain similarities with continental occurrences.

The above patterns suggest that volcanic occurrences increasingly farther from areas of more intense magmatism are less likely to tap shallow enriched sources and are isotopically more similar to DM. Furthermore, horizontal variability in EM signatures also seem to reflect vertical variability in both continental sectors, with the nature (i.e. EM-I or EM-II) and the degree of EM influences changing according to lithospheric thickness and tectonic context. For instance, in the Cameroon Line, the isotopic differences between the Adamawa plateau (strong EM-II) and the OCB (strong EM-I) must also reflect differences in lithospheric thickness since they are respectively the areas least and most affected by continental separation. The same applies to the central segment of the MQVL (strong EM-II) and the Brazilian OCB (strong EM-I). The vertical variability of isotopic influences is also highlighted in the shallower melts of the Borborema basins, although these patterns are also affected by the larger degrees of partial melting in these localities, which must also reflect greater assimilation of lithospheric material as well as shallower depths.

Proposed model

A model for Cenozoic volcanism in the two conjugate margins needs to accommodate both the similarities and individual internal variability of the

two provinces. It should also account for the lithospheric structure discussed above. We propose a model that combines the concept of edge-driven convection, specifically in the mantle underlying the continental block, a thin continental lithosphere and the rheological and compositional characteristics of the subcontinental thermal boundary layer (TBL). We argue that the rheological characteristics of the TBL must lead to distinct, albeit limited, compositional characteristics in the timescales considered here. In other words, magmatism results from the effects that the continental lithospheric morphology may have on the thermal structure of the underlying mantle, and the rheological and compositional vertical stratification at the lithospheric base, including its underlying TBL. We will demonstrate that combining these elements can account for the time delay in the onset of synchronous volcanism in both conjugate margins since continental separations, their matching geographical positions and their identical geochemistry, as well as continental lithospheric thinning through thermal erosion and a locally elevated geotherm, thereby agreeing with both our analyses and other studies.

Edge-driven convection

The concept of edge-driven convection as applied to mantle dynamics refers to the convection cell formed as a result of horizontal temperature gradients between the asthenosphere and the lithosphere (Foulger, 2010). When asthenospheric material abutting colder lithosphere cools and sinks, it causes the upwelling of hotter material to take its place, and thereby triggers a convection cell that is coupled with the initial lateral temperature gradient. It was initially explored as an attempt to explain the formation of continental flood basalts (CFB) during adiabatic melting (Mutter *et al.*, 1988; King and Anderson, 1995, 1998), through the proposition that a convection cell forms in the lateral temperature gradient between upwelling asthenosphere under thinned lithosphere and its lateral contact with lithosphere of original thickness. The result would be the rapid circulation of fertile material through

the melting zone under extensional settings, allowing substantially larger quantities of magma to be generated than simply through adiabatic upwelling. Subsequently, the model expanded to include the effects of the convection cell on the local heat flux, whereby thermal anomalies may form at zones of more rapid upwelling and thereby affect the production of melt (Keen and Boutilier, 1995; King and Anderson, 1995, 1998; King and Ritsema, 2000). Keen and Boutilier (1995) have calculated that heat flux can be up to 8% higher under continental terranes affected by edge-driven convection during a rift stage. In these studies, melt production is often modelled numerically according to the model developed by McKenzie and Bickle (1988), in order to determine if melting will occur and how much melt will be produced under specific temperature and pressure conditions, given the characteristics of the local geotherm and solidus. Such thermal anomalies are sometimes also referred to as 'hotspots' (e.g. Almeida, 2006) but should not be confused with the same terminology used for deep mantle plumes. By considering heat flux, the edge-driven convection model started to be applied to the lateral temperature gradient created by large thickness variations along the lithosphere, such as between continental and oceanic, and cratonic and non-cratonic terranes (King and Anderson, 1998; King and Ritsema, 2000; King, 2005), and its effects on dynamic topography and lithospheric basal erosion (Vogt, 1991; Demidjuk *et al.*, 2007; Sacek and Ussami, 2013; Sacek, 2017).

By definition, edge-driven convection implies some delay between the establishment of the morphological conditions for the formation of a convection cell, and the full establishment of a localised thermal anomaly. King and Ritsema (2000) estimate that a thermal anomaly should already be present ~50 m.y. after the formation of the lithospheric morphological conditions, and peak between 80 and 100 m.y., with flow gradually decreasing in vigour after that. Their results are in remarkable agreement with seismic tomographic models for the mantle under the South American and African Atlantic passive margins. King and Anderson (1998) estimate

that edge-driven flow becomes dominant 40-60 m.y. after the initial thermal disturbance, although time also depends on the magnitude of the disturbance. In this case, the disturbance is defined as changes to the local thermal structure that will trigger the convection cell, such as the formation of the temperature gradient itself or changes in the magnitude of an already existing gradient. Demidjuk et al. (2007) estimates a time delay just under 40 m.y. for the onset of edge-driven convection in the Newer volcanic province in South Australia, using the methods from King and Anderson (1998). Models of dynamic topography based on edge-driven convection also argue for oscillatory patterns on a scale of ~10 m.y. in the upwelling caused by the convection cell (Keen and Boutilier, 1995; Demidjuk *et al.*, 2007; Sacek and Ussami, 2013; Sacek, 2017).

Another important effect of edge-driven convection is the potential erosion of the lithospheric base. The model by Sacek (2017) shows how subcontinental edge-driven convection may have little impact on highly viscous cratonic keels (i.e. cold, old and potentially depleted), but may erode the base of somewhat less viscous lithosphere under mobile belts (i.e. warmer, younger and potentially enriched). Lithospheric basal erosion is accompanied by upwelling of warmer asthenosphere.

Thermal boundary layer

The TBL is a rheological layer between the asthenosphere and lithosphere whose intermediate rheology precludes a clear-cut boundary between the lithosphere and the asthenosphere (Anderson, 1995). As a concept, it has been formally developed by Parsons and McKenzie (1978), who define the TBL as a layer of small-scale convective instabilities that form the transition from the advective to the conductive geotherm in the mantle, and developed further by McKenzie (1989) and McKenzie and Bickle (1988). In this framework, the lithosphere and the asthenosphere are defined in terms of their dominant mode of heat transport (i.e. conduction and advection, respectively). Conversely, although dependent on the thermal

structure of the lithosphere and the asthenosphere, the TBL is defined in terms of rheology as a layer that is not fully static to transport heat exclusively by conduction, but is not moving vigorously enough to be fully advective, showing both forms of heat transport and comprising parts of both the lithosphere and the asthenosphere depending on whether conduction or advection is the dominant process (Figure 5-1). The equations used to define these structures are given in McKenzie and Bickle (1988) and presented in Appendix D. They show the strong dependence of the structure of the TBL, including its thickness and temperature variability, to the surrounding thermal structure, which includes the characteristics of the lithosphere and the asthenosphere, and the local heat flux. Therefore, the base of the lithosphere contains a layer that, although part of the lithosphere, is not fully permanent, is rheologically unstable and highly sensitive to the thermal structure of the upper mantle. Meanwhile, the top of the asthenosphere contains a layer that is moving more slowly than its main convecting body. It has been estimated that the movement of the TBL precludes the development of enriched isotopic signatures as found in the lithosphere, which may take between 100 to 1000 m.y. to form (McKenzie and Bickle, 1988; McKenzie, 1989).

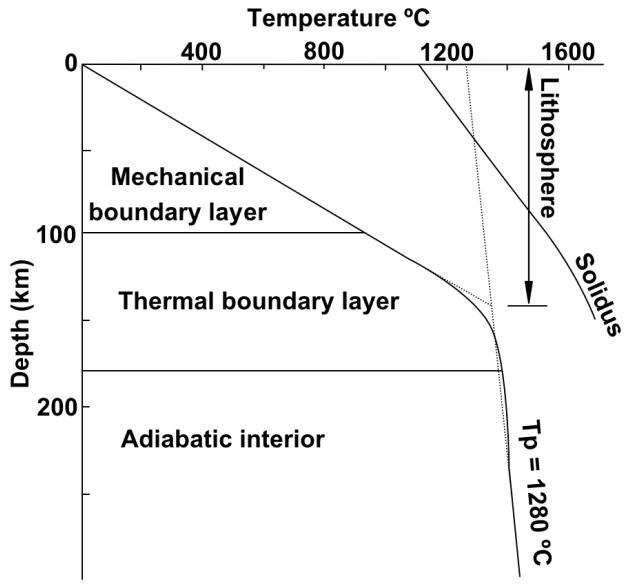

Figure 5-1: Geotherm in relation to the lithosphere and the upper mantle boundary layers (i.e. mechanical and thermal). Adapted from Mckenzie and Bickle (1988).

The point where the mantle shifts from advective to conductive behaviour is controlled by the steady-state equilibrium of the amount of heat input at the base of the convective layer, and the output at the top of the conductive layer. As the lithosphere cools, the mechanical (rigid) boundary layer increases in thickness until the amount of heat lost through the lithosphere by conduction is equal to the amount of heat delivered to the base of the lithosphere by advection. In the oceanic environment, this means a lithosphere 125 km thick or slightly less (Parsons and McKenzie, 1978; McKenzie and Bickle, 1988). For the continental lithosphere there is great variability between different continental terranes, but values ~200-250 km are often used (McKenzie, 1989; Anderson, 1995; King and Ritsema, 2000; King, 2005). Estimates for the thickness of the TBL based on these values range from 30 to 80 km (Parsons and McKenzie, 1978; McKenzie and Bickle, 1988). However, equations in Appendix D show how an increase in the heat flux affects the Rayleigh number in a way that decreases the thickness of the TBL and increases the magnitude of its temperature variability. Hence, thinning the TBL means that some of its material must return to the convecting asthenosphere after a potentially long period of sluggish movement (i.e. 10s to a few 100s of m.y.) and potential coupling with the overlying plate. A qualitative comparison with Figure 5-1 also shows how a thinner TBL and greater magnitude of temperature variability may push the geotherm closer to the solidus.

Although the TBL will be the first layer to cross the solidus during melting, its condition as an intermediate rheological layer is rarely explicitly considered by geochemists, leading to confusing and sometimes contradictory definitions that lump it together either with the lithosphere or the asthenosphere depending on convenience, or treat is as the ‘weak’ and/or ‘hot’ base of the lithosphere (Anderson, 1995, 1998). However, the TBL must be a geochemical reservoir that is distinct from the mechanical lithosphere and the adiabatic asthenosphere, especially in Phanerozoic timescales, since it is not fully permanent but neither does it flow in the same rate as the

asthenosphere. Therefore, it will not be fully stirred like the asthenosphere nor will it accumulate the effects of enrichment over long periods of time like the lithosphere, but it will show the short-term effects of relatively recent enrichment processes. For instance, despite its limitations in developing distinct isotopic signatures, the Cenozoic TBL under continents is likely to carry the effects of metasomatism and enrichment processes caused by small-scale mantle melting (e.g. carbonatites) or subduction zones that were active at least in the Mesozoic and Late Palaeozoic. Thus, the TBL's position as an intermediate layer in the mantle thermal structure and rheology may also translate into intermediate levels of enrichment, placing it between the lithosphere and the asthenosphere. Ultimately, we argue that the TBL should be more clearly defined in terms of composition by geochemists, despite the difficulties in separating it from the underlying asthenosphere or the overlying lithosphere. Therefore, we use the term TBL to mean neither the lithosphere nor the asthenosphere, but an intermediate layer that is also impermanent and an open geochemical system, being affect by enrichment events, but not retaining their effects over long periods of time as the lithosphere.

Due to its unstable nature, intermediate rheology and dependence on the thermal structure of the upper mantle, the TBL may be pushed into more viscous or more ductile behaviour according to the surrounding thermal conditions. The most significant variable in the rheology of the upper mantle is temperature (Keen and Boutilier, 1995; McKenzie *et al.*, 2005; Priestley and McKenzie, 2006), and therefore changes in thermal conditions may cause the continental sublithospheric TBL to slowly start moving if it becomes warmer. The initial movement of a warm TBL, before it is absorbed by full mantle convection, would be lateral, since it cannot move upwards due to the presence of the mechanical boundary layer. Its recent warming and, in the case of our model, the presence of the upwelling branch of a convection cell would also hinder downwards movement. Lateral movement would allow it to extend underneath the oceanic lithosphere. The exposure of a somewhat enriched TBL to higher temperatures may potentially also cause

melting if the lithosphere is thin enough, which may eventually occur if it is already thin to begin with and becomes further eroded by this process. Potential melting may also occur if the enriched TBL moves towards thinner lithosphere.

Discussion

Subcontinental leakage

The variability of present-day lithospheric thickness along the South American and African passive margins has been illustrated in Chapter 3 (Figure 3-36), using the model given by Priestley and McKenzie (2013). Edge-driven convection cells established at the thickness gradient between the oceanic and continental lithospheres have been proposed as a model for several oceanic islands along the South American and African passive margins (Vogt, 1991; King and Ritsema, 2000; Almeida, 2006; King, 2007). Yet, these interpretations fail to explain why only certain places along the margins produce volcanic islands. They also rely heavily on the thickness gradient between oceanic lithosphere and continental cratons. However, superimposing the distribution of cratons, adapted from Heilbron et al. (2008), Priestley et al. (2008) and Priestley and McKenzie (2013), over a satellite image shows that, along the South American and African Atlantic passive margins, seamounts are completely absent where oceanic lithosphere abuts continental cratons, and instead only occur aligned with continental mobile belts surrounding cratons (Figure 5-2). More specifically, seamount chains along both the South American and African Atlantic passive margins tend to develop in alignment with adjacent continental sutures between cratons and mobile belts.

Such correlation between seamounts along the Atlantic passive margins and their adjacent continental terranes is striking. There simply aren't any seamounts where cratons abut the oceanic lithosphere, but they suddenly appear again precisely where cratons end. These patterns are very

obvious in satellite images (Figure 5-2) but have never been considered in any discussion of intraplate volcanism, despite the long noticed pattern of continental large igneous provinces (LIPs) concentrating around craton margins (Menzies, 1992; Anderson, 1995, 1998, King and Anderson, 1995, 1998). Although there could be some uncertainty about the exact position of cratons in South America and Africa, surface geological mapping and interpretation of seismic data are consistent, and errors would not be in a scale that affects the patterns in Figure 5-2. Therefore, seamount distribution in the equatorial and south Atlantic seriously undermines the idea that edge-driven convection cells at oceanic-cratonic lithospheric thickness gradients may be responsible for oceanic intraplate volcanism, and shows that even if edge-driven convection happens in these localities, it is not capable of generating magmatism. For example, the Bermuda rise along virtually the entire North American east coast has been associated with edge-driven convection at the margins between oceanic lithosphere and the North American shield, but only has the Bermuda seamount and the New England seamount chain as volcanic occurrences, and the latter is often attributed to a deep mantle plume (Vogt, 1991) despite the problems with such interpretation.

Alternatively, we propose that edge-driven convection may work as a source of magmatism if it operates entirely under the continental lithosphere, on the thickness gradients between cratons and younger mobile belts. This arrangement exposes a potentially enriched and more fusible subcontinental TBL to a thermal anomaly and may cause it to flow and ‘leak’ sideways towards shallower depths under thinner lithosphere, such as oceanic basins. In the latter case, the thickness gradient between where the flow starts and where it moves to does not have to be significant. Pushing the TBL to shallower depths and/or higher temperatures may also lead to melting depending on the degrees of such changes and local levels of enrichment. The proposition that the Cameroon Line is triggered by an exclusively subcontinental edge-driven convection cell that leads to lateral movement of

material towards the oceanic lithosphere was made by Reusch et al. (2010), based on exclusively seismic analyses of the mantle underneath the volcanic chain. It is not unreasonable to assume that a similar process is affecting Northeast Brazil, since it represents the continuation of the same lithospheric structure. This proposition is further supported by the identical nature of volcanism in both provinces. A magma source in the subcontinental TBL would also explain the coupling of material with the overlying lithosphere since continental breakup and its subsequent flow from continent to ocean when mobilised by a thermal anomaly that, according to edge-driven convection models, should come into effect 30-50 m.y. after continental separation (Figure 5-3).

The notion that enriched material may flow at the base of the lithosphere towards thinner domains is not new (Fitton, 1987; Sleep, 1996; Ebinger and Sleep, 1998; Foulger, 2010), but the concept of upward drainage is usually done in association with deep mantle plume material. The concept is that upwelling hot material makes use of the topographic relief at the base of the lithosphere, creating patterns of channelized flow and potential ponding of enriched material. Ebinger and Sleep (1998) and Sleep (2003, 1996) have examined the possibility that magmatism in the Cameroon Line and Northeast Brazil are the result of very distal outpourings of supposed plumes under east Africa and the Paraná LIP, respectively. However, these propositions cannot account for synchronous and geochemically identical volcanism on both conjugate margins. Measurements of anisotropy along the Cameroon Line have been used in an attempt to identify flow patterns within the low-velocity anomaly, but results are mixed. Adams et al. (2015) argued that anisotropy is mainly oriented N-S, which could be evidence for lack of lateral flow but would support edge-driven convection abutting the Congo craton. Elsheikh et al. (2014) obtained opposite results in a more detailed anisotropy analysis, indicating a strong WSW-ENE flow along the lineament. Koch et al. (2012) find less clear results, but show the predominance of roughly N-S directions but also with

NE-SW elements. If edge-driven convection is active and the TBL is being mobilised to flow, it would bring material both against the Congo craton and along the Cameroon Line, potentially creating anisotropy in both directions at different depths, or anisotropy results that might overprint each other, which seems to be the case.

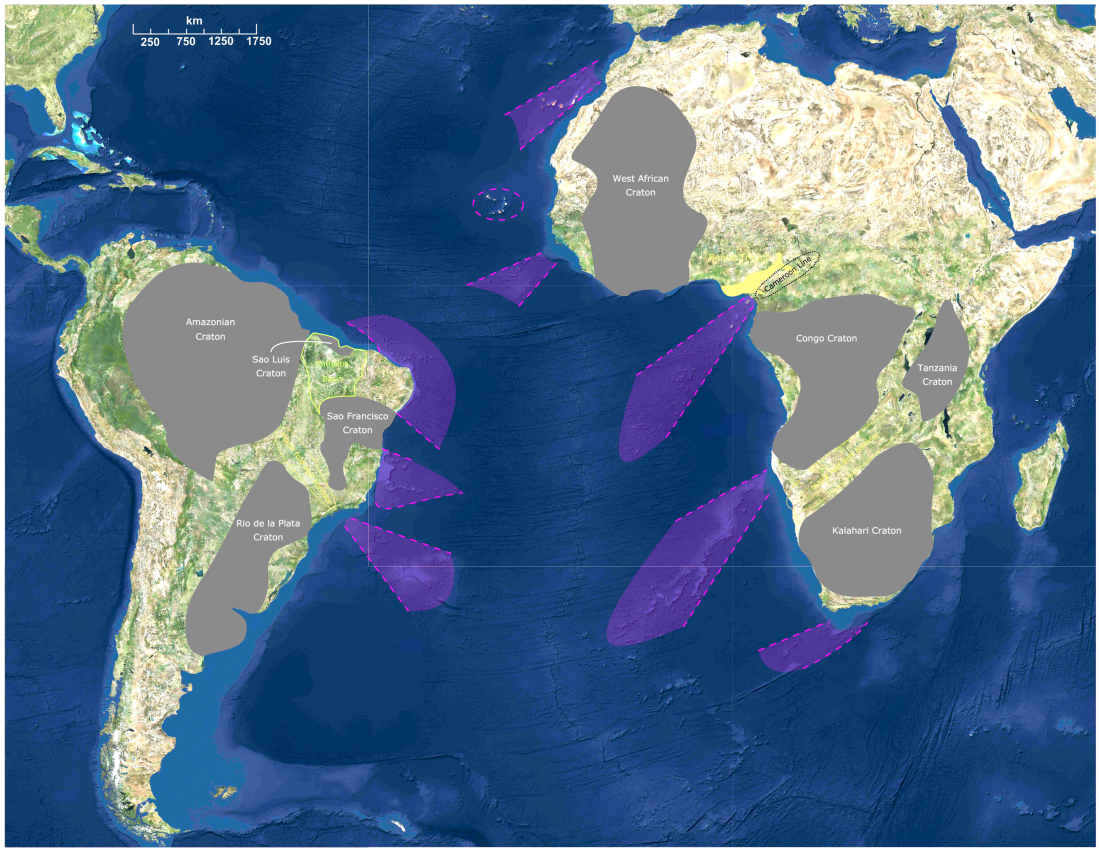

Figure 5-2: Relationship between seamounts (highlighted in *purple*) and cratons (*grey*) along the South American and African Atlantic passive margins. It is clear how seamount occurrences avoid cratons, and instead align with the suture zones between cratons and their surrounding terranes. All seamounts connected to the continental block follow this pattern, and the clear-cut relationship with adjacent cratonic terranes is particularly obvious in the seamount distribution along the Brazilian east coast. Cape Verde is also highlighted due to its size, but it is not connected to the continental passive margin by a seamount chain and may result from a different process than the model we propose.

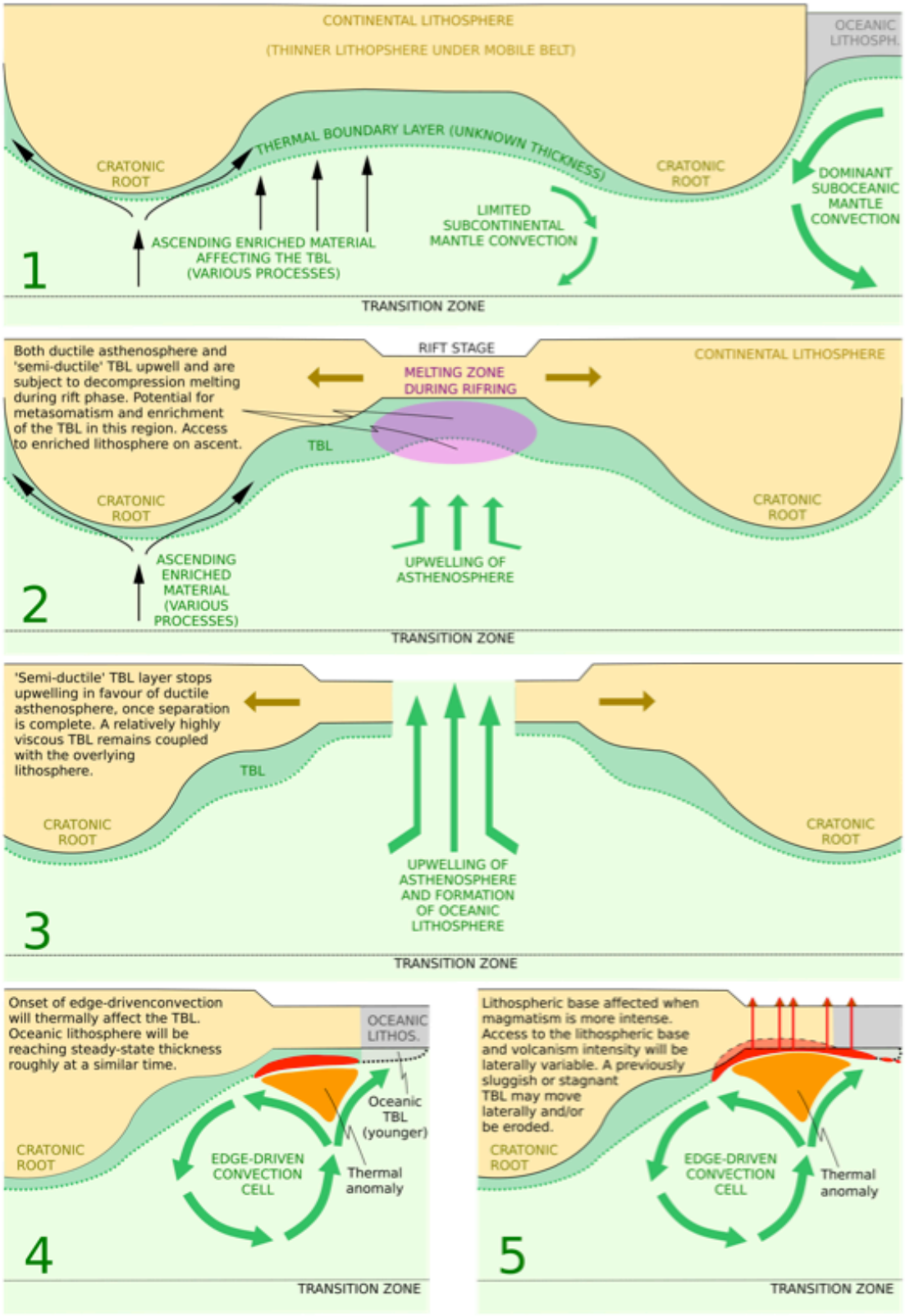
CONTINENTAL LITHOSPHERE
(THINNER LITHOPSHERE UNDER MOBILE BELT)
OCEANIC LITHOSPH.
THERMAL BOUNDARY LAYER (UNKNOWN THICKNESS)
CRATONIC ROOT
CRATONIC ROOT
DOMINANT SUBOCEANIC MANTLE CONVECTION
LIMITED SUBCONTINENTAL MANTLE CONVECTION
ASCENDING ENRICHED MATERIAL AFFECTING THE TBL (VARIOUS PROCESSES)
1
TRANSITION ZONE
RIFT STAGE
Both ductile asthenosphere and 'semi-ductile' TBL upwell and are subject to decompression melting during rift phase. Potential for metasomatism and enrichment of the TBL in this region. Access to enriched lithosphere on ascent.
MELTING ZONE DURING RIFRING
CONTINENTAL LITHOSPHERE
TBL
CRATONIC ROOT
CRATONIC ROOT
ASCENDING ENRICHED MATERIAL (VARIOUS PROCESSES)
UPWELLING OF ASTHENOSPHERE
2
TRANSITION ZONE
'Semi-ductile' TBL layer stops upwelling in favour of ductile asthenosphere, once separation is complete. A relatively highly viscous TBL remains coupled with the overlying lithosphere.
TBL
CRATONIC ROOT
CRATONIC ROOT
UPWELLING OF ASTHENOSPHERE AND FORMATION OF OCEANIC LITHOSPHERE
3
TRANSITION ZONE
Onset of edge-drivenconvection will thermally affect the TBL. Oceanic lithosphere will be reaching steady-state thickness roughly at a similar time.
OCEANIC LITHOS.
Oceanic TBL (younger)
CRATONIC ROOT
EDGE-DRIVEN CONVECTION CELL
Thermal anomaly
4
TRANSITION ZONE
Lithospheric base affected when magmatism is more intense. Access to the lithospheric base and volcanism intensity will be laterally variable. A previously sluggish or stagnant TBL may move laterally and/or be eroded.
CRATONIC ROOT
EDGE-DRIVEN CONVECTION CELL
Thermal anomaly
5
TRANSITION ZONE

Figure 5-3: (*previous page*) Block diagram of the proposed model. Lateral variability in the intensity of volcanism in *block 5* is concomitant with a centre of stronger activity directly on top of the thermal anomaly. Although the TBL will have mainly asthenospheric composition, it may be enriched in its incompatible trace element signatures, but not isotopic ones in any significant degree. Contributions of the actual continental lithosphere will increase gradually with degrees of partial melting and shallower depths, and will include more enriched isotopic and trace element signatures, the latter also potentially including evidence of the past effects of subduction zones, such as low Nb relative to similarly incompatible elements. Although this is a 2D representation, the same would apply to a 3D approach where the lateral flow of the TBL is perpendicular to the flow of the edge-driven convection cell, which would be the case for the Cameroon Line.

This model of lateral flow would explain the seamount patterns on Figure 5-2. Furthermore, the proposition that magmatism and flow of material affects layers previously coupled with the lithosphere and therefore affected by similar processes of enrichment also finds support in the great geochemical similarity of Northeast Brazil and the Cameroon Line with the Canaries and the East African Rift (Chapter 4). If geochemical similarity is due to relatively recent (i.e. Mesozoic) enrichment processes, they could correlate with geographical proximity and association with the same continental block. Although seamount chains do not always continue onto continents, the presence and abundance of continental occurrences may be limited by the lithospheric thickness under the fold belts and the intensity of the underlying convection cell, the latter controlled by local lithospheric morphology. For instance, the Cameroon Line and Borborema, the most vigorous provinces of intraplate Cenozoic volcanism on both continental margins, also represent the thinnest segments of continental lithosphere along the Atlantic conjugate margins (Priestley and McKenzie, 2013; Chapters 3 and 4; Figure 3-36). In other instances along the two passive margins, volcanism may only manifest itself once material moves into the oceanic domain and its thinner lithosphere.

The flow of subcontinental material may continue towards thinner lithosphere and potentially towards spreading ridges, which may produce a discontinuous distribution of enriched mid-ocean ridge basalts (E-MORB) that will be more abundant in younger spreading ridges closer to continental

blocks. A brief look at E-MORB occurrences at mid-ocean ridges around the world seems to support this hypothesis (Humler and Besse, 2002; Fitton, 2007). Although it has been noted that seamounts favour oceanic lithosphere closer to continental blocks, these patterns have been attributed to differences in the thickness between older/colder and younger/hotter oceanic lithospheres and their effects of depth of melting (Fitton, 2007). The proposed model also accommodates a heterogeneous mantle composed of a dominantly depleted matrix containing blobs and slivers of more enriched material (Fitton *et al.*, 1997; Meibom and Anderson, 2004; Fitton, 2007; Foulger, 2010), but adds a possible extra source for these enriched bodies other than subducted slabs, and associates them with seamount patterns. The model also implies that these sources are continuously formed and tapped according to global and local tectonic processes.

The proposition of an enriched sublithospheric mantle layer has been previously put forward by Anderson in his concept of the *perisphere* (Anderson, 1995, 1998), but his hypothesis included both continental and oceanic domains. It was subsequently questioned in Fitton (2007), who argues that the lack of enriched signatures in samples of old oceanic crust at the oceanic-continental boundary in a North Atlantic locality seriously undermines this model, as, according to Anderson, such signatures should be most prevalent at the time of continental separation. We believe that our model addresses this issue by placing this enriched layer under the continents but recognising that they may be too viscous to be readily mobilised. Instead, mobilisation requires specific lithospheric morphology, mantle flow and thermal conditions, and the TBL may not play a significant role in the early formation of the oceanic lithosphere if it is viscous enough to remain coupled with the separating plates. Although it will stretch and may be affected by adiabatic melting during the rift stage, once the plate separates

all the upwelling material (and therefore the early segments of the oceanic crust) will be dominated by asthenospheric material.

Northeast Brazil and the Cameroon Line

The timeframe for the onset of Cenozoic volcanism in Northeast Brazil and the Cameroon Line in relation to continental separation fits well in the timescales given by edge-driven convection models. The chronological intervals proposed by the models discussed above are illustrated in Figure 5-4 in relation to these two conjugate margins, and show how volcanism in both provinces may be associated with a ~50 m.y. interval since the separation of Borborema and Cameroon, which developed from ~118 to ~100 Ma and marks the final stage of a long process of separation between South America and Africa (Nürnberg and Müller, 1991). A subsequent interval of 30-50 m.y., which would be expected until the convection cell reaches flow peak (King and Ritsema, 2000), roughly matches the onset of activity in the oceanic sectors. The small-scale cyclicity of Cenozoic volcanism in Northeast Brazil, including its recent apparent extinction and its clear peak at ~20-25 Ma followed by ~6 m.y. of quiescence (Chapter 2), is also within the proposed timeframe for edge-driven convection cyclicity (Demidjuk *et al.*, 2007; Sacek and Ussami, 2013; Sacek, 2017). Such oscillatory patterns are not clear in the Cameroon Line, but this could reflect the lack of more precise dating for its older occurrences or simply the dilution of small-scale patterns in a much larger and vigorous volcanic province where the effects of edge-driven convection and/or the subcontinental lithospheric structure might not be horizontally uniform.

Figure 5-4: (next page) Chronological development of volcanic activity in Northeast Brazil and the Cameroon Line, and its relationship to the edge-driven convection timeframe proposed by King and Ritsema (2000). The convection 'peak' is outlined in relation to the onset of magmatism in both conjugate margins. Onset of magmatism is in turn chronologically associated with the timing of continental separation by a 50 m.y. interval. The timing of continental separation follows Nürnberg and Müller (1991) with the separation of Borborema from Cameroon specifically highlighted in *purple*. According to King and Anderson (1998), the 50 m.y. gap could vary between 40 and 60 m.y., which is still within our proposed timeframes. *NB: Northeast Brazil; CL: Cameroon Line; EDC: Edge-driven convection*.

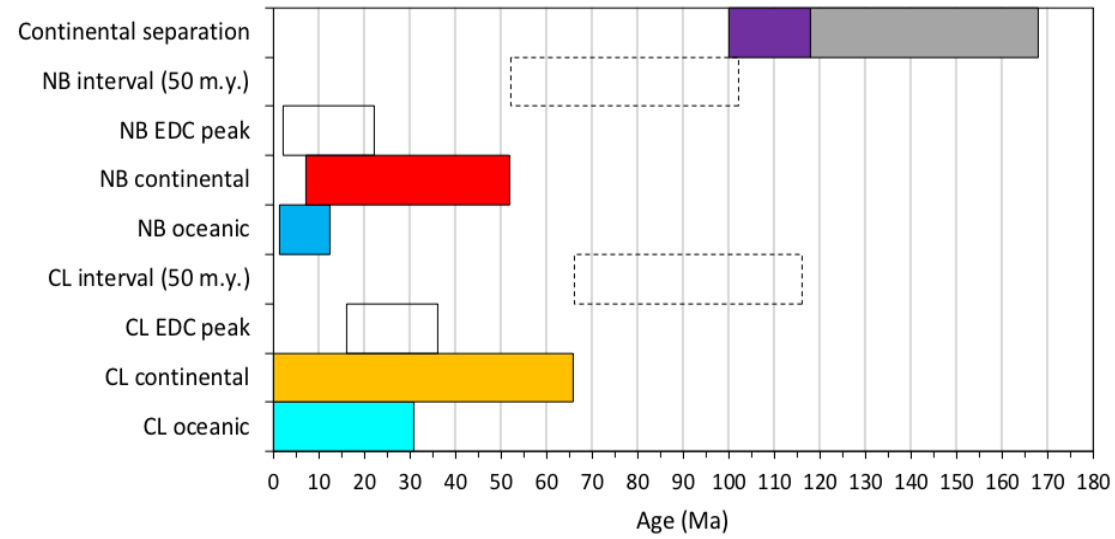

Figure 5-4: Caption on previous page.

It is not clear why volcanism is so much more intense in the Cameroon Line than in Northeast Brazil, but the length of the suture between the Congo craton and the adjacent mobile belt in Africa is much longer than what exists in Borborema. Furthermore, some lithospheric morphological differences between the two provinces may be inferred from the concave-oceanward and convex-oceanward geometries of the Cameroon Line and Borborema respectively. Sacek and Ussami (2013), using the Santos basin of Southeast Brazil, show through numerical modelling and an assessment of the basin's sedimentation how the 3D arrangement of such convex and concave geometries may affect the flow of edge-driven convection cells. Their results indicate that concave-oceanward geometries, where the effects of the continental block are stronger, allow much more vigorous convection that may be up to 70% faster than convex-oceanward shapes that are more dominated by the oceanic terrane. More vigorous volcanism on the African side may have allowed greater assimilation of continental material, which would apply to both sectors if one assumes that magmatism is centred under the continental sector and flows laterally. The most significant difference between the two conjugate margins as two distinct groups (independently of their oceanic and continental characteristics) is the significantly lower Ba and

somewhat lower Sr values on the Brazilian side, which are elements that may be associated with contamination by continental lithospheric material (Chapter 3; Fitton et al., 1991; Fodor et al., 1998; Sun and McDonough, 1989).

The vertical compositional and isotopic stratification identified in Northeast Brazil, and the horizontal isotopic variability matching lithospheric thickness in both conjugate margins fit well in a model where the source is at least to some extent coupled with the base of the lithosphere, despite its mainly asthenospheric composition. This is further reinforced by the greater similarities between the two continental sectors with each other than with their respective oceanic counterparts, which also applies to the two oceanic sectors. It is also noteworthy that both continental sectors have stronger OIB-like trace element signatures than their oceanic counterparts. These observations also support the interpretation that the centre of volcanic activity is under the continents, but stretches laterally to the oceanic sector.

In addition, isotopic patterns show that lavas in the continental sector are marked by relatively higher EM contributions, which increase at shallower depths, higher melt fractions and around the most active volcanic centres in the continental block. In Northeast Brazil, higher EM contributions are accompanied by higher Ba content and relatively lower Nb (Figure 5-5), which may be linked to some form of vertical stratification (Chapter 3). Although lavas with longer residence time in the lithosphere (i.e. those from the MQVL basins) show stronger EM signatures, such isotopic characteristics cannot be the exclusive result of crustal contamination because lavas generated at great depth and crossing thick segments of continental lithospheres are also somewhat affected by it. Furthermore, EM signatures seem to correlate directly with spinel lherzolite contributions to the source, and not melt evolution that could indicate longer residence time in the lithosphere. Instead, variability in EM signatures is greater between volcanic centres that are located in the central segment and basins of the MQVL on the one hand (or the OCB and continental hinterland next to the

Congo craton in the case of the Cameroon Line), and, on the other hand, those that are not. This layer with stronger EM characteristics must be underlain by another with dominantly DM isotopic signatures, which is more prevalent amongst lower melt fractions, at greater distances from thinner segments of the continental lithosphere, away from the most active volcanic centres in both continental sectors, and farther into the oceanic sector. Isotopic EM-I signatures are horizontally focused in the OCB, with a limited spread over both the continental and oceanic sectors (i.e. it is limited to volcanic centres along the coast and to ocean islands abutting the continental shelf). All these signatures are relative and subtle, and the lavas are still predominantly close to asthenospheric composition and DM characteristics. This makes the TBL (which will retain strong asthenospheric characteristics) a strong candidate for their source, with small assimilation of continental material under some circumstances. For instance, EM signatures increase as melting encroaches the shallower and more 'permanent' layers of the continental TBL and lithosphere, with EM-I representing shallower levels that are only accessible in areas of intense lithospheric stretching such as the OCB (Figure 5-3).

The Nb and Ba trends observed in Northeast Brazil also support the proposed model. Whilst Nb depletion is characteristic of arc magmatism, Ba behaves as a highly mobile element independently of the type of magmatic process and would become enriched at the base of the lithosphere in most metasomatic events. Therefore, in Northeast Brazil, Ba indicates that shallower depths may be gradually more affected by previous metasomatic events (high Ba) than deeper ones (low Ba), whilst Nb indicates that such events change from metasomatism caused by small degrees of mantle melting at deeper levels (relatively younger layers, where Nb behaves like Ba) to subduction zone signatures at shallower ones (relatively older layers, where Nb shows a sudden depletion; Chapter 3), with depth indicated by variability in spinel lherzolite contributions to the source. These processes indicate vertical stratification from the base of the TBL to its transition into

more permanent lithosphere, which, in turn, can only be explained if in the timescales relevant for our analyses the source is at least to some extent isolated from whole mantle convection and its concomitant homogenisation. We propose that such isolation is achieved by some degree of coupling of compositionally asthenospheric material with the continental lithosphere.

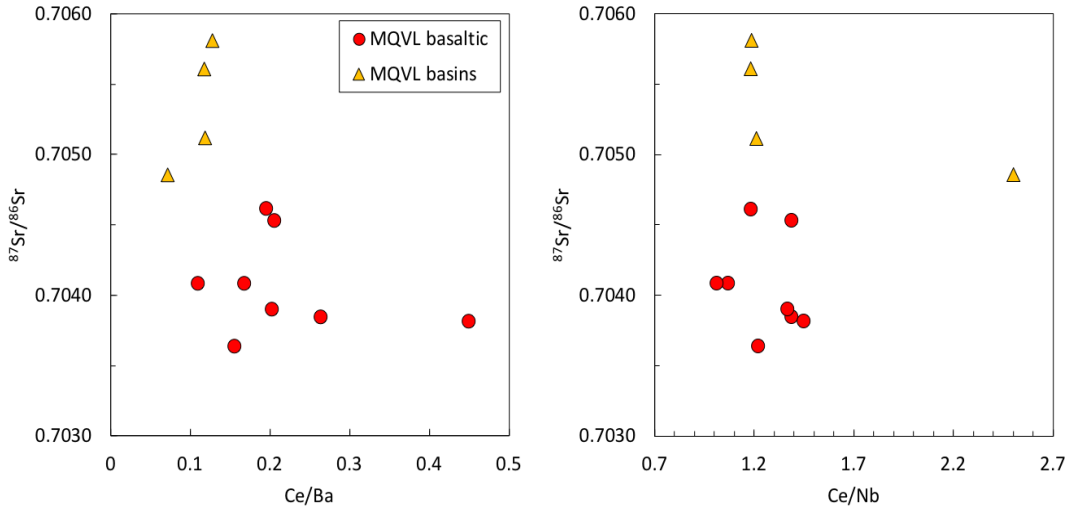

Figure 5-5:The relationship of $^{87}Sr/^{86}Sr$ with both Ce/Ba and Ce/Nb in the MQVL, which expands on the points made in Chapter 3 and shows how enriched isotopic signatures correlate with the patterns of contributions of continental lithospheric material, such as the high Ba content (i.e. low Ce/Ba) for shallow and high melt fractions (i.e. basin samples), and a shift in Nb behaviour. Nb should behave similarly to Ba, but instead, the diagram on the *right* shows unexpectedly high Ce/Nb for higher $^{87}Sr/^{86}Sr$ (i.e. the MQVL basins), which may indicate greater contributions of old subduction zone signatures (see Chapter 3).

Both Northeast Brazil and the Cameroon Line are mostly isotopically depleted in relation to bulk silicate Earth (BSE) but enriched in relation to mid-ocean ridge basalts and depleted mantle (MORB and DM sources, respectively). Both conjugate margins are also enriched in terms of incompatible trace element composition in relation to MORB. This overall pattern also characterises a significant proportion of ocean island basalt (OIB). A mantle source under Northeast Brazil and the Cameroon Line that is mainly asthenospheric in composition but affected by Mesozoic-Cenozoic enrichment processes that still survive in a sluggishly moving layer somewhat coupled with the overlying lithosphere, such as the TBL, is

therefore not unreasonable, and could produce the observed patterns. A similar logic may also be key to understating other OIB and E-MORB signatures.

It is not clear why edge-driven convection based on continental lithospheric morphology would not be active in the areas discussed here before continental breakup, but it should be clear that the thermal structure beneath a large stable continent will be different from what comes after its breakup, if nothing else because newly developed adjacent oceanic lithosphere will have a distinct thermal structure. Differences in thermal structure may also be due to continental insulation of the underlying mantle during periods of supercontinent stability (Humler and Besse, 2002; Brandl *et al.*, 2013), which argues that subcontinental asthenosphere might become warmer during periods of supercontinent stability. This scenario could hinder downwelling and the onset of a convection cell. A very thick overlying continental block may also preclude the onset of volcanism, even if a magmatic process is occurring underneath, similarly to what we propose as the reason why some seamount chains connected with the continental block lack or have more subdued continental volcanic occurrences associated with them. Furthermore, warming of the TBL in an area surrounded by cratons may cause the material to remain ponded under the continental block, hindering further convection. Models proposed by Sleep (2003) show how significant convection cells within such closed spaces may be temporally limited and often relatively short-lived in the case of ponded material derived from deep mantle plumes.

Another approach to the lack of volcanism before continental separation is to insert the system into a larger tectonic context. Some edge-driven convection models suggest that, where it occurs between continental and oceanic lithospheres, the mantle even under a newly formed continent must be somewhat warmer in order to provide the necessary thermal disturbance to trigger the convection cell (King and Anderson, 1995, 1998). Furthermore, for volcanism to occur, the overlying lithosphere must also be

stretching, which would provide the conditions for magma ascent (ibid.). In this model, edge driven convection would not happen close to subduction zones, as these would cool the underlying mantle, or right after the assembling of supercontinents if it is assumed that these are likely to form over colder mantle, where continental blocks will converge (Anderson, 1994). Therefore, the conditions for edge-driven convection would only develop towards the end of a supercontinent cycle and away from active subduction zones, of which at least the former condition fits the context of Cenozoic intraplate volcanism in Africa and South America.

In addition to providing the conditions for magmatism, the basal morphology and relief of the continental lithosphere could also be the reason behind the remarkable geometrical resemblance between the Cameroon volcanic line and the Benue Trough. There is evidence that the Benue Trough has subsided since opening, especially on the SW of the main basin in the widest segment of the Trough and along the northern arm, but apparently less so along the eastern arm (Adams et al., 2015; Chapter 1, Figure 1-9). The resulting arrangement at the base of the lithosphere could curb sublithospheric asthenospheric or TBL flow on a local scale, concentrating movement of material between the subsided basin and the craton's deep roots, especially towards the SW. Even though subsidence is less substantial in the NE of the Trough, which explains why the volcanic chain crosses over some of the rifted areas there, volcanism still avoids the rifts themselves, suggesting that subsidence within rifts may indeed work as barriers for volcanism.

Detailed studies of other passive margins with volcanic occurrences straddling both continental and oceanic sectors could further test our proposed mechanism. For instance, it would be interesting to compare the Canary Islands with adjacent continental Cenozoic volcanism, such as the Azrou and Oulmés volcanic fields in Morocco. Furthermore, the locality of Djebel Targou in Central Morocco and Mt. Etinde in the Cameroon Line not only have produced very similar nephelinite, but their unusual assemblages

also have the only reported occurrences anywhere in the world of strontian melilite, testifying to the strong similarities between these volcanic centres (Velde and En-noufous Rachdi, 1988). Interestingly, volcanism in the Canaries and Morocco also matches the New England volcanic chain in North America in a geographic fit akin to Northeast Brazil and the Cameroon Line. The New England volcanic chain also happens to be the only continuous volcanic lineament straddling across both continental and oceanic lithosphere (i.e. from Mont Royal in Montreal, to the Nashville seamount over 1400 km off the coast of New England) and the only place where seamounts occur directly abutting the continental block in the North American Atlantic passive margin (Figure 5-6). Both volcanic provinces also postdate continental separation in the Mesozoic. Although there has been attempts to associate the New England seamount chain with the Bermuda rise and therefore the Bermuda seamount (Vogt, 1991), the latter has no connection with the continental block, similarly to Cape Verde on the African coast. In the South Atlantic, there is also a matching pattern between the Rio Grande and Walvis ridges, although their origin may be mixed up with the Paraná-Etendeka LIP (O'Connor and Duncan, 1990).

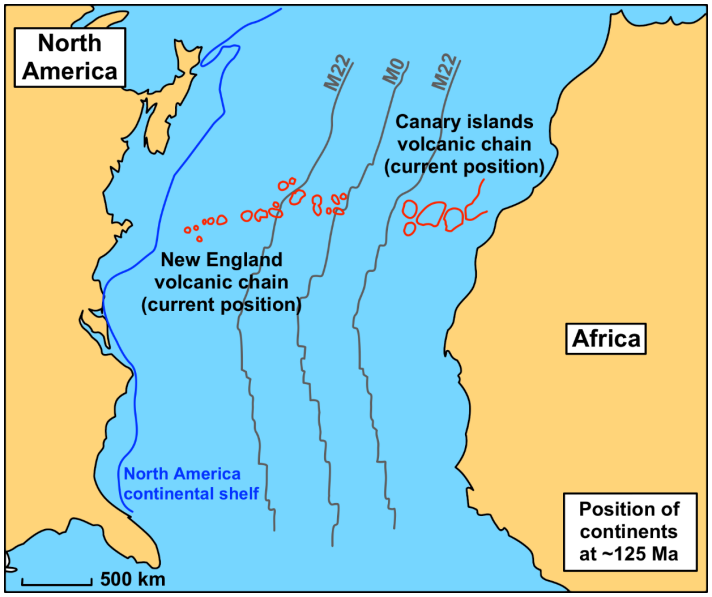

Figure 5-6:Current position of the New England seamount chain and the Canaries in relation to their respective continental blocks, with the continental position at ~125 Ma (Early Cretaceous), around the time when oceanic volcanism on both provinces started. Adapted from Labails et al. (2010). The New England seamount chain is the only occurrence of seamounts on the North American Atlantic coast that continues onto the continental block. For the African seamounts see Figure 5-2.

Conclusions

Explaining synchronous and geochemically identical volcanism at conjugate points of the South American and African passive margins, tens of millions of years after continental separation, requires that both the sources and mechanisms responsible for magmatism are inherent to the respective continental blocks. The continental blocks of Borborema and the Cameroon Line are the shared element between the two provinces that were adjacent to one another before continental separation, and what distinguishes them from other areas along the Atlantic passive margins of Africa and South America where no significant Cenozoic volcanism is found. However, the evidence discussed in previous chapters also indicates that the main source of magmatism is sublithospheric, allowing it to extend across both oceanic and continental lithospheres whilst remaining virtually identical and completely independent of the overlying geological terranes. Therefore, a model for the two provinces must correlate sublithospheric mantle dynamics with the characteristics of the overlying continental block, and the effects that continental breakup had on both.

Placing the source of melts of Cenozoic volcanism in Northeast Brazil and the Cameroon Line in the subcontinental TBL accounts for both coupling of the source with the lithosphere during continental separation and its subsequent mobilisation by a thermal anomaly, thereby explaining their identical geochemistry. The lithospheric morphology of these two provinces provide the right conditions for the development of edge-driven convection, which in turn also leads to a local thermal anomaly and explains the somewhat elevated geotherm in the region and the synchronous onset of volcanism. A TBL with intermediate rheology may also explain compositional vertical stratification, developed during relatively recent events of metasomatism and/or exposure to subduction zones that have not yet been fully reincorporated in the convecting asthenosphere but cannot be considered to be equal to the lithosphere either. Continental volcanism also requires a substantially thin continental lithosphere, with thickness

approaching that of the oceanic block. Along the South American and African passive margins, this condition is only met to a significant degree in Northeast Brazil and the Cameroon Line. Edge-driven convection may also cause lithospheric thermal erosion, which would thin the continental lithosphere even more than the adjacent oceanic block, further mobilising the enriched TBL and lithospheric mantle, and provide a positive feedback to magmatism through adiabatic upwelling.

The trends observed in Northeast Brazil and the Cameroon Line expose patterns of intraplate volcanism along the Atlantic passive margins that have not previously been considered and may shed light on the mechanisms behind such magmatic provinces. We have shown how identical and synchronous volcanism in both conjugate margins results from the same magmatic process and is not a coincidence. Furthermore, there appears to be other matching volcanic provinces postdating continental separation along the Atlantic, reinforcing that this may be a recurrent pattern of intraplate volcanism that has so far gone unrecognised. The model proposed above not only accounts for all the patterns in Cenozoic volcanism in Northeast Brazil and the Cameroon Line discussed in previous chapters, but may also be tested against other intraplate volcanic occurrences along the Atlantic passive margins, especially the Canaries-Morocco volcanism and the New England volcanic chain.

References

Adams, A. N., Wiens, D. A., Nyblade, A. A., Euler, G. G., Shore, P. J. & Tibi, R. (2015). Lithospheric instability and the source of the Cameroon Volcanic Line: Evidence from Rayleigh wave phase velocity tomography. *Journal of Geophysical Research: Solid Earth* **120**, 1708–1727.

Aka, F. T., Nagao, K., Kusakabe, M., Sumino, H., Tanyileke, G., Ateba, B. & Hell, J. (2004). Symmetrical Helium isotope distribution on the Cameroon Volcanic Line, West Africa. *Chemical Geology* **203**, 205–223.

Allègre, C. J. & Minster, J. F. (1978). Quantitative models of trace element behavior in magmatic processes. *Earth and Planetary Science Letters* **38**, 1–25.

Almeida, F. (1955). *Geologia e petrologia do arquipelago de Fernando de Noronha*. DNPM/DGM, Rio de Janeiro.

Almeida, F. (2006). Ilhas oceânicas brasileiras e suas relações com a tectônica atlântica. *Terrae Didatica* **2**, 3–18.

Almeida, F. F. M., Carneiro, C. D. R., Machado Jr., D. . & Dehira, L. . (1988). Magmatismo Pós- Paleozóico no Nordeste Oriental do Brasil. *Revista Brasileira de Geociências* **18**, 451–462.

Anderson, D. L. (1994). Superplume or supercontinents? *Geology* **22**, 39–42.

Anderson, D. L. (1995). Lithosphere, asthenosphere, and perisphere. *Reviews of Geophysics* **33**, 125–149.

Anderson, D. L. (1998). The edges of the mantle. In: Gurnis, M., Wysession, M. E., Knittle, E. & Buffett, B. A. (eds) *The Core-Mantle Boundary Region*. American Geophysical Union, Geodynamics **28**, 255–271.

Arthaud, M., Caby, R., Fuck, R. A., Dantas, E. L. & Parente, C. V. (2008). Geology of the northern Borborema Province, NE Brazil and its correlation with Nigeria, NW Africa. In: Pankhurst, R. J., Trouw, R. A. J. & Brito Neves, B. B. (eds) *West Gondwana: Pre-Cenozoic correlations across the South Atlantic region*. Geological Society, London, Special Publications **294**, 49–67.

Baker, M. B. & Stolper, E. M. (1994). Determining the composition of high-pressure mantle melts using diamond aggregates. *Geochimica et Cosmochimica Acta* **58**, 2811–2827.

Ballentine, C. J., Lee, D.-C. & Halliday, A. N. (1997). Hafnium isotopic studies of the Cameroon line and new HIMU paradoxes. *Chemical Geology* **139**, 111–124.

Brandl, P. a., Regelous, M., Beier, C. & Haase, K. M. (2013). High mantle temperatures following rifting caused by continental insulation. *Nature Geoscience* **6**, 391–394.

Castro, D. L. de, Bezerra, F. H. R., Sousa, M. O. L. & Fuck, R. a. (2012). Influence of Neoproterozoic tectonic fabric on the origin of the Potiguar Basin, northeastern Brazil and its links with West Africa based on gravity and magnetic data. *Journal of Geodynamics* **54**, 29–42.

Comin-Chiaramonti, P., Demarchi, G., Girardi, V. a. V., Principalle, F. &

Sinigoi, S. (1986). Evidence of mantle metasomatism and heterogeneity from peridotite inclusions of northeastern Brazil and Paraguay. *Earth and Planetary Science Letters* **77**, 203–217.
Cordani, U. G. (1970). Idade do vulcanismo no Oceano Atlântico Sul. *Boletim IGA* **1**, 9–75.
Cordani, U. G., Milani, E. J., Thomaz Filho, A. & Campos, D. A. (2000). Tectonic evolution of south america. *31st International Geological Congress*. Rio de Janeiro.
Cordani, U. G. & Sato, K. (1999). Crustal evolution of the South American Platform, based on Nd isotopic systematics on granitoid rocks. *Episodes* **22**, 167–173.
De Jongh, W. K. (1973). X-Ray fluorescence analysis applying theoretical matrix corrections. Stainless steel. *X-ray spectrometry* **2**, 151–158.
Deer, W. A., Howie, R. A. & Zussman, J. (1992). *An introduction to the rock-forming minerals*. Harlow: Pearson Education.
Demidjuk, Z., Turner, S., Sandiford, M., George, R., Foden, J. & Etheridge, M. (2007). U-series isotope and geodynamic constraints on mantle melting processes beneath the Newer Volcanic Province in South Australia. *Earth and Planetary Science Letters* **261**, 517–533.
Ebinger, C. J. & Sleep, N. H. (1998). Cenozoic magmatism throughout east Africa resulting from impact of a single plume. *Nature* **395**, 788–791.
Eggins, S. M., Woodhead, J. D., Kinsley, L. P. J., Mortimer, G. E., Sylvester, P., McCulloch, M. T., Hergt, J. M. & Handler, M. R. (1997). A simple method for the precise determination of ≥ 40 trace elements in geological samples by ICPMS using enriched isotope internal standardisation. *Chemical Geology* **134**, 311–326.
Elsheikh, A. A., Gao, S. S. & Liu, K. H. (2014). Formation of the Cameroon Volcanic Line by lithospheric basal erosion: Insight from mantle seismic anisotropy. *Journal of African Earth Sciences* **100**, 96–108.
Ernesto, M. (2005). Paleomagnetism of the Post-Paleozoic Alkaline Magmatism in the Brazilian Platform : Questioning the Mantle Plume Model. In: Comin-Chiaramonti, P. & Barros Gomes, C. (eds) *Mesozoic to Cenozoic Alkaline Magmatism in the Brazilian Platform*. São Paulo: EDUSP/FAPESP, 689–705.
Fairhead, J. D. & Okereke, C. S. (1987). A regional gravity study of the West African rift system in Nigeria and Cameroon and its tectonic interpretation. *Tectonophysics* **143**, 141–159.
Fairhead, J. D. & Okereke, C. S. (1991). Crustal thinning and extension beneath the Benue Trough based on gravity studies. *Journal of African Earth Sciences* **11**, 329–335.
Fitton, J. G. (1980). The Benue trough and cameroon line - A migrating rift system in West Africa. *Earth and Planetary Science Letters* **51**, 132–138.
Fitton, J. G. (1987). The Cameroon line, West Africa: a comparison between oceanic and continental alkaline volcanism. In: Fitton, J. G. & Upton, B. G. J. (eds) *Alkaline igneous rocks*. Geological Society, London, Special

Publications **30**, 273–291.
Fitton, J. G. (2007). The OIB paradox. In: Foulger, G. R. & Jurdy, D. M. (eds) *Plates, plumes and planetary processes*. The Geological Society of America Special Papers **430**, 387–412.
Fitton, J. G. & Dunlop, H. M. (1985). The Cameroon line, West Africa, and its bearing on the origin of oceanic and continental alkali basalt. *Earth and Planetary Science Letters* **72**, 23–38.
Fitton, J. G. & Godard, M. (2004). Origin and evolution of magmas on the Ontong Java Plateau. In: Fitton, J. G., Mahoney, J. J., Wallace, P. J. & Saunders, A. D. (eds) *Origin and evolution of the Ontong Java Plateau*. Geological Society, London, Special Publications **229**, 151–178.
Fitton, J. G., James, D. & Leeman, W. P. (1991). Basic magmatism associated with Late Cenozoic extension in the western United States: Compositional variations in space and time. *Journal of Geophysical Research* **96**, 13693.
Fitton, J. G., Saunders, A. D., Norry, M. J., Hardarson, B. S. & Taylor, R. N. (1997). Thermal and chemical structure of the Iceland plume. *Earth and Planetary Science LettersEarth and Planetary Science Letters* **153**, 197–208.
Fitton, J. G., Saunders, A. D., Larsen, L. M., Hardarson, B. S. & Norry, M. J. (1998). Volcanic rocks from the southeast Greenland Margin at 63°N: composition, petrogenesis, and mantle sources. *Proceedings of the Ocean Drilling Program, Scientific Results* **152**.
Fitton, J. G., Williams, R., Saunders, A. & Barry, T. (in press). The origin of magmas in the Louisville and Emperor seamounts. *Journal of Petrology*.
Fodor, R. V., Mukasa, S. B. & Sial, A. N. (1998). Isotopic and trace-element indications of lithospheric and asthenospheric components in Tertiary alkalic basalts, northeastern Brazil. *Lithos* **43**, 197–217.
Fodor, R. V., Sial, A. N. & Gandhok, G. (2002). Petrology of spinel peridotite xenoliths from northeastern Brazil: Lithosphere with a high geothermal gradient imparted by Fernando de Noronha plume. *Journal of South American Earth Sciences* **15**, 199–214.
Foulger, G. R. (2010). *Plates vs Plumes: A Geological Controversy*. Oxford: Wiley-Blackwell.
Gerlach, D. C., Stormer, J. C. & Mueller, P. a. (1987). Isotopic geochemistry of Fernando de Noronha. *Earth and Planetary Science Letters* **85**, 129–144.
Gill, R. (2010). *Igneous rocks and processes: a practical guide*. Oxford: Wiley-Blackwell.
Govindaraju, K. (1994). Compilation of working values and descriptions for 383 geostandards. *Geostandards Newsletter* **18**, 1–158.
Green, T. H. & Pearson, N. J. (1987). An experimental study of Nb and Ta partitioning between Ti-rich minerals and silicate liquids at high pressure and temperature. *Geochimica et Cosmochimica Acta* **51**, 55–62.
Guimarães, I. P., Sial, A. N. & Silva Filho, A. F. (1982). Petrologia e geoquímica da província alcalina terciária Fortaleza, Ceara. *Anais do*

XXXII congresso brasileiro de geologia, Salvador, Bahia, 577–588.
Halliday, A. N., Davidson, J. P., Holden, P., DeWolf, C., Lee, D.-C. & Fitton, J. G. (1990). Trace-element fractionation in plumes and the origin of HIMU mantle beneath the Cameroon line. *Nature* **347**, 523–528.
Halliday, A. N., Dickin, A. P., Fallick, A. E. & Fitton, J. G. (1988). Mantle dynamics: A Nd, Sr, Pb and O isotopic study of the Cameroon line volcanic chain. *Journal of Petrology* **29**, 181–211.
Heilbron, M., Valeriano, C. M., Tassinari, C., Almeida, J., Tupinambá, M., Siga, O. & Trouw, R. A. J. (2008). Correlation of Neoproterozoic terrane between te Ribeira Belt, SE Brazil and its African countepart: comparative tectonic evolution and open questions. In: Pankhurst, R. J., Trouw, R. A. J. & Brito Neves, B. B. (eds) *West Gondwana: Pre-Cenozoic correlations across the South Atlantic region*. Geological Society, London, Special Publications **294**, 2011–237.
Humler, E. & Besse, J. (2002). A correlation between mid-ocean-ridge basalt chemistry and distance to continents. *Nature* **419**, 607–609.
Jacquemin, H., Sheppard, S. M. F. & Vidal, P. (1982). Isotopic geochemistry (O, Sr, Pb) of the Golda Zuelva and Mboutou anorogenic complexes, North Cameroun: mantle origin with evidence for crustal contamination. *Earth and Planetary Science Letters* **61**, 97–111.
Jochum, K. P., Seufert, H. M. & Thirlwall, M. F. (1990). High-sensitivity Nb analysis by spark-source mass spectrometry (SSMS) and calibration of XRF Nb and Zr. *Chemical Geology* **81**, 1–16.
Jourdan, F., Matzel, J. P. & Renne, P. R. (2007). ^{39}Ar and ^{37}Ar recoil loss during neutron irradiation of sanidine and plagioclase. *Geochimica et Cosmochimica Acta* **71**, 2791–2808.
Jourdan, F. & Renne, P. R. (2013). Neutron-induced ^{37}Ar recoil ejection in Ca-rich minerals and implications for ^{40}Ar/^{39}Ar dating. In: Jourdan, F., Mark, D. F. & Verati, C. (eds) *Advances in ^{40}Ar/^{39}Ar dating: from archaeology to planetary sciences*. Geological Society, London, Special Publications **378**, 33–52.
Kamdem, J. B., Kraml, M., Keller, J. & Henjes-Kunst, F. (2002). Cameroon Line magmatism: Conventional K/Ar and single-crystal laser ^{40}Ar/^{39}Ar ages of rocks and minerals from the Hossere Nigo anorogenic complex, Cameroon. *Journal of African Earth Sciences* **35**, 99–105.
Kampunzu, A. B. & Mohr, P. (1991). Magmatic Evolution and Petrogenesis in the East African Rift System. In: Kampunzu, A. B. & Lubala, R. T. (eds) *Magmatism in Extensional Structural Settings*. Berlin: Springer, 85–136.
Keen, C. E. & Boutilier, R. R. (1995). Lithosphere-Asthenosphere interactions below rifts. In: Banda, E., Torné, M. & Talwani, M. (eds) *Rifted Ocean-Continent Boundaries*. Dordrecht: Springer, 17–30.
King, S. D. (2005). Archean cratons and mantle dynamics. *Earth and Planetary Science Letters* **234**, 1–14.
King, S. D. (2007). Hotspots and edge-driven convection. *Geology* **35**, 223–226.
King, S. D. & Anderson, D. L. (1995). An alternative mechanism of flood

basalt formation. *Earth and Planetary Science Letters* **136**, 269–279.
King, S. D. & Anderson, D. L. (1998). Edge-driven convection. *Earth and Planetary Science Letters* **160**, 289–296.
King, S. D. & Ritsema, J. (2000). African hot spot volcanism: small-scale convection in the upper mantle beneath cratons. *Science* **290**, 1137–1140.
Klöcking, M. (2017). *Continental Magmatism and Dynamic Topography* Doctoral thesis. University of Cambridge, UK.
Knesel, K. M., Souza, Z. S., Vasconcelos, P. M., Cohen, B. E. & Silveira, F. V. (2011). Young volcanism in the Borborema Province, NE Brazil, shows no evidence for a trace of the Fernando de Noronha plume on the continent. *Earth and Planetary Science Letters* **302**, 38–50.
Koch, F. W., Wiens, D. A., Nyblade, A. A., Shore, P. J., Tibi, R., Ateba, B., Tabod, C. T. & Nnange, J. M. (2012). Upper-mantle anisotropy beneath the Cameroon Volcanic Line and Congo Craton from shear wave splitting measurements. *Geophysical Journal International* **190**, 75–86.
Koppers, A. A. P., Staudigel, H. & Duncan, R. A. (2003). High-resolution $^{40}Ar/^{39}Ar$ dating of the oldest oceanic basement basalts in the western Pacific basin. *Geochemistry, Geophysics, Geosystems* **4 (11)**.
Koppers, A. A. P., Staudigel, H. & Wijbrans, J. R. (2000). Dating crystalline groundmass separates of altered Cretaceous seamount basalts by the40Ar/39Ar incremental heating technique. *Chemical Geology* **166**, 139–158.
Kuepouo, G., Tchouankoue, J. P., Nagao, T. & Sato, H. (2006). Transitional tholeiitic basalts in the Tertiary Bana volcano-plutonic complex, Cameroon Line. *Journal of African Earth Sciences* **45**, 318–332.
Labails, C., Olivet, J. L., Aslanian, D. & Roest, W. R. (2010). An alternative early opening scenario for the Central Atlantic Ocean. *Earth and Planetary Science Letters* **297**, 355–368.
Le Maitre, R. W. (ed.) (2002). *Igneous rocks: a classification and glossary of terms*. Cambridge: Cambridge University Press.
Lee, D. C., Halliday, A. N., Fitton, J. G. & Poli, G. (1994). Isotopic variations with distance and time in the volcanic islands of the Cameroon line: evidence for a mantle plume origin. *Earth and Planetary Science Letters* **123**, 119–138.
Lee, J. Y., Marti, K., Severinghaus, J. P., Kawamura, K., Yoo, H. S., Lee, J. B. & Kim, J. S. (2006). A redetermination of the isotopic abundances of atmospheric Ar. *Geochimica et Cosmochimica Acta* **70**, 4507–4512.
Leonhardt, R., Matzka, J. & Menor, E. A. (2003). Absolute paleointensities and paleodirections of miocene and pliocene lavas from Fernando de Noronha, Brazil. *Physics of the Earth and Planetary Interiors* **139**, 285–303.
Lopes, R. P. (1997). *Petrologia dos Fonólitos do Arquipélago de Fernando de Noronha, PE*. Masters dissertation. Instituto de Geociências, University of São Paulo, Brazil.
Lopes, R. P. (2002). *O vulcanismo do arquipélago de Fernando de Noronha,*

PE: química mineral e geoquímica. Doctoral thesis. Instituto de Geociências, University of São Paulo, Brazil.
Lopes, R. P., Ulbrich, M. N. C. & Ulbrich, H. (2014). The volcanic-subvolcanic rocks of the Fernando de Noronha Archipelago , southern Atlantic Ocean: Mineral chemistry. *Central European Journal of Geosciences* **6**, 422–456.
MacDonald, G. A. & Katsura, T. (1964). Chemical composition of Hawaiian Lavas. *Journal of Petrology* **5**, 82–133.
Mackenzie, W. S., Donaldson, C. H. & Guilford, C. (1982). *Atlas of igneous rocks and their textures*. Harlow: Longman.
Mark, D. F., Barfod, D., Stuart, F. M. & Imlach, J. (2009). The ARGUS multicollector noble gas mass spectrometer: Performance for $^{40}Ar/^{39}Ar$ geochronology. *Geochemistry, Geophysics, Geosystems* **10 (2)**.
Marzoli, A., Renne, P. R., Piccirillo, E. M., Castorina, F., Bellieni, G., Melfi, A. J., Nyobe, J. B. & N'ni, J. (1999). Silicic magmas from the continental Cameroon Volcanic Line (Oku, Bambouto and Ngaoundere): ^{40}Ar-^{39}Ar dates, petrology, Sr-Nd-O isotopes and their petrogenetic significance. *Contributions to Mineralogy and Petrology* **135**, 133–150.
Matos, R. M. D. De (1992). The northeast Brazilian rift system. *Tectonics* **11**, 766–791.
McDonough, W. F. & Sun, S. s. (1995). The composition of the Earth. *Chemical Geology* **120**, 223–253.
McDougall, I. & Harrison, T. M. (1999). *Geochronology and Thermochronology by the $^{40}Ar/^{39}Ar$ method* (2nd edition). Oxford: Oxford University Press.
McKenzie, D. (1989). Some remarks on the movement of small melt fractions in the mantle. *Earth and Planetary Science Letters* **95**, 53–72.
McKenzie, D. & Bickle, M. J. (1988). The volume and composition of melt generated by extension of the lithosphere. *Journal of Petrology* **29**, 625–679.
McKenzie, D., Jackson, J. & Priestley, K. (2005). Thermal structure of oceanic and continental lithosphere. *Earth and Planetary Science Letters* **233**, 337–349.
Meibom, A. & Anderson, D. L. (2004). The statistical upper mantle assemblage. *Earth and Planetary Science Letters* **217**, 123–139.
Menzies, M. A. (1992). The lower lithosphere as a major source for continental flood basalts: a re-appraisal. In: Storey, B. C., Alabaster, T. & Pankhurst, R. J. (eds) *Magmatism and the causes of continental break-up*. Geological Society, London, Special Publications **68**, 31–39.
Milelli, L., Fourel, L. & Jaupart, C. (2012). A lithospheric instability origin for the Cameroon Volcanic Line. *Earth and Planetary Science Letters* **335–336**, 80–87.
Minster, J. F. & Allègre, C. J. (1978). Systematic use of trace elements in igneous processes, part III: Inverse problem of batch partial melting in volcnic suites *Contributions to Mineralogy and Petrology* **68**, 37–52.
Mitchell-Thomé, R. C. (1970). *Geology of the South Atlantic Islands*.

Gebrüder Borntraeger.
Mizusaki, A. M. P., Thomaz-Filho, A., Milani, E. J. & De Césero, P. (2002). Mesozoic and Cenozoic igneous activity and its tectonic control in northeastern Brazil. *Journal of South American Earth Sciences* **15**, 183–198.
Morgan, W. J. (1971). Convection plumes in the lower mantle. *Nature* **230**, 42–43.
Morgan, W. J. (1983). Hotspot tracks and the early rifting of the Atlantic. *Tectonophysics* **94**, 123–139.
Mutter, J. C., Buck, W. R. & Zehnder, C. M. (1988). Convective partial melting, 1: A model for the formation of thick basaltic sequences during the initiation of spreading. *Journal of Geophysical Research* **93**, 1031–1048.
Ngounouno, I., Déruelle, B. & Demaiffe, D. (2000). Petrology of the bimodal Cenozoic volcanism of the Kapsiki plateau (northernmost Cameroon, Central Africa). *Journal of Volcanology and Geothermal Research* **102**, 21–44.
Njome, M. S. & de Wit, M. J. (2014). The Cameroon Line: Analysis of an intraplate magmatic province transecting both oceanic and continental lithospheres: Constraints, controversies and models. *Earth-Science Reviews* **139**, 168–194.
Norrish, K. & Hutton, J. . (1969). An accurate X-ray spectrographic method for the analysis of a wide range of geological samples. *Geochimica et Cosmochimica Acta* **33**, 431–453.
Nürnberg, D. & Müller, R. D. (1991). The tectonic evolution of the South Atlantic from Late Jurassic to present. *Tectonophysics* **191**, 27–53.
O'Connor, J. M. & Duncan, R. A. (1990). Evolution of the Walvis Ridge-Rio Grande Rise hot spot system: Implications for African and South American plate motions over plumes. *Journal of Geophysical Research* **95**, 17475.
Onstott, T. C., Miller, M. L., Ewing, R. C., Arnold, G. W. & Walsh, D. S. (1995). Recoil refinements: Implications for the $^{40}Ar/^{39}Ar$ dating technique. *Geochimica et Cosmochimica Acta* **59**, 1821–1834.
Parsons, B. & McKenzie, D. (1978). Mantle convection and the thermal structure of the plates. *Journal of Geophysical Research: Solid Earth* **83**, 4485–4496.
Pearce, J. A. (1976). Statistical analysis of major element patterns in basalts. *Journal of Petrology* **17**, 15–43.
Pérez-Diaz, L. & Eagles, G. (2014). Constraining South Atlantic growth with seafloor spreading data. *Tectonics* **33**, 1848–1873.
Pérez-Díaz, L. & Eagles, G. (2017). A new high-resolution seafloor age grid for the South Atlantic. *Geochemistry, Geophysics, Geosystems* **18**, 457–470.
Perlingeiro, G., Vasconcelos, P. M., Knesel, K. M., Thiede, D. S. & Cordani, U. G. (2013). $^{40}Ar/^{39}Ar$ geochronology of the Fernando de Noronha Archipelago and implications for the origin of alkaline volcanism in the

NE Brazil. *Journal of Volcanology and Geothermal Research*. Elsevier B.V. **249**, 140–154.
Pin, C. & Bassin, C. (1992). Evaluation of a strontium-specific extraction chromatographic method for isotopic analysis in geological materials. *Analytica Chimica Acta* **269**, 249–255.
Pin, C. & Zalduegui, J. F. S. (1997). Sequential separation of light rare-earth elements, thorium and uranium by miniaturized extraction chromatography: Application to isotopic analyses of silicate rocks. *Analytica Chimica Acta* **339**, 79–89.
Pinheiro, A. G. & Julià, J. (2014). Normal thickness of the upper mantle transition zone in NE Brazil does not favour mantle plumes as origin for intraplate Cenozoic volcanism. *Geophysical Journal International* **199**, 996–1005.
Poudjom Djomani, Y. H., Diament, M. & Wilson, M. (1997). Lithospheric structure across the Adamawa plateau (Cameroon) from gravity studies. *Tectonophysics* **273**, 317–327.
Poudjom Djomani, Y. H., Nnange, J. M., Diament, M., Ebinger, C. J. & Fairhead, J. D. (1995). Effective elastic thickness and crustal thickness variations in west central Africa inferred from gravity data. *Journal of Geophysical Research* **100**, 22,047-22,070.
Priestley, K. & McKenzie, D. (2006). The thermal structure of the lithosphere from shear wave velocities. *Earth and Planetary Science Letters* **244**, 285–301.
Priestley, K. & McKenzie, D. (2013). The relationship between shear wave velocity, temperature, attenuation and viscosity in the shallow part of the mantle. *Earth and Planetary Science Letters* **381**, 78–91.
Priestley, K., Mckenzie, D., Debayle, E. & Pilidou, S. (2008). The African upper mantle and its relationship to tectonics and surface geology. *Geophysical Journal International* **175**, 1108–1126.
Princivalle, F., Salviulo, G., Fabro, C. & Demarchi, G. (1994). Inter- and intra-crystalline temperature and pressure estimates on pyroxenes from NE Brazil mantle xenoliths. *Contributions to Mineralogy and Petrology* **116**, 1–6.
Princivalle, F., Secco, L., Demarchi, G., Trieste, U., Europa, P., Padova, U. & Garibaldi, C. (1989). Crystal chemistry of a clinopyroxene series in ultrafemic xenoliths from North-Eastern Brazil. *Contributions to Mineralogy and Petrology* 131–135.
Rankenburg, K., Lassiter, J. C. & Brey, G. (2005). The role of continental crust and lithospheric mantle in the genesis of Cameroon Volcanic Line lavas: Constraints from isotopic variations in lavas and megacrysts from the Biu and Jos Plateaux. *Journal of Petrology* **46**, 169–190.
Rao, A. B. & Sial, A. N. (1972). Observations on alkaline plugs near Fortaleza city, Ceará State, Brazil. *24th International Geological Congress*, 56–61.
Renne, P. R., Balco, G., Ludwig, K. R., Mundil, R. & Min, K. (2011). Response to the comment by W.H. Schwarz *et al.* on “Joint

determination of ^{40}K decay constants and $^{40}Ar^*/^{40}K$ for the Fish Canyon sanidine standard, and improved accuracy for $^{40}Ar/^{39}Ar$ geochronology" by P.R. Renne *et al.* (2010). *Geochimica et Cosmochimica Acta* **75**, 5097–5100.

Renne, P. R., Mundil, R., Balco, G., Min, K. & Ludwig, K. R. (2010). Joint determination of ^{40}K decay constants and $^{40}Ar^*/^{40}K$ for the Fish Canyon sanidine standard, and improved accuracy for $^{40}Ar/^{39}Ar$ geochronology. *Geochimica et Cosmochimica Acta* **74**, 5349–5367.

Reusch, A. M., Nyblade, A. A., Tibi, R., Wiens, D. A., Shore, P. J., Bekoa, A., Tabod, C. T. & Nnange, J. M. (2011). Mantle transition zone thickness beneath Cameroon: Evidence for an upper mantle origin for the Cameroon Volcanic Line. *Geophysical Journal International* **187**, 1146–1150.

Reusch, A. M., Nyblade, A. A., Wiens, D. A., Shore, P. J., Ateba, B., Tabod, C. T. & Nnange, J. M. (2010). Upper mantle structure beneath Cameroon from body wave tomography and the origin of the Cameroon Volcanic Line. *Geochemistry, Geophysics, Geosystems* **11 (10)**.

Reynolds, R. C. (1963). Matrix corrections in trace element analysis by X-ray fluorescence: Estimation of the mass absorption coefficient by Compton scattering. *The American Mineralogist* **48**, 1133–43.

Rivalenti, G., Mazzucchelli, M., Girardi, V. a. V., Vannucci, R., Barbieri, M. A., Zanetti, A. & Goldstein, S. L. (2000). Composition and processes of the mantle lithosphere in northeastern Brazil and Fernando de Noronha: evidence from mantle xenoliths. *Contributions to Mineralogy and Petrology* **138**, 308–325.

Rivalenti, G., Zanetti, A., Girardi, V. A. V, Mazzucchelli, M., Tassinari, C. C. G. & Bertotto, G. W. (2007). The effect of the Fernando de Noronha plume on the mantle lithosphere in north-eastern Brazil. *Lithos* **94**, 111–131.

Rollinson, H. (1993). *Using geochemical data: evaluation, presentation, interpretation*. Harlow: Pearson Prentice Hall.

Sacek, V. (2017). Post-rift influence of small-scale convection on the landscape evolution at divergent continental margins. *Earth and Planetary Science Letters* **459**, 48–57.

Sacek, V. & Ussami, N. (2013). Upper mantle viscosity and dynamic subsidence of curved continental margins. *Nature Communications* **4**, 1–6.

Santos, T. J. S. dos, Fetter, A. H. & Neto, J. A. N. (2008). Comparisons between the northwestern Borborema Province, NE Brazil, and the southwestern Pharusian Dahomey Belt, SW Central Africa. In: Pankhurst, R. J., Trouw, R. A. J. & Brito Neves, B. B. (eds) *West Gondwana: Pre-Cenozoic correlations across the South Atlantic region*. Geological Society, London, Special Publications **294**, 101–120.

Schwarz, W. H., Kossert, K., Trieloff, M. & Hopp, J. (2011). Comment on the " Joint determination of ^{40}K decay constants and $^{40}Ar^*/^{40}K$ for the Fish Canyon sanidine standard, and improved accuracy for $^{40}Ar/^{39}Ar$

geochronology" by Paul R. Renne et al. (2010). *Geochimica et Cosmochimica Acta* **75**, 5094–5096.
Sial, A. N. (1975a). Fracionamento de Ni entre olivina e augita e a temperatura de cristalização dos basaltos terciários do Rio Grande do Norte e Paraíba. *Atas do VII simpósio de geografia*. Fortaleza: Dept. Geologia. Centro Tecnologia UFPE, 243–246.
Sial, A. N. (1975b). Profundidade de formação do magma basáltico terciário do Rio Grando do Norte e Paraíba, deduzida de suas inclusões peridotíticas. *Atas do VII simpósio de geografia*, 173–184.
Sial, A. N. (1976a). The Rio Grande do Norte alkali-olivine basalt association, Northeast Brazil. *Revista Brasileira de Geociências* **6**, 1–14.
Sial, A. N. (1976b). The post-Paleozoic volcanism of Northeast Brazil and its tectonic significance. *Anais da Academia Brasileira de Ciências* **48**, 299–311.
Sial, A. N., Long, L. N., Pessoa, D. A. R. & Kawashita, K. (1981). Potassium-argon ages and strontium isotope geochemistry of Mesozoic and Tertiary basaltic rocks, northeastern Brazil. *Anais da Academia Brasileira de Ciências*, 115–122.
Silveira, F. V (2006). *Magmatismo cenozóico da porção central do Rio Grande do Norte, NE do Brasil*. Doctoral thesis. Centro de Ciências Exatas e da Terra, Federal University of Rio Grande do Norte, Brazil.
Sleep, N. H. (1996). Lateral flow of hot plume material ponded at sublithospheric depths. *Journal of Geophysical Research* **101**, 28065–28083.
Sleep, N. H. (2003). Fate of mantle plume material trapped within a lithospheric catchment with reference to Brazil. *Geochemistry, Geophysics, Geosystems* **4 (7)**.
Souza, Z. S. de, Nascimento, M. A. L. do, Barbosa, R. V. N. & Dias, L. G. da S. (2005). Geology and tectonics of the Boa Vista Basin (Paraíba, northeastern Brazil) and geochemistry of associated Cenozoic tholeiitic magmatism. *Journal of South American Earth Sciences* **18**, 391–405.
Souza, Z. S. de, Vasconcelos, P. M., Knesel, K. M., Dias, L. G. da S., Roesner, E. H., Farias, P. R. C. de & Morais Neto, J. M. de (2013). The tectonic evolution of Cenozoic extensional basins, northeast Brazil: Geochronological constraints from continental basalt 40Ar/39Ar ages. *Journal of South American Earth Sciences* **48**, 159–172.
Sparks, R. S. J., Folkes, C. B., Humphreys, M. C. S., Barfod, D. N., Clavero, J., Sunagua, M. C., McNutt, S. R. & Pritchard, M. E. (2008). Uturuncu volcano, Bolivia: Volcanic unrest due to mid-crustal magma intrusion. *American Journal of Science* **308**, 727–769.
Sun, S. -s. & McDonough, W. F. (1989). Chemical and isotopic systematics of oceanic basalts: implications for mantle composition and processes. In: Saunders, A. D. & Norry, M. J. (eds) *Magmatism in the ocean basins*. Geological Society, London, Special Publications **42**, 313–345.
Thompson, R. N. (1984). Dispatches from the Basalt Front. I. Experiments. *Proceedings of the Geologists' Association*. The Geologists' Association

95, 249–262.
Turner, S., Regelous, M., Kelley, S., Hawkesworth, C. & Mantovani, M. (1994). Magmatism and continental break-up in the South Atlantic: high precision ^{40}Ar-^{39}Ar geochronology. *Earth and Planetary Science Letters* **121**, 333–348.
Ulbrich, M. (1993). Petrography of alkaline volcanic-subvolcanic rocks from the brazilian Fernando de Noronha archipelago, Southern Atlantic Ocean. *Boletim IG-USP. Série Científica* **24**, 77–94.
Ulbrich, M. N. C. & Lopes, R. P. (2000). Xenólitos de origem subvulcânica na Formação Remédios, arquipélago de Fernando de Noronha: petrografia, textura e química mineral. *Geochimica Brasiliensis* **14**, 097-114.
Ulbrich, M. N. C., Maringolo, V. & Ruberti, E. (1994). The geochemistry of alkaline volcanic-subvolcanic rocks from the Brazilian Fernando de Noronha Archipelago, southern Atlantic Ocean. *Geochimica Brasiliensis* **8**, 21–39.
van Schmus, W. R., Oliveira, E. P., da Silva Filho, A. F., Toteu, S. F., Penaye, J. & Guimaraes, I. P. (2008). Proterozoic links between the Borborema Province, NE Brazil, and the Central African Fold Belt. In: Pankhurst, R. J., Trouw, R. A. J. & Brito Neves, B. B. (eds) *West Gondwana: Pre-Cenozoic correlations across the South Atlantic region*. Geological Society, London, Special Publications **294**, 69–99.
Velde, D. & En-Noufous Rachdi, H. (1988). Influence of Sr on an established petrological incompatibility: The association melilite + K-Feldspar in a nephelinite from Djebel Targou, Central Morocco. *Journal of Petrology* **29**, 585–597.
Vogt, P. R. (1991). Bermuda and Appalachian-Labrador rises: common non-hotspot processes? *Geology* **19**, 41–44.
Walter, M. J. (1998). Melting of garnet peridotite and the origin of komatiite and depleted lithosphere. *Journal of Petrology* **39**, 29–60.
Weaver, B. L. (1990). Geochemistry of highly-undersaturated ocean island basalt suites from the South Atlantic Ocean: Fernando de Noronha and Trindade islands. *Contributions to Mineralogy and Petrology* **105**, 502–515.
White, W. M. (2015). *Isotope geochemistry*. Oxford: Wiley.
Winter, J. D. (2010). *An introduction to igneous and metamorphic petrology*. New Jersey: Pearson Prentice Hall.

Appendix A: Methods

Preliminary sample preparation for XRF and ICP-MS

Samples were collected during 2 weeks of fieldwork in Fernando de Noronha in September 2014, and during 2 weeks in the Borborema Province in October 2015. Sample localities and locality characteristics were given in Chapter 1. From those collected, 50 samples from Fernando de Noronha and 30 from Borborema were prepared and analysed by X-Ray Fluorescence (XRF) at the University of Edinburgh, and by Inductively Coupled Plasma Mass Spectrometry (ICP-MS) at the University of Cambridge. Preliminary sample preparation of samples from Fernando de Noronha were conducted at the University of Edinburgh, and of samples from Borborema at the University of Cambridge.

The samples were cut with a diamond saw to obtain a fresh core ~100-200 g with no originally exposed surfaces and no detectable xenoliths with the naked eye. They were subsequently dried overnight in an oven at 110^{o}C, and crushed with a tungsten carbide reciprocating rock crusher. Xenoliths detected with the naked eye were picked out. Samples from Fernando de Noronha were ground for 6-8 minutes in an agate barrel swing mill, and samples from Borborema were ground for 12 minutes in an agate barrel ball mill. The obtained powders were used for the XRF, ICP-MS and isotope analyses.

XRF

Sample preparation

Major element concentrations were measured on fused glass disks and trace element ones on pressed powder pellets. One glass disk and one powder pellet were produced for each sample. The glass disks were prepared by a method similar to that of Norrish & Hutton (1969). Unignited

fine rock powder was first dried overnight at 110°C. In a Pt90Au10 crucible, 0.9-1.0g of each sample was weighed and heated at 1100°C for 20 minutes in order to decompose carbonates and hydrous silicates. Samples were then weighed again, in order to obtain a value for the initial loss of mass on ignition (LOI). An amount of borate flux (Johnson and Mathey Spectroflux 105, which consists of a mixture of 47% lithium tetraborate, $Li_2B_4O_7$, 37% lithium oxide, Li_2O, and 16% lanthanum oxide, La_2O_3, as an x-ray heavy absorber) was added to the crucible in order to reach a total mass equal to 6 times the mass of the initial unignited sample (± 0.0003), and gently mixed. In between stages and before each weighing stage, samples were always kept in a desiccator jar to avoid re-absorption of moisture. The mixture was placed in an oven at 1100°C for 20 minutes in a lidded crucible, then swirled and cooled for 10 minutes. Further borate flux was added to compensate for any loss of mass during the second firing stage (± 0.0003). The lidded crucible was placed over a Meker burner, and the sample fused again with the added borate flux for about 3 minutes, being swirled thoroughly during this time (3x for 30 seconds). The resulting melt was then immediately cast onto a graphite plate over a hotplate at 220°C, and a glass disk formed by using an Al plunger and a steel guide ring. The glass disk was annealed for at least 15 minutes, then transferred to a hotplate at 110°C and annealed for another 15 minutes before being left to cool. Finally, excess glass around the pellets was trimmed with pliers and a self-adhesive label with the sample details fixed to the back of the disk.

The powder pellets were produced by adding 8 drops of a poly-vinyl acetate (PVA) binding solution (2% PVA solution) to 8 ± 0.1 g of fine rock powder and mixing thoroughly until evenly distributed. The mixture was then put in a tapered Al pellet cup inside a steel mould assembly and compressed between two 40mm tungsten carbide (WC) die at 8 tonnes for 2 minutes

using an automated hydraulic press, with decompression regulated at 0.3 minutes.

Analyses

Samples were analysed at the School of Geosciences at the University of Edinburgh using a Philips PW2404 wavelength dispersive sequential X-ray spectrometer fitted with a Rh anode end window X-ray tube. Analytical methods are detailed in Fitton *et al.* (1998). The spectrometer was calibrated using the international standard samples ALI, BCR, BEN, BHVO-1 and BIR-1, for major elements, and with all values listed in Govindaraju (1994), except for Nb and Zr, which are given in Jochum et al. (1990). Data for standards are given in Appendix C, including measured values and those listed in the aforementioned references, allowing for an assessment of precision and accuracy.

Analytical lines (fluorescence peaks) are chosen to provide high intensity with minimal interference from other elements. Line overlap factors were calculated using international standards for calibration combined with synthetic standards for trace element overlaps. The synthetic standards were prepared from AnalaR-grade pure oxides mixtures of basalt and granite bulk compositions spiked with stoichiometric trace element compounds. The mixtures were ground, fused and pressed into pellets as described above. Line overlap corrections are applied to Rb on Y, Sr on Zr, Nb on V & Ba, V on Cr, Cr on Ce, Ce on Nd, Ca on Sc, Sc on Ba, Sr on U, Rb on U & Th. Major elements corrections were applied to for Ca on Mg, Ti & P, Mg on Na.

The use of a heavy absorber (La_2O_3) in the flux composition for major elements analyses allows the production of glass disks with relatively constant matrix composition. However, linearity of calibration is improved by correcting the intensities of major elements lines for matrix effects using theoretical alpha coefficients that are calculated ‘on-line’ (De Jongh, 1973). These coefficients are calculated to allow for volatile components (H_2O +

CO_2) in the sample which are replaced by flux. Analytical total should be, therefore, 100% minus LOI.

The intensities of the Rb, Sr, Y, Zr and Nb lines are corrected for matrix effects using the count rate from the Rh Kα Compton scatter line as an internal standard (Reynolds, 1963). All other trace element intensities are corrected for matrix effects using theoretical alpha coefficients based on major element concentrations measured on powder pellets at the same time.

ICP-MS

All ICP-MS procedures were conducted in the Department of Earth Sciences at the University of Cambridge by Marthe Klöcking, who also wrote the following two subsections following Klöcking (2017). Precision and accuracy estimated based on comparing measured with published (see below) standard values are given in Appendix C.

Sample preparation (*Marthe Klöcking*)

For each sample, 0.1000 g of finely ground rock powder was digested using 4 ml HF plus 1 ml HNO_3 in sealed PFA vials. The acids used for sample preparation were ppb grade and were further distilled in house using Teflon or quartz stills. An Evapoclean® (Analab, France) system consisting of a temperature-controlled Teflon-covered graphite block was used for digestions and evaporations in a closed, clean PFA environment, avoiding the need for sample preparation to be carried out in a clean lab. Blanks and standards were prepared with each set of samples to monitor the quality of the sample preparation method.

Analyses (*Marthe Klöcking*)

All samples were analysed on a PerkinElmer SCIEX Elan DRC II quadrupole ICP-MS (Inductively Coupled Plasma – Mass Spectrometer). The method of analysis is similar to that used in Eggins *et al.* (1997) and based

on the use of international rock standards for matrix matched calibration. ICP-MS internal standards were 10 ppb Rh, In and Re and each sample was diluted x5000 for analysis in 1% HNO_3. Under the conditions used, instrumental drift was less than 5% measured for the internal standard intensity during the entire analytical run (40 or more solutions per batch). Solutions were analysed using a Micromist nebuliser (FM05, Glass Expansion, Australia) and a quartz cyclonic baffled spray chamber with platinum sampler and skimmer cones. ICP-MS sensitivity in this configuration was 5 x 10^4 cps/ppb In with CeO/Ce ratios of 2%. Appropriate corrections were made using oxide/metal correction factors calculated by analysing pure single-element standard solutions. Instrument calibration was performed using preferred values from the GeoReM database (version 9, 2009; http://georem.mpch-mainz.gwdg.de/) by analysing matrix-matched USGS rock standards BIR-1, AGV-1, BHVO-2, and BCR-2 (all values given in Appendix C), which were dissolved using the same procedures as the samples. Concentrations were calculated in a spreadsheet from raw intensities by blank subtraction, internal standard normalisation, and rare earth oxide correction. The calibration method was a simple linear calibration curve to calculated slopes and the intercept was set to zero. All results (unknowns and standards) were accurately corrected for dilutions by mass. Total procedural blanks for all elements were very low, with abundances slightly higher than the ultra-pure 1% HNO_3 rinse solution but negligible compared to the sample intensities. External reproducibility, based on replicate analysis of standards and samples within batches, is 2-5% for all analytes. Accuracy for the analysis of rock standards such as BCR-2 during

the run for most elements was within ~2% of the GeoReM preferred values and better than 5% (n = 5) for the rest of the elements studied.

$^{40}Ar/^{39}Ar$ dating

$^{40}Ar/^{39}Ar$ analyses were conducted at the Scottish Universities Environmental Research Centre (SUERC), East Kilbride, by Dr. Dan Barfod. All samples preparation was conducted by the author at the same facilities.

Sample preparation

The samples were cut with a diamond saw to obtain a fresh core around 100-200 grams with no originally exposed surfaces and no detectable xenoliths with the naked eye, and subsequently dried overnight in an oven at 110°C. They were then crushed using a Retsch DM 200 disk mill, and dry sieved to separate grains between 250-500 μm. These were washed using with deionised water and left to dry overnight in a 70°C heated cupboard. Mafic and felsic groundmass samples were then leached in a glass beaker with 25% dilute HNO_3 while immersed in an ultrasonic bath for 30 minutes. They were subsequently rinsed 3 times with deionised water (18 mega ohms) and returned to the ultrasonic bath with the beakers refilled with deionised water for another 30 minutes. The rinsing procedure was repeated until water was clear. Sanidine crystals (all from phonolite samples) were leached in Teflon beakers with 5% dilute HF immersed in an ultrasonic bath for 3 minutes. They were subsequently rinsed 10 times with deionised water and returned to the ultrasonic bath with the beakers refilled with deionised water for another 30 minutes. The rinsing procedure was repeated 3 times. Samples were then dried overnight in a 70°C heated cupboard.

All samples were then magnetically separated using a Frantz magnetic barrier laboratory separator, in order to separate groundmass from phenocrysts (i.e. olivine in the case of mafic samples, and sanidine and nepheline in the case of felsic samples). This process also allows the

separation of groundmass grains dominated by phenocrysts. This process was repeated until the desired level of purity was obtained. All groundmass separates were then handpicked under a binocular microscope to further remove phenocrysts and altered grains. Sanidine phenocrysts were also handpicked from the felsic phenocryst separates, favouring clear, non-fractured euhedral crystals that could not be confused with other minerals. The goal was to obtain groundmass grains free of phenocrysts. However, despite all the stages involved in processing the grains, it is not possible to completely eliminate all phenocrysts, especially when they are < 250 μm and could be fully enclosed in grains of the selected size range.

Irradiation and analyses

Samples and neutron flux monitors were packaged in copper foil packets and stacked in quartz tubes with the relative positions of packets precisely measured for later reconstruction of neutron flux gradients. The sample package was irradiated in the Oregon State University reactor, Cd-shielded facility. Fish Canyon sanidine (28.294 ± 0.036 (1σ) Ma; Renne et al. 2011)[2] was used as standard to monitor ^{39}Ar production and establish neutron flux values (*J*) for the samples.

Gas was extracted from samples via step-heating using a mid-infrared (10.6 *μ*m) CO_2 laser with a non-gaussian, uniform energy profile and a 3.5 mm beam diameter. The samples were housed in a doubly-pumped ZnS-window laser cell and 50 mg aliquots loaded into a copper planchette containing nine 1 cm^2 square wells. Liberated Ar was purified of active gases (e.g. CO_2, H_2O, H_2, N_2 and CH_4) using three Zr-Al getters, one at 16°C and two at 400°C. Data were collected on a GVi Instruments ARGUS V multi-collector mass spectrometer using a variable sensitivity faraday collector array in static collection (non-peak hopping) mode (Sparks *et al.*, 2008; Mark *et al.*, 2009). Time-intensity data were regressed to inlet time with second-

[2] In reference to Renne et al. (2010) and Schwarz et al. (2011).

order polynomial fits to the data. The average total system blank for laser extractions, measured between each sample run, was $1.1 \pm 0.4 \times 10^{-15}$ mol ^{40}Ar, $1.5 \pm 2.0 \times 10^{-17}$ mol ^{39}Ar, $5.2 \pm 2.4 \times 10^{-18}$ mol ^{36}Ar. Mass discrimination was monitored on a daily basis between sample runs by analysis of an air standard aliquot delivered by an automated pipette system. All blank, interference and mass discrimination calculations were performed with the MassSpec software package (MassSpec, version 8.058, authored by Al Deino, Berkeley Geochronology Center, Version 8.058).

Inverse-variance-weighted plateau ages were chosen as the best estimates of the emplacement ages. Plateau ages were defined following the following criteria:

1) Steps overlap in age within 2σ uncertainty;
2) Minimum ^{39}Ar content for a step being ≥ 0.1% of total ^{39}Ar release;
3) Minimum of three contiguous steps;
4) Minimum of 50% of ^{39}Ar in the chosen steps;
5) The inverse isochron formed by the plateau steps yields an age indistinguishable from the plateau age at 2σ uncertainty;
6) The trapped component composition, derived from the inverse isochron, is indistinguishable from the composition of air at the 2σ uncertainty level;
7) Age and uncertainty were calculated using the mean weighted by the inverse variance of each step;
8) For replicated samples, an error-weighted plateau for each aliquot was independently calculated and the accepted steps for each aliquot combined into a composite plateau.

Isotopes

Isotope analyses were conducted at the Scottish Universities Environmental Research Centre (SUERC), East Kilbride, by Mrs Anne Kelly

(*column chemistry*) and Mr. Vincent Gallagher (*analyses*), with the author working as an assistant. All samples preparation was conducted by the author at the same facilities.

Column chemistry

Around 0.2000g of finely crushed rock powder was put into a PFA Teflon (savillex) beaker, and digested in steps using ultrapure HF, HNO_3 and HCl over a hotplate at 140-150^{o}C. Sr and REE fractions were separated by standard cation exchange column chemistry using Bio-Rad analytical grade cation exchange resin AG 50W x 8 hydrogen form in a quartz glass column with approximate column volume of 12 ml. In order to further separate Rb from the Sr fraction, samples were passed through Triskem Sr spec resin columns, using methods from Pin & Bassin (1992), and the Sr fraction collected. Rare earth elements fractions from cation columns were passed though small columns containing Triskem/Eichrom Ln resin (Pin and Zalduegui, 1997), and the Nd fractions collected.

Analyses

Sr samples were loaded onto Re filaments using a Ta emitter solution, and Nd samples were loaded onto Ta side-filaments in a triple filament arrangement. Analyses were then carried out on a VG sector 54-30 Thermal Ionisation Mass Spectrometer.

Comparison between XRF and ICP-MS

Overall, there is very good agreement between the XRF and ICP-MS datasets for Fernando de Noronha and Borborema (Figure A-1). However, samples from Fernando de Noronha have shown some scattering for some elements when the XRF and ICP-MS data are compared. The elements most affected were Zn, Cu, Ni, Cr, V, Ba, Sc, La, Ce and Nd. Elements such as Nb, Zr and Y showed no differences. Cu, Sc and V all showed linear trends

that were not 1:1 between the XRF and ICP-MS results, but a linear trend was still maintained, especially for Borborema, suggesting that it could be a calibration issue. Even under these circumstances, the scatter in the Fernando de Noronha results was larger. A second round of analyses produced no improvements in these differences. A third round of analyses was undertaken for Zn, Cu, Ni, Cr, V, Ba and Sc after the Fernando de Noronha samples were grounded further in the same agate barrel swing mill, and the results showed some improvements. Regrinding the samples from Fernando de Noronha was done in order to test the effects of potential differences in grain size in these differences, since powders from Fernando de Noronha and the Borborema Province were initially ground in different machines. Some elements (i.e. La, Ce and Nd) however were not reanalysed for all samples. The scattering was somewhat reduced for La, Zn, Ni and V, and more so for Cr and Ba. However, Cu and Sc showed little and no improvements respectively. The scattering for Cu was initially relatively small, whilst that for Sc was the greatest in the dataset, but these elements showed such effects in both the Borborema and Fernando de Noronha datasets, suggesting that they may occur for a different reason than the other elements, and were therefore unaffected by the regrinding of powders. Nonetheless, differences between the XRF and ICP-MS measurements for Fernando de Noronha were relatively small overall, and their magnitude did not affect the results discussed in this work. A simple statistical assessment of these differences between the XRF and ICP-MS measurements has also shown that they are statistically not significant (Klöcking, 2017). However, the potential problems that may arise from differences in powder grain size are highlighted in this brief comparison.

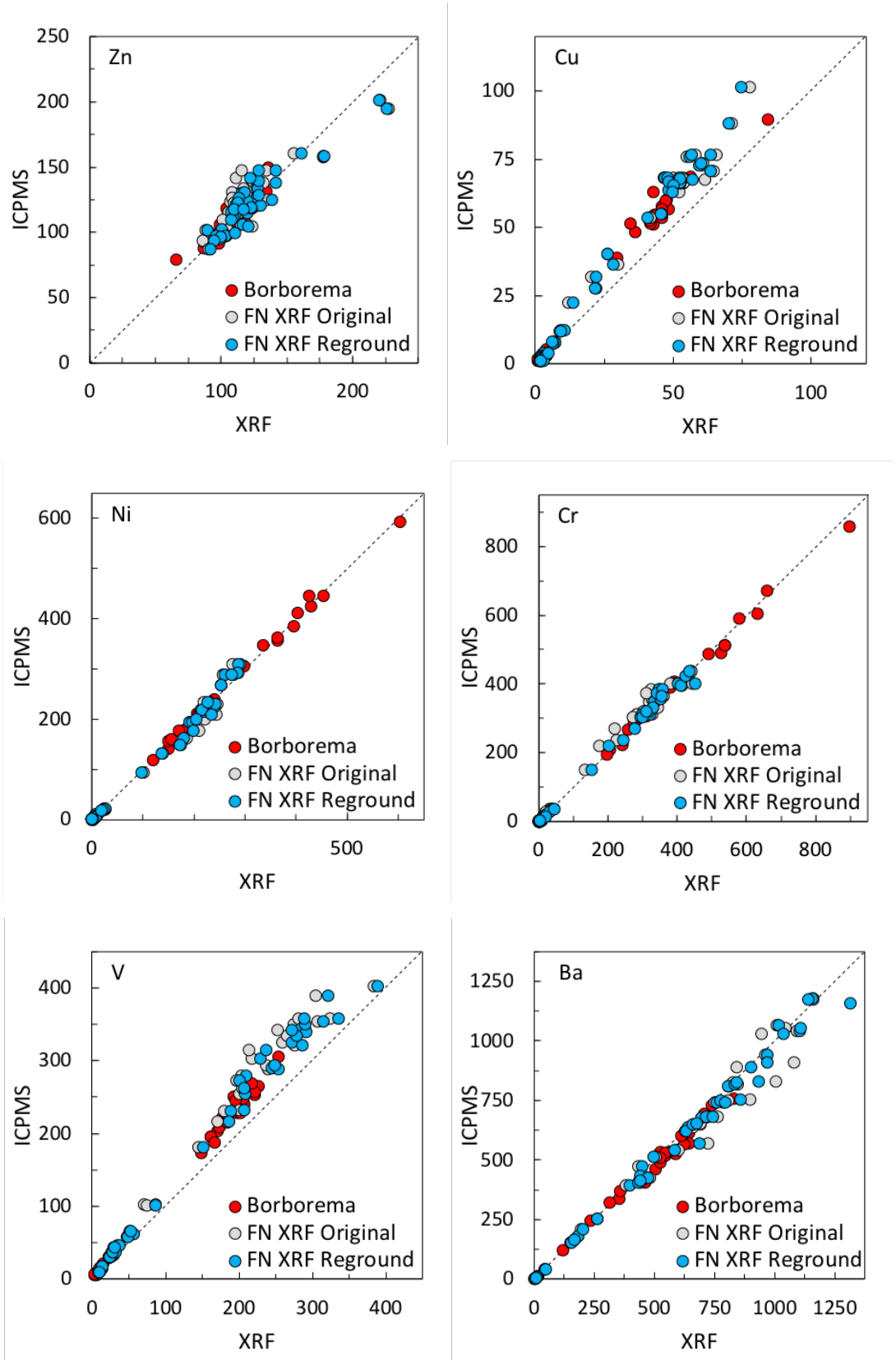

Figure A-1: Continues on the next page.

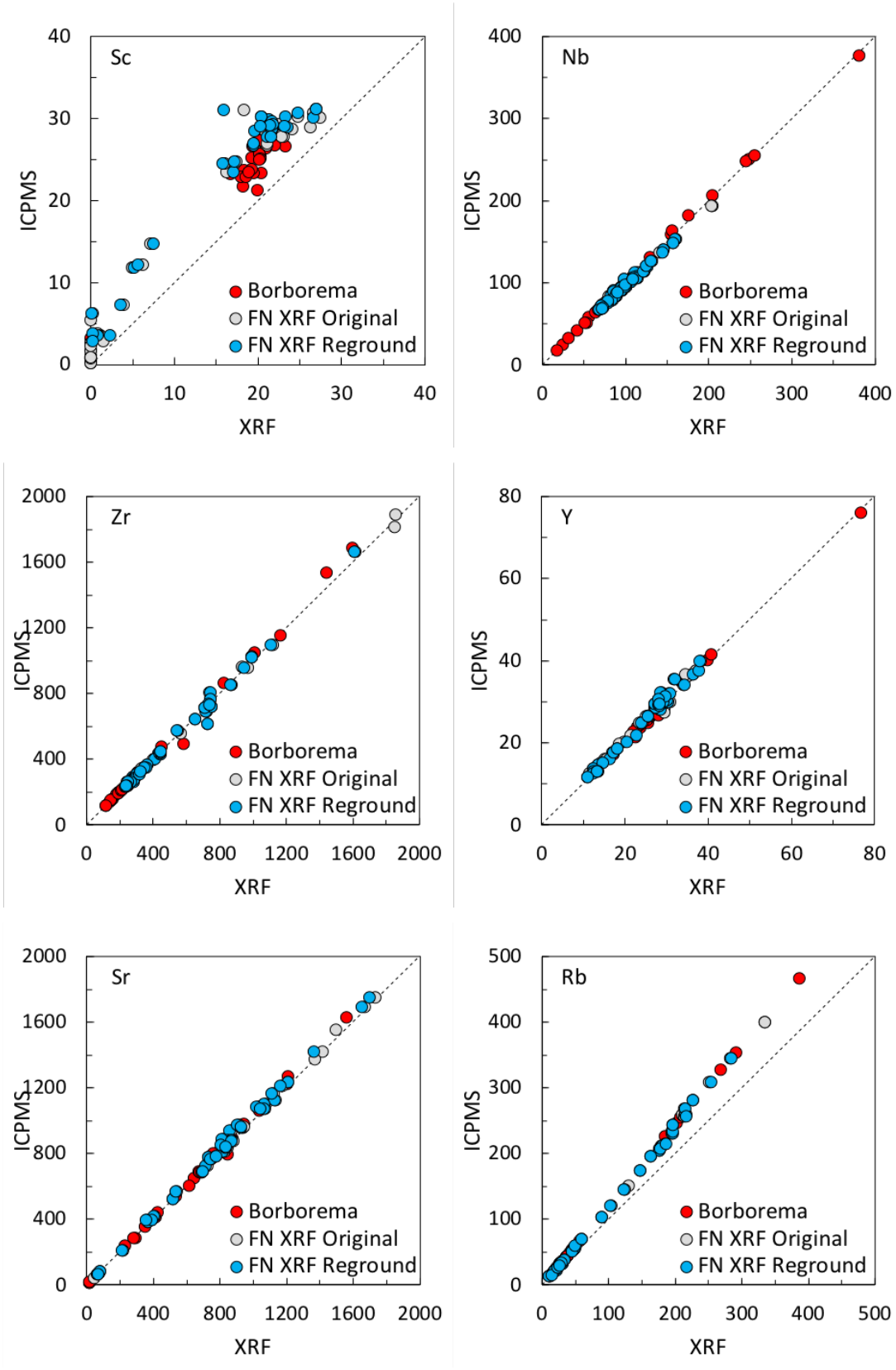

Figure A-1: Continues on the next page.

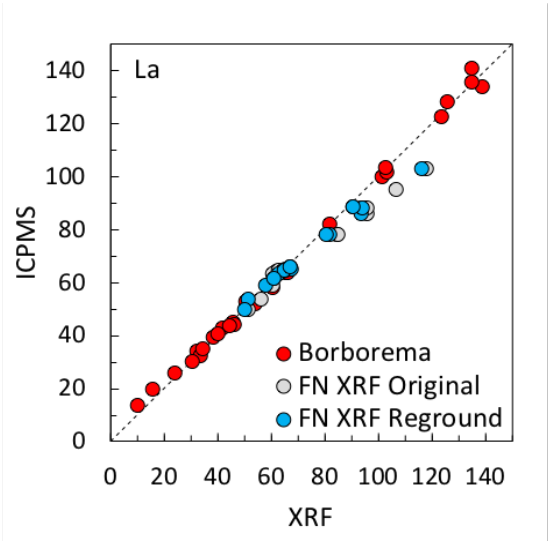

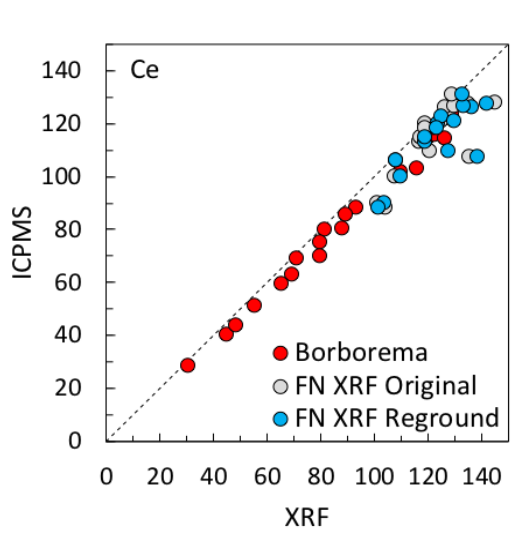

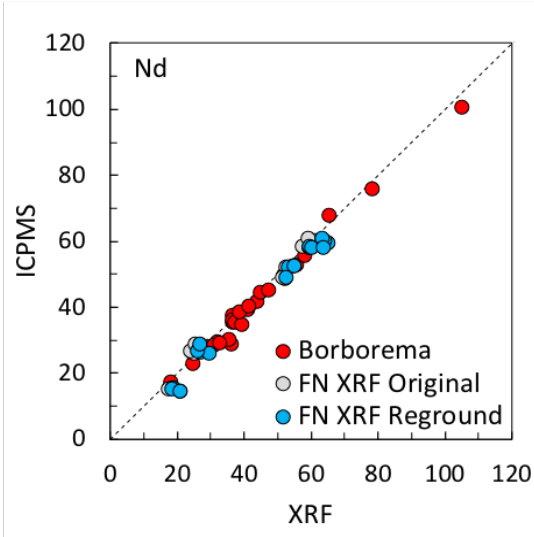

Figure A-1: Comparison between XRF and ICP-MS measurements.

Appendix B: $^{40}Ar/^{39}Ar$ dating dataset

$^{40}Ar/^{39}Ar$ dating dataset table including laboratory reference information and *J* values (Table B-2). The full, raw dataset is given in Appendix F in Volume 2 of 2 of this thesis. Other relevant information and colour guide to the table are also given below, including the values for nucleogenic production ratios, isotopic constants and decay rates used in the analyses (Table B-1). Samples were irradiated in the Oregon State University reactor, Cd-shielded facility. Fish Canyon sanidine (28.294 ± 0.036 (1σ) Ma, Renne et al., 2011) was used to establish neutron flux values (*J*). Decay constants are listed in Renne et al. (2011).

Table B-1: Nucelogenic production ratios, isotopic constants and decay rates used in the analyses.

Nucleogenic production ratios		Isotopic constants and decay rates	
$(^{36}Ar/^{37}Ar)Ca$	2.64×10^{-4}	$\lambda(^{40}K_e)/yr$	$5.757 \pm 0.016 \times 10^{-11}$
$(^{39}Ar/^{37}Ar)Ca$	6.5×10^{-4}	$\lambda(^{40}K_{\beta-})/yr$	$4.955 \pm 0.013 \times 10^{-10}$
$(^{38}Ar/^{37}Ar)Ca$	$0.196 \pm 0.00816 \times 10^{-4}$	$\lambda(^{37}Ar)/d$	$1.983 \pm 0.0045 \times 10^{-2}$
$(^{40}Ar/^{39}Ar)K$	8.5×10^{-3}	$\lambda(^{39}Ar)/d$	$7.068 \pm 0.0788 \times 10^{-6}$
$(^{38}Ar/^{39}Ar)K$	$1.22 \pm 0.0027 \times 10^{-2}$	$\lambda(^{36}Cl)/d$	$6.308 \pm 0 \times 10^{-9}$
$(^{36}Ar/^{38}Ar)Cl$	$2.629 \pm 0.011 \times 10^{2}$	$(^{40}Ar/^{36}Ar)_{Atm}$	298.56 ± 0.31
$^{37}Ar/^{39}Ar$ to Ca/K	1.96	$(^{40}Ar/^{38}Ar)_{Atm}$	1583.5 ± 2.5
$^{38}Ar/^{39}Ar$ to Cl/K	2.9	$^{40}K/K_{Total}$	0.01167 ± 0.00002

Colour code to Table B-2:

Sample info
Plateau data
Isochron data
Integrated age data
Accepted ages
Notes

Table B-2: Dataset for the $^{40}Ar/^{39}Ar$ dating analyses. Colour codes given above. Trapped components in *bold* are higher than current atmospheric values. *g.m.* = groundmass; *n.p.* = no plateau; *n.r.a.* = no resolvable age.

	MQVL						
Sample	**15BP1-1**	**15BP1-1**	**15BP1-1**	**15BP3-2**	**15BP3-3b**	**15BP3-3b**	**15BP3-3b**
Run ID	92902-1	92902-2	92902-1, 92902-2	92900-1	92897-1	92897-1	92897-2
Iradiat.	EK73 BV1	EK73 BV1	EK73 BV1	EK73 BV1	EK73 BV1	EK73 BV1	EK73 BV1
Material	g.m.	g.m.	g.m.	g.m.	g.m.	g.m.	g.m.
***J* value**	0.00163	0.00163	0.00163	0.00164	0.00164	0.00164	0.00164
± 2σ	1.7E-06	1.7E-06	1.7E-06	1E-06	1.7E-06	1.7E-06	1.7E-06
Integrated Ca/K	38.8	50.4	43.5	6.9	21.9	21.9	23.9
± 2σ	22.0	13.8	11.5	3.4	6.4	6.4	5.5
Integrated $^{40}Ar^*/^{39}K$	10.5434	10.5893	10.5587	7.1555	10.3205	8.4625	10.0420
± 2σ	0.4467	0.2923	0.2238	0.0351	0.9610	0.6479	0.8167
Integrated age (Ma)	30.8	30.9	30.8	21.1	30.4	25.0	29.6
± 2σ	2.6	1.7	1.3	0.2	5.6	3.8	4.8
Trapped $^{40}Ar/^{36}Ar$	298.6	298.6	298.6	298.6	298.6	**562.5**	298.6
% rad	0	0	0	0	0	0	0
Plateau Age (Ma)				21.09		22.50	
±2σ (without *J*)				0.04		0.31	
±2σ (with *J*)	n.p.	n.p.	n.p.	0.05	n.p.	0.32	n.p.
MSWD				1.8		1.0	
p				0.07		0.43	
steps				g-o		g-o	
n (steps)				9		9	
n_{tot}				12		14	
Plateau Ca/K				7		23	
± 2σ				4		8	
% ^{39}Ar release				82.0		56.3	
mol ^{39}Ar				3.58E-15		5.47E-16	
Isochron age (Ma)				20.87		22.50	
±2σ (without *J*)				0.22		2.65	
±2σ (with *J*)				0.22		2.65	
n				9		9	
MSWD	164.1			1.0		1.2	
p	0.00			0.41		0.33	
$^{40}Ar/^{36}Ar_{(i)}$				432.9		562.5	
± 2σ				139.9		169.4	
Status	-			accepted		accepted	
Notes	n.r.a.				Excess argon. Plateau calculation uses trapped component from inverse isochron analysis.		

Table B-2 (cont.)

	MQVL (cont.)				
Sample	**15BP3-5**	**15BP4-6**	**15BP4-6**	**15BP4-7**	**15BP4-7**
Run ID	92912-1	92910-1	92910-2	92907-1	92907-2
Iradiat.	EK73 BV2	EK73 BV2	EK73 BV2	EK73 BV2	EK73 BV2
Material	g.m.	g.m.	g.m.	g.m.	g.m.
***J* value**	0.00161	0.00163	0.00163	0.00163	0.00163
± 2σ	1.4E-06	1.1E-06	1.1E-06	9.4E-07	9.4E-07
Integrated Ca/K	10.1	335	275	79	58
± 2σ	5.0	203	90	49	33
Integrated $^{40}Ar^*/^{39}K$	8.4279	25.9173	25.2082	10.9532	10.7376
± 2σ	0.0884	2.5434	1.6029	0.3916	0.2513
Integrated age (Ma)	24.4	75.0	72.8	32.1	31.4
± 2σ	0.5	14.0	9.1	2.3	1.5
Trapped $^{40}Ar/^{36}Ar$	298.6	298.6	298.6	298.6	298.6
% rad	0	0	0	0	0
Plateau Age (Ma)	24.50				
±2σ (without *J*)	0.05				
±2σ (with *J*)	0.08	n.p.	n.p.	n.p.	n.p.
MSWD	1.1				
p	0.38				
steps	e-j				
n (steps)	6				
n_{tot}	14				
Plateau Ca/K	1.7				
± 2σ	0.3				
% ^{39}Ar release	75.4				
mol ^{39}Ar	2.18E-15				
Isochron age (Ma)	24.55				
±2σ (without *J*)	0.10				
±2σ (with *J*)	0.11				
n	6				
MSWD	1.0	165	79	1221	263
p	0.42	0.00	0.00	0.00	0.00
$^{40}Ar/^{36}Ar_{(i)}$	282.1				
± 2σ	27.6				
Status	accepted	-		-	
Notes		n.r.a.		n.r.a.	

Table B-2 (cont.)

	MQVL (cont.)					
Sample	**15BP5-8**	**15BP5-8**	**15BP5-8**	**15BP5-9**	**15BP5-10**	**15BP7-14**
Run ID	92905-1	92905-2	92905-all plat. steps	92922-2	93274-1	92920-2
Iradiat.	EK73 BV2	EK73 BV2	EK73 BV2	EK73 BV3	EK73 B21	EK73 BV3
Material	g.m.	g.m.	g.m.	g.m.	g.m.	g.m.
***J* value**	0.0016192	0.0016192	0.0016192	0.0016282	0.0015447	0.0016464
± 2σ	1.02E-06	1.02E-06	1.02E-06	3.97E-06	0.0000013	2.57E-06
Integrated Ca/K	74	79	1.4	245	8.2	56
± 2σ	40	30	0.3	68	2.3	21
Integrated $^{40}Ar^*/^{39}K$	11.4993	11.3288	11.7218	12.0634	10.44	7.0933
± 2σ	0.3429	0.3235	0.0284	0.7041	0.10	0.1386
Integrated age (Ma)	33.4	32.9	34.0	35.2	28.9	21.0
± 2σ	2.0	1.9	0.2	4.1	0.5	0.8
Trapped $^{40}Ar/^{36}Ar$	298.6	298.6	298.6	298.6	298.6	298.6
% rad	0	0	0	0	0	0
Plateau Age (Ma)	34.01	33.99	34.00	33.91	29.29	21.60
±2σ (without *J*)	0.47	0.06	0.16	0.91	0.081	0.57
±2σ (with *J*)	0.47	0.09	0.17	0.94	0.11	0.58
MSWD	4.1	1.2	2.1	1.3	0.9	2.4
p	0.00	0.31	0.01	0.25	0.48	0.02
steps	b-g	b-m	b-m	m-t	I-Q	a-g
n (steps)	6	12	17	8	9	7
n_{tot}	14	21	18	22	22	22
Plateau Ca/K	1.4	1.6	1.4	251	1.418	3.1
± 2σ	0.5	0.5	0.3	147	0.003	0.8
% ^{39}Ar release	70.7	68.5	99.8	58.1	51.4	42.5
mol ^{39}Ar	1.04E-15	1.01E-15	2.04E-15	1.13E-16	4.4E-15	4.96E-16
Isochron age (Ma)	34.00	33.97	33.98	33.51	29.15	21.45
±2σ (without *J*)	0.09	0.07	0.05	1.67	0.19	0.23
±2σ (with *J*)	0.10	0.08	0.07	1.67	0.19	0.24
n	6	12	18	8	9	7
MSWD	5.0	1.0	1.9	1.5	0.59	2.2
p	0.00	0.46	0.02	0.19	0.77	0.05
$^{40}Ar/^{36}Ar_{(i)}$	300.2	301.2	300.8	315.1	325.4	302.6
± 2σ	3.7	3.2	2.4	59.8	31.3	4.4
Status		accepted		accepted	accepted	accepted
Notes	Plateau forced from steps *b* to *g* in the 1st run, producing a high MSWD. Highest precision run chosen as the best age. The third set of data combines plateau steps from the two runs, with the smallest step, 2*b*, omitted by the software.				Caution. Similar disturbs. at beginning and end when compared to other samples.	MSWD is slightly high.

Table B-2 (cont.)

	MQVL (cont.)		Mecejana			
Sample	**15BP7-15**	**15BP12-26**	**15BP9-19a**	**15BP9-19c**	**15BP9-19c**	**15BP9-19c**
Run ID	93281-1	93282-1	92917-1	92916-1	92916-2	92916-all plat. steps
Iradiat.	EK73 B22	EK73 B22	EK73 BV3	EK73 BV3	EK73 BV3	EK73 BV3
Material	g.m.	g.m.	Sanidine	g.m.	g.m.	g.m.
***J* value**	0.0015447	0.0015447	0.0016455	0.0016438	0.0016438	0.0016438
± 2σ	0.0000013	0.0000013	2.54E-06	2.64E-06	2.64E-06	2.64E-06
Integrated Ca/K	174.0	23.6	0.26	0.06	3.9	-0.4
± 2σ	59.6	7.1	0.92	0.03	10.9	1.3
Integrated $^{40}Ar^*/^{39}K$	4.44	9.24	11.3421	11.1829	11.1858	11.1787
± 2σ	0.15	0.16	0.0474	0.0647	0.0615	0.0213
Integrated age (Ma)	12.36	25.63	33.4	32.9	32.9	32.9
± 2σ	0.84	0.87	0.3	0.4	0.4	0.1
Trapped $^{40}Ar/^{36}Ar$	298.6	298.6	298.6	298.6	298.6	298.6
% rad	0	0	0	0	0	0
Plateau Age (Ma)	12.39		33.48	32.88	32.96	32.92
±2σ (without *J*)	0.23		0.04	0.04	0.03	0.07
±2σ (with *J*)	0.24	n.p.	0.15	0.15	0.15	0.16
MSWD	1.2		1.2	1.0	1.3	1.7
p	0.24		0.30	0.44	0.24	0.03
steps	E-V		d-s	f-l	h-t	f-t
n (steps)	18		16	7	13	20
n_{tot}	22		18	18	22	20
Plateau Ca/K	174.8		-0.1	0.02	-0.2	-0.4
± 2σ	0.3		0.5	0.02	0.4	1.3
% ^{39}Ar release	88.5		97.7	54.4	72.1	100
mol ^{39}Ar	4.5E-16		8.08E-15	3.54E-15	4.00E-15	7.53E-15
Isochron age (Ma)	12.50	no isochron	33.57	33.21	32.97	
±2σ (without *J*)	0.29		0.10	0.17	0.12	
±2σ (with *J*)	0.29		0.14	0.20	0.16	
n	18		16	9	13	
MSWD	1.19		1.0	1.1	1.4	
p	0.26		0.46	0.36	0.17	
$^{40}Ar/^{36}Ar_{(i)}$	297.2		263.8	249.5	297.4	
± 2σ	2.1		36.5	26.4	16.4	
Status			accepted		accepted	
Notes		n.r.a.		The run with atmospheric trapped component was chosen as the best age.		

Table B-2 (cont.)

Sample	Mecejana (cont.) 15BP10-20 (a)	15BP10-20 (a)	15BP10-20 (a)	15BP10-20 (b)	15BP10-21a	15BP10-21b
Run ID	92915-1	92915-2	92915-all plat. steps	92944-1	92943-1	92942-1
Iradiat.	EK73 BV3	EK73 BV3	EK73 BV3	EK73 BV4	EK73 BV4	EK73 BV4
Material	g.m.	g.m.	g.m.	Sanidine	Sanidine	Sanidine
J value	0.0016339	0.0016339	0.0016339	0.0016058	0.0016118	0.0016183
± 2σ	3.26E-06	3.26E-06	3.26E-06	3.89E-06	4.28E-06	4.67E-06
Integrated Ca/K	0.03	0.16	0.04	1.4	0.066	-
± 2σ	0.01	0.05	0.01	1.6	0.025	-
Integrated $^{40}Ar^*/^{39}K$	8.597154	8.587239	8.373011	10.7291	11.7775	12.0803
± 2σ	0.242692	0.223906	0.032363	0.0732	0.0778	0.0410
Integrated age (Ma)	25.2	25.2	24.6	34.0	34.0	35.0
± 2σ	1.4	1.3	0.2	0.5	0.5	0.2
Trapped $^{40}Ar/^{36}Ar$	298.6	298.6	298.6	298.6	298.6	298.6
% rad	0	0	0	0	0	0
Plateau Age (Ma)	24.65	24.50	24.57	30.80	33.94	35.03
±2σ (without *J*)	0.06	0.06	0.16	0.05	0.03	0.03
±2σ (with *J*)	0.15	0.15	0.21	0.22	0.25	0.28
MSWD	2	1.9	3.3	1.6	1.4	1.4
p	0.07	0.1	0.0	0.11	0.21	0.13
steps	j-o	r-v	j-v	g-p	f-m	d-s
n (steps)	6	5	11	10	8	16
n_{tot}	14	22	11	19	18	18
Plateau Ca/K	0.04	0.03	0.04	0.06	-	-
± 2σ	0.02	0.01	0.01	0.01	-	-
% ^{39}Ar release	40.6	26.1	100	67.1	71.0	96.2
mol ^{39}Ar	4.06E-15	2.72E-15	6.78E-15	2.23E-15	7.94E-15	6.10E-15
Isochron age (Ma)	25.89	27.29		31.22	33.98	35.03
±2σ (without *J*)	1.26	1.24		0.29	0.20	0.14
±2σ (with *J*)	1.27	1.25		0.33	0.27	0.24
n	6	5		10	8	16
MSWD	2.0	0.8		1.0	1.7	1.5
p	0.09	0.48		0.43	0.12	0.10
$^{40}Ar/^{36}Ar_{(i)}$	215.6	109.4		261.6	292.4	294.8
± 2σ	87.7	80.3		26.0	23.9	58.6
Status		rejected		accepted	accepted	accepted
Notes	See main text for the reasons for rejecting the ages for this sample.					

Table B-2 (cont.)

Sample	Mecejana (cont.) 15BP10-22 (a)	15BP10-22 (a)	15BP10-22 (a)	15BP10-22 (b)	15BP10-22 (b)	15BP10-23
Run ID	92939-1	92939-2	92939-all plat. steps	92937-1	92937-1	92936-2
Iradiat.	EK73 BV4	EK73 BV4	EK73 BV4	EK73 BV4	EK73 BV4	EK73 BV4
Material	g.m.	g.m.	g.m.	Sanidine	Sanidine	Sanidine
J value	0.0016336	0.0016336	0.0016336	0.0016356	0.0016356	0.0016345
± 2σ	5.12E-06	5.12E-06	5.12E-06	4.34E-06	4.34E-06	3.93E-06
Integrated Ca/K	0.13	0.42	0.13	0.05	0.05	0.09
± 2σ	0.02	0.36	0.02	0.03	0.03	0.06
Integrated $^{40}Ar^*/^{39}K$	11.0432	11.0313	10.9013	12.3831	12.2053	11.8185
± 2σ	0.1139	0.1151	0.0454	0.2707	0.2266	0.0314
Integrated age (Ma)	32.3	32.3	31.9	36.3	35.7	34.6
± 2σ	0.7	0.7	0.3	1.6	1.3	0.18
Trapped $^{40}Ar/^{36}Ar$	298.6	298.6	298.6	298.6	**411.4**	298.6
% rad	0	0	0	0	0	0
Plateau Age (Ma)	32.00	31.81	31.92	35.43	34.92	34.61
±2σ (without *J*)	0.06	0.07	0.17	0.05	0.06	0.015
±2σ (with *J*)	0.29	0.29	0.33	0.27	0.27	0.23
MSWD	1.8	1.6	2.8	2.0	0.4	1.5
p	0.10	0.16	0.00	0.06	0.88	0.12
steps	i-o	q-v	i-v	g-n	g-n	ca-n
n (steps)	7	6	13	8	8	12
n_{tot}	14	21	13	18	18	15
Plateau Ca/K	0.13	0.13	0.13	0.03	0.03	0.09
± 2σ	0.02	0.05	0.02	0.01	0.01	0.08
% ^{39}Ar release	53.7	52.0	100	48.1	48.1	91.9
mol ^{39}Ar	5.88E-15	6.24E-15	1.21E-14	2.94E-15	2.94E-15	4.90E-15
Isochron age (Ma)	32.13	31.01		34.92		34.62
±2σ (without *J*)	0.62	1.18		0.36		0.03
±2σ (with *J*)	0.65	1.20		0.41		0.17
n	7	6		8		12
MSWD	1.9	1.3		0.5		1.641
p	0.10	0.26		0.81		0.09
$^{40}Ar/^{36}Ar_{(i)}$	291.7	341.2		411.4		293.8
± 2σ	31.2	61.8		80.1		17.6
Status	accepted				accepted	accepted
Notes				Chosen run contains excess argon. Plateau calculation therefore uses trapped component from inverse isochron analysis.		

Appendix C: Geochemical data tables

X-ray fluorescence (XRF) major and trace element data for Northeast Brazil, including the Macau-Queimadas volcanic lineament (MQVL), the Mecejana volcanic field and Fernando de Noronha are given on Table C-1. Standards for the XRF major and trace element analyses are given Tables C-2 and C-3, respectively. Inductively coupled plasma mass spectrometry (ICP-MS) trace element data for the same areas, excluding rare-earth elements (REE), are given Table C-4, whilst REE are given on Table C-5. Standards for the ICP-MS analyses are given on Table C-6. Data were acquired following the methods described in Appendix A. Data for the Cameroon Line obtained in the same XRF laboratory using the same techniques are given on Table C-7. The latter do not have a registered loss on ignition (LOI), which was therefore calculated as the difference between total sum of major element oxides in weight% and 100%. All rock types were defined through the geochemical classification scheme based on the total-alkalis and silica diagram, according to Le Maitre et al. (2004), sometimes combining petrographic observations when required by the classification method. The XRF major element data have not been normalised on a volatile-free basis and total iron is given as Fe_2O_3. All major element data are given in weight% (wt.%) and all trace element data given in parts per million (ppm). Detailed petrographic descriptions for Northeast Brazil are given in Appendix E. No petrography was done for the Cameroon Line samples.

Table C-1: (next pages) Northeast Brazil XRF data for major and trace elements. The former given in weight% (wt.%) and the latter in parts per million (ppm). Rock type determined through the total alkalis and silica (TAS) diagram classification according to Le Maitre et al. (2004). * = rock types that differ from the petrographic classification.

Table C-1: Caption on previous page. MQVL

Sample	15BP1-1	15BP3-2	15BP4-6	15BP4-7	15BP5-8	15BP5-9	15BP5-10	15BP5-11	15BP6-12a	15BP6-13	15BP7-15	15BP7-16
Rock type	Basanite	Alkali basalt	Basanite	*Alkali basalt	Basanite	Basanite	Alkali basalt	Alkali basalt	Alkali basalt	Alkali basalt	Nephelinite	Alkali basalt
SiO_2	44.24	47.23	42.14	45.66	43.52	42.2	47.17	46.59	44.43	45.3	40.12	44.65
Al_2O_3	12.27	13.47	10.69	11.02	9.98	10.97	12.93	13.47	11.08	12.48	9.85	11.75
Fe_2O_3	11.68	10.73	12.34	11.1	11.57	12.93	10.61	10.78	11.86	11.65	12.04	12.13
MgO	12.6	8.12	14.05	14.6	17.35	13.92	12.52	10.71	13.91	11.77	16.15	13.46
CaO	9.92	10.51	10.88	10.49	9.26	10.88	9.41	9.4	9.62	11.08	12.11	9.5
Na_2O	4.12	2.78	4.04	2.36	3.09	4.01	2.45	2.7	3.25	2.47	3.73	3.18
K_2O	1.437	1.605	1.021	1.187	1.161	0.859	1.339	1.696	0.719	1.349	1.143	1.163
TiO_2	2.078	2.416	2.456	1.833	2.001	2.334	1.72	2.354	2.606	2.387	2.492	2.348
MnO	0.169	0.16	0.183	0.172	0.172	0.191	0.156	0.159	0.166	0.17	0.2	0.18
P_2O_5	0.747	0.499	0.841	0.502	0.618	0.781	0.379	0.559	0.773	0.527	1.325	0.651
LOI	0.74	1.95	1.22	0.61	1	0.57	0.73	1.62	1.36	0.6	0.73	0.74
Total	100	99.47	99.85	99.53	99.72	99.66	99.42	100.03	99.77	99.78	99.89	99.75
Zn	111.3	98.9	107.5	88.6	109.6	123.5	87	94.7	111.5	104.2	105.9	108.6
Cu	45.6	43.1	47.7	84.4	29.6	44.3	45.8	41.3	36.1	47.6	42.8	46
Ni	299	120.7	363.4	429.3	604.6	363.4	336.1	229	396.3	239.1	453.3	402.6
Cr	380.2	257.6	538.7	896.8	659.6	490	392	318.9	525.8	400.6	631	537
V	162.3	193.1	197.5	201.8	173.1	184.5	183.4	161.9	206.8	208.9	220.9	205.5
Ba	736.8	594.7	586.4	460.5	684.6	622.2	454.4	559.1	543.7	505.4	704.7	525
Sc	16.7	18.3	19.2	22.9	17.9	18.5	19.2	18.9	19.9	21	22	20.3
La	41.9	32.3	45.7	33.6	65.4	66.1	30.6	38.5	50.6	34.6	101.3	40
Ce	81.2	70.9	93	68.8	119.5	121.8	64.9	79.4	109.4	79.5	190.8	87.7
Nd	36.5	36.4	43.7	31.9	44.9	51.8	28.8	36.4	47.2	37.1	78.2	41
U	1.5	1	1.5	1.2	2.5	2.4	1.1	1.3	1.6	1.7	3.6	2.1
Th	6.6	6.1	5.8	5.8	17.8	14.4	5.3	7.3	7.6	5.2	15.4	6.2
Pb	3.4	4.1	3.5	3.2	4.6	6.4	2.8	3.6	3.5	2.8	3.5	3.5
Nb	74	55.6	87.5	53	89.2	97.6	50.6	72	81.3	63.3	129.3	67.4
Zr	180.5	188.5	245	151.9	209.9	246.6	141.6	216	249.8	187.1	311.3	205.8
Y	23.6	25.2	23	22.5	25.9	29.5	24	25.3	24.3	25.9	33.5	29.4
Sr	786.7	641.5	1210.1	615.1	761.8	846	531.1	673.5	811.6	676.8	1202.6	688.5
Rb	41.8	56.8	38.1	32.2	47.1	29.9	36.9	48.6	48.7	36	19.9	30.5

Table C-1 (cont.). MQVL **MQVL basins** **Mecejana**

Sample	15BP8-17	15BP8-18	15BP11-24	15BP12-25	15BP12-26	15BP3-3a	15BP3-3b	15BP3-4	15BP3-5	15BP7-14	15BP9-19a	15BP9-19c
Rock type	Basanite	Alkali basalt	Alkali basalt	Nephelinite	Alkali basalt	Basaltic andesite	Basaltic andesite	Basalt	Alkali basalt	Basaltic andesite	Phonolite	Phonolite
SiO_2	43.02	44	45.07	38.82	44.58	54.02	52.77	49.17	48.57	53.15	54.23	55.95
Al_2O_3	11.56	11.74	11.88	10.54	11.47	14.51	14.18	13.48	12.91	14.54	21.03	21.95
Fe_2O_3	12.81	12.63	12.28	14.15	12.04	10.34	9.39	11.1	11.41	10.73	2.81	2.41
MgO	11.05	11.19	9.88	10.99	14.47	5.85	6.32	9.22	9.97	5.49	0.49	0.12
CaO	11.52	10.93	10.49	13.76	9.49	8.71	9.42	9.07	8.38	9.23	1.74	1.18
Na_2O	2.82	2.52	3.46	4.03	2.74	3.01	3.34	2.98	2.89	2.7	8.65	9.8
K_2O	1.486	2.034	1.311	1.453	1.478	0.833	0.505	1.018	1.298	0.569	5.712	6.223
TiO_2	2.868	2.834	2.811	3.311	2.144	1.933	1.884	1.99	2.103	1.834	0.525	0.395
MnO	0.183	0.177	0.169	0.225	0.181	0.141	0.158	0.161	0.159	0.112	0.13	0.165
P_2O_5	0.83	0.749	0.948	1.409	0.655	0.26	0.268	0.345	0.416	0.192	0.102	0.079
LOI	1.57	1.15	1.41	1.07	0.55	0.32	1.54	1.1	1.68	0.98	4.45	1.37
Total	99.72	99.95	99.71	99.77	99.8	99.93	99.78	99.65	99.79	99.53	99.86	99.64
Zn	114.8	111.8	116.7	135.4	109.5	115.8	118.6	110.9	109.4	97.9	66.1	105.5
Cu	53.2	56.1	47.3	34.3	45.8	42.9	42.7	41.8	46.6	48.2	4	2.2
Ni	206.3	209.3	149.5	154.8	424.9	131.5	184.7	171.4	233.7	150.2	5.6	0
Cr	275	285.2	205.9	196.5	579.9	245.2	240.5	293.8	311.5	310.9	11.2	1.7
V	226.8	221.5	217.4	253.6	194.9	163.8	149	177.2	170.2	167.3	22.8	13.4
Ba	642.7	622.5	612.4	545.7	525.4	246.6	235.1	354.8	828.2	644.3	523.4	356.3
Sc	20.1	20.2	20.1	19.3	20.1	21.7	20.4	19.4	18.2	23.3	0.5	0
La	60.5	53.9	62.1	123.8	44.7	-	10	15.6	24.1	46.4	81.7	103.1
Ce	125.9	115.3	128.7	244.7	88.9	-	30.2	44.7	54.9	48.3	121.4	155
Nd	55.7	52.2	58.1	105	41.2	-	18.2	24.8	26	39.4	26.4	30.8
U	1.6	1.1	2.2	2.6	1.7	-	0	1	0.5	0.3	3.4	11.5
Th	6.4	6.2	9.6	14.6	7	-	2.7	1.9	4	2.4	19	33.7
Pb	3.2	3.4	5	5.9	3.6	-	1.7	2.4	3.4	1.9	9.7	14.6
Nb	82.5	76.8	88.4	155.5	71.5	25.8	24.9	31.9	41.3	17.6	155.1	247.8
Zr	305.3	287	305.5	451.8	214	122.6	117.6	137.4	155.7	114	581.3	1163.5
Y	28.1	26.5	27.3	40.7	28.6	23.5	22.4	23.7	25.4	76.7	17.2	22.4
Sr	1035.7	873.7	944.9	1556.8	757.7	342	346.4	414.7	843.8	289.9	424.2	281
Rb	33	49.8	35.6	37.4	44.6	22.8	22	25.2	36.8	18	201.9	291.7

Table C-1 (cont.). Mecejana **Fernando de Noronha**

Sample	15BP10-20	15BP10-21a	15BP10-21b	15BP10-22	15BP10-23	FN01-01	FN01-02	FN02-03	FN03-04	FN04-05	FN04-06	FN05-07
Rock type	Phonolite	Phonolite	Phonolite	Phonolite	Phonolite	Trachyte	Trachyte	Phonolite	Phonolite	Alkali basalt	Alkali basalt	Alkali basalt
SiO_2	56.23	56.01	56.78	58.61	59.71	61.67	60.75	54.85	54.73	44.12	44.21	44.9
Al_2O_3	21.81	20.76	21.98	21.06	19.95	20.66	19.77	22.26	22.13	12.06	12.09	11.11
Fe_2O_3	2.46	2.62	2.17	1.99	2.56	2.5	2.43	2.23	2.22	12.74	12.57	12.7
MgO	0.03	0.28	0.02	0.05	0.15	0.29	0.34	0.07	0.13	10.23	10.52	10.13
CaO	0.57	1.34	0.56	0.86	1.19	0.95	1.9	1.45	1.44	11.73	11.5	11.63
Na_2O	9.91	9	11.26	9.72	8.48	4.33	5.8	9.36	9.3	3.21	2.67	3.14
K_2O	5.573	6.089	5.471	5.755	6.235	6.512	6.161	6.369	6.207	0.7	0.505	0.766
TiO_2	0.27	0.443	0.205	0.173	0.381	0.47	0.429	0.251	0.239	3.019	3.029	3.058
MnO	0.284	0.152	0.21	0.227	0.228	0.065	0.137	0.12	0.122	0.178	0.18	0.198
P_2O_5	0.046	0.085	0.023	0.019	0.05	0.074	0.061	0.043	0.042	0.807	0.79	0.841
LOI	2.31	3.1	1.06	1.25	0.88	2.29	2.09	2.84	3	1.1	1.6	1.24
Total	99.49	99.88	99.74	99.71	99.82	99.82	99.87	99.85	99.56	99.9	99.66	99.7
Zn	177.3	87.6	134.4	119.8	104.3	155.4	88.4	102	104.4	113.5	125.4	121.9
Cu	1.6	2.5	0.7	1	1.4	3	3.1	3.2	2.9	50.7	77.7	46.7
Ni	0	0	0	0	0	4.2	2.4	1.7	1.1	192.7	196.3	216.7
Cr	1.8	2.9	2.5	2	2.3	1.6	0.5	1.4	1.2	340.1	327.8	319.9
V	4.8	15.5	5.7	3.4	3.2	27.6	34.6	26.1	23	258.5	241.2	274.9
Ba	6.3	313.8	15.4	42.5	120.3	1157.9	1159.4	184.2	152.8	658.3	625.7	807.9
Sc	0	0	0	0	0	0	0	0	0	21.1	23	22.3
La	138.8	102.8	125.6	135	135.1	95	106.6	84.6	84.8	56.4	51.3	60.6
Ce	205.3	166.4	189.9	197.4	244	134.8	144.4	100.5	103.6	107.5	107.1	118.7
Nd	36	38.6	35.3	32.8	65.4	24.3	26.1	18.6	17.5	52.5	51.4	57.2
U	20	6.5	12.9	7.9	7.3	-	-	-	-	-	-	-
Th	57.1	23.4	43.6	29.5	28.2	-	-	-	-	-	-	-
Pb	22.2	11.9	18.4	13	13	-	-	-	-	-	-	-
Nb	380.2	175.5	245	204	255.4	112.7	108.9	83.5	82.3	86	85.9	98
Zr	1594.6	821	1440.2	1008.4	993.3	965.9	932	739.7	745.1	275.6	280.2	297.8
Y	28	22.1	27.9	25.4	39.8	13.4	15	12.3	12.4	28.6	27.5	31.8
Sr	15.3	226.8	11.6	17.2	72	722.9	744.6	404.8	368.8	867.3	814	913.9
Rb	386.5	184.3	267.5	208.3	210.3	216.2	209.9	213.8	225.9	12.1	10.6	27.9

Table C-1 (cont.). Fernando de Noronha

Sample	FN06-08	FN07-09	FN07-10	FN10-14	FN10-15	FN10-16	FN11-17	FN14-18	FN15-19	FN15-20	FN13-21	FN13-22	FN13-25
Rock type	Basanite	Basanite	Basanite	Trachyte	Phonolite	Phonolite	Phonolite	Foidite	Tephrite	Foidite	Trachyte	*Tephrite	Trachy-andesite
SiO_2	43.08	40.58	40.34	56.17	53.94	55.23	57.02	40.08	40.59	39.33	61.86	42.66	52.68
Al_2O_3	11.33	10.94	11.25	22.19	21.44	21.65	22.25	10.7	10.75	10.52	20.07	11.93	18.26
Fe_2O_3	12.83	13.41	13.43	3.26	3.09	3.31	2.05	12.9	12.99	12.78	3.03	13.06	6.8
MgO	10.76	11.89	11.32	0.95	0.67	0.77	0.54	13.14	12.74	14.01	0.5	8.11	2.27
CaO	12.06	12.77	12.93	2.49	2.09	2.5	0.77	13.24	13.31	13.61	1.65	11.45	5.18
Na_2O	3.14	3.02	3.02	5.11	7.1	6.58	7.21	3.34	2.06	2.35	5.15	2.26	3.36
K_2O	0.541	1.399	1.535	5.727	6.321	5.875	5.482	1.971	0.938	1.505	5.497	2.137	5.032
TiO_2	3.101	3.375	3.379	0.629	0.614	0.678	0.171	3.176	3.247	3.163	0.421	3.597	2.471
MnO	0.199	0.205	0.207	0.124	0.128	0.135	0.148	0.182	0.192	0.185	0.081	0.187	0.162
P_2O_5	0.825	0.938	1.006	0.111	0.114	0.123	0.025	0.997	1.054	0.966	0.072	0.946	0.695
LOI	1.97	1.32	1.43	2.92	4.12	2.89	4.27	0.06	1.82	1.22	1.33	3.66	3.08
Total	99.84	99.85	99.84	99.68	99.63	99.75	99.94	99.78	99.68	99.64	99.65	100	99.99
Zn	120.9	108.3	106.7	114.6	103.7	94.5	123.3	105	119.1	105.4	108.8	132.1	117.05
Cu	50	54.8	71.1	7	6.3	6.7	1.9	41.6	58.1	53.5	2.7	53.8	11.85
Ni	236.2	223.8	216.3	10.9	9.5	10.9	1.7	229.1	240.4	245.1	9.2	186.2	9.65
Cr	328.2	305.5	274.6	32.4	15.3	20.3	1.1	379.3	413.9	433.2	0.3	224.4	0.35
V	241.3	280.6	282	50.1	47.4	51.4	10.3	274.9	275.9	281.1	30.2	306.9	201.2
Ba	751.9	709.3	721	381.3	434.7	503.1	45.1	692.5	804.6	760.6	1006.4	1003.4	961.85
Sc	21.5	26.3	24.1	1.1	0.2	0.8	0	26.6	27.4	26.9	0	16.2	3.85
La	60.4	62.7	65.5	95.6	95.7	90.5	118	64.4	67	60.9	136.7	92.3	124.55
Ce	116.2	127.3	125.9	120.4	116.8	118.7	135.1	129.6	128.6	124.6	190.5	188.2	222
Nd	54.5	59.6	60.6	25	24	25.5	20.7	61.3	59.1	59.3	38.9	85.4	84.05
U	-	-	-	-	-	-	-	-	-	-	-	-	-
Th	-	-	-	-	-	-	-	-	-	-	-	-	-
Pb	-	-	-	-	-	-	-	-	-	-	-	-	-
Nb	100.3	96.9	93.4	114.1	110.1	125.5	113.9	88.4	106.1	88.8	121.9	89.1	146.05
Zr	272.7	282.3	283.7	717.5	430.4	746	1118.4	272.5	275.5	260.3	869.7	404.2	649.45
Y	28	29.1	30.8	15.5	14.2	16.9	13.1	28.3	28.9	27.1	19.8	36.1	37.1
Sr	850	827.6	844.8	691.7	731.7	742.3	214.3	934.2	867.3	1131.1	772.9	1077.4	1207.5
Rb	15.8	20.4	29.7	176.3	179.3	176	194.6	48.4	19.4	47.9	184.2	44.4	147.4

Table C-1 (cont.). Fernando de Noronha

Sample	FN16-27	FN17-29	FN18-30	FN19-31	FN12-32	FN12-33	FN12-34	FN12-35	FN12-36	FN20-40	FN20-41	FN21-42
Rock type	Tephrite	Phonolite	Phonolite	Tephrite	Trachy-andesite	Trachy-andesite	*Picro-basalt	Alkali basalt	Basaltic trachyandesite	Basaltic trachyandesite	*Tephrite	Phonolite
SiO_2	42.53	55.61	55.22	42.24	55.04	54.66	39.14	42.79	49.31	48.81	42.23	56.84
Al_2O_3	10.69	22.38	22.61	10.44	21.51	19.59	13.02	14.12	17.28	16.63	13.82	21.71
Fe_2O_3	13.59	2.16	2.26	13.71	4.24	4.62	11.19	10.49	7.21	8.12	10.5	2.32
MgO	10.53	0.08	0.26	10.91	1.81	1.97	7.4	7.53	5.01	5.54	7.41	0.17
CaO	12.07	1.41	1.61	12.75	3.27	4.24	16.36	12.9	6.57	7.57	11.44	0.52
Na_2O	3.48	9.85	8.7	3.3	3.42	3.29	0.58	2.12	2.93	2.62	4.28	10.18
K_2O	0.769	6.311	5.856	0.957	5.267	5.799	1.014	2.007	4.818	3.15	2.053	4.891
TiO_2	3.745	0.246	0.291	3.569	1.052	1.232	3.415	2.778	1.784	2.196	2.704	0.183
MnO	0.181	0.119	0.118	0.191	0.124	0.126	0.229	0.193	0.153	0.149	0.183	0.225
P_2O_5	1.11	0.045	0.051	1.108	0.212	0.276	0.804	0.625	0.42	0.537	0.625	0.024
LOI	1.3	1.33	2.71	0.83	3.88	4.2	6.85	4.45	4.52	4.51	4.38	2.52
Total	99.99	99.54	99.69	100	99.84	100.01	100	100.01	100	99.83	99.63	99.59
Zn	123.7	97.4	99.8	111.3	85.85	101.9	135	113.4	101.1	112.4	123.7	220.8
Cu	53.5	2.5	3	53.5	9.3	8.8	64.6	46	21.9	30.05	61.4	2.6
Ni	213.6	1.1	1.4	219.8	24.5	7.6	175.2	243.4	101.4	138.25	220.8	2.3
Cr	283.5	1.1	0	272.8	21.55	2.25	219.8	327.5	133.9	176.35	343.4	1
V	266	23.2	26.2	253.1	71.05	75.1	383.1	239.8	144.8	179.75	237	9.7
Ba	845.9	166.2	261.1	1079.8	945.4	842.45	721.4	897	1091	1044.6	787.8	14
Sc	22.5	0	0	21.9	0.85	1.5	21.8	16	4.9	7.1	18.3	0
La	71.8	77.3	83.4	75.1	104.65	93.7	79.3	73.5	112.7	119.4	70.3	161.5
Ce	153.9	95	101.3	151.3	212.55	136.6	154.4	133	167	186.8	128.9	197.9
Nd	73.9	15.3	16.9	72.2	95.6	34.85	69.1	52.6	50.8	61.75	53.3	32.6
U	-	-	-	-	-	-	-	-	-	-	-	-
Th	-	-	-	-	-	-	-	-	-	-	-	-
Pb	-	-	-	-	-	-	-	-	-	-	-	-
Nb	107.6	81.4	83.9	99.7	116.6	140.7	95.6	100.2	124.6	131.95	100.8	204.1
Zr	439.3	731.6	711.2	396.5	562.4	723	361.4	353	442.9	440.2	340.2	1853.7
Y	34	11.5	12.3	34.6	18.45	21.4	28.7	25	23.5	27.05	25.4	29.5
Sr	1070.5	388.2	518.3	1366.2	1492.8	873.55	541.3	1121.8	1671.3	1730.7	1034.6	42.2
Rb	13.8	213.6	194.8	24.7	129.9	162.3	31.8	32.8	103.6	51.1	58.5	335.1

Table C-1 (cont.). Fernando de Noronha **Fernando de Noronha São José**

Sample	FN22-43	FN24-45	FN25-46	FN25-47	FN26-49	FN27-50	FN28-51	FN29-52	FN30-53	FN30-54	FN30-55	FN30-56
Rock type	Phonolite	Phonolite	Trachy-basalt	Basaltic trachyandesite	Trachyte	Alkali basalt	Alkali basalt	Phonolite	Alkali basalt	Alkali basalt	Alkali basalt	Alkali basalt
SiO_2	55.64	56.98	46.14	51.01	57.62	48.15	42.57	61.25	46.09	45.44	44.53	45
Al_2O_3	21.23	22.3	15.3	18.29	23.34	12.7	10.68	23.65	11.44	12	11.68	11.73
Fe_2O_3	2.27	2.25	12.82	7.96	2.66	12.66	12.25	2.3	13.12	12.09	12.08	12.06
MgO	0.08	0.17	5.48	3.17	0.4	11.65	9.03	0.05	9.75	11.25	12.2	11.87
CaO	0.68	1.11	9.52	5.52	1.28	11.62	10.4	0.95	11.31	11.01	11.39	11.3
Na_2O	9.93	9.29	2.85	2.9	2.61	3.02	2.93	9.78	2.6	2.73	2.61	2.97
K_2O	4.747	6.189	2.272	4.082	6.544	1.123	0.797	5.654	0.921	1.022	1.102	1.043
TiO_2	0.174	0.182	3.291	2.305	0.36	2.706	2.838	0.196	3.005	2.526	2.518	2.497
MnO	0.225	0.134	0.201	0.157	0.099	0.181	0.176	0.205	0.181	0.167	0.172	0.169
P_2O_5	0.017	0.02	0.797	0.607	0.06	0.741	0.739	0.025	0.788	0.702	0.754	0.734
LOI	4.42	1.25	1.02	3.65	4.54	-4.57	7.47	-4.57	0.57	0.59	0.67	0.33
Total	99.41	99.88	99.7	99.65	99.53	99.97	99.87	99.49	99.78	99.52	99.71	99.69
Zn	227.7	121	134	119.1	90.5	108.2	115.5	177.7	108.46	109.9	110.3	116.2
Cu	1.5	1.9	26	20.3	4.4	49.5	49.2	1.5	51.08	60.5	52.1	60.8
Ni	1.8	0.7	26.5	19.9	3.7	286.7	276.1	2.6	255.98	253.5	287.2	277.6
Cr	0.7	1.8	36.7	11.7	2.1	324.7	310.2	2.3	349.78	304.1	441.1	361.8
V	8.5	12.6	304.6	170.4	29.6	217.9	213.6	9.9	202.76	196.8	200.4	204.6
Ba	9.4	1.7	450.6	823.85	193.9	598.7	691.5	7.1	454	441	482.1	437.9
Sc	0	0	17.4	6.15	0	20.8	20.4	0	21.24	21.1	21.1	22.8
La	163.9	94.6	61.2	107.5	74.1	52.1	55.8	142.8	49.38	48.8	54.4	50.2
Ce	202.7	108.3	141.6	168.05	91.8	112	116.6	165.7	106.04	100.9	108.2	109
Nd	33.5	15.9	69.2	55.25	16.5	53.5	56.9	25	51.02	48.4	54.1	51.3
U	-	-	-	-	-	-	-	-	-	-	-	-
Th	-	-	-	-	-	-	-	-	-	-	-	-
Pb	-	-	-	-	-	-	-	-	-	-	-	-
Nb	203.4	109	78.9	160.4	90.7	77.4	80.3	157.5	70.34	67.9	72.9	71.5
Zr	1848.3	991.1	443.4	738.3	547.9	320.6	326.3	1615.7	241.12	229.1	238.5	234.5
Y	29.3	12.8	38.2	30.5	10.9	29.9	34.4	18.1	27.92	27.7	28.2	28.2
Sr	61.1	79.5	1054.1	1175.3	359.1	944.8	844.9	64.1	821.38	808.4	877.3	837.1
Rb	334.3	251	89.8	124.55	195.9	23.6	21.7	282.8	25.92	25.9	28.7	25.7

Table C-2: Standards for XRF major element analyses. International standards were compared with values from Govindaraju (1994). Precision was estimated from multiple runs of randomly selected samples. x_s = reference value; $\bar{x}$ = mean; n = number of analyses; σ = standard deviation; V = coefficient of variation ($100\bar{x}/\sigma$); S = accuracy ($100\bar{x}/x_s$).

Sample		SiO_2	Al_2O_3	Fe_2O_3	MgO	CaO	Na_2O	K_2O	TiO_2	MnO	P_2O_5
ALI		70.11	18.83	0.07	-0.04	0.34	10.86	0.136	0.012	0.002	0.04
	x_s	69.34	18.59	0.075	0.035	0.384	10.59	0.14	0.012	0.004	0.038
	S	101	101	93	-114	89	103	97	100	50	105
BEN		39.05	10.23	12.73	13.73	13.88	3.35	1.389	2.593	0.202	1.211
	x_s	38.2	10.07	12.84	13.15	13.87	3.18	1.39	2.61	0.2	1.05
	S	102	102	99	104	100	105	100	99	101	115
BHVO-1		50.55	13.82	12.27	7.27	11.52	2.85	0.535	2.723	0.176	0.287
	x_s	49.94	13.8	12.23	7.23	11.4	2.26	0.52	2.71	0.168	0.273
	S	101	100	100	101	101	126	103	100	105	105
BIR-1		48.73	16.14	11.31	10.05	13.11	1.89	0.024	0.935	0.174	0.019
	x_s	47.77	15.35	11.26	10.05	13.24	1.75	0.027	0.96	0.171	0.046
	S	102	105	100	100	99	108	89	97	102	41
FN01-02	$\bar{x}$ (n = 3)	60.38	19.63	2.45	0.33	1.89	6.20	6.21	0.43	0.14	0.06
	σ	0.08	0.06	0.01	0.01	0.01	0.06	0.04	0.00	0.00	0.00
	V	0.14	0.33	0.37	3.57	0.50	0.94	0.70	1.03	0.55	3.98
FN06-08	$\bar{x}$ (n = 7)	42.04	11.35	13.18	10.82	12.14	3.38	0.56	3.12	0.21	0.93
	σ	0.23	0.12	0.41	0.06	0.07	0.03	0.01	0.02	0.00	0.01
	V	0.55	1.04	3.08	0.59	0.56	0.87	1.26	0.58	0.63	0.75
FN14-18	$\bar{x}$ (n = 4)	39.61	10.60	13.00	13.16	13.26	3.54	1.97	3.17	0.19	1.12
	σ	0.03	0.03	0.04	0.08	0.03	0.02	0.01	0.01	0.00	0.00
	V	0.08	0.27	0.32	0.60	0.25	0.52	0.71	0.29	1.02	0.37
FN12-34	$\bar{x}$ (n = 3)	38.57	12.76	11.19	7.35	16.32	0.62	1.00	3.41	0.23	0.89
	σ	0.08	0.02	0.04	0.03	0.06	0.03	0.00	0.01	0.00	0.00
	V	0.22	0.19	0.32	0.43	0.39	5.49	0.41	0.39	0.48	0.12
FN17-29	$\bar{x}$ (n = 4)	55.30	22.41	2.19	0.06	1.40	10.36	6.31	0.24	0.12	0.04
	σ	0.33	0.20	0.01	0.03	0.02	0.38	0.08	0.00	0.00	0.00
	V	0.60	0.91	0.41	54.88	1.68	3.63	1.24	0.83	0.69	6.12
15BP3-3a	$\bar{x}$ (n = 2)	53.98	14.55	10.31	5.86	8.67	3.00	0.83	1.93	0.14	0.26
	σ	0.05	0.06	0.05	0.01	0.05	0.01	0.00	0.01	0.00	0.00
	V	0.09	0.38	0.46	0.13	0.58	0.37	0.31	0.34	1.57	1.07

Table C-3: Standards for XRF trace element analyses. International standards were compared with values from Govindaraju (1994). Precision was estimated from multiple runs of samples. x_s = reference value; $\bar{x}$ = mean; *n* = number of analyses; σ = standard deviation; V = coefficient of variation ($100\bar{x}/\sigma$); S = accuracy ($100\bar{x}/x_s$).

Sample		Zn	Cu	Ni	Cr	V	Ba	Sc	La	Ce	Nd	Nb	Zr	Y	Sr	Rb
BCR	x_s	129.5	19.0	13.0	16.0	407.0	681.0	32.6	24.9	53.7	28.8	14.0	190.0	38.0	330.0	47.2
	$\bar{x}$ (n = 3)	124.9	17.9	13.5	4.1	397.8	690.9	30.6	-	-	-	12.7	192.4	37.9	333.5	47.6
	σ	0.8	0.2	0.2	0.5	0.7	1.1	0.3	-	-	-	0.1	1.1	0.3	2.9	0.3
	V	0.6	1.4	1.3	13.4	0.2	0.2	0.9	-	-	-	0.9	0.6	0.8	0.9	0.7
	S	96.4	94.4	104.1	25.4	97.7	101.4	93.9	-	-	-	90.4	101.2	99.7	101.1	100.8
BEN	x_s	120.0	72.0	267.0	360.0	235.0	1025.0	22.0	82.0	152.0	67.0	105.0	260.0	30.0	1370.0	47.0
	$\bar{x}$ (n = 3)	133.2	76.6	280.9	382.1	248.5	1058.0	24.7	91.9	156.1	69.9	117.3	266.8	29.8	1383.3	47.5
	σ	0.4	0.6	0.6	0.0	1.5	1.6	0.3	1.4	0.6	0.5	0.3	1.0	0.2	4.7	0.2
	V	0.3	0.7	0.2	0.0	0.6	0.1	1.1	1.5	0.4	0.7	0.3	0.4	0.5	0.3	0.5
	S	111.0	106.3	105.2	106.1	105.8	103.2	112.4	112.0	102.7	104.3	111.7	102.6	99.4	101.0	101.0
BHVO-1	x_s	105.0	136.0	121.0	289.0	317.0	139.0	31.8	15.8	39.0	25.2	19.0	179.0	27.6	403.0	11.0
	$\bar{x}$ (n = 3)	103.8	132.7	116.9	283.3	311.3	127.6	32.4	13.5	39.5	26.1	19.4	173.7	27.1	391.8	9.9
	σ	0.5	0.2	0.5	1.1	2.2	0.4	0.7	1.4	0.9	1.3	0.1	0.6	0.2	0.8	0.1
	V	0.5	0.2	0.5	0.4	0.7	0.3	2.2	10.0	2.3	4.8	0.3	0.3	0.8	0.2	1.5
	S	98.9	97.5	96.6	98.0	98.2	91.8	101.9	85.2	101.3	103.7	101.9	97.1	98.1	97.2	89.7
BIR	x_s	71.0	126.0	166.0	382.0	313.0	7.0	44.0	0.6	2.0	2.5	0.6	15.5	16.0	108.0	0.3
	$\bar{x}$ (n = 3)	66.9	123.7	153.7	369.2	310.0	4.7	40.3	3.5	3.7	2.4	0.7	17.2	16.3	107.7	0.5
	σ	0.6	0.8	0.5	0.3	1.6	2.9	0.5	0.2	0.8	0.9	0.0	0.5	0.2	0.3	0.1
	V	0.8	0.6	0.3	0.1	0.5	62.0	1.1	4.8	21.6	35.5	7.1	3.0	1.2	0.3	17.5
	S	94.3	98.2	92.6	96.6	99.0	67.6	91.6	569.9	191.5	96.0	111.1	111.2	102.1	99.8	186.7

Table C-4: Northeast Brazil ICP-MS data for trace elements given in parts per million (ppm) and excluding rare-earth elements (REE). The latter are given on Table C-5.

(ppm)	MQVL 15BP1-1	15BP3-2	15BP4-6	15BP4-7	15BP5-8	15BP5-9	15BP5-10	15BP5-11	15BP6-12a	15BP6-13	15BP7-15	15BP7-16	15BP8-17
Li	8.08	9.73	9.26	7.53	9.38	9.8	10.16	12.54	7.16	8.5	8.81	9.08	8.12
Be	1.61	1.51	2.01	1.24	2.025	2.24	1.31	1.57	1.87	1.48	2.52	1.7	1.85
P	3361	2154	3518	2170	2933	3483	1795	2428	3456	2323	5962	2876	3579
K	11895	12592	8208	9684	10340	7106	10833	13734	5879	10860	9304	9185	11968
Sc	23.3	23.7	23.87	28.12	22.845	22.93	25.2	23.51	21.28	26.42	26.77	25.46	25.69
Ti	12861	15109	14900	11250	12449	13999	10626	14325	15240	14427	14960	14673	17316
V	195.0	250.4	227.8	228.0	209.3	218.7	215.1	195.4	240.1	260.4	253.8	248.2	264.5
Cr	388.6	267.8	512.3	857.8	670.8	487.5	407.6	317.9	489.8	405.0	605.2	512.1	286.3
Mn	1381	1189	1385	1316	1376	1467	1238	1264	1257	1336	1535	1374	1372
Co	54.4	41.15	56.08	55.15	65.78	58.18	53.2	45.26	57.89	53.03	58.24	55.65	54.01
Ni	305.1	119.0	356.2	425.7	593.6	362.8	346.8	224.4	385.2	240.3	445.7	411.7	210.8
Cu	53.8	54.76	60.21	89.49	39	54.59	53.51	52.44	48.45	57.1	62.99	57.85	67.15
Zn	111.8	105.9	112.1	89.3	107.9	124.3	87.7	98.8	111.7	102.0	105.2	108.3	121.9
Ga	19.42	20	18.19	15.36	16.935	19.11	17.45	18.99	18.27	18.64	17.19	18.33	19.37
Rb	49.78	67	43.87	37.04	57.245	35.8	44.63	57.3	56.44	41.95	23.71	36.14	38.91
Sr	806.4	650.5	1271.6	604.6	791.0	851.2	541.8	692.6	829.1	687.3	1224.1	683.3	1062.6
Y	23.71	26.03	23.97	22.72	26.32	30.78	25.01	25.58	25.16	26.39	34.89	30.29	30.12
Zr	186.4	196.4	237.2	152.2	210.4	246.4	150.1	220.4	256.0	192.7	319.2	210.1	312.3
Nb	74.81	58.31	87.52	51.85	89.23	98.04	51.78	73.2	82.91	63.62	131.8	67.61	84.1
Sn	1.56	1.54	1.94	1.29	1.595	1.72	1.16	1.61	1.67	1.46	1.82	1.56	1.79
Cs	0.69	1.34	0.68	0.6	1.255	2.16	0.95	0.94	0.46	0.58	0.5	0.71	0.52
Ba	728.2	540.5	525.9	405.8	651.9	592.3	423.4	531.5	517.0	460.3	692.2	491.2	568.3
Hf	3.98	4.62	5.32	3.47	4.64	5.46	3.47	4.9	5.42	4.25	6.49	4.59	6.62
Ta	3.74	3.21	4.88	2.66	4.6	5.01	2.88	4.05	4.27	3.48	6.51	3.65	4.81
Tl	0.05	0.08	0.08	0.02	0.01	0.07	0.02	0.03	0.03	0.02	0	0.02	0.04
Pb	3.32	3.68	3.13	2.82	4.82	6.54	3.24	3.56	3.31	2.72	3.65	3.37	3.34
Th	6.25	5.81	5.96	4.89	14.42	12.9	4.92	6.08	6.98	4.99	13.68	6.09	6.49
U	1.6	1.32	1.83	1.26	2.705	2.53	1.17	1.48	2.01	1.31	3.86	1.55	1.92

Table C-4 (cont.)

	MQVL				MQVL basins					Mecejana		
(ppm)	15BP8-18	15BP11-24	15BP12-25	15BP12-26	15BP3-3a	15BP3-3b	15BP3-4	15BP3-5	15BP7-14	15BP9-19a	15BP9-19c	15BP10-20
Li	7.58	10.02	12.15	10.76	12	7.17	8.29	9.51	4.2	22.54	30.34	74.24
Be	1.67	2.175	2.82	2	1.06	1.17	1.05	1.21	4.7	4.07	6.83	9.03
P	3237	4335	6616	3094	1223	1246	1526	1761	873	456	358	207
K	16191	11576	12455	12033	7086	4135	8042	10237	4555	46866	49784	47436
Sc	25.12	24.98	26.67	27.26	24.88	23.33	23.36	21.71	26.67	3.35	0.67	0.73
Ti	17222	17969	21408	13272	12472	11003	12723	12770	10866	3219	2381	1589
V	257.5	269.0	305.4	245.0	167.4	173.5	222.4	203.2	187.1	28.7	16.4	7.8
Cr	298.6	207.3	194.6	590.9	217.1	221.3	302.3	309.1	306.8	9.1	0.6	0.2
Mn	1347	1348	1810	1428	1068	1135	1256	1230	851	1071	1293	2208
Co	53.01	50.75	53.37	58.58	34.33	41.7	46.52	46.48	29.58	2.8	1.07	0.16
Ni	209.8	156.8	159.4	446.7	114.7	180.4	177.1	232.7	141.9	7.0	1.2	0.8
Cu	68.43	59.79	51.55	56.8	46.38	50.99	51.56	56.54	56.84	5.32	3.28	1.81
Zn	116.3	123.2	149.4	112.7	98.4	107.8	110.5	120.0	91.7	79.4	101.4	158.0
Ga	19.38	20.955	20.72	19.04	19.09	19.83	20.24	18.65	19.13	26.54	34.37	43.08
Rb	58.28	43.05	44.53	53.59	26.2	26.06	30.13	42.87	21.03	247.39	353.77	467.22
Sr	891.9	979.4	1630.8	803.0	319.2	358.2	415.0	797.5	286.6	442.7	287.0	16.4
Y	26.85	29.095	41.49	29.43	23.31	22.83	24.31	24.86	76.12	17.27	21.41	26.76
Zr	291.1	319.6	477.7	215.6	120.0	118.8	142.0	160.0	118.1	495.0	1152.9	1687.8
Nb	77.21	89.185	164.09	73.46	22.15	24.33	33.41	42.23	17.57	158.73	250.37	376.94
Sn	1.94	2.04	2.5	1.73	1.15	1.25	1.3	1.52	1.21	1.02	1.41	1.76
Cs	0.43	0.53	0.62	0.95	0.58	0.53	0.41	0.58	0.29	2.39	4.74	5.99
Ba	565.4	602.4	529.4	509.0	252.5	244.1	339.4	757.4	612.6	535.1	368.9	4.0
Hf	6.42	7.01	9.54	4.94	3.23	3.16	3.5	3.77	3.2	9.68	18.63	25.48
Ta	4.52	4.885	8.59	4.07	1.36	1.34	1.85	2.34	0.98	6.65	9.42	11.57
Tl	0.06	0.045	0.02	0.05	0.06	0.12	0.05	0.14	0.2	0.26	0.39	0.41
Pb	3.33	4.74	6.3	3.73	1.97	1.87	2.04	3.01	1.59	10.44	16.26	25.12
Th	6.05	9.02	14.61	6.72	2.37	2.23	2.7	4.06	1.78	17.99	33.05	56.67
U	1.77	2.38	4.19	1.76	0.63	0.59	0.7	0.99	0.4	3.8	11.3	20.2

Table C-4 (cont.)

	Mecejana				Fernando de Noronha							
(ppm)	15BP10-21a	15BP10-21b	15BP10-22	15BP10-23	FN01-01	FN01-02	FN02-03	FN03-04	FN04-05	FN04-06	FN05-07	FN06-08
Li	24.83	41.96	29.66	29.875	29.39	32.31	29.38	37	8.5	9.09	8.81	8.82
Be	5.29	9.52	7.02	6.79	5.24	5.72	5.43	5.65	1.84	1.84	1.97	1.66
P	371	99	62	225	304	277	150	179	3841	3684	3938	3725
K	48694	46746	49277	56739	51721	55852	56440	52743	5769	4280	6814	4652
Sc	3.17	0.77	0.39	1.695	0.96	2.59	0.99	1.72	29.89	27.76	28.74	29.59
Ti	2781	1196	1017	2395	2864	2715	1593	1410	19272	18916	20444	19350
V	21.0	6.2	5.1	7.2	33.0	45.6	32.4	30.8	324.6	291.8	342.0	290.1
Cr	0.7	0.0	0.2	-0.2	0.3	-0.4	-0.3	-0.5	359.2	346.0	347.2	311.6
Mn	1189	1526	1743	1839	529	1167	1005	978	1498	1424	1710	1597
Co	1.59	0.26	0.21	0.335	2.19	1.36	2.28	1.63	56.39	57.74	62.69	61.28
Ni	1.5	0.4	1.0	0.6	2.5	0.6	0.6	0.5	194.5	193.5	214.5	217.8
Cu	3.66	1.33	1.93	2.34	3.32	3.83	2.95	2.73	65.86	101.53	68.07	68.23
Zn	92.3	131.2	118.6	118.1	160.9	101.3	98.6	102.5	130.1	126.6	134.0	119.8
Ga	29.25	39.88	30.46	29.815	32.73	32.58	34.73	34.1	21.93	21.58	21.25	19.68
Rb	226.39	328.46	254.98	257.54	260.4	259.76	268.52	281.09	14.31	12.94	34.25	17.83
Sr	241.9	12.3	18.0	73.5	728.1	766.8	421.5	384.6	937.6	866.4	977.7	882.8
Y	22.71	28.31	26.52	40.205	14.8	15.98	13.72	13.15	32.28	29.23	35.46	29.4
Zr	867.5	1536.7	1051.4	1024.8	957.5	966.0	809.0	766.0	294.6	288.4	311.5	266.9
Nb	181.71	248.77	206.76	255.64	112.95	108.14	85.77	83.65	91.08	89.56	105.23	96.26
Sn	1.57	2.03	1.98	3.04	1.3	1.29	0.64	0.64	2.12	2.15	2.01	2.12
Cs	2.41	4.19	2.87	2.55	2.02	20.02	2.88	3.42	0.84	1.15	1.33	1.08
Ba	322.3	13.1	41.9	122.1	1176.5	1175.4	181.8	154.0	639.2	620.5	808.2	740.9
Hf	15.92	26.12	18.73	19.92	16.27	15.84	10.11	10.36	6.37	6.39	7	6.08
Ta	8.5	8.11	6.21	13.95	3.48	3.19	1.33	1.27	5.08	5	5.89	5.28
Tl	0.28	0.44	0.28	0.295	0.28	0.34	0.31	0.36	0.02	0.01	0.03	0.01
Pb	13.65	22.25	15.41	14.35	19.14	18.09	19.45	19.85	3.68	3.37	2.73	3.2
Th	24.09	42.57	28.72	27.875	26.91	25.82	27.49	27.7	6.72	6.2	7.7	7.36
U	6.78	12.72	7.99	7.45	3.8	6.88	9.98	10.04	1.97	1.86	2.36	2.01

Table C-4 (cont.)

	Fernando de Noronha												
(ppm)	FN07-09	FN07-10	FN10-14	FN10-15	FN10-16	FN11-17	FN14-18	FN15-19	FN15-20	FN13-21	FN13-22	FN13-25	FN16-27
Li	6.46	8.87	17.58	26.13	26.88	49.35	9.19	14.25	8.85	14.75	16.49	24.3	9.51
Be	1.86	1.62	3.34	4.31	3.57	5.66	1.65	1.73	1.49	3.91	2.18	3.65	2.21
P	4262	4487	460	476	549	95	4454	4715	4216	305	4023	2946	4950
K	11516	12689	46285	51661	50379	46912	17500	8035	13222	47470	18654	44865	6698
Sc	28.98	28.73	3.54	6.23	3.79	5.4	30.69	30.07	31.11	2.58	23.51	7.28	29.32
Ti	19931	19582	3549	3549	3960	937	19253	19442	20117	2457	21550	14848	22964
V	343.6	339.6	61.8	57.5	66.0	14.9	349.6	321.9	358.5	37.2	354.3	232.4	334.8
Cr	319.6	303.3	36.1	15.9	19.3	-0.3	401.5	394.3	422.5	0.4	235.7	3.4	311.0
Mn	1599	1679	989	1005	1083	1187	1450	1504	1494	637	1412	1216	1424
Co	61.94	65.56	4.79	4.54	5.46	0.71	59.39	59.93	62.9	5.65	60.81	15.7	57.4
Ni	226.7	218.8	10.3	8.2	9.8	0.3	233.0	223.6	230.6	7.4	162.9	6.3	219.7
Cu	76	88.05	7.62	7.53	8.01	1.04	53.6	76.62	66.28	2.76	66.36	22.33	68.33
Zn	121.1	123.2	106.1	97.1	97.2	104.7	112.3	117.9	115.2	111.1	138.1	133.7	139.3
Ga	19.25	19.93	32.41	30.67	31.33	36.25	18.61	18.57	18.04	32.35	23.08	29.8	21.85
Rb	22.51	32.8	205.2	212.01	207.44	230.23	55.26	21.97	54.71	215.55	50.85	173.91	15.59
Sr	813.7	834.8	689.3	776.4	768.7	211.1	960.4	878.5	1123.2	785.6	1105.2	1236.3	1076.4
Y	29.33	29.89	16.1	15.08	17.74	13.03	28.22	29.59	28.55	20.25	36.59	37.51	34.04
Zr	284.0	284.2	690.7	438.9	722.9	1094.4	263.4	275.6	264.0	854.7	401.5	647.6	432.2
Nb	97	93.97	107.94	106.78	119.66	106.24	87.09	101.64	87.25	113.71	84.31	140.24	105.2
Sn	1.73	2	0.93	0.88	0.91	0.81	2	1.9	2.07	1.36	2.62	2.39	2.75
Cs	0.67	0.58	1.43	1.71	2.51	4.23	0.46	0.91	0.32	1.39	4.59	2.74	0.92
Ba	678.2	680.5	392.3	472.7	512.3	43.0	648.8	749.4	681.6	1066.8	831.3	942.4	818.4
Hf	6.29	6.12	10.93	9.27	11.13	15.05	6.04	5.87	5.73	15.11	8.87	11.89	9.39
Ta	5.65	5.39	3.07	3.17	3.33	1.49	4.82	5.42	4.74	2.8	4.54	7.35	5.48
Tl	0.01	0.01	0.49	0.24	0.11	0.31	0.01	0.01	0.01	0.25	0.13	0.29	0.03
Pb	4.11	7.59	14.23	24.24	12.72	23.25	5.79	1.96	4.21	15.98	7.63	13.82	4.07
Th	7.38	7.16	20.94	25.24	19.37	32	7.64	8.53	7.35	24.77	10.57	19.08	7.48
U	1.82	1.73	5.5	1.92	7.64	12.91	1.87	2.29	1.91	3.29	2.58	4.79	1.93

Table C-4 (cont.)

	Fernando de Noronha												
(ppm)	FN17-29	FN18-30	FN19-31	FN12-32	FN12-33	FN12-34	FN12-35	FN12-36	FN20-40	FN20-41	FN21-42	FN22-43	FN24-45
Li	40.27	25.06	9.75	32.13	37.05	19.81	15.16	15.32	25.22	12.65	83.06	65.05	26.62
Be	5.79	4.68	2.34	3.63	4.04	2.21	2.04	2.31	2.41	2.25	13.92	14.11	6.98
P	194	208	4807	859	1217	3467	2761	1906	2427	2889	85	76	89
K	55751	52711	8603	45677	51109	8705	17577	41747	28188	19315	46601	45111	59083
Sc	0.17	0.91	29.03	3.56	2.88	29.13	24.52	11.85	14.79	31.01	0.24	0.73	2.28
Ti	1410	1761	22069	6246	7528	20614	17013	10873	13524	17544	1148	1010	1060
V	30.6	37.0	341.8	102.5	100.9	401.9	289.1	181.1	231.2	294.1	11.2	9.2	17.4
Cr	0.3	-0.4	303.4	27.7	2.8	270.6	357.1	151.3	220.0	332.2	0.1	-0.6	-1.0
Mn	965	995	1555	1001	1054	1733	1450	1212	1203	1523	1915	1718	1146
Co	2.12	2.17	60.12	9.51	8.19	52.59	46.75	25.69	34.39	49.34	1.43	0.95	1.23
Ni	0.9	0.6	233.2	22.9	5.2	149.4	210.1	93.6	131.8	199.2	1.3	0.2	0.2
Cu	2.8	2.6	67.82	12.27	12.04	70.64	54.82	27.86	36.53	67.54	2.56	1.15	1.02
Zn	95.1	96.6	141.9	93.8	99.7	125.3	114.9	109.5	124.5	118.1	201.0	194.7	119.4
Ga	34.45	34.26	21.27	27.55	26.71	21.55	20.83	24.1	23.97	21.86	54.49	53.23	40.7
Rb	257.45	233.66	27.37	151.02	196.01	37.33	38.54	120.94	59.75	70.66	400.75	399.85	308.32
Sr	397.7	520.7	1376.1	1552.3	884.2	568.2	1164.3	1691.8	1750.3	1087.9	43.3	64.1	82.2
Y	12.51	12.95	36.08	19.78	21.87	30.07	26.41	24.77	29.5	26.49	28.46	27.44	13.12
Zr	737.9	715.4	396.5	555.6	616.7	365.6	351.1	436.3	444.8	351.5	1890.4	1813.9	1021.4
Nb	78.48	79.47	100.07	112.39	137.22	91.36	95.11	120.44	126.52	97.2	193.55	194.28	104.26
Sn	0.58	0.59	2.54	1.07	1.48	1.9	1.86	1.55	1.67	1.83	1.18	1.27	0.78
Cs	2.61	1.16	0.9	1.61	1.84	0.57	0.9	1.41	0.89	0.78	6.96	6.66	3.77
Ba	166.5	252.0	907.7	1028.6	889.2	569.9	752.3	1041.0	1052.9	741.5	9.2	6.2	2.1
Hf	9.78	9.45	8.89	8.51	9.27	6.53	6.66	7.59	7.81	6.65	23.32	23.51	13.64
Ta	1.21	1.36	5.34	3.78	5.28	4.8	4.51	5.03	5.49	4.64	2.13	2.11	1.4
Tl	0.31	0.3	0.03	0.12	0.16	0.11	0.08	0.06	0.07	0.17	0.5	0.53	0.41
Pb	20.78	17.57	4.43	12.32	17.58	5.31	5.13	6.68	6.33	6.27	40.71	41.18	25.82
Th	25.64	24.04	7.61	17.21	24.25	9.54	9.59	11.43	11	9.76	68.75	68.73	36.98
U	9.04	8.97	2.22	3.89	7.7	3.63	2.88	3.6	3.84	3.08	23.17	23.23	12.37

Table C-4 (cont.)

	Fernando de Noronha									
(ppm)	FN25-46	FN25-47	FN26-49	FN27-50	FN28-51	FN29-52	FN30-53	FN30-54	FN30-55	FN30-56
Li	16.26	27.45	24.83	9.36	9.44	74.69	9.84	9.21	8.93	7.56
Be	2.07	3.25	4.25	1.92	1.93	9.2	1.68	1.61	1.62	1.46
P	3648	2751	269	3781	3895	74	3570	3494	3664	3600
K	21211	37183	64318	8541	8842	48475	10857	10358	10798	10331
Sc	24.7	12.24	0.94	28.51	30.24	-0.18	29.08	26.72	27.02	27.78
Ti	21908	14338	2237	19402	20444	1080	17232	16939	15855	16948
V	389.7	216.9	43.0	302.4	315.1	9.9	279.3	273.1	254.9	263.0
Cr	34.3	14.6	2.3	383.6	372.2	-0.5	384.7	321.1	436.4	363.9
Mn	1738	1318	869	1491	1667	1612	1540	1457	1492	1453
Co	36.18	21.7	1.89	63.17	65.93	1.03	58.64	57.2	60.03	58.83
Ni	21.1	19.2	1.9	310.3	309.6	0.6	289.7	268.4	292.8	289.0
Cu	40.13	31.89	3.8	63.73	66.65	1.16	65.43	72.73	63.06	73.6
Zn	147.8	128.3	87.3	130.7	147.6	158.5	126.4	122.6	117.5	117.4
Ga	28.03	30.74	36.55	20.65	21.84	49.55	20.82	19.97	18.92	19.37
Rb	103.42	145.05	243.16	27.04	25.35	345.22	32.13	30.66	33.39	30.2
Sr	1074.5	1213.2	395.7	961.8	869.2	67.8	887.2	855.3	875.2	841.1
Y	39.98	32.11	11.72	31.32	36.72	18.52	30.64	29.2	29.11	29.45
Zr	448.4	730.4	574.6	328.6	345.4	1661.5	264.7	234.9	238.3	239.0
Nb	75.49	152.85	88.14	78.01	83.85	149	71.78	67.2	69.57	68.45
Sn	2.8	1.91	0.79	2.14	2.23	1.08	1.77	1.81	1.71	1.7
Cs	0.89	0.91	1.22	0.82	0.93	4.66	0.47	0.26	0.34	0.37
Ba	419.5	826.5	210.3	539.9	652.9	3.4	433.8	403.7	425.5	413.6
Hf	9.85	12.38	9.48	7.04	7.4	21.8	5.61	5.16	5.22	5.26
Ta	4.46	6.1	1.99	4.58	4.91	2.08	3.91	3.56	3.67	3.55
Tl	0.16	0.2	0.23	0.05	0.07	0.56	0.02	0.03	0.04	0.03
Pb	5.61	15.86	14.7	3.41	4.09	30.23	3.99	4.56	4.41	4.53
Th	7.72	24.16	24.19	5.79	6.22	47.45	6.41	5.91	6.26	5.98
U	2.01	6.98	5.25	1.79	1.82	22.97	2.24	1.8	1.83	1.79

Table C-5: Northeast Brazil ICP-MS data for rare-earth elements (REE) given in parts per million (ppm). MQVL

(ppm)	15BP1-1	15BP3-2	15BP4-6	15BP4-7	15BP5-8	15BP5-9	15BP5-10	15BP5-11	15BP6-12a	15BP6-13	15BP7-15	15BP7-16	15BP8-17
La	42.95	34.31	45.25	32.52	63.755	63.6	30.31	39.3	53.05	35.09	100.14	40.85	58.07
Ce	80.06	69.19	88.42	63.21	114.43	115.89	59.66	75.34	101.91	70.17	182.76	80.5	114.8
Pr	9.25	8.47	10.38	7.4	12.145	12.7	6.97	8.76	11.48	8.29	20.08	9.48	13.41
Nd	37.44	35.56	41.77	29.41	44.685	49.83	28.23	36.07	45.4	35.51	76.02	39.42	52.85
Sm	7.62	7.76	8.33	6.13	8.1	9.86	5.57	7.32	8.31	7.41	12.74	8.26	10.1
Eu	2.47	2.34	2.63	1.94	2.465	3.06	1.78	2.29	2.64	2.3	3.76	2.56	3.08
Gd	6.95	7.03	7.31	5.66	7.24	9.01	5.44	6.76	7.47	6.86	10.68	7.72	8.83
Tb	0.98	0.99	1.01	0.83	1.025	1.24	0.83	0.95	1	1.01	1.41	1.1	1.18
Dy	5.05	5.18	5.06	4.37	5.265	6.47	4.63	5.1	4.99	5.33	7.13	5.84	5.97
Ho	0.87	0.89	0.83	0.79	0.92	1.03	0.86	0.9	0.86	0.91	1.19	1.04	1.02
Er	2.11	2.2	2.03	2.03	2.225	2.49	2.26	2.16	2.07	2.23	2.91	2.58	2.45
Tm	0.27	0.28	0.25	0.28	0.28	0.31	0.3	0.29	0.26	0.3	0.38	0.34	0.31
Yb	1.49	1.62	1.44	1.58	1.57	1.66	1.72	1.64	1.48	1.67	2.09	1.96	1.74
Lu	0.2	0.22	0.19	0.22	0.215	0.22	0.23	0.22	0.19	0.22	0.27	0.27	0.23

	MQVL				**MQVL basins**					**Mecejana**		
(ppm)	15BP8-18	15BP11-24	15BP12-25	15BP12-26	15BP3-3a	15BP3-3b	15BP3-4	15BP3-5	15BP7-14	15BP9-19a	15BP9-19c	15BP10-20
La	51.83	64.45	122.51	43.93	14.47	13.84	19.67	25.71	44.08	82.26	101.49	133.75
Ce	103.47	123.59	237.66	85.71	29.1	28.81	40.45	51.47	43.99	118.5	139.44	178.69
Pr	12.02	14.1	26.33	10.09	3.8	3.71	5.12	6.34	8.12	9.73	10.75	12.41
Nd	48.58	55.515	100.64	40.48	17.69	17.24	22.85	27.17	34.84	27.67	28.54	28.86
Sm	9.24	10.125	17.58	8.16	4.97	4.66	5.4	6.21	8.12	3.57	3.43	3.18
Eu	2.94	3.065	5.1	2.59	1.74	1.66	1.86	1.97	2.65	1.01	0.89	0.64
Gd	8.11	8.63	14.02	7.82	5.58	5.13	5.7	6.31	10.49	2.77	2.71	2.41
Tb	1.09	1.125	1.83	1.1	0.83	0.8	0.85	0.92	1.7	0.43	0.45	0.47
Dy	5.51	5.78	8.83	5.92	4.65	4.43	4.68	5.08	10.15	2.6	2.84	3.08
Ho	0.96	0.97	1.48	1.03	0.84	0.82	0.86	0.91	2.07	0.52	0.64	0.72
Er	2.32	2.365	3.5	2.58	2.12	1.96	2.16	2.21	5.72	1.62	2.13	2.7
Tm	0.3	0.295	0.42	0.35	0.28	0.26	0.29	0.29	0.79	0.27	0.38	0.51
Yb	1.67	1.7	2.32	1.93	1.63	1.54	1.68	1.67	4.42	1.9	2.83	4.08
Lu	0.23	0.225	0.31	0.27	0.22	0.2	0.23	0.23	0.67	0.3	0.47	0.66

Table C-5 (cont.). Mecejana **Fernando de Noronha**

(ppm)	15BP10-21a	15BP10-21b	15BP10-22	15BP10-23	FN01-01	FN01-02	FN02-03	FN03-04	FN04-05	FN04-06	FN05-07	FN06-08
La	103.51	128.17	135.76	140.735	88.4	95.26	78.08	78	53.6	49.66	63.33	58.84
Ce	159.05	171.17	185.68	247.32	127.83	128.18	90.03	88.56	106.37	100.38	120.48	113.47
Pr	13.57	12.41	12.9	23.09	9.67	9.99	6.16	6.03	12.71	12	14.34	13.27
Nd	38.45	30.29	29.2	67.945	26.39	26.48	15.69	15.16	52.24	49.02	58.45	52.46
Sm	4.74	3.35	2.87	8.455	3.19	3.08	1.87	1.86	10.17	9.67	11.14	9.8
Eu	1.23	0.68	0.52	1.79	0.89	0.84	0.5	0.52	3.1	3.01	3.41	3.1
Gd	3.51	2.63	2	5.89	2.32	2.25	1.47	1.41	9.02	8.47	9.9	8.81
Tb	0.57	0.49	0.4	0.97	0.36	0.35	0.25	0.25	1.22	1.18	1.33	1.13
Dy	3.41	3.25	2.75	5.75	2.11	2.08	1.54	1.51	6.37	6.13	6.6	5.96
Ho	0.69	0.74	0.66	1.2	0.43	0.45	0.34	0.35	1.06	1.01	1.17	1.01
Er	2.1	2.68	2.46	3.715	1.3	1.46	1.18	1.2	2.52	2.48	2.71	2.44
Tm	0.35	0.48	0.46	0.58	0.23	0.25	0.22	0.22	0.32	0.31	0.34	0.3
Yb	2.39	3.5	3.37	3.875	1.65	1.74	1.64	1.6	1.78	1.76	1.85	1.65
Lu	0.36	0.57	0.55	0.59	0.25	0.28	0.25	0.26	0.24	0.23	0.24	0.23

Fernando de Noronha

(ppm)	FN07-09	FN07-10	FN10-14	FN10-15	FN10-16	FN11-17	FN14-18	FN15-19	FN15-20	FN13-21	FN13-22	FN13-25	FN16-27
La	64.88	65.25	85.96	88.29	88.5	103.17	64.56	66.1	61.6	115.32	82.23	108.06	71.57
Ce	122.8	126.46	109.68	114.93	118.69	107.76	126.95	131.23	121.33	165.22	166.71	198.16	147.21
Pr	14.43	14.93	8.96	9.33	9.78	6.55	15.08	15.42	14.46	12.99	19.66	21.2	17.62
Nd	58.09	59.69	26.17	26.84	28.69	14.52	60.32	61.03	58.1	35.56	77.61	77.11	71.43
Sm	10.78	10.93	3.34	3.43	3.82	1.47	11.05	11.06	10.56	4.08	13.83	12.77	13.11
Eu	3.19	3.34	0.98	1.03	1.11	0.35	3.33	3.33	3.2	1.18	4.04	3.68	3.88
Gd	9.48	9.5	2.75	2.7	2.94	1.15	9.18	9.55	9.19	3.05	11.55	10.23	11.12
Tb	1.21	1.23	0.42	0.41	0.45	0.22	1.2	1.24	1.16	0.46	1.5	1.36	1.42
Dy	6.04	6.2	2.35	2.31	2.66	1.4	6.03	6.18	5.76	2.7	7.53	7.15	7.17
Ho	1	1.03	0.48	0.45	0.52	0.34	0.99	1.02	0.97	0.55	1.26	1.24	1.2
Er	2.38	2.48	1.49	1.43	1.64	1.28	2.37	2.47	2.3	1.84	2.98	3.21	2.79
Tm	0.29	0.31	0.24	0.22	0.25	0.23	0.29	0.29	0.29	0.3	0.37	0.41	0.33
Yb	1.6	1.65	1.68	1.53	1.76	1.82	1.61	1.66	1.52	2.05	1.95	2.4	1.81
Lu	0.22	0.22	0.27	0.24	0.27	0.31	0.21	0.22	0.21	0.33	0.26	0.32	0.24

Table C-5 (cont.). Fernando de Noronha

(ppm)	FN17-29	FN18-30	FN19-31	FN12-32	FN12-33	FN12-34	FN12-35	FN12-36	FN20-40	FN20-41	FN21-42	FN22-43	FN24-45
La	74.17	73.87	74.14	84.13	95.84	62.95	63.74	103.4	104.73	63.64	139.8	140.14	88.31
Ce	84.52	86.51	147.69	123.68	143.55	120.74	116.02	164.16	172.32	118.16	154.94	153.54	87.86
Pr	5.79	6.15	17.93	11	12.92	14.04	12.9	16.04	17.22	13.1	9.96	9.84	5.27
Nd	14.85	15.99	71.8	34.98	41.45	54.98	49.58	54.49	60.41	50.72	22.67	22.68	11.19
Sm	1.68	1.81	13.21	5.03	6.11	10.05	8.81	8.15	9.42	8.81	2.51	2.47	1.11
Eu	0.49	0.52	4.01	1.49	1.77	3.1	2.65	2.41	2.78	2.72	0.62	0.62	0.29
Gd	1.36	1.43	11.29	4.01	4.75	8.85	7.65	6.6	7.53	7.54	2.18	2.05	0.89
Tb	0.23	0.25	1.47	0.59	0.69	1.19	1.01	0.88	1.04	1.01	0.42	0.42	0.19
Dy	1.44	1.49	7.34	3.21	3.72	5.77	5.11	4.62	5.29	5.15	2.86	2.78	1.25
Ho	0.32	0.34	1.25	0.61	0.69	1	0.89	0.83	0.92	0.88	0.7	0.69	0.32
Er	1.17	1.16	2.82	1.76	1.97	2.48	2.18	2.18	2.44	2.2	2.65	2.57	1.23
Tm	0.2	0.21	0.35	0.26	0.28	0.31	0.28	0.29	0.31	0.28	0.49	0.49	0.23
Yb	1.5	1.48	1.9	1.72	1.78	1.71	1.61	1.74	1.85	1.6	3.74	3.72	1.78
Lu	0.24	0.25	0.24	0.26	0.26	0.24	0.22	0.24	0.26	0.22	0.62	0.63	0.3

	Fernando de Noronha						Fernando de Noronha São José			
(ppm)	FN25-46	FN25-47	FN26-49	FN27-50	FN28-51	FN29-52	FN30-53	FN30-54	FN30-55	FN30-56
La	58.16	105.34	66.6	49.65	55.15	122.71	50.14	45.99	49.5	47.91
Ce	125.35	171.39	81.54	100.62	108.17	123.53	102.07	94.06	100.9	98.47
Pr	15.42	17.05	5.95	12.11	13.24	7.48	12.34	11.28	12.06	11.79
Nd	62.92	60.25	15.63	49.44	55.06	16.07	50.13	45.72	48.27	47.82
Sm	12.08	9.64	1.88	9.67	10.37	1.71	9.64	9.08	9.32	9.2
Eu	3.63	2.82	0.53	2.99	3.25	0.37	3.04	2.87	2.89	2.89
Gd	10.27	7.69	1.53	8.53	9.62	1.29	8.54	8.2	8.38	8.24
Tb	1.4	1.08	0.25	1.18	1.3	0.26	1.18	1.09	1.11	1.08
Dy	7.39	5.63	1.47	6.08	6.68	1.77	6.01	5.71	5.61	5.64
Ho	1.29	1.02	0.34	1.06	1.19	0.43	1.02	0.97	0.98	0.94
Er	3.32	2.75	1.12	2.56	2.87	1.67	2.56	2.37	2.36	2.37
Tm	0.43	0.39	0.19	0.32	0.34	0.31	0.31	0.3	0.29	0.29
Yb	2.42	2.41	1.51	1.78	1.96	2.44	1.73	1.63	1.64	1.67
Lu	0.35	0.35	0.26	0.25	0.27	0.43	0.24	0.23	0.23	0.23

Table C-6: Standards for ICP-MS trace element analyses. Accuracy was estimated by comparing the analyses of USGS standards BCR-2 and BHVO-2 with reference values from the GeoReM database. Precision was estimated from multiple analyses of randomly selected samples. x_s = reference value; $\bar{x}$ = mean; n = number of analyses; σ = standard deviation; V = coefficient of variation ($100\bar{x}/\sigma$); S = accuracy ($100\bar{x}/x_s$).

	BCR-2	n = 14				BHVO-2	n = 14			
(ppm)	x_s	$\bar{x}$	σ	V	S	x_s	$\bar{x}$	σ	V	S
Li	9.00	10.94	1.13	10.33	122	4.8	5.75	1.66	28.9	120
Be	1.75	2.39	0.2	8.37	137	1	1.18	0.34	28.8	118
P	1527	1591	69	4.34	104	1178	1273	124	9.7	108
K	14860	15363	1239	8.06	103	4280	5263	3129	59.5	123
Sc	33.00	44.3	2.76	6.23	134	32	40.22	2.19	5.4	126
Ti	13549	13960	561	4.02	103	16367	16597	706	4.3	101
V	416.0	421	48.5	11.52	101	317	375.8	49.1	13.1	119
Cr	18.00	14.31	0.49	3.42	80	280	267.05	73	27.3	95
Mn	1520	1595	72	4.51	105	1290	1372	98	7.1	106
Co	37.00	37.49	1.7	4.53	101	45	44.13	2.63	6.0	98
Ni	17.70	12.24	0.43	3.51	69	119	109.33	27.99	25.6	92
Cu	21.00	29.15	0.47	1.61	139	127	133.05	30.14	22.7	105
Zn	127.0	128.9	3.9	3.03	101	103	108.3	6.6	6.1	105
Ga	20.60	22.02	0.48	2.18	107	21.7	21.33	0.45	2.1	98
Rb	46.90	54.7	0.56	1.02	117	9.08	13.83	11.81	85.4	152
Sr	340.0	341	8.5	2.49	100	396	390.1	17.3	4.4	99
Y	37.00	38.41	0.82	2.13	104	26	28.43	2.79	9.8	109
Zr	188.0	189.1	4.1	2.17	101	172	173.7	4.6	2.6	101
Nb	12.60	12.58	0.18	1.43	100	18.1	18.19	1.69	9.3	100
Sn	2.00	2.1	0.05	2.38	105	1.7	1.78	0.09	5.1	105
Cs	1.07	1.08	0.02	1.85	101	0.09	0.17	0.26	152.9	189
Ba	677.0	658.8	17.1	2.60	97	131	163.5	140.2	85.7	125
La	24.90	24.16	0.56	2.32	97	15.2	15.15	2.47	16.3	100
Ce	52.90	50.26	1.16	2.31	95	37.5	36.47	3.93	10.8	97
Pr	6.57	6.46	0.11	1.70	98	5.29	5.13	0.37	7.2	97
Nd	28.70	27.89	0.56	2.01	97	24.5	24	1.2	5.0	98
Sm	6.58	6.3	0.17	2.70	96	6.07	5.84	0.15	2.6	96
Eu	1.96	1.87	0.03	1.60	95	2.07	1.99	0.05	2.5	96
Gd	6.75	6.52	0.18	2.76	97	6.24	6.06	0.18	3.0	97
Tb	1.07	1.04	0.03	2.88	97	0.936	0.92	0.03	3.3	98
Dy	6.41	6.29	0.13	2.07	98	5.31	5.32	0.27	5.1	100
Ho	1.30	1.27	0.02	1.57	98	0.972	0.98	0.08	8.2	101
Er	3.66	3.61	0.06	1.66	99	2.54	2.58	0.3	11.6	102
Tm	0.54	0.52	0.02	3.85	96	0.33	0.35	0.05	14.3	106
Yb	3.38	3.34	0.06	1.80	99	2	2.06	0.35	17.0	103
Lu	0.50	0.5	0	0.00	99	0.274	0.29	0.06	20.7	106
Hf	4.90	4.87	0.06	1.23	99	4.36	4.43	0.15	3.4	102
Ta	0.74	0.77	0.01	1.30	104	1.14	1.11	0.1	9.0	97
Tl	0.26	0.26	0.01	3.85	100	0.022	0.04	0.06	150.0	182
Pb	11.00	10.39	0.13	1.25	94	1.6	2.32	2.36	101.7	145
Th	5.70	5.98	0.09	1.51	105	1.22	1.56	1.26	80.8	128
U	1.69	1.74	0.02	1.15	103	0.39	0.52	0.35	67.3	133

Table C-6 (cont.)

	15BP5-8	n = 2		15BP10-23	n = 2	
(ppm)	$\bar{x}$	σ	V	$\bar{x}$	σ	V
Li	9.38	0.64	6.8	29.88	2.73	9.2
Be	2.03	0.20	9.6	6.79	0.40	5.8
P	2933	393	13.4	225	8	3.7
K	10340	1134	11.0	56739	6562	11.6
Sc	22.84	1.63	7.1	1.70	0.22	12.9
Ti	12449	760	6.1	2395	145	6.1
V	209.3	8.9	4.2	7.2	0.6	8.0
Cr	670.79	20.53	3.1	-0.20	0.43	-217.0
Mn	1376	89	6.5	1839	128	7.0
Co	65.78	2.98	4.5	0.33	0.02	6.5
Ni	593.57	18.24	3.1	0.61	0.05	8.1
Cu	39.00	0.06	0.2	2.34	0.05	2.3
Zn	107.9	2.7	2.5	118.1	5.5	4.7
Ga	16.94	0.70	4.1	29.82	0.78	2.6
Rb	57.25	0.49	0.9	257.54	0.60	0.2
Sr	791.0	30.5	3.9	73.5	2.7	3.6
Y	26.32	0.74	2.8	40.20	0.97	2.4
Zr	210.4	3.6	1.7	1024.8	19.5	1.9
Nb	89.23	2.16	2.4	255.64	7.96	3.1
Sn	1.59	0.00	0.2	3.04	0.00	0.0
Cs	1.26	0.05	4.4	2.55	0.11	4.5
Ba	651.9	15.8	2.4	122.1	4.0	3.3
La	63.76	2.81	4.4	140.73	6.11	4.3
Ce	114.43	4.77	4.2	247.32	11.50	4.7
Pr	12.15	0.40	3.3	23.09	0.65	2.8
Nd	44.69	1.95	4.4	67.94	2.57	3.8
Sm	8.10	0.38	4.7	8.46	0.46	5.5
Eu	2.46	0.15	6.0	1.79	0.02	1.4
Gd	7.24	0.35	4.9	5.89	0.31	5.3
Tb	1.03	0.05	4.7	0.97	0.06	5.8
Dy	5.26	0.29	5.5	5.75	0.25	4.4
Ho	0.92	0.02	2.2	1.20	0.05	4.2
Er	2.23	0.05	2.2	3.71	0.05	1.3
Tm	0.28	0.01	4.3	0.58	0.02	4.2
Yb	1.57	0.06	3.8	3.88	0.15	3.9
Lu	0.21	0.01	4.8	0.59	0.01	1.7
Hf	4.64	0.09	1.9	19.92	0.20	1.0
Ta	4.60	0.17	3.7	13.95	0.41	2.9
Tl	0.01	0.00	8.9	0.30	0.01	4.5
Pb	4.82	0.17	3.5	14.35	0.29	2.0
Th	14.42	0.45	3.1	27.88	0.63	2.3
U	2.70	0.07	2.5	7.45	0.11	1.5

Table C-6 (cont.)

	15BP11-24	n = 2		FN01-02	n = 2	
(ppm)	$\bar{x}$	σ	V	$\bar{x}$	σ	V
Li	10.02	0.75	7.5	32.31	4.48	13.9
Be	2.17	0.18	8.3	5.72	0.28	4.8
P	4335	244	5.6	277	22	7.9
K	11576	1192	10.3	55852	5284	9.5
Sc	24.98	0.66	2.6	2.59	0.39	15.0
Ti	17969	1101	6.1	2715	130	4.8
V	269.0	9.2	3.4	45.6	4.3	9.4
Cr	207.31	2.48	1.2	-0.44	0.31	-70.9
Mn	1348	95	7.1	1166	37	3.2
Co	50.75	2.05	4.0	1.36	0.01	0.9
Ni	156.85	3.23	2.1	0.62	0.04	6.2
Cu	59.79	0.99	1.7	3.82	0.20	5.2
Zn	123.2	4.4	3.6	101.3	3.7	3.7
Ga	20.95	0.56	2.7	32.58	0.50	1.5
Rb	43.05	0.16	0.4	259.76	1.14	0.4
Sr	979.4	23.5	2.4	766.8	7.3	1.0
Y	29.10	0.76	2.6	15.98	0.35	2.2
Zr	319.6	10.5	3.3	966.0	1.2	0.1
Nb	89.18	3.19	3.6	108.13	3.99	3.7
Sn	2.04	0.05	2.3	1.29	0.04	3.0
Cs	0.53	0.04	7.7	20.02	0.90	4.5
Ba	602.4	30.7	5.1	1175.4	38.5	3.3
La	64.45	3.78	5.9	95.26	3.41	3.6
Ce	123.59	7.69	6.2	128.18	4.64	3.6
Pr	14.10	0.68	4.8	9.98	0.33	3.3
Nd	55.52	2.61	4.7	26.48	0.77	2.9
Sm	10.12	0.71	7.0	3.08	0.09	2.9
Eu	3.07	0.14	4.4	0.85	0.04	5.0
Gd	8.63	0.62	7.2	2.25	0.10	4.6
Tb	1.13	0.08	6.8	0.36	0.03	7.1
Dy	5.78	0.33	5.7	2.08	0.13	6.1
Ho	0.97	0.06	6.2	0.44	0.01	2.3
Er	2.36	0.06	2.5	1.46	0.05	3.4
Tm	0.30	0.02	6.7	0.25	0.01	4.0
Yb	1.70	0.10	5.9	1.74	0.03	1.7
Lu	0.23	0.00	1.1	0.28	0.01	2.6
Hf	7.01	0.17	2.4	15.84	0.37	2.4
Ta	4.89	0.17	3.4	3.19	0.08	2.4
Tl	0.05	0.00	10.5	0.34	0.01	3.8
Pb	4.74	0.17	3.5	18.09	0.53	2.9
Th	9.02	0.34	3.7	25.82	0.88	3.4
U	2.38	0.10	4.3	6.88	0.19	2.8

Table C-7: (next pages) Cameroon Line XRF data for major and trace elements, given in weight% (wt.%) and parts per million (ppm), respectively. Rock type determined as in Table C-1. Loss on ignition (LOI) values determined as the difference between the total weight % of all major elements and 100 wt.%.

Table C-7: Caption on the previous page. Cameroon Line continental

Locality-Sample	Bambouto-C100	Bambouto-C101	Bambouto-C102	Bambouto-C103	Bambouto-C104	Bambouto-C105	Bambouto-C106	Bambouto-C107	Bambouto-C108	Bambouto-C109	Bambouto-C110	Bambouto-C111
Rock Type	Rhyolite	Trachyte	Alkali basalt	Trachyte	Rhyolite	Rhyolite	Trachyte-Trachydacite	Trachyte	Trachy-basalt	Trachyte	Alkali basalt	Trachyte
SiO2	68.89	63.75	45.73	62.91	68.56	68.5	63.82	66.51	46.2	63.72	44.05	63.31
Al2O3	13.81	15.64	15.95	15.5	13.08	12.33	12.33	14.43	16.57	15.83	14.2	14.72
Fe2O3	5.09	5.08	11.83	5.93	5.75	6.71	8.93	5.77	13.21	5.39	13.01	6.71
MgO	0.09	0.59	5.97	0.47	0.05	0.12	0.05	0.07	4.78	0.46	9.27	0.59
CaO	0.04	0.36	9.56	0.43	0.44	0.21	0.41	0.17	8.19	0.39	10.42	0.61
Na2O	5.62	6.91	3.26	6.41	5.87	5.19	5.06	6.27	3.73	7.05	2.73	6.57
K2O	4.149	5.466	1.392	5.254	4.806	4.798	4.517	4.731	2.012	5.448	1.278	5.01
TiO2	0.221	0.795	3.062	0.723	0.352	0.459	0.552	0.491	3.343	0.743	3.136	0.775
MnO	0.131	0.17	0.203	0.501	0.133	0.115	0.577	0.354	0.216	0.188	0.197	0.503
P2O5	0.002	0.05	1.053	0.037	0.006	0.001	0.028	0.029	0.935	0.069	0.832	0.039
Total	98.04	98.81	98.01	98.17	99.05	98.43	96.27	98.83	99.19	99.29	99.12	98.84
LOI	1.96	1.19	1.99	1.83	0.95	1.57	3.73	1.17	0.81	0.71	0.88	1.16
Zn	265.8	135.3	98.8	628.9	299.6	402.7	297.7	254.4	109.5	141.5	98.2	358.3
Cu	-20.7	-7	34.5	-9.1	-11	-8.4	-5.6	-8.7	22.9	-8.5	54.3	-11.1
Ni	2.6	2	47.7	1.5	2.8	5.8	1.6	1.3	10.1	1.5	182.4	2
Cr	1.3	3.2	117.3	3.8	3	3.3	3.5	4.1	6.9	3.8	304.2	4.1
V	-9.6	-9.4	181	-4.7	-6.3	-12.9	-3.1	-5.3	182.6	-13.3	248.8	-7
Ba	41.9	8.6	918.3	41.4	31.4	10.9	1266.6	833	487.1	59.5	709.5	46.1
Sc	-0.9	8.5	20.2	5.8	-1.6	-0.7	1	2.5	15.1	5.3	24.4	6.3
La	754.2	293.2	46	185.3	248.8	486.9	124.8	154.6	71.9	595.3	35.2	225
Ce	252	373.5	99.1	376.8	398	537	271.1	326.3	145.8	376.1	76.5	450
Nd	565.6	253.1	48.7	137.9	188.4	401.4	117.9	127.8	64.5	315.4	39.2	161.8
Pb	17.6	11.1	3.9	17.5	18.2	3.7	11.1	13.9	3.4	14.1	2.2	21.4
Nb	507.1	214.1	60.7	278	283.9	190.1	174.9	233.2	103.9	280.7	54.7	347.4
Zr	2546.6	876.5	234.1	1225.4	1371.5	1008.9	770.9	1059.8	445.4	1237.9	211.6	1509.8
Y	205.3	93.4	28.7	80.9	112.1	314.7	70.8	88.7	35.7	174.1	27.7	123.9
Sr	3.5	4.8	1536	14	6.1	5.9	15.3	27.1	1015.6	13.1	1032.2	20
Rb	168.6	109.6	30.2	100.6	133.2	103.2	87.5	84	55.5	117.5	29.5	102.4

Table C-7 (cont.). Cameroon Line continental

Locality-Sample	Bambouto-C112	Bambouto-C113	Bambouto-C114	Bambouto-C115	Bambouto-C116	Bambouto-C117	Bambouto-C118	Bambouto-C119	Bambouto-C120	Bambouto-C121	Bambouto-C122	Bambouto-C123
Rock type	Basanite-Tephrite	Trachyte	Trachyte	Trachyte	Trachyte	Trachyte	Trachyte-Trachydacite	Trachyte	Trachyte	Basanite-Tephrite	Trachyte	Basanite-Tephrite
SiO_2	43.85	67.55	62.96	60.8	58.19	66.09	65.11	62.76	63.75	42.37	63.5	43.13
Al_2O_3	13.65	12.72	15.86	18.2	19.5	15.83	11.61	15.98	15.2	15.61	16.01	14.97
Fe_2O_3	12.52	5.86	5.25	4.66	4.39	4.1	7.18	6.87	6.22	13.08	4.35	14.7
MgO	9.21	0.41	0.56	0.65	0.8	0.08	0.21	0.16	0.54	6.1	0.53	6.73
CaO	10.55	0.37	0.62	1.41	2.88	0.38	0.61	2.32	0.52	11	0.66	9.47
Na_2O	3.47	6.15	6.62	7.57	7.77	7.32	5.3	5.14	6.98	2.74	7.07	3.18
K_2O	1.465	5.016	5.42	5.39	4.257	4.958	4.573	5.462	5.281	1.121	5.515	1.498
TiO_2	3.1	0.793	0.798	0.54	0.906	0.161	0.735	0.455	0.697	3.966	0.699	3.938
MnO	0.194	0.294	0.385	0.211	0.206	0.204	0.68	0.2	0.222	0.192	0.174	0.213
P_2O_5	1.027	0.028	0.026	0.128	0.199	0.009	0.045	0.091	0.033	1.589	0.122	1.271
Total	99.04	99.19	98.5	99.56	99.1	99.13	96.05	99.44	99.44	97.77	98.63	99.1
LOI	0.96	0.81	1.5	0.44	0.9	0.87	3.95	0.56	0.56	2.23	1.37	0.9
Zn	95.8	258.8	248.1	127.4	75	281.5	549.3	135.6	410.3	94.1	134.7	113.3
Cu	43	-17.4	-9.4	-3.6	-1.7	-11.3	-13.8	-2.3	-11.3	32.8	-5.7	29.7
Ni	148.1	0.9	1.5	1.3	1.8	1.6	1.2	1.5	1.7	30.1	1.7	40
Cr	458.8	3.8	3.6	3.8	2.8	3	4.8	2.8	4.6	41.9	3.1	82.5
V	231.6	-0.9	6.4	-4.8	2.2	-5.3	-2.9	-5.8	-10.9	242.4	-3.6	198.8
Ba	874.4	38.1	7.1	404.1	2500.6	20.2	27.9	1925.3	26.7	1844.1	46.9	499.1
Sc	23.2	5.7	5.9	1	-0.5	-0.6	9	13.5	4.8	19	5.8	20.5
La	42.9	199.3	187.4	89.1	116.3	312.4	303.2	109.4	144.9	53	71.3	60.8
Ce	88.8	411.9	385.5	186.5	183	593.8	601.5	228.5	315.9	109.7	155.8	127.1
Nd	45.8	147.4	139.6	68.8	72.6	190.3	219.7	99.5	107.8	65.9	64	64.2
Pb	0.4	36.7	17.3	11.9	6.7	25.4	32.8	13	22.1	-3.4	13.6	0.2
Nb	63.5	470.6	279.1	168.4	172.3	531	375.3	105.4	334.9	53.9	132.2	80.2
Zr	190.3	2280.7	1106.8	723.2	557.5	1461	1773.8	853.5	1489.5	191.5	662.6	316.9
Y	26.2	122.5	82.2	42.4	49.3	107.6	137.8	58.1	58.5	29.7	25.9	35.5
Sr	1241.8	7.9	14.7	105.8	1549	10.7	6.6	135.4	7.4	2039	7.2	1276.5
Rb	31.7	228.2	137.9	106.7	100.5	232.4	151.6	92.7	152.6	25.5	93.5	29.3

Table C-7 (cont.). Cameroon Line continental

Locality-Sample	Bambouto-C124	Bambouto-C125	Bambouto-C73	Bambouto-C74	Bambouto-C75	Bambouto-C82	Bambouto-C83	Bambouto-C99	Biu-N1	Biu-N10	Biu-N11	Biu-N13
Rock type	Basanite-Tephrite	Trachy-basalt	Basanite-Tephrite	Alkali basalt	Trachyte-Trachydacite	Trachyte-Trachydacite	Trachyte	Basanite-Tephrite	Alkali basalt	Alkali basalt	Alkali basalt	Trachy-basalt
SiO_2	42.16	46.05	42.83	46.04	65.12	64.97	65.25	41.95	44.59	46.72	45.32	47.84
Al_2O_3	12.21	16.4	12.69	14.92	12.86	12.61	13.03	11.17	12.5	13.14	13.3	13.89
Fe_2O_3	14.19	13.14	12.94	10.67	7.87	9.29	7.74	13.2	11.52	11.64	11.66	11.17
MgO	11.29	4.98	10.94	5.93	0.23	0.02	0.23	14.51	10.91	10.44	9.6	8.56
CaO	10.48	8.52	10.87	10.68	1.02	0.07	0.82	10.49	10.48	10.27	10.1	8.43
Na_2O	2.49	3.57	3.2	2.73	5.4	5.05	5.92	2.49	1.96	3.3	2.9	3.96
K_2O	0.779	1.844	1.417	1.519	4.336	4.505	4.499	0.814	1.678	1.351	1.545	1.516
TiO_2	3.77	3.533	3.209	2.807	0.625	0.61	0.633	2.816	2.637	2.701	2.492	2.812
MnO	0.189	0.22	0.218	0.172	0.406	0.412	0.381	0.197	0.158	0.17	0.182	0.158
P_2O_5	0.457	0.88	0.979	0.757	0.049	0.034	0.037	0.988	0.589	0.506	0.761	0.732
Total	98.02	99.14	99.29	96.23	97.92	97.57	98.54	98.63	97.02	100.24	97.86	99.07
LOI	1.98	0.86	0.71	3.77	2.08	2.43	1.46	1.37	2.98	-0.24	2.14	0.93
Zn	96	103	94.1	98.6	266.1	251.1	431	100.5	88.8	90.4	110.3	111.3
Cu	27.5	19.4	53.9	44	-6.2	-3.1	-5.8	47	19.6	58	44	34.6
Ni	139.4	10	230.2	69.6	1.1	1.6	1.2	392.7	240.8	248.4	184.1	186.3
Cr	417.3	8.6	377.3	162.6	2.9	3.2	4	679	442.9	369	244.6	194.7
V	329.6	174.6	235.3	264.4	-4.1	-5	-11.2	220.9	355.5	363.5	342.7	368.8
Ba	266.6	494.8	811.2	842.9	26.3	560.1	148.7	720.9	541.5	458.5	663.4	654.6
Sc	34.7	15.4	23.4	23	4.2	-0.8	5.4	24.1	21.2	24.1	20.2	20.3
La	38.9	66	49.8	41.3	143.2	129.8	163.8	44.8	42.4	37.9	60.5	65.6
Ce	73.5	146.1	101.4	83.2	300.5	265.1	333.4	85.7	81.4	72.9	110.1	121.5
Nd	37.2	63.7	47.7	39.4	125.2	123.1	148	42	36.6	32	46.6	51.3
Pb	3	5.9	3.9	6.2	13.9	13.9	12.5	4.8	4.3	3.5	5	7.4
Nb	54.7	99.1	72.3	53.4	205.9	156.9	208.6	60.9	71.6	64.1	95.1	97.6
Zr	250	414.1	213.4	232.7	866.3	671.2	884.5	176.8	204.1	215.5	276.5	336.5
Y	26.2	35.4	27.8	26.8	77.6	70.6	102.3	25.2	23.3	25.3	28.7	29.3
Sr	559.6	1118.8	1196.3	993.7	5.1	8.7	13.8	1063.6	614.1	651.5	841	885.3
Rb	23.9	38	34.5	43	81.5	75.2	61.5	28.2	37.8	33.1	51.2	140.2

Table C-7 (cont.). Cameroon Line continental

Locality-Sample	Biu-N14	Biu-N15	Biu-N16	Biu-N17	Biu-N18	Biu-N19	Biu-N2	Biu-N20	Biu-N21	Biu-N22	Biu-N23	Biu-N24	Biu-N25
Rock type	Trachy-basalt	Alkali basalt	Trachy-basalt	Alkali basalt	Alkali basalt	Alkali basalt	Basalt	Alkali basalt	Alkali basalt	Alkali basalt	Alkali basalt	Alkali basalt	Basalt
SiO_2	44.24	47.1	46.45	45.89	45.91	46.36	48.75	49.09	48.38	44.75	48.97	46.21	47.55
Al_2O_3	12.3	14.08	13.48	12.9	12.98	13.15	13.41	14.65	14.34	12.08	14.47	12.88	12.71
Fe_2O_3	12.38	11.83	11.3	11.31	11.48	11.68	10.8	11.17	11.04	12.29	11.15	11.53	10.74
MgO	10.78	9.49	9.23	9.73	10.11	10.19	10.31	8.11	8.78	11.05	8.56	9.8	10.69
CaO	10.53	9.57	8.73	9.8	10.05	9.83	9.27	9.14	8.67	10.21	9.12	10.39	8.4
Na_2O	3.33	3.24	3.74	2.4	2.1	2.18	2.44	3.38	2.87	3.25	3.34	2.94	2.33
K_2O	1.64	1.385	1.235	1.279	1.426	1.33	1.299	1.162	1.204	1.53	1.223	1.323	1.313
TiO_2	2.967	2.43	2.67	2.379	2.814	2.905	2.123	1.866	1.93	2.638	1.942	2.26	2.354
MnO	0.201	0.164	0.172	0.152	0.157	0.153	0.151	0.15	0.153	0.192	0.152	0.184	0.147
P_2O_5	0.894	0.566	0.77	0.461	0.557	0.58	0.416	0.399	0.423	0.81	0.419	0.717	0.414
Total	99.26	99.86	97.78	96.3	97.58	98.36	98.97	99.12	97.79	98.8	99.35	98.23	96.65
LOI	0.74	0.14	2.22	3.7	2.42	1.64	1.03	0.88	2.21	1.2	0.65	1.77	3.35
Zn	112	95.1	119.8	89.4	98.1	94.9	89.7	89.9	92.9	121.6	94.8	110.8	95.1
Cu	47.1	58.3	36.7	45.7	49.9	45	55.9	52.8	54.5	51.1	55	56.1	39.5
Ni	257.4	199.6	210.8	235	200	210.4	223.7	165.9	167.8	285.4	169.6	224.8	248.7
Cr	313.2	266.6	252.7	390.3	300.4	339.8	395.5	262.1	254.1	470.9	252.4	327	440.7
V	397.5	329.6	334.3	307.5	364.4	372.6	305.2	268.7	285.9	390.7	293.2	343.2	321.7
Ba	841.6	497.3	741	509.3	558.5	460.6	504.1	420	431.1	641.6	457	740.4	452.9
Sc	23.3	24.9	18.4	23.4	24	22.5	21.3	24.1	22.8	25	24.6	24	19.2
La	69.6	41.1	68.7	31.7	38.5	40	34.2	30.6	30.9	74.3	33.8	68	34.4
Ce	132.4	77.1	129.1	59.5	80.2	78.4	63.7	57.8	51.9	137.5	56.8	119.4	65.5
Nd	56.5	34.7	54.8	28.7	38.2	37.2	28.9	25.1	24.9	58.8	24.5	48.3	30.7
Pb	5.3	4.1	4.6	7.1	4.5	4.1	5.3	6.6	6.5	-0.1	4.7	3.6	5.7
Nb	99.8	67.1	105	55.2	68.3	66.9	50.3	48.7	51.5	100.5	52.7	89.2	54.9
Zr	336.1	205.5	373.7	165	245.7	238.1	171	162.1	169.2	329.7	170.7	264	192.6
Y	33	26.6	29.6	22.3	27.3	26.6	22.3	23	24	34.3	24.3	31.8	22.8
Sr	909.7	690.1	1050.8	988.1	1114.5	750.8	767.6	560.2	573.9	892.8	575.8	836.5	490.5
Rb	44.4	35.6	66.2	35.8	32.5	39.6	31.6	29.6	28.8	46	30.2	38	31.8

Table C-7 (cont.). Cameroon Line continental

Locality-Sample	Biu-N26	Biu-N27	Biu-N29	Biu-N3	Biu-N31	Biu-N32	Biu-N33	Biu-N34	Biu-N35	Biu-N36	Biu-N37	Biu-N38	Biu-N4
Rock type	Basaltic andesite	Alkali basalt	Basaltic trachy-andesite	Alkali basalt	Trachy-basalt	Alkali basalt	Trachy-basalt	Alkali basalt	Trachy-basalt	Alkali basalt	Alkali basalt	Trachy-basalt	Alkali basalt
SiO_2	51.48	49.87	51.07	47.12	49.18	46.96	46.77	49.12	49.37	45.48	46.5	44.8	45.4
Al_2O_3	14.25	14.58	16.28	13.69	13.69	13	13.5	14.64	14.26	12.86	13.45	12.76	12.99
Fe_2O_3	10.9	10.42	9.22	12.33	10.94	12.7	11.79	10.76	10.67	11.4	11.34	13.05	11.97
MgO	4.98	7.99	4.06	7.09	9.78	7.92	8.94	7.89	8.76	10.18	9.92	9.92	8.69
CaO	8.23	9.41	6.93	9.65	7.94	9.83	9.69	8.97	8.6	9.64	9.69	10.38	9.72
Na_2O	3.54	3.44	4.32	3.37	3.42	2.35	3.78	3.2	3.42	2.92	2.47	3.54	2.93
K_2O	1.192	1.206	2.845	1.423	1.569	1.245	1.655	1.379	1.516	1.69	1.437	1.43	1.273
TiO_2	2.704	2.073	2.228	3.319	2.167	3.295	2.655	2.078	2.07	2.674	2.6	2.655	3.368
MnO	0.165	0.143	0.09	0.132	0.153	0.154	0.179	0.155	0.141	0.163	0.145	0.201	0.152
P_2O_5	0.465	0.57	0.931	0.625	0.468	0.572	0.654	0.542	0.504	0.808	0.695	0.838	0.562
Total	97.91	99.7	97.97	98.75	99.31	98.03	99.61	98.73	99.31	97.82	98.25	99.57	97.06
LOI	2.09	0.3	2.03	1.25	0.69	1.97	0.39	1.27	0.69	2.18	1.75	0.43	2.94
Zn	123.9	91.2	132.6	103.4	96.1	103	104.2	89.4	94.9	114.4	97.2	118.3	99.3
Cu	40.4	45.3	16.2	50.7	44	46.5	51.4	52.6	48.4	45	53.4	51.9	42.6
Ni	155.7	165.1	82.4	138.8	281.7	246.5	201.3	172.6	210.8	260.7	269.2	221.2	165.9
Cr	222.4	237.8	83.9	138.1	376.1	366.8	323	243.8	285.6	321.5	351.8	271.9	174.4
V	311.7	291.8	240.2	388.8	294.5	443	357.4	291.6	299.6	371.5	365.1	372.8	393.6
Ba	480.6	457.3	1021.1	559.9	526.7	423.9	686.2	512.9	525.6	588.4	534.1	692.7	415
Sc	16.6	21	5.3	19.9	23.5	26.5	22.7	23.2	21.9	21.8	21.4	23.7	21.5
La	28.8	45.7	66	39.3	37.2	39.2	58.8	44.7	41.1	62.8	43	70.4	36.1
Ce	59	84.7	130.4	75.6	77.1	74.7	106.9	75.3	75.6	124.7	83	133.9	75.1
Nd	32.7	35.5	57.4	40.3	32.8	38.7	47.1	33.9	32.3	52.8	36.5	57.3	39
Pb	4	5.2	6	5.3	7.7	7.9	4.4	6.3	5.7	5.1	5.1	3.6	8.5
Nb	45.1	64.3	108.6	55.6	62.3	57.9	87.2	64.2	64.7	96.8	72.7	94.4	54
Zr	232.5	207.1	338.1	296	239.3	267	277.8	200.8	215.1	303.2	214.7	330.6	274.1
Y	23.9	23.1	17.9	29.2	26.7	32.2	31	25.2	23.4	30.2	26	35.1	28.6
Sr	615.6	685.1	1191.6	715	631.7	592.7	828.7	719.4	653.7	1175.3	1577.4	859.3	667
Rb	26.5	29.1	75.1	29.8	35.1	26.6	42.7	30.8	34.9	53.1	32.1	40.7	28.2

Table C-7 (cont.). Cameroon Line continental

Locality-Sample	Biu-N5	Biu-N6	Biu-N7	Biu-N8	Biu-N9	Foumbot-C190	Foumbot-C191	Kerawa-N39	Kerawa-N40	Kerawa-N40A	Kumba-C38	Mandara-C135	Mandara-C136
Rock type	Alkali basalt	Alkali basalt	Basalt	Trachy-basalt	Alkali basalt	Basanite-Tephrite	Basanite-Tephrite	Rhyolite	Rhyolite	Rhyolite	Alkali basalt	Basanite-Tephrite	Rhyolite
SiO_2	46.51	46.8	49.84	47.81	46.48	44.03	43.9	72.37	70.7	71.09	44.34	43.66	70.73
Al_2O_3	13.39	13.42	13.93	13.99	12.89	12.77	12.91	12.99	12.87	11.69	12.88	12.56	14.96
Fe_2O_3	11.97	11.6	11.29	12.39	11.51	13.38	13.21	3.35	4.06	5.94	13.3	11.78	1.44
MgO	8.83	9.09	8.31	7.61	10.64	12.59	11.99	0.15	0.26	0.33	10.77	11.34	0.2
CaO	9.74	11.44	9.74	9.09	10.59	9.79	9.79	0.39	0.44	0.45	11.09	10.39	0.13
Na_2O	3.29	3.06	2.95	3.46	2.85	3.6	3.69	4.29	4.61	5.31	2.65	3.5	6.17
K_2O	1.115	0.908	0.954	1.539	1.133	1.534	1.585	5.008	5.128	2.827	1.057	1.113	4.436
TiO_2	3.323	1.842	2.029	3.162	2.332	2.667	2.66	0.208	0.315	0.455	2.987	3.152	0.142
MnO	0.15	0.155	0.16	0.159	0.161	0.195	0.201	0.058	0.219	0.301	0.192	0.183	0.005
P_2O_5	0.586	0.33	0.328	0.845	0.445	0.62	0.634	0.014	0.024	0.023	0.576	0.725	0.016
Total	98.9	98.65	99.53	100.06	99.03	101.18	100.57	98.83	98.63	98.42	99.84	98.4	98.23
LOI	1.1	1.35	0.47	-0.06	0.97	-1.18	-0.57	1.17	1.37	1.58	0.16	1.6	1.77
Zn	98.1	82	89.9	118.4	88.6	105.1	104.6	217.5	257.1	269.3	101.1	99.3	38.7
Cu	40.7	70.1	50.7	39.3	62.2	54.7	52.7	-6.7	-5.7	-8.4	60.5	70	-9.7
Ni	173.9	217.5	247.1	142.3	271.9	296	274.7	0.6	1.8	1.6	212.8	285.2	1.5
Cr	236.6	345	382.2	189.5	387.5	341.3	337.6	2	2.7	1.3	324.5	481.5	2.5
V	390.7	294.3	287.2	341.4	336.9	228.7	215.9	11.7	18.1	26.6	255.1	453.9	8
Ba	453.6	470.8	390.1	469.5	661	627.2	661.5	3.5	180.7	169.6	373.5	558.8	6.3
Sc	22.9	22	24.4	18.6	24.1	23.9	22.9	0.6	2.8	8.1	24.7	25.2	-1.6
La	41.4	23.9	24.1	47	35.2	56.8	57.5	160	136.4	91.5	29.1	60.6	114.5
Ce	81.3	41.7	43.2	101.2	57.9	100	109.1	311.5	248.8	215.5	58.6	115.6	182.8
Nd	40.3	20.2	20.7	52	28.3	39.4	41.3	127.1	118	86.7	30.1	48.9	66.4
Pb	3.3	5.6	4.5	5.5	4.4	3.2	5.5	19.7	14.9	16.7	5.6	4	19.2
Nb	63.5	42.8	37.5	69.6	57.9	88.3	89.6	209.7	165	182.5	47.7	104.2	532.8
Zr	265.9	120.8	135.9	377.4	174.1	249	259.7	1249.2	1065.4	1410.7	185.8	298.7	1072.7
Y	28.8	23.4	25.1	31.3	23.6	25.8	25.5	98.1	87.9	75.9	23.9	27.4	67.3
Sr	695.2	501.2	456	828.3	636.8	807.6	827.1	5.9	23.5	19.7	631.7	1022.4	10.3
Rb	46.2	22.3	21.8	33.3	26.6	37.4	36.5	175.2	131.9	85.7	23	22.1	275.2

Table C-7 (cont.). Cameroon Line continental

Locality-Sample	Mandara-C137	Mandara-C138	Mandara-C139	Mandara-C140	Mandara-C141	Mandara-C142	Mandara-C143	Mandara-C144	Mandara-C145	Mandara-C146	Mandara-C147	Manengouba-C48
Rock type	Rhyolite	Rhyolite	Rhyolite	Rhyolite	Trachyte	Rhyolite	Trachyte	Rhyolite	Trachyte	Basanite-Tephrite	Trachy-basalt	Alkali basalt
SiO_2	74.44	69.95	73.49	72.35	67.32	72.31	67.53	74.08	65.87	40.04	43.6	44.79
Al_2O_3	13.04	15.17	16.41	12.44	15.91	12.33	16.64	11.4	15.62	11.8	14.5	15.02
Fe_2O_3	1.69	2.1	0.46	3.51	3.05	3.35	1.59	3.49	2.93	14.19	12.66	13.35
MgO	0.18	0.17	0.23	0.3	0.26	0.24	0.34	0.17	0.43	10.19	7.42	7.61
CaO	0.18	0.16	0.14	0.25	0.19	0.18	0.44	0.09	0.41	11.68	9.78	9.15
Na_2O	4.52	5.6	1.28	4.17	5.75	5.63	6.15	5.26	7.02	3.62	3.32	2.87
K_2O	4.017	4.748	1.422	4.159	5.158	4.374	5.105	4.051	5.305	0.98	1.542	1.636
TiO_2	0.124	0.201	0.219	0.315	0.49	0.279	0.472	0.121	0.427	3.711	3.908	3.236
MnO	-0.013	-0.005	-0.001	0.004	0.066	0.158	0.008	0.104	0.324	0.208	0.157	0.188
P_2O_5	0.075	0.043	0.063	0.059	0.064	0.014	0.102	0.011	0.067	1.13	0.743	0.702
Total	98.25	98.14	93.71	97.56	98.26	98.87	98.38	98.78	98.4	97.55	97.63	98.55
LOI	1.75	1.86	6.29	2.44	1.74	1.13	1.62	1.22	1.6	2.45	2.37	1.45
Zn	42.7	79.9	7.3	165	123.4	282	31	307.3	162.2	108	90.1	117.5
Cu	-7.8	-3.4	-7.7	-16.9	-3.2	-13.9	-4.8	-14	-7.7	47.8	43.2	47
Ni	4	1.3	1.2	3	4.3	1	1.8	0.6	1.9	165.8	87.6	119.1
Cr	3	3.3	2.3	2.4	1.7	3.1	1.7	3.2	1.9	273.8	128.9	142.7
V	6.1	11	11.4	23.9	38.3	19.9	35.1	6.9	27.3	534.6	503.2	245
Ba	23.1	7.2	38.4	11.9	133.5	35.2	376.2	8.7	50.4	609.1	485.4	547.6
Sc	-1.4	0	0.5	0	1.7	0.1	3.6	-1.4	4.7	26.2	19.4	22.6
La	101.1	173.5	170.7	121.6	142.5	25.4	136.6	40.8	197.8	62.1	44.7	60.5
Ce	193.3	294.1	303.4	283.4	270.9	126.3	240	153.1	365.1	118.1	87.1	123.7
Nd	72.3	86.9	97	105.3	86.2	36.6	82.9	29.3	109	52.9	44.4	55.9
Pb	20.1	11	12.6	15.3	14.6	29.8	9.3	36.9	13.6	4.3	5.8	5.5
Nb	234.6	254.4	290.4	471.5	255.3	485.4	154.3	650.3	201.7	101	70.2	88.1
Zr	893.3	632	660	2354.9	859.7	1925.3	918	1938.1	1365.1	264.2	250.3	354.6
Y	73	45.2	54	100.1	54.5	93.8	45.4	78.4	53.3	32.2	25.3	30.2
Sr	94.1	10.9	62.5	16.1	35.3	6.2	97.5	3.8	15.7	1156.7	1110.2	921.9
Rb	265.7	167.4	58.2	237.6	171.8	259.2	84.2	401.7	137.6	24.5	33.9	40.1

Table C-7 (cont.). Cameroon Line continental

Locality-Sample	Manengouba-C49	Manengouba-C50	Manengouba-C51	Manengouba-C52	Manengouba-C53	Manengouba-C54	Manengouba-C55	Manengouba-C56	Manengouba-C57	Manengouba-C58
Rock type	Basaltic trachyandesite	Basaltic trachyandesite	Trachybasalt	Basaltic trachyandesite	Trachybasalt	Trachyte	Trachybasalt	Alkali basalt	Basaltic trachyandesite	Trachybasalt
SiO_2	51.05	49.9	47.68	49.38	49.25	64.66	49.64	49.36	52.12	47.05
Al_2O_3	17.58	17.72	14.65	16.69	15.76	16.35	15.91	15.32	15.52	16.3
Fe_2O_3	10.43	10.61	12.51	10.52	12.27	5.07	12.39	12.54	11.52	12.36
MgO	3.5	4.04	6.95	4.52	5.79	0.28	4.11	5.74	3.07	4.99
CaO	5.67	6.48	9.07	7.14	8.79	1.33	7.8	9.1	6.46	7.74
Na_2O	4.59	4	3.56	4.86	3.75	5.33	4.05	3.46	4.63	3.92
K_2O	2.588	1.917	1.434	2.496	1.688	5.367	1.488	0.957	2.051	2.312
TiO_2	2.255	2.452	2.543	2.62	2.584	0.478	2.84	2.524	2.46	3.016
MnO	0.166	0.171	0.177	0.191	0.19	0.161	0.189	0.171	0.245	0.196
P_2O_5	0.688	0.679	0.633	0.805	0.736	0.088	0.754	0.463	1.061	0.84
Total	98.52	97.97	99.21	99.22	100.81	99.11	99.17	99.64	99.14	98.72
LOI	1.48	2.03	0.79	0.78	-0.81	0.89	0.83	0.36	0.86	1.28
Zn	133.7	117.2	116.4	117.1	128	105.5	127.8	113.6	143.1	120.5
Cu	18.4	24.9	54.9	21.3	45.6	-4.6	14.2	53.7	6.2	27.3
Ni	22.9	61.5	133.3	33.4	81.1	2	27.3	72.3	2.5	37.7
Cr	15.7	60.5	219.5	27.5	127.5	4.1	44.2	147	6.4	24.9
V	104.6	143.4	188.2	145.2	166	-7.4	168.5	204.5	80.2	171.2
Ba	716.6	656	438.5	698.2	519.2	1277	424	345.8	770.8	775.5
Sc	7.5	12.6	20.4	14	17.5	3.8	16.7	23.3	16.8	14.5
La	73.3	60.6	46.1	83.6	64.6	97.1	47.4	29.2	68.2	84.2
Ce	150.3	115	95.5	165.2	133.1	202	94.7	53.9	138.6	172.2
Nd	64.6	53.2	46.3	68	58.4	82.7	45.6	26.9	69.1	70.7
Pb	6.6	7	3.3	8.3	6	11.1	6	2.6	3.2	5.3
Nb	112.4	84.2	67.4	120.9	90.6	109.7	70.2	43.9	87.9	122.7
Zr	562.9	411.1	321.9	540.9	412.5	817	312.4	213.6	365	501.3
Y	31	31.6	28.5	34.3	36.8	47.7	34.4	28.2	45.3	37.5
Sr	868.8	687.7	756.5	1086.9	868.4	163.1	636.1	480.5	753.1	1194.3
Rb	68.6	45.3	36.8	65.5	45.7	88.9	35.7	15.7	46.3	58.3

Table C-7 (cont.). Cameroon Line continental

Locality-Sample	Manengouba-C59	Manengouba-C60	Manengouba-C62	Manengouba-C63	Manengouba-C64	Manengouba-C65	Manengouba-C66	Manengouba-C67	Manengouba-C68	Manengouba-C69
Rock type	Alkali basalt	Trachybasalt	Trachy-andesite	Trachy-andesite	Basaltic trachyandesite	Alkali basalt	Alkali basalt	Basaltic trachyandesite	Basaltic trachyandesite	Trachy-andesite
SiO_2	45.45	46.59	52.59	52.72	51.76	49.77	48.92	52.46	50.69	54.39
Al_2O_3	14.86	16.15	18.42	16.65	17.1	13.86	14.17	17.21	14.53	18.51
Fe_2O_3	13.86	13.25	8.55	8.98	8.93	12.52	12.2	9.59	10.95	8
MgO	7.59	4.85	2.52	3.28	2.82	7.78	8.2	3.32	5.82	2.29
CaO	9.33	7.25	4.95	5.39	7.66	7.46	8.52	8.48	7.4	6.19
Na_2O	2.79	3.32	4.93	5.16	4.47	3.35	3.25	4.36	4.19	5.36
K_2O	1.638	2.036	2.929	3.09	1.651	1.381	1.275	1.413	1.676	2.296
TiO_2	3.32	3.316	1.669	1.967	2.271	2.227	2.267	2.43	2.147	1.762
MnO	0.176	0.183	0.179	0.164	0.136	0.175	0.164	0.136	0.182	0.159
P_2O_5	0.698	0.789	0.694	0.622	0.407	0.386	0.401	0.44	0.427	0.68
Total	99.71	97.73	97.43	98.02	97.21	98.91	99.37	99.84	98.01	99.64
LOI	0.29	2.27	2.57	1.98	2.79	1.09	0.63	0.16	1.99	0.36
Zn	119	120.1	108.6	105.8	99.2	121.9	103.5	101.3	115	96.8
Cu	48.6	22.2	7.8	14	55.8	56.6	53.2	68.4	51.7	19.4
Ni	127.9	28.9	11.1	23.6	41	196.8	202.3	46.7	112	10.6
Cr	152.8	18	10	22	45.6	275.3	275.8	71	177.9	10.7
V	245.3	190.1	66.4	91.3	158.1	193.3	191.7	166.3	160.9	62.5
Ba	518.6	658.7	857.3	701.3	491	457.6	466.3	440.2	492.8	658.4
Sc	23.4	16.2	5.5	8.8	12.7	23.2	19.8	16.5	18.7	8.9
La	60.9	72.4	86.8	76.3	38.1	41.3	36	39.6	47.1	70.5
Ce	119.2	141.7	170.6	147.8	76.9	63.9	66.7	75.8	89.3	139.3
Nd	55.9	60.6	66	58.1	35.5	33.2	30.5	34.8	37.8	60.1
Pb	5.1	6.6	9.5	9.8	7.1	5.5	6.4	12.9	4.9	7.9
Nb	86.2	107.1	132	121.7	60.8	53.5	46.6	52.6	65.6	95.7
Zr	338.4	430.4	607.9	643	336.5	298.9	254.4	299.9	364.4	456.4
Y	30.8	35.6	34.2	32.4	27.6	29.1	24.9	30.4	29.5	40.3
Sr	945.4	1149.8	1005.8	856.2	566.3	428.7	587.5	545.6	463.2	787.8
Rb	36.7	48	80.1	87.1	41	30.7	26.5	31.6	38	62

Table C-7 (cont.). Cameroon Line continental

Locality-Sample	Manengouba-C70	Manengouba-C71	Manengouba-C72	Mt Cameroon-C1	Mt Cameroon-C10	Mt Cameroon-C11	Mt Cameroon-C12	Mt Cameroon-C13	Mt Cameroon-C14
Rock type	Trachybasalt	Basaltic trachyandesite	Trachybasalt	Basanite-Tephrite	Trachybasalt	Alkali basalt	Basanite-Tephrite	Basanite-Tephrite	Basanite-Tephrite
SiO_2	45.93	51.57	45.72	46.57	47.5	45.57	42.4	42.96	46.35
Al_2O_3	14.54	18.17	14.5	16.26	16.09	12.83	13.7	13.36	16.39
Fe_2O_3	13.38	8.93	13.16	11.69	11.43	12.63	13.38	13.59	11.6
MgO	8.43	3.07	7.55	5.41	5.37	9.12	7.65	7.66	4.77
CaO	9.11	7.6	9.01	10.2	9.91	13.06	12.12	12.85	9.98
Na_2O	3.69	4.64	3.36	4.45	4.43	2.35	4.07	3.22	4.36
K_2O	1.659	2.033	1.737	1.791	1.563	0.907	1.435	1.495	1.795
TiO_2	2.924	2.355	3.141	3.172	2.817	2.674	3.623	3.772	3.204
MnO	0.19	0.153	0.172	0.205	0.199	0.198	0.208	0.197	0.214
P_2O_5	0.625	0.816	0.665	0.816	0.524	0.345	0.802	0.613	0.798
Total	100.48	99.34	99.02	100.56	99.83	99.68	99.39	99.72	99.46
LOI	-0.48	0.66	0.98	-0.56	0.17	0.32	0.61	0.28	0.54
Zn	115.3	104.9	122.3	99.7	105.9	97.5	113	105.6	116.1
Cu	52.7	21.4	44.2	66.5	67.8	113.6	59.7	92.3	34.7
Ni	162.8	12.9	130.8	43.5	48.5	132.4	92.3	96.7	25.3
Cr	212.1	13.5	150.4	63.1	81.3	355.6	206.1	212.7	41.6
V	219.3	105.8	239.2	216	247.6	332.6	301.6	343.4	253.4
Ba	497.2	821.6	525.7	599.4	570.5	367.9	601.6	476.4	565.9
Sc	27.5	10.9	21.8	15	18.5	38.6	24.5	27.8	13.3
La	48.5	67.1	60.4	86.8	88.3	55.5	92	80	91.2
Ce	94.2	138.4	119.8	181.5	175.3	105.9	190	157.3	180.3
Nd	42.9	59.5	53.8	76.2	71.2	44.1	80.8	65.5	76.9
Pb	5.1	9.1	3.9	8.5	7.8	7.1	7.4	7.1	6.8
Nb	79	93.3	87.5	116.5	122.9	69.5	125.1	104.5	121.8
Zr	308.2	383.5	349.2	407.3	438.2	267.8	422.9	356.7	413.2
Y	32	33.4	30.7	35.5	34.1	26.5	32.8	30.8	35.7
Sr	733.2	994.7	918.1	1136.1	1099.4	742	1167.2	1006.6	1100.8
Rb	41.9	53.6	42.7	42.8	45.2	27.3	51.2	34.9	42.5

Table C-7 (cont.). Cameroon Line continental

Locality-Sample	Mt Cameroon-C15	Mt Cameroon-C16	Mt Cameroon-C17	Mt Cameroon-C18	Mt Cameroon-C19	Mt Cameroon-C2	Mt Cameroon-C25	Mt Cameroon-C26	Mt Cameroon-C27
Rock type	Basanite-Tephrite	Alkali basalt	Basalt	Basaltic trachyandesite	Trachybasalt	Trachybasalt	Basanite-Tephrite	Basanite-Tephrite	Trachybasalt
SiO_2	46.59	44.48	45.39	50.02	47.51	47.11	43.24	42.79	46.76
Al_2O_3	16.5	13.84	9.79	16.77	15.63	16.68	12.05	13.09	15.95
Fe_2O_3	11.58	12.96	11.99	10.87	11.77	11.6	13.52	13.72	11.74
MgO	4.69	8.29	14.52	3.57	6.51	4.43	10.52	8.85	5.39
CaO	9.88	12.12	12.72	8.12	10.16	9.6	11.64	11.71	10.14
Na_2O	4.52	3.12	1.79	3.94	3.77	4.2	3.03	3.19	3.89
K_2O	1.838	1.449	0.663	2.329	1.367	1.911	1.403	1.539	1.49
TiO_2	3.19	3.008	2.308	3.056	2.935	3.053	3.076	3.377	3.089
MnO	0.216	0.203	0.172	0.167	0.193	0.208	0.215	0.207	0.183
P_2O_5	0.794	0.657	0.307	0.634	0.583	0.676	0.726	0.764	0.606
Total	99.8	100.13	99.65	99.48	100.43	99.47	99.42	99.24	99.24
LOI	0.2	-0.13	0.35	0.52	-0.43	0.53	0.58	0.76	0.76
Zn	114.3	104.6	88.9	112.5	100.5	111.6	110.9	110.9	99.7
Cu	29.8	64.4	90.3	12.9	69.5	32.9	60.5	71.2	84.1
Ni	23.1	117.7	337.3	6.4	86.4	18.3	179.3	135.3	52.2
Cr	35.5	303.7	1122.3	7.9	172.8	20	477.2	329.5	82.1
V	249.2	322.1	252.6	219.1	230.1	195.9	285.6	313.8	257.6
Ba	563.4	490.5	242	670.9	433.5	585	479.3	511.6	451.5
Sc	13.3	25.4	39.8	15.9	21.3	11.4	32.5	30	20.7
La	88.5	74.6	38.1	85	58.5	86.2	82.9	86.6	69.1
Ce	181.7	151.3	76	170.7	126.8	170	163.5	176.7	133.3
Nd	77.2	61.7	34.6	76.6	55.3	67.7	70.2	73.3	55.6
Pb	4.8	6	5.1	12.7	6	3.5	6.2	7.2	7.2
Nb	121.8	101.3	48	99.2	83.6	118.7	104.5	110.1	88.6
Zr	413.5	301.5	192.7	428.3	333.7	380.3	355.8	368.1	347.8
Y	34.9	27.3	21.5	35.9	29.2	34.5	29.4	32.2	30.5
Sr	1110.1	976.1	528.5	918.1	855.9	1142.8	989	1071.1	901.3
Rb	42.9	34.3	19.9	70.9	32.6	44	35.9	38.8	37.5

Table C-7 (cont.). Cameroon Line continental

Locality-Sample	Mt Cameroon-C28	Mt Cameroon-C29	Mt Cameroon-C3	Mt Cameroon-C30	Mt Cameroon-C37	Mt Cameroon-C4	Mt Cameroon-C5	Mt Cameroon-C6	Mt Cameroon-C7
Rock type	Basanite-Tephrite	Trachybasalt	Basaltic trachyandesite	Alkali basalt	Trachybasalt	Alkali basalt	Tephrite-Basanite	Tephrite-Basanite	Tephrite-Basanite
SiO_2	42.98	44.74	51.15	44.72	46.79	45.62	47.3	47.85	48.04
Al_2O_3	12.05	15.01	17.24	10.04	16.19	12.92	17.2	17.39	17.39
Fe_2O_3	13.62	13.1	9.89	12.79	10.86	12.63	10.32	10.14	10.2
MgO	9.07	6.22	3.63	12.81	5.35	9.06	4.25	4.1	4.13
CaO	11.73	11.64	7.86	13.5	9.74	13.45	8.87	8.72	8.78
Na_2O	3.8	3.51	4.95	2.27	4.38	2.19	5.26	5.26	5.13
K_2O	1.609	1.438	1.853	0.757	1.894	0.847	2.09	2.123	2.105
TiO_2	2.975	3.343	2.583	2.579	2.993	2.692	2.931	2.912	2.938
MnO	0.235	0.204	0.193	0.181	0.212	0.192	0.201	0.199	0.198
P_2O_5	1.099	0.667	0.663	0.444	0.792	0.342	0.922	0.953	0.946
Total	99.17	99.87	100.01	100.09	99.2	99.94	99.34	99.65	99.86
LOI	0.83	0.13	-0.01	-0.09	0.8	0.06	0.66	0.35	0.14
Zn	134.9	106	115.6	89.9	107.4	102.6	103.4	101.4	100.8
Cu	57	46.9	40.1	95.5	29.7	113.3	29.6	29.7	28.6
Ni	153.6	51.4	13.5	260.4	36.7	130.8	18	13	15.1
Cr	318.9	126.7	16.5	872.2	98.8	374.8	24.7	16.4	18.3
V	249	319.6	132.2	299	234.7	321.8	176.9	167.7	178.4
Ba	687.2	485.6	613.9	292.1	570.7	361.8	649.5	664.7	668.2
Sc	25.7	21.1	10.9	41.1	14.9	40.5	9.7	8.3	9.9
La	125.1	67.7	93.7	45.1	81	55.9	96.5	97.5	95.4
Ce	254	138.6	192.9	99.4	172	105.9	198.8	199.7	198.8
Nd	100.7	59.7	78.5	44.4	71.3	45.5	81	82.4	78.4
Pb	5.8	8.5	9.8	7.2	8.2	6.1	6	5.9	6.2
Nb	153.3	91.6	126.2	62.1	118.3	70.6	134	135.4	135.5
Zr	521.5	321.9	528.1	240	398.1	269.9	461.4	466.6	466.7
Y	37.1	30.8	39	22.9	33.6	26	37.6	38.4	37.7
Sr	1368.8	953.3	986.6	624.9	1040.3	735.2	1201.8	1220.4	1224.7
Rb	50.5	34	48.8	22.2	44.1	20.6	51.1	51.3	51

Table C-7 (cont.). Cameroon Line continental

Locality-Sample	Mt Cameroon-C8	Mt Cameroon-C9	Mt Koupe-C41	Mt Koupe-C42	Mt Koupe-C43	Mt Koupe-C45	Mt Koupe-C47	Ngaoundere-C155	Ngaoundere-C156	Ngaoundere-C157	Ngaoundere-C158
Rock type	Trachybasalt	Trachybasalt	Alkali basalt	Trachy-basalt	Alkali basalt	Alkali basalt	Trachy-basalt	Phonolite	Basanite-Tephrite	Basanite-Tephrite	Trachyte
SiO_2	47.8	48.85	45.3	46.99	44.11	48.63	46.71	55.75	43.2	43.92	58.77
Al_2O_3	17.09	16.13	14.9	16.86	14.82	15.46	16.84	22.05	11.68	15.58	18.88
Fe_2O_3	10.85	9.81	14.23	13.09	13.48	12.68	13.37	2.29	13.35	12.98	3.5
MgO	4.26	5.67	7.83	4.9	8.04	6.6	5.24	0.09	11.08	5.04	0.69
CaO	9.51	9.67	10.19	7.73	10.04	8.81	8.03	1.08	11.77	10.1	3.37
Na_2O	4.64	4.01	2.85	3.88	2.74	3.48	4.05	10.93	3.13	3.25	5.01
K_2O	1.738	1.811	0.872	1.563	1.261	1.079	1.191	5.537	0.625	2.213	5.791
TiO_2	2.969	2.353	3.219	3.133	3.44	2.805	3.258	0.349	3.36	3.601	0.621
MnO	0.205	0.182	0.187	0.167	0.181	0.167	0.17	0.185	0.2	0.245	0.245
P_2O_5	0.891	0.586	0.412	0.632	0.539	0.459	0.541	0.084	0.629	1.75	0.154
Total	99.95	99.07	99.99	98.95	98.65	100.17	99.4	98.35	99.02	98.68	97.03
LOI	0.05	0.93	0.01	1.05	1.35	-0.17	0.6	1.65	0.98	1.32	2.97
Zn	116.8	96.5	115.6	108.4	107.1	116.5	117.3	131.3	96.8	130.5	128.5
Cu	23.5	59.3	60.8	23.7	42.6	43.2	20.9	-7.8	50.7	7.4	-4
Ni	12.2	72.3	114.2	15	101.8	82.9	26.4	2	184.3	3.6	2.4
Cr	16	191.1	169.9	8.2	130.5	154.1	12.8	4.7	440.2	6.2	3.7
V	220.3	197.7	298.4	164.2	284.2	194.1	217.5	14.4	281.7	167.4	13.7
Ba	567.2	599.4	336.7	538.9	506.4	307.4	448.8	406.3	553.7	811.4	872
Sc	12.5	19.2	28.2	14.3	23.7	22	18.9	-0.5	28	9.2	-0.4
La	90.9	96.7	32.9	52.1	48.7	28.5	41.4	60.4	56.1	87	146.1
Ce	191.3	188.8	59.5	103.6	95.7	60.5	82.1	104.5	98.6	174.4	245.8
Nd	77.5	69.8	31.5	47.9	42.1	32	38.9	27	44.5	82.3	71.2
Pb	6	9.7	3.5	6.5	5.9	7.7	3.3	16.9	1.6	3.5	15.2
Nb	126.8	127	49.5	78	75.3	48	61.7	188.7	75.8	118.6	209.4
Zr	459.7	455.9	196.7	306.6	266.3	208.8	255.2	1291.3	311.2	450.6	756.5
Y	36.1	32.9	28.5	30.5	29.2	29.4	30.8	22	26.9	42.5	41.4
Sr	1171.4	1031.1	613.7	917.3	980.4	577.7	793.4	465.6	707.6	1593	723.2
Rb	45.2	49.1	17	35	28.5	21.3	17.9	211.7	41.5	56.3	156.7

Table C-7 (cont.). Cameroon Line continental

Locality-Sample	Ngaoundere-C159	Ngaoundere-C160	Ngaoundere-C161	Ngaoundere-C162	Ngaoundere-C163	Ngaoundere-C164	Ngaoundere-C165	Ngaoundere-C166	Ngaoundere-C167	Ngaoundere-C168
Rock type	Trachyte	Basanite-Tephrite	Basanite-Tephrite	Basanite-Tephrite	Trachyte	Alkali basalt	Basanite-Tephrite	Trachyte	Alkali basalt	Picro-basalt
SiO_2	62.72	43.65	44.12	44.4	62.18	45.03	43.62	60.85	44.31	41.97
Al_2O_3	16.91	14.13	12.95	13.51	18	11.49	12.37	19.03	13.82	11.68
Fe_2O_3	4.92	12.27	12.91	12.17	3.68	11.96	13.53	2.82	13.23	14.84
MgO	0.6	9.47	11.66	10.44	0.57	10.28	12.11	0.5	8.91	10.61
CaO	1.03	10.51	10.2	10.62	1.4	14.48	10.29	2.25	9.28	12.21
Na_2O	6.61	4.06	2.69	3.1	6.6	1.55	3.44	6.42	2.96	2.03
K_2O	5.561	1.834	1.328	1.686	5.607	0.998	0.885	5.944	1.614	0.71
TiO_2	0.34	2.944	2.758	2.938	0.434	2.906	2.954	0.461	3.433	4.018
MnO	0.311	0.207	0.199	0.204	0.353	0.173	0.18	0.253	0.191	0.163
P_2O_5	0.125	0.942	0.686	0.916	0.066	0.36	0.617	0.061	0.873	0.458
Total	99.13	100.02	99.5	99.98	98.89	99.23	100	98.59	98.62	98.69
LOI	0.87	-0.02	0.5	0.02	1.11	0.77	0	1.41	1.38	1.31
Zn	157.6	105.3	121.7	109	171.5	76.8	101.9	125.6	119.3	102.7
Cu	-3.7	42.8	45.4	39.6	-7.7	61.2	59.8	-8.8	41.5	37.7
Ni	1.8	164.6	266.2	199.8	1.6	118.6	279.4	2.4	125.2	125.9
Cr	3.5	270.2	492.7	367.9	3.4	433.9	442.9	3.2	245.8	354.7
V	-5.9	210.7	244.8	213.6	-8.1	319.7	257.3	3.7	219	340.4
Ba	157.5	840.6	629.6	752.6	125.9	390.6	496	219.9	569.3	440.3
Sc	1.8	19.2	27.9	21.6	-1	44.1	26.7	-1	22	31.8
La	128.5	84.6	63.5	75.8	161.6	26	50.6	161.1	59.6	37.9
Ce	235.8	149	118.5	137.8	309.4	46.4	65.5	286.2	110.2	60.4
Nd	73.2	58.5	49.3	55.2	100.8	23.6	24.9	79.3	49	32
Pb	18.5	6.6	7.2	5.1	18.8	6.6	5.2	17.1	4.3	4.6
Nb	202.3	116.2	95	98.2	277.3	36.5	69.7	283.9	88	52.1
Zr	964	331.7	326.6	341.8	1212.6	187.7	233	1315.1	376.2	232.2
Y	39.5	28	28.3	28.9	51.6	20.3	23.2	47.3	29.9	25.4
Sr	18.6	1110.1	828.1	1107.7	31.1	529.6	706.7	115.4	877.9	598.1
Rb	144	45.6	37	44.8	177.4	18.4	17.7	168.4	31.9	23.8

Table C-7 (cont.). Cameroon Line continental

Locality-Sample	Ngaoundere-C169	Ngaoundere-C170	Ngaoundere-C171	Ngaoundere-C172	Ngaoundere-C173	Ngaoundere-C174	Ngaoundere-C175	Ngaoundere-C176	Ngaoundere-C177	Ngaoundere-C178
Rock type	Basanite-Tephrite	Basanite-Tephrite	Tephrite-Basanite	Basanite-Tephrite	Basanite-Tephrite	Tephrite-Basanite	Basanite-Tephrite	Trachyte	Phonolite	Basanite-Tephrite
SiO_2	42.85	42.17	47.78	44.82	40.94	45.47	46.19	64.77	57.44	40.55
Al_2O_3	11.12	14.68	16.18	16.19	12.15	15.35	14.86	17.45	20.98	13.32
Fe_2O_3	13.87	14.54	11.3	12.89	14.68	11.55	11.79	2.82	2.7	15.41
MgO	11.71	6.39	5.65	5.49	10.41	5.47	7.57	0.27	0.24	8.81
CaO	12.47	10.18	8.66	9.42	12.02	9.34	8.19	0.61	1.45	10.92
Na_2O	2.39	3.65	4.83	4.19	3.54	5.08	4.14	7.08	9.9	3.55
K_2O	1.004	0.832	2.423	2.392	1.575	2.863	2.141	5.617	5.51	0.911
TiO_2	3.592	4.512	2.539	3.617	3.414	2.576	3.192	0.466	0.307	4.383
MnO	0.179	0.229	0.18	0.174	0.206	0.261	0.144	0.211	0.154	0.2
P_2O_5	0.508	1.087	0.606	0.801	0.997	0.906	0.909	0.064	0.039	0.878
Total	99.69	98.27	100.15	99.98	99.93	98.87	99.13	99.36	98.72	98.93
LOI	0.31	1.73	-0.15	0.02	0.07	1.13	0.87	0.64	1.28	1.07
Zn	100.9	119.8	117.8	115.9	119.4	122.3	128.3	126.8	114.8	120.5
Cu	31.5	16.3	44.7	35.3	60.9	35.2	22.5	-9.3	-3.9	59.1
Ni	162.8	12.3	61.8	31.4	164.6	53.7	115.4	1.5	1.5	98.2
Cr	496	13.1	156.6	31.9	339.4	115.6	145.3	3	3.7	156.7
V	347.4	253.8	176.3	254.4	286.8	184.6	152.7	-1.3	10.2	331.2
Ba	395.7	711.3	859.5	884.3	658.2	1000	684.7	241.8	947.9	455.5
Sc	35.8	16.1	16.5	19.6	28.7	15.4	14	0.8	-1.2	28.5
La	39.8	66.2	73	69.2	82.4	108.5	74.1	116.4	105.5	62.5
Ce	68.2	129.8	123.9	118.2	157.2	179.5	140.8	195.6	121.3	118.3
Nd	31.7	59.5	46	49.3	66.7	64.7	60.3	67.4	20.4	54.7
Pb	5	2.9	5.4	5.9	5.1	5.7	4.5	15.4	19.7	-0.4
Nb	58.3	97.9	93.1	91.5	97.2	129.6	114.7	224	177.2	91.9
Zr	245.5	381.7	368.3	329.6	317.1	475.6	438.6	1205.5	744	369.4
Y	25.5	36.6	28.7	29.3	32.9	33.8	25.6	24	16.8	32.1
Sr	588.7	1037	1169.7	1159.7	1164.4	1266.4	991.6	23.1	430.3	845.3
Rb	34.9	44.6	59.5	78.1	94.9	73.8	50.1	128.3	170	39.4

Table C-7 (cont.). Cameroon Line continental

Locality-Sample	Ngaoundere-C179	Ngaoundere-C180	Ngaoundere-C181	Ngaoundere-C182	Ngaoundere-C183	Ngaoundere-C184	Ngaoundere-C185	Ngaoundere-C186	Ngaoundere-C187	Ngaoundere-C188
Rock type	Basanite-Tephrite	Alkali basalt	Trachyte	Basanite-Tephrite	Basanite-Tephrite	Basanite-Tephrite	Alkali basalt	Basanite-Tephrite	Basanite-Tephrite	Basanite-Tephrite
SiO_2	40.24	45.88	58.21	42.48	43.03	41.91	46.01	41.94	39.76	41.49
Al_2O_3	12.19	14.01	19.02	12.73	13.06	12.65	14.25	12.08	13.69	13.87
Fe_2O_3	15.74	10.91	4.55	12.8	13.69	11.97	11.1	14.68	14.53	14.92
MgO	10.61	8.87	0.96	11.5	10.16	11.75	9.91	11.5	5.86	7.69
CaO	11.26	10.18	3.73	10.73	10.31	11.62	9.85	10.73	12.4	11.18
Na_2O	2.73	2.73	6.98	3.54	2.96	3.53	3.24	2.39	3.63	3.55
K_2O	1.543	1.657	4.214	1.548	1.479	1.429	1.216	0.832	0.948	0.851
TiO_2	3.995	2.427	0.992	3.153	3.763	2.806	2.517	3.409	4.435	4.354
MnO	0.183	0.154	0.221	0.194	0.182	0.203	0.154	0.192	0.245	0.207
P_2O_5	0.75	0.661	0.189	0.927	0.768	1.096	0.609	0.676	2.167	1.044
Total	99.24	97.48	99.07	99.6	99.4	98.96	98.86	98.43	97.67	99.16
LOI	0.76	2.52	0.93	0.4	0.6	1.04	1.14	1.57	2.33	0.84
Zn	124.7	84.9	123.6	102.7	101.7	100.2	84.1	112.4	144.1	122.4
Cu	59.5	47	-4	35.7	39.6	40.6	49	56	11.7	37
Ni	169.1	151.9	2.2	213.7	162.9	242.7	199.4	217	6.2	55.3
Cr	219.4	259	4	337.7	225.2	372.7	339.4	305.5	7.6	70.2
V	306.5	191.3	16.2	229.4	222.5	230.4	204.4	261.9	221.8	297.2
Ba	510.7	620.8	1474.2	825.8	657.4	879.7	616.2	449.4	804.4	576.8
Sc	26.4	20	-0.1	23.4	20.5	22.6	23.2	24.5	12.6	23
La	56.8	51.8	123.3	70.1	58.5	91.3	48.8	46.6	96.3	72.9
Ce	103.8	90.2	252.4	131.7	100.8	159.1	76.5	70.9	193.3	140
Nd	46.1	39.2	94.8	56.7	44.4	61.1	31.5	30.8	92.3	57.7
Pb	4.8	5.4	10.2	5.9	4.5	5.6	6.8	5.5	2.1	2.9
Nb	78.8	71.5	210.7	96.8	91	122.6	72.1	59.9	128.3	103.8
Zr	285.7	232.5	838.2	306.7	302.7	334	211.5	245.6	508.5	406.7
Y	25.2	24.4	49.5	28.2	26.1	29.7	20.8	23.1	43.3	35.3
Sr	789.1	746.3	1208.1	1008.7	1067.5	1341.1	866.9	729.6	1613	932.4
Rb	36.3	63.3	102.3	46.2	33.7	52.9	32.5	20.9	48.6	82.6

Table C-7 (cont.). Cameroon Line continental

Locality-Sample	Ngaoundere-C189	Oku-C76	Oku-C77	Oku-C78	Oku-C79	Oku-C80	Oku-C81	Oku-C84	Oku-C85	Oku-C86	Oku-C87	Oku-C88	Oku-C89
Rock type	Basanite-Tephrite	Rhyolite	Trachy-basalt	Trachy-basalt	Alkali basalt	Trachy-basalt	Trachyte	Rhyolite	Rhyolite	Trachyte	Rhyolite	Basaltic trachy-andesite	Alkali basalt
SiO_2	41.09	75.68	46.79	45.22	43.87	46.22	58.75	73.17	72.7	65.63	71.13	48.72	46.62
Al_2O_3	12.52	11.86	15.02	14.76	13.92	14.64	15.74	10.43	10.74	12.67	12.56	15.96	16.86
Fe_2O_3	15.72	2.16	12.4	13.32	12.01	12.66	8.48	5.86	5.69	7.99	3.31	11.68	12.5
MgO	9.49	0.01	7.22	6.8	8.93	7.78	0.21	0.06	0.04	0.12	0.04	3.67	5.56
CaO	11.1	-0.03	9.06	8.63	8.7	9.19	0.76	0.14	0.12	0.24	0.02	5.97	8.5
Na_2O	2.83	4.43	3.56	3.19	3.2	3.91	5.21	4.33	4.72	6.86	5.68	4.49	3.39
K_2O	1.526	4.758	1.735	1.964	1.349	1.629	3.958	4.527	4.574	4.989	5.263	2.251	1.368
TiO_2	4.114	0.226	2.933	3.187	2.684	2.952	0.872	0.347	0.368	0.599	0.678	2.046	3.177
MnO	0.204	0.025	0.202	0.201	0.183	0.188	0.405	0.058	0.091	0.181	0.033	0.227	0.192
P_2O_5	1.07	0.003	0.835	0.779	0.797	0.756	0.226	0.001	0.003	0.022	0.089	1.096	0.856
Total	99.66	99.12	99.76	98.05	95.64	99.93	94.61	98.92	99.05	99.3	98.8	96.11	99.02
LOI	0.34	0.88	0.24	1.95	4.36	0.07	5.39	1.08	0.95	0.7	1.2	3.89	0.98
Zn	122.3	121.7	110.5	116.8	110.5	108.8	128.7	314.3	140.7	329.1	261.4	128.6	98.2
Cu	49.5	-1.8	36.4	29.7	38.3	43.2	-3.6	-9.4	-11.6	-11.6	-17.2	1.9	22.3
Ni	126.5	0.8	85.7	78.8	215.6	117.4	0.8	1.1	1	0.7	0.9	1.1	29.4
Cr	157.1	2.3	170.9	85.7	334.4	179.2	2.5	3.2	3.7	4.1	4.8	4	45.5
V	263.1	-1.8	186	188	195.3	205.9	-3	-2.3	-6.2	-11.3	-3.4	54.4	181.8
Ba	629.6	6.4	765.6	669.3	639.7	603	3468.3	13.6	3.7	10.2	80.1	672.4	516.8
Sc	23.5	-1.4	18.7	16.1	19.5	22.9	20	-1.4	-1.6	1.8	2.1	12	19.4
La	68.6	154.3	55.2	63.2	50.6	40.6	88.9	29.4	20.4	217.8	324.6	70.1	46
Ce	119.8	308.6	106.9	121.6	99.3	85.4	193.4	77.4	18.1	379.7	659.3	149.6	93.6
Nd	52.5	129.8	48.2	53.1	44.2	40	90.9	40.1	19	157.1	267.2	73.5	48.2
Pb	2.3	20	4.4	5	7.5	5.7	2.9	28.8	17.9	23.9	21	6.6	4.2
Nb	90.9	164.4	78.2	92.2	74.9	66.3	109.1	245.4	287.8	350.1	427.8	88.7	52.8
Zr	306.2	1054.1	302	360.1	276.4	256.7	524.6	1358.3	1404.7	1634.5	2070.6	482.9	253.9
Y	29.4	82.7	28.5	32	27	28	49.2	81.9	25.5	62.5	165.4	40.7	28.2
Sr	957.2	4.8	1038	1064.5	872.4	795.2	357.7	7	3.5	3.9	14.6	839.2	1005.2
Rb	30.4	205	41.7	50.5	49.6	47.7	54.6	205.6	171.7	197.1	206.9	38.8	22.2

Table C-7 (cont.). Cameroon Line continental **Cameroon Line oceanic**

Locality-Sample	Oku-C90	Oku-C91	Oku-C92	Oku-C93	Oku-C94	Oku-C95	Oku-C96	Oku-C97	Oku-C98	Bioko-FP1	Bioko-FP11	Bioko-FP13	Bioko-FP15
Rock type	Alkali basalt	Trachy-basalt	Rhyolite	Basaltic trachy-andesite	Trachy-basalt	Rhyolite	Trachy-basalt	Alkali basalt	Trachy-basalt	Alkali basalt	Alkali basalt	Trachy-basalt	Alkali basalt
SiO_2	44.08	47.31	71.03	51.88	46.51	75.16	46.93	45.43	47.21	46.46	45.32	47.24	45.66
Al_2O_3	11.92	16.54	11.94	16.33	14.21	12.77	15.45	15.51	16.67	12.93	12.6	15.94	11.56
Fe_2O_3	12.74	12.26	3.69	11.68	12.3	1.36	12.71	13.91	13.11	13.01	13.16	10.81	12.8
MgO	14.24	4.83	0.06	3.06	9.31	0.03	6.27	6.16	4.86	8.06	10.38	5.32	13.05
CaO	9.2	7.69	0.04	5.97	8.34	0	7.55	9.22	7.02	11.23	10.82	9.3	9.27
Na_2O	2.07	3.99	5.21	3.44	3.77	4.34	3.42	2.99	3.83	2.53	2.63	4.25	2.71
K_2O	0.904	1.979	4.867	2.738	1.65	5.188	1.782	0.992	1.671	1.149	0.843	2.235	1.223
TiO_2	2.775	3.218	0.628	2.018	2.841	0.267	3.144	3.8	3.127	3.682	2.867	3.327	3.018
MnO	0.177	0.179	0.096	0.243	0.207	0.019	0.187	0.187	0.19	0.192	0.17	0.172	0.161
P_2O_5	0.647	0.965	0.076	1.042	0.717	0.011	1.061	0.86	0.721	0.521	0.862	0.877	0.619
Total	98.75	98.96	97.64	98.4	99.86	99.15	98.5	99.06	98.41	99.76	99.65	99.47	100.08
LOI	1.25	1.04	2.36	1.6	0.14	0.85	1.5	0.94	1.59	0.24	0.35	0.53	-0.08
Zn	98.2	89.6	229.6	136.1	100.4	116.9	111.6	110.8	107	110.2	116.2	111.5	112.8
Cu	49	21.6	-16	6.2	31.6	-6.4	29.2	37.1	8.5	64.9	60.6	38	51
Ni	399.5	16.2	2.3	3.1	160.1	1.2	62.8	46.2	3.5	236.6	259.5	54.6	400.7
Cr	595.1	27.5	2.6	5.2	281.1	2.3	107.1	55.5	6.9	388.3	363.6	107.3	440.7
V	212.8	157.4	-5.9	94	179.1	-4.7	128.7	241.9	159.3	319.1	233.8	235.8	249.5
Ba	456.2	736.6	89.4	1202.5	486.9	13.9	675	543.6	514.8	448.8	448.7	820.4	408.1
Sc	24.2	14.2	1.1	18.6	19.2	-0.6	15.9	20.3	16.9	24.8	23.4	13.3	22.2
La	25.1	39.4	294.3	71.7	44.2	319.8	53.8	37.9	50.1	44.3	53.2	86.7	42.2
Ce	63.2	93.3	604.9	157.1	87.3	635	117	86.2	109	99.6	114.5	178.9	88.4
Nd	32.4	47.4	249.8	73.8	40.1	233.4	55.6	44.8	52.5	47.4	52.3	75.6	42.6
Pb	4.5	4.1	23.4	8.6	5.2	13.2	4.4	1.1	6	4.3	6	7.9	7.5
Nb	42.4	59.1	363.3	74.8	68.1	161.2	67.6	48.7	70.1	63.4	56	120.5	58.2
Zr	173	259.8	1892.9	397.5	275.4	1138.8	313.6	229.3	344.8	287.8	234.4	473.3	273.4
Y	22.2	25.5	133	41.7	28.9	75.3	30.1	30.6	32.6	30.4	30.5	37.5	25.6
Sr	870.4	1410.5	11	692.2	847.1	4.3	1216.2	806.2	936.6	726.3	861.9	1195.4	670
Rb	17.2	31	192.1	53.6	36.1	156	27.5	19.8	35.8	25.5	16.2	58.5	30.8

Table C-7 (cont.). Cameroon Line oceanic

Locality-Sample	Bioko-FP16	Bioko-FP20	Bioko-FP23	Bioko-FP26	Bioko-FP29	Bioko-FP31	Bioko-FP32	Bioko-FP33	Bioko-FP37	Bioko-FP38	Bioko-FP39	Bioko-FP41	Bioko-FP42
Rock type	Basanite-Tephrite	Basanite-Tephrite	Alkali basalt	Basanite-Tephrite	Basalt	Basanite-Tephrite	Basanite-Tephrite	Alkali basalt	Alkali basalt	Alkali basalt	Alkali basalt	Basanite-Tephrite	Alkali basalt
SiO_2	42.62	45.27	45.34	42.64	47.81	45.63	45.58	44.96	46.07	45.99	45.66	43.73	44.66
Al_2O_3	13.44	15.51	11.53	15.17	10.74	15.83	15.96	12.45	15.37	11.82	12.32	13.09	12.44
Fe_2O_3	15.38	14.69	13.61	15.06	11.9	13.47	13.64	13.08	12.28	13.45	13.83	14.62	13.63
MgO	7.13	4.72	9.44	6.29	9.73	4.37	4.26	10.38	4.75	10.85	9.48	9.41	11.16
CaO	11.14	8.89	12.33	10.29	13.91	9.15	9.15	11.71	10.35	11.18	10.6	9.7	10.83
Na_2O	1.81	3.71	2.42	3.65	1.86	4.5	4.55	2.36	3.44	2.42	2.45	2.9	2.83
K_2O	1.187	2.039	1.118	1.807	1.141	2.047	2.049	1.144	1.455	0.967	1.037	1.442	1.076
TiO_2	4.162	3.408	3.726	3.709	2.413	3.386	3.421	2.958	4.546	3.371	3.71	4.091	3.009
MnO	0.183	0.229	0.179	0.207	0.166	0.223	0.235	0.178	0.159	0.172	0.186	0.166	0.181
P_2O_5	0.847	0.942	0.523	0.731	0.373	0.876	0.878	0.495	0.794	0.482	0.512	0.651	0.743
Total	97.89	99.4	100.22	99.55	100.05	99.48	99.7	99.71	99.21	100.69	99.78	99.8	100.56
LOI	2.11	0.6	-0.22	0.45	-0.05	0.52	0.3	0.29	0.79	-0.69	0.22	0.2	-0.56
Zn	137.5	133.6	93.9	122.5	89.3	125.2	117.3	99.3	137	105.2	112.3	136.6	114.8
Cu	98.6	15.8	104.7	59.8	86.9	15.6	12.1	91.5	38.9	96.2	91.4	50	65.3
Ni	161.5	7.4	158.8	38.2	161	6.1	4.8	224.9	47.9	248.4	220.1	205.4	261
Cr	370.9	9.5	442.8	17.7	580.3	9.5	5.9	590.8	24.4	516	357.3	239.5	441.5
V	332.3	218.1	316.9	354.7	346.8	224.3	222.3	320.1	345.5	286.8	324.3	288.5	252.6
Ba	686.6	807.5	406.1	688.5	460.9	816.6	835.9	463.8	559.6	352.6	379.8	492	442.8
Sc	20	14.3	27.7	23	42.2	12.5	12.1	31.5	17.2	29.6	30	21.6	23.7
La	72.3	94.3	60.4	85.7	39.6	98.7	98.8	52.3	63.9	41.5	48.6	45.9	52
Ce	160.7	193.6	125.7	169.9	85.4	202.1	199.8	110.2	135.9	86.5	91.4	99.8	112.5
Nd	69.7	77.9	54.6	66	39.8	78.7	78.7	47.6	63.1	42.8	51.6	48.1	50.7
Pb	8.6	8.2	7.1	3.1	5	5.1	5.9	4.3	5.2	7	2.2	4	6.6
Nb	100.2	128.5	69.3	114.5	48.3	136.5	135.4	69.4	87.7	53.5	56.9	69.5	64.8
Zr	381.4	399.4	297.8	336.3	202.4	385.4	392.7	231.7	368.1	274.3	290.3	311.4	244
Y	33.8	39.1	28.4	35	24	38.8	39.6	26.7	36.7	28.4	40.4	29.8	28.3
Sr	941.2	1203.6	685.2	989	573.6	1175.7	1199	688.8	937.4	647	635.1	855.1	799.6
Rb	24.7	55.4	26.3	54.8	27.3	61.9	61.3	25.4	32.9	25	22.4	33.7	26.1

Table C-7 (cont.). Cameroon Line oceanic

Locality-Sample	Bioko-FP43	Bioko-FP44	Bioko-FP5	Bioko-FP7	Bioko-FP8	Bioko-FP9	Pagalu-AN1	Pagalu-AN10	Pagalu-AN11	Pagalu-AN12	Pagalu-AN13	Pagalu-AN14	Pagalu-AN15
Rock type	Basanite-Tephrite	Alkali basalt	Alkali basalt	Basanite-Tephrite	Basanite-Tephrite	Alkali basalt	Basanite-Tephrite	Basanite-Tephrite	Alkali basalt	Basanite-Tephrite	Basanite-Tephrite	Basanite-Tephrite	Basanite-Tephrite
SiO_2	45.67	44.4	45.7	43.14	43.4	44.1	40.46	42.38	45.92	43.41	42.21	41.79	41.67
Al_2O_3	15.87	10.8	12.7	11.94	12.82	12.84	12.77	10.8	13.2	11.36	10.62	12.61	10.62
Fe_2O_3	13.84	13.33	13.11	14.06	14.51	14.34	15.08	13.84	12.82	14.15	13.81	14.46	13.76
MgO	4.56	10.8	10.33	10.47	10.88	10.31	10.32	14.5	8.08	12.85	14.81	10.47	15.52
CaO	9.23	12.58	10.44	11.39	9.68	9.87	10.99	9.95	9.96	10.08	9.98	11	9.7
Na_2O	4.41	2.48	2.69	2.35	1.83	2.23	2.47	3.08	2.57	2.1	3.08	2.7	2.36
K_2O	2.013	1.186	0.789	1.24	1.339	1.334	0.688	0.645	1.77	1.297	0.638	0.674	0.846
TiO_2	3.432	3.513	2.829	3.662	3.453	3.488	3.003	3.122	3.81	3.072	3.076	2.945	3.124
MnO	0.238	0.187	0.171	0.165	0.177	0.174	0.222	0.189	0.167	0.176	0.186	0.21	0.188
P_2O_5	0.969	0.632	0.79	0.898	0.534	0.528	1.696	0.872	0.847	0.895	0.85	1.467	0.822
Total	100.22	99.9	99.55	99.31	98.62	99.21	97.7	99.38	99.13	99.4	99.25	98.32	98.61
LOI	-0.22	0.1	0.45	0.69	1.38	0.79	2.3	0.62	0.87	0.6	0.75	1.68	1.39
Zn	129.3	106.7	117.1	124.8	120.2	119.3	159.2	125.8	117.9	141.7	123.2	163.4	118.3
Cu	17.4	71.6	60.6	62.7	65.7	60.8	41.6	45.5	59.5	37.7	41.4	36.8	43.4
Ni	4.6	215.2	265.4	223.5	285.3	237.3	221.5	504.7	224.7	405.6	506	251.9	569
Cr	8.1	521.2	357.3	418.1	386.8	360.2	263.2	710.4	335.3	514.2	541.4	298.7	588.3
V	210.9	294.1	232	288.6	292	282.8	268.9	271.7	300	265.3	266.3	278.8	268
Ba	823	562.2	447.1	435.7	487.6	482.8	855.4	543.9	605.8	570.9	515.6	742.8	516.3
Sc	12.9	29.8	24.3	24.4	25	25.3	27.9	25.7	24.2	25.7	25.2	28.6	24.9
La	102.7	58.3	49.3	48.9	52.2	47.5	82.5	50	47.2	50.1	47.1	75.3	58.3
Ce	206.6	121.1	107.7	102.2	102.1	98.3	168.8	100.9	109	106.9	100.3	152.1	90.4
Nd	82.4	59.3	49.9	52.3	46.7	44.1	73.8	46.5	56.5	50.7	47.7	69.9	42.7
Pb	4	7.5	5.7	3.9	4.2	3.4	3	5.3	4.2	5.5	4.5	5.4	5.9
Nb	138	74.2	52.2	67.8	69.4	68.4	98.4	70.3	58.7	73.6	69.6	87.5	64.5
Zr	408	336.3	227.2	263.7	250.6	248.7	397	278.1	364.8	304.7	274.7	351.9	253.2
Y	39.6	31.9	30.3	31.3	28.2	28.3	42.8	32.1	32.4	32.2	31.4	40.7	30
Sr	1164.5	822.6	831	771	754.3	718.7	1625.6	823.4	789.5	815.5	821.2	998.8	778.7
Rb	60.8	32.5	14.5	26	27	26.5	3.1	44	34	21.3	42.5	12.6	36.6

Table C-7 (cont.). Cameroon Line oceanic

Locality-Sample	Pagalu-AN17	Pagalu-AN18	Pagalu-AN19	Pagalu-AN20	Pagalu-AN3	Pagalu-AN4	Pagalu-AN7	Pagalu-AN8	Pagalu-ANBM7	Principe-P1	Principe-P10	Principe-P11	Principe-P12
Rock type	Basanite-Tephrite	Basanite-Tephrite	Basanite-Tephrite	Basanite-Tephrite	Alkali basalt	Alkali basalt	Alkali basalt	Trachy-basalt	Basanite-Tephrite	Phonolite	Phonolite	Phonolite	Trachy-andesite
SiO_2	43.16	43	43.41	43.57	45.99	44.51	47.38	47.65	43.12	54.33	55.85	54.57	53.75
Al_2O_3	12.49	12.46	12.29	12.41	12.55	12.48	13.95	15.41	12.36	21.99	22.24	22.37	19.46
Fe_2O_3	14.34	14.46	13.78	14.08	13.09	13.72	12.79	12.71	14.31	2.48	2.93	3.12	4.83
MgO	9.26	9.39	10.82	10.63	8.48	8.16	6.38	4.55	10.62	0.22	0.41	0.42	1.44
CaO	10.98	11.17	10.53	10.66	10.58	10.94	9.46	9.06	9.98	1.29	1.73	1.97	5.1
Na_2O	2.76	2.91	3	2.75	2.57	2.79	2.49	3.21	3	10.71	9.8	9.82	5.4
K_2O	0.96	0.633	1.168	1.304	1.537	1.194	1.77	1.845	1.73	5.26	5.657	6.106	4.482
TiO_2	3.061	3.062	2.743	2.943	3.438	3.974	3.606	3.839	3.26	0.386	0.51	0.48	1.079
MnO	0.195	0.203	0.201	0.227	0.166	0.176	0.141	0.147	0.182	0.146	0.134	0.108	0.114
P_2O_5	1.101	1.054	0.952	1.006	0.644	0.9	0.75	0.798	0.82	0.074	0.072	0.088	0.24
Total	98.31	98.33	98.89	99.59	99.05	98.84	98.71	99.22	99.38	96.88	99.32	99.05	95.89
LOI	1.69	1.67	1.11	0.41	0.95	1.16	1.29	0.78	0.62	3.12	0.68	0.95	4.11
Zn	135.7	137.3	142.1	134.4	110	123.3	113.9	109.8	142	134.8	102.1	78.6	86.6
Cu	55.8	51.7	48.8	59.5	65.3	52.4	44.3	41.4	47.7	-6.9	-1	0.6	4.3
Ni	267	252.1	245.2	269.3	255.8	229.2	179.5	103.7	204.2	1.9	2.6	2.6	10.7
Cr	376.3	378.9	345.1	348.3	561.2	395.5	337.9	137.4	245.6	4.3	4.4	4.5	14
V	299.8	307.4	251	275	302.4	310.7	315.7	320.5	274.1	13.8	19.3	44.6	55.5
Ba	647.9	617.5	639.6	664.7	526.1	725.2	674.8	578.9	669.4	546.9	934.5	1087.1	757.7
Sc	27.7	28.6	29.4	24.8	23.5	26.5	25.8	21.2	26.2	-0.5	-1.1	-0.9	1.6
La	61.1	62.1	66.7	58.2	41.1	60.7	51.4	50.6	50.3	69.1	85.5	64.9	68
Ce	125.3	121.9	136.2	119.4	87	136.4	119.1	120.2	106.2	118.8	132	93	111.1
Nd	57.2	56	58.7	55.2	42	66	57.2	59.3	49.1	31.7	31.1	22.9	35.5
Pb	1.1	5.3	5.8	5.6	4.8	7.1	6.5	6.3	6.2	14.5	13.8	6.6	15.6
Nb	77.6	73.3	76.4	76.9	59	71.4	60.5	61.4	80.4	237.1	158.6	90.1	135.2
Zr	322.1	310.8	312.4	313	290.9	474.3	405.2	403.9	339.3	1310.8	589.1	431	719
Y	35.2	35.6	36.9	34.8	29.3	34	32.1	35.8	32.7	22.3	18.7	15.1	19.9
Sr	936.4	901.6	911.5	845.4	713.4	904.7	751.3	760.4	798.4	676.9	562.3	958.7	1114.5
Rb	36.7	49	49.2	30.3	35.6	42.8	32.8	36	41.7	202	144.3	132.7	180.2

Table C-7 (cont.). Cameroon Line oceanic

Locality-Sample	Principe-P13	Principe-P15	Principe-P16	Principe-P17	Principe-P18	Principe-P19	Principe-P2	Principe-P20	Principe-P21	Principe-P22	Principe-P23	Principe-P24	Principe-P25
Rock type	Trachy-andesite	Basalt	Phonolite	Alkali basalt	Foidite	Basanite-Tephrite	Phonolite	Basanite-Tephrite	Alkali basalt	Phonolite	Picro-basalt	Picro-basalt	Alkali basalt
SiO_2	55.12	46.89	55.93	44.62	37.89	41.88	56.83	42.57	44.88	53.38	42.5	42.45	45.21
Al_2O_3	19.69	12.1	21.49	12.09	10.51	12.31	21.56	12.98	13.8	21.25	10.99	10.87	15.43
Fe_2O_3	4.72	12.69	2.36	12.15	14.22	14.24	2.68	13.75	14.95	4.09	13.33	13.22	13.32
MgO	1.33	8.96	0.12	10.95	11.59	8.94	0.12	8.28	6.67	0.6	12.66	12.55	5.57
CaO	3.58	10.02	2.02	11.97	13.24	10.99	0.83	10.42	10.47	2.72	12.36	12.83	9.82
Na_2O	6.16	2.45	8.72	2.12	3.06	3.1	11.04	3.59	2.75	9.77	1.82	1.61	3.23
K_2O	4.652	0.476	4.972	1.174	1.607	1.941	5.669	2.12	0.999	5.246	1.073	0.823	1.389
TiO_2	0.965	2.346	0.155	2.917	4.054	3.5	0.184	3.385	3.892	0.794	3.033	3.032	3.993
MnO	0.192	0.146	0.168	0.149	0.198	0.188	0.149	0.19	0.165	0.164	0.171	0.162	0.174
P_2O_5	0.227	0.407	0.017	0.573	1.431	1.045	0.024	1.063	0.541	0.167	0.751	0.726	0.776
Total	96.64	96.49	95.94	98.72	97.79	98.14	99.08	98.34	99.11	98.17	98.69	98.26	98.92
LOI	3.36	3.51	4.06	1.28	2.21	1.86	0.92	1.66	0.89	1.83	1.31	1.74	1.08
Zn	94.7	113.2	185.3	94.7	108.2	107	161.9	108.1	120.6	141	94.5	90.3	125
Cu	1.8	60	-11	55.2	55.9	38.7	-5.7	41.6	35	-3.2	63.3	64.4	28.2
Ni	9.1	235.9	1.8	207	193.2	119.5	2.6	108.6	73.5	2.7	257.9	264.1	26.1
Cr	11.5	350.5	3.7	359.8	337.7	163.2	3.5	147.1	139.7	4.4	454.6	460.6	30
V	54.3	214.6	4.8	249	306.5	225.2	8.3	212.4	372.7	51.8	259	254.1	255
Ba	889.4	173.7	10.6	396.5	986.6	684.1	15.4	758.9	323.2	1138.3	503.1	522.3	400.1
Sc	0.7	24	-0.6	26.5	26.2	21	-1.4	18.9	27.3	0	27.3	26	19.8
La	75.9	16.3	97.9	42.1	103	71.3	85.3	76.9	39.4	90.5	43.2	47.5	47.3
Ce	124	39.9	109.6	87	203.1	140.1	105.9	154.7	67.4	156	98.5	93.7	100.8
Nd	36.6	22.2	17.1	39.7	84.6	63.7	17.3	66.6	34.8	47.4	42.9	44.4	46.9
Pb	17.4	5.2	30.7	5.4	4.2	3.6	24.3	2.2	6.3	13.9	3	6	3.7
Nb	161.1	28.8	154.4	57.5	133.8	88.7	148.1	100.3	54.6	238.2	58.4	54.2	68.5
Zr	608.9	131.3	1745.1	230.7	337.3	320	1053.4	335.5	239	1021.8	196	192.9	301.6
Y	21.6	22.8	19	24.1	34.9	33.3	17.4	34.7	27.5	28.2	25.4	26.2	33.8
Sr	1187.6	443.8	10.5	764.8	1297	1153	42	1175.6	598.9	1227	740	729.5	879.5
Rb	185.2	12.7	314	29.7	39.7	42.5	244.1	40.9	21.8	177.5	24.3	18.7	27.7

Table C-7 (cont.). Cameroon Line oceanic

Locality-Sample	Principe-P26	Principe-P27	Principe-P28	Principe-P29	Principe-P3	Principe-P30	Principe-P31	Principe-P32	Principe-P33	Principe-P34	Principe-P35	Principe-P36	Principe-P37
Rock type	Trachy-basalt	Alkali basalt	Alkali basalt	Basaltic trachy-andesite	Trachy-basalt	Basaltic trachy-andesite	Alkali basalt	Basalt	Trachy-basalt	Basanite-Tephrite	Phonolite	Trachy-basalt	Trachy-basalt
SiO_2	45.95	46.29	47.12	51.68	47.33	48.96	47.83	47.36	47.95	40.98	54.47	46.43	47.71
Al_2O_3	15.83	15.75	11.94	16.3	14.18	15.48	13.75	12.65	15.94	11.72	21.57	14.32	13.97
Fe_2O_3	12.72	12.46	13.55	9.59	11.34	10.72	11.82	12.43	12.18	12.81	2.7	11.32	11.8
MgO	5.13	4.63	10.25	3.41	3.51	3.88	7.98	8.31	4.52	10.55	0.35	4.04	4.97
CaO	9.89	9.48	8.12	6.98	7.6	7.94	8.09	9	8.01	12.18	1.38	8.06	8.14
Na_2O	3.43	3.26	2.8	4.41	4.55	4.16	3.02	2.25	3.85	3.79	10.46	3.84	3.89
K_2O	1.518	1.457	1.328	2.22	1.042	2.204	1.704	1.345	1.909	0.611	5.255	2.103	1.667
TiO_2	3.8	3.752	3.033	2.525	3.718	3.053	2.949	2.945	3.326	3.155	0.349	3.92	3.218
MnO	0.17	0.166	0.153	0.106	0.138	0.162	0.146	0.159	0.168	0.18	0.122	0.12	0.146
P_2O_5	0.799	1.012	0.55	0.822	0.79	1.371	0.654	0.567	1.044	0.882	0.074	0.768	0.545
Total	99.24	98.26	98.84	98.05	94.2	97.94	97.95	97.02	98.9	96.85	96.73	94.91	96.06
LOI	0.76	1.74	1.16	1.95	5.8	2.06	2.05	2.98	1.1	3.15	3.27	5.09	3.94
Zn	119.6	123.5	121.6	123.8	124.9	138.8	111.6	112.4	131.5	115.3	137.6	120.3	120.9
Cu	20.1	20.7	26.5	16.4	58.2	6	41.5	56.2	19.9	52.8	-6.9	52.2	61.1
Ni	14.7	9.3	272.7	24.8	57.6	1.4	167.4	248.3	14.6	211.8	2.6	46.3	57.1
Cr	14.7	4.6	303.8	14.9	4.4	4.7	231.1	379	8.6	342.6	4.2	13.6	73.7
V	218.2	211	207.3	142	287.3	154.6	231.1	233.9	173.3	254.9	17.4	322.6	274.5
Ba	465.2	433.3	346.5	557.3	339.9	644.2	438.9	375.3	539.7	464.8	208.2	581.2	415.5
Sc	17.5	15.2	23.1	13.7	21.7	12.9	20.8	21.2	14	26	-1	23.3	24.1
La	44.9	48.9	31	63.8	46.8	73.7	43.3	34.5	58.6	54	78.7	45.5	31.1
Ce	100.7	103.1	70.9	135.3	98.4	155.5	87.5	75.1	128.5	114.2	101.6	95.6	71.1
Nd	52.2	51.6	34.7	63.3	46	72.2	41.1	36.2	61.4	52.5	21.4	49	36.6
Pb	8.3	3.6	6.5	7	7.4	6.4	8.1	3.5	3.2	5.8	27.2	6.1	4.7
Nb	71.6	69.5	42.3	77.3	65.9	96.2	56	45.8	80.1	79.4	129.4	64.1	42.8
Zr	317.6	297.4	259.6	391.5	354.6	423.7	327.1	259.3	382.6	293.8	1358.7	340.1	261.7
Y	34.5	35.7	25.4	34.6	32.3	41.4	28.6	27	36.9	30.1	18.6	31.8	29.3
Sr	918.1	899.4	572.1	781.6	713.2	871.4	625.2	531.8	948	846.3	295.4	716.6	666.3
Rb	27	26.9	26.2	45.8	14.3	45.9	37.5	28.7	36.2	59.5	296.9	44.3	34.1

Table C-7 (cont.). Cameroon Line oceanic

Locality-Sample	Principe-P38	Principe-P39	Principe-P40	Principe-P41	Principe-P45	Principe-P46	Principe-P47	Principe-P48	Principe-P49	Principe-P5	Principe-P50	Principe-P51	Principe-P6
Rock type	Phonolite	Phonolite	Phonolite	Trachyte	Picro-basalt	Trachy-basalt	Trachy-basalt	Basaltic trachy-andesite	Trachy-basalt	Phonolite	Picro-basalt	Basanite-Tephrite	Trachy-basalt
SiO_2	54.17	55.99	55.83	58.82	42.6	46.91	47.98	49.93	46.67	54.38	42.25	43.06	47.45
Al_2O_3	21.54	21.95	22.12	19.59	10.59	13.56	15.98	17.11	16.05	22.04	10.54	10.15	16.77
Fe_2O_3	3.13	2.22	2.63	3.08	13.53	11.53	11.14	10.05	12.44	2.41	16.58	12.52	11.3
MgO	0.41	0.16	0.23	0.78	12.45	8.43	5.15	3.7	5.07	0.23	11.89	12.67	4.44
CaO	1.92	0.97	1.04	1.86	13.15	9.62	8.26	7.48	8.85	0.94	10.93	13.82	8.63
Na_2O	10.33	10.65	10.57	7.41	1.57	3.79	3.59	4.19	3.3	11.67	1.93	2.11	3.57
K_2O	5.23	5.584	5.911	5.367	0.944	1.741	1.795	2.033	1.65	5.097	0.488	1.017	1.613
TiO_2	0.522	0.172	0.322	0.573	3.034	2.482	2.813	2.465	3.593	0.205	3.851	3.003	3.311
MnO	0.162	0.135	0.168	0.122	0.166	0.164	0.16	0.18	0.153	0.14	0.155	0.138	0.148
P_2O_5	0.111	0.024	0.03	0.092	0.686	0.598	1.143	1.126	0.742	0.045	0.445	0.616	0.905
Total	97.53	97.85	98.84	97.68	98.71	98.82	98	98.26	98.52	97.14	99.06	99.1	98.13
LOI	2.47	2.15	1.16	2.32	1.29	1.18	2	1.74	1.48	2.86	0.94	0.9	1.87
Zn	131	148.5	142.9	87.6	96.5	111.7	124.4	137.3	112.8	186.9	121.7	92.9	121.8
Cu	-3.5	-7.5	-2.6	-3.8	55.3	52.2	18	3.9	20.2	-11.2	45.3	50.3	7.5
Ni	3.1	1.7	3	3.3	269.7	182.4	42.3	1.1	15	3.1	227.1	261	4.3
Cr	5.4	3.7	3.9	4.8	489.1	321.7	60.2	4.1	14.5	4.5	465.1	589.9	6.5
V	29.6	8	17	23.5	278	192.4	145	93.8	200.7	11.1	394.6	281.8	201
Ba	1171.7	50.8	142.8	822.8	437.4	576.2	495.6	555.8	406.5	51.2	253	393.5	503.9
Sc	0.1	-1.1	-1	-0.8	32.2	20.9	12.1	5.8	16.1	-1	32.8	37.2	11.8
La	75	80.1	83.4	74	39.1	48.4	63.1	73.5	50.5	97.2	31.2	38	61.9
Ce	137.5	95.3	114.4	111.5	85.7	103	134.4	156.4	98.4	109.7	57.8	79.7	123.9
Nd	38.7	16.7	23.2	27.3	44.2	43.9	63.1	71.8	47.6	18.4	28.4	38.6	58.4
Pb	14.2	24.6	19.1	15.9	3.4	3.9	6.6	6.1	3.7	36.3	4.9	1.9	6
Nb	231.8	106.4	167.7	145.4	52.7	83.4	86.3	104.4	67.5	142.1	44	52.5	87.1
Zr	1008.6	1282.3	934.1	783.3	193.8	331.4	392.8	473.4	302.7	1946.8	198.2	209.7	377.3
Y	25.4	16	19.1	17.1	25.9	25.7	35	40.4	34.5	22	23.9	24.6	35.2
Sr	1201.9	79.3	239.7	483.7	677.3	850.1	1015.1	1071.2	894.7	85.7	708.6	658.4	935.3
Rb	191.5	270.6	216.4	174.4	19.1	50.2	37.4	41.1	32.8	392.8	6	22.1	17.7

Table C-7 (cont.). Cameroon Line oceanic

Locality-Sample	Principe-P7	Principe-P8	Principe-P9	Sao Tome-ST1	Sao Tome-ST10	Sao Tome-ST100	Sao Tome-ST101	Sao Tome-ST102	Sao Tome-ST103	Sao Tome-ST104	Sao Tome-ST105	Sao Tome-ST106
Rock type	Alkali basalt	Basanite-Tephrite	Picro-basalt	Phonolite	Phonolite	Trachy-andesite	Alkali basalt	Alkali basalt	Basanite-Tephrite	Alkali basalt	Basanite-Tephrite	Basanite-Tephrite
SiO_2	43.86	43.97	43.47	58.95	57.13	55.64	43.33	45.66	43.79	45.24	41.91	44.08
Al_2O_3	14.31	14.02	10.83	19.81	22.02	19.66	14.8	13.73	10.68	15.06	11.75	11.03
Fe_2O_3	14.79	15.14	11.85	2.94	2.19	4.77	12.21	12.13	13.55	12.64	14.01	13.85
MgO	5.57	6.2	12.03	0.47	0.22	1.37	5.31	8.37	13.28	6.13	9.92	13.19
CaO	10.57	10.72	14	1.97	1.24	4.08	10.29	10.46	10.28	10.8	12.44	10.13
Na_2O	2.36	2.66	1.93	7.21	9.84	5.92	2.55	2.5	2.87	3.06	2.91	2.16
K_2O	1.321	1.212	0.968	5.944	6.127	4.139	1.645	1.167	1.096	1.602	0.855	1.178
TiO_2	4.426	4.43	3.089	0.566	0.24	1.076	3.363	3.359	2.713	3.543	3.543	2.794
MnO	0.163	0.163	0.144	0.148	0.148	0.16	0.19	0.149	0.165	0.173	0.206	0.172
P_2O_5	0.834	0.81	0.528	0.067	0.038	0.284	0.821	0.842	0.818	0.859	1.223	0.824
Total	98.19	99.32	98.84	98.07	99.18	97.09	94.49	98.37	99.24	99.11	98.78	99.4
LOI	1.81	0.68	1.16	1.93	0.82	2.91	5.51	1.63	0.76	0.89	1.22	0.6
Zn	125.9	123.4	84.6	100.2	113.7	103.5	121.8	110	126.7	117.8	124	133.7
Cu	49.4	49.9	46.2	-3.7	-3.6	-1.3	33.4	52.2	52.7	49.8	72.4	45.3
Ni	50	54.7	224.2	1	1.8	2.6	50.1	172.2	388.7	58.7	205.1	389.5
Cr	33	46.7	400.1	5.1	4.2	4.2	110.7	279.5	443	129.4	446.4	459.4
V	353.8	344.8	296.4	6.2	14.9	55.7	268.6	261	214	283.6	290.5	242.1
Ba	348.3	340.7	404.3	1170.8	153.6	1134	600.4	470.5	467.4	501.2	644.1	528.2
Sc	25.3	26.7	35.8	-1	-1.3	1.1	17.1	22.9	24.1	23.4	24.8	25.2
La	43.7	43.2	41.1	104.3	75.5	93.6	71.1	55.3	54.5	54.5	79.3	55.7
Ce	93.4	86.9	86.3	182.9	95.2	149.4	144	106.5	109.2	116.1	163.4	112.2
Nd	46	44.6	43.2	50	18	39.4	63.6	51.4	48.2	54.5	74.9	51.1
Pb	3.5	2.5	3.8	11.8	21.2	18.2	6.9	8.1	8.1	9.8	3.3	6.5
Nb	60.4	58.6	50.8	212	93.5	137.3	98.5	68.5	69	81.9	96.6	70.5
Zr	274	266.6	244.2	840.8	964.8	679.3	364.2	302.6	265.8	317.1	326.3	272.5
Y	30.7	31.1	26.1	28.1	12.9	24	32.7	27.9	27.3	30.3	32.9	27.5
Sr	772	790.9	642	211.9	110.1	1204.2	1031.7	1596	838.2	867.7	1066.2	835.7
Rb	32.7	21.7	22.1	163.7	223.1	138.9	38.9	27.5	64.1	37.4	16.1	29.4

Table C-7 (cont.). Cameroon Line oceanic

Locality-Sample	Sao Tome-ST107	Sao Tome-ST108	Sao Tome-ST109	Sao Tome-ST11	Sao Tome-ST110	Sao Tome-ST111	Sao Tome-ST112	Sao Tome-ST113	Sao Tome-ST114	Sao Tome-ST115	Sao Tome-ST116	Sao Tome-ST117
Rock type	Trachy-basalt	Basanite-Tephrite	Alkali basalt	Phonolite	Tephri-phonolite	Alkali basalt	Phono-tephrite	Basanite-Tephrite	Phonolite	Basalt	Picro-basalt	Tephri-phonolite
SiO_2	46.59	42.15	46.23	56.66	53.62	44.17	49.23	44.88	55.72	43.9	42.31	55.42
Al_2O_3	15.24	12.24	13.29	20.56	18.78	15.33	16.9	14.94	21.12	9.76	11.04	19.97
Fe_2O_3	10.9	13.69	13.11	3.41	6.49	13.77	10.06	12.58	2.76	13.18	14.02	5.06
MgO	6.34	10.35	9.12	0.61	1.84	5.67	3.45	5.44	0.12	12.06	12.56	1.89
CaO	9.12	11.68	9.81	2.39	4.98	10.19	7.7	11.08	0.73	13.97	12.77	4.04
Na_2O	3.79	2.59	3.67	7.23	7.32	3	5.55	4.22	11.07	1.58	1.66	7.63
K_2O	2.155	0.642	1.263	6.541	3.726	1.844	2.858	1.998	4.896	0.327	0.855	4.064
TiO_2	2.914	3.425	2.966	0.682	1.625	4.142	2.787	3.462	0.131	3.065	3.369	1.107
MnO	0.182	0.174	0.171	0.132	0.153	0.18	0.179	0.165	0.245	0.169	0.15	0.139
P_2O_5	0.764	1.143	0.641	0.127	0.433	0.927	0.876	0.965	0.001	0.36	0.526	0.318
Total	97.99	98.09	100.27	98.34	98.96	99.23	99.59	99.73	96.8	98.38	99.26	99.64
LOI	2.01	1.91	-0.27	1.66	1.04	0.77	0.41	0.27	3.2	1.62	0.74	0.36
Zn	118.1	115.4	114.1	75.9	117.3	121.2	126.4	109.8	239.9	86.4	101.5	82.2
Cu	34.3	53.4	55.5	-0.5	6.5	32.8	21.6	55	-13.3	152.4	62.3	7.8
Ni	84.1	186.8	183.5	2.9	5.8	20.1	9.4	53.1	0.9	229.1	287.3	25.4
Cr	188.2	326.3	298.2	4.3	5.4	30.8	9.8	19.5	5.2	708.9	551.5	31.3
V	210.5	262.6	202	44.6	78.7	254.5	143.3	258.2	3.4	363.4	345.8	58.9
Ba	749.5	765.7	451.8	872.7	845.4	571.1	806.5	701	3.9	370.1	331	1111.8
Sc	16.9	23.4	21.9	0	3.9	19.3	7.4	18.6	-1.1	50.2	34	2.5
La	89.2	72.9	49.3	63.4	78.6	65.2	87.7	84.9	161.9	34.7	37.5	72.7
Ce	167.9	145.6	97.9	93.4	147.7	132.3	166	160.9	184.2	68.6	74.4	128.5
Nd	65	64.2	43.6	24.1	52.3	60.6	68.3	69.1	22.8	30	37.1	38.8
Pb	11.9	5.8	6.3	16.2	13.3	5.5	9.5	2	30.4	6.9	1.7	11.3
Nb	116.9	84.2	68.3	94	131.8	91.8	133.1	101.2	191.7	46.6	46.6	106.7
Zr	501.1	335.7	282.4	545.1	751.2	365.5	611	370.6	1938.5	203.3	202.5	590.2
Y	32.3	30.9	28.3	14.9	26.9	33	33.9	35.1	18.3	22	23.2	21.3
Sr	1101.5	1266.8	823.6	615.9	1128	999.4	1245.4	1165.5	8.8	425.4	648.8	1183.2
Rb	62.4	99.1	28.7	172.2	113.9	41.8	78.6	50.3	316.1	36	18.7	101.7

Table C-7 (cont.). Cameroon Line oceanic

Locality-Sample	Sao Tome-ST118	Sao Tome-ST119	Sao Tome-ST12	Sao Tome-ST13	Sao Tome-ST15	Sao Tome-ST16	Sao Tome-ST17	Sao Tome-ST18	Sao Tome-ST19	Sao Tome-ST2	Sao Tome-ST20	Sao Tome-ST21
Rock type	Basanite-Tephrite	Tephri-phonolite	Tephri-phonolite	Alkali basalt	Trachy-basalt	Trachy-andesite	Alkali basalt	Basanite-Tephrite	Basanite-Tephrite	Phonolite	Basanite-Tephrite	Trachy-basalt
SiO_2	41.97	50.78	52.45	43.49	48.26	51.91	43.61	44.13	44.6	58.84	42.14	45.59
Al_2O_3	10.71	17.76	18.92	14.28	16.26	18.93	11.74	13.61	14.88	19.72	11.7	16.03
Fe_2O_3	13.28	8.23	6.12	13.02	11.01	6.52	13.22	12.44	12.93	3.06	13.42	12.71
MgO	12.53	2.49	1.62	6.21	4.81	3.27	10.29	8.46	5.5	0.36	11.49	4.6
CaO	10.1	6.16	5.05	10.54	7.03	4.81	10.31	9.88	9.6	1.32	12.05	10.13
Na_2O	2.37	6.82	6.07	3.22	3.83	4.51	2.04	3.24	4.62	8.35	2.07	3.21
K_2O	1.744	3.455	5.071	1.039	2.366	3.857	1.256	2.112	2.182	6.039	1.236	1.812
TiO_2	3.112	2.099	1.703	4.153	2.781	1.63	3.21	3.359	3.764	0.58	3.348	3.663
MnO	0.181	0.171	0.133	0.199	0.17	0.178	0.188	0.183	0.186	0.161	0.178	0.184
P_2O_5	0.787	0.6	0.379	1.244	0.856	0.325	0.64	0.762	1.002	0.073	0.74	0.902
Total	96.78	98.57	97.52	97.39	97.37	95.95	96.5	98.19	99.26	98.5	98.38	98.82
LOI	3.22	1.43	2.48	2.61	2.63	4.05	3.5	1.81	0.74	1.5	1.62	1.18
Zn	125	122.7	72.1	138.3	113.3	132.5	111.5	122	132.7	94.9	104.8	121.1
Cu	47.3	14.1	9.8	46.9	19.8	3.3	58.7	44.1	41.1	-4.1	71.7	39.1
Ni	363.1	8.9	8.7	48.9	9.4	10.5	206.8	155.1	43.2	2.6	224	38.5
Cr	606.3	5.9	4.2	69.4	1.8	11.9	458.7	259.4	33.3	5.8	526.1	47.3
V	240.8	105.2	104.8	284.1	185.2	82.5	307.9	240.4	234	4.7	286.5	269.8
Ba	748.4	920.3	2344.3	815.1	715.7	1451.8	425.2	766.4	728.1	1139.1	521.3	586.6
Sc	20.2	6	2.4	18.3	11.5	1.6	29.5	19.6	15.9	-1	29.6	19
La	65.3	91.4	67.3	87.1	70.2	116.6	42.3	77.8	83.3	109.9	55.6	64.4
Ce	130.2	154	118.5	183.3	139.1	213.4	85	144	162.9	191.6	107.9	138.5
Nd	57.9	58.5	43.9	81	57.4	68.7	42.5	61.3	71.7	51.1	48	62.1
Pb	4.2	10.7	11.2	3.2	8	13.4	8.2	7.2	6.6	18.2	9.1	5.2
Nb	91.7	133.6	118.5	114.1	100.7	200	56.4	107.9	111.8	223.4	72.7	99.1
Zr	315.3	637.7	527.6	513.1	395.1	907.7	248.5	394.5	472	894.5	246.6	387.9
Y	23.9	29.6	22.6	37.2	32.5	35.6	26.8	28.9	35.5	29.3	27	32.6
Sr	916.6	1277.9	1528	1180.7	878.8	1967	549.9	971.5	1113.2	200.5	791.2	944.2
Rb	49.8	94.4	125.7	17.6	66.7	100	29.7	57.6	59.7	174.7	27.2	42.9

Table C-7 (cont.). Cameroon Line oceanic

Locality-Sample	Sao Tome-ST22	Sao Tome-ST23	Sao Tome-ST24	Sao Tome-ST25	Sao Tome-ST26	Sao Tome-ST27	Sao Tome-ST28	Sao Tome-ST29	Sao Tome-ST3	Sao Tome-ST30	Sao Tome-ST31	Sao Tome-ST32
Rock type	Trachy-basalt	Basanite-Tephrite	Alkali basalt	Basanite-Tephrite	Basanite-Tephrite	Alkali basalt	Alkali basalt	Basanite-Tephrite	Phonolite	Basanite-Tephrite	Basanite-Tephrite	Basanite-Tephrite
SiO_2	45.7	47	45.26	43.76	43.38	45.83	44.08	43	59.12	45.28	44.91	44.16
Al_2O_3	16.1	16.89	11.56	15.18	13.36	14.95	13.76	13.56	19.68	15.17	15.35	13.33
Fe_2O_3	12.58	11.11	13.35	13.96	13.71	12.67	13.54	13.24	3.01	11.88	12.42	12.53
MgO	4.61	4.2	11.68	5.38	8.59	5.8	6.98	7.96	0.46	5.27	4.88	8.43
CaO	10.11	9.62	10.97	11.23	11.66	11.21	11.45	12.04	1.41	9.42	10.35	10.39
Na_2O	3.42	4.51	2.54	2.87	2.92	2.98	3.02	3.62	7.84	3.97	4.13	4.48
K_2O	1.83	2.38	0.936	0.801	1.423	1.209	1.331	1.658	5.865	2.477	1.581	0.935
TiO_2	3.624	3.502	2.962	4.29	3.549	3.539	3.724	3.625	0.579	3.303	3.519	3.167
MnO	0.177	0.187	0.168	0.176	0.188	0.165	0.171	0.199	0.163	0.16	0.157	0.201
P_2O_5	0.885	0.865	0.694	1.236	1.038	0.765	0.927	1.161	0.069	1.374	1.032	0.922
Total	99.04	100.25	100.11	98.89	99.81	99.11	98.99	100.05	98.19	98.3	98.33	98.54
LOI	0.96	-0.25	-0.11	1.11	0.19	0.89	1.01	-0.05	1.81	1.7	1.67	1.46
Zn	121	135.8	107.5	113.2	116.1	109	118.1	117.5	96.8	127.3	117	116.5
Cu	34.6	22.3	69.5	52.4	86.7	56.5	58.2	49.1	-5	45.6	50.9	35.2
Ni	33.5	14.3	300.5	43.7	160.7	58.6	92.2	113.4	1.5	49.3	49.7	170.9
Cr	39	11.5	502.6	46.9	291.6	75.3	143.1	261.1	4.8	70.2	13.8	256.9
V	272.3	202.9	258	311.7	296.5	269.3	297	278	4.9	205.9	252.1	208.6
Ba	588.1	964.6	356.2	630.9	536.1	439.2	496.6	664.2	1192.2	934.7	779.4	826.6
Sc	18	9.5	27.1	18.6	25.6	20.4	23.2	20.4	-1.2	14.5	15.4	16.8
La	67.4	79.8	38.7	66.8	62.5	41.5	56.7	73.9	110.3	110.6	89.2	97
Ce	138.1	174.2	79.8	139.7	127.1	92	115.3	153.6	195.5	213.9	175.2	186
Nd	63.4	81.6	38.9	64.4	57.6	44.7	54.7	67.2	52.1	89.3	74.3	78.2
Pb	8.7	6.4	9.4	5.9	5.8	8.4	9.7	6.6	16.6	8.9	7.4	8.3
Nb	101	126.2	48.5	90.7	78.4	61.9	73.7	98.5	224.5	129.5	114.5	122
Zr	391.1	530	215	353.2	307.3	250.7	276.4	325.8	894.2	504.5	403	402.2
Y	32.6	40.3	24.9	33.7	29.8	28.6	29.8	33.4	29.3	39.7	35.7	35.1
Sr	949.6	1496	688.6	1074.6	896.2	854	904.6	1126.3	220.8	1392.5	1222.5	1269.6
Rb	42.6	59.3	21.5	42.2	34	23.3	31.9	38.1	160.2	57.5	30.5	40.7

Table C-7 (cont.). Cameroon Line oceanic

Locality-Sample	Sao Tome-ST33	Sao Tome-ST34	Sao Tome-ST35	Sao Tome-ST36	Sao Tome-ST37	Sao Tome-ST38	Sao Tome-ST39	Sao Tome-ST4	Sao Tome-ST40	Sao Tome-ST41	Sao Tome-ST42	Sao Tome-ST43
Rock type	Tephrite-Basanite	Basanite-Tephrite	Tephri-phonolite	Basanite-Tephrite	Alkali basalt	Alkali basalt	Trachyte	Picro-basalt	Basanite-Tephrite	Alkali basalt	Basanite-Tephrite	Trachyte
SiO_2	45.27	43.36	51.83	42.94	43.59	45.83	60.23	43.28	43.85	45.95	43.98	61.51
Al_2O_3	16.19	12.19	17.92	12.71	13	15.53	19.42	10.23	15.31	12.19	13.19	19.01
Fe_2O_3	11.96	13.77	7.44	13.43	12.67	12.53	3	13.44	13.79	13.07	12.98	2.74
MgO	4.59	9.95	3.32	9.21	9.59	5.57	0.62	11.59	5.4	10.65	7.86	0.33
CaO	8.48	11.6	5.59	11.85	11.06	10.65	1.59	14.24	10.43	10.22	11.73	1.69
Na_2O	4.46	3.35	5.89	3.54	2.27	2.48	7.5	1.48	4.24	3.11	3.63	7.99
K_2O	2.665	0.561	3.677	1.464	1.554	1.882	5.755	0.377	0.909	1.013	1.766	4.555
TiO_2	3.252	3.547	1.846	3.163	3.249	3.243	0.611	3.451	4.212	2.762	3.758	0.398
MnO	0.179	0.184	0.142	0.189	0.175	0.168	0.119	0.154	0.185	0.184	0.171	0.186
P_2O_5	1.317	0.791	0.59	1.358	0.711	0.653	0.095	0.444	1.088	0.725	0.878	0.055
Total	98.35	99.3	98.24	99.86	97.86	98.53	98.93	98.69	99.41	99.87	99.96	98.47
LOI	1.65	0.7	1.76	0.14	2.14	1.47	1.07	1.31	0.59	0.13	0.04	1.53
Zn	133.6	113.1	99.2	123.5	112.7	113.4	78.4	88.5	127	117.3	113.1	96.9
Cu	56.7	47.7	17.1	59.4	46	41.9	-0.2	61	45.6	52.5	67.9	-6.2
Ni	52.3	203.4	32.1	164.7	183.3	48	3.8	219.1	25.8	267.5	101.3	1.6
Cr	79.3	457.3	56.5	309.2	437.9	90.1	7.5	631.8	10.4	313.5	252	5.1
V	200.7	298	86.2	241.3	258.3	293.7	30	359.5	269.6	213.5	277.2	-1.9
Ba	826.7	458.4	736	780.3	496.2	631.1	523.2	429.5	583.5	391.8	543.7	1341.6
Sc	11.6	27.6	7.6	23.2	23.6	20.1	0.1	44.7	19.9	21.9	26.7	-0.9
La	96.9	49.5	79.9	114.4	56	58.3	95	40.3	71.2	42.2	62.9	106.4
Ce	188.7	102.1	151	223.4	113.1	111.4	132.2	78	144.7	85.9	120.5	177.8
Nd	77.1	46.9	53	93.8	51.5	47.3	30.1	40.3	67	39.9	57.1	46.4
Pb	8	5.6	17	8	8.4	6.1	18.9	8	8.3	3.4	8.4	16
Nb	128	73.1	130.9	99.3	81.2	80	159.6	52.9	96.8	54.4	84.1	168
Zr	456.5	275.9	660	339.7	308.3	308.6	939.9	237.4	414	222.6	343.3	924.9
Y	34	28.4	27.2	38.9	27.3	29.7	19.6	23.5	35.1	27.5	30.9	26.5
Sr	1336	761.3	891.6	1326.3	854.4	828.8	248.4	550.4	1063.3	897.2	897.7	462.6
Rb	61.3	7.3	93.6	36	36.1	41.9	178.3	17.4	147.4	22.7	41.4	129.1

Table C-7 (cont.). Cameroon Line oceanic

Locality-Sample	Sao Tome-ST44	Sao Tome-ST45	Sao Tome-ST46	Sao Tome-ST47	Sao Tome-ST48	Sao Tome-ST49	Sao Tome-ST5	Sao Tome-ST50	Sao Tome-ST51	Sao Tome-ST52	Sao Tome-ST53	Sao Tome-ST54
Rock type	Basanite-Tephrite	Basanite-Tephrite	Alkali basalt	Trachy-basalt	Trachy-basalt	Basanite-Tephrite	Trachy-basalt	Alkali basalt	Alkali basalt	Alkali basalt	Alkali basalt	Phonolite
SiO_2	40.48	43.95	45.01	44.66	44.47	42.16	49.16	47.3	44.99	44.89	45.73	58.43
Al_2O_3	10.95	12.93	13.62	12.84	12.42	12.42	16.23	14.22	12.78	12.73	12.66	20.77
Fe_2O_3	13.96	12.83	13.22	13.33	12.02	13.09	10.16	12.63	13.06	13.09	12.53	2.5
MgO	12.05	8.81	9.03	9.64	11.28	9.61	4.6	7.67	10.07	9.81	10.25	0.28
CaO	11.68	11.32	9.96	10.37	9.35	11.26	8.74	10.04	10.12	10.06	10.35	1.52
Na_2O	2.45	3.49	3.56	3.77	3.03	3.47	3.99	3.12	3.47	3.57	3.25	8.53
K_2O	1.489	1.562	1.036	1.211	1.897	0.745	1.383	1.017	1.298	1.297	1.286	6.27
TiO_2	3.714	3.108	3.383	3.006	2.801	3.701	2.823	3.114	2.982	2.987	2.909	0.363
MnO	0.177	0.205	0.177	0.18	0.168	0.189	0.158	0.157	0.17	0.178	0.179	0.129
P_2O_5	0.871	0.946	0.804	0.863	0.668	0.957	0.884	0.653	0.757	0.733	0.65	0.047
Total	97.82	99.15	99.8	99.87	98.1	97.59	98.13	99.92	99.69	99.35	99.79	98.82
LOI	2.18	0.85	0.2	0.13	1.9	2.41	1.87	0.08	0.31	0.65	0.21	1.18
Zn	121.8	117	122.8	122.6	112.3	120.7	109	113.4	120.2	118.3	109.4	90.2
Cu	50.4	58.7	40.7	53.3	46.7	42.9	15.7	55.5	53.1	55.5	62.2	-3.6
Ni	288.4	159.2	161.7	223.9	252.4	190	34.7	139.4	217	224.2	240.1	1.7
Cr	473.9	360	243.9	288.6	512.4	276	107	189.7	281	287.7	372.1	4.2
V	270.6	235	218.6	211.9	220.3	268.5	194.8	212.2	210.7	205.1	221.5	21.9
Ba	642.7	665.1	629	601	699.6	789.8	880.6	368	499.6	498.3	536.9	1542.3
Sc	24.6	21.7	18.8	19.7	16.1	22.6	13.1	21.4	21.4	21.2	21.5	-0.9
La	62.7	76.4	77.9	62	52.7	76.1	77	42.5	54	51.6	50.5	73.8
Ce	129.1	150.7	156.2	121.2	105.8	154.3	160.7	78.7	102.4	104.2	98.4	94.8
Nd	59.4	64.4	69.8	55.4	45.5	67.7	65.6	40.2	46.2	47.9	43.9	19.7
Pb	4.1	10.2	9.3	10.2	11.2	7.7	5.9	5.3	9.4	8.6	10.6	17.9
Nb	83.5	91.3	118.5	86	87.2	96.9	110.6	54.7	74.5	73.9	74.7	108
Zr	306.7	339.1	410.2	298.1	366.5	359.6	435.8	223.7	281.2	274.6	276.5	751.9
Y	27.4	31.6	35.6	28.3	24.1	29.3	34	27.9	27.9	27.7	26.7	12.5
Sr	1086.8	1017.6	1091.6	1000.6	954.8	1181.4	973.6	720.1	883.4	887.5	868.7	467.9
Rb	39.9	40.8	14.8	22.4	43	29.6	20	18.8	28.4	26.9	27.8	212.7

Table C-7 (cont.). Cameroon Line oceanic

Locality-Sample	Sao Tome-ST55	Sao Tome-ST56	Sao Tome-ST57	Sao Tome-ST58	Sao Tome-ST59	Sao Tome-ST6	Sao Tome-ST60	Sao Tome-ST61	Sao Tome-ST62	Sao Tome-ST63	Sao Tome-ST64	Sao Tome-ST65
Rock type	Phonolite	Phonolite	Trachyte	Trachyte	Alkali basalt	Phonolite	Alkali basalt	Basanite-Tephrite	Trachy-basalt	Picro-basalt	Alkali basalt	Alkali basalt
SiO_2	58.75	56.05	66.14	67.61	47.43	55.8	47.26	43.84	47.31	42.29	46.72	44.62
Al_2O_3	20.89	21.75	18.3	19.14	14.28	20.92	14.4	12.11	17.1	11.99	13.77	14.85
Fe_2O_3	2.53	3.83	2.14	1.43	12.7	3.46	12.74	13.53	10.09	13.69	12.71	12.86
MgO	0.27	0.59	0.15	0.17	7.96	0.77	7.6	10.5	3.89	9.29	7.79	5.91
CaO	1.52	3.27	0.57	0.59	9.92	2.42	10.03	10.87	8.42	12.31	8.33	10.38
Na_2O	8.92	8.75	6.38	6.54	3.04	9.04	3.1	2.46	3.98	2.31	2.87	3.76
K_2O	6.024	5.182	4.404	4.365	1.036	5.205	0.954	1.014	2.216	0.426	1.635	0.927
TiO_2	0.361	0.701	0.31	0.353	3.136	0.684	3.157	3.553	3.082	3.738	2.846	3.818
MnO	0.141	0.162	0.108	0.036	0.177	0.132	0.158	0.169	0.163	0.179	0.268	0.198
P_2O_5	0.042	0.123	0.064	0.063	0.669	0.134	0.617	0.763	1.253	0.72	0.655	0.94
Total	99.43	100.4	98.56	100.28	100.34	98.58	100.01	98.81	97.49	96.93	97.59	98.26
LOI	0.57	-0.4	1.44	-0.28	-0.34	1.42	-0.01	1.19	2.51	3.07	2.41	1.74
Zn	92.2	121.9	78.6	119.8	114.8	92.1	115.4	116.3	126.7	108.1	114.7	112.9
Cu	-3.6	3.6	-3.7	-4.9	53.3	-0.5	47.6	60.1	14.9	80.2	47.7	52.4
Ni	1.6	6.6	1.8	1.4	148.2	3.8	143	213	4.3	176.8	120.1	47.5
Cr	4.5	10.7	4.9	3.5	207.7	6	193.7	402	2.4	364.3	212	60.9
V	18.5	36.6	2.3	2.3	210.1	40.8	217.9	249.6	172.5	344.7	229.8	286.9
Ba	1558.3	1251.5	1360.5	1284.6	401.9	515.2	361.1	519.5	1696.9	612.7	482.4	811.1
Sc	-1.2	-0.5	-0.9	-0.8	22	0.3	22.4	22.9	7.2	30.7	20.4	22.3
La	73.8	99.5	148	120.8	42.6	68.3	41.7	49.5	85.5	54.5	48.6	76.4
Ce	94.5	156.9	254.1	209.9	83.2	98.2	82.9	102	182.6	108.7	97.2	154.6
Nd	19.8	40.5	77.8	68.1	41.6	24.6	42.1	49.2	79.1	49.5	44.8	65.2
Pb	18.4	15.9	16.6	12.2	8.1	22.6	5.3	4.1	3.8	7.9	9.8	9.7
Nb	108.2	153.1	159.6	161.9	57.3	104.8	55.3	75	131.7	76.8	64.4	112
Zr	751.9	794.9	514.6	553.5	235.6	954.8	226.6	277.1	607.1	306.2	305.2	431.8
Y	13.6	23	37.6	29.7	28.3	17.1	28.3	28.1	39.2	28.2	30.4	34.2
Sr	464.6	1387.1	230.5	224.7	721.4	554	710.5	873	1215.5	752.9	500.8	967.8
Rb	193.3	163.7	124.4	124	18.5	201.5	11.9	24	26	7.5	37.6	14

Table C-7 (cont.). Cameroon Line oceanic

Locality-Sample	Sao Tome-ST66	Sao Tome-ST67	Sao Tome-ST68	Sao Tome-ST69	Sao Tome-ST7	Sao Tome-ST70	Sao Tome-ST71	Sao Tome-ST72	Sao Tome-ST73	Sao Tome-ST74	Sao Tome-ST75	Sao Tome-ST76
Rock type	Basanite-Tephrite	Basanite-Tephrite	Basanite-Tephrite	Alkali basalt	Basaltic trachy-andesite	Trachy-basalt	Phono-tephrite	Trachy-basalt	Phono-tephrite	Trachy-basalt	Trachy-basalt	Phonolite
SiO_2	42.9	42.81	42.65	44.02	45.84	44.77	51.44	44.4	48.41	46.82	46.45	56.29
Al_2O_3	12.51	11.63	11.8	13.33	14.82	14.91	18.95	13.75	17.05	16.68	14.97	20.34
Fe_2O_3	13.61	14.54	14.39	13.45	11.22	12.59	8.08	12.48	9.92	11.36	11.74	3.96
MgO	10.03	11.04	10.86	8.18	4.15	5.48	2.63	8.32	3.53	4.53	6.59	0.81
CaO	11.04	11.14	11.32	10.52	6.34	11.15	5.85	10.59	8.18	9.36	9.6	2.22
Na_2O	3.19	2.78	2.9	3.3	5.18	4.09	5.96	3.48	5.41	4.43	4.16	8.79
K_2O	1.664	1.301	1.203	1.502	1.158	1.11	2.851	1.451	2.492	1.608	1.774	4.808
TiO_2	3.807	3.157	3.225	3.343	3.345	3.512	2.118	3.164	2.615	3.344	2.827	0.915
MnO	0.189	0.182	0.174	0.179	0.148	0.159	0.155	0.191	0.197	0.168	0.174	0.141
P_2O_5	1.013	0.98	0.975	0.973	0.825	0.951	0.827	1.024	0.898	0.781	0.999	0.172
Total	99.95	99.56	99.5	98.8	93.02	98.72	98.87	98.83	98.69	99.07	99.28	98.44
LOI	0.05	0.44	0.5	1.2	6.98	1.28	1.13	1.17	1.31	0.93	0.72	1.56
Zn	119.6	132.3	125.2	110.9	125.2	118.5	102.7	114.4	119.7	106.5	118.1	108.3
Cu	55.7	55.1	54.9	55.1	22.7	55	18.7	49.3	20.8	29.9	50.4	-1.7
Ni	179.2	240.9	230.6	139.7	21.9	53.6	15.4	167.8	18.5	25.8	113.7	4.3
Cr	331.4	338.9	326.5	231.5	4.5	20.5	16.4	305.4	23.2	27.4	194.6	5.3
V	265.5	252.9	238	257.5	281.6	280.2	93.4	239.9	172.6	231.2	174	33.6
Ba	550.5	491.5	511.4	533.3	364.9	667.8	920.5	721.8	869.7	696.3	768.2	1108.5
Sc	23.5	24.6	22.3	22.9	17.5	21.1	4.1	19.6	9	15.3	14.8	0.1
La	60.1	53.9	53.7	54.7	54.3	80.4	103.9	81.4	104.7	71.4	82.2	115.5
Ce	125.5	108.4	109.4	117.9	109.4	156.7	189.8	159.5	196.9	146.2	174.2	179.7
Nd	61.2	50.1	52.1	55.5	51.6	68.4	71.3	67.4	78.9	60.9	71.2	51.9
Pb	7.8	3.4	4.8	8.3	5.8	8.3	12.3	11	15.4	10.6	8	18.3
Nb	85	72.9	73.4	71.1	80.7	102.4	144.5	104.9	150.4	105.8	112.6	178.4
Zr	327.8	239.8	246.4	313.9	357.7	368.9	618.4	367.3	599.2	402.8	366.9	906.1
Y	31.7	28	28.3	30.4	31.1	35.6	32.8	33.1	37.5	32.8	34.5	28.4
Sr	933	840.2	835	954	859.4	1118.7	1267.8	1130	1280.9	1056.5	1196.4	727.9
Rb	35.3	27.6	24.8	34.7	28.3	52.4	65.7	46.4	64.4	68.9	55.3	148.5

Table C-7 (cont.). Cameroon Line oceanic

Locality-Sample	Sao Tome-ST77	Sao Tome-ST78	Sao Tome-ST79	Sao Tome-ST8	Sao Tome-ST81	Sao Tome-ST82	Sao Tome-ST83	Sao Tome-ST84	Sao Tome-ST85	Sao Tome-ST86	Sao Tome-ST87	Sao Tome-ST88
Rock type	Basanite-Tephrite	Phonolite	Phonolite	Phonolite	Phonolite	Tephri-phonolite	Phonolite	Trachyte	Basanite-Tephrite	Basanite-Tephrite	Trachy-basalt	Basaltic trachy-andesite
SiO_2	43	56.51	56.86	56.9	56.16	51.5	56.3	61.58	42.76	39.74	47.89	48.09
Al_2O_3	12.87	20.53	20.58	21.86	20.38	18.56	20.35	18.75	10.85	9.94	16.23	16.53
Fe_2O_3	13.56	3.79	3.92	2.28	3.96	7.51	3.95	3.46	13.41	14.48	10.84	9.38
MgO	9.19	0.67	0.68	0.24	0.89	2.42	0.81	0.23	11.91	12.79	4.33	3.53
CaO	11.66	2.35	2.08	1.2	2.52	5.37	2.29	0.93	11.45	12.92	6.8	7.89
Na_2O	3.02	8.63	8.84	10.1	8.7	7.22	8.8	8.02	2.39	2.28	2.91	3.5
K_2O	1.51	4.398	5.052	6.018	4.879	3.598	4.917	5.547	1.222	0.692	3.148	3.491
TiO_2	3.471	0.866	0.891	0.24	0.908	1.768	0.921	0.266	3.053	3.5	2.791	2.568
MnO	0.201	0.148	0.158	0.147	0.153	0.173	0.139	0.225	0.165	0.191	0.176	0.223
P_2O_5	1.078	0.148	0.158	0.044	0.171	0.75	0.176	0.025	0.88	0.982	1.059	0.77
Total	99.56	98.04	99.21	99.01	98.73	98.85	98.66	99.04	98.08	97.51	96.17	95.97
LOI	0.44	1.96	0.79	0.99	1.27	1.15	1.34	0.96	1.92	2.49	3.83	4.03
Zn	118.9	113.6	105.3	120.8	101.4	126.9	103.6	174.3	113.6	122.8	147.5	157.7
Cu	54.1	-4.3	-3.2	-5	-1.2	12.8	-2.4	-7.1	54.9	61.9	9.5	3.5
Ni	164.6	1.9	2.6	0.7	4.1	13.3	3.7	1.1	269.6	286.2	4.9	3.7
Cr	392.2	5.3	5.4	4.6	6.4	9	6.3	4	399.8	446	5.5	2.8
V	280.6	30.3	30.3	15.6	27.8	93.6	34.3	-4.4	261.7	343.6	188.9	123.8
Ba	633.6	1088.4	1120	98.2	1113.7	1079.5	1089.4	70.4	540.6	532.4	871.8	1092.3
Sc	23.2	-0.3	-0.5	-1	-0.5	3.9	-0.6	-1.1	22.2	24.3	8	3.4
La	81	106.4	109.8	74.2	101.8	109	100.8	198.6	56.4	63.9	99.5	121.8
Ce	167.2	179.5	176.8	96.3	172.9	200.2	172.9	337.7	106.8	121.9	209.4	238.8
Nd	71.7	49.3	50	16.8	47.2	67.6	48.2	88.3	50.8	59.5	86	92.9
Pb	3.9	18.7	17.8	22.6	17.1	12.9	16.9	19.4	6.4	2.6	10.4	8
Nb	109.1	181.4	181.5	93.2	175.8	143.6	177.2	298.3	70	93.3	137.2	171.4
Zr	356	920.9	925	984.1	890.6	672.8	904.5	1414.3	258.8	291.5	626.1	845.3
Y	34.7	25.6	28	13.3	25.3	30.9	26.1	42.9	27.4	28.8	37.8	45.4
Sr	1068.1	686.8	682.4	89.1	744.1	1405.8	727.4	18.7	894.4	970.5	1176.5	1207.3
Rb	39	139.1	155.6	225.1	148	101.2	148.7	200.3	25	17.4	98.2	107.7

Table C-7 (cont.). Cameroon Line oceanic

Locality-Sample	Sao Tome-ST89	Sao Tome-ST9	Sao Tome-ST90	Sao Tome-ST91	Sao Tome-ST92	Sao Tome-ST93	Sao Tome-ST94	Sao Tome-ST95	Sao Tome-ST96	Sao Tome-ST97	Sao Tome-ST99
Rock type	Phono-tephrite	Phonolite	Phonolite	Trachyte	Alkali basalt	Alkali basalt	Alkali basalt	Trachy-basalt	Basaltic trachy-andesite	Basanite-Tephrite	Trachy-basalt
SiO_2	47.6	56.21	56.22	61.78	45.6	43.63	42.84	46.78	49.55	41.07	46.22
Al_2O_3	16.45	21.6	21.98	19.37	12.12	17.24	14.19	13.56	17.27	12.58	16.45
Fe_2O_3	9.39	2.2	2.32	2.23	12.89	13.25	12.56	12.64	9.53	15.02	9.91
MgO	2.86	0.21	0.23	0.22	11.21	4.75	6.12	8.65	4.08	7.76	3.22
CaO	7.63	1.17	1.19	1.18	10.66	9.14	11.41	9.44	7.12	11.86	9.97
Na_2O	4.74	10.11	10.46	7.73	2.18	2.69	1.56	3.62	3.72	3.03	3.9
K_2O	3.465	6.13	5.705	5.883	0.912	0.961	1.866	1.52	2.781	0.681	1.381
TiO_2	2.631	0.24	0.178	0.272	3.199	3.855	3.922	2.87	2.497	4.793	3.113
MnO	0.213	0.145	0.182	0.161	0.184	0.208	0.169	0.16	0.191	0.179	0.19
P_2O_5	0.814	0.045	0.025	0.024	0.689	1.252	0.728	0.702	0.979	1.215	0.891
Total	95.78	98.07	98.49	98.85	99.63	96.98	95.35	99.94	97.72	98.18	95.24
LOI	4.22	1.93	1.51	1.15	0.37	3.02	4.65	0.06	2.28	1.82	4.76
Zn	160.7	117.9	145.9	102.2	117.5	130.4	116.1	113.7	128	123.6	123.1
Cu	3.9	-3.9	-7	-6.4	58.3	30	56.1	49.7	9.3	73.5	19.4
Ni	3.7	1.1	1.3	1.9	287.8	17.4	48.8	168.8	7.2	88.5	18.8
Cr	3.9	4.6	4.3	4.9	475.3	16.8	40.3	231.2	4.5	123.9	19.1
V	125.7	14.3	3.5	1.2	246.1	223.3	365.4	193.2	124.2	376.9	230.8
Ba	1099.2	100.5	41.7	1095.2	404.3	799	1401.8	470.9	853.9	709.6	724.3
Sc	3.9	-0.9	-1.1	-1	25.5	12.9	24.2	19.2	5.6	25.6	11.4
La	123	72.7	105.2	105.8	42.1	96.9	68.7	56.1	89	71.6	86.5
Ce	233.7	95.4	131.5	161.1	85.9	196.3	130.1	105.9	180.2	144.3	174
Nd	94.6	15.2	21.9	34.4	41.6	87.3	58.8	46.7	75.8	69.8	72.6
Pb	8.3	21.9	22.5	17.4	6.2	9	4.8	7.4	9.9	5.8	8.7
Nb	171.9	92.1	146.5	151.2	56.6	128.7	88.7	71.9	119.2	86	121.7
Zr	760.8	967.4	1183.6	963.5	247.1	489.8	366.9	322.9	526.6	393.6	469.2
Y	47.7	12.6	18.7	20.7	27.2	42.6	30.4	27.8	36.9	32.9	35.7
Sr	1247.9	87	36.3	204.9	734	1173.5	2369	782.6	1056.4	963.5	1158.1
Rb	96.7	224.5	239.4	176.4	18.1	7.7	58.2	40.4	61.6	9	66.3

Appendix D: Numerical definition of the thermal boundary layer (TBL)

Equations used to define the thermal boundary layer (TBL), according to McKenzie and Bickle (1988). For illustration, see Figure 5-1 in Chapter 5. According to this concept, the thickness of the TBL is the length scale of variability δ in the potential temperature of the geotherm, which becomes fixed in the asthenospheric adiabat. Its structure is also dependant on the magnitude of temperature variability $\Delta\theta$. These values are defined as:

$$\Delta\theta = B\left(\frac{\kappa\nu}{g\alpha d^3}\right)R^{3/4} \tag{12}$$

$$\frac{\delta}{d} = AR^{-1/4} \tag{13}$$

with the Rayleigh number R defined as:

$$R = \frac{g\alpha d^4 F}{k\kappa\nu} \tag{14}$$

where *A* and *B* are numerical constants determined by numerical experiments, α the thermal expansion coefficient, *d* the thickness of the convecting layer, *g* the acceleration due to gravity, κ the thermal diffusivity, *k* the thermal conductivity, ν the viscosity of the solid material of the upper mantle, and *F* the heat flux/unit area through the layer. The TBL is overlain by a rigid and fully conductive mechanical boundary layer, and together these two layers form the boundary layer at the top of the convecting adiabatic mantle. The equations above show the strong dependence of the structure of the TBL, including its thickness and temperature variability, to the surrounding thermal structure, which includes the characteristics of the

lithosphere and the asthenosphere, and the local heat flux, which is part of the definition of the Rayleigh number.

Appendix E: Thin section descriptions and notes

Borborema Province

15BP1-1 (Olivine basanite): Porphyritic hypocrystalline with glassy (mostly) to cryptocrystalline groundmass containing augite and opaques. Olivine phenocrysts. Augite microphenocrysts. Olivine xenocrysts and peridotitic xenoliths.

Olivine phenocrysts are subhedral to euhedral, up to 1 mm, 10-15 modal% and occasional light alteration to smectite along fractures. Augite microphenocrysts are prismatic, subhedral to euhedral, up to 0.3 mm in length (mode 0.1 mm), 50-60 modal% and include occasional titanaugite (which are also the larger crystals) amongst them. Olivine xenocrysts and rare xenoliths (the latter with granular texture) are up to 5 mm, 5-7 modal%, with some smectite alteration (mainly along but not restricted to fractures and crystal rims). They have etched boundaries and evidence for straining in the form of oscillatory extinction. Xenoliths also include orthopyroxenes with sieve texture and reaction textures forming olivine and opaques. Groundmass opaques are equant, subhedral to euhedral, 7-10 modal% and up to 0.05 mm.

Notes: The lack of plagioclase as an obvious phase would indicate that this is a foidite. However, there is no foidite present either. The major element analysis puts it as a basanite, and therefore some plagioclase must be present in the groundmass. Unstable orthopyroxene indicates either a compositionally undersaturated melt, out of the orthopyroxene stability field, or incongruent re-melting of xenoliths. Their reaction textures suggest loss of silica to form Forsterite-rich olivine, which accommodates less Fe and leads to the crystallisation of iron oxides. The sample comes from a neck or plug, and the glassy groundmass and overall texture agree with a hypabyssal intrusion context.

15BP3-2 (Titanaugite-phyric alkali basalt): Porphyritic holocrystalline with fine-grained groundmass containing plagioclase and titanaugite in intergranular texture, as well as olivine and opaques. Phenocrysts of olivine and titanaugite.

Groundmass plagioclase laths are calcic, up to 0.5 mm and 50-60 modal%. Titanaugite phenocrysts are subhedral to euhedral, ocassionally zoned, represent 20-25 modal%, seriate with the groundmass and appear as glomerocrysts up to 3 mm (dominant habit) or smaller crystals < 0.5 mm. Olivine phenocrysts are anhedral to subhedral, 1-1.5 mm, 1-2 modal%, occasionally occur as glomerocrysts and are mostly altered to iddingsite and serpentinite along boundaries and fractures, with smaller crystals sometimes completely altered. Groundmass olivine are 0.1-0.3 mm, mostly rounded or subhedral, and together with phenocrysts represent 15-20 modal%. Both olivine and titanaugite contain rare inclusions. Groundmass opaques are anhedral to subhedral, equant and prismatic, up to 0.2 mm and 5-7 modal%.

Notes: The larger olivine cannot be easily classified as phenocrysts or xenocrysts due to high alteration levels along crystal boundaries. Although they have a bimodal size distribution and larger crystals present etched boundaries, they are still fairly uniform, have good subhedral habits and no strain evidence, and are more likely phenocrysts. The sample comes from a lava flow at ground level, and the lack of a glassy or microcrystalline groundmass suggests the erupted material cooled slowly in a thick flow and/or was dominated by crystal mush when it erupted. The presence of ubiquitous plagioclase and titanaugite in the groundmass in intergranular texture, with phenocrysts of olivine and titanaugite, indicates an alkali basalt, in accordance with the major element analysis.

15BP3-3a, *thin-section 1* (Vesicular olivine-phyric hyalo-basalt): Porphyritic hypocrystalline (hyalo-basalt) with glassy groundmass (black to dark brown in ppl) containing plagioclase and augite. Phenocrysts of plagioclase, olivine and augite. Xenocrysts and xenoliths of olivine, augite and orthopyroxene, and presence of vesicles and amygdales.

Vesicles are 0.5-5 mm, 10-15 modal%, some of which are completely or partially filled with calcite (amygdales). Plagioclase laths are calcic, up to 1 mm, 30-40 modal%, suspended in the glassy groundmass and with small amounts of microcrystalline augite and glass forming interstitial and intersertal textures in lath clusters. Phenocrysts, xenocrysts and xenoliths are up to 3 mm and together represent 5-7 modal%, although much of the olivine has been completely altered. Olivine phenocrysts are subhedral to euhedral, sometimes skeletal and strongly altered to iddingsite, with some crystals completely consumed, leaving a gap lined with alteration products. Augite phenocrysts are subhedral to euhedral, dominated by glomerocrysts, zoned (compositional and/or inclusions), often with rounded edges that sometimes affects whole glomerocrysts, which could indicate xenoliths instead, may contain small inclusions of rounded poykilitic olivine and are somewhat altered, often with sieve texture. Orthopyroxene xenocrysts are anhedral to subhedral and often reacting to form olivine. Xenoliths are very rounded, up to 2 mm and formed by augite (dominant), olivine and orthopyroxene in granular texture.

Notes: It is not always possible to distinguish between phenocrysts and glomerocrysts from xenocrysts and xenoliths, especially in relation to the pyroxenes, and it is possible that some of the very rounded pyroxene glomerocrysts were originally fine-grained pyroxenite xenoliths. However, sometimes they have subhedral habits and clearer glomerophyric texture, making a stronger case for phenocrysts. It is not possible to identify the alteration product for the clinopyroxenes (superficially it is similar to yellow iddingsite). Groundmass with interstitial texture between plagioclase and augite reinforces the idea that the larger augites are xenocrysts, and indicates a subalkaline basalt. Major element analysis puts it as a basaltic andesite.

15BP3-3a, *thin-section 2* (Olivine-phyric hyalo-basalt): Hypocrystalline (hyalo-basalt) with glassy groundmass (clear light beige in ppl) containing plagioclase, olivine and rare augite. Phenocrysts of olivine. Vesicles and amygdales. Zeolite pseudomorphs after olivine.

Pseudomorphs are subhedral to euhedral, apparently with olivine habit, often occur in clusters, and are filled with microcrystalline and/or acicular/spherulitic zeolites. They are up to 0.5 mm, 5-7 modal% and also have smectite or iddingsite (and occasionally opaques) lining their walls. Fractures in the rock have the same materials, and pseudomorphs tend concentrate near them. Vesicles and amygdales represent 2-5 modal%, are mostly round and filled/lined with calcite or zeolites. Occasional tear-shaped examples are aligned and indicate the way-up orientation. Plagioclase is calcic, supported by the glassy matrix, 10-15 modal% and occur mostly as laths up to 0.4 mm but also as rare equant/tabular euhedral microphenocrysts up to 0.6 mm. Olivine occurs solely as phenocrysts up to 0.5 mm, mostly euhedral (some subhedral), 5-7 modal% and with rare inclusions. Olivines may also be skeletal, glomerophyric and altered to iddingsite and/or smectite. There are some rare, small glomerocrysts of plagioclase with augite and possibly orthopyroxene (with the same overall crystal size range), although the precise identification of orthopyroxene in these small examples is difficult.

Notes: Alteration of olivine and pseudomorphs have similar by-products to the previous sample. Also like the previous sample, it is glass-rich. The olivine polymorphs represent a significant proportion of the olivine originally present and could potentially hide previous xenocrysts, which are so common in other samples. The two 15BP3-3a samples (i.e. thin-sections 1 and 2) come from the same exposure and suggest a segregation of crystals to the more vesiculated domains where the glass also seems to be fuller of impurities or perhaps more altered. The possible presence of two pyroxenes is difficult to ascertain due to the small number of occurrences and the small size of crystals, which hinders the observation of cleavage and results in augites showing birefringence that leans towards smaller values. Nonetheless, two pyroxenes would indicate low pressure and melting and would be in accordance with other samples for the area that indicate subalkaline basalts. Major element analysis puts it as a basaltic andesite.

15BP3-3b (Tholeiitic basalt): Hypocrystalline with glassy to microcrystalline groundmass (black to dark brown in ppl) containing plagioclase and olivine. Microphenocrysts of olivine and plagioclase and calcite pseudomorphs after olivine and rare vesicles and amygdales filled or lined with calcite and/or glass.

Groundmass plagioclase occurs as very thin calcic laths (width up to 0.05 and length up to 0.6 mm) with 30-40 modal% in interstitial and intersertal texture with the microcrystalline and glassy materials in the groundmass. Some equant plagioclase crystals around 0.5 mm and seriate with the groundmass are also present as microphenocrysts. Olivine are subhedral to euhedral, equant, up to 0.7 mm, 2-3 modal%, seriate with the groundmass and often skeletal. Olivine may also occur as glomerocrysts and are often strongly altered (partially or completely) to iddingsite or substituted by calcite pseudomorphs. Vesicles and amygdales are irregular or round, up to 0.5 mm and filled and/or lined with calcite and/or very pale green or yellow (ppl) glass with only incipient degrees of devitrification.

Notes: Augites must be present in the groundmass microcrystalline material. The sample indicates a tholeiitic crystallisation sequence (plagioclase before augite) and, together with its very glassy matrix, is in accordance with its pillow lava context. The black glassy matrix hinders the identification of opaques. It is also difficult to assess what part of the microcrystalline material in the groundmass is original or due to later alteration. The overall characteristics indicate a tholeiitic basalt, but the almost lack of olivine suggests some evolution. This would be in accordance with major element analysis that sets it as basaltic andesite instead.

15BP3-3c (Sandy bentonite): Bentonite with cryptocrystalline matrix and very fine-grained quartz grains. Accessory biotite and augite grains.

Quartz is very well-sorted, yet very angular, and < 0.3 mm. Accessory augite is sub-rounded and 0.1 mm. Accessory biotite is subhedral and < 0.3 mm.

Notes: This is a very well-sorted and very fine-grained ash deposit mixed with what is likely volcanoclastic quartz material, and likely distal from the vent and deposited in a small basin in a subaqueous environment. It is associated with pillow lavas but probably comes from a different area. The concentration of quartz is puzzling, as no samples have produced this mineral. A very-well sorted but still very-angular deposit suggests a volcanic plume tephra dispersal.

15BP3-4 (Olivine basalt): Porphyritic holocrystalline with fine-grained to microcrystalline groundmass containing plagioclase with interstitial augite, as well as olivine and opaques. Phenocrysts of augite, olivine and rare plagioclase. Calcite and smectite infillings alteration along interstitial spaces. Possibly some olivine xenocrysts.

Plagioclase is the dominant phase in the groundmass and occurs as calcic laths up to 0.5 mm together with interstitial augite crystals < 0.05 mm. Smectite and calcite (dominant) infilling of interstitial groundmass spaces represent at least 5 modal%. Groundmass opaques are anhedral and represent 7-10 modal%. Phenocrysts are dominated by olivine and augite with some calcic plagioclase, and overall are up to 3 mm, 7-10 modal% and may be glomerophyric, sometimes with calcite infillings radial microlites in what were probably original glass inclusions in glomerocryst cores. Olivine range from anhedral to euhedral, often with etched boundaries, resorption embayments and irregular straight-sided shapes, and altered to smectite along fractures and boundaries, with occasional alteration to iddingsite. Augites are subhedral to euhedral, often with composition/inclusion zoning, may contain poykilitic rounded olivine and may form radial glomerocrysts that are sometimes rounded around the edges. Some of the olivines may be xenocrysts.

Notes: This samples had no definite context in the field but a lava flow stratigraphycally overlaying pillow lavas was inferred. The thin-section texture supports this, although a sill is also a possibility. The ubiquitous groundmass plagioclase with interstitial augite and augite phenocrysts indicates a basalt. The major element analysis puts it as a borderline subalkaline basalt.

15BP3-5 (Olivine basalt): Porphyritic holocrystalline with fine-grained to microcrystalline groundmass containing plagioclase, augite, olivine and opaques with occasional alteration to smectite/serpentine. Phenocrysts and microphenocrysts of augite and olivine.

Plagioclase is the dominant phase in the groundmass and occurs as calcic laths up to 0.5 mm with interstitial augite crystals < 0.05 mm. Groundmass opaques represent 5-7 modal%, and follow thin continuous irregular domains up to 0.05 mm in thickness but up to several mm in length between

plagioclase laths. Olivine phenocrysts and microphenocrysts are anhedral to subhedral, rounded, 5-7 modal%, up to 0.8 mm, altered to smectite along fractures and boundaries and may contain inclusions. Augite phenocrysts are subhedreal to euhedral, up to 2 mm, 3-5 modal% and may include poykilitic very rounded olivine and other micro-inclusions. Microphenocrysts of olivine and augite are seriate with the groundmass. Augite glomerocrysts are up to 4 mm, occasionally include olivine, especially in their cores, and show rounded edges and sometimes apparent granular contact between their crystals, suggesting the possibility of overgrown xenocrysts or some form of recrystallization.

Notes: Sample from a lava flow and very similar to 15BP3-4, but without the groundmass calcite/smectite alteration. It is difficult to confirm an interstitial texture for the plagioclase and augite in the groundmass, suggesting a transitional basalt. This is in accordance with the major element analysis that plots it as borderline alkali basalt, almost together with 15BP3-4.

15BP4-6 (Basanite): Porphyritic holocrystalline with fine-grained to microcrystalline groundmass containing augite, nepheline, olivine, opaques and rare plagioclase. Phenocrysts and possibly xenocrysts of olivine.
Nepheline occurs as anhedral oykocrysts up to 2 mm, poikilitically enclosing augite laths and olivine crystals. This pattern forms the bulk of the groundmass. Plagioclase laths are rare, up to 0.5 mm and occur amidst the nepheline oykocrysts. Augite laths are brown to lilac in ppl, range from microcrystals to 0.5 mm, 40-50 modal% and includes titanaugite. Opaques are up to 0.2 mm, 10-15 modal% and anhedral. Olivine groundmass crystals and phenocrysts are subhedral to euhedral, up to 1 mm, 10-15 modal% and seriate. Possible olivine xenocrysts or phenocrysts are crystals 1-4 mm, 3-5 modal%, with ondulose extinction, resorption embayments, etched boundaries and anhedral irregular shapes often with straight sides. Alteration is rare.

Notes: The sample is very fresh. The relatively large nepheline oikocrysts make it unlikely that the sample comes from a flow and a hypabyssal context is more plausible. The plagioclase Ca content cannot be measured. The presence of late nepheline oikocrysts in an augite and plagioclase groundmass and ubiquitous olivine phenocrysts indicates a basanite, in accordance with the major element analysis.

15BP4-7 (Olivine basalt): Virtually aphyric holocrystalline with microcrystalline groundmass containing plagioclase, augite, fine-grained olivine and opaques. Xenocrysts of olivine. Ocellar reaction features.

Plagioclase and augite occur in similar proportions in the groundmass with no obvious crystallisation sequence. Plagioclase laths are calcic, up to 0.2 mm. Augite is equant to prismatic, very pale green in ppl, up to 0.1 mm and sometimes zoned. Opaques are subhedral, < 0.1 mm and 7-10 modal%. Olivine are subhedral to euhedral, up to 0.5 mm, 15-20 modal% and seriate. Olivine xenocrysts are anhedral to subhedral, often with irregular straight-sided shapes, 1-3 mm, 1-2 modal%, etched boundaries, strong ondulose extinction and ubiquitous alteration to smectite along boundaries and fractures. Ocellar features are 0.5-4 mm, 1-2 modal%, with an outer layer of microcrystalline augite laths, with occasional rounded olivine (up to 0.2 mm) and interstitial glass inclusions (with some devitrification), and a core of slightly larger, equant, tabular olivine with a rough radial arrangement and that may also contain glass inclusions. These features have diffuse boundaries and much less and smaller opaques (apparently euhedral) than in the groundmass (<< 0.1 mm and 1-2 modal%) and may be missing the inner olivine layer.

Notes: The glass inclusions intermingled with the augite in the ocellar texture suggests this material was hot when added to the main matrix or when the sample was extruded. They could represent blebs of hotter immiscible material (perhaps with a clinopyroxenite composition) added to the magma before eruption or the re-melting of previous xenoliths or xenocrysts that contained orthopyroxene. Their opaques seem euhedral but the crystals are too small for a detailed assessment. The overall texture suggests somewhat rapid cooling and therefore the plug/neck must have been shallow. The presence of augite, plagioclase and olivine in the groundmass suggests a basalt. The major element analysis puts it as an alkali basalt.

15BP5-8 (Basanite): Porphyritic hypocrystalline with crypto- to microcrystalline groundmass containing augite (dominant), olivine, little plagioclase and opaques. Phenocrysts and microphenocrysts of olivine. Accessory titanaugite. Ocellar reaction features. Xenocrysts of olivine, orthopyroxene and spinel. Devitrified glass inclusions and biotite alteration. One sandstone xenolith.

Overall, the groundmass is somewhat heterogenous with some alteration to biotite. Devitrified glass inclusions are sub-rounded, ~1-2 mm, with irregular shapes and sharp boundaries. They are completely filled with secondary plagioclase that sometimes contain green euhedral augite laths up to 0.2 mm radiating from the cavity walls. Opaques are anhedral and with 3-5 modal% (difficult to quantify due to dark groundmass). Olivine phenocrysts and microphenocrysts are subhedral to euhedral, seriate with the groundmass, up to 0.5 mm and 10-15 modal%. Olivine xenocrysts are anhedral to subhedral, 1-6 mm, often with irregular straight-sided edges, 5-7 modal%, etched boundaries, ondulose extinction and light alteration to smectite along fractures. Accessory titanaugite phenocrysts and microphenocrysts are subhedral to euhedral, 1-6 mm, ≤ 1 modal%, with poykilitic olivine and sieve texture. Orthopyroxene xenocrysts react to form microcrystalline olivine (degrees varying from partial to complete, which consume the crystals from boundary to core). One sandstone xenolith (1 cm) with glassy devitrified margins and made of well-sorted, angular quartz grains < 0.3 mm, supported by a cryptocrystalline matrix with glassy devitrified margins. A few spinel xenocrysts (possibly chromite), which are brown under ppl, anhedral to subhedral and ~0.5 mm.

Notes: This is a complex sample with a rather heterogenous groundmass (in terms of granularity, types of material and overall colour), but shows the degrees and possibilities of reactions consuming orthopyroxene xenocrysts that are obviously in disequilibrium. The groundmass dominated by augite but with a little plagioclase, the accessory titanaugite and olivine phenocrysts and microphenocrysts indicate a basanite, in accordance with the major element analysis.

15BP5-9 (Basanite): Porphyritic holocrystalline with microcrystalline groundmass containing augite, olivine, opaques and little plagioclase. Phenocrysts and microphenocrysts of titanaugite (rare) and olivine. Possibly xenocrysts of olivine. Ocellar reaction features and one spinel xenocryst.

Groundmass augite occurs as laths <0.1 mm, and opaques as anhedral to subhedral crystals up to 0.1 mm (rare crystals or clusters 0.5 mm) and 7-10 modal%. Olivine phenocrysts are microphenocrysts are subhedral to euhedral, mostly < 0.5 mm but up to 1.5 mm, 7-10 modal%, seriate with the groundmass and with little or no alteration. Possible olivine xenocrysts are anhedral to subhedral, 0.5-4 mm, 5-7 modal%, with etched boundaries, occasional light ondulose extinction and alteration to smectite along fractures or iddingsite in their cores. Titanaugite phenocrysts and microphenocrysts are up to 1 mm, ~1 modal%, subhedral to euhedral and with rare sieve texture. Ocellar reaction features are up to 1 mm and made of microcrystalline olivine and opaque subhedral crystals < 0.1 mm, with occasional layering where opaques concentrate at the rims. One spinel xenocryst that is brown, 0.5 mm and anhedral.

Notes: The ocellar reaction features show textures similar to xenocryst alteration in other samples, and the olivine clusters are likely the reaction products of orthopyroxenes. The groundmass dominated by augite with little plagioclase and all the olivine content put together indicates a basanite, in accordance with the major element analysis.

15BP5-10 (Olivine alkali basalt): Aphyric holocrystalline with microcrystalline groundmass containing plagioclase, augite, olivine and opaques. Xenocrysts of olivine and titanaugite. Ocellar reaction features with olivine, augite and orthopyroxene. Calcite amygdales.

Plagioclase laths are subhedral to euhedral, up to 0.3 mm, seriate, borderline andesine-labradorite composition, often zoned, with sieve textures (especially euhedral crystals) and together with interstitial augite form the bulk of the groundmass that also includes olivine. Olivine are subhedral to euhedral, up to 0.5 mm, seriate, 10-15 modal%, with little alteration and may be skeletal. Opaques are up to 0.05 mm, anhedral, 10-15 modal%, with occasional crystals or clusters of 0.5 mm. Calcite amygdales are irregular in shape, up to 1.5 mm and < 1 modal%, likely filling cavities other than vesicles. Olivine xenocrysts are anhedral to subhedral, 1-10 mm, 2-3 modal%, with etched boundaries, ondulose extinction and moderately altered to smectite along fractures and boundaries.

Rare titanaugite xenocrysts are up to 1 mm, anhedral, with sieve texture and strongly resorbed and etched along the edges. Ocellar reaction features are up to 2 mm, often composed solely of augite, with very fine outer layers (crystals < 0.05 mm) and cores that are prismatic, radial and coarser. They may also contain glass inclusions and clearly have less and finer opaques than the groundmass. Some ocelli contain large concentration of opaques, forming mm-scale domains, and a third layer of olivine in their cores, whilst others are heterogeneous but no obvious layers, and contain olivine, orthopyroxene and clinopyroxene with strong reaction/resorption and sieve textures (in the case of orthopyroxene crystals, they develop olivine coronas). These are clearly the reaction products of previous peridotitic xenoliths or xenocrysts.

Notes: Textures in this sample show clearly that some ocelli are reaction products of resorbed/re-melted xenoliths. They are very similar to those found in other samples, but with stronger radial textures for augites. A groundmass dominated by plagioclase and augite in similar proportions with additional olivine indicate an alkali basalt, in accordance with the major element analysis.

15BP5-11 (Olivine alkali-basalt): Aphyric holocrystalline with microcrystalline to fine-grained groundmass containing plagioclase, titanaugite, olivine and opaques. Microphenocrysts of olivine (dominant), and little titanaugite and plagioclase. Ocellar reaction features, xenoliths and xenocrysts. Calcite amygdales and secondary alteration minerals.

Groundmass comprises calcic plagioclase laths up to 0.5 mm, equant to prismatic titanaugite < 0.05 mm and rounded to subhedral olivine (7-10%) < 0.5 mm, all in seriate texture. Plagioclase is equant and often with sieve texture. Titanaugite are subhedral with rare crystals reaching 2 mm and sometimes with sieve texture. Opaques are up to 0.3 mm, 3-5 modal% and anhedral to subhedral. Olivine xenocrysts are anhedral to subhedral, 0.5-2 mm, < 3 modal%, with etched edges and some ondulose extinction. All olivine shows ubiquitous alteration to smectite along fractures and crystal boundaries, and occasionally to iddingsite. Calcite amygdlaes are up to 1 mm, < 1 modal%, do not show sharp boundaries with the ground mass, and probably represent original glass inclusions lost and filled by a secondary mineral. Ocellar reaction features are often composed solely of augite, with a very fine outer layers (crystals < 0.05 mm) and cores that are prismatic, radial and coarser. They may also contain glass inclusions and clearly less and finer opaques than the groundmass. Other ocelli are made solely of equant olive < 0.2 mm. Augite ocelli tend to be rounded whilst olivine ones tend to be irregular in shape. Some ocelli (one example reaching 2 cm) are layered, with radial olivine in their cores, followed by augite, and large late interstitial or spherulitic plagioclase (up to 1 mm) concentrated at the edges and elongate opaque clusters up to 0.5 mm. These are clearly the reaction products of a resorbed/re-melted peridotitic xenolith.

Notes: Some of the rounded ocelli could be the alteration products immiscible melts. Olivine ocelli are very similar to the alteration of orthopyroxene seen in other samples. Overall, olivine is heavily altered throughout the sample. Ocelli are relatively large and modal% was not estimated (one grain with 2 cm represents around 5% of the entire thin section). The groundmass with plagioclase and titanaugite in similar proportions and some olivine indicates an alkali basalt, in accordance with the major element analysis.

15BP6-12a, *two thin-sections* (Olivine alkali basalt): Porphyritic hypocrystalline with crypto- to microcrystalline groundmass containing olivine, plagioclase, augite and opaques. Phenocrysts of olivine and accessory microphenocrysts of titanaugite. Xenocrysts, xenoliths and glass inclusions.

Groundmass is moderately altered and somewhat heterogeneous in terms of granularity. Olivine phenocrysts are subhedral to euhedral, up to 2 mm, 10-15 modal% and seriate with the groundmass. Accessory titanaugite microphenocrysts are subhedral and up to 0.5 mm. Olivine xenocrysts are anhedral to subhedral, up to 10 mm, 5-7 modal%, with etched boundaries, resorption embayments and occasional ondulose extinction. All olivine show minor alteration to smectite. Xenocrysts and xenoliths include also orthopyroxene, diopside and one greenish brown anhedral spinel. Orthopyroxene is usually heavily altered to microcrystalline olivine clusters (sometimes completely, forming ocelli of irregular shape) and diopside shows thinner reaction coronas or sieve texture. Glass inclusions have often devitrified to plagioclase (often in spherulitic texture) and represent 3-5 modal%. They do not have sharp boundaries with the groundmass and sometimes have green augite

crystals (equant or prismatic and < 0.1 mm) growing close to their walls (often radially). Groundmass opaques are anhedral, < 0.05 mm and 5-7 modal%. Xenoliths are large and modal% was not estimated (one grain alone is 2 cm).

Notes: The sample has good xenolith examples and gives a better idea of reaction textures observed in other samples, especially the reaction of orthopyroxene to form olivine and the possibility that diopside crystals could also be reacting. The crypto- to microcrystalline texture of the groundmass makes it difficult to assess the level of alteration. The presence of plagioclase and augite in the groundmass apparently in similar proportions together with olivine phenocrysts indicate an alkali basalt, in accordance with the major element analysis.

15BP6-12b (Very altered vesicular nepheline olivine alkali basalt): Porphyritic hypocrystalline with crypto- to microcrystalline groundmass containing augite, plagioclase and possibly nepheline, and also opaques. Phenocrysts and microphenocrysts of olivine and augite. Vesicles and glass inclusions.

Groundmass augite occurs in poikilitic texture with plagioclase and possibly nepheline oykocrysts up to 5 mm. Opaques are anhedral, seriate, up to 0.5 mm and 5-7 modal%. Vesicles and glass inclusions are rounded or irregular, up to 1 mm and 5-7 modal%. Sometimes the glass is just lining the cavities. Microphenocrysts and phenocrysts of olivine and titanaugite are seriate with the groundmass. Olivine phenocrysts are anhedral (often rounded) up to 15 mm, 10-15 modal%, and completely altered to iddingsite except for larger crystals, which are only altered along the rims. These could potentially include xenocrysts. Titanaugite phenocrysts are anhedral to subhedral, up to 2 mm, 5-7 modal%, may occur as glomerocrysts and contain strong sieve texture, often with altered or bright green cores.

Notes: This is a strongly altered sample, and the olivine likely include xenocrysts as in other samples, but the levels of alteration make it difficult to confirm. This sample came from a very small leucocratic vein, and is not be included in the overall analysis. The groundmass with augite and oikocrysts of plagioclase and nepheline, and olivine phenocrysts indicate a nepheline olivine alkali basalt, but the major element analysis sets it as a phonotephrite as a result of its strong alteration.

15BP6-13 (Olivine alkali basalt): Porphyritic holocrystalline with fine-grained groundmass containing olivine, titanaugite, plagioclase and opaques. Phenocrysts of olivine.

Groundmass comprises titanaugite prisms (dominant) up to 0.5 mm, may be zoned and sometimes occur as radial glomerocrysts, with plagioclase growing in between them clearly as a later phase. Olivine are 0.1-2 mm, mostly euhedral, 15-20 modal% and include phenocrysts seriate with the groundmass. They also show very little alteration to smectite, may be skeletal and occur as glomerocrysts. Opaques are anhedral, up to 0.5 mm and 5-7 modal%.
Notes: Clear alkaline crystallisation sequence with titanaugite before plagioclase. Sample in very good condition with virtually no alteration. The groundmass with titanaugite and interstitial plagioclase, and olivine phenocrysts indicate an alkali basalt, in accordance with the major element analysis.

15BP7-14 (Olivine tholeiitic basalt): Virtually aphyric hypocrystalline with fine-grained groundmass containing dark glass, olivine and plagioclase. Ubiquitous vesicles.

Olivine are subhedral to euhedral, up to 1 mm, seriate (1-2% microphenocrysts) and strongly altered to iddingsite and smectite, with virtually complete substitution, especially in the larger crystals. Vesicles are irregular in shape (although larger ones are circular), 0.3-5 mm, 5-7 modal% and contain a cryptocrystalline film of alteration along their walls.

Notes: The dark glassy groundmass hinders the identification of opaques. Pyroxenes must be present in the groundmass glass. The presence of only plagioclase and olivine in the groundmass indicates a subalkaline basalt. The major element analysis puts it as a basaltic andesite, but this is strange considering olivine is still crystallising from the groundmass and no pyroxenes have appeared.

15BP7-15 (Olivine-phyric nephelinite): Porphyritic holocrystalline with heterogeneous crypto- to microcrystalline groundmass containing augite, nepheline and opaques. Phenocrysts of olivine and microphenocrysts of augite and olivine. Ocellar reaction features and xenocrysts.

Groundmass is heterogeneous ranging from very crypto- to microcrystalline in irregular domains. Augite microphenocrysts are subhedral, mostly prisms and laths, up to 1 mm, seriate with the groundmass, 1-2 modal% and with common anomalous birefringence. Olivine phenocrysts and microphenocrysts are subhedral to euhedral, up to 1.5 mm, seriate with the groundmass, 7-10 modal% and may be skeletal. Ocellar features are up to 1.5 mm, irregular in shape and contain microcrystalline olivine and opaques (the latter clearly smaller and in less quantity than those in the groundmass). Xenocrysts include anhedral olivine, orthopyroxene, diopside and one spinel crystal, all up to 3 mm, very irregular shapes with etched boundaries, resorption embayments and common ondulose extinction. They probably represent around 5-7 modal%, but it is difficult to assess as they mingle with phenocrysts. There is little alteration of olivine to smectite. Opaques are anhedral to subhedral and 5-7 modal%.

Notes: The ocelli are reminiscent of orthopyroxene reactions to form olivine observed in other samples. The presence of only nepheline and augite in the groundmass, with phenocrysts of olivine indicates a nephelinite, in accordance with the major element analysis.

15BP7-16 (Olivine alkali basalt): Porphyritic holocrystalline with somewhat heterogeneous microcrystalline groundmass containing plagioclase, olivine, titanaugite and opaques. Phenocrysts and microphenocrysts of titanaugite and olivine. Ocellar reaction features and xenocrysts.

Titanaugite phenocrysts and microphenocrysts are euhedral, up to 3 mm, somewhat seriate with the groundmass, ~1 modal%, often with sieve texture with a non-sieved overgrowth, may be zoned and have rare glomerophiric texture. Olivine phenocrysts and microphenocrysts are seriate with the groundmass, mostly subhedral, up to 0.5 mm and 15-20 modal%. Olivine xenocrysts are anhedral, up to 5 mm, 10-15 modal%, with resorbtion embayments, occasional ondulose extinction and etched boundaries. Olivines show little alteration to smectite or very rare iddingsite. Ocellar reaction features are up to 2 mm, generally rounded, free of opaques and monomineralitic, containing microcrystalline to cryptocrystalline augite or olivine; clusters of the latter, however, may be rimmed by opaques, have an irregular shape and rare green glass (altered) cores. Rare orthopyroxene anhedral xenocrysts, up to 2 mm, very resorbed and with microcrystalline olivine coronas. Opaques are anhedral, < 0.1 mm and 10-15 modal%.

Notes: Titanaugite sieve textures and overgrowths are particularly clear in this sample. Coronas over orthopyroxene are more microcrystalline than in other samples. The ubiquitous presence of plagioclase in the groundmass, together with titanaugite and olivine indicates an alkali basalt, in accordance with the major element analysis.

15BP8-17 (Titanaugite-phyric basanite): Porhyritic hypocrystalline (virtually holocrystalline) with microcrystalline groundmass containing titanaugite, olivine, plagioclase and opaques. Phenocrysts and microphenocrysts of olivine, titanaugite and plagioclase. Devitrified glass inclusions and ocellar reaction features.
The groundmass is dominated by titanaugite and occasional microcrystalline and glassy material. Devitrified glass inclusions are substituted by plagioclase, up to 0.5 mm, contain small titanaugite crystals and mostly don't show a sharp boundary with the groundmass. Titanaugite phenocrysts and microphenocrysts are subhedral to euhedral, up to 2 mm, somewhat seriate with the groundmass, 15-20 modal%, zoned, may poykilitically enclose olivine clusters and form glomerocrysts. Olivine phenocrysts and microphenocrysts are subhedral to euhedral, up to 6 mm, somewhat seriate with the groundmass, 10-15 modal% and may be skeletal. Some rare olivine crystals are anhedral, with very irregular shapes, etched boundaries and ondulose extinction, and might be xenocrysts. Overall there is little alteration of the olivine to smectite. Ocellar reaction features are up to 2 mm, < 1 modal%, monomineralitic, free of opaques, irregular in shape and containing microcrystalline olivine. Occasionally they are layered, with augite rims and/or glassy cores. Opaques are anhedral to subhedral and 10-15 modal%.

Notes: The presence of xenocrysts in this sample is dubious when compared with the other samples so far. There are only a few phenocrysts with the right characteristics and little ocellar reaction features. The presence of plagioclase in a groundmass dominated by titanaugite, and phenocrysts of titanaugite and olivine indicate a basanite, in accordance with the major element analysis.

15BP8-18, *three thin sections* (Olivine alkali basalt): Porphyritic hypocrystalline (virtually holocrystalline) with microcrystalline groundmass containing olivine, titanaugite, plagioclase and opaques. Phenocrysts and microphenocrysts of olivine and titanaugite. Glass inclusions, ocellar reactions features and xenocrysts or xenoliths.

Groundmass dominated by titanaugite with devitrified glass inclusions substituted by plagioclase that is sometimes spherulitic. The latter are up to 0.5 mm, with irregular rounded shapes, may contain small titanaugite crystals and boundaries that range from sharp to merging with the groundmass. Titanaugite phenocrysts and microphenocrysts are subhedral to euhedral, up to 4 mm, seriate with the groundmass, 15-20 modal%, zoned (compositionally and in terms of opaque inclusions), may poikilitically enclose olivine clusters, have sieve texture and form glomerocrysts. Olivines phenocrysts and microphenocrysts are subhedral to euhedral, up to 2 mm, seriate with the groundmass and 10-15 modal%. Olivine xenocrysts are anhedral, up to 3 mm, represent < 2 modal% and have etched boundaries. Overall, there is little olivine alteration to smectite. Ocellar reaction features tend to be up to 3 mm and layered, which includes an outer layer of brown glass, crypto- to microcrystalline augite (< 0.1 mm) and somewhat larger titanaugite, and a core of radial olivine up to 0.3 mm and brown glass, all with little or no opaques (very fine). Groundmass opaques are subhedral to euhedral and 10-15 modal%.

Notes: The three thin sections are very similar and the freshest one was chosen for description. In the other thin sections there is strong alteration of olivine to iddingsite in some places. The zoned glassy ocelli reinforce the idea of re-melted xenoliths or xenocrysts. Alternatively, they could indicate immiscible melt material that cooled faster than the surrounding matrix either during mixing or extrusion. Sample very similar to 15BP8-17 (from the same locality) but seem to have scarcer plagioclase. The presence of titanaugite and plagioclase in the groundmass, with phenocrysts of olivine and titanaugite indicate an alkali basalt, in accordance with the major element analysis.

15BP9-19a (Phonolite): Porphyritic holocrystalline with strongly altered microcrystalline groundmass containing sanidine (dominant), aegirine and opaques. Phenocrysts of sanidine, titanaugite, amphibole and possibly nepheline. Clusters of microcrystalline aegirine. Accessory sphene and large opaques. Calcite and cryptocrystalline alteration products that likely include sericite.

Sanidine phenocrysts (20-25 modal% and sometimes glomerophiric) and groundmass laths are subhedral to euhedral, respectively reaching 5 and 0.5 mm and strongly altered to sericite. The groundmass also shows areas with calcite infilling. Titanaugite phenocrysts are up to 2 mm, < 2 modal%, with aegirine coronas, very rounded (possibly resorbed) and may be glomerophyric. Amphibole phenocrysts are dark brown, lightly pleochroic, with very high or anomalous birefringence and likely to be kaersutite. They are up to 2 mm, < 2 modal%, strongly resorbed and with coronas of aegirine and opaques, the latter sometimes substituting the whole crystal. Aegirine microcrystalline clusters are irregular (almost like blebs), up to 1.5 mm, 2-3 modal% and often associated with clusters of opaques. Accessory sphene is subhedral to euhedral and up to 1 mm. Accessory nepheline strongly altered and difficult to assess. Opaques are < 0.05 mm, anhedral and 3-5 modal%, with occasional mm-scale anhedral crystals or clusters.

Notes: Amphibole interpreted as kaersutite, although in the literature a Ti-richterite interpretation seems to predominate. Overall the rock is strongly altered. The levels of alteration make it difficult to ascertain the presence of nepheline amongst the phenocrysts, but because it is present in other samples from the same locality, it reinforces the interpretation of some phenocrysts as nephelines. The sample comes from the same locality as 15BP9-19b and c. The titanaugite and amphiboles are obviously in disequilibrium. The aegirine microcrystalline clusters likely represent the complete recrystallization of amphiboles or titanaugite. The groundmass dominated by sanidine, with some aegirine, and phenocrysts of sanidine and nepheline indicate a phonolite, in accordance with the major element analysis.

15BP9-19b, *two thin-sections*: As 15BP9-19a but with stronger alteration and weathering. These thin-sections illustrate a typical vein found in the area, with analcime, calcite, smectite and cryptocrystalline infillings.

Notes: The veined sample is more altered than vein-free specimens.

15BP9-19c (Phonolite): Porphyritic holocrystalline with microcrystalline groundmass with light trachytic texture containing sanidine (dominant), aegirine and nepheline. Phenocrysts and microphenocrysts of sanidine and nepheline. Phenocrysts of amphibole and haüyne/nosean. Microcrystalline clusters of aegirine. Devitrified glass inclusions. Accessory sphene and opaques. Calcite and microcrystalline alteration products.

Glass inclusions are irregular, up to 2 mm, 1-2 modal%, with no sharp boundaries with the groundmass and contain laths of sanidine. They are devitrified and substituted by K-feldspar apparently. Sanidine phenocrysts and microphenocrysts are subhedral to euhedral, up to 5 mm, seriate with the groundmass, 15-20 modal%, often glomerophyric and generally lightly but pervasively fractured (with alteration along them). Nepheline phenocrysts are euhedral, up to 3 mm, seriate with the groundmass and 3-5 modal%. Amphibole phenocrysts are dark brown, pleochroic, with very high or anomalous birefringence and likely to be kaersutite. They are up to 3 mm, < 2 modal%, strongly resorbed and with coronas of aegirine and opaques. Aegirine microcrystalline clusters are irregular (almost like blebs), up to 1 mm and 2-3 modal% and probably result from a full reaction of amphibole. Haüyne/nosean phenocrysts are anhedral to subhedral, up to 1.5 mm and 1-2 modal%. Accessory sphene is rounded or euhedral and up to 0.5 mm. Accessory opaques are anhedral and mostly < 0.1 mm.

Notes: The haüyne/nosean crystals show weak birefringence in their cores, which is sometimes described as a characteristic of inclusion-rich nosean. The light and dark phonolites from the Caruru quarry (respectively 15BP9-19a and 15BP9-19c) come from different depths in the quarry and seem to present different assemblages: i.e. the dark phonolite is from shallower levels and contain nosean, whereas the deeper samples are lighter in colour, contain resorbed and reacting crystals of titanaugite. A large (10 cm) euhedral K-feldspar megacryst was found in the quarry. The groundmass dominated by sanidine, with aegirine and nepheline, together with phenocrysts of sanidine and nepheline indicate a phonolite, in accordance with the major element analysis.

15BP10-20, *two thin sections* (Aegirine-phyric phonolite): Porphyritic holocrystalline with strongly altered crypto- to microcrystalline groundmass containing nepheline and sanidine. Phenocrysts of nepheline, aegirine and rare sanidine. Some alteration material and rare devitrified glass inclusions.

The groundmass is heterogeneous in its texture, granularity and weathering, showing alteration to microcrystalline or reddish brown to opaque material. Devitrified glass inclusions are rounded, irregular in shape, may contain aegirine laths, have no sharp boundaries with the groundmass and are substituted by very low birefringence material. Nepheline phenocrysts are euhedral, up to 0.5 mm, 3-5 modal%, may be zoned and substitute by isotropic material (likely analcime or a sodalite mineral) in the more altered domains. Sanidine phenocrysts are rare, subhedral, prismatic, 1-7 mm, strongly resorbed and often with sieve textures. Aegirine phenocrysts appear as branching dendritic crystals, up to 5 mm, 3-5 modal% and postdate nepheline phenocrysts.

Notes: Second thin section much more altered, with the nepheline sometimes altered to almost isotropic material showing hourglass zoning patterns. Ubiquitous nepheline and relatively scarce sanidine takes it to the blurry phonolite-foidite boundary, in accordance with major element analysis.

15BP10-21a (Aegirine-phyric phonolite): Porhyritic holocrystaline with microcrystalline to fine-grained groundmass with trachytic texture containing sanidine (dominant) and nepheline. Phenocrysts and microphehenocrysts of nepheline, aegrine and sanidine. Accessory amphibole.

Nepheline phenocrysts are euhedral, up to 2.5 mm, 5-7 modal% and occasionally zoned. Sanidine phenocrysts are subhedral to euhedral, prismatic, up to 5 mm, 2-3 modal%, with occasional ondulose extinction, no twinning and may be weakly or moderately resorbed or altered, especially along

boundaries and fractures. Aegirine phenocrysts are branching and dendritic, pervasively following the trachytic texture of the groundmass, up to 5 mm and 7-10 modal%. One resorbed 3 mm phenocryst of amphibole that is dark brown, pleochroic, with a corona of aegirine and very high or anomalous birefringence, which likely to be kaersutite.

Notes: The sample is very pristine, but some sanidine phenocrysts seem to show evidence of being strained, and together with the lack of twinning, these could actually be xenocrysts of a different K-feldspar. A groundmass with sanidine and nepheline, together with phenocrysts of nepheline and aegirine indicate a phonolite, in accordance with the major element analysis.

15BP10-21b (Aegirine phonolite): Porphyritic holocrystaline with very altered microcrystalline felty groundmass containing sanidine (dominant), nepheline and aegirine. Phenocrysts of sanidine, nepheline, amphibole and augite. Microphenocrysts os aegirine. Devitrified or altered glass inclusions. Accessory sphene and opaques.

Groundmass shows strong alteration to cryptocrystalline material. Glass inclusions are irregular in shape (up to 3 mm) or vein like, < 1 modal% and mostly substituted by nepheline or calcite alteration. Sanidine phenocrysts are euhedral prisms, up to 7 mm, may be glomerophyric, with ondulose extinction and strongly altered (especially along boundaries and fractures). Nepheline phenocrysts are euhedral, prismatic or equant, up to 5 mm, strongly altered but much less prone to show ondulose extinction (although some crystals do have it). Together, sanidine and nepheline phenocrysts represent 10-15 modal%. Aegirine microphenocrysts are prismatic, with incipient branching dendritic texture, ≤ 0.5 mm and 3-5 modal%. Amphiboles are strongly resorbed, dark brown with very high or anomalous birefringence and are likely kaersutite. They are up to 1 mm, 1-2 modal% and have aegirine coronas. Aegirine also forms clusters with opaques that are probably the result of full amphibole reaction. Opaques are subhedral to euhedral, 0.1-1.5 mm. Sphene is subhedral to euhedral and up to 0.6 mm. Rare resorbed and rounded augite glomerocrysts 2 mm across and with aegirine coronas.

Notes: The proportions of nepheline in the groundmass cannot be ascertained due to the size of crystals and levels of alteration. Although from the same locality as 15BP20-21a, this sample is different, lacking the trachytic texture and producing augite glomerocrysts, more amphibole, less aegirine and more accessory minerals. The groundmass with sanidine and nepheline, together with nepheline, sanidine and aegirine phenocrysts indicate a phonolite, in accordance with the major element analysis.

15BP10-21c (Aegirine phonolite): Veined heterogeneous sample with porphyritic microcrystalline groundmass containing sanidine, nepheline and aegirine. Microphenocrysts and rare phenocrysts of the same minerals. Veins are filled with brecciated material containing fine- to medium-grained clasts of hornblende, biotite, aegirine and apatite, as well as orthoclase, anorthoclase and possibly plagioclase, all in a crypto- to microcrystalline groundmass containing sanidine, aegirine and nepheline. Microcrystalline domains in the veined material are finer than the dominant groundmass, and contain microphenocrysts of nepheline.

Veins are lined and often defined by microcrystalline aegirine, and include clasts of the host rock. Coarser clasts are sub-angular to sub-rounded, very altered, with etched boundaries and with granular texture in multimineralitic examples. Sometimes they have thin coronas (< 0.1 mm) of aegirine microcrystalline prisms. Phenocrysts and microphenocrysts in the host rock include nepheline, sanidine and aegirine. Nepheline is euhedral, zoned, up to 1.5 mm and 5-7 modal%. Sanidine is subhedral, up to 3 mm, 3-5 modal%, moderately to strongly altered, with ondulose extinction and may form glomerocrysts. Aegirine is dendritic, up to 1 mm and 5-7 modal%. Microphenocrysts in the groundmass of vein material include subhedral nepheline, < 0.4 mm and 2-3 modal%.

Notes: Veined material is uncannily similar to the amphibole nodules found in Fernando de Noronha, although their appearance in a phonolite is unusual. It is difficult to ascertain if the sanidine glomerocrysts, which contain the most altered sanidine crystals in the groundmass, are part of the groundmass or if they are xenoclasts. It seems that the vein material intruded the host rock whilst still hot and not fully solid (i.e. crystal much). The presence of sanidine, nepheline and aegirine both as

phenocrysts and in the groundmass indicate a phonolite. This sample was not analysed for major or trace elements, due to its strong heterogeneity.

15BP10-22 (Phonolite): Virtually aphyric holocrystaline with fine-grained, moderately altered groundmass (with some cryptocrystalline material) with light trachytic texture containing sanidine (dominant), nepheline and aegirine. Accessory phenocrysts of sanidine and microphenocrysts of amphibole and sphene.

Sanidine phenocrysts are subhedral prisms up to 2.5 mm. Amphibole microphenocrysts are anhedral, up to 1.5 mm, strongly resorbed and with coronas of aegirine and opaques, sometimes causing complete substitution of the crystals. They are brown, with very high birefringence and are probably kaersutite. Sphene is rounded and up to 0.5 mm.

Notes: The virtual absence of phenocrysts is unusual relative to the other samples. A groundmass with sanidine, nepheline and aegirine indicates either a trachyte or a phonolite, but the almost complete absence of phenocrysts makes it difficult to place it either as one or the other. The major element analysis puts it as a phonolite.

15BP10-23 (Aegirine phonolite): Porphyritic holocrystalline with fine-grained, moderately altered groundmass with light trachytic texture containing sanidine (dominant), nepheline, aegirine and little opaques. Phenocrysts of sanidine and nepheline. Microphenocrysts of aegirine and opaques. Accessory sphene.

Sanidine phenocrysts are prismatic, subhedral to euhedral, up to 5 mm, 7-10 modal%, moderately altered and may be glomerophyric. Nepheline phenocrysts are tabular, subhedral to euhedral, up to 1 mm and ≤ 1 modal%. Aegirine microphenocrysts are subhedral, prismatic or equant, 0.2-0.5 mm, 1-2 modal% and may be zoned. Opaques microphenocrysts are subhedral, 0.1-1 mm, 1 modal% and are often associated with aegirine microphenocrysts. Sphene is euhedral and up to 0.5 mm.

Notes: Although levels of weathering and alteration are only moderate, they are pervasive and very homogeneous throughout the sample and include both groundmass and phenocrysts. The trachytic texture has the largest sanidine laths in the Mecejana assemblage. The groundmass with sanidine, nepheline and aegirine, and phenocrysts of sanidine and nepheline indicate a phonolite, in accordance with the major element analysis.

15BP11-24 (Olivine alkali basalt): Porphyritic hypocrystalline (virtually holocrystalline) with mostly cryptocrystalline groundmass containing plagioclase, augite, olivine and opaques. Phenocrysts and microphenocrysts of olivine. Ocellar reaction features that include glass. Possibly xenocrysts of plagioclase (and possibly another feldspar), orthopyroxene, augite/diopside, one spinel and possibly olivine.

Olivine phenocrysts and microphenocrysts are subhedral to euhedral, up to 2 mm, somewhat seriate with the groundmass, 10-15 modal% and often altered to smectite. Possible xenocrysts are anhedral, often with irregular straight-sided faces, up to 2 mm, 2-3 modal%, have etched boundaries and include plagioclase and augite/diopside with sieve textures, and possibly olivine. One spinel xenocryst, 0.5 mm, rounded and dark green in ppl. Anhedral opaques in the groundmass are ubiquitous and represent 25-30 modal%. Layered ocellar features are rounded, up to 3 mm, 2-3 modal%, and have an outer layer of microcrystalline augite with glass and may include augite and olivine microphenocrysts (up to 0.2 mm), followed by radial olivine and sometimes cores of brown glass with microcrystalline needles, or an orthopyroxene xenocryst. Sometimes, the glass in the ocellar features has been replaced by calcite or zeolites.

Notes: The ocellar features in the sample are mostly small, but ubiquitous. The disequilibrium of plagioclase and orthopyroxene xenocrysts is obvious. The olivine phenocrysts and microphenocrysts are very small, giving the rock an almost aphyric look. The presence of augite a plagioclase in the groundmass, but with plagioclase xenocrysts in disequilibrium and olivine phenocrysts indicate an alkali basalt, in accordance with the major element analysis.

15BP12-25 (Olivine-phyric nephelinite): Porphyritic holocrystalline with microcrystalline groundmass containting augite, nepheline, olivine and opaques. Phenocrysts and microphenocrysts of olivine and titanaugite. Occasional alteration to smectite. It is possible that some rare olivine xenocrysts are also present. One amygdale.

Olivine phenocrysts and microphenocrysts are subhedral to euhedral, up to 2.5 mm, 5-7 modal%, seriate with the groundmass and often skeletal. Some rare examples are very anhedral, with etched edges and occur in clusters with apparent granular texture, and might be xenocrysts. Olivine shows some alteration to smectite. Titanaugite phenocrysts and microphenocrysts are subhedral to euhedral, up to 1.5 mm, 3-5 modal%, seriate with the groundmass and occasionally forming glomerocrysts or showing polysynthetic twinning. They are often zoned, with green cores showing very strong sieve textures and opaque inclusions, contrasting with clean titanaugite overgrowths. Groundmass opaques are anhedral and represent 20-25 modal%, but opaques also occur as rare anhedral, rounded and weakly resorbed xenocrysts or clusters of smaller crystals up to 0.5 mm. One amygdale 2 mm long, with irregular shape, no sharp boundary with the groundmass and filled with spherulitic zeolites that likely substitutes and original glass inclusion.

Notes: Possible olivine xenocrysts are rare. No plagioclase can be identified and the presence of nepheline in the groundmass and olivine phenocrysts would indicate a nephelinite, in accordance with the major element analysis.

15BP12-26 (Olivine alkali basalt): Porphyritic holocrystalline with microcrystalline to fine-grained groundmass containing plagioclase, titanaugite, olivine and opaques. Phenocrysts of olivine and titanaugite. Ocellar reaction features and xenocrysts.

Groundmass opaques represent 7-10 modal%. Olivine phenocrysts are subhedral to euhedral, seriate with the groundmass, up to 1 mm, 10-15 modal% and with little alteration to smectite. Olivine xenocrysts are rounded or anhedral, mm-scale (up to 5 mm), 3-5 modal%, have etched boundaries, resorption embayments, rare ondulose extinction and moderate alteration to smectite. Sometimes they are still attached to strongly reacting orthopyroxene. Titanaugite phenocrysts are subhedral to euhedral, up to 5 mm, 3-5 modal%, often zoned and with sieve texture in their cores, which may also be green, and clean titanaugite overgrowths. Opaques also occur as clusters of crystals, which are rounded, up to 1 mm and in one example enclosure a round, anhedral spinel crystal 0.5 mm. Ocellar reaction features are irregular in shape, with no sharp boundaries, up to 5 mm, 1-2 modal% and free from opaques. They are also layered, with an outer zone of microcrystalline augite that may include microphenocrysts of titanaugite and olivine, followed by radial olivine, and sometimes cores containing either glass or orthopyroxene.

Notes: The spinel crystal is similar to the one in 15BP12-25. Orthopyroxene reactions are clear in this sample. The margins of the ocelli have no sharp boundary with the groundmass. The presence of plagioclase and augite in the groundmass and olivine phenocrysts indicates an alkali basalt, in accordance with major element analysis.

Fernando de Noronha

FN01-01 (Trachyte): Porphyritic holocrystalline with microcrystalline trachytic groundmass containing sanidine and opaques. Phenocrysts of sanidine and anorthoclase, sodalite-group minerals and one aegerine crystal. Accessory nepheline, sphene and opaques.

Sanidine phenocrysts are subhedral to euhedral, 0.3-5 mm, 3-5 modal%, sometimes occurring as overgrowths over anorthoclase and often much fractured and with internal cavities. Sodalite-group phenocrysts are mostly euhedral, 0.3-1.5 mm and 3-5 modal%. Accessory nepheline occurs as microphenocrysts that are mostly euhedral, < 0.7 mm and very weathered and pitted. Opaques (anhedral to subhedral) and sphene (mostly euhedral) are 0.2-0.5 mm, < 1 modal% and often associated with each other. One euhedral microphenocryst of aegerine, 0.5 mm.

Notes: This is the same rock as FN01-02 although the latter seems to have produced more aegerine and no nepheline. The identification of nepheline, however, is difficult, and based on the straight extinction of rectangular crystals that are relatively thin and small. Dominance of sanidine both in the groundmass and as phenocrysts, small amounts of ferromagnesian minerals and accessory nepheline indicate a borderline trachyte.

FN01-02 (Trachyte): Porphyritic almost aphyric, holocrystalline with microcrystalline trachytic groundmass containing sanidine (dominant), aegerine and opaques. Phenocrysts of sanidine and microphenocrysts of aegerine and opaques. Zeolite pseudomorphs after sodalite-group minerals. Accessory sphene and sodalite-group minerals.

Groundmass shows flow orientations. Sanidine phenocrysts are subhedral to euhedral, 0.4-1 mm, 2-3 modal% and sometimes grow over previous anorthoclase crystals. Aegerine microphenocrysts are mostly euhedral, 0.1-0.8 mm, around 1 modal%, occasionally zoned (subtle) or with amphibole cores. Accessory sphene microphenocrysts are mostly euhedral, 0.1-1.5 mm and just under 1 modal%. Opaque microphenocrysts are anhedral to subhedral, 0.1-1 mm, around 1 modal% and occasionally associated with orange-yellow alteration material. Microphenocrysts of aegerine, opaques and sphene sometimes occur together as glomerocrysts. Zeolite pseudomorphs are subhedral to euhedral, tabular or hexagonal, 0.1-0.8 mm, 1-2 modal%, contain micro inclusions and are sometimes poikilitically enclosed within sanidine phenocrysts. These are likely substituting sodalite-group minerals. One sodalite-group subhedral microphenocryst was also identified.

Notes: The opaque-aegerine-sphene associations are probably the result of break down reaction of kaersutite. Dominance of sanidine both in the groundmass and as phenocrysts, small amounts of ferromagnesian minerals and absence of nepheline indicates a trachyte.

FN02-03 (Sodalite/haüyne/nosean-phyric phonolite): Porphyritic holocrystalline with crypto- to microcrystalline groundmass with incipient trachytic texture, and containing sanidine (dominant), aegerine and opaques. Phenocrysts of sanidine, nepheline and sodalite-group minerals, and microphenocrysts of aegerine and kaersutite. Accessory sphene.

Sanidine phenocrysts are mostly euhedral, lamellar, 1-8 mm and 2-3 modal%. Nepheline phenocrysts are mostly euhedral, 1-3 mm, with occasional crystals < 1 mm, 3-7 modal% and occasionally together as glomerocrysts or containing poikilitically enclosed small crystals of aegerine, sphene or sodalite-group minerals. Aegerine microphenocrysts are anhedral to subhedral, 0.1-0.5 mm and occasionally with titanaugite cores and zoned. Sodalite-group phenocrysts are anhedral to subhedral, 0.2-2 mm, 2-3 modal% and with ubiquitous alteration to calcite. Kaersutite microphenocrysts are anhedral to subhedral, 0.3-3 mm (mostly < 0.5 mm), 1-2 modal% and often with aegerine overgrowths and/or opaque coronas, in the latter case sometimes causing complete substitution. Accessory sphene is euhedral and 0.1-0.5 mm.

Notes: The nepheline phenocrysts together with dominant sanidine both in the groundmass and as phenocrysts indicate a phonolite. The breakdown of amphibole maybe suggests that these evolved rocks spent some time in shallow reservoirs outside of the amphibole stability field.

FN03-04 (Sodalite/haüyne/nosean-phyric phonolite): Porphyritic holocrystalline with crypto- to microcrystalline groundmass with trachytic texture containing sanidine (dominant) and aegerine. Phenocrysts of sanidine, nepheline and sodalite-group minerals. Microphenocrysts of aegerine and kaersutite. Accessory sphene and opaques.

Sanidine phenocrysts are mostly euhedral, 1-3 mm and 1-2 modal%. Nepheline phenocrysts are mostly euhedral, 0.2-4 mm (mostly in the larger end of the range), 3-7 modal%, sometimes with strong cleavage or zoning, may occur as overgrowths on sodalite-group minerals and may contain inclusions of aegerine, sphene, haüyne/nosen and opaques. Aegerine microphenocrysts anhedral (often rounded) to subhedral (lamellar), 0.1-0.5 mm, 1-2 modal% and may have titanaugite cores. Sodalite-group phenocrysts are anhedral to subhedral, 0.3-2 mm, 1-2 modal%, with common alteration to calcite and rare inclusions of relatively large (0.5-1 mm) opaques or euhedral sphene. Kaersutite microphenocrysts are anhedral, 0.1-1.5 mm, around 1 modal% and may have aegerine

and/or opaque coronas, in the latter case sometimes causing complete substitution. Accessory sphene is euhedral and 0.2-0.8 mm.

Notes: Sample very similar to FN02-03. Nepheline phenocrysts together with sanidine both in the groundmass and as phenocrysts indicate a phonolite.

FN04-05 (Olivine alkali basalt): Porphyritic holocrystalline with microcrystalline groundmass containing augite, plagioclase (sometimes poikilitically enclosing augites) and opaques all in roughly similar proportions. Phenocrysts of olivine and microphenocrysts of titanaugite.

Olivine phenocrysts are subhedral to euhedral, 0.1-3 mm, seriate, 7-10 modal%, always with iddingsite coronas that often cause complete mineral substitution of smaller crystals, occasional alteration to smectite along fractures and occasional skeletal textures. Titanaugite microphenocryts are mostly subhedral, lamellar to tabular, 0.1-0.5 mm, 2-3 modal%, occasionally zoned and forming glomerocrysts.

Notes: Crystallisation of augite followed by plagioclase, and olivine phenocrysts indicate an alkali basalt.

FN04-06 (Olivine alkali basalt): Porphyritic hypocrystalline with heterogeneous crypto- to microcrystalline groundmass containing augite, opaques and possibly plagioclase. Highly vesicular and sometimes with altered glass inclusions. Phenocrysts of olivine. Microphenocrysts of titanaugite.

Vesicles are rounded and often interconnected, with total cavity sizes 0.1-6 mm and 5-7 modal%. Glass inclusions line or completely or partially fill some of the vesicles, are pale brownish yellow and mostly altered to low birefringence material that could indicate some devitrification. Olivine phenocrysts are mostly euhedral, 0.1-3 mm, seriate, 3-5 modal%, with some rare skeletal textures, ubiquitous iddingsite alteration along boundaries (occasionally along fractures as well) and occasionally forming glomerocrysts. Titanaugite microphenocrysts are mostly subhedral, lamellar, < 0.5 mm, seriate with the groundmass, 5-7 modal%, often zoned and forming glomerocrysts that are mostly radial.

Notes: The presence or not of significant plagioclase in the groundmass would be the difference between an alkali basalt and a basanite. The major element analysis points to the former though. This is part of the highest sequences of the Quixaba Formation and all these rocks plot as alkali basalts to basanites, as opposed to the foidites to basanites of the lower lava sequences.

FN05-07 (Olivine alkali basalt): Porphyritic hypocrystalline with cryptocrystalline heterogeneous groundmass with some augite microlites, opaques and possibly plagioclase. Phenocrysts of olivine. Microphenocrysts of titanaugite. Ubiquitous irregular spaces in the groundmass filled with feldspars and analcime.

Groundmass contains domains that are elongated and very irregular in shape and merging with the groundmass (no sharp boundaries), sometimes with 'floating' microlites. They represent 3-5 modal%, are filled with feldspars (possibly both low-Ca plagioclase and K-feldspar) and analcime and sometimes contain bubbles. These are likely previous glass inclusions with more evolved melts that are now at different stages of devitrification. Olivine phenocrysts are subhedral to euhedral, 0.1-5 mm, seriate, 10-15 modal%, often skeletal and with iddingsite coronas that causes complete mineral substitution in smaller crystals. Titanaugite microphenocrysts are subhedral to euhedral laths, 0.1-0.5 mm, seriate, 7-10 modal% and occasionally zoned and forming glomerocrysts.

Notes: It is likely that this rock contained glass inclusions similar to FN04-06. The plagioclase-rich devitrified material and the major element chemical analysis indicate plagioclase in the groundmass. Heterogeneous and poor-quality groundmass due to outcrop weathering.

FN06-08 (Basanite): Porphyritic hypocrystalline with crypto- to microcrystalline (often with clear distinct domains) very heterogeneous groundmass containing augite and opaques. Devitrified glass domains and veins completely or partially filled with very low birefringence, almost isotropic

cryptocrystalline material (possibly leucite- or analcime-rich in composition) or, very rarely, nepheline or plagioclase. Highly oxidised olivine phenocrysts, and augite microphenocrysts and phenocrysts. Accessory opaques.

Olivine phenocrysts are subhedral to euhedral, 0.1-2 mm, seriate, 10-15 modal%, highly oxidised, often causing complete substitution of smaller crystals, and with rare iddingsite alteration along fractures. Augite phenocrysts are subhedral to euhedral, lamellar, 0.5-1 mm, 1-2 modal% and with some titaniferous content. Augite microphenocryst laths are anhedral to subhedral, 0.1-0.5 mm, 7-10 modal% and may form glomerocrysts (< 1 modal% and < 1 mm) of homogeneous size crystals around accessory opaques. Devitrified glass domains are irregular in shape but mostly sub-rounded, 0.1-3 mm and represent 7-10 modal% of microcrystalline domains but 25-30 modal% of cryptocrystalline ones. They probably indicate devitrified or altered glass. Veins are up to 0.3 mm thick. Accessory opaques are anhedral, < 1 mm and invariable associated with augite glomerocrysts.

Notes: Overall the rock is very heterogeneous, and the groundmass seems to be in poor condition. No plagioclase was identified except for small quantities in the devitrified material, which suggests a basanite (>10% modal olivine), in accordance with the major element analysis. Heterogeneous and poor-quality groundmass due to outcrop weathering.

FN07-09 (Basanite): Porphyritic hypocrystalline with microcrystalline groundmass containing titanaugite, opaques and nepheline oikocrysts. Devitrified glass domains completely or partially filled with very low birefringence, almost isotropic material (possibly leucite- or analcime-rich in composition), and containing accessory biotite. Phenocrysts of olivine and very rarely of titanaugite.

Groundmass nepheline grows poikilitically over titanaugite and opaques. Olivine phenocrysts are subhedral to euhedral, 0.2-4 mm, 10-15 modal%, often skeletal, always with a bright orange iddingsite altered rim that causes complete substitution of smaller crystals and sometimes with opaque coronas when close to larger glass domains. Titanaugite phenocrysts are subhedral, 0.5-1 mm and accessory. Devitrified glass domains are mostly round but may also be elongated and irregular in shape, 0.2-6 mm, 3-5 modal%, with no sharp boundaries with the groundmass and lined or filled with low birefringence microcrystalline material. Accessory biotite is anhedral, up to 0.4 mm and almost always associated with vesicles.
Notes: No plagioclase present. Very similar to FN04-05 but somewhat coarser. This sample should be classified as a nephelinite based on petrography, but major element analysis puts it as a borderline basanite (>10% modal olivine). There must be some groundmass plagioclase.

FN07-10 (Basanite): Porphyritic hypocrystalline with microcrystalline groundmass containing titanaugite, olivine, nepheline and opaques. Irregular glass domains completely or partially filled with very low birefringence, almost isotropic devitrified material (possibly leucite- or analcime-rich in composition), and containing accessory biotite. Phenocrysts of olivine and very rarely of titanaugite. Accessory plagioclase.

Olivine phenocrysts are subhedral to euhedral, 0.2-5 mm, 10-15 modal%, often skeletal, always with a bright orange iddingsite altered rim that causes complete substitution of smaller crystals, some smectite alteration along fractures and in crystal cores and sometimes with overgrowth of opaque microlites. Titanaugite phenocrysts are subhedral, 0.3-0.5 mm and accessory. Glass domains are mostly irregular in shape, 0.2-6 mm, 3-5 modal% and may be lined with radially growing feldspar or augite microlites. Accessory biotite is anhedral, up to 0.5 mm and almost always associated with devitrified glass.

Notes: Very similar to FN04-05 and, although somewhat finer-grained, to FN07-09. The clusters of microcrystalline augite are interpreted as late crystallising liquid domains. The small amounts of late plagioclase in a dominantly augite groundmass and olivine phenocrysts indicates a basanite (>10% modal olivine).

FN08-11 (Olivine-phyric nephelinite): Porphyritic holocrystalline with cryptocrystalline groundmass containing augite and opaques. Rare vesicles irregular in shape. Phenocrysts of olivine and, very rarely, titanaugite. Very rare possible olivine xenocrysts.

Olivine phenocrysts are subhedral to euhedral, 0.1-3 mm, seriate, 10-15 modal%, often skeletal and with occasional iddingsite alteration. Titanaugite microphenocrysts are anhedral to subhedral, < 0.5 mm, accessory and form glomerocrysts up to 1 mm. Olivine xenocrysts are anhedral to subhedral, ~ 4 mm, accessory, with subtle ondulose extinction, etched boundaries and inclusions of orthopyroxene reacting out to form microcrystalline material containing olivine. Vesicles are irregular in shape, < 0.5 mm and << 1 modal%.

Notes: This rock is a clast in volcanic agglomerate or pyroclastic flow. No identifiable plagioclase or nepheline. The rock is classified as a foidite, although no obvious foid minerals could also indicate a basanite, but a foidite is in accordance with major element analysis.

FN08-12 (Basanite): Porphyritic holocrystalline with crypto- to microcrystalline groundmass containing augite, nepheline and opaques. Phenocrysts of olivine and microphenocrysts of augite. Rare devitrified glass domains and one xenolith.

Devitrified glass domains are rounded, < 0.5 mm, << 1 modal% and completely or partially filled with very low birefringence, almost isotropic material (possibly leucite- or analcime-rich in composition). Olivine phenocrysts are anhedral to subhedral, 0.2-5 mm, seriate, 10-15 modal%, highly oxidised, which causes complete substitution of smaller crystals, and with occasional alteration to iddingsite in larger crystals. Augite microphenocrysts are anhedral to subhedral, 0.1-0.5 mm, seriate with the groundmass and forming rare glomerocrysts up to 2 mm together with opaques and nepheline around opaque cores. The one xenolith is very rounded, 10 mm and highly vesiculated. It has a cryptocrystalline groundmass with olivine phenocrysts similar to the host rock, and vesicles are mostly rounded, 0.1-0.5 mm, 25-30 modal% and filled with cryptocrystalline material and microlites of augite and nepheline.

Notes: The augite glomerocrysts and reaction textures are similar to textures observed in some Borborema basaltic rocks. This rock is a clast in a volcanic agglomerate or pyroclastic flow. No identifiable plagioclase, and the sample should be classified as a nephelinite based on petrography, but major element analysis puts it as a borderline basanite. There must be some groundmass plagioclase content.

FN08-13 (Pyroclastic breccia): Volcanic breccia containing mafic clasts and crystals, sometimes partially molten, poorly sorted with a glassy to cryptocrystalline vesicular matrix.

Crystals are dominated by highly oxidised anhedral to subhedral olivine that is 0.1-2 mm, 3-5 modal% and occasionally altered to iddingsite. Partially molten clasts are more irregular in shape, vesiculated (vesicles 10-40 modal%) and with augite microlites up to 0.2 mm and < 5 modal%. Clasts are dominated by basanite-nephelinite but possibly also alkali-basalt and basalt that are crypto- to microcrystalline with lath-shaped cavities that suggest previous presence of augite or plagioclase. Matrix vesicles are irregular in shape, up to 3 mm and filled with calcite.

Notes: The missing laths are difficult to interpret and if they represent plagioclase some of the clasts must oversaturated basalt. This would indicate a different earlier compositional trend for the island, which has not produced any oversaturated samples in the current analysis. Such basalt clasts could, however, also come from the local oceanic crust. The glass matrix excludes the possibility of an agglomerate.

FN10-14 (Sodalite/haüyne/nosean-phyric phonolite): Porphyritic holocrystalline with microcrystalline groundmass containing sanidine (dominant), aegerine and few opaques. Phenocrysts of sanidine, nepheline, aegerine, sodalite-group minerals and amphibole. Accessory sphene and opaques.

Sanidine phenocrysts are subhedral to euhedral, 0.3-6 mm, 3-5 modal%, occasionally zoned and may be glomerophiric and enclose sodalite-group minerals in poikilitic texture. Nepheline phenocrysts are subhedral to euhedral, 0.4-5 mm, 2-3 modal% and are sometimes rounded and apparently not in full equilibrium. Aegerine phenocrysts are subhedral to euhedral, 0.4-2 mm, 1-2 modal%, occasionally

skeletal, may contain titanaugite cores and microlites are occasionally glomerophiric with clusters up to 0.7 mm. Sodalite-group phenocrysts are subhedral to euhedral, 0.2-2 mm, 3-5 modal%, rarely skeletal and often rich in opaque and yellowish inclusions. Amphibole phenocrysts are greenish brown, and probably kaersutite. They are anhedral to subhedral, 0.1-2 mm, 3-5 modal% and with opaque coronas that cause complete substitution of smaller crystals. Accessory opaques are anhedral, 0.1-0.5 mm and often associated with aegerine. Sphene is euhedral, 0.2-1.5 mm and relatively common, possibly reaching 1 modal%.

Notes: This rock is the richest in sodalite-group minerals and sphene in Fernando de Noronha yet. The presence of nepheline phenocrysts indicates a sodalite/haüyne/nosean phonolite in petrographic terms. However, the major element analysis puts it as a borderline trachyte, and this could be the justification for the somewhat poor conditions (disequilibrium) of nepheline phenocrysts, although this could also be the result of the apparent overall alteration that seems to affect the rocks from Fernando de Noronha and lead to loss of Na.

FN10-15 (Phonolite): Pophyritic holocrystalline with microcrystalline groundmass containing sanidine, aegerine and opaques. Phenocrysts of sanidine, aegerine, nepheline and amphibole. Calcite and zeolite pseudomorphs after sodalite-group minerals. Accessory opaques and sphene, and one ocellar feature.

Sanidine phenocrysts are lamellar, subhedral to euhedral, 0.3-7 mm, 3-5 modal% and may be glomerophiric and may poikilitically enclose sphene. Nepheline phenocrysts are subhedral to euhedral, 0.2-3 mm, 2-3 modal% and may poikilitically enclose sanidine and amphibole. Aegerine phenocrysts are 0.1-2.5 mm, seriate, 1-2 modal%, may be glomerophyric, contain titanaugite cores and poikilitically enclose sphene, amphiboles and opaques. Amphibole phenocrysts are greenish brown, and probably kaersutite. They are anhedral to euhedral, 0.1-2 mm, 3-5 modal% and seem to be reacting-out, with aegerine overgrowths and opaque coronas that sometimes cause complete substitution of smaller crystals. Calcite and zeolite pseudomorphs after sodalite-group minerals are euhedral, 2 mm and 1-2 modal%. Accessory sphene is euhedral and 0.2-1.5 mm. Accessory opaques are anhedral, up to 0.5 mm and virtually always associated with aegerine phenocrysts. One tear-shaped occellar feature 5 mm long, containing a calcite core, surrounded by opaques, which are in turn surrounded by a layer containing microlites of augite, olivine and opaques, and finally a biotite rim.

Notes: Very similar to FN10-14, but with more groundmass aegerine and somewhat less altered. The calcite pseudomorphs after sodalite-group minerals support the idea that they may be haüyne more specifically, which could provide the necessary Ca, although the association between nosean and calcite is not uncommon in the literature. Same rock as FN10-16. The presence of nepheline phenocrysts indicates a phonolite, in accordance with the major element analysis.

FN10-16: Same as FN10-15 but somewhat more altered, with calcite alteration affecting also sanidine and nepheline phenocrysts in addition to the sodalite-group minerals.

Notes: This sample was taken from the same outcrop as FN10-15, only a few meters apart. It is clearer here that the aegerine-opaque clusters are reaction products of kaersutite resorption. Aegerine with titanaugite cores are also clearer. Additional evidence to classify the amphiboles as kaersutite are the opaque coronas, which are described by Deer et al. (1966) as a common feature of these minerals.

FN11-17 (Phonolite): Aphyric holocrystalline with crypto- to microcrystalline groundmass containing sanidine, aegerine and small proportions of opaques. Very rare phenocrysts of sanidine, nepheline, sodalite-group minerals and amphibole, and represent ~1 modal% in total. The sample is macroscopically variolitic.

Groundmass is slightly dominated by sanidine, with mostly dendritic aegerine. Sanidine phenocrysts are euhedral and 1-4 mm. Nepheline phenocrysts are euhedral, 0.5-1 mm and often altered. A single amphibole phenocryst is anhedral, 0.4 mm and with a corona of microcrystalline aegerine and opaques. Sodalite-group phenocrysts are subhedral, 0.5-2 mm, and almost completely altered to cryptocrystalline material or calcite.

Notes: It is difficult to assess the level of alteration of this rock. It has an interesting variolitic texture in hand specimen. It is dotted by lighter coloured spherules up to 5 mm that are more resistant to weathering, causing them to stand out in weathered surfaces. The presence of the very few nepheline phenocrysts indicates a borderline phonolite, in accordance with the major element analysis.

FN14-18 (Olivine-phyric nephelinite): Porphyritic holocrystalline with microcrystalline groundmass containing augite, nepheline and opaques. Olivine phenocrysts and rare titanaugite microphenocrysts.

Olivine phenocrysts are subhedral to euhedral, 0.1-4 mm, 7-10 modal%, often skeletal, always with a bright orange iddingsite alteration rim causing complete substitution of smaller crystals and rare smectite alteration along fractures and in crystal cores. There are possibly one or two olivine xenocrysts, which are oversized crystals (5 mm), with straight sides that do not correspond to crystal habit and with etched and resorbed boundaries. Titanaugite microphenocrysts are anhedral to subhedral, often lamellar, up to 0.5 mm, < 1 modal% and may form glomerocrysts.

Notes: A typical ankaramite flow from the Quixaba Formation. The ubiquitous nepheline in the groundmass, lack of obvious plagioclase and ubiquitous olivine phenocrysts indicate a nephelinite, in accordance with the major element analysis.

FN15-19 (Tephrite): Porphyritic hypocrystalline with microcrystalline groundmass containing augite, little nepheline and perhaps plagioclase, and opaques. Vesicles and amygdales that include devitrified or altered original glass inclusions. Olivine phenocrysts and accessory titanaugite microphenocrysts.

Vesicles and devitrified glass domains are 0.1-3 mm, 15-20 modal%, mostly round (although irregular cavities are also present) and sometimes completely or partially filled with very low birefringence, almost isotropic material (possibly zeolites), forming amygdales, which also affects cavities within olivine phenocrysts. Some irregular cavities also do not have sharp boundaries with the groundmass and are likely original glass inclusions that have been altered or devitrified. Olivine phenocrysts are subhedral to euhedral, 0.1-2.5 mm, 5-7 modal%, rarely skeletal, highly oxidised and with rare alteration to iddingsite in crystal cores. Accessory titanaugite microphenocrysts are lamellar, euhedral, up to 0.5 mm and may be glomerophyric.

Notes: A typical ankaramite Quixaba flow, although vesiculated and somewhat finer-grained. The nepheline in the groundmass with some possible plagioclase and proportions of olivine phenocrysts (< 10%) indicate a tephrite, in accordance with the major element analysis.

FN15-20 (Olivine-phyric nephelinite): Porphyritic hypocrystalline with microcrystalline groundmass containing augite, little nepheline and opaques. Irregular vesicles and devitrified glass domains lined with opaques and filled with spherulitic zeolites and possibly nepheline, as well as augite crystals and other microlites. Olivine phenocrysts and accessory titanaugite microphenocrysts.

Vesicles and devitrified glass domains are irregular in shape, 3-5 modal%, mostly < 1 mm but sometimes forming veins a few cm long, containing euhedral augite crystals and other microlites irradiating from the walls or 'floating' within it. Olivine phenocrysts are 0.1-5 mm, 5-7 modal%, range from anhedral to euhedral, sometimes skeletal and with occasional oxidised rims. Accessory titanaugite microphenocrysts are lamellar, euhedral, up to 0.5 mm and may be glomerophyric.

Notes: Very similar to FN15-19, but without the pervasive oxidation of olivine phenocrysts and total absence of rounded vesicles and amygdales. The nepheline in the groundmass, lack of obvious plagioclase and ubiquitous olivine phenocrysts indicate a nephelinite, in accordance with the major element analysis.

FN13-21 (Trachyte): Porphyritic almost aphyric holocrystalline with microcrystalline to fine-grained trachytic groundmass containing sanidine and little opaques. Rare small irregular cavities. Rare phenocrysts of sanidine (dominant). Phenocrysts and microphenocrysts of aegerine and hornblende. Accessory sphene and opaques.

Cavities are rounded, < 0.2 mm and << 1 modal%. All phenocrysts represent 1-2 modal% in total. Sanidine phenocrysts are dominant, subhedral to euhedral, somewhat seriate with the groundmass but up to 3 mm, may form glomerocrysts with the other phenocrysts and sometimes occur as overgrowths over previous albite or anorthoclase. Amphiboles are greenish brown and likely hornblendes. They are anhedral to subhderal, up to 2.5 mm and may form glomerocrysts, usually in poor condition (perhaps resorbed). Sphene is euhedral, 0.3-0.7 mm and occurs as part of sanidine-amphibole glomerocrysts. Accessory opaques are anhedral, < 0.5 mm and occur as part of sanidine-amphibole glomerocrysts.

Notes: The sample comes from a dyke, but the microcrystalline to fine-grained groundmass is rather coarse and could indicate relatively slow cooling in a hypabyssal context. The dominance of sanidine with Na-feldspar cores, no nepheline phenocrysts and little aegerine and hornblende (possibly resorbed) indicates a trachyte, in accordance with the major element analysis.

FN13-22 (Alkali basalt): Porphyritic holocrystalline with microcrystalline groundmass containing titanaugite, plagioclase, nepheline and opaques. Phenocrysts of olivine and titanaugite (dominant). Opaque microphenocrysts. The rock is rather altered.

Olivine phenocrysts are anhedral, 0.3-3 mm, 2-3 modal% and virtually destroyed by alteration/oxidation. Titanaugite phenocrysts are euhedral, 0.3-4 mm, somewhat seriate with the groundmass, 10-15 modal% and may have bright green cores and opaque inclusions. Opaque microphenocrysts are anhedral, < 0.5 mm and 1-2 modal%.

Notes: The bright green cores in the titanaugite clearly suggest an initial different composition (perhaps ferroaugite). The dominance of titanaugite phenocrysts, very little olivine and the presence of nepheline and plagioclase in the groundmass indicate an alkali basalt, in accordance with major element analysis.

FN13-23 (Volcanic agglomerate): Volcanic agglomerate with cryptocrystalline matrix. Clasts are sub-angular to sub-rounded, up to 1 cm, moderately- to poorly-sorted. They include glassy, highly vesiculated mafic grains of tuff, trachyte, phonolite, basanite, nephelinite and alkali basalt, as well as individual olivine and titanaugite crystals.

Notes: The clasts are a good representation of the dominant lithologies in the island, exposed today. Their texture, clast characteristics, cryptocrystalline (clastic) matrix and low consolidation of the rock indicate an agglomerate.

FN13-24 (Olivine-phyric nephelinite): Porphyritic hypocrystalline with microcrystalline to fine-grained groundmass containing titanaugite laths and opaques. Calcite pseudomorphs after olivine phenocrysts. Amygdales filled with zeolites and calcite. Presence of devitrified material.

Amygdales and devitrified domains have very irregular shapes 0.1-3 mm, 3-5 modal% and may form veins. Amygdales are completely filled with zeolites and occasionally calcite. Devitrified domains contain crystals growing from the walls inwards, occasionally calcite and do not show sharp boundaries with the groundmass. Substitution of olivine for calcite is complete, with subhedral to euhedral pseudomorphs 0.1-4 mm, seriate, 7-10 modal%, with some empty cavities in the larger examples and occasional yellow alteration.

Notes: This rock is highly altered. The lack of plagioclase and dominance of titanaugite and (originally) olivine indicate a foidite. The major element analysis, however, puts it as a picro-basalt. This is probably wrong, as both the MgO wt.% and olivine contents are rather low. Alteration must have significantly affected the results. The sample comes from a thin dyke a few 10's of cm thick, from the Caieiras beach, a locality strongly affected by weathering.

FN13-25 (Kaersutite trachyandesite): Porphyritic holocrystalline with microcrystalline, very altered, trachytic groundmass containing sanidine, opaques and some devitrified domains. Phenocrysts of amphibole and accessory augite. One large amphibole xenocryst. Opaque microphenocrysts.

The groundmass trachytic texture has flow orientation, is very altered, with pervasive microcrystalline material and calcite, and has occasional empty elongated vesicles, 1-3 modal%, following the dominant trachytic texture and with no sharp boundary with the groundmass, suggesting they were originally glass inclusions. Amphibole phenocrysts are subhedral to euhedral, 0.2-4 mm, 2-3 modal% and yellowish brown. They are likely kaersutite. Augite phenocrysts are subhedral to euhedral, ~1 modal%, 0.3-1 mm, often with sieve texture and/or resorbed rims. Opaque microphenocrysts 0.3-1 mm, 1-2 modal% and anhedral to subhedral. The one amphibole xenocryst is anhedral but angular, 8 mm, and encloses anhedral to subhedral augites in 7-10 modal% and up to 1.5 mm, and anhedral opaques in 3-5 modal% and up to 0.3 mm, both of which are evenly distributed throughout the crystal. The xenocryst also contains calcite-filled cavities up to 1 mm.

Notes: The amphibole xenocryst is very similar to the amphibole clusters found in the Atalaia rocks, as well as very similar to those amphiboles naturally occurring in the rock, and could support the interpretation that these crystals are forming cumulates from the magma itself, as opposed to older lithospheric xenoliths. The dominance of sanidine in the groundmass with no aegerine or nepheline, and no aegerine or sanidine phenocrysts indicate a trachyandesite, in accordance with the major element analysis.

FN13-26 (Volcanic breccia): Volcanic breccia containing two main groups of trachyte clasts at very different stages of alteration and with different sizes.

Matrix is somewhat altered, porphyritic, crypto- to microcrystalline, containing sanidine (dominant) with a few opaques, and phenocrysts of anorthoclase and sanidine. Calcite alteration concentrates around clast rims or affect phenocrysts. Phenocrysts in total represent ~1 modal% of the matrix, are 0.5-1.5 mm and anhedral to subhedral. Clasts are mainly trachyte and can be divided into two groups. The first is fresh, fine-grained, angular to sub-angular, 3-15 mm, porphyritic (phenocrysts of sanidine and aegerine) and very similar to sample FN13-21. The second group is heavily altered, with the groundmass substituted my cryptocrystalline brown material, sub-angular to sub-rounded, 1-7 mm and porphyritic (phenocrysts of sanidine and amphibole).

Notes: The clasts are mostly local, dominated by the nearby trachyte FN13-21. The presence of anorthoclase in the sanidine-dominated groundmass indicates a trachyandesite or trachyte groundmass. It could be related to the emplacement of rock FN13-25, as opposed to the abutting dyke represented by sample FN13-22, even though direct stratigraphic relations were not available in the field.

FN16-27 (Tephrite): Porphyritic hypocrystalline with heterogeneous crypto- to microcrystalline groundmass containing augite, opaques and rare nepheline, and devitrified, oriented, linear glass domains. Olivine phenocrysts and possibly xenocrysts.

Olivine phenocrysts are subhedral to euhedral, 0.1-4 mm, 7-10 modal%, and apparently bimodal with crystals either < 0.5 mm or > 1 mm. Larger crystals represent 2-3 modal%, are mostly irregular in shape, being either somewhat rounded or with straight sides and rough polygonal forms, indicating they are probably xenocrysts. All olivine have iddingsite alteration along the rims, which amounts to complete substitution of smaller crystals. The rock contains linear devitrified glass domains < 0.5 mm thick, showing the same overall orientation. These merge with the surrounding groundmass, with no sharp border. They are dominated by feldspars, but may also contain biotite, thin needles of pyroxene, and sometimes bubbles that are now filled with zeolite and other alteration material. The groundmass is somewhat heterogeneous, with slightly lighter and darker patches with different granularity.

Notes: The rock seems to be a typical, somewhat altered, nephelinite/ankaramite from the Quixaba Formation. The groundmass comprising almost exclusively augite and opaques suggests a nephelinite, but the feldspar-rich devitrified glass domains indicate the presence of feldspars in the liquid composition. The low modal presence of olivine indicates a tephrite, in accordance with the major element analysis.

FN16-28: No thin-section was made of this sample. It refers to a very rounded beach pebble 15 cm in diameter.

FN17-29 (Sodalite/haüyne/nosean-phyric phonolite): Porphyritic hypocrystalline with somewhat heterogeneous crypto to microcrystalline groundmass containing sanidine and aegerine. Phenocrysts of sanidine, nepheline and sodalite-group minerals. Microphenocrysts of aegerine and accessory amphibole, sphene and opaques. Some occasional linear devitrified glass inclusions.

Groundmass is somewhat trachytic. Occasional linear inclusions resembling small veins have no sharp boundaries, with groundmass crystals growing into them, and low birefringence interiors, indicating these are devitrified glass inclusions. Sanidine phenocrysts are subhedral to euhedral, 0.5-5 mm, 1-2 modal%, with occasional alteration to clays. Nepheline phenocrysts are subhedral to euhedral, 1.5-2.5 mm and around 1 modal%. Sodalite-group phenocrysts are subhedral to euhedral, 0.3-1.5 mm, 2-3 modal% and some are blue under plain polarised light. Aegerine microphenocrysts are mostly subhedral, 0.1-0.4 mm and 2-3 modal%. Presence of one aegerine glomerocryst 5 mm long with crystals 0.2-1 mm, which are zoned from pale green cores, through lilac and to aegerine rims, with little fragments of amphibole < 0.2 mm. Accessory amphibole appears as phenocrysts, which are subhedral to euhedral, 0.1-1 mm, << 1 modal%, with coronas of microcrystalline aegerine and opaques. They are brown pleochroic and likely kaersutite. Accessory sphenes are subhedral to euhedral and 0.1-0.3 mm. Accessory opaques are anhedral, 0.1-0.5 mm and seem to have subtle brown pleochroic cores, suggesting that they are probably the products of amphibole resorption.

Notes: This sample is unusual in its proportions of sodalite-group minerals to sanidine phenocrysts, and the relatively more common blue colour of the former's crystals. The obvious blue colour of sodalite-group minerals and their substitution by zeolites in sample FN17-30 perhaps suggests that these are nosean. The trachytic groundmass, presence of nepheline and sanidine phenocrysts indicates a phonolite, in accordance with the major element analysis.

FN18-30 (Phonolite): Porphyritic holocrystalline with microcrystalline trachytic texture containing sanidine and aegerine. Phenocrysts of sanidine and nepheline. Microphenocrysts of aegerine, amphiboles and opaques. Zeolite pseudomorphs after sodalite-group minerals and accessory sphene.

Sanidine phenocrysts are euhedral, 0.5-6 mm, 1-2 modal% and with occasional alteration to clays. Nepheline phenocrysts are euhedral, 0.5-2 mm, 1 modal% and with occasional alteration to clays. Amphibole microphenocrysts are mostly euhedral, brown, 0.2-0.5 mm, 1 modal%, with coronas of aegerine and opaques that cause completely substitution of some crystals, and are probably kaersutite. Aegerine microphenocrysts are subhedral, 0.1-0.5 mm, 1-2 modal% and occasionally with titanaugite cores. Opaques are anhedral, 0.1-1 mm, 1 modal%, sometimes with aegerine coronas and are probably the products of amphibole reactions/resorption. Zeolite pseudomorphs have sodalite-group habits, but possibly also nepheline, and are 0.2-2 mm with 1-2 modal%. Accessory sphene is subhedral to euhedral and 0.1-0.5 mm.

Notes: The original proportions of sodalite-group minerals in this rock must have been quite high, similar to rock FN17-29 although not as much, but they have been substituted by zeolites. The substitution of sodalite-group minerals by zeolites and their obvious blue colour in rock FN17-29 suggests that perhaps these are nosean. The trachytic groundmass with phenocrysts of nepheline and sanidine indicates a phonolite, in accordance with the major element analysis.

FN19-31 (Titanaugite-phyric tephrite): Porphyritic hypocrystalline with groundmass containing augite, opaques and nepheline, as well as nepheline oykocrysts and irregular mostly devitrified glass inclusions. Phenocrysts of olivine and titanaugite. One xenolith and rare zeolite-filled cracks.

Olivine phenocrysts are subhedral to euhedral, 0.1-5 mm seriate, 5-7 modal%, often skeletal, with common alteration to clays along internal fractures but always with iddingsite rims, which causes complete substitution in smaller crystals. Titanaugite phenocrysts are subhedral to euhedral, 0.1-3 mm seriate, 10-15 modal%, often with sieve textures, opaque inclusions and augite cores, and rarely glomerophyric. Devitrified glass inclusions are irregular in shape, dominated by variolitic feldspar re-crystallisation, 0.5-5 mm and represent < 1 modal%. They may occasionally also contain bubbles lined or completely filled with cryptocrystalline alteration products. One xenolith is 5 mm, sub-rounded, with a darker cryptocrystalline matrix containing augite, and olivine subhedral phenocrysts up to 1 mm and with iddingsite rims. Rare zeolite-filled linear cracks cut across the sample.

Notes: The rock seems to be a typical, somewhat altered, nephelinite/ankaramite from the Quixaba flows. The dominance of feldspar in the devitrified material indicates its presence in the liquid composition, and together with an augite and nepheline groundmass and some olivine phenocrysts, indicate a tephrite, in accordance with the major element analysis.

FN12-32 (Sodalite/haüyne/nosean- kaersutite-phyric tephriphonolite): Porphyritic holocrystalline with microcrystalline felty groundmass containing feldspar, augite or aegerine, opaques and rare nepheline. Phenocrysts of K-feldspar, aegerine, and sodalite-group minerals. Phenocrysts or xenocrysts of amphibole. Microphenocrysts of nepheline. Accessory opaques and sphene.

K-feldspar phenocrysts include sanidine and little anorthoclase, sometimes with microperthitic cores or forming glomerocrysts that may contain micrographic texture. They are subhedral to euhedral (sometimes sub-rounded), tabular or lamellar, 0.3-4 mm, seriate, 3-5 modal%, sometimes zoned and may include xenocrysts amongst them. Aegerine phenocrysts are subhedral to euhedral, 0.2-3 mm, seriate but with great dominance of smaller crystals, 2-3 modal%, with occasional augite-titanaugite cores and glomerocrysts. Amphibole phenocrysts or xenocrysts range from anhedral to euhedral, 0.1-4 mm, seriate, 7-10 modal%, lamellar, tabular or equant and mostly with microcrystalline coronas of aegerine and opaques. They are yellowish brown, somewhat zoned and with greenish brown rims, have high birefringence (high 2nd to 3rd order), occasionally opaque cores, and are likely kaersutite. They are in poor condition and often resorbed, and could be xenocrysts. Sodalite-group phenocrysts are subhedral to euhedral, 0.2-1.5 mm, 5-7 modal%, and often glomerophyric and altered to zeolites. Nepheline microphenocrysts are subhedral, 0.1-0.4 mm, 1-2 modal% and occasionally altered to isotropic material. Accessory sphene is up to 0.7 mm and subhedral to euhedral. Accessory opaques are anhedral, 0.2-0.3 mm, rarer than sphene and often with a yellow alteration halo. K-feldspar and/or sodalite-group mineral glomerocrysts may contain plagioclase cores that is often associated with micrographic textures.

Notes: This rock is unusual so far in its large amounts of amphiboles. The feldspars also show strong evidence for disequilibrium and resorption, and could be xenocrysts. The presence of plagioclase, even if in disequilibrium, together with ubiquitous amphibole, some sanidine and a felty texture with little augite/aegerine indicates a trachyandesite, in accordance with the major element analysis, but the little nepheline suggests tephriphonolite as a more suitable classification.

FN12-33 (Kaersutite-phyric tephriphonolite): Porphyritic hollocrystaline with a somewhat altered micro- to cryptocrystalline groundmass with a felty to somewhat trachytic texture, containing feldspar, pyroxenes and opaques. Irregular cavities filled with calcite. Phenocrysts of K-feldspar, nepheline and amphiboles. Microphenocrysts of sphene and opaques.

Cavities are irregular, mostly elongated, reaching 6 mm, and filled with calcite. K-feldspar phenocrysts are mostly sanidine but with some anorthoclase, subhedral to euhedral, 0.5-3 mm, 10-15 modal%, may be zoned and form glomerocrysts, and are much altered to calcite and zeolites, especially in crystal cores. Nepheline phenocrysts are subhedral to euhedral, 0.2-1.5 mm, 3-5 modal% and often altered to calcite and zeolites. Amphibole phenocrysts range from anhedral to euhedral, are dark yellowish to greenish brown, with high birefringence (high 2nd to 3rd order), somewhat zoned, 0.2-5 mm, seriate, 5-7 modal% and do not show the coronas of aegerine and/or opaques common in other samples. These may be kaersutite. Opaque microphenocrysts are anhedral, 0.1-0.5 mm, 1-2 modal% and often with rusty alteration haloes. Sphene microphenocrysts are subhedral to euhedral, 0.1-0.5 mm and around 1 modal%.

Notes: The large amount of sphene and the absence of aegerine and/or opaque coronas around the amphiboles in this rock are unusual. It is somewhat finer grained than FN12-32, and although the samples come from what looks like distinct alteration domains in the same outcrop, under the microscope they are obviously different. The presence of ubiquitous amphibole, some sanidine and a lightly trachytic texture with apparently no aegerine would indicate a trachyandesite, in accordance with the major element analysis. However, the clear presence of nepheline points to a tephriphonolite instead, and the rock must have been affected by alteration leading to alkali depletion.

FN12-34 (Tephrite): Porphyritic holocrystalline with crypto- to microcrystalline groundmass containing augite and opaques, as well as vesicles and amygdales filled with calcite and zeolites. Calcite pseudomorphs after olivine and titanaugite phenocrysts.

Groundmass is heterogeneous with areas around vesicles and amygdales darker and more altered. It also contains some very rounded opaque-poor domains where the larger and more rounded amygdales are concentrated, and which have sharp boundaries and somewhat coarser pyroxenes that are sometimes oriented. Larger amygdales are mostly rounded, up to 5 mm, 2-3 modal%, completely filled with calcite and occasionally with a thin lining of zeolites. A second group of cavities are filled with calcite and zeolite, irregular, angular, < 0.5 mm and merge with the surrounding groundmass. Calcite pseudomorphs after olivine are subhedral to euhedral, 0.3-2 mm, seriate, 3-5 modal%, lined along the rims with a thin layer of clay minerals and often form glomerocrysts that may include titanaugite. Titanaugite phenocrysts are mostly euhedral, 0.3-3 mm, seriate, 3-5 modal% and often zoned and in glomerocrysts that may include calcite pseudomorphs and opaques somewhat larger than in the groundmass.

Notes: This rock is similar to the Quixaba tephrites but the state, size and proportion of titanaugites seem unusual. It seems as if the titanaugite sometimes nucleate on the surface of previous olivine crystals, and grow into glomerocrysts. The apparent absence of plagioclase in the groundmass would suggest a nephelinite, but the major element analysis indicates a picro-basalt. The rock is likely a tephrite with high levels of alteration, which concentrated on its phenocrysts and led to the complete substitution of all its original olivine. The good condition of the titanaugites is not surprising, as this is a mineral particularly resilient to alteration. This rock has 6.85 wt.% LOI, the second highest amongst the Fernando de Noronha rocks.

FN12-35 (Tephrite): Porphyritic holocrystalline with crypto- to microcrystalline groundmass containing augite, opaques and possibly plagioclase. Amygdales and fractures filled with calcite and smectite. Calcite and smectite pseudomorphs after olivine. Phenocrysts of titanaugite and accessory opaques.

Amygdales are rounded to very rounded, up to 5 mm, around 1 modal%, filled with calcite and sometimes lined with clays. Linear fractures in the rock are ~0.1 mm thick and filled with smectite. Titanaugite phenocrysts are subhedral to euhedral, 0.1-5 mm, seriate, 7-10 modal%, often zoned, with some rare green cores, occasionally with a sieve-textured core and often in glomerocrysts that may include calcite pseudomorphs. Pseudomorphs after olivine are subhedral to euhedral, 0.2-5 mm, 7-10 modal% (only slightly lower than titanaugite phenocrysts), may form glomerocrysts that may include titanaugite phenocrysts, and are dominated by smectite, but sometimes with a small core of calcite. Accessory opaques are anhedral and up to 0.5 mm.

Notes: It seems as if titanaugite sometimes nucleate on the surface of previous olivine crystals and grow into glomerocrysts. The presence of little plagioclase in the groundmass, with phenocrysts of titanaugite and original olivine indicate a basanite, but major element analysis classifies it as a borderline alkali-basalt. The high levels of alteration of the olivine does not seem, however, to have affected the major element composition as it apparently did for FN12-34. This sample does not have a LOI value as high as FN12-34, but it is still high (4.45 wt.%). Another difference is the dominance of smectite substitution of olivine instead of calcite substitution.

FN12-36 (Basaltic trachyandesite): Porphyritic holocrystalline with crypto- to microcrystalline groundmass containing feldspar (dominant and likely plagioclase), augite and opaques. Irregular amygdales filled with analcime and calcite. Phenocrysts of augite, titanaugite and amphiboles. Phenocrysts or xenocrysts of K-feldspar. Calcite and zeolite pseudomorphs. Accessory sphene, ferroaugite and biotite.

Amygdales are very irregular, angular, < 1 mm, 2-3 modal%, filled with analcime or lined with analcime and further filled with calcite. K-feldspar phenocrysts or possibly xenocrysts are anhedral and rounded, 0.3-5 mm, around 1 modal% and partially resorbed. Augite and titanaugite phenocrysts are mostly subhedral, 0.3-3 mm, seriate, 3-5 modal%, sometimes with a green core, zoned or glomerophyric and often heavily fractured. Amphibole phenocrysts are subhedral to euhedral, brown

with high birefringence (high 2nd to 3rd order), 0.2-2 mm, 3-5 modal%, often with microcrystalline coronas or completely substituted by opaques, and are likely kaersutite. They may also show heavily altered cores, dominated by opaques. Calcite and zeolite pseudomorphs are subhedral, have dense opaque rims, cloudy cores caused by micro oxide inclusions and pale yellow-green clay alteration haloes. They seem to substitute sodalite-group minerals. Accessory sphene is subhedral to euhedral and up to 0.5 mm. Accessory biotite is subhedral, up to 1 mm and often associated with calcite/zeolite pseudomorphs. Accessory ferroaugite microphenocrysts are green, subhedral to euhedral and 0.2-1.5 mm.

Notes: Country rock to FN12-35 and probably the same rock as FN12-32. This is a relatively primitive rock but with amphiboles. The green colour of some augites or augite indicates either ferroaugite or sodic augite. The lack of clear feldspar or olivine phenocrysts, with the dominance of titanaugite and some amphibole as phenocrysts indicates an intermediate to primitive rock, in accordance with the major element analysis.

FN12-37 (Sodealite/haüyne/nosean-phyric basaltic trachyandesite): Porphyritic holocrystaline with crypto- to microcrystalline groundmass containing feldspar (dominant), pyroxene and opaques. Phenocrysts of sanidine, titanaugite and augite, amphibole, and sodalite-group minerals. Phenocrysts or xenocrysts of other K-feldspar. Accessory biotite and sphene.

One cavity with irregular shape, 3 mm, filled with calcite. Phenocrysts of titanaugite and augite are subhedral to euhedral, bimodal in size with 0.3-2 mm and a second group around 5-6 mm dominated by titanaugite, total 3-5 modal%, and are also sometimes zoned, with simple twinning or glomerophiric. Augite is likely ferroaugite or sodic augite, with moderate to strong bright green to greenish-brown pleochroism. Sanidine and K-feldspar phenocrysts and possibly xenocrysts are anhedral to subhedral, 2-3 modal%, 0.5-5 mm, often rounded, resorbed, zoned, with bluish anomalous extinction and a subtle corona << 0.1 mm suggesting some regrowth. Sometimes apparently in aggregates with granular texture. They may be glomerophyric together with haÿne/nosean crystals. Amphibole phenocrysts are subhedral to euhedral, 0.2-2 mm, 3-5 modal%, sometimes substituting clinopyroxenes either in lattice continuation or as microcrystalline lath clusters, and strongly oxidised, often with complete substitution by opaques, making identification of the specific type difficult (likely kaersutite due to context). Sodalite-group phenocrysts are subhedral to euhedral, 0.5-3 mm, 3-5 modal%, strongly altered to calcite, especially in their cores. Accessory biotite is subhedral to euhedral, mostly 0.3-1 mm but with occasional crystals up to 3 mm, strongly oxidised along the boundaries and often glomerophiric. Accessory sphene is euhedral and 0.5-1.5 mm.

Notes: This is the same rock as FN12-36 and probably not the same as FN12-32, as was first suggested in the field. It was taken from the same exposure as FN12-36, but it is somewhat more altered. The exposure was rich in amphibole nodules, which were avoided in the preparation of this particular thin-section. The presence of K-feldspar and sanidine, kaersutite and titanaugite without any olivine indicates a basaltic trachyandesite, in accordance with the major element analysis.

FN12-38: Same as rock FN12-37, but heavily fractured. Cracks filled with calcite, smectite and red oxide material, likely hematite. The K-feldspar show better examples of granular textures and clearer evidence of being rounded xenoliths.

Notes: Sample taken from the same exposure as FN12-36 and FN12-37, but from the brecciated zone associated with a dyke emplacement. It is somewhat altered due to (and along) its fractures.

FN12-39 (Kaersutite nodule): Holocrystalline with granular texture containing amphibole, green clinopyroxene, sphene and opaques, all poikilitically enclosing abundant and large apatite crystals. The rock is fractured and altered, with high levels of oxidation, especially the amphiboles, and carbonate, smectite and cryptocrystalline material as alteration products and infillings along fractures and cavities.

Cavities represent 3-5 modal%. Apatite are subhedral to euhedral, 0.1-2 mm, 7-10 modal% and the more dense clusters are associated with sphene. Clinopyroxene are anhedral, pale green and weakly pleochroic from pinkish green to yellowish green, 0.2-5 mm, 30-40 modal%, full of amphibole and

opaque-rich blebs, and it seems to be reacting out to form the amphiboles. Clinopyroxenes are likely omphacites or augites. Amphiboles are strongly pleochroic from dark brown to yellowish or occasionally greenish brown, 0.5-5 mm, 40-50 modal%, and are likely kaersutite. Sphene is anhedral 0.5-5 mm, 5-7 modal%, and also seems to be reacting out in favour of amphiboles.

Notes: The nodule is relatively different from FN25-48 and it seems to represent the alteration of a clinopyroxenite.

FN20-40 (Basaltic trachyandesite): Porphyritic holocrystalline with microcrystalline groundmass containing augite surrounded by plagioclase lath oikocrysts (dominant), opaques and devitrified glass inclusions. Phenocrysts of titanaugite, amphibole and sodalite-group minerals. Calcite and smectite pseudomorphs. Accessory sphene, biotite and opaque phenocrysts.

Clinopyroxene phenocrysts are dominated by titanaugite with occasional bright green crystals or cores of ferroaugite or sodic augite. They are subhedral to euhedral, 0.3-2 mm, 5-7 modal%, often zoned, and occasionally glomerophyric and with simple twinning. Amphiboles are subhedral to euhedral, 0.3-2 mm, 1-2 modal%, dark brown or dark yellowish brown (likely kaersutite) and strongly oxidised, with coronas of opaques that may cause complete substitution of the original crystal. Sodalite-group minerals are subhedral to euhedral, 0.5-2 mm, 1-2 modal% and sometimes somewhat yellowish. Calcite and smectite pseudomorphs are subhedral to euhedral, 0.5-2 mm, 2-3 modal% and seem to replace clinopyroxene. Devitrified glass inclusions are irregular in shape, 0.5-2 mm, 2-3 modal%, and sometimes contain calcite cores, indicating cavities, but the devitrified material consists of nepheline and probably analcime. Accessory biotite is anhedral to subhedral, 0.3-2 mm and often with coronas of opaques. Accessory sphene is euhedral and 0.5-1 mm.

Notes: This is supposedly the same rock as FN12-36 and FN12-37, but has a somewhat coarser groundmass. It the country rock to the same mafic dykes and amphibole nodules. The dominance of titanaugite phenocrysts with some incipient amphibole, in a plagioclase groundmass poykilitically enclosing some augite indicates an intermediate to primitive transitional rock that we classify as a basaltic trachyandesite, in accordance with the major element analysis.

FN20-41 (Titanaugite-phyric basanite/tephrite): Porphyritic hypocrystalline with glassy to cryptocrystlline groundmass containing augite, opaques and amygdales. Phenocrysts of titanaugite. Calcite, smecite and zeolite pseudomorphs after olivine. Orthoclace xenocrysts.

Titanaugite is euhedral, 0.1-3 mm, seriate, 10-15 modal%, often zoned and occasionally with green, sodic cores or forming glomerocrysts either independently or as 0.1-0.2 mm microlites around the pseudomorphs and xenocrysts. Calcite, smectite snd zeolite pseudomorhs are subhedral to euhedral, 0.2-5 mm, seriate, 7-15 modal% and seem to replace olivine. Amygdales are irregular in shape, 0.2-1 mm, 1-2 modal% and infilled with calcite, smectite, zeolites or hematite. Orthoclase xenocrysts are very rounded, 0.3-1.5 mm and << 1 modal%.

Notes: This rock plots as a basanite/tephrite and petrography would indicate a basanite if the olivine had not been substituted by pseudomorphs, but it could potentially also be a tephrite, similarly to other dykes nearby. The groundmass must contain some plagioclase content. It is somewhat different from the other dykes sampled nearby, namely FN12-34 and FN12-35.

FN21-42 (Phonolitic nephelinite): Virtually aphyric holocrystalline with crypto- to microcrystalline groundmass containing nepheline. Accessory (<< 1 modal%) phenocrysts of sanidine and nepheline. Sanidines are euhedral and 0.5-3 mm. Nephelines are euhedral and 0.1-1 mm.

Notes: The groundmass must also contain some sanidine but crystals are not recognisable in the crypto- to microcrystalline groundmass. Virtually no opaques present. The rock is somewhat altered. The nepheline groundmass with sanidine and nepheline phenocrysts indicates a phonolitic nephelinite, although the major element analysis puts it as a phonolite.

FN22-43 (Phonolite): Virtually aphyric holocrystalline with trachytic groundmass containing sanidine (dominant), nepheline (2-3 modal%) and dendritic aegerine (15-20 modal%). Accessory (< 1

modal%) phenocrysts of sanidine and nepheline. Sanidine phenocrysts are euhedral, 1.5-2.5 mm and somewhat altered. Nepheline phenocrysts are euhedral and 0.2-2 mm.

Notes: No opaques present. Phenocrysts are somewhat more present than in rock FN21-42. The nepheline and sanidine groundmass with sanidine and nepheline phenocrysts indicates a phonolite, in accordance with the major element analysis.

FN23-44 (Amphibole- titanaugite-phyric phonotephrite): Porphyritic holocrystalline and very heterogeneous in its inclusions and degrees of groundmass alteration. Crypto- to microcrystalline groundmass containing augite, plagioclase and opaques. Presence of veins and amygdales. Phenocrysts of titanaugite and augite, amphibole and opaques. Xenoliths. Xenocrysts of amphibole, titanaugite and K-feldspar. Accessory sphene.

The groundmass includes bright orange vein-like domains 1-3 mm thick. Amygdales are irregular, up to 1 mm and filled with zeolites, analcime, calcite and/or smectite. Veins are either empty or filled with the same material, mostly 0.1 mm thick and oriented. Clinopyroxene phenocrysts are dominated by titanaugite, occasionally with green cores, but also includes whole bright green sodic or ferroaugite crystals. They are subhedral to euhedral, 0.2-3 mm, 7-10 modal% and often zoned. Amphiboles are subhedral to euhedral, 0.1-2 mm, 5-7 modal% and dark brown or yellowish brown (likely kaersutite). Opaques are mostly anhedral, 0.1-0.5 mm and 3-5 modal%. Accessory sphene is euhedral and 0.2-0.5 mm. Xenoliths are 1-10 mm, rounded to very rounded, strongly altered (especially the orthoclases) and often resorbed. They include alkali basalts rich in opaques, clasts comprising fine-grained granular orthoclase, and a 10 mm angular clast dominated by euhedral titanaugite (0.2-3 mm and 30-40 modal%), subhedral to euhedral zeolite pseudomorphs likely substituting sodalite-group minerals (0.2- 2 mm and 15-20 modal%), anhedral to subhedral opaques (0.3-1 mm and 7-10 modal%) and euhedral apatites (0.2-1 mm and 7-10 modal%), all in a microcrystalline basaltic groundmass containing plagioclase and augite. Xenocrysts include rounded to very rounded sanidine and orthoclase up to 6 mm, anhedral subrounded to subangular titanaugite and amphiboles up to 3 mm and very similar to those naturally occurring in the rock.

Notes: This is one of the most heterogeneous rocks collected in the archipelago, and the basaltic xenolith assemblage is in accordance with what is found there, but the granular orthoclase seem to come from a plutonic source. The plagioclase and augite groundmass with titanaugite and amphibole phenocrysts indicates an intermediate to primitive alkaline rock, in accordance with the major element analysis.

FN24-45 (Nepheline-phyric phonolite): Porphyritic (almost aphyric) holocrystalline with microcrystalline groundmass with felty to trachytic texture containing sanidine (dominant), aegerine (25-30 modal%) and nepheline. Phenocrysts of sanidine and nepheline. Microphenocrysts of aegerine. Accessory sphene and opaques.

Phenocrysts amount to only 1-2 modal% and are dominated by nepheline. Nepheline is euhedral and 0.3-3 mm. Sanidines form euhedral laths 0.3-3 mm long. Aegerine microphenocrysts are rare (<< 1 modal%), subhedral and around 0.3 mm. One crystal of sphene and one opaque were identified, both anhedral and with aegerine microphenocrysts nucleating on them.

Notes: The rock is very similar to FN22-43, only with somewhat higher, but still very small proportions of phenocrysts and accessories. The sanidine, aegerine and nepheline groundmass with nepheline and sanidine phenocrysts indicates a phonolite, in accordance with the major element analysis.

FN25-46 (Trachybasalt): Virtually aphyric holocrystalline with microcrystalline groundmass containing ubiquitous opaques (25-30 modal%), laths of plagioclase and augite more or less in equal proportions and a dark brownish green almost opaque mineral. Microphenocrysts of opaques. Possible xenocrysts of K-feldspar, titanaugite, augite. Possibly amphibole xenocrysts. Opaques.

Groundmass contains altered domains along fractures, rich in bright red-orange material (hematite). Opaque microphenocrysts are subhedral to euhedral, 0.05-0.3 mm and 2-3 modal%. Phenocrysts and

xenocrysts amount to < 1 modal%, are subrounded to rounded and 0.5-3 mm. Clinopyroxene xenocrysts often have opaques nucleated on their surfaces. K-feldspar xenocrysts are strongly altered and resorbed. Many opaque xenocrysts have etched boundaries. One large xenocryst is 7 mm, dark brown, anhedral, apparently with resorption embaymetns, strongly altered and oxidised (almost completely opaque), containing very rounded 1 mm inclusions of pyroxene and K-feldspar, and is likely to be an amphibole (likely kaersutite).

Notes: The xenocrysts in this rock are in accordance with the assemblages found on the island, but the large size of a couple of them (amphibole and one augite) suggest a granular origin, possibly plutonic. The plagioclase and augite groundmass with a lack of olivine or another pyroxene indicates a borderline trachybasalt, in accordance with the major element analysis.

FN25-47 (Augite amphibole-phyric basaltic trachyandesite): Porphyritic holocrystaline with microcrystalline to fine-grained groundmass containing plagioclase laths, augite and opaques. Vesicles and amygdales. Phenocrysts of amphibole, titanaugite, augite, sodalite-group minerals and opaques. Accessory sphene.

Vesicles and amygdales (completely or partially filled with zeolites and smectite) are rounded, 0.3-5 mm and 3-5 modal%. Clinopyroxenes include titanaugite and sodic or ferroaugite, and are mostly subhedral, 0.2-2 mm, 2-3 modal%, often zoned and alternating between green and lilac layers. Amphibole phenocrysts are subhedral to euhedral, 0.1-3 mm, seriate, 5-7 modal%, dark brown to orange brown (likely kaersutite) and sometimes overgrowing clinopyroxenes. Opaques are anhedral to subhedral, 0.1-0.2 mm and 1-2 modal%. Sodalite-group minerals are subhedral to euhedral, 0.5-1 mm and 1 modal%. Accessory sphene is euhedral and 0.4-1 mm.

Notes: This rock has produced the largest amphibole nodules, and the context favours the hypothesis that these are cumulates. It comes from a dyke a few metres wide and its microcrystalline to fine-grained groundmass, together with vesicles, suggests it was emplaced close to the surface but perhaps in rocks still relatively hot. It is a very similar rock to FN12-36, FN12-37 and perhaps FN20-40, but with less sodalite-group phenocrysts. The presence of amphibole and titanaugite phenocrysts in a plagioclase and augite groundmass and lack of olivine indicates an intermediate to primitive alkaline rock, in accordance with the major element analysis.

FN25-48 (Kaersutite nodule): Holocrystalline, layered, fine- to medium-grained granular texture containing amphibole, plagioclase, orthoclase, clinopyroxene and opaques, all anhedral. Accessory anhedral sphene and subhedral apatite.

Layers go from a fine-grained assemblage containing feldspar (30-40 modal% and including Ca-poor plagioclase), amphibole (40-50 modal%) pyroxene (5-7 modal%) and accessory apatite, to a medium-grained assemblage with amphibole, orthoclase (3-5 modal%), pyroxene (5-7 modal%) and accessory apatite, and finally to a fine- to medium-grained assemblage containing solely amphibole and accessory feldspar, pyroxene and sphene. All layers include interstitial opaques of irregular shape, 0.2-2 mm and 2-5 modal%. Amphiboles are anhedral, 0.3-5 mm, brown to dark or greenish brown and with serrated, sometimes blurred contacts between crystals. Orthoclase is 0.1-1 mm and interstitial, but sometimes also occurs as chadacrysts within amphiboles. Plagioclase is 0.2-1 mm and restricted to one layer. Clinopyroxene is up to 1 mm and mostly in very poor condition with sieve texture and resorbed boundaries. Orange-red alteration is ubiquitous in the feldspar-rich layer.

Notes: It is possible that the amphiboles are deposited in a cumulate texture that was then somehow tectonised, but the overall texture is not that of an obvious cumulate. Serrated boundaries are a common feature in heavily compacted sediments that undergo boundary pressure dissolution. This nodule is different from FN12-39.

FN26-49 (Sodalite/haüyne/nosean trachyte): Porphyritic holocrystalline with microcrystalline somewhat heterogeneous groundmass containing sanidine and aegerine (25-30 modal%). Phenocrysts of sanidine, aegerine and sodalite-group minerals (or perhaps analcime). Microphenocrysts of aegerine. Possible orthoclase and sanidine xenocrysts. Accessory amphibole and sphene.

The groundmass is mostly microcrystalline but contains some small cryptocrystalline domains. K-feldspars include phenocrysts of subhedral sanidine and possibly xenocrysts of sanidine and orthoclase. Most crystals are either shattered, angular and with irregular etched boundaries, or rounded and resorbed, suggesting a distinction between phenocrysts and possible xenocrysts. Larger crystals are 1-2 mm, 1-2 modal%, sometime with simple twinning and often associated with irregular fragments 0.1-0.3 mm. Sodalite-group (or perhaps analcime) phenocrysts are subhedral to euhedral, 0.3-1.5 mm and 2-3 modal%. Aegerine phenocrysts are subhedral to euhedral 0.5-2 mm, < 1 modal%, sometimes with titanaugite cores, and sometimes associated with amphibole or sodalite-group minerals. Aegerine microphenocrysts are subhedral to euhedral, with tabular or lath habits, 0.1-03 mm and 1-2 modal%. Amphiboles are subhedral to euhedral, 0.3-1 mm, dark brown to yellowish brown, often with coronas of microcrystalline opaques and occasionally ly oxidised. Sphene is subhedral to euhedral and 0.2-1 mm.

Notes: The shattered crystals in this rock still seem to stay together or associated with each other or larger crystals. Resorption and disequilibrium also seem common. The sanidine and aegerine groundmass with phenocrysts of sanidine, aegerine and sodalite-group minerals (or perhaps analcime), as well as the absence of obvious nepheline indicates a trachyte, in accordance with the major element analysis.

FN27-50 (Olivine alkali basalt): Porphyritic holocrystalline with microcrystalline groundmass containing plagioclase, augite and opaques. Phenocrysts of altered olivine. Microphenocrysts of titanaugite with a few larger crystals. Veins and devitrified domains.

Groundmass plagioclase poikilitically encloses augite. Devitrified domains are irregular in shape, 0.5-2 mm, and may be lined with cryptocrystalline material, zeolites or devitrified crystals of plagioclase. Veins are < 0.1 mm, may cut across phenocrysts, and are filled with cryptocrystalline material or zeolites. Olivine phenocrysts are subhedral to euhedral, overall 20-25 modal% with a bimodal size distribution with groups 0.1-0.5 mm (microphenocrysts and dominant) and 1-4 mm. Virtually all olivine crystals are completely altered to iddingsite, with a few altered to smectite along boundaries and fractures. Titanaugite microphenocrysts are seriate with the groundmass, subhedral to euhedral, tabular, 1-2 modal%, mostly 0.1-0.5 mm, with some rare crystals reaching 2 mm, which are also often zoned.

Notes: In spite of the ubiquitous alteration of olivine, the groundmass is in good condition. Together with FN28-51, this rock represents the stratigraphically higher lava flows and both plot as alkali basalts rather than the ankaramites of the lower sequences. Both seem more akin to the São José rocks, which are also supposedly late in the Remédios sequence. The plagioclase and augite groundmass with olivine phenocrysts and titanaugite microphenocrysts indicates an alkali basalt, in accordance with the major element analysis.

FN28-51 (Olivine alkali basalt): Porphyritic holocrystalline with microcrystalline groundmass containing titanaugite and opaques enclosed by plagioclase oikocrysts. Phenocrysts of altered olivine. Titanaugite microphenocrysts seriate with the groundmass. Veins and devitrified domains.

Veins and vesicles represent ~1 modal%. Veins are < 0.05 mm, filled with zeolites and cut across phenocrysts and oikocrysts. Devitrified domains have irregular shapes, are < 2 mm, lined with cryptocrystalline material, zeolites or completely void. Olivine phenocrysts are subhedral to euhedral, overall 15-25 modal% and bimodal size distribution with a group of microphenocrysts 0.1-0.5 mm (dominant) and a larger group 1-3 mm, virtually all completely altered to iddingsite with a few altered to smectite in their cores. The very largest crystals are anhedral to subhedral with etched boundaries, resorption embayments and more ubiquitous alteration to smectite than smaller crystals. Plagioclase oikocrysts engulf groundmass titanaugite, are 0.5-3 mm and 25-30 modal%. Titanaugite microphenocrysts are subhedral to euhedral, tabular, 0.1-2 mm, 2-3 modal%, seriate and larger crystals are often zoned.

Notes: The rock seems to be the virtually the same as FN27-50, with the only differences being the plagioclase crystallisation as oikocrysts and the somewhat smaller olivine content. The augite

groundmass with plagioclase oikocrysts, as well as olivine phenocrysts and titanaugite microphenocrysts indicate an alkali basalt, in accordance with the major element analysis.

FN29-52 (Phonolite): Aphyric holocrystalline mostly cryptocrystalline rock with some microcrystalline domains containing nepheline and sanidine laths with incipient trachytic texture. Very rare (<< 1 modal%) subhedral to euhedral nepheline micophenocrysts, 0.3-1 mm.

Notes: It seems that at least some of the cryptocrystalline material in this rock is due to alteration. The sanidine groundmass, with the presence of nepheline both in the groundmass and as microphenocrysts indicate a phonolite, in accordance with the major element analysis.

FN30-53 (Olivine alkali basalt): Porphyritic holocrystalline with microcrystalline groundmass containing augite, plagioclase (sometimes poikilitically enclosing augites), olivine and opaques. Phenocrysts of olivine (possibly xenocrysts), augite and titanaugite. Rare plagioclase oikocrysts. Olivine microphenocrysts. Ocellar reaction structures. Accessory opaque microphenocrysts. Altered glass domains. Amygdales filled with calcite and occasional fractures.

Fractures are < 0.1 mm with some limited alteration along them. Amygdales have irregular shapes, are < 0.5 mm and filled with calcite. Altered glass domains have irregular shapes, are < 0.5 mm and mostly altered to microcrystalline material (palagonite?). Most olivine phenocrysts and some in the groundmass are altered to smectite along fractures and crystal boundaries. Olivine microphenocrysts are subhedral to euhedral, up to 0.5 mm, seriate with the groundmass and 7-10 modal%. Olivine phenocrysts are anhedral to subhedral, 0.8-3 mm, 1-2 modal%, occasionally rounded, with etched boundaries and could be xenocrysts. Augite and titanaugite phenocrysts are anhedral (mostly) to subhedral but sometimes rounded, 0.3-2 mm, 3-5 modal%, often zoned, with strong sieve textures and also seem to be somewhat in disequilibrium. Plagioclase oikocrysts are very rare (<< 1 modal%), anhedral and up to 1 mm. Ocellar reaction structures represent << 1 modal%, are 0.5-4 mm, layered with an outer layer of augite and/or olivine microlites that may include occasional titanaugite microphenocrysts < 0.3 mm, a layer of olivine and titanaugite microphenocrysts < 0.3 mm growing radially inwards and a core of altered glass. Smaller examples may contain only the outer or the first two layers. Accessory opaque microphenocrysts are anhedral, 0.1-0.5 mm and with irregular boundaries.

Notes: This is the same rock as FN30-54 to 56, although with a somewhat finer groundmass than FN30-54. The ocellar structures are very similar to those seen in rocks from Borborema, and likely represent the resorption of xenocrysts. The presence of augite and plagioclase (sometimes as oikocrysts) in the groundmass and olivine phenocrysts indicate an alkali basalt, in accordance with the major element analysis.

FN30-54 (Olivine alkali basalt): Porphyritic holocrystalline with microcrystalline groundmass containing augite, plagioclase (sometimes poikilitically enclosing augites), olivine and opaques. Phenocrysts of olivine and titanaugite. Orthopyroxene xenocryst and one ocellar reaction structure.

Most olivine show alteration to smectite along fractures. Groundmass olivine crystals are up to 0.3 mm, often rounded and somewhat larger than the other groundmass crystals. Olivine phenocrysts are anhedral to subhedral, 0.5-2 mm, 1-2 modal% and occasionally with ondulose extinction. Titanaugite phenocrysts are anhedral to subhedral, 0.5-2 mm, sometimes with a bright green core, often zoned and with strong sieve texture. They often occur as 0.5-2 mm glomerocrysts of crystals < 0.5 mm and with granular texture. The ocellar structure is at least 5 mm, irregular in shape but rounded, with irregular zones of augite microlites and somewhat larger olivine reacting with orthopyroxene xenocryst at its core.

Notes: This is the same rock as FN30-53, 55 and 56, although with a somewhat coarser groundmass than FN30-53 and 55. The ocellar structure is similar to those seen in the rocks from Borborema, and here the resorption of orthopyroxene is clear. The presence of augite and plagioclase in the groundmass in this order of crystallisation, as well as olivine phenocrysts indicate an alkali basalt, in accordance with the major element analysis.

FN30-55 (Olivine alkali basalt): Porphyritic holocrystalline with microcrystalline groundmass containing augite, plagioclase (sometimes poikilitically enclosing augites), olivine and opaques. Phenocrysts of olivine (possibly xenocrysts) and titanaugite. Olivine microphenocrysts. Accessory opaques.

Most olivine show low-grade alteration to smectite along fractures, with only occasional crystals being completely or nearly completely substituted. Olivine microphenocrysts are subhedral to euhedral, although smaller crystals are sometimes somewhat rounded, 0.1-0.5 mm, seriate with the groundmass, 7-10 modal%, occasionally forming glomerocrysts or with skeletal crystals > 1 mm. Olivine possible xenocrysts are anhedral to subhedral, 1-2 mm, ~ 1 modal%, with etched irregular boundaries and occasional ondulose extinction. Titanaugite phenocrysts are subhedral to euhedral, 0.2-2 mm, 5-7 modal%, with ubiquitous sieve textures, and may contain low titanium cores in crystallographic continuity. Occasionally they form glomerocrysts with anhedral to subhedral crystals with irregular boundaries in granular texture, and overall the titanaugite could be in disequilibrium. Accessory opaques are anhedral, up to 0.3 mm and with irregular boundaries, and seem to be clusters of smaller crystals.

Notes: This is the same rock as FN30-53 to 54 and FN30-56, although with a somewhat coarser groundmass than FN30-53, 54 and 56. No ocellar structures were identified. The presence of augite and plagioclase in the groundmass in this order of crystallisation, as well as olivine phenocrysts indicate an alkali basalt, in accordance with the major element analysis.

FN30-56 (Olivine alkali basalt): Porphyritic hypocrystalline with crypto- to microcrystalline groundmass containing augite, plagioclase, olivine and opaques. Phenocrysts of olivine (possibly xenocrysts) and titanaugite. Olivine microphenocrysts, xenoliths and glass inclusions.

All olivine show occasional low-grade alteration to smectite along fractures. Olivine microphenocrysts are subhedral to anhedral, 0.1-0.5 mm, seriate with the groundmass and with occasional crystals > 1 mm, 10-15 modal% and occasionally skeletal. Olivine possible xenocrysts are anhedral to subhedral, 1-3 mm, < 1 modal% and with etched irregular boundaries. Titanaugite phenocrysts are subhedral to euhedral, 0.2-1 mm (rare crystals reach 3 mm), 2-3 modal%, with ubiquitous sieve textures, may be somewhat rounded or show etched boundaries, and may contain low titanium cores in crystallographic continuity. Occasionally they form glomerocrysts with anhedral to subhedral crystals with irregular boundaries in granular texture. One crystal contains anhedral spinel inclusions. Xenoliths include a few peridotite angular grains, around 3 mm, containing olivine and pyroxene, and one basalt rounded grain, 3 mm, with microcrystalline groundmass containing plagioclase, augite and opaques and olivine microphenocrysts, which is very similar to the other São José rocks. Glass inclusions are irregular, 0.2-1 mm, 2-3 modal% and mostly brown. Some examples or domains within brown inclusions are yellowish green, do not mix with the brown areas and may contain what appear to be bubbles that have been mostly substituted by calcite. All glass inclusions may be rimmed by radially growing groundmass crystals.

Notes: This is a rock worth taking to the microprobe. The basalt xenolith seems to be a grain of FN30-53, FN30-54 or FN30-55, which are simply different domains of the same rock. This one is somewhat finer and contain glass inclusions, indicating more rapid cooling. No ocellar structures were identified, but the presence of xenoliths and the titanaugite textures suggest that the glomerocrysts of the latter could be the reaction products of recrystallized mantle diopside or augite. The presence of augite and plagioclase in the groundmass and olivine phenocrysts indicate an alkali basalt, in accordance with the major element analysis.